EFFECTS OF LONG-DURATION GROUND MOTIONS ON LIQUEFACTION HAZARDS

Michael W. Greenfield

A dissertation

submitted in partial fulfillment of the

requirements for the degree of

Doctor of Philosophy

University of Washington

2017

Committee:

Steven L. Kramer, Chair

Brett Maurer

Jeffrey William Berman

Kenneth Creager, Graduate School Representative

Program Authorized to Offer Degree:

Civil & Environmental Engineering

University of Washington

Abstract

EFFECTS OF LONG-DURATION GROUND MOTIONS ON LIQUEFACTION HAZARDS

Michael W. Greenfield

Chair of the Supervisory Committee:
Professor Steven L. Kramer
Civil & Environmental Engineering

Soil liquefaction during past earthquakes has caused extensive damage to buildings, bridges, dam, pipelines and other elements of infrastructure. Geotechnical engineers use empirical observations from earthquake case histories in conjunction with soil mechanics to predict the behavior of liquefiable soils. However, current empirical databases are insufficient to evaluate the behavior of soils subject to long-duration earthquakes, such as a possible M_w = 9.0 Cascadia Subduction Zone earthquake.

The objective of this research is to develop insight into the triggering and effects of liquefaction due to long-duration ground motions and to provide recommendations for analysis and design. Recorded ground motions from 21 case histories with surficial evidence of liquefaction showed marked differences in soil behavior before and after liquefaction was triggered. In some cases, strong shaking continued for several minutes after the soil liquefied, and a variety of behaviors were observed including dilation pulses, continued softening due to soil fabric degradation, and soil stiffening due to pore pressure dissipation and drainage. Supplemental field and laboratory investigations were performed at three sites that liquefied during the 2011 M_w = 9.0 Tohoku earthquake. The recorded ground motions and field investigation data were used in conjunction with laboratory observations, analytical models, and numerical models to evaluate the behavior of liquefiable soils subjected to long-duration ground motions.

Observations from the case histories inspired a framework to predict ground deformations based on the differences in soil behavior before and after liquefaction has triggered. This

framework decouples the intensity of shaking necessary to trigger liquefaction from the intensity of shaking that drives deformation by identifying the time when liquefaction triggers. The timing-based framework promises to dramatically reduce the uncertainty in deformation estimates compared to conventional, empirically-based procedures.

TABLE OF CONTENTS

LIST OF FIGURES

LIST OF TABLES

ACKNOWLEDGEMENTS

I would like to thank Profs. Jon Stewart and Steven Kramer of the for providing support for this work through PEER's Next Generation Liquefaction Project. I would also like to thank Profs. John Vidale, Dan Abramson, Jeff Berman, Ann Bostrom, and Alison Duvall, who provided support through the University of Washington's M9 project. I appreciate the guidance of my reading committee and am also grateful for their contributions to this work. In general, I am fortunate to be a part of the University of Washington community.

Most importantly, I would like to extend my appreciation and gratitude to Prof. Steven Kramer who has served as my advisor and friend. He has guided much of this work, and I am absolutely indebted to him.

DEDICATION

This work could not have been possible without my wife, Sarah. Whenever I needed help, she supported me. Whenever I doubted myself, she told me to persevere. Whenever I needed a friend, she was there for me. The years of work that went into this dissertation represent but a single step in the journey of our lives. Wherever we go together, we can accomplish anything.

[This page intentionally left blank]

Chapter 1. INTRODUCTION

Soil liquefaction has been observed in numerous earthquakes and has caused extensive damage to buildings, bridges, dam, pipelines and other elements of infrastructure. Geotechnical engineers use empirical observations in conjunction with soil mechanics principles to predict the behavior of soil for liquefaction triggering and post-triggering analyses. The procedures for evaluating the behavior of liquefiable soils are based on documented case histories where liquefaction was observed. These case histories are primarily from the past 50 to 60 years, which is very short in geologic time and short with respect to the return periods of large-magnitude events. The case history database, therefore, contains insufficient information about the large-magnitude earthquakes that typically produce long-duration ground motions.

Without case histories to constrain predictive models for long-duration ground motions, other means must be taken to investigate and understand the effects of long-duration motions on soil liquefaction. The relevant characteristics of long-duration motions compared to short-duration motions may provide insight into the effects of ground motion duration on liquefaction hazards. Long-duration motions have many more cycles of loading than short duration motions, and long-duration motions can trigger liquefaction at lower shear stress amplitudes. Motions with many cycles of loading also greatly increase the consequences of liquefaction. During long-duration motions, liquefaction could be triggered relatively early during the motion, and the soil may be subjected to many cycles of loading after liquefaction has been triggered. The soil fabric degrades and softens with each cycle of loading, so, if liquefaction is triggered at a site with gently sloping ground, multiple cycles of post-triggering loading could cause very large deformations. Conversely, pore pressures generated during strong shaking may have time to dissipate during long-duration motions, which may delay liquefaction triggering or lead to soil stiffening of the soil after liquefaction has been triggered.

Long-duration motions generally result from large magnitude earthquakes, which have large rupture areas and low corner frequencies, leading to greater low-frequency energy content than smaller magnitude earthquakes. These low-frequency components of motion may have a

limited effect on the triggering of liquefaction, which is typically associated with peak acceleration. However, after the soil liquefies, the low-frequency components of motion may induce large shear strains in the soft, liquefied soil. Low-frequency components may be amplified by sedimentary basins, such as the Seattle, Tacoma, or Tualatin basins.

1.1 OBJECTIVES

The objective of this study is to develop insight into the triggering and effects of liquefaction of soils subjected to long-duration ground motions and to provide recommendations for analysis and design. These objectives were completed by characterizing intensity measures for earthquake duration, evaluating the evolutionary response of recorded ground motions from sites where liquefaction was triggered, and evaluating the post-triggering behavior of the soil. The significant findings from each of these tasks were then tied together to create a framework for improved prediction of liquefaction-induced deformation.

1.2 ORGANIZATION OF DISSERTATION

Each chapter in this document presents a specific aspect related to the effects of liquefaction hazards from long-duration ground motions.

Chapter 2 provides details and a summary about the current state-of-practice with respect to liquefaction triggering and deformation analyses. The mechanics of liquefiable soils, laboratory and field-based observations, the state-of-practice procedures and recommendations presented in this chapter all provide the fundamental building blocks for subsequent analyses in this study.

Chapter 3 reviews intensity measures that have been developed to represent the duration of a ground motion. These intensity measures can be used to characterize the potential effects of long-duration motions. Several factors that affect the ground motion duration, including earthquake magnitude, rupture distance, site amplification, and basin effects were identified. Long-duration ground motions impact liquefaction hazards differently than shorter-duration earthquakes and can trigger liquefaction at greater distances and in denser soils. During long-duration ground motions, intense shaking can continue after liquefaction has been triggered, and additional factors can impact the behavior of liquefied soils, including pore pressure dissipation and continued soil fabric degradation.

Chapter 4 presents a generally robust time-frequency analysis to identify the time when liquefaction was triggered. Ground motions and subsurface information from 21 case histories with surficial evidence of liquefaction were identified. Each of these ground motions showed a rapid shift in the frequency content once liquefaction was triggered. Once the time of liquefaction was identified, the intensity of shaking and frequency content before and after triggering could be isolated for additional analyses.

Chapter 5 presents an analytical solution to illustrate the competing effects of pore pressure generation due to shaking and dissipation due to drainage. This solution shows that drainage during long-duration motions explains some of the post-triggering changes in frequency content observed in the case histories. The solution underscores the need to consider the potential for pore pressure dissipation or redistribution during shaking, particularly during long-duration ground motions.

Chapter 6 presents the details of the Cocktail Glass constitutive model in the finite element program FLIP. This model is used to predict deformations at sites underlain by liquefied soils, which can then be used to supplement empirically-based observations when limited data are available. The Cocktail Glass model was calibrated to match empirical and semi-empirical observations that are commonly used to evaluate liquefaction triggering and post-triggering behavior in U.S.-based practice.

Chapter 7 presents supplemental investigations that were performed at three sites in Japan where surficial evidence of liquefaction was observed following long-duration motions produced by the 2011 M_w = 9.0 Tohoku earthquake. Liquefaction at each of these sites occurred in unique conditions, especially since limited liquefaction observations are available from very large magnitude earthquakes. Details from these studies show that the frequency content of the ground motions changed very significantly and the amplitude of the ground motions increased substantially once liquefaction was triggered.

Chapter 8 presents a framework that decouples the intensity of shaking necessary to trigger liquefaction from the post-triggering intensity of shaking that drives deformation. The framework is referred to as the timing-based framework because it uses the time of liquefaction to decouple the pre- and post-triggering motions. Compared to conventional methods, this framework generally reduces the uncertainty in predicting deformation, even though no additional information is required.

Chapter 9 presents a database of 21 liquefaction case histories that all showed rapid shifts from high to low modal frequencies once liquefaction was triggered. Multi-linear regression was performed to develop equations to predict the evolving frequency content of these ground motions. Predictions of the post-triggering modal frequency can then be used to evaluate the site response when liquefaction is triggered or identify intensity measures that are most closely associated with liquefaction-induced settlement and lateral spreading deformations.

Chapter 10 ends with a short summary of the research and the conclusions that can be drawn from each of the previous chapters. Recommendations for future research are also provided.

Chapter 2. LIQUEFACTION

Liquefaction from cyclic loading occurs when the pore pressure in a saturated soil approaches the overburden pressure and the effective stress between soil grains becomes zero. Liquefied soil is extremely soft, has very low strength, and may temporarily behave as a viscous fluid. A range of phenomenon can cause elevated pore pressure and soften the soil, but liquefaction is typically described in terms of elevated pore pressures in saturated, low-plasticity or non-plastic soil due to strong shaking where the soil behaves in an undrained manner.

Liquefaction has caused some of the most catastrophic failures in geotechnical engineering. Extremely soft and weak liquefied soil can develop very large shear strains, which has led to devastating deformation of slopes and earthen dams and the complete failure of the bridge and building foundations. Photos from four catastrophic failures caused by liquefaction are shown in Figure 2.1. In Figure 2.1(a) the soil supporting the shallow foundations in the Kawagishi-Cho apartment buildings liquefied during the 1964 Niigata earthquake and multiple buildings sank, tilted severely, and toppled. Figure 2.1(b) shows damage due to liquefaction-induced lateral spreading that bent the foundation and supports of the Showa Bridge during the Niigata earthquake. Multiple simply-supported decks were knocked off the bridge. In Figure 2.1(c), the Upper San Fernando dam experienced a catastrophic liquefaction-induced slope failure during the 1971 M_W = 6.6 San Fernando earthquake. The upstream slope of the dam failed and was nearly breached. Over 80,000 people were evacuated from the downstream inundation area resulting from the near-complete failure (National Information Service for Earthquake Engineering, 2016). In Figure 2.1(d), much of the near-surface soil in the Central Business District and surrounding areas of Christchurch liquefied during the 2010-2011 Canterbury Earthquake sequence. Severe surficial liquefaction and sand boils damaged houses, buildings, roadways, pipelines, and nearly every element of the built environment. Many of the sites liquefied multiple times in the sequence of earthquakes. Nearly 200 people were killed, the critical infrastructure was heavily damaged, and over 8,000 buildings were damaged significantly enough that they were later demolished (Cubrinovski et al., 2011).

Figure 2.1: Photos of damage due to liquefaction. (a) Foundation failure of the Kawagishi-Cho apartments from the 1964 Niigata earthquake (from National Information Service for Earthquake Engineering, 2016). (b) Lateral spreading failure of the Showa Bridge from the 1964 Niigata earthquake (from National Information Service for Earthquake Engineering, 2016). (c) Crest failure of the Lower San Fernando Dam after the 1971 San Fernando earthquake (from National Information Service for Earthquake Engineering, 2016). (d) Large sand boil in Christchurch from the 2011 Christchurch earthquake (from Cubrinovski et al., 2011).

2.1 MECHANICS OF LIQUEFACTION

Unlike many other engineering materials, soils tend to change volume as shear stress is applied. Loose, dry sand tends to densify, or contract, during shearing, while dense, dry sand tends to loosen or dilate. If loose sand is saturated and cannot drain during shaking, pore pressure is generated as the soil attempts to contract. The excess pore pressure, u_e, is often used to describe the amount of pore pressure that is above the hydrostatic pore pressure level, u_0. Once the excess pore pressure equals the initial effective stress, σ_0', the effective stress, σ', between the soil grains is zero and the soil has liquefied. In this state, cohesionless soils have no strength.

$$u_e = u - u_0 \tag{2.1}$$

$$u_e = \sigma_0' - \sigma' \tag{2.2}$$

The ratio of excess pore pressure to the initial effective stress, r_u, is also used to describe the level of excess pore pressure in relative terms. Before shaking begins, the excess pore pressure is zero and r_u is zero. During shaking, the pore pressure increases in response to the volume change tendencies of the soil. Excess pore pressure develops incrementally with each cycle of loading during shaking. Once r_u reaches 1.0, the soil has liquefied.

$$r_u = \frac{u_e}{\sigma_{v0}'} = 1 - \frac{\sigma_v{}'}{\sigma_{v0}'} \tag{2.3}$$

Liquefied soils are extremely soft since cohesionless soils develop their strength and stiffness through friction between soil grains. Many material models for soil show that the shear stiffness of the soil is directly related to the effective stress of the soil (e.g. Been and Jefferies, 1991; Beaty and Byrne, 2011; Kramer et al., 2013; Boulanger and Ziotopotolou, 2015; etc.). A simple soil model illustrates the change in shear stiffness, G, as a function of mean effective stress, $\sigma_m{}'$, normalized by the atmospheric pressure, p_a, with an exponent m that is based on material properties (Kramer et al., 2013). The expression for shear stiffness as a function of effective stress can be defined in terms of the pore pressure ratio and the initial mean effective stress, $\sigma_{m0}{}'$.

$$\mathrm{G} = \mathrm{G}_{1\ \mathrm{atm}} \left(\frac{\sigma_m{}'}{p_a}\right)^m \tag{2.4}$$

$$\mathrm{G} = \mathrm{G}_{1\ \mathrm{atm}} \left(\frac{\sigma_{m0}{}'}{p_a}[1 - r_u]\right)^m \tag{2.5}$$

As the pore pressure ratio approaches 1.0, equations (2.4) and (2.5) indicate that the shear stiffness also approaches zero, and this simple material model implies that the soil has no shear stiffness when r_u equals 1.0. In a liquefied state, the soil may temporarily behave as a viscous fluid, rather than a solid (Kawakiami et al., 1994). This state of zero stiffness is temporary, and even loose soils dilate if they are sheared to high enough shear strains. As soils dilate in response to shear they regain stiffness, although the stiffness of liquefied soil during dilation is generally much lower than the soil's initial stiffness.

2.2 LIQUEFACTION SUSCEPTIBILITY

Not all soils are susceptible to liquefaction. Soils that are not susceptible to liquefaction do not liquefy under any realistic loading condition. This includes soils above the groundwater table that are unsaturated, cemented or heavily consolidated soils, and soils with moderate or higher plasticity. Although these soils may soften or develop pore pressure during shaking, the extreme decrease in stiffness and loss of shear strength associated with liquefaction does not occur.

Screening for soils that are susceptible to liquefaction is the first step in a liquefaction analysis. The liquefaction susceptibility can be judged by historical, geologic, hydrologic, and compositional factors (Kramer, 2008). Each one of these factors provides evidence or likelihood of a soil's susceptibility to liquefaction. Historical observations of liquefaction are the most obvious, and probably the highest confidence, measure of susceptibility to liquefaction. If a site has liquefied in the past, it is susceptible to liquefaction, although its resistance to liquefaction triggering may have changed.

Youd (1998) developed recommendations for rapidly screening sites for soils that are susceptible to liquefaction. The recommendations, to some regard, mix factors for triggering and susceptibility, which are evaluated separately in contemporary analyses. The general recommendations provide geologic criteria that are ranked from very high to very low susceptibility to liquefaction. Recent alluvial soils, loess, and uncontrolled fill are highly to very highly susceptibility to liquefaction. Older alluvial soils, lacustrine and estuarine soils, colluvium, and dunes are moderately susceptible to liquefaction. Pleistocene and older soils generally have a low to very low susceptibility to liquefaction. Figure 2.2 provides general guidelines for screening liquefaction susceptibility based on geologic deposit.

For significant pore water pressure to be generated, soils that are susceptible to liquefaction must be saturated or very nearly saturated. Unsaturated and drained soils are not susceptible to liquefaction because the pore pressure can never reach the overburden pressure. However, the loading rate of earthquake shaking is very fast, and very few soils drain rapidly enough that so little pore pressure is generated that the soil cannot liquefy under any realistic loading condition. Even gravels with high permeability have been shown to liquefy, especially if the gravel layer is confined by low permeability materials. For practical purposes, it is commonly assumed that gravels are susceptible to liquefaction (Allen, 2015).

Type of deposit	sediments in General distribution of cohesionless deposits	Likelihood that cohesionless sediments, when saturated, would be susceptible to liquefaction (by age of deposit)			
		< 500 yr	Holocene	Pleistocene	Pre-pleistocene
(1)	(2)	(3)	(4)	(5)	(6)
(a) Continental Deposits					
River channel	Locally variable	Very high	High	Low	Very low
Flood plain	Locally variable	High	Moderate	Low	Very low
Alluvial fan and plain	Widespread	Moderate	Low	Low	Very low
Marine terraces and plains	Widespread	-	Low	Very low	Very low
Delta and fan-delta	Widespread	High	Moderate	Low	Very low
Lacustrine and playa	Variable	High	Moderate	Low	Very low
Colluvium	Variable	High	Moderate	Low	Very low
Talus	Widespread	Low	Low	Very low	Very low
Dunes	Widespread	High	Moderate	Low	Very low
Loess	Variable	High	High	High	Unknown
Glacial till	Variable	Low	Low	Very low	Very low
Tuff	Rare	Low	Low	Very low	Very low
Tephra	Widespread	High	High	?	?
Residual soils	Rare	Low	Low	Very low	Very low
Sebka	Locally variable	High	Moderate	Low	Very low
(b) Coastal Zone					
Delta	Widespread	Very high	High	Low	Very low
Esturine	Locally variable	High	Moderate	Low	Very low
Beach					
High wave energy	Widespread	Moderate	Low	Very low	Very low
Low wave energy	Widespread	High	Moderate	Low	Very low
Lagoonal	Locally variable	High	Moderate	Low	Very low
Fore shore	Locally variable	High	Moderate	Low	Very low
(c) Artificial Fill					
Uncompacted fill	Variable	Very high	-	-	-
Compacted fill	Variable	Low	-	-	-

Figure 2.2: Liquefaction susceptibility for sediments at a geologic deposit-level scale (from Youd, 1998)

The liquefaction susceptibility of soils also depends on the soil's composition. Clay soils may soften during shaking, but do not liquefy in the same manner as clean, uniformly graded, loose sand. Even a modest amount of clay in a soil may prevent liquefaction from occurring. Plasticity index is the most commonly used measure of clay content of the soils for liquefaction susceptibility screening. Two major studies (Boulanger and Idriss, 2006; Bray and Sancio, 2006) proposed criteria for evaluating the liquefaction susceptibility of fine-grained soils. Both criteria were developed using the results of field observations and laboratory tests by well-respected

leaders of the geotechnical engineering profession. Both research groups recognized that high-quality sampling of soils with appreciable fines contents is feasible and recommended that the susceptibility of fine-grained soils could be evaluated by laboratory testing if the soil does not clearly fall into the categories of susceptible or not susceptible to liquefaction. At the present time, data that proves one method is more reliable than the other does not exist, so both methods must be considered plausible, and both methods should be considered in a liquefaction susceptibility evaluation.

Boulanger and Idriss (2006) reviewed case histories and laboratory tests involving cyclic loading of different fine-grained soils. They identified two types of behavior that they described as "sand-like" and "clay-like" based on stress normalization and stress-strain behavior. Soils exhibiting sand-like behavior were considered susceptible to liquefaction and soils exhibiting clay-like behavior were considered not susceptible to liquefaction. Boulanger and Idriss proposed that the distinction between sand-like or clay-like soils could be made based solely on plasticity index, PI. Figure 2.3(a) shows the transition between sand-like and clay-like behavior observed by Boulanger and Idriss. The soil was expected to be clearly sand-like at PI < 3 and to be clearly clay-like at PI > 8.5. The clay-like or sand-like behavior described in this figure is defined in terms of the cyclic resistance ratio, CRR, of the soils. While the transitional nature of the soil behavior was emphasized, a simple, conservative guideline of PI = 7 was recommended when detailed laboratory testing results are not available.

Bray and Sancio (2006) investigated fine-grained soils that liquefied during 1994 Northridge, 1999 Kocaeli, and 1999 Chi-Chi earthquakes and proposed new compositional criteria for liquefaction susceptibility evaluation. In addition to plasticity index, Bray and Sancio also found the ratio of water content to liquid limit (w_c/LL) influenced liquefaction susceptibility. This approach mixes liquefaction susceptibility with triggering criteria, since the water content of saturated soil is directly related to the void ratio and relative density of soil, while Atterberg Limits, LL and PL, are independent of the soil's natural water content. Bray and Sancio found soils with PI < 12 and w_c/LL > 0.85 were consistently susceptible to liquefaction, and soils with PI > 18 or w_c/LL < 0.80 were consistently not susceptible to liquefaction. Soils in between the ranges of PI and w_c/LL were moderately susceptible to liquefaction and additional cyclic testing was recommended to establish the cyclic behavior of these soils. Figure 2.3(b) shows the boundaries

of susceptible, moderately susceptible, and not susceptible zones of liquefaction recommended by Bray and Sancio (2006).

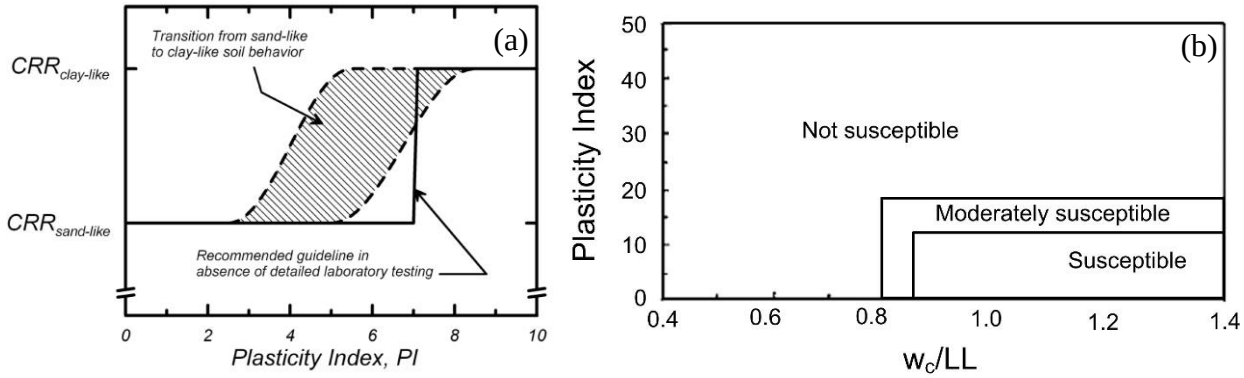

Figure 2.3: Liquefaction susceptibility based on soil plasticity. (a) Transition from sand-like to clay-like behavior (from Boulanger and Idriss, 2006). (b) Liquefaction susceptibility based on plasticity index and water content (from Bray and Sancio, 2006).

Both research groups noted that the presence of soils that were not susceptible to liquefaction did not imply that damage and large deformation could not occur. Boulanger and Idriss pointed out that some soils that were not susceptible to liquefaction were still subject to cyclic softening behavior, like soft clays for example, that could lead to severe earthquake damage. Although cyclic softening of clay soils is a concern, this study is focused on the triggering and consequences of non-plastic or low-plasticity saturated soils.

2.3 LIQUEFACTION TRIGGERING

Soils that are susceptible to liquefaction liquefy only if shaking from an earthquake is sufficiently intense to raise the excess pore pressure to a level where the pore pressure is equal to the overburden stress. The potential for liquefaction is usually evaluated by comparing measures of earthquake loading and resistance and calculating a factor of safety against liquefaction. The intensity measure for cyclic loading during an earthquake is usually defined by the cyclic shear stress amplitude normalized by the initial vertical effective stress. This quantity is referred to as the cyclic stress ratio, CSR.

$$\mathrm{CSR} = \frac{\tau_{\mathrm{cyc}}}{\sigma_{v,o}{}'} \tag{2.6}$$

where τ_{cyc} is the amplitude of the cyclic shear stress and $\sigma_{v,o}'$ is the initial overburden effective stress. The measure for liquefaction resistance is typically derived from empirical soil properties found during subsurface investigation, like the standard penetration test N-values, cone penetration test q_c values, or shear wave velocity. The quantity for measuring cyclic resistance is referred to as cyclic resistance ratio, CRR. The potential for liquefaction is described in terms of a factor of safety against liquefaction, FS_L, which is the ratio of the cyclic resistance ratio to the cyclic stress ratio. An FS_L less than 1.0 indicates liquefaction is likely.

$$\mathrm{FS}_L = \frac{\mathrm{CRR}}{\mathrm{CSR}} \tag{2.7}$$

2.3.1 *Cyclic stress*

The original evaluation of liquefaction triggering was developed from observations of laboratory tests where the cyclic stress amplitude was generally held constant. However, in field conditions, the horizontal shear stress, τ_{cyc}, cannot be recorded during actual earthquake loading, but it can be estimated using recorded motions at the ground surface. The horizontal stresses at any depth in a soil deposit can be approximated as the stress required to counteract the horizontal acceleration of the mass of soil above that depth. For a rigid mass shearing a layer of potentially liquefiable soil, the maximum cyclic shear stress in the soil layer, τ_{max}, is equal to the product of the peak ground acceleration, PGA, and the total overburden stress at the depth of interest. However, soil layers are deformable, rather than rigid, and do not necessarily obey such simple mechanics. Seed et al. (1983) defined a "simplified procedure" for estimating the cyclic stress ratio during an earthquake with commonly available information. A depth reduction factor, r_d, was used to account for the decrease in shear stress wave amplitude below the ground surface. The factors of effective and total stresses, peak ground acceleration, and a depth reduction factor combine to form a general expression for cyclic stress ratio.

$$\mathrm{CSR} = 0.65\,\frac{\mathrm{PGA}\;\sigma_v\;r_d}{\sigma_{v0}'} \tag{2.8}$$

The choice of 0.65 as a reference stress level in equation (2.8) was originally proposed by Seed and Idriss (1971) as a factor to compare the stress from transient shear stress loading to the cyclic, constant amplitude, uniform amplitude harmonic loading applied in lab tests. This factor of 0.65 has carried through to modern day practice.

2.3.2 *Cyclic resistance*

Seed and Idriss (1975) showed that cyclic resistance of soil to liquefaction depended largely on the soil's relative density and to a lesser extent on fines content of the soil and the overburden pressure. Early liquefaction evaluation was performed by either sampling or reconstituting samples to the appropriate relative density in the lab, and then subjecting the soil to cyclic shear stresses that were representative of a design earthquake. The number of loading cycles required to trigger liquefaction was counted and compared to the estimated number of cycles from a deterministic design earthquake. Liquefaction was determined to be likely if the number of cycles required to trigger liquefaction was less than the number of cycles expected to occur during a design earthquake.

However, sand samples are difficult to sample, and the behavior of sand depends on fabric properties which vary between different methods of preparation. Seed et al. (1983) developed an empirical method to estimate the cyclic resistance of soil based on field observations from previous earthquakes. The cyclic resistance was derived from readily available field test data, such as the standard penetration test (SPT) resistance and fines content. In this empirical method, the recorded blow counts were corrected for overburden pressure, hammer energy, and fines content to create an index parameter, the equivalent clean sand blowcounts or $(N_1)_{60cs}$. The equivalent blowcounts provided a measure of the soil's relative density. Values of $(N_1)_{60cs}$ collected from available case histories were compared based on binary field observations of either the presence or absence of liquefaction and the intensity of shaking. A function was fit to separate the binary case history observations of liquefaction on a plot of intensity measures versus $(N_1)_{60cs}$. The cyclic stress ratio was initially used as the intensity measure used for this approach, but other intensity measures have been used in more recent studies (Kramer and Mitchell, 2006; Kayen et al. 2013; and Boulanger and Idriss, 2014). In the Seed et al. (1982) approach, the curve that best separated the liquefied versus not liquefied case histories was used as a deterministic decision function for liquefaction triggering. Figure 2.4 shows the decision functions from several authors (Seed, 1979; Seed and Idriss, 1982; Youd et al., 1997; Seed et al. 2001; and Idriss and Boulanger, 2004) that separated case histories where liquefaction occurred from case histories where liquefaction did not occur. Note that at low values of $(N_1)_{60cs}$ and CSR the decision functions agree very well, but at high values of $(N_1)_{60cs}$ and CSR the decision functions diverge quickly where limited data was

available. Different authors refer to the corrected SPT values of liquefaction triggering analysis as $(N_1)_{60}$ or $N_{1,60}$, often without the "clean sand" subscript.

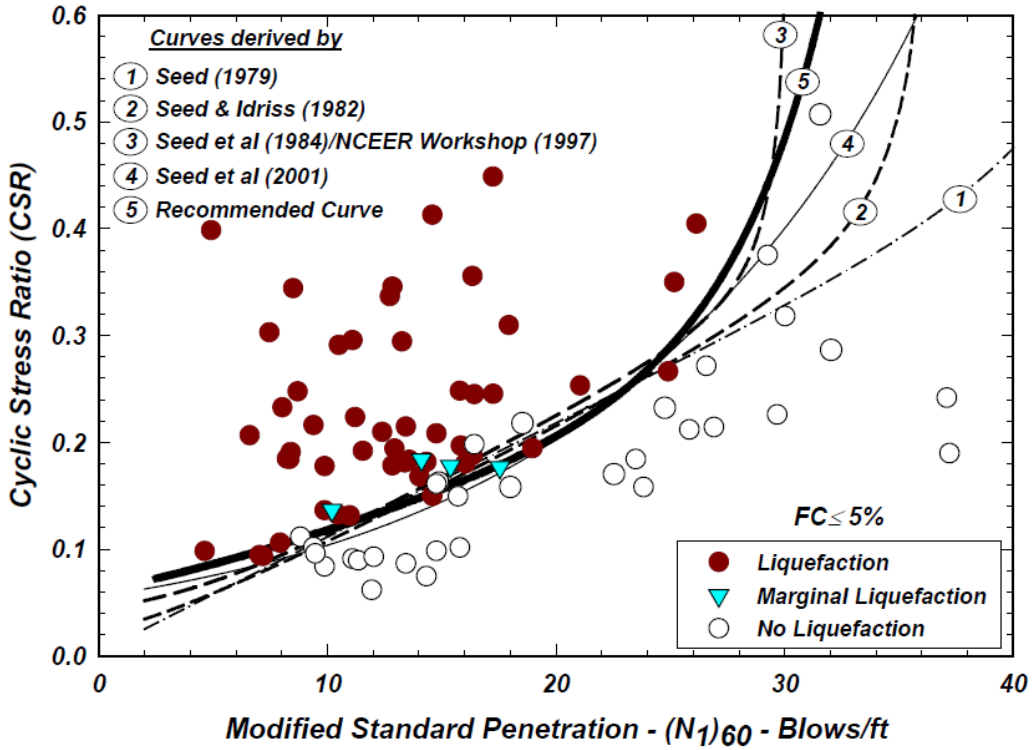

Figure 2.4: Liquefaction triggering functions (from Idriss and Boulanger, 2004). Decision functions from authors as noted.

The original relationships for CRR versus $(N_1)_{60cs}$ were developed from field observations of earthquakes ranging from M_w = 7.3 to 7.8, with an average of about M_w = 7.5. Because the earthquakes used in the initial development of CRR had similar magnitudes and durations, equations for estimating the factor of safety against liquefaction were developed without any measures to accounted for earthquake duration. Early laboratory testing showed that the resistance of soil to liquefaction decreased with increasing number of cycles. Seed et al. (1975) developed a cycle counting procedure to adjust cyclic stresses from an irregular time history with a peak stress of τ_{max} to an equivalent number of constant-amplitude cycles at 0.65 τ_{max}. The original liquefaction triggering framework was developed for earthquakes around M_w = 7.5, and a magnitude scaling factor, MSF, was created to adjust the cyclic resistance ratios to arbitrary magnitude earthquakes. The magnitude scaling factor was included in the computation of CRR, which created an intensity measure, $CRR_{7.5}$, that was normalized for arbitrary magnitudes.

$$CRR_{7.5} = CRR \cdot MSF \quad (2.9)$$

Table 2.1 shows the number of equivalent cycles and the appropriate magnitude scaling factor for earthquakes ranging from M_w = 5.25 to 8.5 (Seed et al. 1983).

Table 2.1: Magnitude scaling factor (after Seed et al. 1983)

Magnitude, M	Number of equivalent cycles at 0.65 τ_{max}	Magnitude scaling factor, MSF
8.5	26	0.89
7.5	15	1.0
6.75	10	1.13
6	5	1.32
5.25	2-3	1.5

Laboratory tests at high overburden pressure indicated that the CRR of soils at a constant relative density decreased with increasing isotropic pressure. So, the cyclic resistance of an empirical field-based method for estimated liquefaction potential should also vary with overburden pressure, even after field SPT values have been corrected to $(N_1)_{60}$. An overburden correction factor, K_σ, was initially proposed by Seed (1983) to extend the available case history data using data from laboratory observations. The overburden correction factor was applied to the $CRR_{7.5}$ to generate a new intensity measure, $CRR_{7.5,\,1\,atm}$.

$$CRR_{7.5,1\,atm} = CRR \cdot MSF \cdot K_\sigma \quad (2.10)$$

Contemporary methods (Cetin et al., 2004; Idriss and Boulanger, 2010) use the same general framework as the original simplified procedure (Seed et al. 1983), but the data used to develop the contemporary methods for liquefaction triggering included many more earthquakes with a wide range of cyclic stresses and earthquake magnitudes. The decision functions used to separate the binary liquefaction observations were also defined more rigorously in terms of engineering mechanics and field and laboratory observations. In recent years, the simplified procedure has become increasingly debated and is anything but simple. Two prominent groups of researchers (Cetin et al., 2004; Idriss and Boulanger, 2010; Boulanger and Idriss, 2014) have produced different procedures for estimating liquefaction triggering potential. Both procedures produce similar results (i.e. the presence or absence of liquefaction) in most situations, however, each procedure has some important differences.

Cetin et al. (2004) noted that many of the variables used to calculate the CSR or CRR in the case histories contained significant uncertainty. They calculated distributions of CSR and CRR that included uncertainties in the depth of the critical layer, depth of the groundwater, peak acceleration at the site, hammer energy, fines content, etc. The depth reduction factor, r_d, was estimated by performing over 2,100 equivalent linear site response analyses to account for the effects of earthquake magnitude and stochastic uncertainty in earthquake ground motions. A probability of liquefaction, P_L, was estimated using Bayesian updating with terms for the penetration resistance, $N_{1,60}$, fines content, FC, cyclic stress ratio, CSR, earthquake moment magnitude, M_w, and overburden pressure normalized by the atmospheric pressure, $\frac{\sigma_{v'}}{p_a}$. The resulting CRR from the data was log-normally distributed, and the probability of liquefaction was computed as equation (2.11).

$$\begin{aligned} P_L = \mathbf{\Phi}\Bigg[-\frac{1}{2.70}\Bigg(&N_{1,60}(1 + 0.004\ FC) \\ &- 13.32\ln(CSR) \\ &- 29.53\ln(M_w) - 3.70\ln\left(\frac{\sigma_v{}'}{p_a}\right) + 0.05\ FC + 16.85\Bigg)\Bigg] \end{aligned} \tag{2.11}$$

where $\mathbf{\Phi}$ represents the cumulative normal distribution. Functions describing the CSR versus the SPT penetration resistance could be computed for different probabilities of liquefaction. A decision function was calculated that separated cases where liquefaction was likely liquefy from cases where liquefaction is unlikely. The decision function was defined a probability of liquefaction $P_L = 0.5$ and $\mathbf{\Phi}^{-1}[P_L] = 0$. Cetin et al. (2004) recommend using a $P_L = 0.15$ for deterministic calculations when $FS_L = 1.0$. This recommendation implied that $\mathbf{\Phi}^{-1}[P_L] = -1.04$ should be used for deterministic calculations. Equation (2.11) shows the recommended relationship for CRR.

$$\begin{aligned} CRR = \exp\Bigg[\frac{1}{13.32}\Bigg(&N_{1,60}(1 + 0.004\ FC) \\ &- 29.53\ln(M_w) - 3.70\ln\left(\frac{\sigma_v{}'}{p_a}\right) + 0.05\ FC + 14.04\Bigg)\Bigg] \end{aligned} \tag{2.12}$$

The rigorously defined Bayesian updating and regression used in the Cetin et al. (2004) procedure improved the estimation of liquefaction triggering by using results from equivalent linear analysis to calculate r_d and accounted for the uncertainty in field measurements. However,

their analysis did not account for soil behavior that has been observed in the laboratory. Boulanger and Idriss (2014) developed a procedure that included recommendations and data from other studies that accounted for trends observed in laboratory tests. These trends included CRR correction at high overburden stress with an overburden correction factor, K_σ, (Youd et al., 2001) and a magnitude scaling factor that was a function of the relative density of the soil (Kishida and Tsai, 2014). The effects of the magnitude scaling factor are significant for long duration earthquakes and are discussed in detail in Chapter 3. These considerations based on laboratory observations changed the expression for the probability of liquefaction and the decision function compared to the Cetin et al. (2004) procedure. Boulanger and Idriss (2014) also used a 4-th order polynomial to fit the overburden, energy, and fines corrected penetration resistance, $(N_1)_{60cs}$, whereas Cetin et al. (2004) used a linear term. The case history database used by Boulanger and Idriss also included slightly different interpretations of key case histories than the database used by Cetin et al. (2004). In both procedures, since the probabilistic likelihood function included many variables and the number of observations was limited, certain case histories had very large leverage in the decision function. The resulting probability of liquefaction proposed by Boulanger and Idriss (2014) tended to indicate that the probability of liquefaction was slightly lower than the probability of liquefaction calculated using the Cetin et al. (2004) procedure for the same earthquake and soil conditions. Equation (2.13) describes the probability of liquefaction estimated using the Boulanger and Idriss procedure.

$$P_L = \mathbf{\Phi}\left[-\frac{1}{0.13}\left(\frac{(N_1)_{60cs}}{14.1}+\left(\frac{(N_1)_{60cs}}{126}\right)^2-\left(\frac{(N_1)_{60cs}}{23.6}\right)^3+\left(\frac{(N_1)_{60cs}}{25.4}\right)^4-2.67-\ln\left(CSR\,\frac{1}{MSF\,K_\sigma}\right)\right)\right] \quad (2.13)$$

Boulanger and Idriss (2014) recommended considering a probability of liquefaction about 15% for deterministic calculations.

$$CRR = (MSF\,K_\sigma)\exp\left[\frac{(N_1)_{60cs}}{14.1}+\left(\frac{(N_1)_{60cs}}{126}\right)^2-\left(\frac{(N_1)_{60cs}}{23.6}\right)^3+\left(\frac{(N_1)_{60cs}}{25.4}\right)^4-2.80\right] \quad (2.14)$$

In contemporary liquefaction triggering analyses, it is common to consider both the Cetin et al. (2004) and Boulanger and Idriss (2014) procedures. Figure 2.5 shows plots of the decision

function for both procedures with clean sand at 1 atm of overburden pressure for M_w = 6, 7.5 and 9 earthquakes. It should be noted that the cyclic resistance ratio for a M_w = 9 earthquake is an extrapolation for both procedures, and the largest magnitude in either database is the M_w = 8.1 Michoacan earthquake. The procedures have different methods of correcting $(N_1)_{60}$ and for calculating the depth reduction factor, r_d, so a direct comparison of the CRR from each method is not necessarily straightforward. Some key case histories in both procedures have been disputed, leading to the differences in cyclic resistance ratio between the procedures, and it is important to consider these differences when comparing the procedures.

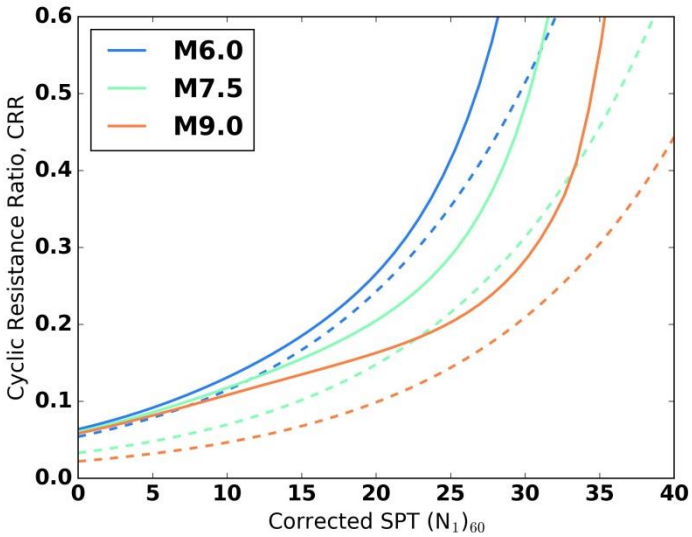

Figure 2.5: Comparison of contemporary deterministic liquefaction triggering functions. Solid lines are from Boulanger and Idriss (2014). Dashed lines are from Cetin et al. (2004).

2.4 LIQUEFIED MATERIAL BEHAVIOR

Loose granular soils tend to contract during shearing. If the soil is saturated and unable to drain, the tendency for volumetric contraction is manifested as increased pore water pressure. In conditions where the permeability of the soil is too low to drain or the layer of soil cannot drain, because it is bounded by lower permeable layers, the pore pressure between the soil grains increases until the pore pressure is equal to the overburden pressure. Once the pore pressure is equal to the overburden pressure the effective stress is zero and the soil has liquefied.

The rate of pore pressure generated during harmonic loading in laboratory tests is commonly described using the number of cycles of loading, N, relative to the number of cycles

required to initiate liquefaction, N_L. DeAlba et al. (1975) developed an empirical equation based on the results of laboratory testing that relates the number of cycles of loading to the pore pressure ratio, r_u. The expression was later simplified by Booker et al. (1976). Figure 2.6 shows the pore pressure ratio for several values of an empirical material property, α. This figure indicated that, pore pressure initially developed rapidly during the first few cycles of loading, but then the rate of generation slowed once the pore pressure ratio approached values around 0.2 to 0.4. The pore pressure ratio continued to increase slowly as the number of cycles of loading increases. Once the pore pressure ratio approached values around 0.8 or 0.9, pore pressure developed rapidly until the soil liquefied and the pore pressure ratio was equal to 1.0.

$$r_u = \frac{1}{2} + \frac{1}{\pi}\arcsin\left[2\left(\frac{N}{N_l}\right)^{1/\alpha} - 1\right] \tag{2.15}$$

$$r_u = \frac{2}{\pi}\arcsin\left[\left(\frac{N}{N_l}\right)^{1/2\alpha}\right] \tag{2.16}$$

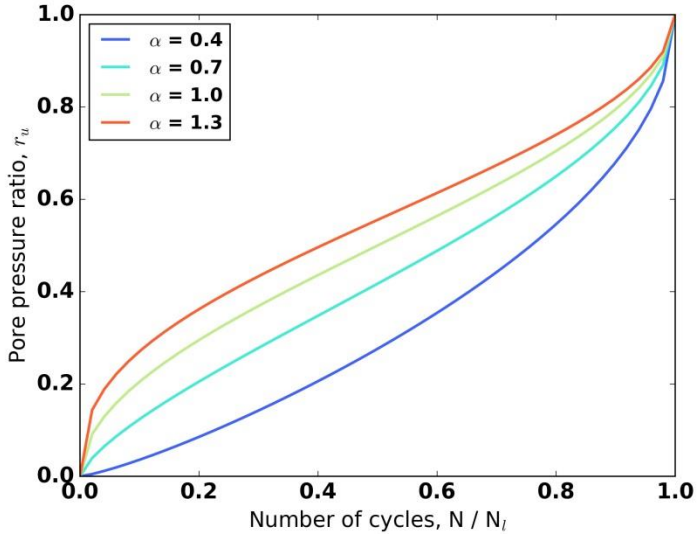

Figure 2.6: Rate of pore pressure generation (after DeAlba, 1975).

The contractive or dilative behavior of soil is largely determined by the effective stress and relative density of the soil. Soils in a contractive state tend to generate pore pressure during shearing, and soils in a dilative state tend to reduce pore pressure during shearing. Sands tend to contract and generate excess pore pressure at low shear stress ratios and dilate and reduce excess pore pressure at high shear stress ratios. The stress dependent change from contractive into dilative

behavior is due to changes in the micromechanical structure of the soil during deformation (Iai et al., 2011). The point of transformation from a contractive into a dilative phase is commonly defined by a constant volume friction angle or phase transformation angle, ϕ_p. At the phase transformation angle, the soil exhibits no volumetric strain during shearing. At shear stress ratios less than the phase transformation angle, soils exhibit contractive behavior, and at shear stress ratios greater than the phase transformation angle, soils exhibit dilative behavior. Figure 2.7 illustrates a monotonically-loaded stress path that undergoes phase transformation from contractive to dilative behavior.

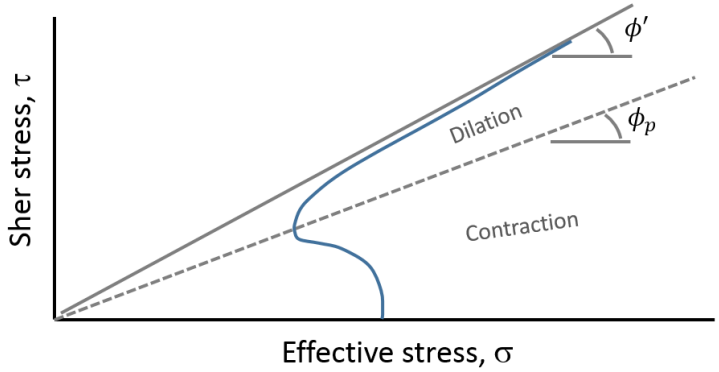

Figure 2.7: Stress path showing dilation and contraction behavior

The actual stress states associated with phase transformation is not completely well-defined. Been et al. (1991) noted that phase transformation should be distinguished from the critical state of sand, where no volumetric strain occurs during shearing at a constant shear stress and shear strain rate. The critical state occurred at relatively large shear strains and was a unique function of void ratio and mean effective stress, whereas the phase transformation can occur at relatively small strains early on during cyclic loading. The point of phase transformation also depended on other factors such as the stress path, sample preparation, fabric, age, etc.

The DeAlba et al. (1975) relationship reflected the general trend of pore pressure generated during cyclic loading but did not account for the phase transformation behavior that occurred within each cycle of loading. The rapid increase in the rate of pore pressure generated as r_u approached values of 0.8 to 0.9 could be explained by the cycles of contraction and dilation that soils undergo at high shear stress ratios. Figure 2.8 shows the results of a cyclic direct simple shear test of medium dense sand and the pore pressure ratio compared to the DeAlba (1975) function. The rate of contraction became very rapid once the soil changed from a contractive to a

dilative phase and back again. Dilation and contraction within each cycle of loading caused the pore pressure ratio to differ from the equation proposed by DeAlba (1975) at high shear stress ratios. The rate of contraction or dilation depended on the relative density of the soil, and loose sands tended to dilate at a relatively modest rate above the phase transformation line, and contract rapidly upon unloading. Dense sand tended to contract slightly at low shear stress ratios, but then dilate very rapidly at high shear stress ratios.

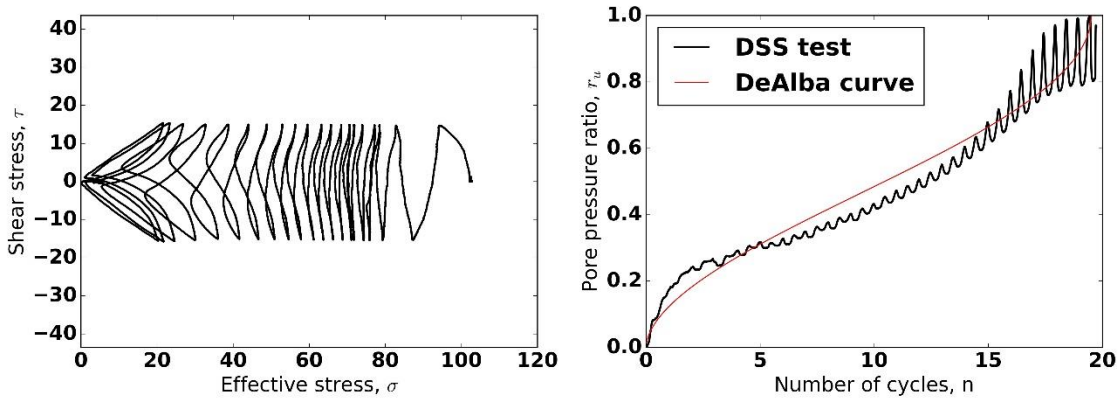

Figure 2.8: Rate of pore pressure generation from a laboratory test. Example DSS test (Kwan et al., 2015) showing the generation of pore pressure with phase transformation at high shear stress ratios.

The example DSS test showed that the stress path stabilized as the soil approached a liquefied state during cyclic loading and r_u varied from about 0.8 to 1.0. The pore pressure after the initiation of liquefaction depended on the shear stress on the soil and the state of loading or unloading. Shear loading after liquefaction caused the pore pressure to decrease and the stress path to travel up the phase transformation line as dilation occurred. Unloading caused the pore pressure to increase due to contraction until the effective stress becomes zero again. The resulting stress path had a "butterfly-like" appearance.

Changes in effective stress due to dilation and contraction also affected the stiffness of the soil. The simple constitutive soil model discussed earlier (Kramer et al., 2013) illustrated that the soil stiffness, G, was a function of the mean effective stress, σ_m', normalized by the atmospheric pressure, p_a. With the very simple relationship between stiffness and effective stress in equations (2.4) and (2.5), the stiffness is proportional to $(1 - r_u)^{0.25}$. At r_u of 0.9, the stiffness of the soil was about 30% of the initial stiffness before shearing. At r_u of 0.99, the shear stiffness was about 10% of the initial stiffness, and as r_u approached 1.0, the shear stiffness approached 0. The

tendency for soil to dilate and contract has important consequences for the behavior of soil leading up to and after liquefaction. The shear modulus of the soil, G, can be defined by the ratio of the change in shear stress, $\delta\tau$, and change in shear strain, $\delta\gamma$.

$$\mathrm{G} = \frac{\delta\tau}{\delta\gamma} \tag{2.17}$$

In the simple model for the stiffness of soil, as pore pressure approached the overburden pressure, the shear modulus became very small. Relatively small changes in shear stress, $\delta\tau$, can result in very large changes in shear strain, $\delta\gamma$, especially compared to the changes in shear strain when the excess pore pressure was low. In a liquefied state, shear strain can accumulate very rapidly. Figure 2.9 shows shear stress, pore pressure ratio, and shear strain time histories for the example cyclic direct simple stress test. Continued cycles of loading after the soil liquefied caused dilation and contraction resulting in changes in effective stress and shear stiffness that varied over several orders of magnitude. Even though continued cycles of loading after the soil liquefied had nearly identical stress paths, the overall secant stiffness of soils continued to decrease as the soil fabric degraded with additional cycles of loading. This phenomenon led to increased shear strain amplitude as additional cycles of loading were applied after the soil liquefied.

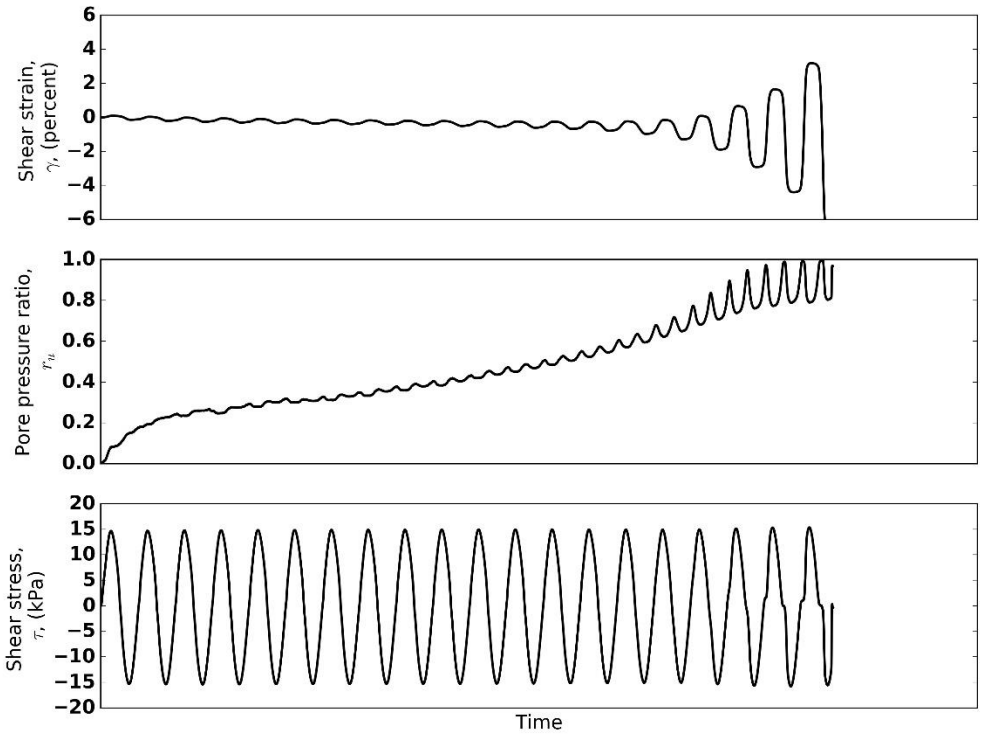

Figure 2.9: Shear strain amplitude from a laboratory test. Example DSS tests showing increase in shear strain amplitude as the pore pressure ratio approaches 1.0 and the soil liquefies

Ishihara and Yoshimine (1992) compiled data from many cyclic simple shear tests on Fuji river sand reconstituted to different relative densities. They found that the maximum cyclic shear strain that developed during cyclic loading, γ_{max}, was related to the factor of safety against liquefaction, FS_L, and the soil's initial relative density, D_r. The factor of safety depended on the number of cycles of loading through the magnitude scaling factor, and continued to decrease with additional cycles of loading after the soil liquefied. After liquefaction, shear strains developed much more rapidly for loose sands than in dense sands.

Seed et al. (1979) proposed that the maximum shear strain that developed during undrained cyclic loading was fundamentally limited by the dilative characteristics of sand. Under cyclic loading with a constant shear stress amplitude, they proposed that the shear strain could not exceed a certain limit, regardless of the number of cycles of loading. Loose soils reached their limiting shear strain with fewer cycles of loading after liquefaction than dense soils. The concept of a limiting maximum shear strain is adopted by Zhang et al. (2004) to modify Ishihara and Yoshimine's (1992) laboratory results to include a limiting shear strain, γ_{lim}. Modified curves of

maximum shear strain during cyclic loading versus factor of safety and relative density are shown on Figure 2.10.

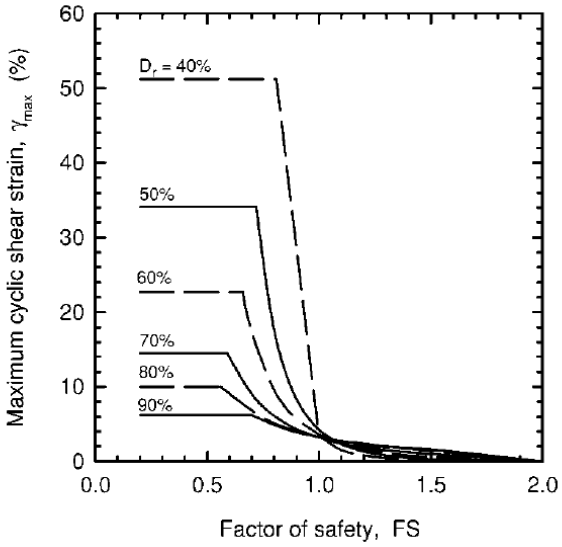

Figure 2.10: Maximum cyclic shear strain (from Zhang et al., 2004). Data from Ishihara and Yoshimine (1992).

Idriss and Boulanger (2008) created an analytical expression for the maximum cyclic shear strain from the plot shown in Figure 2.10. Per the recommendations by Seed et al. (1979), the limiting maximum cyclic shear strain, γ_{max}, depended on the relative density of the soil. In Idriss and Boulanger's expression, the shear strain was limited for factors of safety less than a threshold factor of safety, F_α, that depends on the soil's relative density.

$$\gamma_{max} = \min\left\{\gamma_{lim}, 0.035(2 - FS_L)\left(\frac{1 - F_\alpha}{FS_L - F_\alpha}\right)\right\} \quad \begin{matrix} 0 & FS_L \geq 2 \\ & 2 > FS_L \geq F_\alpha \\ \gamma_{lim} & FS_L < F_\alpha \end{matrix} \tag{2.18}$$

$$\gamma_{\lim} = 1.859(1.1 - D_R)^3 \tag{2.19}$$

$$F_\alpha = 0.032 + 4.7\, D_R - 6.0\, {D_R}^2 \tag{2.20}$$

Mikami et al. (2016) performed many harmonic stress-controlled cyclic triaxial tests on reconstituted sand samples and proposed that the peak cyclic strain amplitude during each cycle of loading can be modeled as a simple bilinear function on a semi-log axis. Prior to liquefaction, the cyclic shear strain amplitude increases at a constant rate, A, with the log of the number of cycles of loading. After liquefaction, cyclic shear strains accumulated more rapidly and the cyclic

shear strains increased at a faster rate, B. The two lines for the cyclic shear strain amplitude versus the log of the number of cycles of loading intersected at a point, D_{is}. The rates before and after liquefaction, A and B, and the intersection point, D_{is}, were used to construct a function of cyclic shear strain amplitude versus the number of cycles of loading. Liquefaction was assumed to occur once the double-amplitude shear strain reaches 5%. The bilinear function suggested that cyclic shear strain continued to increase after liquefaction without an upper limit, although the number of cycles was plotted on a log scale. The log scale implied that the increase in double-amplitude shear strain from each cycle of loading diminished after many cycles of loading. Recommendations for parameters A, B, and D_{is} are included in Table 2.3, 2.4, and 2.5.

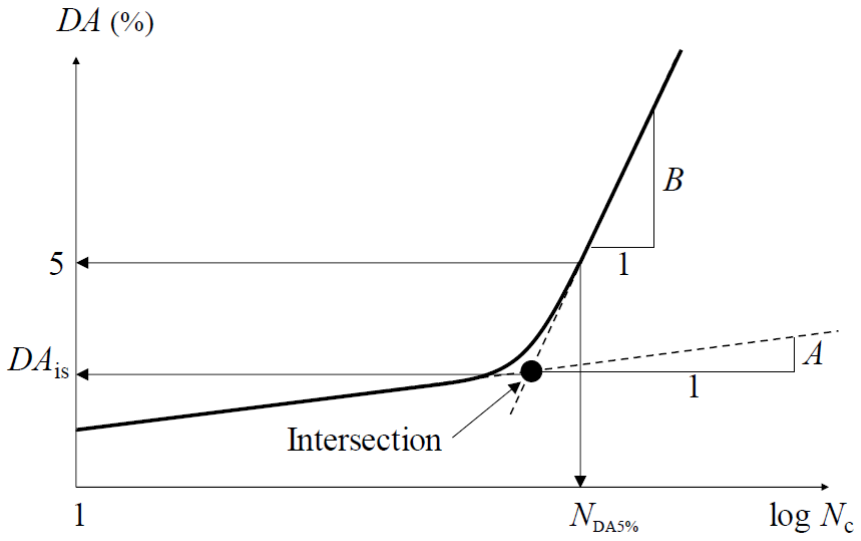

Figure 2.11: Estimated shear strain amplitude (from Mikami et al., 2017).

Table 2.2: Parameter A for Mikami et al. (2017) shear strain estimate

Fines content	$\mathbf{D_R < 50\%}$	$\mathbf{50\% \le D_R < 80\%}$	$\mathbf{D_R > 80\%}$
Less than 10%	$3\ N_{5\%}^{-1.35}$	$10\ N_{5\%}^{-1.35}$	$60\ N_{5\%}^{-1.35}$
10 to 35%	$3\ N_{5\%}^{-1.35}$	$10\ N_{5\%}^{-1.35}$	$60\ N_{5\%}^{-1.35}$
Greater than 35%	$6\ N_{5\%}^{-1.35}$	$20\ N_{5\%}^{-1.35}$	$60\ N_{5\%}^{-1.35}$

Table 2.3: Parameter B for Mikami et al. (2017) shear strain estimate

Fines content	$D_R < 50\%$	$50\% \leq D_R < 80\%$	$D_R > 80\%$
Less than 10%	$35\ N_{5\%}^{0.8}$	$15\ N_{5\%}^{0.6}$	$7\ N_{5\%}^{0.4}$
10 to 35%	$6\ N_{5\%}^{0.8}$	$5\ N_{5\%}^{0.6}$	$4\ N_{5\%}^{0.4}$
Greater than 35%	$6\ N_{5\%}^{0.8}$	$5\ N_{5\%}^{0.6}$	$4\ N_{5\%}^{0.4}$

Table 2.4: Parameter D_{is} for Mikami et al. (2017) shear strain estimate

Fines content	$D_R < 50\%$	$50\% \leq D_R < 80\%$	$D_R > 80\%$
Less than 10%	$1.5\ N_{5\%}^{-0.7}$	$4\ N_{5\%}^{-0.7}$	$17\ N_{5\%}^{-0.7}$
10 to 35%	$1.5\ N_{5\%}^{-0.7}$	$4\ N_{5\%}^{-0.7}$	$17\ N_{5\%}^{-0.7}$
Greater than 35%	$3\ N_{5\%}^{-0.7}$	$7\ N_{5\%}^{-0.7}$	$17\ N_{5\%}^{-0.7}$

As discussed previously, at a critical state, shear strains accumulate indefinitely at a constant rate. The concept of liquefaction at steady state (Been and Jefferies 1991, Iai et al. 2011) suggested that very large strains could develop if the shear stress approached the undrained steady-state shear strength, s_{us}, of the soil. The steady state shear strength surface was uniquely defined by void ratio, effective stress, and shear stress. Figure 2.12 (from Kramer, 1996) illustrates a monotonically loaded undrained triaxial test where the soil reached steady state and the shear strain continued to accumulate indefinitely. Under transient loading, the soil may reach steady state, where strain continues at a constant rate if the shear stress remained equal to s_{us}. Since laboratory tests, such as cyclic triaxial or simple shear tests, do not include all the mechanisms of loading that can occur in the field, the steady state undrained shear strength is difficult to recreate using cyclic laboratory testing. The undrained steady-state shear strength is commonly back-calculated from case histories of flow slides after earthquakes (Olson and Stark, 2002; Kramer and Wang, 2016). Sloping ground or sites near steep riverbanks or cuts may induce static shear stresses that are near s_{us}. These conditions can lead to flow-like behavior where soils with a high static shear stress contract under relatively modest cyclic loading and approach the steady state shear strength of the soil (Kramer, 1996).

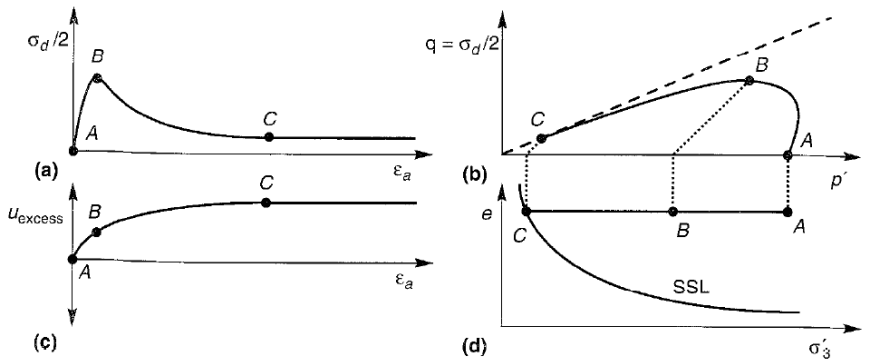

Figure 2.12: Continued shear strain at steady-state (from Kramer, 1996). (a) Shear strain versus deviator stress. Note continued axial strain at a constant deviator stress. (b) Stress path. (c) Excess pore pressure. (d) Presence of steady state line, SSL.

2.5 CONSEQUENCES OF LIQUEFACTION

Soil liquefaction does not always cause damage. The possibility of damage due to liquefaction not only depends on the susceptibility and triggering of liquefaction but also on the behavior of the soil after liquefaction is triggered and the nature of the structures, piers, embankments, dams, etc. that could be impacted by liquefiable soils. An understanding of the consequences of liquefaction is important for assessing the damage caused by liquefaction and designing solutions to mitigate liquefaction. Liquefaction can have many possible consequences, but this section will focus on engineering applications of amplified ground motions and lateral spreading.

Soils become extremely soft during liquefaction, and the dynamic characteristics of the liquefiable soil layers are very different before and after liquefaction. Equations (2.4) and (2.5) illustrated the decrease in shear modulus as pore pressure increased during shaking. The maximum amplification of a soil profile occurs at frequencies near the soil profile's characteristic frequency, f_s. As pore pressure is generated and the soil profile becomes softer during shaking, the characteristic site frequency decreases, and lower frequency components of motion are amplified. For a simple example of a single layer of soil with an initial shear wave velocity, v_{s0}, the characteristic frequency of the soil layer is $v_{s0}/4H$. The decrease in characteristic site frequency becomes very rapid as r_u approaches 1.0. Figure 2.13 shows the ratio of the characteristic site frequency, f_s, and period, T_s, relative to the initial characteristic site frequency and period, f_0 and T_{s0} (Kramer et al., 2013).

$$f_s = \frac{v_s}{4H} = \frac{\sqrt{\mathrm{G}/\rho}}{4H} \tag{2.21}$$

$$f_s = \frac{1}{T_s} = \frac{\sqrt{\frac{\mathrm{G}_{1\ atm}}{\rho}\left(\frac{\sigma_{mo}'(1-r_u)}{p_a}\right)^m}}{4H} = \frac{v_{s0}}{4H}\left(\frac{\sigma_{mo}'(1-r_u)}{p_a}\right)^{0.5m} \tag{2.22}$$

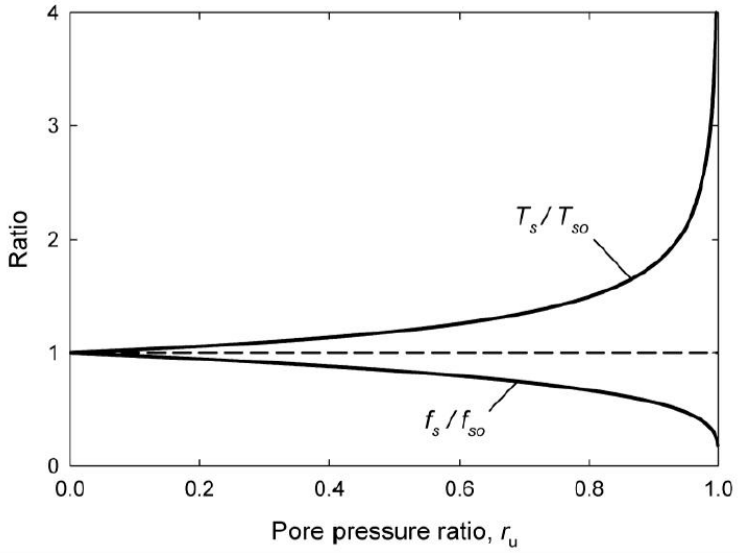

Figure 2.13: Characteristic site period and frequency versus pore pressure ratio (from Kramer et at., 2013).

At the onset of liquefaction, the liquefied layer is extremely soft can only transmit very low-frequency motions. However, strong shaking once the soil has liquefied may cause the soil to dilate, leading to temporary stiffening and amplification of higher frequencies of motion. Degradation of the soil fabric results in overall softening as strong shaking continues and large strains develop. However, if pore pressure can dissipate via drainage during shaking, the soil may stiffen over time and regain some of its ability to transmit higher frequency motions. The effects of extreme softening, soil fabric degradation, dilation, and drainage create very complicated behavior that can affect the response spectrum at sites where liquefaction occurs. Hartvigsen (2007) compared many nonlinear site response analyses with and without consideration for softening due to pore pressure generation. The ratio of the response spectra of effective stress and total stress analyses, RSR, provided insight into the possible consequences of liquefaction for site response analysis. An RSR greater than 1.0 indicated liquefied soils amplified the spectral

acceleration of a 1D oscillator, and an RSR less than 1.0 indicated the soil deamplified the spectral acceleration. The complicated behavior of liquefied soil resulted in a large variance in RSR, but in general, softening due to pore pressure generation decreased the short period spectral acceleration and increased the long period spectral acceleration. The effects of liquefaction on the RSR became more pronounced as the factor of safety against liquefaction decreases. Figure 2.14 shows the results of Harvigsen (2007) for three different ranges of factor of safety.

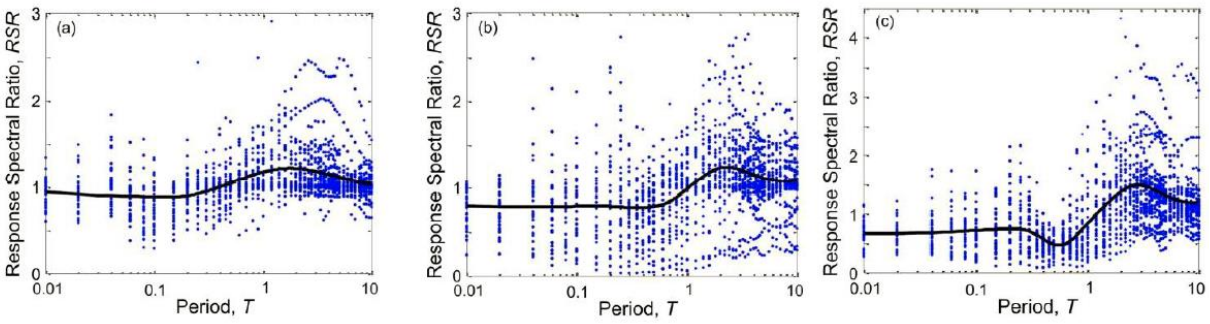

Figure 2.14: Response spectrum ratio for effective stress and total stress analyses (from Kramer et al., 2011). (a) Factor of safety against liquefaction between 1.7 and 2.5. (b) Factor of safety between 0.8 and 1.0. (c) Factor of safety between 0.5 and 0.6.

Gingery (2014) investigated site response behavior at 19 sites with strong motion records where the spectral acceleration was impacted by liquefied soil. The recorded spectral acceleration was compared to the spectral acceleration that was estimated using a GMPE. An amplification factor due to liquefaction was defined as AF_{liq}.

$$\mathrm{AF}_{liq} = \ln\left(S_{\mathrm{a},liq}\right) - \ln\left(S_{a,GMPE}\right) \tag{2.23}$$

Values of AF_{liq} were estimated based on the metadata from the NGA West-2 database, including PGA, $v_{s,30}$, and M_w. However, the values of AF_{liq} was not calculated with considerations of soil properties or subsurface conditions.

During past major earthquakes, severe damage to engineered structures and lifelines has been caused by liquefaction induced ground failures (Zhang et al., 2004). Large shear strains can develop in liquefied soil from even relatively small static shear stresses. Permanent lateral deformation due to a combination of strain developed during shaking and gravitational forces is called lateral spreading. The transient shear stresses during an earthquake combined with static gravitational loading can lead to "ratcheting" stress-strain behavior where the soil permanently

strains downhill at gently sloping sites, or towards a free-face at steep riverbanks or cut slopes. Figure 2.15 shows a simulated laboratory triaxial test with a constant shear stress bias, which illustrates the mechanics of lateral spreading were permanent shear strains develop.

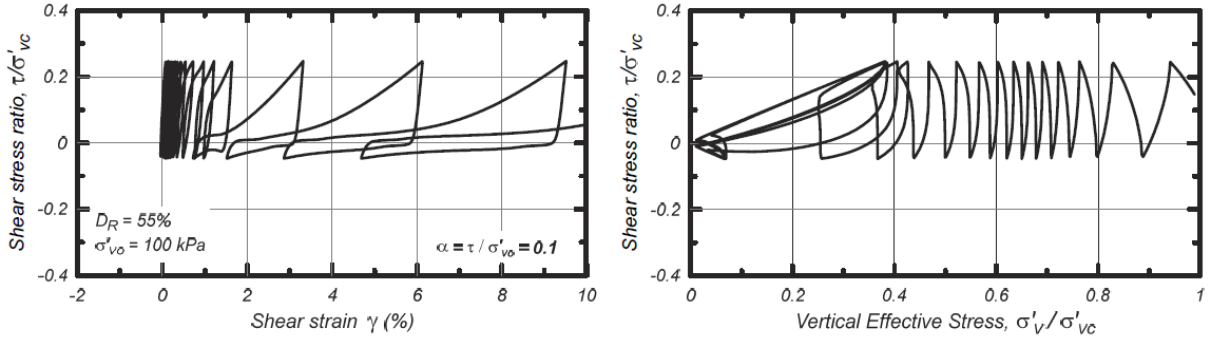

Figure 2.15: Stress-strain curve and stress path of a simulated laboratory triaxial test with a constant shear stress bias (from Boulanger and Ziotopoulou, 2015). Shear stress ratios normalized by initial vertical confining stress, $\sigma_{vc}{}'$

Since the mechanics of lateral spreading can be very complicated, estimates of lateral spreading deformations are commonly based on empirical or semi-empirical observations. Youd et al. (2002) combined case histories of lateral spreading with available subsurface data to estimate permanent deformation using multiple linear regression (MLR). Their regression analysis indicated that earthquake moment magnitude, M_w, horizontal site to source distance, R, cumulative thickness of saturated layers with $(N_1)_{60} < 15$, T_{15}, the average fines content in T_{15}, and the median grain size within T_{15}, provided sufficient features to estimate the lateral spreading deformation at a site that is a distance, L, away from a steep riverbank or cut with height, H. For the empirical regression, the average finest content, F_{15}, is in percent, the median grain size, $D50_{15}$, is in units of mm, and lateral deformation, LD, is in units of m.

$$\log(\mathrm{LD}) = -16.713 + 1.532M - 1.406\log R^* - 0.012R + 0.594\log\frac{\mathrm{H}}{\mathrm{L}} + 0.450\log T_{15} + 3.413\log(100 - F_{15}) - 0.795\log(D50_{15} + 0.1\mathrm{mm}) \quad (2.24)$$

$$R^* = R + 10^{(0.89M - 5.64)} \quad (2.25)$$

The variance of the estimated deformation using this approach is relatively large, and Youd et al. (2002) indicate that 90% of the data lies between factors of 0.5 and 2 times the predicted values. Assuming a log-normal distribution, the residuals of the estimates corresponds to a

standard deviation, $\sigma_{\ln \delta}$, of 0.46 (Franke and Kramer, 2014). The empirical databases do not cover the full range of conditions that are encountered in practice, and extending MLR lateral spreading models outside the range of conditions may result in unrealistic predictions of deformations. Youd et al. warranted caution in using this approach when the ratio of the height of the free face, H, to the distance to the top of the free face, L, exceeded 0.20. Sites that are closer than 0.20 H/L have initial static shear stresses than may cause slumping or flow failures, which were not accounted for in the Youd et al. (2002) model. The Youd et al. (2002) database included only one earthquake with $M_w > 7.8$, so estimated deformations for larger magnitude earthquake extrapolate beyond the data used to create the model. Figure 2.16 shows the predicted lateral spreading deformation versus measured deformation from the case histories in the Youd et al. (2002) database.

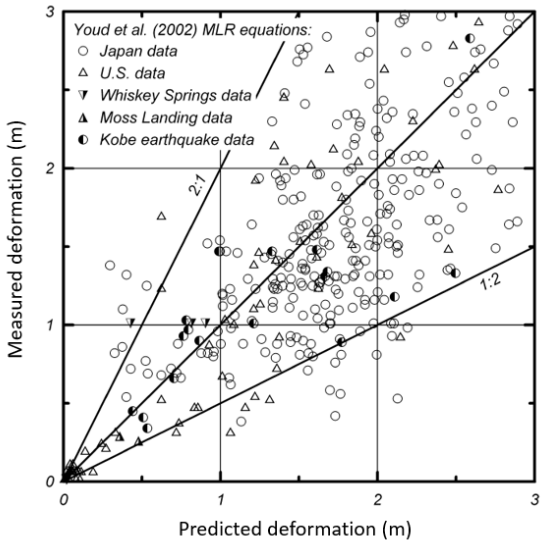

Figure 2.16: Measured versus predicted deformation (from Youd et al. 2002).

Lateral spreading deformation typically results from the accumulation of shear strain across layers of soil, rather than slip along a discrete failure plane. Zhang et al. (2004) used the concept of maximum shear strain from laboratory tests, γ_{max}, with empirical observations from case histories to develop a semi-empirical procedure for predicting lateral spread deformation. Most cyclic laboratory tests are performed with no static shear bias, which simulates level-ground conditions. Research with these types of tests indicate that the maximum cyclic shear strain is a function of the factor of safety against liquefaction and the relative density of the soil (Ishihara and Yoshimine, 1992). Zhang et al. (2004) defined a parameter known as the lateral displacement index (LDI) to estimate the potential for lateral spreading, that was independent of static shear

stresses. The LDI was calculated as the integral of the maximum potential cyclic shear strain in each layer at a site. Chu et al. (2006) found that the depth of soils that contribute to the computation of LDI and the permanent lateral spreading deformation can be restricted to about twice the height of the free face, 2H.

$$\text{LDI} = \int_0^{2H} \gamma_{max}\, dx \tag{2.26}$$

The stress-strain behavior of the liquefied soil is characterized by "banana-shaped" hysteresis loops where the shear stress remains low until large shear strains develop. Dilation then occurs and the soil stiffness increases. Since the soil is very soft before dilation occurs, even a relatively modest static shear stress can cause substantial shear strains. Static shear stresses drive the shear strain of liquefied soil towards γ_{max}. As the static shear stress increases at a site, the permanent deformation caused by liquefaction increases relative to the LDI. Empirical factors from lateral spreading case histories can be used to adjust the LDI to match the observed lateral spreading deformation, LD. The adjustment factor for LDI is a function of the height of the free face, H, and distance from the site to the free face, L.

$$\text{LD} = \text{LDI} \cdot 6\left(\frac{\text{L}}{\text{H}}\right)^{-0.8} \tag{2.27}$$

The concept of maximum shear strain potential is useful since it incorporated soil mechanics into the computation of lateral spreading. However, it did not account for wave mechanics or the actual kinematic behavior that may occur during an earthquake. Accounting for the soil behavior, site geometry, kinematic behavior, and wave mechanics require, at a minimum, nonlinear finite element or finite difference analysis.

It has recently been common practice to base lateral spreading displacement estimates on sliding block analyses with residual strengths used to represent soil resistance. Compilations of multiple sliding block analyses have been developed by several investigators, among the most commonly used of which are those by Bray and Travasarou (2007) and Saygili and Rathje (2008). The very low, and variable shear strength of liquefied soil leads to a large amount of uncertainty using these approaches. The shear resistance of the soil does not typically exhibit a uniform, constant strength that these sliding block methods imply for lateral spreading. Olson and Johnson (2008) have back-calculated approximate shear strengths from 39 case histories using sliding block analysis. They found that the back-calculated mobilized shear strength, $s_{u,\text{mob}}$, for sliding block

analysis was consistent with the mobilized shears strength presented by Olson and Stark (2002) for residual strength flow analysis.

$$\frac{s_{u,\mathrm{mob}}}{\sigma_v{}'} = \begin{Bmatrix} 0.03 + 0.0075\ (\mathrm{N}_1)_{60} \\ 0.03 + 0.0143\ q_{c1} \end{Bmatrix} \tag{2.28}$$

Olson and Johnson (2008) indicated the relationship in equation (2.28) was limited to $(N_1)_{60}$ values less than 16 and q_{c1} values less than 10 MPa. The authors acknowledged that the mechanism of the sliding block method did not properly model the strain mechanism associated with lateral spreading, but indicated that the method was useful for estimating deformations based on empirical regression.

The variation of lateral spreading displacement between the methods discussed here was compared at an example site with a 2% slope and R_{rup} = 20 km. The site was underlain by 7 m of loose, saturated, clean sand. Lateral spreading was evaluated for earthquakes ranging from M_w = 5 to M_w = 9. Intensity measures for liquefaction analysis were estimated using the BCHydro GMPE (Abrahamson et al., 2016). The estimated lateral spreading deformations versus earthquake magnitude, assuming liquefaction was triggered, are shown in Figure 2.17. Since the method presented by Zhang et al. (2004) was based on the factor of safety against liquefaction, very little deformation was predicted for magnitudes that did not trigger liquefaction. Likewise, an upper bound on shear strain was assumed in that method, which leads to a maximum lateral deformation even for large earthquake magnitudes. The models presented in Figure 3.16 were applicable to magnitudes up to M_w = 7.5 to 8.5. Extrapolations beyond the recommended moment magnitudes are shown as dashed lines in the figure. The methods predict very different deformation at all magnitudes, illustrating the uncertainty in lateral spreading prediction and the variability that can be caused by different assumptions about the data, mechanics, and model. Extrapolating these methods up to M_w = 9 led to estimates of lateral spreading that varied by factors of more than 20.

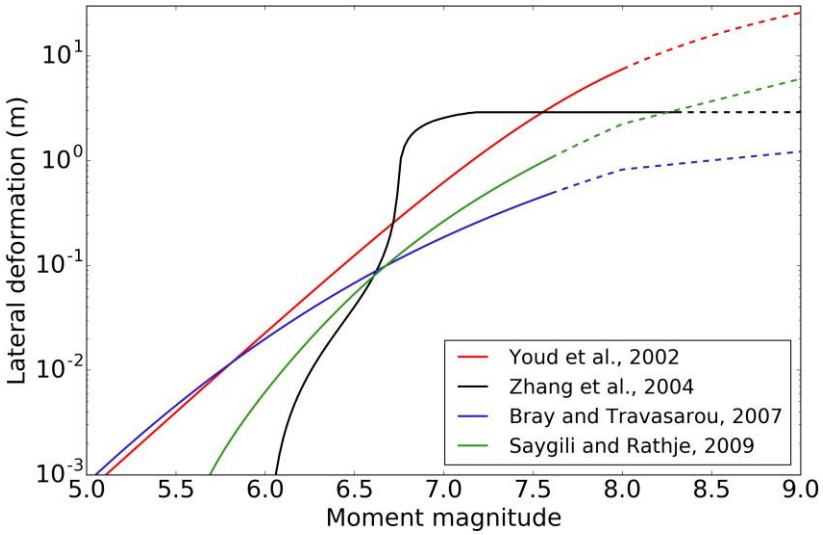

Figure 2.17: Variation in lateral spreading deformation estimates (from Kramer and Greenfield, 2017).

Recent application of the lateral spreading methods to the Canterbury sequence earthquakes (Bowen et al., 2012; Khoshnevisan et al., 2015) indicated that the current lateral spreading methods were relatively poor at predicting deformations for future earthquakes. The databases for developing the lateral spreading methods did not include earthquakes in the Canterbury sequence, and these new case histories varied significantly from the predicted values. The databases used to develop the models may contain insufficient data or prediction variables for estimating the lateral spreading deformation from future earthquakes. Reprocessing of the Zhang et al. (2004) database to include data from the Canterbury sequence earthquake dramatically reduced the misfit of observation versus prediction.

Chapter 3. CHARACTERIZATION OF LONG-DURATION GROUND MOTIONS

A complete description of a ground motion consists of descriptions of frequency content, amplitude, and duration characteristics (Kramer, 1996). The duration of an earthquake may have important consequences for both liquefaction triggering and post-triggering behavior. However, no single measure completely encompasses the effects of earthquake duration for liquefaction and intensity measures for duration have not been developed with long-duration ground motions from subduction zone earthquakes in mind. This section provides a review of commonly used intensity measures for duration and compares suites of ground motions that isolate the effects of ground motion duration. The objective of this study is to identify duration characteristics of ground motions that are important for liquefaction analysis, and to develop suites of motions that have specific duration characteristics to use in subsequent analysis.

3.1 FACTORS AFFECTING GROUND MOTION DURATION

Earthquake magnitude, rupture distance, rupture mechanisms, and directivity all affect the duration of ground shaking at a site. Larger magnitude earthquakes tend to produce longer duration shaking than smaller magnitude earthquakes, and the duration of ground motions can be related to earthquake magnitude and rupture distance using basic principles of seismology. Earthquake moment magnitude, M_w, is defined in terms of the seismic moment, M_o, which is measured in units of dyne-cm (Hanks and Kanamori, 1977).

$$M_w = \frac{2}{3}\log M_o - 10.7 \tag{3.1}$$

The seismic moment, M_o, is a measure of the energy released from a fault rupture due to the displacement of the fault. Based on the principle of work, the seismic moment equals the average fault displacement, $\overline{D}$, over an offset area, A, with an average shear modulus, μ.

$$M_o = \mu A \overline{D} \tag{3.2}$$

The product of the shear modulus and the average displacement along the fault rupture is equal to the stress drop, $\Delta\sigma$, along the fault. Brune (1970) developed a theoretical solution for the Fourier amplitude at a site based on a circular rupture in an elastic medium. Brune's solution indicates the upper limit of seismic moment can be defined by the stress drop and circular rupture volume, r^3.

$$\mathrm{M_o} = \frac{16}{7}\Delta\sigma r^3 \tag{3.3}$$

Observations from many earthquakes have indicated that the initial stress drop from the fault rupture is independent of earthquake magnitude (Frankel, 2009), and is typically about 100 bars the western United States. Since the stress drop is assumed to be constant, the energy released during an earthquake, and the earthquake magnitude, is roughly proportional to the area of fault rupture. The entire area of the fault does not rupture simultaneously, but rather the time from initial fault rupture at the hypocenter to the final fault rupture depends on the velocity of the rupture and size of the rupture area. Madariaga (1976) indicated the velocity of the fault rupture is typically about 90% of the shear wave velocity of the medium, which is constant within a geologic region. Seismic body waves travel through elastic media at a constant velocity, so waves propagating from different parts of a fault should arrive at a site at different times. Both the rupture area and the distance over which the waves travel contribute to the overall duration of shaking, and the total duration of shaking is, at a minimum, the sum of the time required for the fault to completely rupture and the time required for waves to travel from the fault to the site.

The solution proposed by Brune (1970) resulted in a Fourier amplitude spectrum where the amplitude of the motion was relatively constant between lower-bound corner frequencies to upper-bound cut-off frequencies. Figure 3.1 shows the theoretical Fourier amplitude spectrum for the Brune (1970) solution with earthquakes ranging from M_w = 4 to 7. The lower bound corner frequency depended on earthquake magnitude, and the Fourier amplitude of frequencies less than the corner frequency diminished rapidly. The peak Fourier amplitude of the spectrum increased with earthquake magnitude, and the corner frequency also decreased with earthquake magnitude, indicating that higher magnitude earthquakes have much more low-frequency energy than smaller magnitude earthquakes (Boore, 1983).

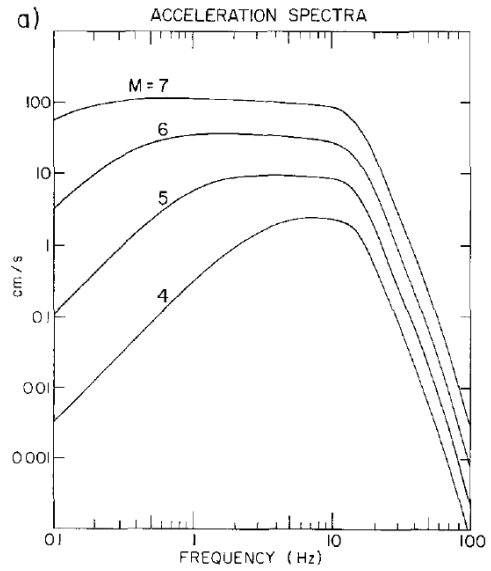

Figure 3.1: Theoretical Fourier amplitude spectrum (from Boore, 1983).

The amount of low-frequency energy can affect the ground motion duration in a couple of ways. Material damping in seismology is based on the frequency content of the wave, and damping is proportional to the number of cycles of a wave as it propagates through a medium. Lower frequency waves have longer wavelengths and require fewer cycles to travel the same distance as higher frequency waves. This means that low-frequency motions can travel farther, have less damping, and arrive at a site with higher amplitude than high-frequency waves. In addition, since the period of low-frequency waves is longer, each cycle of low-frequency waves has a longer duration than a high-frequency wave, leading to a longer overall duration for low-frequency motions than for high-frequency motions.

Sites that are far from the fault rupture tend to experience a longer relative earthquake duration than sites close to the fault rupture, although the amplitude of the shaking certainly tends to decrease with distance from the fault rupture. Different types of waves travel at different velocities, and the arrival time of the different wave types depends on the rupture distance and wave velocity. P-waves travel faster than s-waves through homogeneous elastic media, and velocity of the p- and s-waves, v_p and v_s, depends on the Poisson's ratio of the medium (Kramer, 1996).

$$\frac{v_p}{v_s} = \sqrt{\frac{2-2\nu}{1-2\nu}} \tag{3.4}$$

For a Poisson's ratio of 0.3, which is typical for the earth's crust, the p-wave velocity is about 1.9 times faster than the s-wave velocity. Because of this difference in wave velocity, the length of time between the arrival of p- and s-waves increases as the distance from the fault increases. Surface waves travel slower than s-waves and also increase the overall duration of motion. The velocity of surface waves is frequency dependent, and the time between the arrival of the fastest and slowest surface waves increases as the distance to the fault rupture increases. Surface waves attenuate at a lower rate than body waves, so they can propagate longer distances with less damping and arrive distant sites with significant dispersion.

Fault directivity and the nature of the earthquake rupture also play roles in the duration of strong shaking. Sites that are in the direction of fault rupture may experience short, intense shaking due to constructive interference. Sites that are in the opposite direction of fault rupture may experience less intense shaking, but a longer overall duration due to destructive interference. This effect is analogous to the Doppler effect with sound and light waves, and the constructive and destructive wave interference near the fault rupture leads to an azimuthal-dependence of earthquake duration (Kramer, 1996). Large earthquakes also have asperities or spots of higher slip within the overall fault rupture. Asperities tend to produce high-frequency acceleration pulses with a higher amplitude than the background rupture. Asperities may rupture at different times throughout the earthquake, leading to bursts of high frequency, high amplitude pulses of acceleration at irregular times. Since very large faults may slip over a period of seconds to minutes, asperities that are located far away from each other may rupture a long time after the initial fault rupture, which could produce strong pulses late in the earthquake record. Noguchi and Fumumura (2011) showed the multiple asperity ruptures contributed to the very long duration of the Tohoku earthquake. When waves from an asperity arrive a significantly long time after the initial earthquake rupture, the acceleration time history tends to show a rapid increase in amplitude with increased high-frequency content. The accelerations records plotted in Figure 3.2 show the arrival of ground motions from at least three asperities from the Tohoku earthquake.

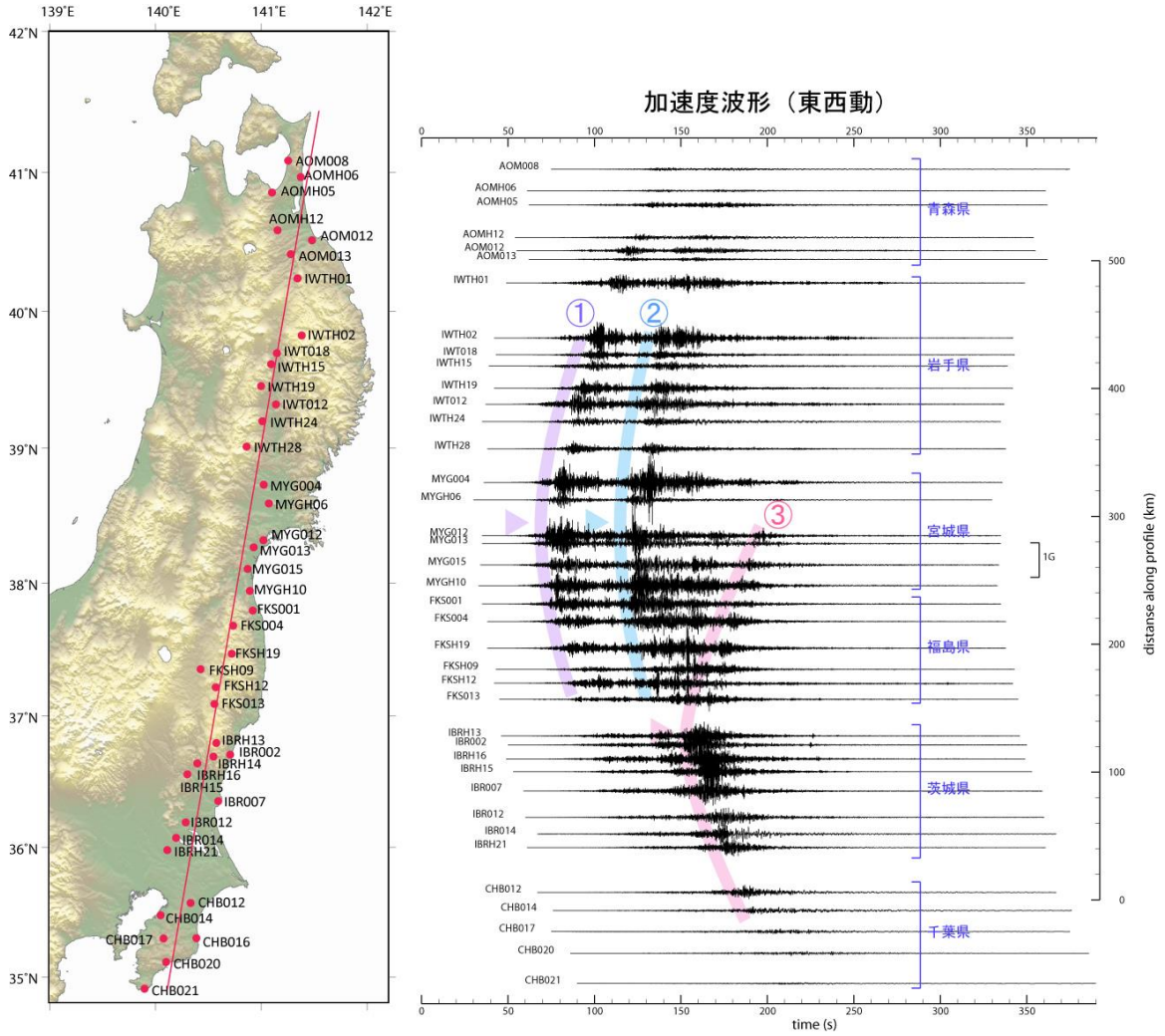

Figure 3.2: Sub-events within the 2011 Tohoku Earthquake (from Noguchi and Fumumura, 2011). Acceleration time histories are plotted versus distance along the profile. The arrival times of three asperities can be seen on the right.

Earthquakes ground motions can be modeled as stochastic, nonstationary processes. One of the properties of this nonstationary process is the duration of the ground motion. Earthquake ground motions tend to begin with relatively high-frequency content due to the arrival of p-waves, transition to a moderate frequency content once s-waves arrive, and then finally transition to low-frequency surface waves. Saragoni and Hart (1974) simulated the earthquake acceleration, $a(t)$, by filtered white noise with a time-domain envelope. They modeled each region of the earthquake (p, s, and surface waves) as frequency filtered white noise, $S_i(t)$. The arrival time of each of these wave regions varied, so each region was filtered in time with a rectangular function, $\Lambda_i(t)$, that began at the estimated time of wave arrival. They superimposed the p, s, and surfaces waves, and

then enveloped the resulting time history by a function, $\psi(t)$, which represented the variation in wave amplitude with time. The general form of the acceleration time history, $a(t)$, is

$$a(t) = \psi(t) \sum_{i=\{\text{p,s,surf}\}} \Lambda_i(t) S_i(t) \tag{3.5}$$

where rectangular functions, $\Lambda_i(t)$, and independent white noise functions, $S_i(t)$, from p-, s-, and surface-wave regions are combined. The time-domain envelope provided a function that constrained the shape of the ground motion amplitude and the duration of the ground motion. Saragoni and Hart modeled the functional form and parameters of the time-domain envelope to represent the observed shape of recorded motions from several earthquakes.

$$\psi(t) = t^{0.5\gamma} e^{-0.5\alpha t} \sqrt{\beta} \tag{3.6}$$

where the parameters γ and α are shape factors that control the duration of the ground motion. The parameter β is an intensity measure that controls the amplitude of the ground motion.

3.2 INTENSITY MEASURES FOR DURATION

Scalar intensity measures are useful for predicting the response of physical systems due to earthquake shaking. Intensity measures for duration have been shown to correspond well with degradation of materials and damage in ductile systems. Ductile systems develop damage if the load on the system exceeds the elastic limit, which causes permanent plastic strain to develop. Repeated cycles of loading that exceed the elastic limit cause incremental damage to the system. Long duration motions have many cycles of loading and can cause more damage to plastic systems than short duration motions with similar amplitudes. Brittle, non-ductile systems do not exhibit incremental damage but can fail catastrophically if the loading meets the failure limit. However, the duration of the ground motion does not affect the behavior of non-ductile systems if the amplitude of the loading is below the failure limit. Figure 3.3 shows an example load deformation curve with non-ductile and ductile systems. Soils respond plastically to high shear stresses and intensity measures that model damage in ductile systems are useful for predicting the behavior of soils.

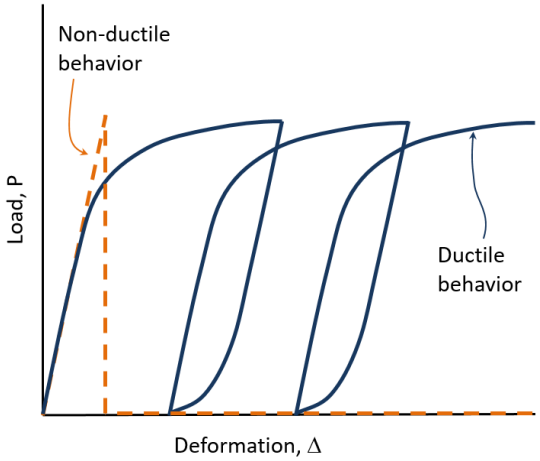

Figure 3.3: Ductile versus non-ductile system behavior.

Not all intensity measures capture the ground motion duration and provide a representative scaler term for evaluating ductile behavior. Common intensity measures associated with earthquake ground motion amplitude and frequency content are peak ground acceleration or spectral acceleration. These intensity measures do not necessarily capture aspects of the earthquake duration. Sideras and Kramer (2012) created suites of motions that all have the same spectral acceleration but have varying durations to show that spectral acceleration can be independent of duration. Intensity measures that characterize the potential effects of earthquake duration are typically derived from a combination of mechanical principles, laboratory testing, or empirical observations. These types of intensity measures typically evolve with time during an earthquake and, when combined with an amplitude intensity measure, are useful for predicting liquefaction triggering and deformation.

3.2.1 *Mechanics-based intensity measures*

Mechanics-based duration intensity measures include bracketed, uniform, or significant duration (Bommer and Martinez-Pereira, 1999). Bracketed duration, t_b, is the time between the first and last exceedances of a threshold acceleration, which is usually 0.05 g. Uniform duration is the total length of time the acceleration is greater than an absolute threshold value, which is usually 0.05 g. Significant duration is the length of time over which a fraction of the total energy or intensity of the ground motion occurs. The time between 5 and 75%, $t_{5\text{-}75}$, or 5 and 95%, $t_{5\text{-}75}$, of the Arias

intensity, I_a, of the ground motion is a common parameter for significant duration. Equations (3.7) and (3.8) define calculations for Arias intensity and significant duration.

$$I_a(t) = \frac{\pi}{2g}\int_0^t a(t)^2 dt \tag{3.7}$$

$$t_{b-c} \equiv I_a\left(t = \frac{c}{100} I_a\right) - I_a\left(t = \frac{b}{100} I_a\right) \tag{3.8}$$

where $a(t)$ is the acceleration time history, g is the acceleration of gravity, and *b* and *c* are percent limits of the evolved intensity.

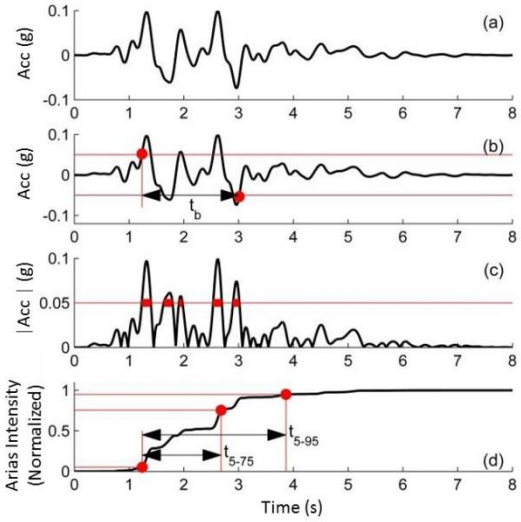

Figure 3.4: Example duration intensity measures (from Sideras and Kramer, 2012). (a) Example acceleration time history. (b) Bracketed duration, t_b. (c) Uniform duration. (d) Significant duration, $t_{5\text{-}75}$ and $t_{5\text{-}95}$.

Several investigators (Kempton and Stewart, 2006; Bommer et al., 2006; Lee and Green, 2014; Afshari and Stewart, 2016) have recently developed ground motion prediction equations (GMPEs) for duration. These GMPEs are based on different data sets that cover different ranges of magnitudes. Figure 3.5 shows the range of 5-95 significant duration versus magnitude for an example site in the western U.S. with v_{s30} = 200 m/s located 5 km from the fault rupture. The ground motion durations were estimated for a range of earthquake magnitudes. Figure 3.5 shows that the duration increases with increasing magnitude, and the rate of increase becomes larger for large magnitude earthquakes. The data used to create these GMPEs generally included observations from ground motions with maximum magnitudes of about M_w = 7.6 or 7.9, depending

on the GMPE. The plots in Figure 3.5 show duration estimates that extrapolate beyond the maximum magnitude as dashed lines. The duration estimates tend to diverge wildly at larger magnitudes, showing that additional data to constrain the behavior for large-magnitude events is needed. At present, predicting ground motion duration for very large magnitude earthquakes is difficult.

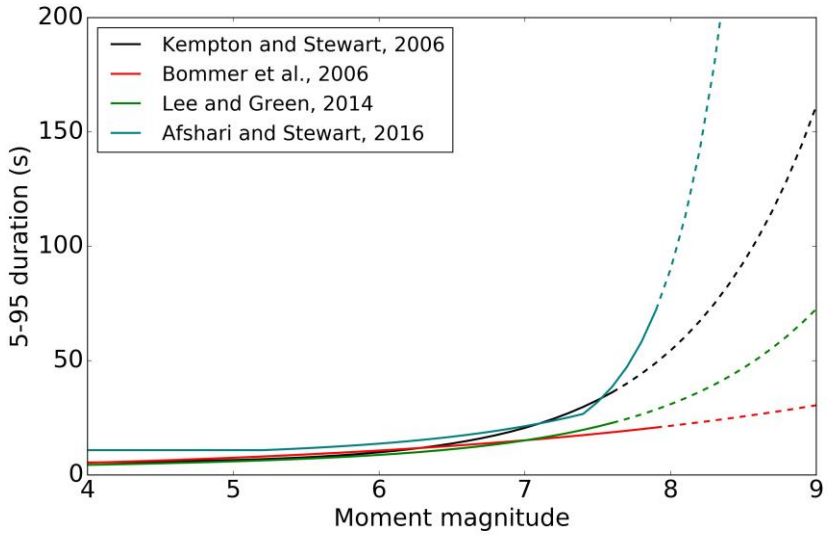

Figure 3.5: Variation of GMPEs for significant duration (from Kramer and Greenfield, 2017). Estimates based on a site in the western U.S. located 5 km from a fault rupture with v_{s30} = 200 m/sec.

3.2.2 *Laboratory-based intensity measures*

Earthquake duration intensity measures associated with liquefaction triggering were originally derived from laboratory testing. Laboratory tests are subject to constraints of stresses, strains, and boundary conditions that can be produced with available testing equipment. In this regard, earthquake loading must be approximated to some degree. Typically, cyclic laboratory testing is limited to the application of constant amplitude loads or deformations, where the frequency of loading is generally controlled and held constant. Liu et al. (2001) showed that the number of loading cycles correlates well with earthquake duration, and that the number of cycles of loading serves as a proxy for ground motion duration. Seed et al. (1975) found that the number of cycles required to initiate liquefaction, n, at cyclic stress amplitude, τ, can be expressed as a simple relationship, which was later formulated as a power law (Idriss and Boulanger, 2008).

$$\frac{\tau}{\tau_{\text{ref}}} = \left(\frac{n}{n_{\text{ref}}}\right)^{-b} \tag{3.9}$$

where τ_{ref} is a reference shear stress, n_{ref} is a reference number of cycles, and b is a soil degradation parameter. The number of cycles of loading, n, is a convenient measure for constant amplitude cyclic loading, but is not applicable for transient loading, as in actual ground motions. Seed et al. (1975) developed a cycle counting procedure to transform a transient shear stress time history into an equivalent number of uniform cycles. Cyclic stress weighting factors, w, used by Seed et al. (1975) were largely based on empirical laboratory evidence and engineering judgment. Their counting procedure indicated that, if one large pulse at τ_{max} triggered liquefaction, then three cycles at a stress 0.65 τ_{max}, and 14 cycles at 0.50 τ_{max}, would also trigger liquefaction. Seed et al. disregarded cycles less than 0.30 τ_{max}, assuming that the shear stress was too low to produce pore pressure and contribute to the overall stress history. They weighted each stress level and summed the weighted number of cycles to develop an equivalent number of uniform cycles at 0.65 τ_{max}. The number of uniform cycles represented the duration of loading for assessing liquefaction potential. This procedure of counting equivalent weighted cycles continues into modern practice. Table 3.1 provides a summary of common equivalent weighting factors for different levels of shear stress (Liu et al., 2001).

$$n = \sum_i w(\tau_i) n_i \tag{3.10}$$

Table 3.1: Equivalent number of cycles at 0.65 τ_{max} (after Liu et al., 2001)

Cycle stress ratio, τ_i / τ_{max}	Weight factor, $w(\tau_i)$	Cycle stress ratio, τ_i / τ_{max}	Weight factor, $w(\tau_i)$
1.0	3.0	0.60	0.7
0.95	2.7	0.55	0.4
0.90	2.4	0.50	0.2
0.85	2.05	0.45	0.1
0.80	1.7	0.40	0.04
0.75	1.4	0.35	0.02
0.70	1.2	<0.30	0.00
0.65	1.0		

Liu et al. (2001) performed regression from over 1,600 ground motion records to estimate the equivalent number of cycles in each record. Equation (3.11) shows the expression for the number of equivalent cycles based on earthquake magnitude, site-to-source distance, and site conditions.

$$\ln n = \ln \left[\frac{\left(\frac{\exp\left(b_1 + b_2 (M_w - m^*)\right)}{10^{1.5\, M_w + 16.05}} \right)^{-\frac{1}{3}}}{4.9 \times 10^6\, \beta} + S\, c_1 + R\, c_2 \right] \tag{3.11}$$

where M_w is the earthquake moment magnitude and β is the shear wave velocity of the source, which is generally equal to 3.2 km/s in the western United States, and R is the site-to-source distance. Variable S is 0 for rock sites and 1 for soil sites. Liu et al. determined coefficients b_1, b_2, m^*, c_1, and c_2 through regression. Regression with field data and laboratory data produced different values of the coefficients, b_1, b_2, c_1, and c_2. Table 3.2 shows the estimated values for these coefficients. Liu et al. recommended averaging the field and laboratory coefficients for future predictions.

Table 3.2: Coefficients for Liu et al. (2001) equation

Coefficient	Laboratory data	Field data	Average
b_1	1.89	0.95	1.53
b_2	1.61	1.35	1.51
c_1	0.668	0.93	0.75
c_2	0.081	0.123	0.095

Kishida and Tsai (2014) also developed a regression procedure to estimate the equivalent number of cycles of loading from transient ground motions records. Their estimates included more detailed parameters to model the amplitude and frequency content in a layer of soil using site response analysis. Additional parameters included the fundamental period of the soil above the layer of interest, T_s, and soil degradation parameter, b. Kishida and Tsai performed equivalent linear site response analyses with different values of T_s, ranging from 0 to 0.6 seconds, values of b ranging from 0.05 to 0.45. They generated over 120,000 data points as part of this analysis, and used the data for regression to estimate the equivalent number of cycles based on several source, path, and

site parameters. Equation (3.11) shows Kishida and Tsai's (2014) GMPE to calculate the equivalent number of cycles.

$$\ln n = \ln\left[\frac{\exp(c_0 + c_1 \ln \mathrm{PGA} + c_2 \ln \mathrm{S_1} + c_3 \mathrm{M_w} + c_4 \ln b + c_5 bT_s) + 0.5}{0.65^{1/b}}\right] \qquad (3.12)$$

where $\mathrm{M_w}$ is the earthquake moment magnitude, PGA is the peak ground acceleration, and $\mathrm{S_1}$ is the ratio of the spectral acceleration at 1.0 and 0.2 s. Figure 3.6 shows a comparison of the equivalent number of cycles of loading based on earthquake magnitude using the procedures from Seed et al. (1983), Liu et al. (2001), and Kishida and Tsai (2014). The data in Figure 3.6 is based on a soil site located 20 km from a fault. Values of PGA and S_1 were calculated using the BCHydro GMPE (Abrahamson et al. 2016). The equivalent number of cycles was calculated for a site with parameters b and T_s equal to 0.3 and 0.1, respectively, for the Kishida and Tsai (2014) method.

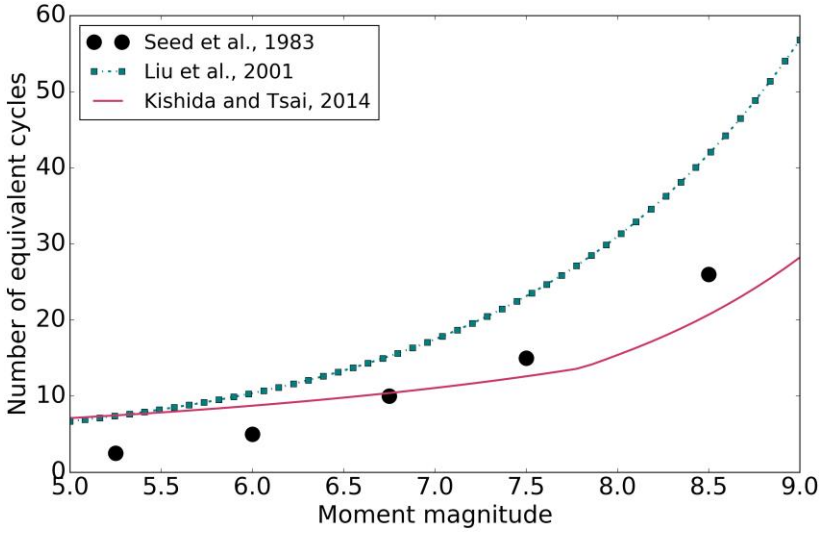

Figure 3.6: Variation of the number of equivalent cycles of loading from different procedures (from Kramer and Greenfield, 2017). Estimates based on a soil site located 20 km from a fault rupture.

Although several methods of cycle counting have been developed for liquefaction triggering analysis, the method of counting cycles is not a trivial consideration for comparing the loading from transient time histories to harmonic loading (Hancock and Bommer, 2004). For transient motions, a rain flow counting definition (Dowling, 1999) is desirable since it counts all the peaks without over-weighting non-zero crossing peaks. Green and Terri (2005) developed a cycle counting procedure for evaluating liquefaction triggering based on work dissipation

principles commonly used for metal fatigue analysis. They normalized individual cycles of loading relative to the number of cycles required to initiate failure, n_{ref}. They also normalized the absorbed energy throughout each cycle of loading, or cumulative work of the system, required to cause failure, w_{ref}. The normalized number of cycles of loading, n_i, and the normalized work, w_i, are proportaional.

$$\sum_i \frac{w_i}{w_{\text{ref}}} = \sum_i \frac{n_i}{n_{\text{ref}}} \tag{3.13}$$

If equivalent linear, elastic stress-strain principles are assumed, the equivalent number of loading cycles can be calculated in terms of applied stress without terms for the shear strain. Green and Terris used a range-mean counting method (Dowling, 1972) to count the shear stress cycles. This approach most closely represented the shear stress-strain hysteresis loops observed in laboratory testing.

$$n = \sum_i \left(n_i \left[\frac{1}{0.65} \frac{\tau_i}{\tau_{\max}} \right]^2 \right) \tag{3.14}$$

The order of cycles has also affects the generation of pore pressure and the triggering of liquefaction. Green and Lee (2006) extended the Green and Terri (2005) framework to an alternative energy-based formulation that accounted for the order of loading cycles based on metal fatigue analysis. The Richart-Newmark Hypothesis assumed that materials exhibit load-dependent cumulative damage in a recursive formulation. The damage parameter, D, is based on the previous level of damage plus the ratio of the current loading cycle with exponent, r_m, which is based on material properties.

$$D_m = \left[(D_{m-1})^{1/r_m} + \left(\frac{n_m}{n_{\text{ref}}} \right) \right]^{r_m} \tag{3.15}$$

Figure 3.7 shows the effects of the Richart-Newmark hypothesis on damage potential for two loading conditions: one condition case where a large pulse occurred early in the motion and a second condition where a large pulse occurs late in the motion. The motion with the large pulse later in the recorded caused greater damage.

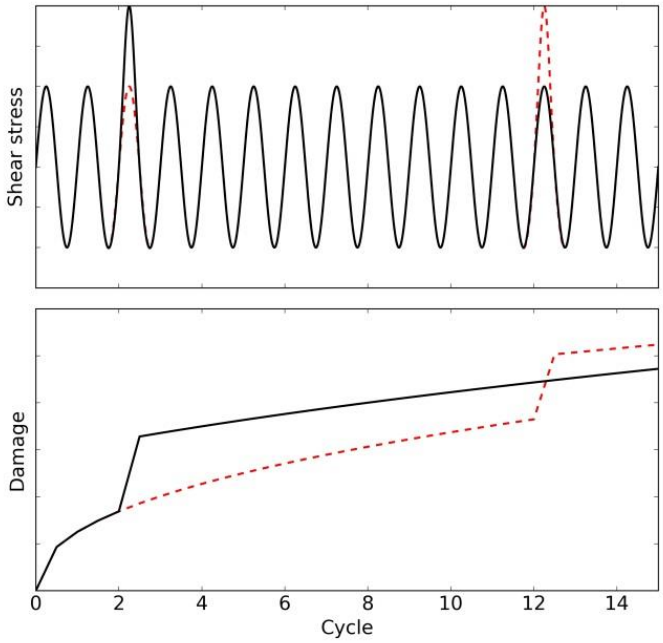

Figure 3.7: Example of Richart-Newmark damage hypothesis. The solid black line represents a motion where a high-amplitude pulse occurs early in the motion and the dashed red line represents a motion where a high-amplitude pulse occurs later in the motion.

Laboratory observations and analyses based on the principles of work require detailed measurements of shear stress and strain. Since the shear stresses and strains cannot be directly measured within a soil layer during an earthquake, recorded ground surface motions are used to estimate the transient shear stresses in soil layers below the ground surface. Many procedures use either equivalent linear site response analysis (Cetin et al. 2004) or rigid body mechanics with a factor to account for wave dynamics (Seed and Idriss, 1971; Youd et al., 2001) to estimate the shear stress within a soil layer during an earthquake. Because the shear stress time history must be inferred through a separate analysis, the number of cycles of loading from transient earthquake shaking is not necessarily convenient or easy to calculate for liquefaction predictions. In the "simplified procedure" for liquefaction triggering analysis (Seed et al., 1983; Cetin et al., 2004; Boulanger and Idriss, 2014), a depth reduction term, r_d, is used to account for the variation in shear stress with respect to depth, and the magnitude scaling factor is used to account for the number of cycles of loading. The simplified liquefaction triggering procedure was introduced and discussed in Chapter 2, but important details about the magnitude scaling factor are discussed subsequently.

3.2.3 *Magnitude scaling factor*

Since earthquake magnitude is related to earthquake duration, a magnitude scaling factor, MSF, is usually used as a proxy for the number of cycles of loading for liquefaction analysis. Seed et al. (1971) developed empirically based magnitude scaling factors for the simplified liquefaction triggering procedure. For liquefaction analysis, they normalized the cyclic resistance ratio by the MSF to account for the variation of the number of cycles of loading for different earthquake magnitudes.

$$\mathrm{FS} = \frac{\mathrm{CRR}_{7.5}}{\mathrm{CSR} \cdot \mathrm{MSF}} \tag{3.16}$$

where $\mathrm{CRR}_{7.5}$ is the cyclic resistance ratio for a $\mathrm{M}_w = 7.5$ earthquake. The results from laboratory tests discussed previously indicated that the normalized shear stress was related to the number of cycles of loading by a power law.

$$\mathrm{MSF} = \frac{\tau}{\tau_{\mathrm{ref}}} = \left(\frac{n}{n_{\mathrm{ref}}}\right)^{-b} \tag{3.17}$$

Seed et al. (1971) proposed that the reference number of cycles, n_{ref}, was 15 for a $\mathrm{M_w}$ = 7.5 earthquake. Hence, the MSF is equal to 1.0 for M_w = 7.5 earthquakes, is greater than 1.0 for M_w < 7.5, and is less than 1.0 for M_w > 7.5. The initial equations relating the number of equivalent cycles, earthquake magnitude, and magnitude scaling factor were proposed largely based on engineering judgement. Table 2.1 provides the magnitude scaling factors used in early liquefaction triggering analysis (Seed et al., 1983).

Since its initial proposal, the functional form of the magnitude scaling factor has been investigated by many authors (e.g. Arango, 1996; Bommer and Martinez-Pereira, 1999; Youd et al., 2001; Green and Terri, 2005; Cetin and Bilge, 2012; Boulanger and Idriss, 2014; etc.). Data collected from liquefaction case histories in the 1980's indicated that the original Seed et al. (1983) magnitude scaling factors were overly conservative for earthquakes with $\mathrm{M_w}$ < 7.5. Ambraseys (1988) performed a statistical analysis of the average stress ratios necessary to trigger liquefaction. He developed magnitude scaling factors by separating the liquefaction case histories into different bins of varying earthquake magnitudes, and then analyzed the relationship between CSR and SPT penetration resistance within each of bins. These magnitude scaling factors tended to be much greater than the Seed and Idriss (1982) magnitude scaling factors for earthquakes with $\mathrm{M_w}$ < 7.5,

and much lower for earthquakes with $M_w > 7.5$, indicating the original magnitude scaling factors proposed by Seed and Idriss (1982) were not sensitive enough to earthquake magnitude.

Arango (1996) developed two separate magnitude scaling factors based on fundamental principles of energy. The first magnitude scaling factor used ground motion prediction equations with observations of the furthest effects of liquefaction to estimate the minimum energy required to trigger liquefaction. The second magnitude scaling factor used principals of absorbed energy from transient motions with the original scaling factors proposed by Seed et al. (1983). The analysis of the absorbed energy indicated the value of b in equation (3.17) should be equal to 0.5. These two magnitude scaling factors did not necessarily agree, but rather bracketed the range of possible magnitude scaling factors.

Two workshops in 1996 and 1998 (Youd and Idriss, 2001) attempted to update the simplified liquefaction triggering procedure and incorporate findings that had occurred since Seed et al. (1983) published their original findings. One of the many purposes of the workshops was to review the available magnitude scaling factors and develop a consensus of which MSFs were appropriate for practical use. Many of the MSFs were formulated as a power law with respect to earthquake magnitude.

$$\text{MSF} = \left(\frac{7.5}{M_w}\right)^c \tag{3.18}$$

The results presented by Andrus and Stokoe (1997), Arango (1996), and Ambraseys (1988) were relatively similar and represented an upper bound of MSF for practical purposes with an exponent, $c = 2.56$. Youd and Nobel (1997) recommended different magnitude scaling factors depending on the probability of liquefaction. For a probability of liquefaction less than 50%, they recommend a value of c as high as 4.21. There is no theoretical reason that the earthquake magnitude and number of equivalent cycles of loading are related as a power law, as in equation (3.18), and Idriss (1999) proposed an alternative expression for MSF.

$$\text{MSF} = 6.9 \exp\left(\frac{-M_w}{4}\right) - 0.06 \tag{3.19}$$

The conclusion of the workshop was that a range of possible magnitude scaling factors should be considered, rather than one specific magnitude scaling factor. They recommended greater conservatism for large magnitude earthquakes since very few case histories are available for $M_w > 8$.

The magnitude scaling factors presented by Youd et al. (2001) only include source terms (M_w) and did not consider possible path and site effects that could impact the number of cycles of loading and would be important for liquefaction triggering analysis. Liu et al. (2001) combined estimates of an equivalent number of cycles based on magnitude, distance, and site characteristics (rock or soil) with the Arango (1996) energy-based magnitude scaling factor to develop an alternative expression for magnitude scaling factor.

$$\ln(\text{MSF}) = a_1 + a_2 \cdot \ln(n) \tag{3.20}$$

where n is the number of equivalent cycles of loading. They found strong correlation between the number of equivalent cycles of loading and the earthquake magnitude and distance, and weaker correlation between the number of cycles of loading and site conditions and near-fault directivity effects. They determined different coefficients based on the regressions with field and laboratory liquefaction observations. Values for a_1 and a_2 were equal to 1.7 and -0.5 based on the field-based observations, and 1.1 and -0.37 based on the laboratory observations. Liu et al. recommended mean values of 1.3 and -0.41 for liquefaction analysis. The functional form of this magnitude scaling factor was the same as the power law proposed in equation (3.18), but the number of reference cycles was not necessarily equal to 15. Liu et al.'s findings implied that magnitude scaling factors were greater in field conditions than in laboratory conditions, and the number of cycles for an M_w = 7.5 earthquake was 24, based on the recommended coefficients.

Cetin et al. (2004) used available case histories with Bayesian updating to develop an expression for the probability of liquefaction based on liquefaction case histories with SPT penetration resistance. They used earthquake magnitude a variable in their regression analysis, so the resulting equation for the probability of liquefaction did not explicitly depend on the number of cycles of loading or magnitude scaling factor. Additional discussion about the Cetin et al. (2004) procedure is provided in Chapter 2. Moss et al. (2006) used data from the Cetin et al. (2004) procedure to develop a similar probabilistic framework for cone penetration resistance. They recommended a power law magnitude scaling factor, equation (3.18), with exponent $c = 1.43$.

Cetin and Bilge (2012) showed that the magnitude scaling factors depended not only on the number of equivalent cycles of loading but also on the level of shear strain or pore pressure ratio for estimating the MSF at factors of safety other than 1.0. These performance-based magnitude scaling factors varied from the MSFs developed from the analysis of binary case

histories, which were intended to predict a decisions function where FS = 1.0. Cetin and Bilge created two separate magnitude scaling factors based on performance levels of either the maximum pore pressure ratio or maximum shear strain. The exponent b in equation (3.17) was calculated using regression to laboratory data.

$$\ln(-b) = \ln\Big(-0.621\left[{r_u}^{4.803}(2.506\ \ln D_R - 19.134) + {r_u}^{5.549}\left(0.645\ \ln \sigma'_{v,0} + 7.798\right) + 0.621\right]\Big) \tag{3.21}$$

$$\ln(-b) = \ln\Big(-0.03\left[{\gamma_{\max}}^{1.308}(1.953\ \ln D_R - 6.719) + {\gamma_{\max}}^{1.687}\left(0.529\ \ln \sigma'_{v,0} - 1.538\right) + 0.231\right]\Big) \tag{3.22}$$

where r_u is pore pressure, is $\gamma_{\max}$ the maximum shear strain, D_R is the relative density, and $\sigma'_{v,0}$ is the initial effective overburden pressure. Cetin and Bilge used the resulting values for b with empirically observed field data to calculate a relationship between the number of cycles of loading and a magnitude scaling factor. The relationship was relatively insensitive to fault rupture distance, and exponent c in equation (3.18) was directly related to the material property b.

$$\ln(c) = \ln([-6.0591 + 0.312\ S]\ b^{1.4391}) \tag{3.23}$$

where $S = 0$ for rock sites and $S = 1$ for soil sites. Cetin and Bilge then used the maximum shear strain with empirical observations from case histories to estimate the shear strain associated with surface manifestation of liquefaction. Looser soils appeared to manifest surface characteristics of liquefaction at a lower shear strain than denser soils, indicating the magnitude scaling factor should be function of the dilatational characteristics of the soil. A magnitude scaling factor that incorporated different levels of shear strain or pore pressure was also useful for performance-based earthquake engineering, where varying levels of deformation may be tolerable over a wide range of return periods. However, the dependence of magnitude scaling factor on material properties complicates the computation of the cyclic stress ratio and the probability of liquefaction for probabilistic seismic hazard analysis.

Kishida and Tsai (2014) indicated the equivalent number of cycles of loading depends not only on the earthquake magnitude but also on the properties of the fundamental frequency of the site and properties of the soil layers. They proposed a refinement of typical liquefaction demand parameters that incorporated PGA, a depth reduction factor, r_d, and the number of cycles of loading, n. Their GMPE relationship predicted an equivalent number of cycles of loading, the equation for n is provided in equation (3.12). Kishida and Tsai formulated a demand parameter,

$K_{1\text{cyc}}$, to incorporate the aleatoric uncertainty in PGA, r_d, and n. They also calculated the variance of loading intensity, $\sigma^2_{\ln K_{1\text{cyc}}}$, using this parameter.

$$\ln K_{1\text{cyc}} = \ln \frac{0.65}{\text{g}} + \mathbf{b'\mu} \tag{3.24}$$

$$\sigma^2_{\ln K_{1\text{cyc}}} = \mathbf{b'V^{1/2}\rho V^{1/2}b} \tag{3.25}$$

$$\mathbf{b'} = [1 \quad 1 \quad b] \tag{3.26}$$

$$\boldsymbol{\mu} = [\text{E}[\ln PGA] \quad \text{E}[\ln r_d] \quad \text{E}[\ln n]] \tag{3.27}$$

where $\mathbf{V^{1/2}\rho V^{1/2}}$ is the covariance matrix of $\ln PGA$, $\ln r_d$, and $\ln n$. Kishida and Tsai's framework can incorporate many earthquake sources into a multi-hazard or performance-based analysis. They analyzed several different architype sites using data from the PEER NGA database (Bozorgnia et al., 2014). They then calculated magnitude scaling factors at each site using different soil and site parameters to calculate the uncertainty in magnitude scaling factors. They defined the magnitude scaling factors in the same ways as equation (3.17), but the reference number of cycles for a M_w = 7.5 earthquake varied depending on site and loading conditions. For example, Kishida and Tsai's procedure indicated that a M_w = 7.5 earthquake produced about 13 cycles of loading for the example in Figure 3.6.

Recent updates to the liquefaction analysis procedures (Boulanger and Idriss, 2014) included an MSF that was based on earthquake magnitude and properties related to the relative density and dilatational characteristics of the soil, such as $(\text{N}_1)_{60\text{cs}}$. Previous magnitude scaling factors used by Idriss and Boulanger (2008) implied that the value of exponent b was equal to 0.34 for sand and 0.135 for clays. However, laboratory tests indicated that the value of b depended on the relative density of the soil, and approached zero as the relative density approached zero. The exponent b was specifically important for a limiting maximum magnitude scaling factor in the framework proposed by Boulanger and Idriss (2014). They calculated the maximum magnitude scaling factor based on a single acceleration pulse, which corresponded to ¾ of a cycle of loading.

$$n_{\min} = \left(\frac{1.0}{0.65}\right)^{\frac{1}{b}} \left(\frac{3}{4} \text{ cycle}\right) \tag{3.28}$$

$$\mathrm{MSF}_{\max} = \left(\frac{n_{\min}}{n_{\mathrm{ref}}}\right)^{-b} \tag{3.29}$$

Since the exponent b varied with relative density, the maximum magnitude scaling factor also varied with relative density. The maximum magnitude scaling factor was, therefore, also a function of the penetration resistance of the soil.

$$\mathrm{MSF} = 1 + (\mathrm{MSF}_{\max} - 1)\left[8.64 \exp\left(\frac{-M}{4}\right) - 1.325\right] \tag{3.30}$$

$$\mathrm{MSF}_{\max} = 1.09 + \left[\frac{(\mathrm{N}_1)_{60\mathrm{cs}}}{31.5}\right]^2 \leq 2.2 \tag{3.31}$$

Figure 3.8 shows the magnitude scaling factors relationship versus the number of cycles of loading recommended by Idriss and Boulanger (2014) and Cetin and Bilge (2012). Idriss and Boulager (2014) limited the CSR at a low number of cycles by limiting the magnitude scaling factor to a maximum value, $\mathrm{MSF}_{\max}$. The value of b using Cetin and Bilge's (2012) recommendations was based on a maximum cyclic shear strain of 3%.

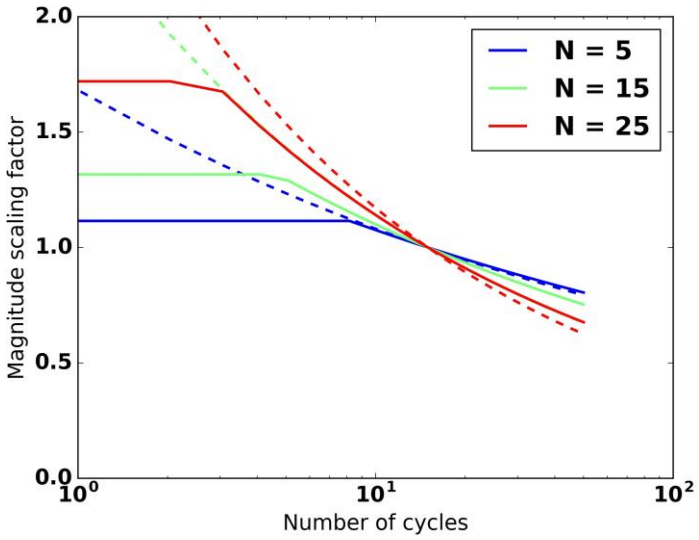

Figure 3.8: Magnitude scaling factor and the number of cycles of loading. Solid lines from Boulanger and Idriss (2014). Dashed lines from Cetin and Bilge (2012).

Kramer et al. (2016) redefined the MSF produced by Boulanger and Idriss as a product of two independent terms, $\mathrm{MSF}_{\mathrm{L}} \cdot K_M$, where $\mathrm{MSF}_{\mathrm{L}}$ was independent of relative density.

$$\mathrm{MSF}_L = 0.580 + 2.737 \exp(-M/4) \tag{3.32}$$

$$K_M = \frac{1 + (\mathrm{MSF}_{max} - 1)\,(8.64\exp[-M/4] - 1.325)}{0.580 + 2.737\exp(-M/4)} \tag{3.33}$$

The calculation of MSF_L was equivalent to the calculation of MSF using Boulanger and Idriss's procedure (2014) for $N_{1,60}$ = 15 blows/ft. To compare liquefaction triggering potential for actual ground motions, Kramer et al. calculated values of MSF_L using equations (3.28) and (3.29) for an equivalent number of cycles of loading. These equations indicate that, when n_{ref} = 15 cycles, exponent b = 0.236. These values are consistent with the CPT-based values of b published by Boulanger and Idriss, which are shown in Figure 3.9.

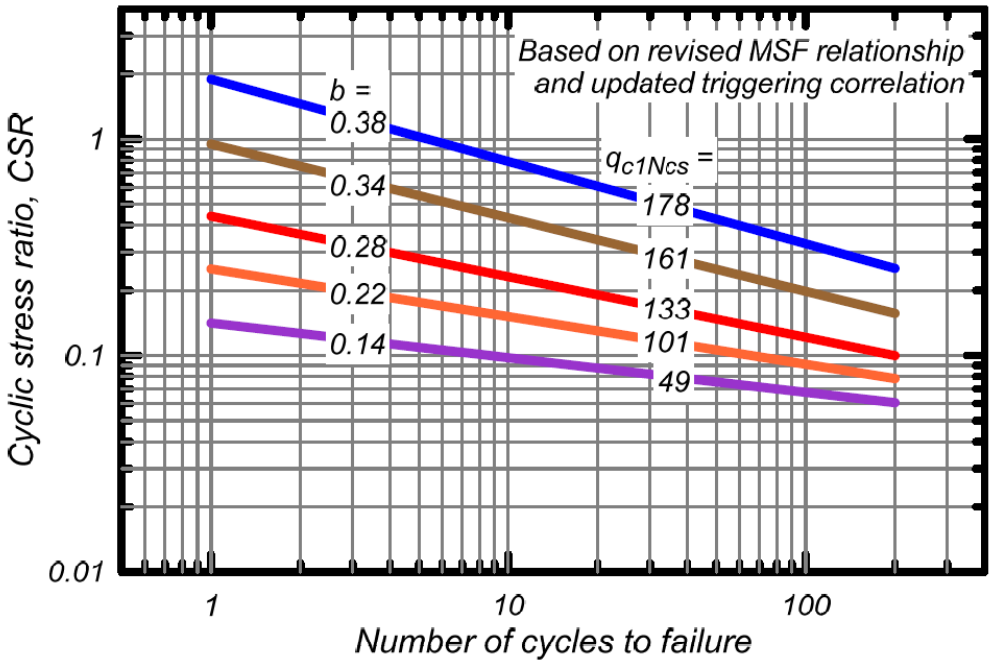

Figure 3.9: Cyclic stress ratio for Boulanger and Idriss's (2014) CPT-based procedure.

With these values, an intensity measure for magnitude-adjusted PGA that is independent of the relative density of the soil can be calculated. Calculating an intensity measure that is independent of subsurface properties is generally advantageous for probabilistic seismic hazard analysis and performance-based liquefaction analysis. Equation (3.32) can be used to calculate an intensity measure for liquefaction triggering, $\mathrm{PGA_M}$, as long as the MSF is less than $\mathrm{MSF_{max}}$, which was 1.317 for $(N_1)_{60}$ = 15.

$$\mathrm{PGA}_M = \frac{\mathrm{PGA}}{\mathrm{MSF}_L} \tag{3.34}$$

3.2.4 *Empirically-based duration intensity measures*

Regression to other intensity measures based on empirical observations has also been used to approximate the effects of earthquake duration for liquefaction analysis. As discussed in the previous section, most laboratory-based liquefaction triggering intensity measures are based on the number of cycles of loading. For transient stresses induced by earthquakes, Hancock and Bommer (2004) showed that no single intensity measure fully encompassed the number of cycles of loading. Uniform duration appeared to provide the best correlation to the number of cycles of loading, although no liquefaction triggering procedures have been developed to include the effects of uniform duration.

Other intensity measures that included the effects of duration for liquefaction triggering analysis have been considered. Kayen and Mitchell (1997) developed a liquefaction triggering procedure based on Arias intensity. Green and Mitchell (2003) indicated that Arias intensity inherently included the amplitude, duration, and frequency content of earthquake ground motions. Parameters like Arias intensity are related to fatigue in other engineering materials. Arias intensity can be formulated to accommodate multiaxial loading, although multiaxial loading has recently been incorporated into the calculation of CSR as well (Cetin and Bilge, 2012). Despite the promise of and Arias intensity-based procedure for liquefaction triggering analysis, further development may be necessary before liquefaction triggering can be evaluated (Green and Lee, 2006).

Kramer and Mitchell (2006) studied over 300 intensity measures to determine which intensity measure had the lowest variance for estimating the pore pressure ratio in a series of numerical analyses. In their study, pore pressure ratios from 450 input motions at nine hypothetical sites were simulated using finite-difference analysis. Cumulative absolute velocity (CAV) with a cutoff at 5 gals (CAV_5) had the best correlation with pore pressure generation.

$$\mathrm{CAV}(t) = \int_0^t |a(t)|dt \tag{3.35}$$

$$\mathrm{CAV}_5(t) = \int_0^t \begin{Bmatrix} |a(t)| & |a(t)| \geq 0.005g \\ 0 & |a(t)| < 0.005g \end{Bmatrix} dt \tag{3.36}$$

An integrated, evolutionary parameter such as CAV inherently incorporates the earthquake duration. Through their analysis, Kramer and Mitchell (2006) also indicated pore pressure

generation was more closely related to shear strain than shear stress. In an elastic medium, the shear strain, γ, is related to the particle velocity, $\dot{u}$, through simple differentiation.

$$\gamma = \frac{\partial u}{\partial z} = \frac{\partial u/\partial t}{\partial z/\partial t} = \frac{\dot{u}}{v_s} \tag{3.37}$$

So, a parameter related to ground surface velocity should be a good predictor of shear strain and pore pressure through simple mechanics. Using CAV_5 as opposed to CAV reduced the effect of low amplitude strain cycles, which may not contribute significantly to the generation of excess pore pressure.

3.2.5 *Limitations of available data*

Despite efforts to develop liquefaction triggering relationships for long duration earthquakes, limited case histories are currently available. The liquefaction observation from the largest magnitude earthquake in the Cetin et al. (2004) liquefaction triggering database was the 1968 M_w = 8.3 Tokachi-Oki earthquake. The Boulanger and Idriss (2014) database included very few observations for earthquake magnitude $M_w > 7.8$. Figure 3.10 shows histograms of the liquefaction databases versus earthquake magnitude (NASEM, 2016).

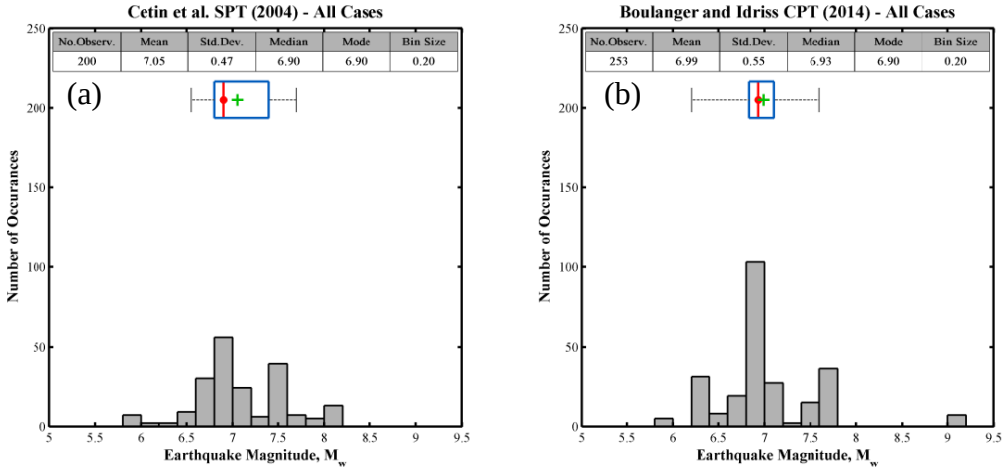

Figure 3.10: Histograms of earthquake magnitude in liquefaction databases (from NASME, 2016). (a) Cetin et al. (2004) data. (b) Boulanger and Idriss (2014) data.

Evaluating liquefaction potential for very large magnitude earthquakes, which have very long durations, extrapolated beyond the data used to develop the liquefaction triggering procedures. Magnitude scaling factors based on laboratory data alone tended to underestimate the

cyclic resistance of the soil for earthquakes with $M_w < 7.5$ and overestimate the cyclic resistance for earthquakes with $M_w > 7.5$. To understand the effects of long duration motions, suites of ground motions have been developed to isolate the characteristics of long-duration ground motions. These suites of motions can be used to identify aspects of the motions that may affect the behavior of liquefiable soil.

3.3 GROUND MOTIONS WITH SPECIFIC DURATION CHARACTERISTICS

Several suites of ground motions have been created for this study to isolate the effects of duration from those of amplitude and frequency content. Each suite of motions either isolates the duration of the ground motions or isolates factors that contribute to long-duration motions. Table 3.3 provides a summary of the suites of ground motions collected for this study.

Table 3.3: Summary of ground motion suites

• Band-limited white noise	Synthetic motions with the same Fourier amplitude spectrum, but with different time-domain envelopes. This suite isolates ground motion duration.
• High-passed filtered white noise	Synthetic motions with filtered low-frequency content. This suite of shows the correlation between frequency content and duration.
• Liquefaction-consistent motions	Recorded motions from crustal and subduction zone earthquakes with similar magnitude-adjusted PGAs.
• Spectrum-compatible motions	Spectrally matched motions with similar response spectra.
• Basin motions	Recorded motions from Japanese earthquakes that include ground motions inside and outside of basins. This suite shows the effects of deep sedimentary basins on duration.
• Cascadia Subduction Zone	Synthetic simulations of a $M_w = 9.0$ Cascadia Subduction Zone rupture. This suite shows the effects of basins, asperity sub-events, and directivity on an event of local interest.

Intensity measures for duration were calculated from the motions in each of these suites. These intensity measures represent unique measures that capture specific aspects of the ground motion. Table 3.4 lists the intensity measures that were analyzed in this study.

Table 3.4: Intensity measures for duration

Intensity measure	Captures
Significant duration	Duration
Bracketed duration	Duration, and some aspects of amplitude
Arias intensity	Duration, amplitude, and frequency content
Cumulative absolute velocity	Duration, amplitude, and frequency content
Magnitude-adjusted PGA	Amplitude and duration

The magnitude-adjusted PGA depends on the magnitude scaling factor, and many possible MSFs are available to calculate the number of cycles of loading. A distinction must be made between MSFs calculated using earthquake metadata (M_w), and MSFs calculated using the equivalent number of cycles calculated from a recorded ground motion. To avoid confusion, in this section, intensity measures calculated using M_w are referred to as magnitude-adjusted PGA, and intensity measures calculated using an equivalent number of cycles are referred to as cycle-adjusted PGA. For general conditions, the magnitude-adjusted PGA was calculated using the recommendations provided by Boulanger and Idriss (2014) with $(N_1)_{60}$ = 15 blows/ft. The cycle-adjusted PGA was calculated by counting the number of cycles of loading, adjusting the cycles to an equivalent number of cycles at $0.65\,\tau_{max}$, and then calculating a MSF using both the recommendations from by Liu et al. (2001) and an adaptation of Boulanger and Idriss (2014).

3.3.1 *Isolation of duration effects: band-limited white noise*

Brune (1970) developed a theoretical expression for the Fourier amplitude spectrum the resulted from a circular rupture to simulate an earthquake. A suite of motions was produced based on a constant Fourier amplitude spectrum that was calculated using the Brune solution. Each of the motions in the suite had a different duration, which was defined by a Saragoni and Hart (1974) time-domain envelope. To generate these motion, the Fourier amplitude spectrum was combined with a random phase component (white noise) and then inverted into the time domain. The Saragoni and Hart (1974) envelope function was used to create a suite of 100 motions with significant duration ranging from 10 to 110 seconds by appropriately varying the parameters of in the time-domain window. Based on the method by which these motions were created, the distribution of the duration should be nearly uniform.

To calculate these motions, the corner frequency of the Brune spectrum was set to 0.5 Hz, and a cutoff frequency of 10 Hz was applied. The motions were scaled in the time domain such that the peak acceleration was equal to 0.30 g. Figure 3.11 shows histograms of the duration intensity measures for the suite of band-limited white noise.

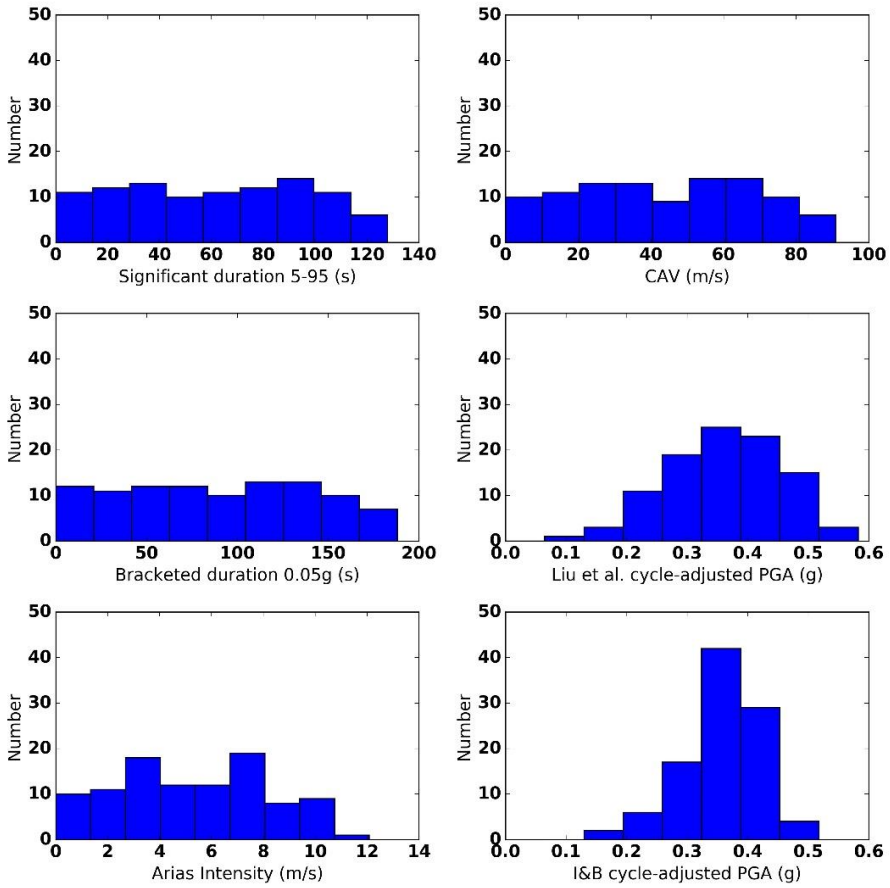

Figure 3.11: Duration intensity measures for band-limited white noise

By design, the ground motions in Figure 3.10 should have a uniform distribution of duration. However, due to the stochastic differences of the ground motions, the shape of the time envelope window, and other aspects of the ground motions that influenced the intensity measures, the distribution was not necessarily uniform. Significant duration appeared to be the best representation of the uniform distribution of duration. Bracketed duration, cumulative absolute velocity, and Arias intensity also produced good representations of the uniform distribution. The cycle-adjusted PGA produced distributions that were approximately normally distributed and were

inconsistent with a uniform distribution of duration. These *IM*s primarily captured the peak ground acceleration of the motions, which was set to 0.30 g.

3.3.2 *Isolation of low-frequency effect: high-pass filtered white noise*

The frequency content of earthquake motions is not uniform across all frequencies and tends to be band-limited between a lower-bound corner frequency and an upper-bound cutoff frequency. Within a geographic region, the lower-bound corner frequency depends primarily on the earthquake magnitude, and the amplitude of frequencies less than the corner frequency diminish quickly. A suite of ground motions that all have the same duration and amplitude characteristics, but different corner frequencies illustrate the effect of different corner frequencies. A suite of 100 filtered motions was created using a Saragoni and Hart (1974) time-domain envelope window with a duration of about 60 seconds. The motions were then filtered using a first-order high-pass Butterworth filter with a corner frequency ranging from about 0.01 to 5 Hz to create motions with variable low-frequency content. The motions were also low-passed filtered with a cut-off frequency of 10 Hz. After high and low-pass filtering, the motions were rescaled to a PGA of 0.30 g. Plots of spectral acceleration best illustrate the effects of the variable corner frequency on the low-frequency components of motion. The variation in corner frequency generally affected the long period spectral accelerations the greatest, and the motions with high corner frequencies had much less long-period spectral acceleration than the motions with low corner frequencies. The effect of varying the corner frequency also diminished the peak acceleration of the motions before rescaling. The rescaling caused some of the motions with a high corner frequency to have a larger short period spectral acceleration than motions with a lower corner frequency. Figure 3.12 shows a plot of the spectral acceleration of the filtered white noise motions.

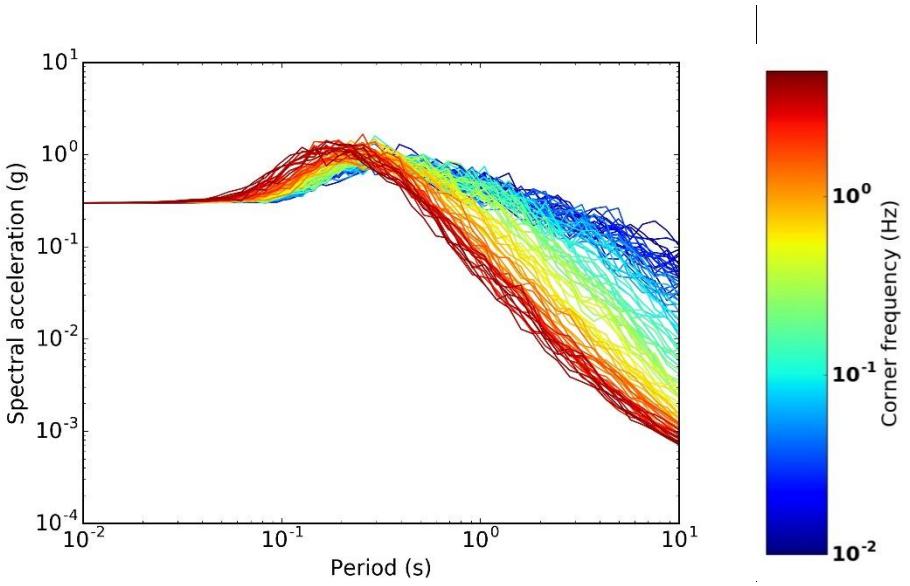

Figure 3.12: High-pass filtered band limited white noise. Motions designed to have the same duration, but with different corner frequencies.

By design, this suite of the motions should not vary in duration and intensity measures that are not influenced by the frequency content of ground motions should be identically distributed. Intensity measures that also captured the frequency content of the motions would vary based on the corner frequency. Figure 3.13 shows histograms of the six duration metrics.

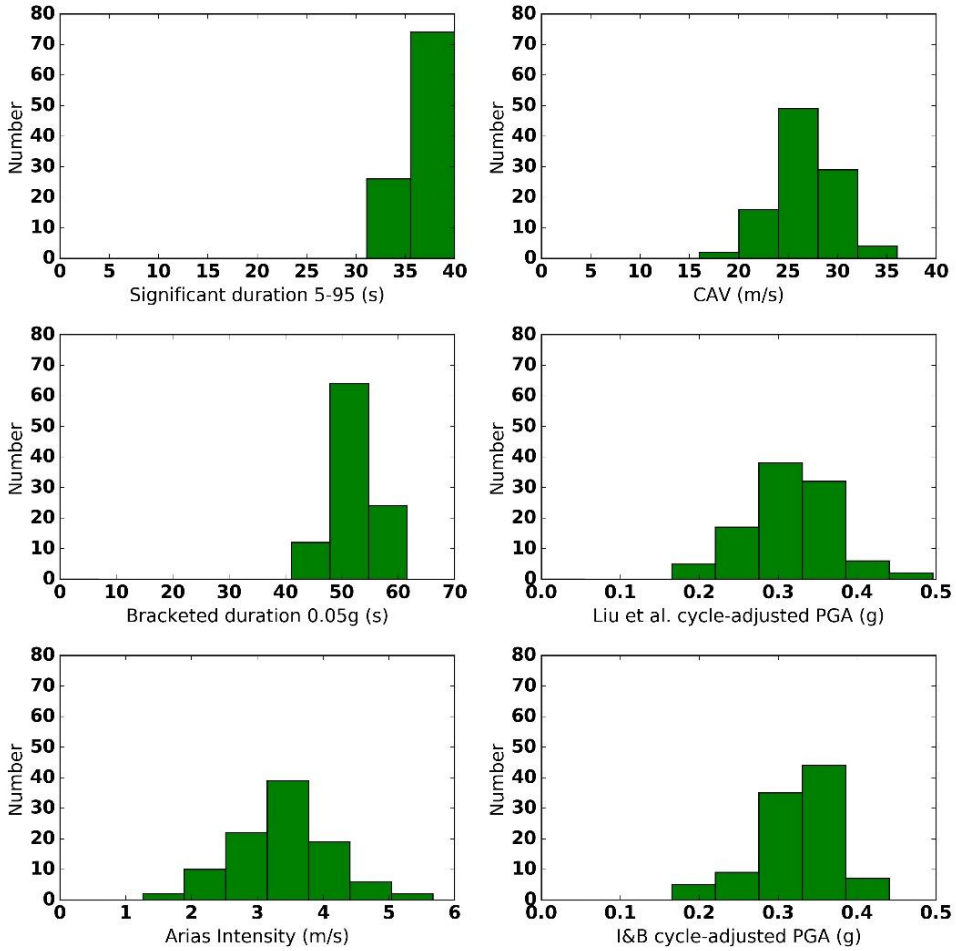

Figure 3.13: Duration intensity measures for filtered white noise.

Significant duration and bracketed duration had the lowest variance, indicating that changes in the frequency content did not greatly affect these intensity measures. In general, significant duration and bracketed duration only captured the duration of the motion. Arias intensity, cumulative absolute velocity, and cycle-adjusted PGA were all affected by variation in corner frequency, and these intensity measures capture not only on the duration of the motion, but also the frequency content of the motion.

3.3.3 *Crustal ground motions*

The NGA West-2 (Bozorgnia et al., 2014) project has produced a flatfile with metadata from over 21,000 earthquakes. The data were filtered for strong motion records with PGA greater than 0.05 g, earthquake magnitude $M_w > 5.25$, and sites on stiff ground or rock ($v_{s30} > 600$ m/s) to eliminate

amplification or frequency content changes that may have been caused by layers of soft soil. Records from 229 ground motions matched the criteria. The selected ground motions included a range of different earthquake magnitudes and distances, all with different ground motion durations, amplitudes, and frequency contents. Figure 3.14 shows the six duration intensity measures plotted against earthquake magnitude. The data is plotted on a semilog scale, which had better correlation with the duration intensity measures than data on a linear scale. Table 3.5 shows the correlation coefficient of each of the intensity measures with earthquake magnitude.

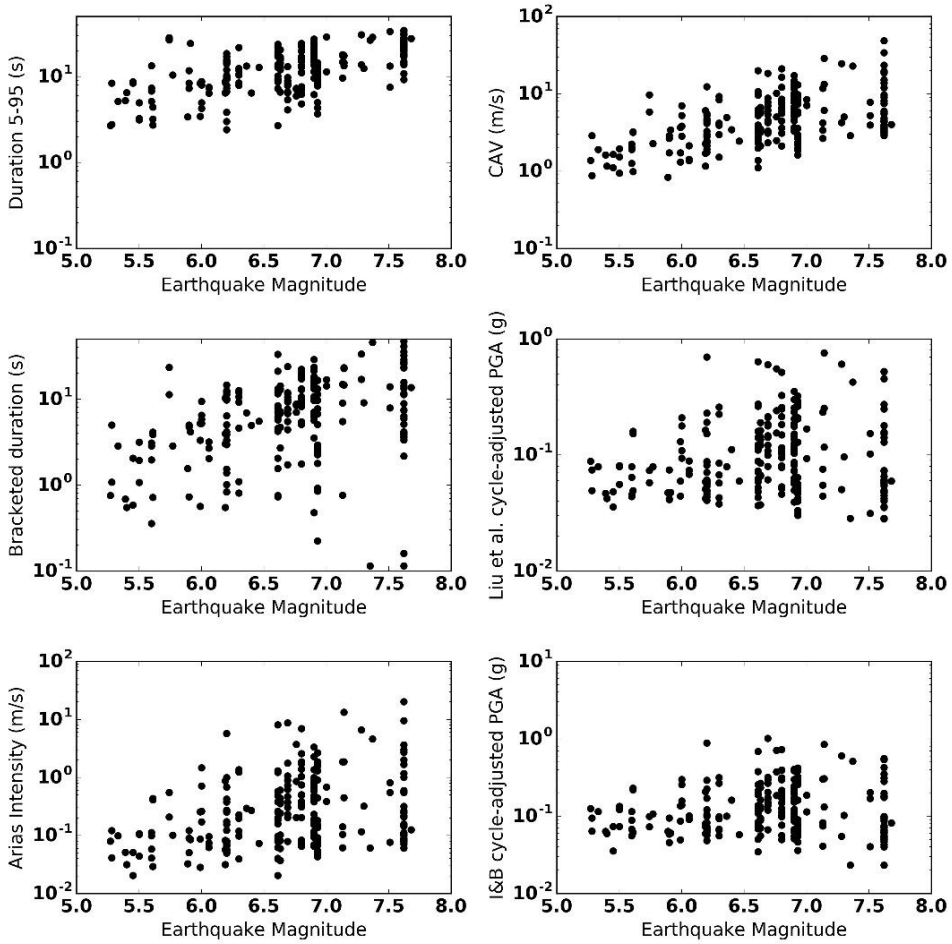

Figure 3.14: Correlation of duration intensity measures with earthquake magnitude for crustal ground motions.

Table 3.5: Correlation of duration intensity measures with earthquake magnitude for crustal ground motions

Intensity measure, *IM*	Transformation	Correlation Coefficient
Duration, 5-95	Exponential	0.59
Bracketed duration	Exponential	0.25
Arias intensity	Exponential	0.31
Cumulative absolute velocity	Exponential	0.51
Cycle-adjusted PGA (Liu et al., 2001)	Exponential	0.13
Cycle-adjusted PGA (Boulanger and Idriss, 2014)	Exponential	0.09

In general, large magnitude earthquakes should have longer durations than smaller magnitude earthquakes. The amplitude and frequency content of ground motions also depends on the rupture distance, so intensity measures that are not influenced by ground motion amplitude or frequency content should be very well correlated with earthquake magnitude. Significant duration was largely independent of the frequency content and amplitude of the motion and had the strongest correlation with earthquake magnitude. Cumulative absolute velocity (CAV) was also somewhat correlated with earthquake magnitude and showed a better correlation with earthquake magnitude than Arias Intensity. Cycle-adjusted PGA inherently includes the number of cycles of loading, so it was nearly independent of earthquake magnitude.

The duration intensity measures were also plotted against rupture distance to show trends in duration versus distance. Figure 3.15 shows a scatter plot of the duration intensity measures versus rupture distance and Table 3.6 shows the correlation coefficient between each of the intensity measures. The data was fit to a log-log scale, which had better correlation with the duration intensity measures than data on a linear scale.

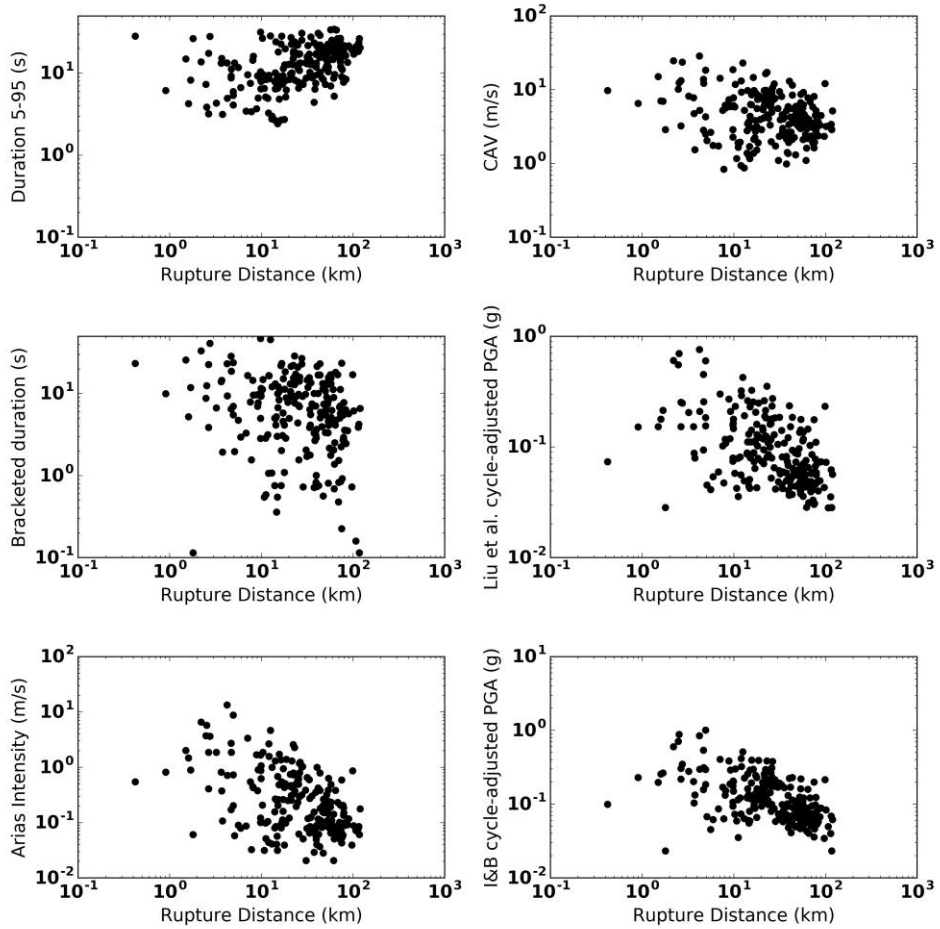

Figure 3.15: Correlation of duration intensity measures and rupture distance for crustal ground motions.

Table 3.6: Correlation of duration intensity measures and rupture distance for crustal ground motions.

Intensity measure, *IM*	**Transformation**	**Correlation Coefficient**
Duration, 5-95	Power	0.30
Bracketed duration	Power	-0.31
Arias intensity	Power	-0.59
Cumulative absolute velocity	Power	-0.42
Cycle-adjusted PGA (Liu et al., 2001)	Power	-0.58
Cycle-adjusted PGA (Boulanger and Idriss, 2014)	Power	-0.59

Ground motions at large distances tended to have longer significant duration, but the correlation was not exceptionally strong. Since bracketed duration, Arias intensity and cumulative

absolute velocity were all functions of ground motion amplitude, they exhibited an inverse correlation with rupture distance.

Magnitude-adjusted PGA is the intensity measure usually associated with liquefaction triggering analysis. Details about magnitude-adjusted PGA have been discussed previously, but the magnitude-adjusted peak acceleration can be calculated using metadata from each recorded ground motion. Magnitude-adjusted PGA and cycle-adjusted PGA should obviously be very closely correlated, but some uncertainty remains in the correlation between earthquake magnitude and the number of cycles of loading. Figure 3.16 shows a scatterplot of duration intensity measures versus magnitude-adjusted PGA, and Table 3.7 shows the correlation coefficients. The correlation was improved by plotting the data on a log-log scale.

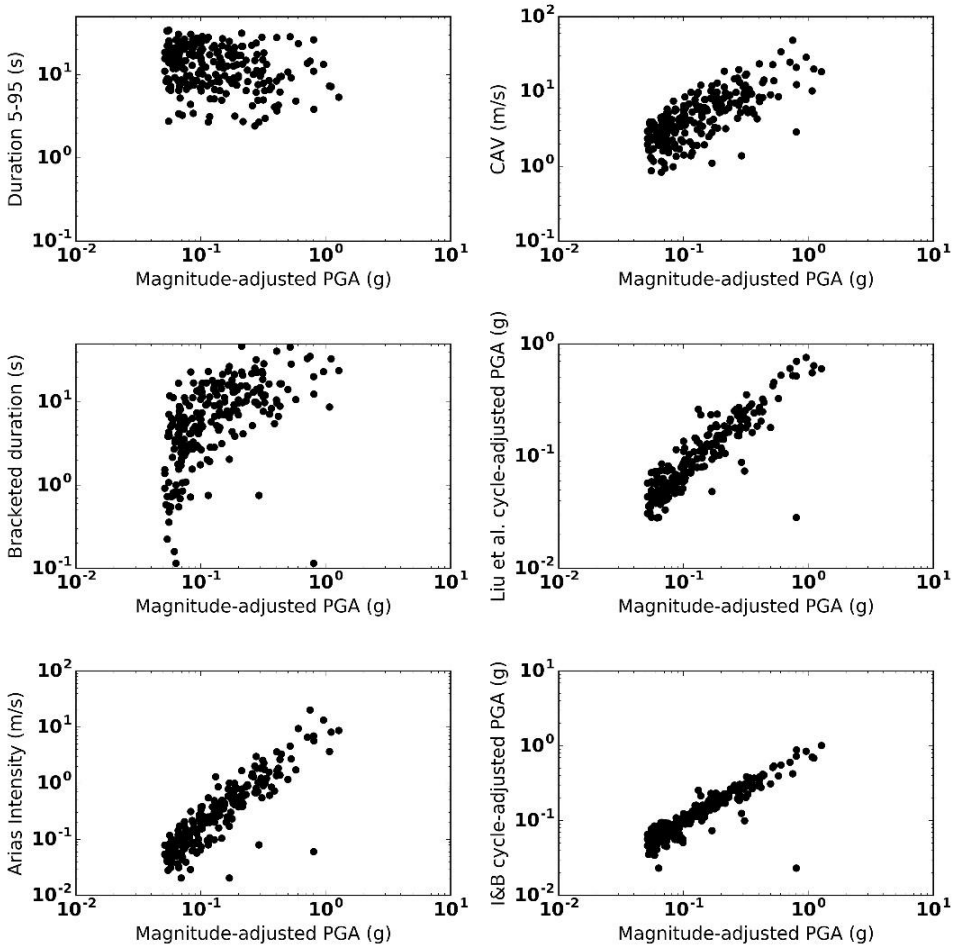

Figure 3.16: Correlation of duration intensity measures and magnitude-adjusted PGA for crustal ground motion.

Table 3.7: Correlation of duration intensity measures and magnitude-adjusted PGA for crustal ground motion

Intensity measure, IM	Transformation	Correlation Coefficient
Duration, 5-95	Power	-0.25
Bracketed duration	Power	0.57
Arias intensity	Power	0.89
Cumulative absolute velocity	Power	0.73
Cycle-adjusted PGA (Liu et al. 2001)	Power	0.89
Cycle-adjusted PGA (Boulanger and Idriss 2014)	Power	0.90

As expected, the cycle-adjusted PGA showed very strong correlation with magnitude-adjusted PGA, although some uncertainty remained. Arias intensity and magnitude-adjusted PGA were also very strongly correlated, followed by cumulative absolute velocity which was slightly less well-correlated. Significant duration was uncorrelated with cycle-adjusted PGA and exhibited a slight negative correlation.

3.3.4 *Isolated liquefaction-consistent motions*

From the filtered NGA flatfile, groups of motions with similar magnitude-adjusted PGA were sorted into bins centered at 0.1, 0.2, 0.3, and 0.4 g. The motions in each bin had magnitude-adjusted PGA values within 0.02 g of the bin centers. The amplitude of the motions in each bin were then scaled to match the central magnitude-adjusted PGA. The ground motions in each bin all had the exact same liquefaction triggering potential, but since the ground motions had a range of different earthquakes magnitudes and distances, each bin also included a range of durations. Figure 3.17 shows histograms of the each of the different earthquake magnitude in each of the liquefaction-consistent bins.

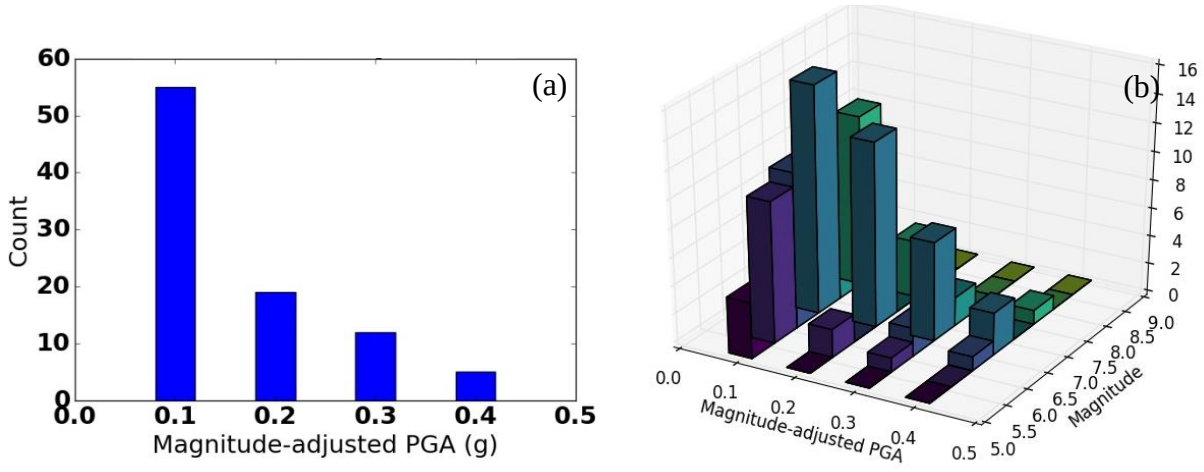

Figure 3.17: Histograms of magnitude-adjusted PGA for liquefaction-consistent ground motions. (a) NGA-west 2 liquefaction consistent motions on stiff ground. (b) NGA-west 2 liquefaction consistent motions on stiff ground separated by magnitude.

Isolating one of the bins and evaluating the duration intensity measures within that bin shows the correlation of ground motion duration with liquefaction potential. The motions within the PGA_M = 0.2 g bin were selected for this comparison. Although the motions in that bin were scaled to a consistent value of PGA_M, the PGA and spectral acceleration varied within the liquefaction-consistent bin of motions. Figure 3.18 shows the spectra acceleration of the motions in the 0.2 g bin.

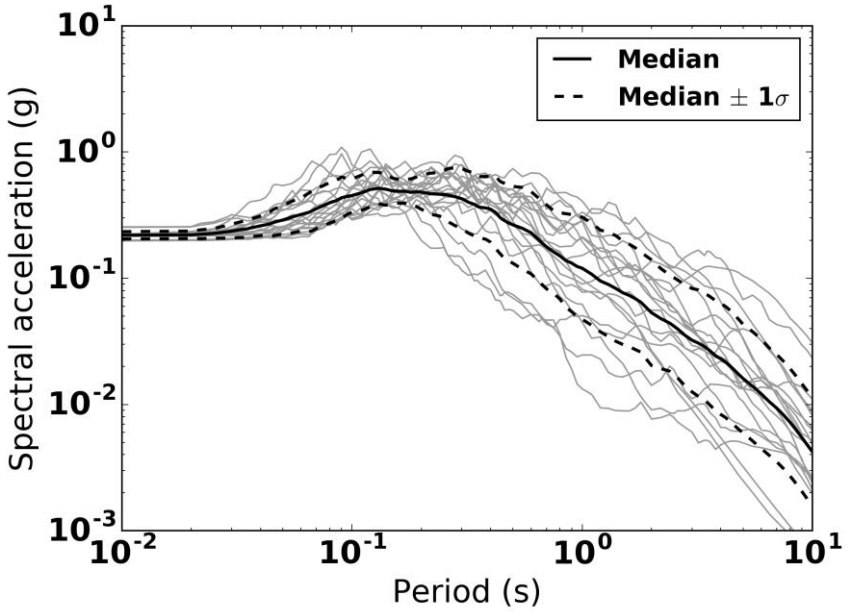

Figure 3.18: Spectral acceleration of crustal liquefaction-constant ground motions. For magnitude-adjusted 0.2 g bin.

Duration intensity measures were calculated for each of the motions in the 0.2 g-bin of liquefaction-consistent motions, and Figure 3.19 shows histograms of the duration intensity measures. Table 3.8 shows the mean, standard deviation, and coefficient of variation for each of the intensity measures.

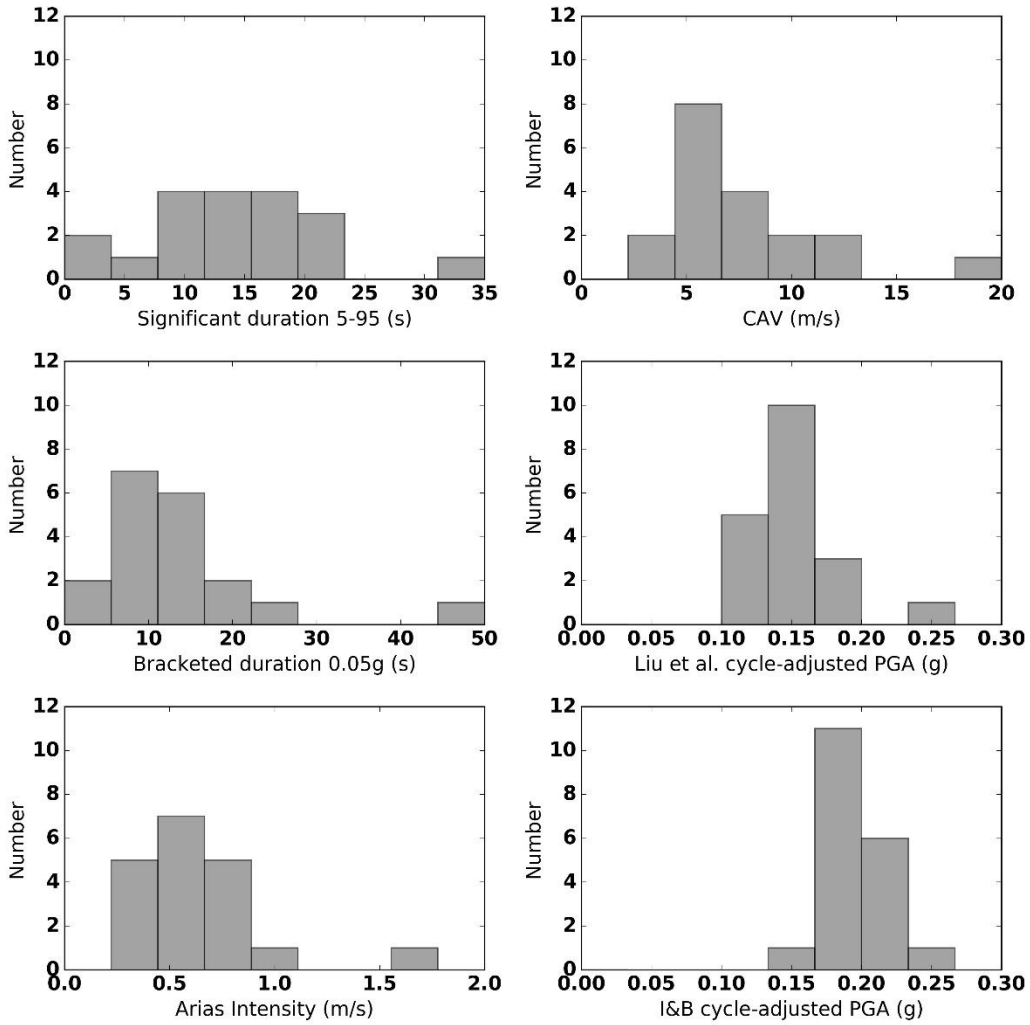

Figure 3.19: Histograms of duration intensity measures for crustal liquefaction-consistent ground motions. For magnitude-adjusted 0.2 g bin.

Table 3.8: Variation of duration intensity measures for liquefaction-consistent ground motions

Intensity measure, *IM*	Mean value	Standard deviation	Coefficient of variation
Duration, 5-95	14.2 s	7.0 s	0.49
Bracketed duration	14.1 s	9.4 s	0.66
Arias intensity	0.65 m/s	0.29 m/s	0.45
Cumulative absolute velocity	7.8 m/s	3.6 m/s	0.45
Cycle-adjusted PGA (Liu et al. 2001)	0.15 g	0.032 g	0.21
Cycle-adjusted PGA (Boulanger and Idriss 2014)	0.19 g	0.024 g	0.12

All the motions within the 0.2 g bin exhibited identical liquefaction potential, but the liquefaction-consistent motions in the 0.2 g bin exhibited moderate variance in duration intensity measures. As expected, cycle-adjusted PGA had the lowest coefficient of variation, since it was most closely related to magnitude-adjusted PGA. Arias intensity and CAV had slightly larger coefficients of variation, and significant duration and bracketed duration had relatively large coefficients of variation. As observed in the scatterplots of duration versus magnitude-adjusted PGA (Figure 3.14), significant duration and bracketed duration were uncorrelated with magnitude-adjusted PGA.

In this suite of motions, if no uncertainty existed in the correlation between magnitude-adjusted PGA and cycle adjusted PGA, the mean of the cycle-adjusted PGA values should be about 0.2 g. However, the cycle-adjusted PGA using the Liu et al. (2001) recommendations tended to be slightly lower than the magnitude-adjusted PGA of 0.2 g used to create the suite of motions. These differences were expected since the reference number of cycles used by Liu et al. (2001) was greater for field observations than the reference number of cycles used by Boulanger and Idriss (2014). The cycle-adjusted PGA values using the Liu et al. (2001) recommendations, therefore, tended to be smaller than the recommendations by Boulanger and Idriss (2014).

3.3.5 *Spectrum-compatible motions*

Spectral acceleration incorporates both the effects of ground motion amplitude and frequency content but does not account for the effects of duration. A suite of ground motions with similar response spectra was created to isolate duration intensity measures from amplitude and frequency

content intensity measures. Individual ground motions were adjusted to match a target spectral acceleration using time-domain wavelet spectral matching (Abrahamson, 1992; Aderkristi and Eatherton, 2015). The procedure was specifically designed to match a target spectrum while maintaining the rate of energy development and nonstationary behavior of the ground motion while minimizing changes in the frequency content. Figure 3.20 shows an example ground motion that was matched to a target spectrum. The spectrally matched acceleration time histories similar to the original time history, but the spectral acceleration of the modified time histories matched the target spectral acceleration very well.

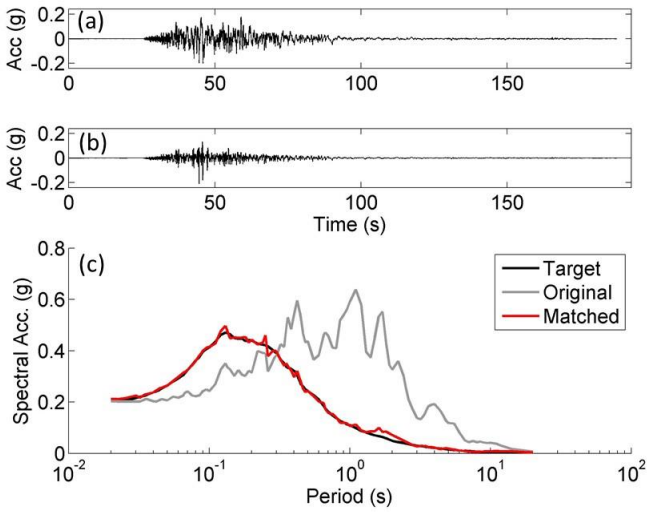

Figure 3.20: Example of spectral matching. (a) Original time history. (b) Wavelet modified spectrally-matched time history. (c) Target, original, and matched time history.

The target spectrum for this analysis was selected as the median spectral acceleration of the liquefaction-consistent crustal records in the 0.2 g bin. The motions in that bin were spectrally matched to the median values, and Figure 3.21 shows the response spectra before and after spectral matching.

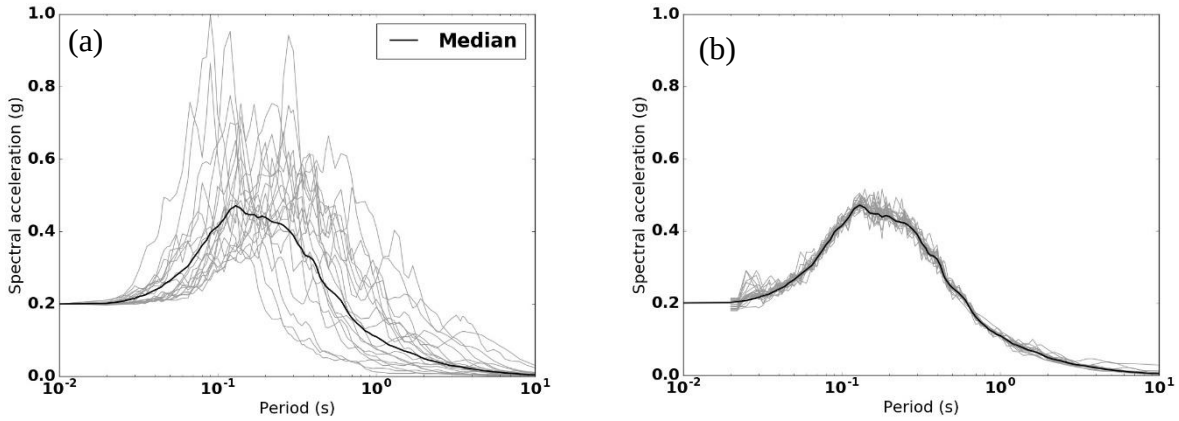

Figure 3.21: Spectral acceleration of spectrum-compatible ground motions. (a) Original crustal liquefaction-consistent motions. (b) Crustal liquefaction-consistent motions spectrally matched to the median.

The effects of spectral matching changed the duration and liquefaction potential of the ground motions, and histograms of the duration intensity measures are shown in Figure 3.22. The figure also includes histograms of the 0.2 g liquefaction consistent motions before the motions were spectral matched. Table 3.9 shows the mean, standard deviation, and coefficient of variation for each of the intensity measures. These values were compared to the values in Table 3.8 to determine the effects of spectral matching on the intensity measures for ground motion duration and liquefaction potential.

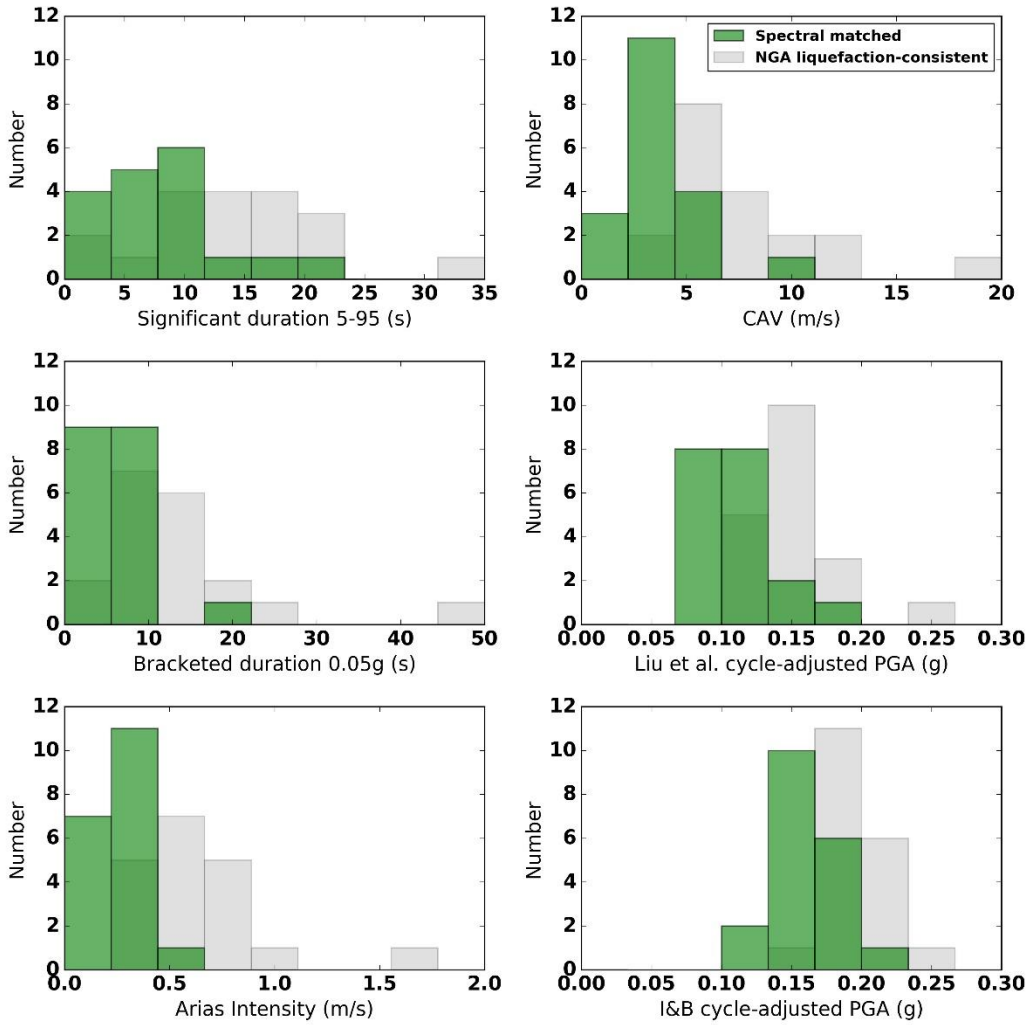

Figure 3.22: Histograms of duration intensity measures for spectrum-compatible ground motions. Motions from the NGA magnitude-adjusted 0.2 g bin, spectrally matched to the median spectral acceleration.

Table 3.9: Variation of duration intensity measures for spectrum-compatible ground motions

Intensity measure, *IM*	Mean value	Standard deviation	Coefficient of variation
Duration, 5-95	10.0 sec	8.8 sec	0.88
Bracketed duration	6.7 sec	4.4 sec	0.66
Arias intensity	0.27 m/s	0.11 m/s	0.42
Cumulative absolute velocity	4.0 m/s	2.1 m/s	0.51
Cycle-adjusted PGA (Liu et al., 2001)	0.11 g	0.03 g	0.27
Cycle-adjusted PGA (Boulanger and Idriss, 2014)	0.16 g	0.02 g	0.15

Based on Tables 3.8 and 3.9, the cycle-adjusted PGA has the lowest coefficient of variation both before and after spectral matching, but the coefficient of variation increased slightly when the motions were spectrally matched. This increase in the coefficient of variation indicated that the process of spectral matching affected the ground motions with respect to liquefaction triggering, and spectral matching did not necessarily maintain the acceleration amplitude or number of cycles of loading. The mean values of the duration intensity measures in the spectrum-compatible suite tended to be much smaller than the corresponding intensity measures in the liquefaction-consistent suite. This indicated that the spectral matching process tended to shorten the overall duration of the motion.

3.3.6 *Subduction liquefaction-consistent motions*

The NGA database includes only motions from crustal earthquakes, with a maximum $M_w = 7.8$. These ground motions were typically shorter in duration than those from subduction zone earthquakes. A suite of motions was collected from subduction zone earthquakes from K-net, KiK-net, USGS, and COSMOS. Over 1,500 motions from the 1985 $M_w = 8.0$ Valparaiso, 2003 $M_w = 8.3$ Tokachi-Oki, 2010 $M_w = 8.8$ Maule and 2011 $M_w = 9$ Tohoku earthquakes had available shear wave velocity profiles. These records were filtered for sites located on stiff ground or rock ($v_{s30} > 600$ m/s) to eliminate the effects of soft soil amplification or frequency content shift on the ground motions. From the suite of subduction zone motions on stiff soil or rock, only motions with PGA greater than 0.05 g were selected. 123 motions matched these criteria.

Since these motions were generated from large magnitudes earthquakes, the subduction zone records can be used to extend the relationships of duration and earthquake magnitude. The combined suites of crustal and subduction zone ground motions are referred to as the CS-data set. Figure 3.23 shows scatterplots of the duration intensity measures versus earthquake magnitude for the ground motions in the CS-data set, and Table 3.10 shows the correlation between the duration intensity measures and earthquake magnitude. A better correlation was obtained when the data were plotted on a semi-log axis.

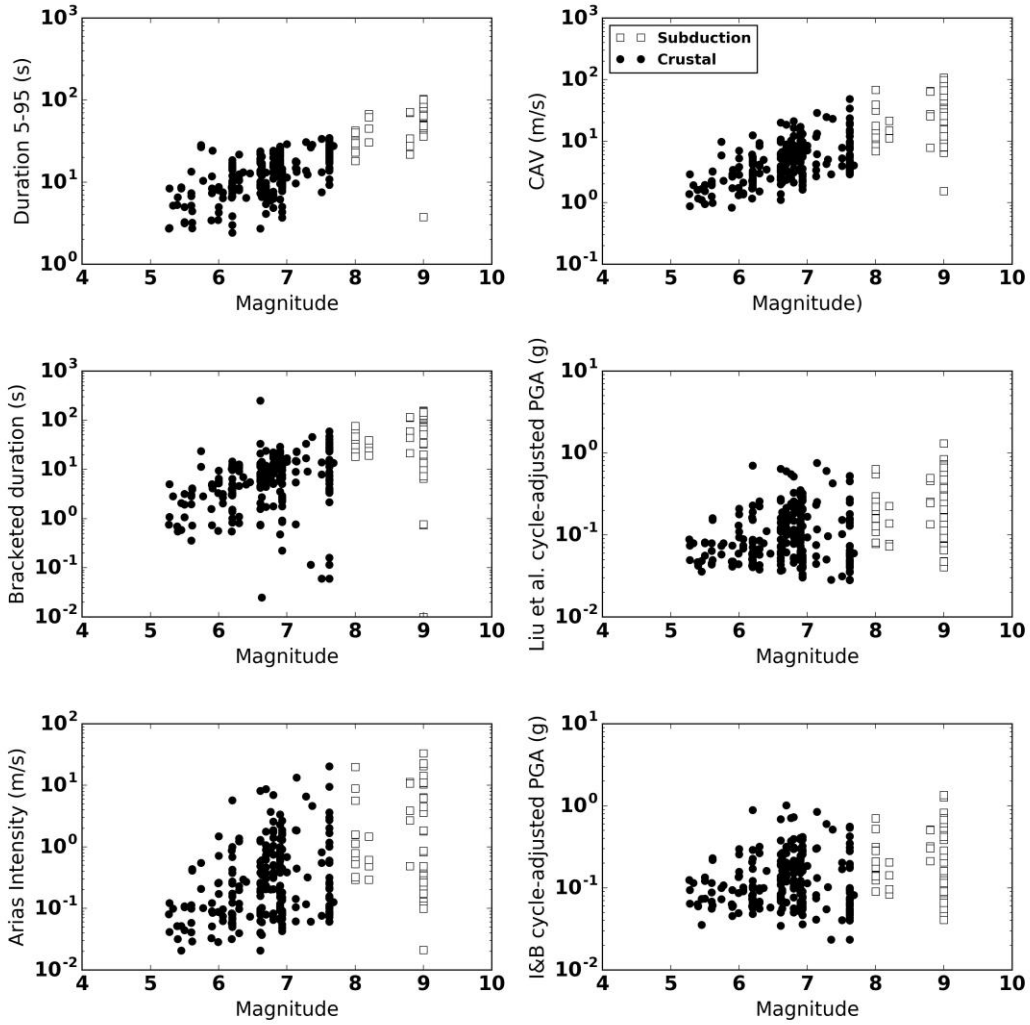

Figure 3.23: Correlation of intensity measures for duration and earthquake magnitude for subduction ground motions.

Table 3.10: Correlation of duration intensity measures and earthquake magnitude for combined crustal and subduction ground motions

Intensity measure, *IM*	Transformation	Correlation Coefficient
Duration, 5-95	Exponential	0.80
Bracketed duration	Exponential	0.45
Arias intensity	Exponential	0.46
Cumulative absolute velocity	Exponential	0.69
Cycle-adjusted PGA (Liu et al., 2001)	Exponential	0.33
Cycle-adjusted PGA (Boulanger and Idriss, 2014)	Exponential	0.27

The relationship of duration versus earthquake magnitude exhibits similar trends in both the suites of subduction and crustal earthquake motions. Extending the range of earthquake magnitudes by combining the two data sets shows the trends more clearly. Significant duration has a very strong correlation with earthquake magnitude, and cumulative absolute velocity also correlates very well with earthquake magnitude. Cycle-adjusted PGA shows some correlation with earthquake magnitude, but if the magnitude scaling factor fully accounted for the effects of earthquake magnitude, the cycle-adjusted PGA should be independent of earthquake magnitude.

The duration intensity measures were also compared to magnitude-adjusted PGA. Figure 3.24 shows scatterplots of the duration intensity measures versus magnitude-adjusted PGA. Magnitude scaling factors were calculated using the procedure described by Boulanger and Idriss (2014) for $(N_1)_{60} = 15$ and an effective overburden stress of 1 atm. Table 3.11 shows the correlation between the duration intensity measures and magnitude-adjusted PGA. Better correlation with the duration intensity measures was obtained when the data were plotted on a log-log scale.

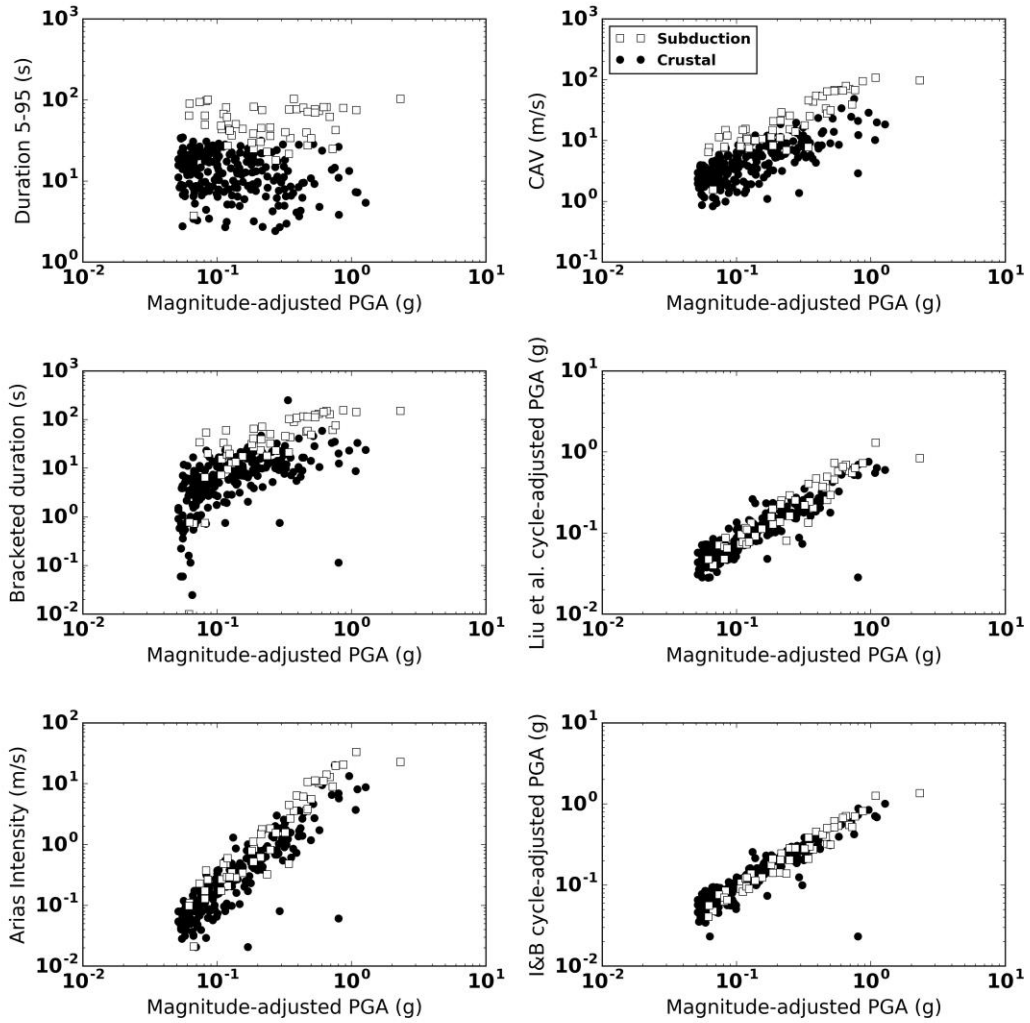

Figure 3.24: Correlation of duration intensity measures and magnitude-adjusted PGA for subduction ground motions. The figure also includes crustal motions for comparison.

Table 3.11 Correlation of duration intensity measures and magnitude-adjusted PGA for combined crustal and subduction ground motions

Intensity measure, *IM*	Transformation	Correlation Coefficient
Duration, 5-95	Power	0.09
Bracketed duration	Power	0.65
Arias intensity	Power	0.91
Cumulative absolute velocity	Power	0.77
Cycle-adjusted PGA (Liu et al., 2001)	Power	0.92
Cycle-adjusted PGA (Boulanger and Idriss, 2014)	Power	0.94

As observed with the crustal suite of motions, cycle-adjusted PGA is very strongly correlated with magnitude-adjusted PGA. Arias intensity and magnitude-adjusted PGA are also very strongly correlated. Cumulative absolute velocity is well-correlated with magnitude-adjusted PGA, but not as strongly as Arias intensity. Significant duration and bracketed duration are largely independent of magnitude-adjusted PGA.

The liquefaction triggering procedures (Cetin et al. 2004; Boulanger and Idriss, 2014) were primarily based on data from crustal earthquakes. The intensity measures from the subduction zone data set showed that the correlations between magnitude-adjusted PGA and cyclic-adjusted PGA remained relatively consistent for larger magnitude earthquakes. Based on these observations, the calculation of magnitude scaling factor can be extended from shorter-duration crustal earthquake motions to longer-duration, large-magnitude subduction zone motions.

Arias Intensity and cumulative absolute velocity both show some dependence on the earthquake magnitude. Figure 3.24 shows that the subduction zone motions tend to have slightly larger Arias Intensity and cumulative absolute velocity than their crustal motion counterparts. However, GMPEs for Arias Intensity and cumulative absolute velocity based on subduction-zone records are not available. Correlations between these intensity measures and magnitude-adjusted PGA are necessary to predict intensity measures from subduction zone earthquakes. The CS-dataset was used to estimate equations to calculate Arias intensity and cumulative absolute velocity based on the magnitude-adjusted PGA. Simple linear regression was performed using the data shown in Figure 3.24, and equations predicting ln I_a or ln CAV based on ln PGA_M were produced. The regression analysis showed that

$$\ln \frac{\mathrm{I}_a}{1\ \mathrm{m/s}} = 2.60 + 1.91 \ln \frac{\mathrm{PGA}_M}{1\ \mathrm{g}} + \sigma_{\ln \mathrm{I}_a \mid \ln \mathrm{PGA}_M} \varepsilon_{\ln \mathrm{I}_a \mid \ln \mathrm{PGA}_M} \tag{3.38}$$

$$\ln \frac{\mathrm{CAV}}{1\ \mathrm{m/s}} = 3.54 + 0.93 \ln \frac{\mathrm{PGA}_M}{1\ \mathrm{g}} + \sigma_{\ln \mathrm{CAV} \mid \ln \mathrm{PGA}_M} \varepsilon_{\ln \mathrm{CAV} \mid \ln \mathrm{PGA}_M} \tag{3.39}$$

where the conditional standard deviation, $\sigma_{\ln \mathrm{I}_a \mid \ln \mathrm{PGA}_M}$ is equal to 0.51 and $\sigma_{\ln \mathrm{CAV} \mid \ln \mathrm{PGA}_M}$ is equal to 0.58. $\varepsilon_{\ln \mathrm{I}_a \mid \ln \mathrm{PGA}_M}$ and $\varepsilon_{\ln \mathrm{CAV} \mid \ln \mathrm{PGA}_M}$ are both standard normally distributed random variables.

3.3.7 *Basin-influenced ground motions*

Amplification of long period spectral acceleration within deep basins is well-known (Boore, et al., 2014; Campbell and Bozorgnia, 2014). Basins are typically composed of deep deposits of soil or sedimentary rocks, and these materials typically have lower shear wave velocities than the underlying bedrock. The shear wave velocity contrast between the bedrock and basin can amplify lower frequency motions relative to sites located outside of the basin. This change in frequency content may influence intensity measures associated with liquefaction triggering and deformation.

Basins have characteristically low shear wave velocity profiles, which persist to great depths. Ground motion prediction equations (GMPEs) typically consider the effects of deep basins with scaler terms based on the depth to shear wave velocities that exceed 1.0 or 2.5 km/s, $z_{1.0}$ or $z_{2.5}$. Deeper basins, with larger values of $z_{1.0}$ or $z_{2.5}$, should produce greater amplification of lower frequency motions than shallower basins.

Basin terms in the GMPEs typically have less influence on the PGA than on intensity measures that capture lower frequency motions (Campbell and Bozorgnia, 2014). In fact, many GMPEs do not include basin terms, such as the BCHydro GMPE (Abrahamson et al. 2015), which is typically used for subduction zones, and the BSSA GMPE (Boore et al. 2014), which was developed using the NGA West-2 crustal data set. Even when basin terms are included in a GMPE, they do not significantly reduce the overall variance of the prediction equation, suggesting that the basin terms may not be strong predictors of PGA. Both the 2014 BSSA GMPE, which does not consider basin effects, and the 2014 CB GMPE (Campbell and Bozorgnia, 2014), which does consider basin effects, predict similar values of the total standard deviation, $\sigma_{\ln \mathrm{PGA}}$ = 0.58 and 0.60. This comparison indicates that, while basin terms should be included in GMPEs based on the mechanisms associated with the shear wave velocity contrast between the bedrock and basin,

including these terms does not have a strong effect on reducing the uncertainty in predicting intensity measures.

Despite the relatively minor influence on PGA, basins tend to amplify low-frequency motions and may influence intensity measures associated with post-triggering deformation, like Arias intensity and cumulative absolute velocity. Campbell and Bozorgnia (2008, 2010, 2012) developed GMPEs based on suites of crustal ground motions for PGA, Arias intensity and cumulative absolute velocity. These GMPEs included a basin term that was a function of $z_{2.5}$. The general form of these GMPEs was

$$\ln(IM) = f_{mag}(\mathrm{M}_w) + f_{dis}(\mathrm{M}_w, \mathrm{R}_{rup}) + \cdots + f_{sed}(\mathrm{z}_{2.5}) + \varepsilon + \eta \tag{3.40}$$

where $f_{sed}(\mathrm{z}_{2.5})$ is a function to account for the effects of sedimentary basin and η and ε are random variables corresponding to inter-event and within-event uncertainty. Equation (3.40) can be formulated to estimate intensity measure amplification factors as a function of f_{sed}. The general expression can be used for any arbitrary IM, as long as the GMPE has a term f_{sed}.

$$\mathrm{AF}_{IM} = \exp\left(\frac{f_{sed}(\mathrm{z}_{2.5})}{f_{sed}(\mathrm{z}_{2.5,\mathrm{ref}})}\right) \tag{3.41}$$

where AF_{IM} is an amplification factor for IM and $\mathrm{z}_{2.5,\mathrm{ref}}$ is a reference value for sites located outside of the basin. Using Cambell and Bozorgnia's GMPE's, amplification factors for PGA, Arias intensity, and cumulative absolute velocity are shown on Figure 3.25. These plots show that the amplification factors at sites with $z_{2.5} < 3$ km are negligible or small, as these sites are generally considered to be outside of basins. Sites with $z_{2.5} > 3$ km amplify Arias Intensity the most, followed by cumulative absolute velocity. Deep basins amplify the PGA the least.

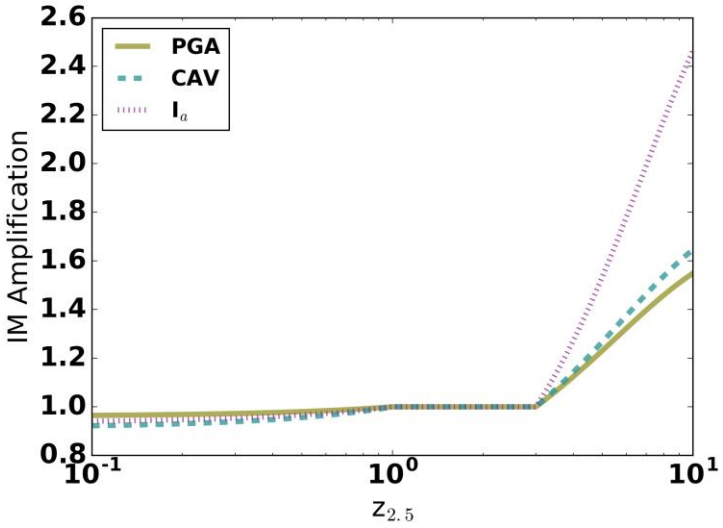

Figure 3.25: Basin amplification factors (after Campbell and Bozorgnia, 2008, 2010, and 2012).

The intensity measures typically used for liquefaction triggering analysis is magnitude-adjusted PGA, which is a combination of the PGA and a magnitude scaling factor. Campbell and Bozorgnia (2010) indicated that the presence of deep sedimentary basins amplifies the PGA, but the presence of basins may also influence the number of cycles of loading and the magnitude scaling factor. Contemporary methods for predicting the number of cycles of loading (Liu et al., 2001; Kishida and Tsai, 2014) do not have terms to account for the effects of basins. However, the K-net and Kik-net seismic networks in Japan include many stations that were located within basins. Since these networks began recording ground motions, very strong earthquakes have shaken several of these basins. For example, the 2003 M_w = 8.3 Tokachi-Oki earthquake produced very strong ground motions in the Yufutsu basin on Hokkaido, and the 2011 M_w = 9.0 Tohoku earthquake produced very strong ground motions in the Kanto basin near Tokyo. Figure 3.26 (from Marafi et al., 2017) shows the location of four deep sedimentary basins in Japan, all of which have recorded ground motions from earthquakes stronger than M_w > 7.0.

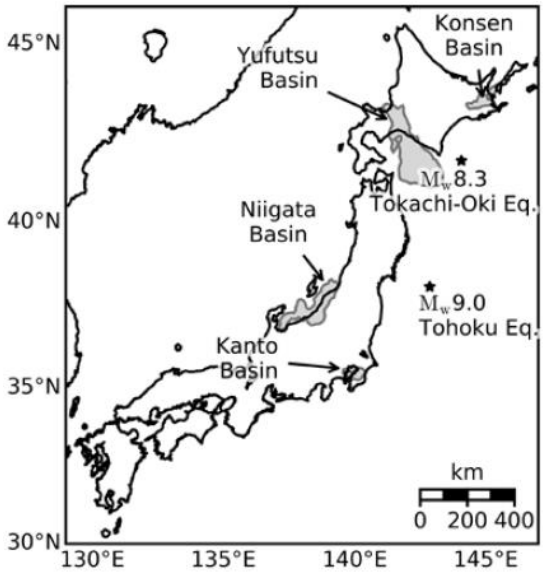

Figure 3.26: Basin locations in Japan (from Marafi et al., 2017).

A large number of recorded ground motions can be used to identify basin effects. A suite of motions was collected from the K-net and KiK-net databases with recorded motions from the six large earthquakes that shook at least one of the four basins shown in Figure 3.26. This suite included ground motions from both inside and outside of the basins. Dawood et al. (2015) provided metadata for the Kik-net recording stations, and Marafi et al. (2017) provided metadata for the K-net recording stations. Metadata from these stations included both shear wave velocity and basin depth parameters. The selected motions were filtered for records with PGA greater than 0.05 g, and Table 3.12 shows the number of motions selected from each earthquake and the closest basin. Figure 3.27 shows the relative distribution of sites with $z_{1.0}$ > 0.3 km or $z_{2.5}$ > 1.0 km for each of the earthquakes in this suite of motions.

Table 3.12: Strong earthquakes near sedimentary basins in Japan

Earthquake	Magnitude	Nearest basin	Number of records with PGA > 0.05 g
2003 Miyagi-Oki	7.0	Niigata	154
2007 West Coast Honshu	6.6	Niigata	58
2005 Honshu	6.3	Kanto	21
2004 Hokkaido	7.0	Konsen	55
2003 Tokachi-Oki	8.3	Yufutsu	142
2011 Tohoku	9.0	Kanto	377

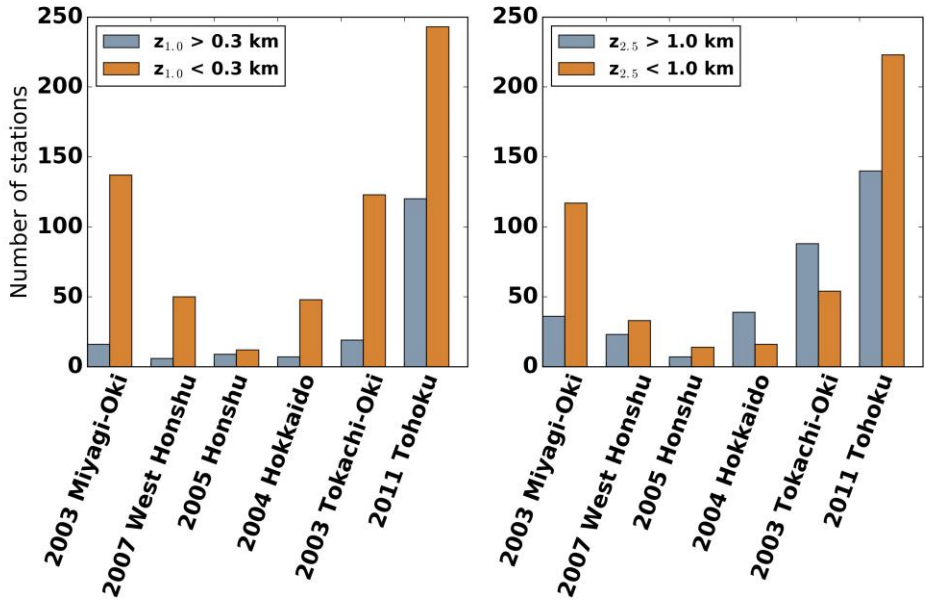

Figure 3.27: Basin and deep soil site data from selected earthquakes

Each of the over 800 motions was baseline-corrected by detrending the waveform, filtering out frequencies above 35 Hz and below 0.1 Hz, and removing a high-order polynomial from the data. The baseline correction method was similar to the approach by Boore et al. (2002). Intensity measures were calculated for each ground motion. Figure 3.28 shows a scatterplot of magnitude-adjusted PGA and Arias Intensity versus moment magnitude and rupture distance. This figure illustrates the range of intensity measures, earthquake magnitudes, and rupture distances that were included in this suite of motions.

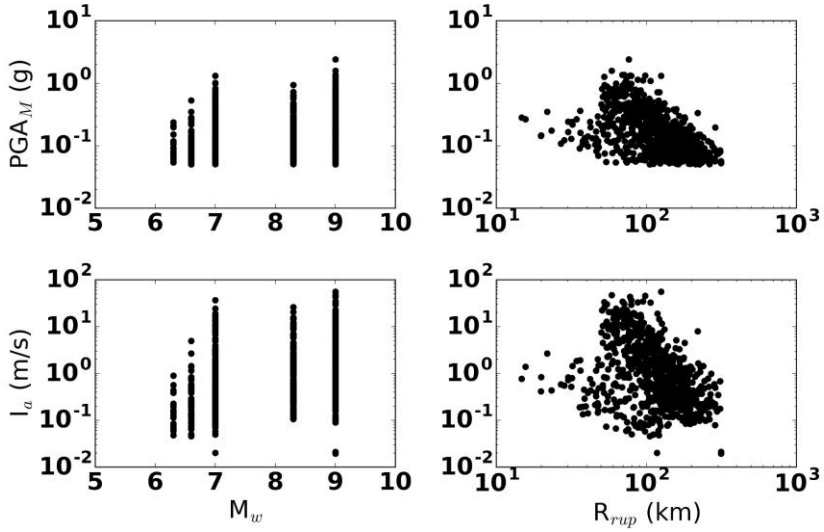

Figure 3.28: Intensity measures for basin-influenced motions

The ground motion metadata from the Japan basin data set was used to predict an equivalent number of cycles of loading, n, using Kishida and Tsai's (2014) procedure. Figure 3.29 shows the calculated versus predicted values of n for the motions in this data set. The predicted values of n showed a wide range of uncertainty, but some of this uncertainty may be due to the effects of basins, which were not considered in the prediction equations. If the presence of deep basins affected n, then residuals versus $z_{1.0}$ or $z_{2.5}$ should show definitive trends. Figure 3.30 shows the residuals versus $z_{1.0}$ and $z_{2.5}$.

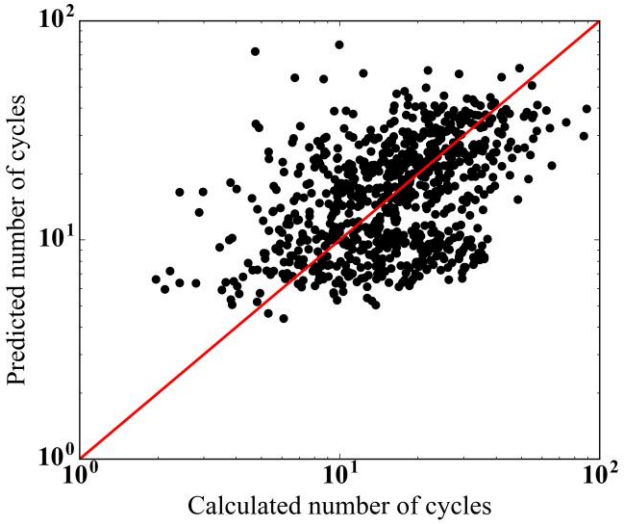

Figure 3.29: Calculated versus predicted number of cycles for basin-influenced motions

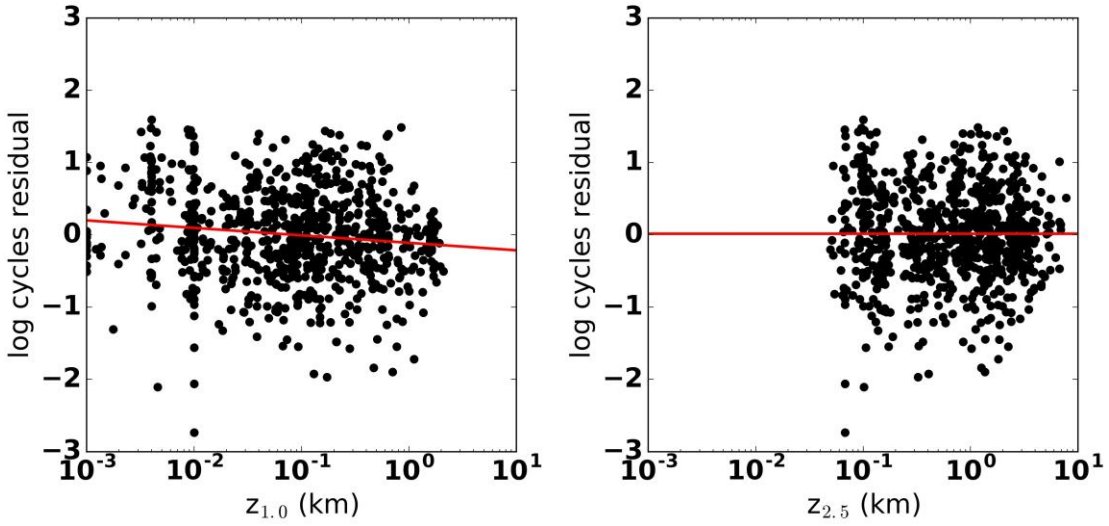

Figure 3.30: Residuals to the recorded number of cycles for basin-influenced motions.

Figure 3.30 shows a weak trend of the number of cycles decreasing with increasing $z_{1.0}$. This trend implies that the number of cycles decreases as the depth of the basin increases. Sedimentary basins should amplify certain ground motion frequencies and de-amplify other frequencies. The isolation of certain frequencies may cause an overall reduction in the number of cycles of loading, but based on the slope of the line in Figure 3.30, the effect is relatively minor. A simple, linear expression was added to the Kishida and Tsai's equations to account for the trend in residual values versus $z_{1.0}$.

$$\ln n = \ln n_{\text{K\&T}} + a \ln z_{1.0} + b \tag{3.42}$$

where n is the estimated number of cycles of loading with consideration for basin effects and $n_{\text{K\&T}}$ is the number of cycles calculated using Kishida and Tsai's procedure. Based on the trendline in Figure 3.30, a = 0.20 and b = -0.045.

While deep basins slightly amplify the PGA, they also reduce the number of cycles of loading. These effects have competing influences on the PGA_M, so to determine if basins increase or decrease the liquefaction triggering hazard, PGA_M amplification factors were calculated for a range of $z_{1.0}$ values. Cambell and Bozorgnia's (2010) amplification factors for PGA are based on $z_{2.5}$, while the number of cycles of loading, n, had the strongest trend with $z_{1.0}$. Choi (2004) describes correlations between $z_{1.0}$ and $z_{2.5}$, so $z_{2.5}$ can be calculated as a function of $z_{1.0}$. PGA

values were calculated using Cambell and Bozorgnia's (2010) amplification factors for PGA, and values of n were calculated using equation (3.39) with adjustment for basin effects. A magnitude scaling factor was the calculated using the values of n adjusted for basin effects. Figure 3.31 shows an amplification factor for PGA_M versus $z_{1.0}$.

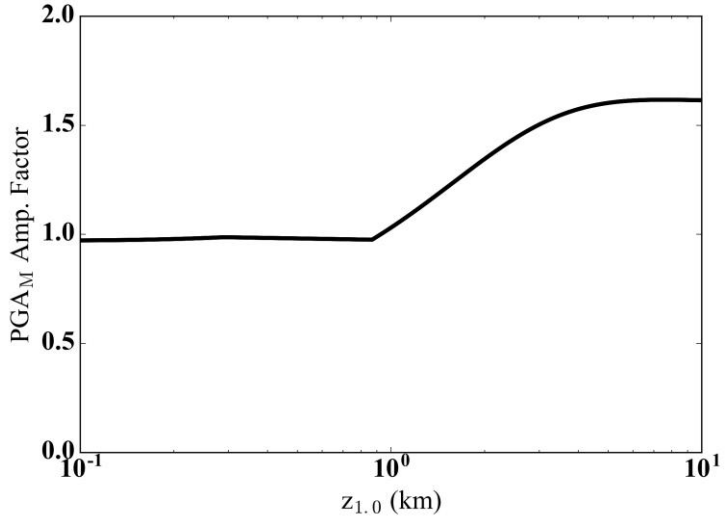

Figure 3.31: Estimated basin amplification factor for PGA_M.

For liquefaction triggering analysis, the presence of deep sedimentary basins caused a combination of increases in PGA and relatively minor decreases in the number of cycles of loading. The net combination resulted in amplification of the magnitude-adjusted PGA for liquefaction triggering analysis. Campbell and Bozorgnia (2012) indicated that lower-frequency intensity measures, such as Arias intensity and cumulative absolute velocity, were amplified significantly at sites established in deep basins. These intensity measures are more closely associated with the post-triggering deformation, and basin amplification likely increases post-triggering deformation.

3.3.8 *Cascadia subduction zone motions*

Simulations have been performed by the University of Washington's M9 team (Wirth et al., 2017) to estimate ground motions from a M_w = 9 Cascadia Subduction Zone rupture. These physics-based simulations captured the source effects of an interface rupture by simulating areas of very high stress-drop sub-events within a large background rupture. Wirth et al. evaluated path effects using finite-difference analyses of the waves generated by the source traveling through a detailed

3D velocity model of the region. This model included the velocity structures of the Puget lowlands near Seattle and Tualatin basin near Portland. For a Cascadia Subduction Zone to generate M_w = 9 earthquake, the entire length of the fault was assumed to have ruptured. The exact mechanism of the rupture was not known, and Wirth et al. performed many simulations to evaluate the effects of potential variations in the rupture mechanics including the hypocenter location, sub-event locations, and the down-dip edge of the rupture. Each simulation represented a realization of a potential rupture mechanism and the potential ground motions. A suite of ground motions was collected from 18 simulations that represented a range of potential rupture scenarios. The variation in rupture mechanism produced a relatively large range of simulated ground motions at individual sites. The location of asperities, or sub-events with high-stress drop, tended to have the strongest effect on ground motions within frequencies of interest. Areas closest to sub-events tended to experience the strongest shaking, but the possible location of sub-events was not explicitly known, and for the various simulations, Wirth et al. assumed between three and five high-stress drop sub-events at various locations. The down-dip edge of the subduction zone rupture also impacted the intensity of shaking at sites near centers of large populations. A rupture further down-dip caused strong shaking in these areas and was another source of uncertainty in the source mechanics.

Wirth et al. produced ground motions from these simulations on an evenly-spaced, 20-km wide grid. Four sites were selected for additional analysis at locations with dense populations where saturated recent alluvium or fill mantled that ground surface. The proximity of these sites to deep sedimentary basins was also considered in their selection. Table 3.13 lists the location of each site, the elements of the built environment that were near each site, the range of potential fault rupture distances, and nearby basins and subsurface conditions that may have affected the ground motions. Strong shaking at any of these selected sites could potentially damage critical elements of the built environment.

Table 3.13: Selected locations of Cascadia subduction zone ground motions

Location	Element of built environment	Range of simulated distance to fault rupture, R_{rup} (km)	Basin and subsurface conditions
Wilbridge	Liquid fuel terminal supplying much of Oregon & SW Washington. Near populations center of Portland.	69 to 127	Edge of Tualatin basin, near-surface Holocene alluvium and fill.
Ronler Acres	Manufacturing center near Portland	53 to 107	Within Tualatin basin, near-surface Pleistocene alluvium and lacustrine sediments.
CenturyLink Field	Near population center of Seattle and significant port infrastructure	97 to 162	Within Seattle basin, near-surface fill.
SeaTac Airport	Significant transportation facility between Tacoma and Seattle.	94 to 160	Outside of Seattle basin, but in Puget lowlands. Near-surface fill, Pleistocene recessional outwash, and till.

The finite-difference velocity model was limited to motions less than 1 Hz. To simulate realistic frequency content of possible ground motions, Wirth et al. stochastically generated high-frequency ground motions and combined these motions into the simulated finite difference results. The combined stochastic and simulated ground motions produced broadband motions that included a wide range of frequencies. Instabilities in the finite difference model occasionally occurred near the end of the earthquake, and these instabilities were removed from the ground motions by applying a tapering function at the end of the record.

In the finite-difference model, the shear wave velocity near the ground surface was limited to a minimum of about 550 m/s. The motions were then baseline-corrected by detrending the waveform, filtering out frequencies above 35 Hz and below 0.1 Hz, and removing a high-order polynomial from to the data. The baseline correction method was similar to the approach by Boore et al. (2002). The spectral acceleration produced by these simulations was compared to the

estimated spectral acceleration calculated using the BCHydro GMPE. The spectral acceleration was estimated using median down-dip limits from the fault rupture model, which corresponded to rupture distances of 62, 81, 124, and 124 km for Ronler Acres, Wilbridge, SeaTac, and CenturyLink sites. Figure 3.32 shows the spectral acceleration from the simulations and the GMPE median.

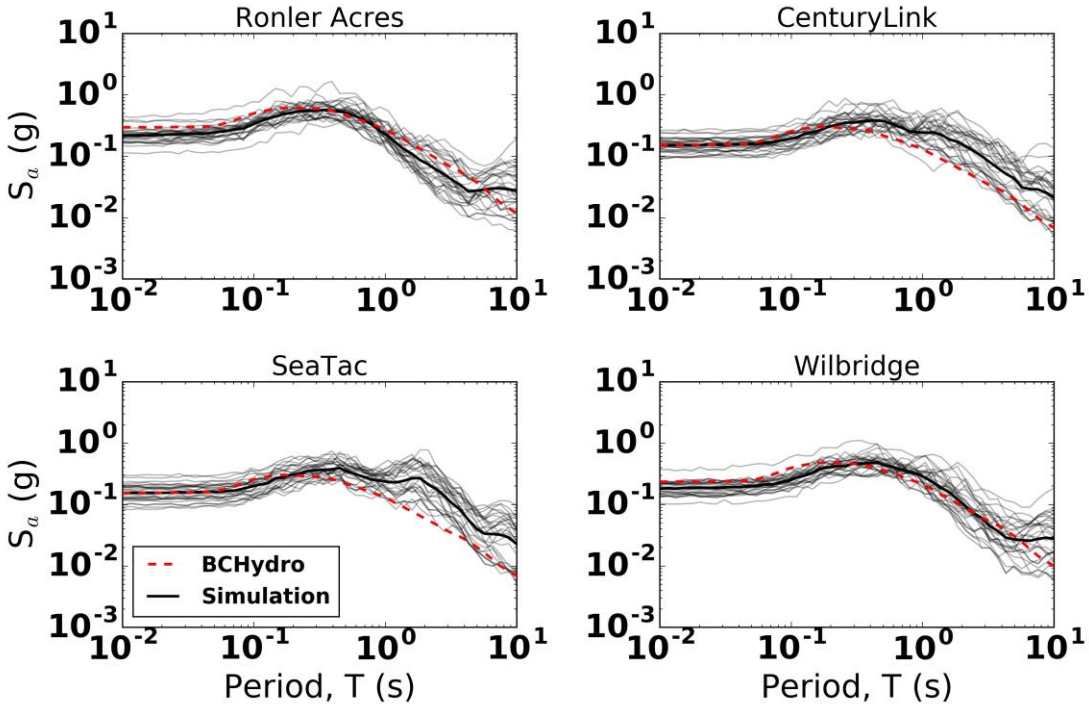

Figure 3.32: Spectral acceleration of Cascadia subduction zone simulations at selected sites.

In general, the simulations and the GMPE produced similar estimates of spectral accelerations between the PGA and a period of 1.0 seconds. The sites located near the Tualatin basin—Wilbridge and Ronler Acres—were closer to the fault rupture and experienced stronger spectral acceleration at short periods than the sites located in the Puget lowlands—SeaTac and CenturyLink. The simulated long period spectral acceleration at the sites in the Puget lowlands was much greater than the GMPE predictions, suggesting that the Puget lowland basin amplified low-frequency motions. However, the simulated long-period spectral acceleration at the sites near the Tualatin basin matched the GMPE relatively well. The Tualatin basin was much shallower

than the Puget lowlands, and the Tualatin basin may not have amplified the low-frequency motions as much as the Puget lowlands.

The equivalent number of cycles of loading was also calculated from each simulated ground motion. Figure 3.33 shows histograms of the number of cycles of loading at the four different sites. The procedure by Boulanger and Idriss (2014) indicated that a $M_w = 9.0$ earthquake would produce about 27 cycles of loading for typical conditions where $N_{1,60} = 15$. On average, the simulated number of cycles of loading was about the same as the estimated number of cycles based on the calculations using Boulanger and Idriss's equations. This observation was consistent with the basin-influenced motion data set, where the number of cycles of loading was not significantly impacted by the presence of deep basins.

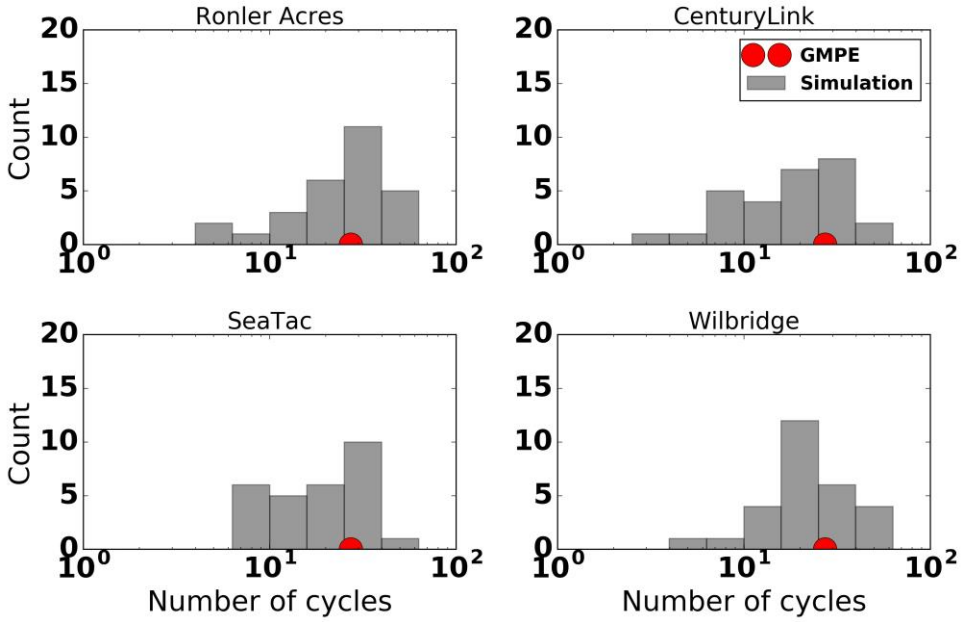

Figure 3.33: Number of cycles of Cascadia subduction zone simulations at selected sites.

A magnitude scaling factor was then calculated using the number of cycles of loading, which was then used to calculate PGA_M. The simulations near the Tualatin basin predicted slightly lower PGAs than the GMPE, and the number of cycles was within the range for a typical $M_w = 9$ earthquake. So, the values of PGA_M near the Tualatin basin were less than GMPEs would predict. Conversely, the simulated PGA values in the Puget lowlands were similar to the GMPE predictions, and the number of cycles of loading was about the same. So, the simulated values of

PGA_M were similar to the GMPE estimates. Figure 3.34 shows histograms of PGA_M from the simulations at the example locations.

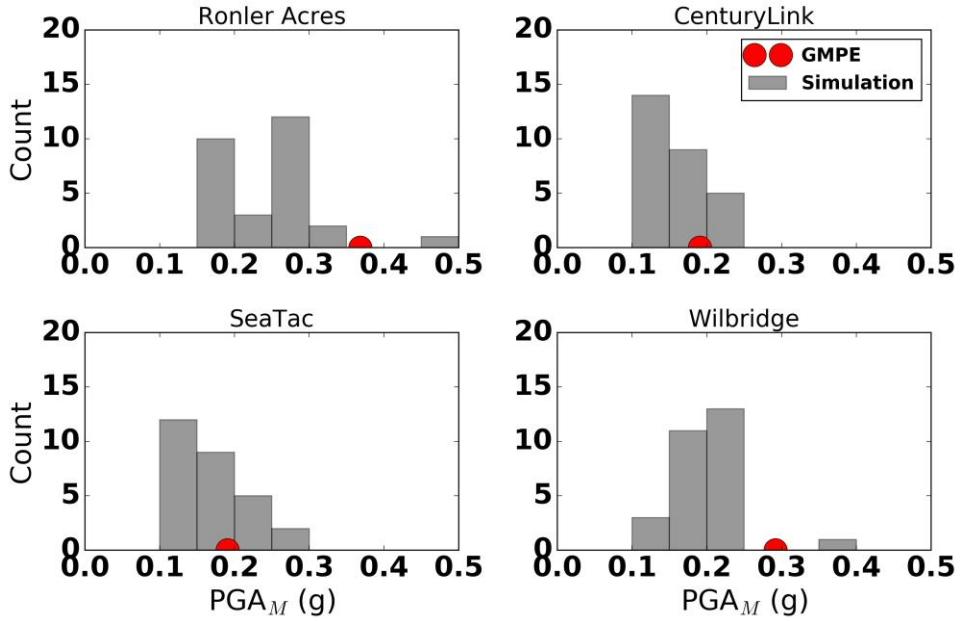

Figure 3.34: Magnitude-adjusted PGA from Cascadia subduction zone simulations at selected sites

3.3.9 *Summary of ground motions suites*

Significant duration as an intensity measure was largely independent of the other aspects of ground motion (amplitude and frequency content) and effectively isolates the ground motion duration. Regardless of the amplitude and frequency content of the motions, the suites of large magnitude earthquakes generally produced longer-duration motions than smaller magnitude earthquakes. Rupture distance modestly increases the ground motion duration, but intensity measures for predicting liquefaction triggering are reduced at larger distances.

Cycle-adjusted PGA, Arias intensity, and cumulative absolute velocity have all been used as intensity measures to predict liquefaction triggering. A distinction was made in this analysis between the cycle-adjusted PGA, which was calculated directly from earthquake ground motions, and the magnitude-adjusted PGA, which was calculated based on earthquake metadata. Cycle-adjusted PGA, Arias intensity, and cumulative absolute velocity all inherently included some measure of earthquake duration. The cycle-adjusted PGA included the number of cycles of

loading, and Arias intensity and cumulative absolute velocity were integrated over time. These intensity measure were not, however, completely independent of ground motion amplitude and frequency content. Cycle-adjusted PGA, Arias intensity, and cumulative absolute velocity were shown to have very strong correlations with magnitude-adjusted PGA.

Correlations of these intensity measures with observations of liquefaction triggering have been developed primarily based on observations from short duration, smaller magnitude (M_w < 7.8), crustal earthquake motions. The analyses in this section implied that the correlations between these intensity measures remained relatively constant even when large magnitude, long duration subduction earthquakes were considered. So, even though the database used to develop equations for calculating magnitude-adjusted PGA did not include many large magnitude earthquakes, the equations still provide reasonable representations of the liquefaction triggering potential.

The presence of deep, sedimentary basins may also influence intensity measures associated with liquefaction triggering and deformation. Data collected from basins in Japan indicated that the correlation between basin depth parameters, $z_{1.0}$ and $z_{2.5}$, and intensity measures for liquefaction triggering were relatively modest. However, Campbell and Bozorgnia (2010, 2012) indicated that lower-frequency intensity measures, that may be associated with post-triggering effects of liquefaction, were indeed amplified by basins.

3.4 SIGNIFICANCE OF LONG-DURATION GROUND MOTIONS ON LIQUEFACTION HAZARDS

The preceding discussions have illustrated the effects of source, path, and site effects on earthquake ground motion duration, and have shown how duration is accounted for in commonly used scaler intensity measures. The procedures for evaluating liquefaction triggering and the subsequent consequences are largely empirical in nature and are based on interpretation of recorded ground motions. The types of motions produced by very large earthquakes, such as those associated with interplate subduction events, have not yet been incorporated into the commonly used empirical models for liquefaction triggering and effects, so the application of predictive models for very long duration motions, therefore, is not well established.

In considering the applicability of predicting earthquake duration, it is useful to determine the unique aspects of very long duration motions from the standpoint of influence on the triggering and consequences of liquefaction. This includes the potential for liquefaction triggering at larger

distances and in denser soils than typically observed for crustal earthquakes, the increased length of time a soil may be subjected to significant shaking while in a liquefied state, and the potential effects of drainage during shaking.

3.4.1 *Liquefaction at greater distances*

The long durations associated with large magnitude earthquakes can produce liquefaction at lower acceleration levels than would occur in smaller magnitude events. For a given element of soil, there are an infinite number of peak acceleration-magnitude combinations that could, in concept, trigger liquefaction. The relationships between the earthquake magnitude and cyclic stress necessary to trigger liquefaction are described in Section 2.1. As an example, Figure 3.35(a) shows the combinations of PGA and M_w that would trigger liquefaction in an element of soil with $(N_1)_{60}$ = 15 blows/ft at a depth of 3 m in a profile of loose to medium dense clean sand with groundwater at a depth of 1 m. Such conditions are representative of sites that have liquefied in past earthquakes. Combinations of PGA and M_w that fall below the curve are insufficient, on average, to trigger liquefaction. The PGA threshold, however, decreases with increasing magnitude – extrapolation of the existing MSF relationship indicates that liquefaction could be triggered by a PGA as low as 0.17 g in a M_w = 9 earthquake when $(N_1)_{60}$ = 15 blows/ft. Figure 3.35(b) shows the same types of curve for $(N_1)_{60}$ = 5, 15, and 25 blows/ft. The curves were superimposed with M_w and R combinations that would produce a given PGA based on the median BCHydro ground motion prediction equation (Abrahamson et al., 2015). The intersections of these two sets of curves define M_w-R combinations corresponding to FS_L = 1 for the reference element assuming different element SPT resistances. Those pairs are plotted for $(N_1)_{60}$ values of 5, 15, and 25 blows/ft in Figure 3.36(a). These curves can be interpreted as representing the maximum distances to which liquefaction would be expected to occur for earthquakes of different magnitudes and are referred to as magnitude bounding curves. The maximum distance where liquefaction is expected increases with increasing magnitude and with decreasing soil density. The curve for $(N_1)_{60}$ = 5 corresponds quite closely to empirical curves of distance to the most distal liquefaction site (Maurer et al., 2015). This observation suggests that the most distant cases of liquefaction generally involve very loose soils. Figure 3.36(b) shows the maximum distance at which liquefaction was observed in many different earthquakes along with the bounding curves of Ambraseys (1988). Figure 3.36(a) illustrates the sensitivity of the maximum distance to

liquefaction to the density of the soil. Consequently, loose sands can liquefy to relatively large distances from the source of an earthquake. Relatively dense soils require strong shaking to liquefy, which occurred only at relatively short source-to-site distances in moderate magnitude events.

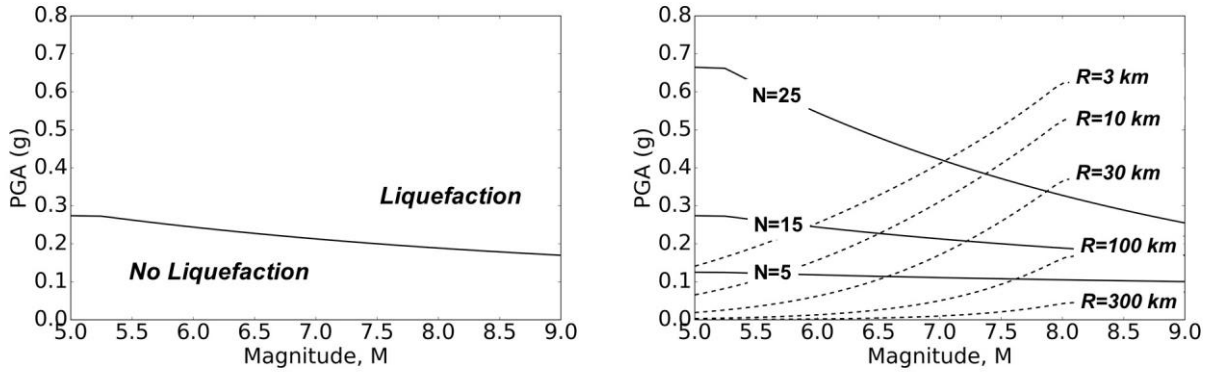

Figure 3.35: Liquefaction triggering for PGA-M pairs (from Kramer and Greenfield, 2017). (a) Magnitude-PGA pairs corresponding to FS=1 for an example site. (b) Magnitude-PGA pairs corresponding to FS=1 for different SPT resistances and different distances.

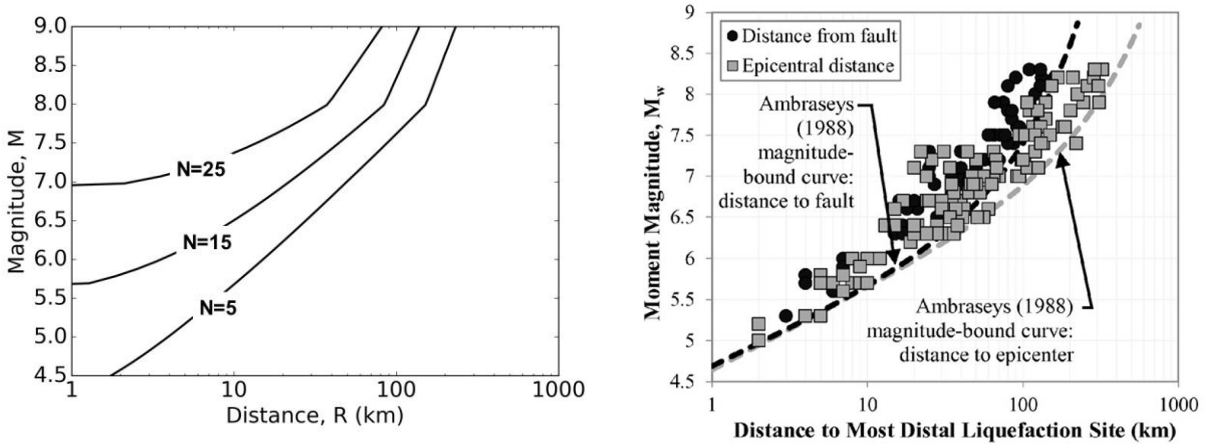

Figure 3.36: Maximum distance of liquefaction. (a) Maximum distance to FS=1 for soils of different density (from Kramer and Greenfield, 2017). (b) Maximum distance of observed liquefaction (from Maurer et al., 2015).

Tohoku case history

During the 2011 Tohoku earthquake, evidence of liquefaction was observed in Ikenouchi, Minamiboso City near the southern end of the Chiba peninsula. The site was 440 km from the epicenter of the earthquake and 192 km from southernmost portion of the rupture (Hata et al., 2013). Sand boils, cracks, and uneven settlement were observed during field reconnaissance Hata et al. (2013) of the area. A subsurface investigation at the site revealed layers of loose silty sand, fine sand, and sandy silt overlying dense sand with gravel. The profile, along with Standard Penetration Test and shear wave velocity measurements, is shown in Figure 3.37.

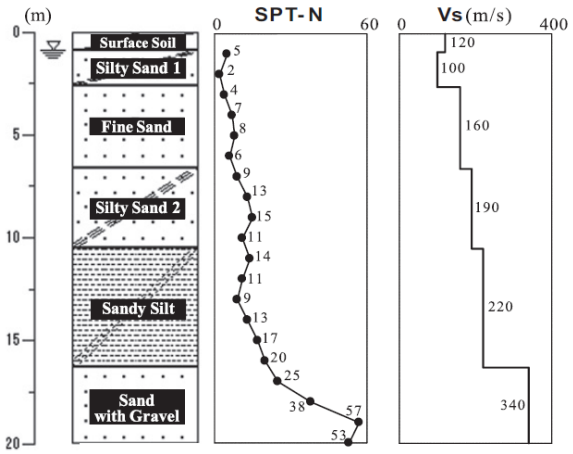

Figure 3.37: Subsurface conditions and soil properties at Ikenouchi liquefaction site (from Hata et al., 2013).

No strong motion instruments were located in the immediate vicinity of the Ikenouchi site, but several stations operated by agencies such as NIED (K-Net and Kik-Net), the Japanese Meteorological Agency, and the Shutoken Kyoshin Network (SK-net) were located nearby. Hata et al. (2013) used microtremor H/V measurements and aftershocks measured by the existing instruments and a temporary array placed at the location of the observed liquefaction to study amplification behavior at the site and characterize the ground motions at the site from the $M_w = 9$ Tohoku event. The amplification and duration behavior at the liquefaction site was found to be different than the locations of the surrounding strong motion instruments, observations thought to possibly be related to topographic and basin effects.

Synthetic time histories were generated by a procedure that produced motions consistent with those recorded at the nearby stations and the amplification consistent with the H/V

microtremor measurements at the Ikenouchi site (Hata et al., 2013). These synthetic motions were used as input motions to one-dimensional finite element analyses of the Ikenouchi liquefaction case history profile. These analyses were performed using the computer program FLIP (http://www.flip.or.jp/flip_english.html) and showed high pore pressures being generated at the case history profile, which was judged to be consistent with the observation of liquefaction at the site. Effective stress analyses of a nearby site with similar subsurface conditions, but for which shorter duration motions were predicted, showed pore pressure ratios limited to the range of 0.5-0.8. Hata et al. (2013) noted the importance of accounting for site-specific ground motion characteristics in addition to site-specific soil conditions. This case history provides an example of liquefaction triggering from a very low amplitude ground motions, but with many cycles of loading.

3.4.2 *Liquefaction of denser soils*

Liquefaction occurs most frequently in loose, saturated soils, many of which are deposited as hydraulic fills or recent alluvium. However, databases of empirical observations (Boulanger and Idriss, 2014; Cetin and Seed, 2004) include cases of liquefaction occurring in very dense soil. The liquefaction triggering curves discussed in Chapter 2.1 do not place an upper-bound limit on the density of soils for liquefaction triggering. For very large magnitude events, the magnitude scaling factor is less than 1.0, which reduces the cyclic resistance of the soil. Figure 3.23 shows that a soil profile with $(N_1)_{60}$ = 25 blows/ft at a source-to-site distance of 70 km would clearly not liquefy under the levels of shaking for earthquake magnitudes M_w < 8.3. However, for a M_w = 9 earthquake, such a profile would be expected to liquefy.

3.4.3 *Increased shaking in a liquefied state*

Liquefaction may occur relatively early during a long duration earthquake and the soil may be subject to many cycles of loading in a liquefied state. Once the soil has liquefied, it is extremely soft and amplifies very low-frequency motions. Because of the difference in stiffness before and after liquefaction, the frequency content of ground surface motions can be very different before and after liquefaction. This dramatic shift in stiffness can affect the site response behavior, and large spectral amplifications have been observed across a range of periods at sites where

liquefaction has occurred. Additional discussion about the changes in frequency content due to liquefaction is discussed in Chapter 4.

After liquefaction, the soil fabric continues to degrade through additional cycles of loading. This causes additional softening, and if liquefaction occurs on a slope or near a free-face, the additional cycles of loading and softening can result in very larger shear strains and lateral spreading.

3.4.4 *Drainage during shaking*

Earthquake loading is usually assumed to occur under undrained conditions in saturated soils. That implies that any redistribution of pore pressure (or void redistribution) would take place after earthquake shaking has ended. The long durations of ground motions produced by very large earthquakes can allow time for significant redistribution of excess pore pressure during the period of shaking. The potential for partial drainage can affect the rate of pore pressure generation and the consequences of liquefaction. The extent to which drainage can affect liquefaction potential and the consequences of liquefaction depend on the permeability of the liquefied soil, the thickness of that soil, and the permeability of the overlying and underlying layers. The effects would be most significant for a relatively thin liquefiable layer sandwiched between two permeable layers. Additional discussion about drainage and pore pressure redistribution during shaking is provided in Chapters 5 and 6.

3.5 SUMMARY

Intensity measures for duration are typically derived from mechanical principals, laboratory test results, or empirical field observations. Several suites of motions have been developed with specific amplitude, frequency content, or duration characteristics. These suites were intended to isolate the characteristics of earthquake motion duration. Synthetic suites of motions that isolated the duration of ground motions from frequency content and amplitude showed that bracketed duration and significant duration largely captured the duration of the motions, and were independent of frequency content and acceleration amplitude. A suite of motions with uniform spectral acceleration appeared to have modest variance with respect to duration intensity measures, indicating that spectral acceleration may not be a good indicator of earthquake duration.

Liquefaction triggering is related not only to the duration of an earthquake but also the acceleration amplitude. Metadata from recorded earthquakes can be used to evaluate the magnitude-adjusted PGA, which is typically associated with field observation of liquefaction triggering. The magnitude-adjusted PGA is similar to, but different than, cycle-adjusted PGA, which is based on a calculated number of cycles in a shear stress time history, rather than a magnitude scaling factor based on earthquake magnitude. As expected, suites of liquefaction-consistent motions showed that magnitude-adjusted PGA was very closely correlated with cycle-adjusted PGA. However, Arias intensity also appeared to be very closely correlated with magnitude-adjusted PGA. Analyzing a suite of subduction zone motions confirmed that larger magnitude earthquakes tended to be longer in duration, and the relationships used to calculate liquefaction triggering intensity measures, which were developed using shorter-duration crustal ground motions, remain consistent for longer-duration subduction zone motions. Basin effects appeared to be relatively limited with respect to liquefaction triggering, and a suite of basin and Cascadia Subduction Zone synthetic motions indicated that recording stations located within basins showed a slight increase in the PGA and a slight reduction in the number of cycles of loading, leading to an overall modest reduction in liquefaction triggering potential. Intensity measures associated with post-triggering deformation, however, did show an increase with basin depth.

Chapter 4. IDENTIFICATION OF THE TIME OF LIQUEFACTION TRIGGERING AT STRONG MOTION RECORDING SITES

Liquefaction effects the motions that are transmitted through the ground to structures and can, therefore, affect structural performance even if ground failure does not occur. Because the great majority of both cyclic and permanent deformations develop after liquefaction is triggered, knowledge of the time when liquefaction is triggered is potentially useful for isolating the behavior of liquefied soil and predicting deformations influenced by liquefaction. Within the past 10-20 years, many strong motion instruments have recorded ground motions at sites that were underlain by liquefiable soil. In this Chapter, the time-frequency behavior of ground motions that were influenced by liquefaction was investigated. A procedure was developed to identify the time at which liquefaction occurred in these records, which can then be used to isolate the behavior of soil after liquefaction occurred.

4.1 EFFECTS OF LIQUEFACTION ON GROUND MOTIONS

The development of high excess pore pressure during an earthquake can lead to a rapid reduction of effective stress and, therefore, a sudden drop in stiffness of the soil. The loss of stiffness affects the dynamic response of the soil profile and changes the frequency content of the motion transmitted to the ground surface. Once the soil liquefies, the ability of a profile to transmit high-frequency motions is greatly reduced while the ability to transmit low-frequency motions to the surface is enhanced. A discussion about the effects of liquefaction with respect to soil stiffness and ground motion amplification is provided in Chapter 2. The rapid change in soil stiffness can have a significant effect on the response of structures supported on or embedded in a profile with liquefiable soil -- the ground surface motion can change from one that induces high forces in structures to one that imposes large deformations on structures.

4.1.1 *Changes in ground motion frequency content*

Earthquake ground motions are affected by different types of waves that travel through the earth's crust. Wave propagation velocities vary depending on the mode and the type of wave. At a site, p-waves arrive first, followed by s-waves, and then surface waves arrive. P-waves typically oscillate at higher frequencies than s-waves, and s-waves oscillate at higher frequencies than surface waves. Thus, earthquake ground motions typically exhibit a general trend of decreasing frequency content with time. If the different waves generated by an earthquake fault rupture arrived discretely, ground motions would exhibit abrupt changes in frequency content with time. Due to extended source and scattering effects, however, the arrival times of the various waves overlap, leading to a more gradual variation of frequency content with time. Indeed, procedures for stochastic simulation of non-stationary synthetic ground motions (e.g., Conte and Peng, 1997; Spanos et al., 2007; Rezaeian and Der Kiureghian, 2010; Yamamoto and Baker, 2013) describe spectral nonstationary behavior using functions that vary relatively smoothly with time.

In liquefiable soils, the soil stiffness changes due to the generation of excess pore pressure during strong shaking. The simple relationship described in Chapter 2 showed that elevated pore pressures affected the site response after liquefaction occurred. The low-strain characteristic site period increased in proportion to $(1\text{-}r_u)^{-0.25}$ as the pore pressure ratio increased. This simple, conceptual relationship implied that the effects of pore pressure generation on the low-strain characteristic site period were relatively modest at pore pressure ratios less than about 0.9. The characteristic site period increased only by 50% at a pore pressure ratio of 0.8 and did not double until the pore pressure ratio reached a value of about 0.94. The simple relationship indicated that:

- the low-strain stiffness of the soil decreases relatively slowly until pore pressure levels become quite high,
- the stiffness decreases rapidly as the pore pressure levels approach initial liquefaction, and
- it is possible to generate relatively high pore pressures without seeing the high levels of softening typically associated with the triggering of liquefaction (Kramer et. al., 2013).

This behavior suggests that the frequency contents of ground surface motions at sites that have liquefied should change quickly at the time of liquefaction. Therefore, rapid changes in frequency content may be used to identify the time at which liquefaction occurs. It should be recognized, however, that changes in frequency content may also result from changes in the motion below the

liquefiable soil. The arrival of s-waves and/or surface waves can also lead to changes in the frequency content at the ground surface.

The stiffness of a soil profile can be estimated in the field through the ratio of Fourier spectra from horizontal and vertical ground surface microtremor motions (Nakamura, 1989). Normalizing the horizontal Fourier spectrum by the vertical spectrum reduces source and path effects that are common to both, leaving an H/V spectral ratio that Nakamura indicated was a close approximation of the shear wave transfer function between the surface and bedrock. Further investigation (e.g., Lermo and Chavez-Garcia, 1994; Fah et al., 1997; Parolai et al., 2004) has shown that Nakamura's technique is reliable for identifying the fundamental frequency of the transfer function.

4.1.2 *Ground motions at liquefiable sites*

Rapid increases in the number of strong ground motion instruments deployed around the world over the past 20 years have yielded many ground motion recordings at sites underlain by liquefiable soils. Many these sites have been subjected to earthquake shaking which was strong enough to produce surficial evidence of liquefaction. Those records show that earthquake-induced liquefaction can alter the amplitude, frequency content, and duration of the recorded ground surface motions. Those parameters have been used to determine if liquefaction was triggered during strong ground motions. The procedures for identifying the presence of absence of liquefaction are generally based on computing ground motion parameters and comparing the values of these parameters with limit values that correspond to the occurrence of soil liquefaction. These procedures are intended to produce a categorical (yes/no/maybe) result indicating whether the given time history came from a deposit that liquefied during the event.

Takada and Ozaki (1997) used a relatively simple parameter, the average ratio of Arias intensities of low-pass filtered and non-filtered orthogonal horizontal acceleration time histories, to identify the occurrence of liquefaction. The method of Suzuki et al. (1998) required analysis of four parameters: (a) PGA, (b) maximum spectral intensity, defined as the integral of the 20% damped velocity response spectrum over periods of 0.1 to 2.5 seconds, (c) maximum horizontal ground displacement due to harmonic vibration, and (d) zero crossing period, a parameter that accounted for the temporal change in frequency content by looking at the number of instances the

acceleration changes sign within a moving time window. Liquefaction was considered to have occurred if all four parameters exceeded threshold values.

Miyajima et al. (1997) used all three components of a recorded ground motion to identify the occurrence of liquefaction based on four parameters: (a) the ratio of vertical and horizontal accelerations that occurred after the PGA, (b) the ratio of the area beneath the Fourier amplitude spectrum at low frequencies (0-2 Hz) compared to the area from 0-10 Hz, (c) an average predominant frequency based on the peak value of a moving window FFT, and (d) the rate of change of the predominant frequency with time.

Kostadinov and Yamazaki (2001) identified liquefaction based on the mean instantaneous frequencies of the horizontal and vertical components of acceleration and peak ground velocity. The occurrence of liquefaction was based on the duration over which the mean instantaneous frequency was above or below certain threshold frequencies, and on whether the peak horizontal ground velocity exceeded a threshold value. Yuxian et al. (2005) used the cumulative time over which the predominant instantaneous frequency, calculated based on the Hilbert-Huang transform (Huang et al. 1998), of the horizontal and vertical acceleration components was above or below given threshold frequencies to identify the occurrence of liquefaction.

As noted, these procedures only attempt to detect the occurrence or non-occurrence of liquefaction and do not offer insight into the time at which liquefaction was triggered. In the following sections, a procedure intended to detect the triggering time of liquefaction is proposed.

4.2 TIME-FREQUENCY REPRESENTATION OF GROUND MOTIONS

A common way of analyzing the frequency content of a signal is usually through Fourier analysis, where a periodic function is expressed as the sum of a series of simple harmonic terms of different frequency, amplitude, and phase (Fourier, 1878/1955). The Fourier series for a time history of acceleration, $a(t)$, is given by

$$A(f) = \int_{-\infty}^{\infty} a(t) e^{-i\,2\pi\,f\,t}\,dt \tag{4.1}$$

where t is time and f is frequency. The frequency content in a Fourier transform is assumed to be stationary, i.e., constant over the duration of the signal. Time-frequency analyses are needed to analyze non-stationary signals with time-varying frequency content. Time-frequency

representations of the recorded motions are most commonly created using short-time Fourier transforms (STFT) or wavelet transforms.

The STFT applies a moving time window to a record so that the Fourier transform can be performed on individual intervals of the signal, rather than on the entire signal. The window localizes the signal in time although the frequency content is smeared over the length of the window. This allows for the development of a spectrogram, which is a plot of short-time Fourier amplitude as a function of both frequency and time. The STFT of a signal can be defined as

$$A(t,f) = \int_{-\infty}^{\infty} a(\tau)\, w(\tau - t)\, e^{-i\,2\pi\, f\, \tau}\, d\tau \tag{4.2}$$

where w is the window function. The width of the window affects the relative resolutions of time and frequency. The STFT spectrogram generally provides very good resolution of frequency, but relatively poor resolution of time.

The wavelet transform, which convolves a signal with a wavelet function (Addison, 2002), can also be used to represent time-frequency behavior. The wavelet function is localized in time and centered about a particular frequency, but the resolution of the wavelet function is smeared over a range of frequencies. The wavelet can be controlled by shifts in time or changes in central frequency by dilating or compressing the width (or scale) of the wavelet with respect to time. The continuous wavelet transform (CWT) can be described by

$$W(t,b) = \frac{1}{\sqrt{b}} \int_{-\infty}^{\infty} a(\tau)\, \Psi\left(\frac{\tau - t}{b}\right) d\tau \tag{4.3}$$

where b is a scale dilation factor that can be related to central frequency, and Ψ is a wavelet function. The wavelet transform allows for the development of a scalogram that provides a representation of variation in scale with respect to time, in which scale can be related to the central frequency of the wavelet (Mayfield, 2008). A wavelet scalogram is defined as the amplitude of the CWT and is generally expressed in terms of central frequency instead of scale dilation factor. The scalogram generally provides very good resolution of time but relatively poor resolution of frequency.

A more recent way of representing time-frequency behavior of recorded motions is through the Stockwell, or S-, transform (Stockwell et al., 1996). The S-transform is an extension of the idea of the continuous wavelet transform and is based on a moving and scalable localizing window. The S-transform is different in that it provides frequency-dependent resolution while maintaining

a direct relationship with the Fourier spectrum. The S-transform of a signal, $a(t)$, defined as CWT with a specific (usually Gaussian) analyzing wavelet multiplied by a phase factor, can be expressed as:

$$S(t,f) = \int_{-\infty}^{\infty} a(\tau)\, \frac{f}{\sqrt{2\pi}} \exp\left[-\frac{1}{2}\,(t-\tau)^2 f^2\right] \exp[-i\,2\pi\, f\, \tau]\, d\tau \qquad (4.4)$$

The Stockwell-transform combines elements of both windowed Fourier transform and wavelet transforms to provide a balanced resolution of both time and frequency. A Stockwell spectrum can be computed as the amplitude of the transformed variable, $S(t,f)$. The Stockwell spectrum provides a balance between the resolutions of the STFT and CWT with better time resolution than the STFT spectrogram and better frequency resolution than the CWT scalogram.

The relative resolutions of the STFT, wavelet, and Stockwell transforms can be illustrated by considering synthetic signals with known frequency contents. Figure 4.1 shows all three time-frequency analyses of a three-part function consisting of simple sinusoids. The three-part function (Figure 4.1(a)) consists of a 1 Hz sinusoid followed by a 4 Hz sinusoid followed by the sum of a 2 Hz sinusoid and a lower amplitude 6 Hz sinusoids. The STFT spectrogram in Figure 4.1(b) clearly identifies the frequencies of the sinusoids but only crudely resolves the times at which the frequencies change – the different frequency bands overlap each other at the times (5 sec and 10 sec) at which the frequency content instantaneously changes. The wavelet scalogram in Figure 4.1(c) shows good resolution of the times at which the frequencies change, but significant smearing of frequency, particularly at higher frequencies. The Stockwell spectrum is shown in Figure 4.1(d) shows time resolution that is far better than that of the STFT, and frequency resolution better than that of the wavelet scalogram. This type of relative behavior was seen in other tests and in the examination of actual earthquake records. The Stockwell transform provides a better indication of time-frequency content than the STFT or wavelet transform for the purposes of this work.

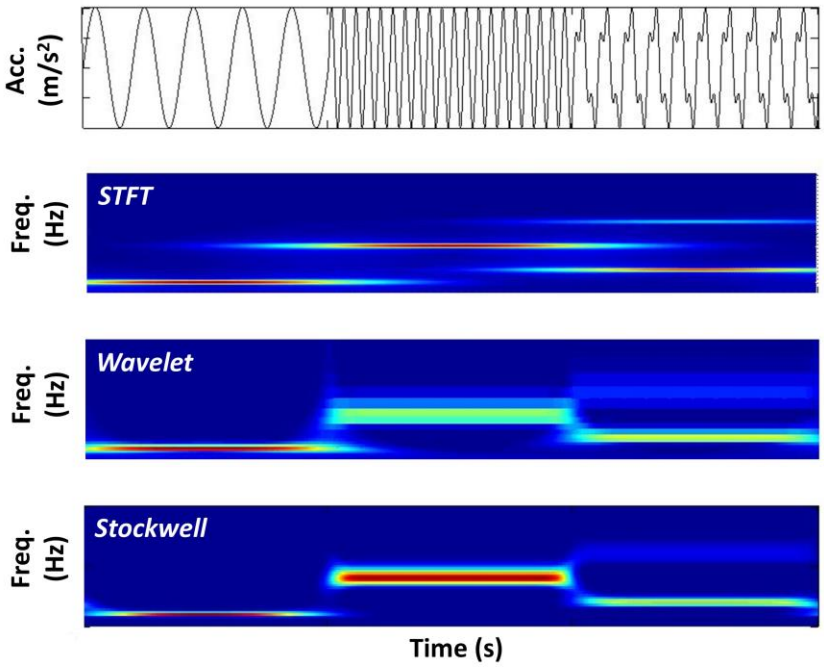

Figure 4.1: Time-frequency analysis of a three-part function.

4.3 IDENTIFICATION OF TRIGGERING FROM VERTICAL ARRAY RECORDS

The frequency content of a ground surface motion can change with time due to changes in the stiffness of the soil profile and/or changes in the frequency content of the motion. The former can be isolated with good resolution when ground motions are also recorded below the soil layer of interest, as in the case of vertical arrays. When both surface and downhole records are available at a site, the ratio of the surface Stockwell spectrum to the downhole Stockwell spectrum shows the evolving amplification behavior of the soil between the two instruments. The liquefied soil between the instruments tends to amplify the low-frequency components of motion and deamplify the high-frequency components of the motion that propagate through the liquefied soil. Because modern strong motion instruments record three orthogonal components of ground motion, horizontal motions can be resolved in any azimuthal direction to check the azimuthal variability of the evolving amplification behavior.

Unfortunately, vertical arrays that are close enough together to interpret the effects of a layer of liquefied soil are not common. Furthermore, only a few vertical arrays have been shaken

strongly enough to trigger liquefaction. The Wildlife and Port Island arrays are the best-known examples where liquefaction occurred in a vertical array. In the following section, the surface and downhole records from the Wildlife and Port Island sites were analyzed to examine changes in the frequency content due to liquefaction.

4.3.1 *Wildlife liquefaction array*

The most well-known and widely studied vertical array subjected to liquefaction is the Wildlife Liquefaction Array (WLA) in southern California. Surface investigations at WLA (Bennett et al., 1983; Zeghal and Elgamal, 1994) indicated that the Wildlife site was mantled by about 2.5 m of lean clay and silt, which was underlain by a layer of sandy silt. The sandy silt transitioned to loose, silty sand about 3.5 m below the ground surface, which extended to a depth of about 6.8 m. The layers of sandy silt and silty sand were saturated, exhibited low plasticity, and were susceptible to liquefaction. Below the silty sand, highly plastic clay was encountered. A downhole accelerometer was installed in the clay layer at a depth of about 7.5 m. A series of piezometers were also installed in the silty sand, and the groundwater level was observed at a depth of about 1.5 m during the initial site investigation. The Wildlife array was subjected to strong shaking in 1987 from the Elmore Ranch and Superstition Hills earthquakes. The Elmore Ranch earthquake of November 23, 1987, was a M_w = 6.2 event epicentered 23 km west of the WLA that did not produce surficial evidence of liquefaction. The Superstition Hills earthquake, a M_w = 6.6 event that occurred about 11 hours later, produced sand boils, ground cracks, and permanent lateral displacements at the site (Elgamal and Zeghal, 1994; Youd and Holzer, 1994).

Figure 4.2 shows Stockwell spectrograms for the NS components of the surface and downhole motions during the Superstition Hills event. The spectrograms were normalized at each time increment by dividing the spectral amplitude by the peak amplitude, which allowed for clear visualization of variations in frequency content over the entire length of the record. In these spectrograms, the deepest blue color represented a normalized spectral amplitude of zero and the deepest red color represented a normalized spectral amplitude of 1.0, which was the peak spectral amplitude and the modal frequency. The normalized surface Stockwell spectrogram, Figure 4.2(a), showed high acceleration amplitude at frequencies greater than 10 Hz during the relatively weak shaking at the beginning of the record. At about 5 seconds, the spectral amplitude at these frequencies decreased, and motions with frequencies around 2-8 Hz dominated the spectrum.

Then, at about 13-14 seconds, the frequency content of the motion shifted rapidly to frequencies less than 1 Hz. The downhole record showed a gradual transition from very high frequencies above 10 Hz to frequencies in the range of 1-5 Hz around 5 seconds. The downhole recording did not show the rapid drop in frequency content around 13 to 14 seconds that was seen in the surface recording, and the frequency content remained relatively constant until about 25 seconds. Both the surface and downhole records showed relatively smooth transitions to very low frequencies (approximately 0.3 Hz) at about 30 seconds, which was likely due to the arrival of surface waves (Holzer and Youd, 2007).

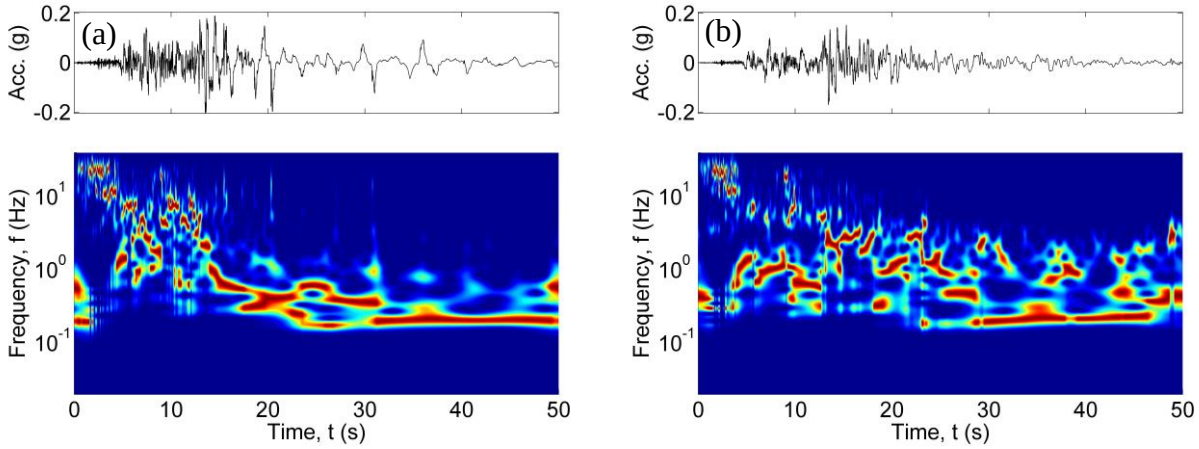

Figure 4.2: Normalized Stockwell spectra for the Superstition Hills NS acceleration time history. (a) surface motion, (b) downhole motion

The behavior of the liquefied soils could be isolated by accounting for the frequency content changes in the downhole recorder, which was installed below the liquefied soil. The downhole record was used to isolate frequency content changes due to liquefaction from frequency content changes due to earthquake source and path effects. Figure 4.3 shows the ratio of the surface to downhole Stockwell spectra for the EW and NS components of the Superstition Hills earthquake. This ratio illustrated the evolving amplification behavior of the soil between the surface and downhole instruments and provided an indication of which frequencies were amplified or deamplified by the soil between the two instruments. Figure 4.3 was created by first smoothing both the horizontal and vertical Stockwell power spectrum slightly with a 2-D digital image processor. The ratio of the spectra was then taken, and then the ratio was normalized at each time increment. The deepest blue color in the figure represents deamplification or no amplification between the instruments, and the deepest red color represents the greatest amplification. The ratio

of spectra indicated that a significant, coinciding change in frequency content in both components of motion occurred at approximately 13-14 seconds. Some very high-frequency amplification (greater than 10 Hz) occurred after 20 seconds, which coincided with dilation spikes which were also seen as sharp pulses in the surface acceleration time histories. The overall results of this analysis implied that the soil between the downhole and surface accelerometers amplified motions in the range of 3-10 Hz at the beginning of the record, but then primarily amplified only low-frequency motions after about 13-14 seconds. The dramatic change in amplification behavior corresponded with evidence that the soil liquefied at about 13-14 seconds. Many investigators (Bonilla et al., 2005; Ziotopoulou et al., 2012; Roten et al., 2014) have analyzed the Wildlife site using one-dimensional, nonlinear, effective stress analyses with advanced constitutive models capable of simulating phase transformation behavior. The models produced very good matches to the recorded surface motions when the recorded downhole motions are used as inputs. These models also showed that pore pressures rose to very high levels and the shear strain amplitude increased substantially around 13-14 seconds. The results of the numerical models were consistent with the shifts in frequency content and amplification behavior shown in Figure 4.3. They are inconsistent, however, with the measured pore pressures (Youd and Holzer, 1994) and the Love wave-based explanation of their apparently delayed nature by Holzer and Youd (2007).

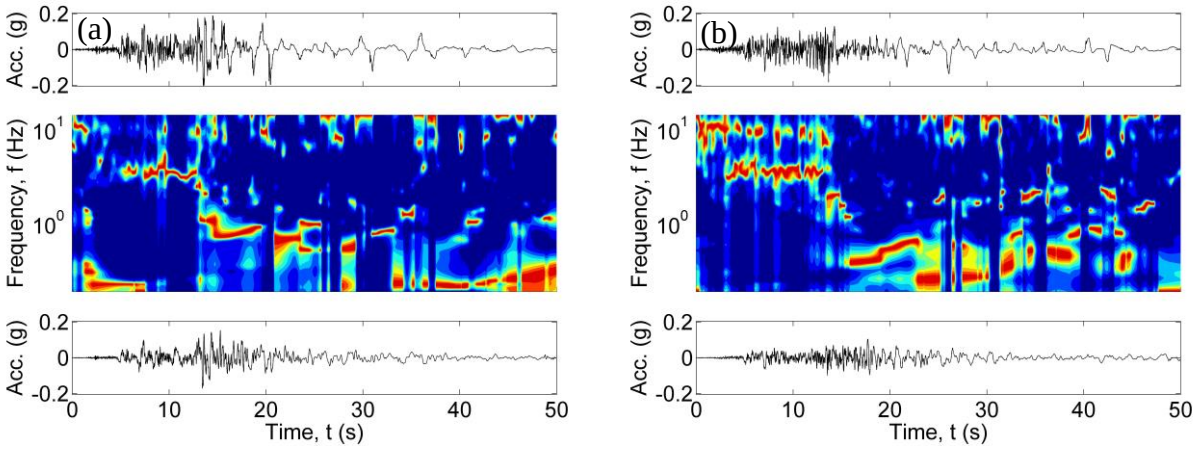

Figure 4.3: Normalized ratio of surface and downhole Stockwell spectra for WLA. (a) EW component. (b) NS component.

4.3.2 *Port Island vertical array*

The Port Island vertical array was located on an artificial island in Kobe Port, Japan. The array was established in 1991 to observe the potential effects of liquefaction on recorded ground motions. Accelerometers were installed at the ground surface and at depths of 16 m, 32 m, and 83 m. Subsurface conditions encountered at the Port Island site during the installation of accelerometers consisted of 19 m of loose sand and gravel fill on top of alluvial Holocene clay. The Holocene clay extended to a depth of about 27 m, where Pleistocene sand, gravel, and clay deposits were encountered. The Pleistocene deposits extended below a depth of 83 m, where the lowest accelerometer was installed (Baise et al., 2001). The groundwater table at the time of installation was about 4 m below the ground surface. Liquefaction was observed at the Port Island array during the January 17, 1995, M_w = 6.9 Hyogo-Ken Nanbu earthquake. The saturated fill between the groundwater table and a depth of about 16 m liquefied during the earthquake. About 3 m of lateral spreading deformation was observed at a caisson-type quay wall located about 400 m from the array (Baise et al., 2001). The lateral spreading deformation caused significant damage to the quay wall.

Ratios of the surface and downhole Stockwell spectra were computed using the ground surface and 16-m depth recordings to evaluate the response of the liquefied fill at Port Island. Figure 4.4 shows the EW and NS components of surface and downhole acceleration time histories along with the ratio of surface to downhole spectra. A significant change in the frequency content of the surface to downhole spectral ratio occurred around 13 seconds as the amplitude of the motion increased. At that time, peak frequencies of the ratio shifted from frequencies primarily above 1 Hz to frequencies primarily below 1 Hz. A second rapid, significant change in the frequency content occurred around 16-17 seconds when the peak frequencies of the surface to downhole spectral ratio dropped from about 1 Hz to below 0.3 Hz. These two decreases in frequency content at 13 seconds and then again at 16-17 seconds were interpreted as:

- first, the arrival of low frequency, high acceleration amplitude waves around 13 seconds, which caused pore pressure to increase and the soil stiffness to decrease; and then
- second, liquefaction between 16-17 seconds, which caused the soil to become extremely soft and only transmit very low-frequency motions to the ground surface recording instrument.

Other observations using cross-correlation analysis between the surface and downhole recordings (Elgamal et al., 1996) showed the average shear wave velocity between the instruments dropped to very low values between about 16 to 18 seconds. This observation was consistent with numerical simulations using advanced nonlinear constitutive models (Zeghal et al., 1996; Cubrinovski et al. 1996; and Sawada et al., 2000), which indicated that pore pressure initially developed during the strong shaking at about 14 seconds, but liquefaction did not occur until about 16 to 18 seconds.

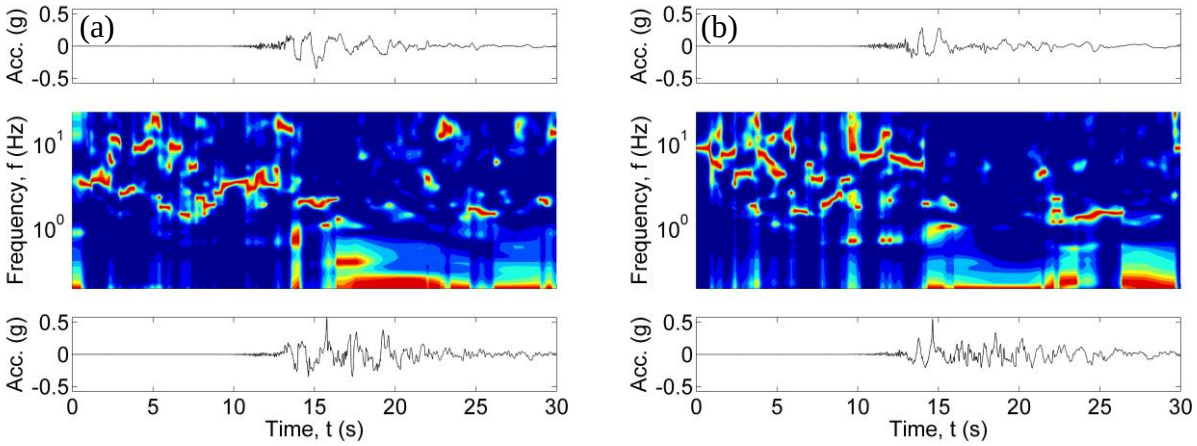

Figure 4.4: Normalized ratio of surface and downhole Stockwell spectra for Port Island. (a) EW component, (b) NS component

4.4 IDENTIFICATION OF TRIGGERING FROM SURFACE GROUND MOTION RECORDS

While vertical arrays in liquefiable soils are quite rare, many more records are available from sites with surface ground motion recordings that were underlain by liquefiable soils. Some of these sites experienced shaking strong enough to generate high pore pressure and produce surficial evidence of liquefaction. Since the generation of excess pore pressure reduced the mean effective stress and softened the soil profiles in all directions, a pore pressure-induced shift in amplification behavior is expected to have occurred in all horizontal directions once the soil liquefied. For sites with surface ground motion records, it may be possible to identify the time when liquefaction occurred from just the surface recordings. A Stockwell transform-based procedure has been developed to identify the time at which liquefaction was triggered by identifying sharp changes in frequency content that are independent of the horizontal direction.

Ground surface strong motion recorders typically have accelerometers in the least two horizontal directions, and frequently have a third accelerometer in the vertical direction. The Stockwell transform from two horizontal acceleration time histories can be reduced into a single time-frequency spectrum by taking the norm of the horizontal Stockwell transforms.

$$S_h(t,f) = (|S_{h1}(t,f)|^2 + |S_{h2}(t,f)|^2)^{0.5} \quad (4.5)$$

where $S_{h1}(t,f)$ is the complex Stockwell transform. The norm maintains some portion of the frequency content of the motion in each direction, which reduced the effects of directionally polarized waves while capturing the shift in frequency content that occurred once the soil liquefied. Taking the power of the Stockwell transform also increased the peaks of the spectrum and improved the visual clarity of the changes in frequency content. Like the surface-to-downhole spectral ratios, normalizing the spectrum at each time increment also helped to clarify the changes in frequency content.

Liquefaction occurred at the Wildlife site during the Superstition Hills earthquake at about 13 to 14 seconds into the record. The norm of the Stockwell power spectra from the ground surface record also showed a rapid frequency drop around 13 to 14 seconds. Since the shift in frequency content due to liquefaction is much more dramatic than the shifts due to earthquake nonstationary behavior, the time of liquefaction can be identified, in some cases, from just the ground surface recordings. Figure 4.5 shows the rapid shift in frequency content at the Wildlife site.

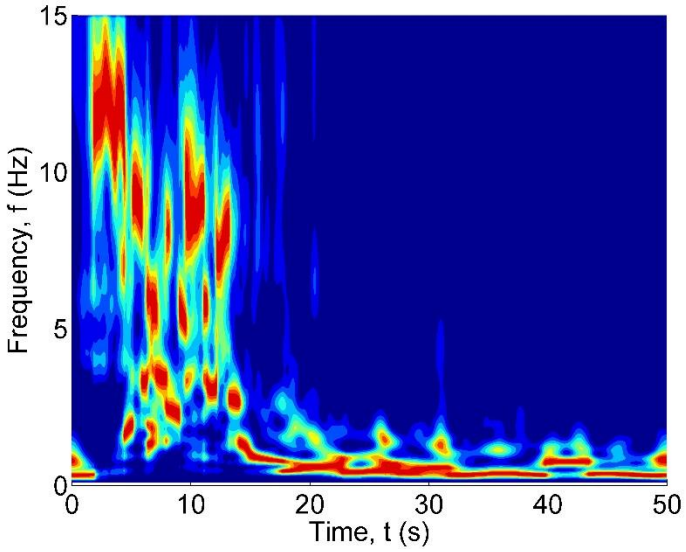

Figure 4.5: Normalized Stockwell power spectrum for the WLA ground surface motion

A procedure has been developed to identify the time of the rapid shift in frequency content caused by liquefaction. Visually, the Stockwell power spectrum clearly shows a rapid shift in frequency content. To identify the time of liquefaction using computational procedures, a time history of the modal frequency, or peak frequency evolving with time, of the ground motion was calculated. Both mean and modal frequencies for evaluating changes in frequency content were investigated. While mean frequencies exhibited more stable behavior, they were (a) less sensitive to the rapid changes in frequency content associated with triggering of liquefaction than modal frequencies and (b) more strongly affected by very high frequencies whose effects were amplified by the variable-width Gaussian window used in the Stockwell transform. Thus, the modal frequency performs better for detecting rapid changes in frequency content with time.

Both the horizontal Stockwell power spectrum (H-spectrum) and the ratio of the horizontal to vertical spectra (H/V spectrum) were used to calculate the modal frequencies evolving with time. The procedure to identify the time of liquefaction using the H-spectrum was based on the modal frequency of the horizontal Stockwell power spectrum. The modal frequency from the H-spectrum was relatively stable from a computational perspective, but frequency shifts from non-stationary behavior, like the arrival of s-waves or surface waves, may also cause the frequency content to change. The procedure based on the H/V spectrum was used to measure the characteristic frequency, or the stiffness, of the soil. The H/V spectrum was calculated using the ratio of horizontal to vertical Stockwell power spectra with a small amount of smoothing to avoid division by very small values. The ratio of spectra provided a measure of the characteristic frequency of the soil, which should be independent of the non-stationary behavior of the ground motions (Nakamura, 1989). However, the ratio of spectra was less stable from a computational perspective and the time of rapid frequency content shifts was not always as clear or obvious in the H/V spectrum as in the H-spectrum. The time at which liquefaction occurred using either procedure was identified by fitting a simple step function to the time history of the modal frequency. The step function implied that the modal frequency of the motion was constant before the time of liquefaction, shifted to a lower frequency at the time of liquefaction, and then remained constant at a low frequency for the remainder of the motion.

The procedure to identify the time at which liquefaction occurred using both the H- and H/V-spectra can be computed in the following steps:

1. Compute the Stockwell transform of each of the horizontal acceleration records

$$S_{hx}(t,f) = \int_{-\infty}^{\infty} a_x(\tau)\ \frac{f}{\sqrt{2\pi}} \exp\left[-\frac{1}{2}\ (t-\ \tau)^2\ f^2\right] \exp[-i\ 2\pi\ f\ \tau]\ d\tau \tag{4.6}$$

where $a_x(t)$ is the acceleration in the direction x.

2. Compute the Stockwell power spectrum using the two horizontal components of motion. The power spectrum helps to visually clarify the peak frequencies of the motion while providing a measure of the amplitude that is independent of direction since frequency shifts due to liquefaction are expected to be azimuthally independent. The horizontal Stockwell power spectrum is computed as:

$$P_{sh}(t,f) = |S_{h1}(t,f)|^2 + |S_{h2}(t,f)|^2 \tag{4.7}$$

where $S_{h1}(t,f)$ and $S_{h2}(t,f)$ are the Stockwell transforms of the two horizontal components of the recorded motion. The Stockwell transforms include real and imaginary components, and the norm of the transform, $S_{hx}(t,f)$, is the amplitude of the motion in direction x.

3. For the H/V spectrogram, calculate steps 1 and 2 with the vertical component of the recorded motion.

$$P_{sv}(t,f) = |S_v(t,f)|^2 \tag{4.8}$$

where $S_v(t,f)$ is the Stockwell transforms of the vertical component of the recorded motion.

4. Smooth the horizontal and vertical Stockwell power spectrograms using a two-way Gaussian filter with a standard deviation of 0.2 sec in time and 0.2 Hz in frequency.

5. Compute the ratio of the smoothed horizontal and vertical Stockwell power spectra. The ratio of the horizontal to vertical power spectra can be interpreted as a time-dependent variant of the previously discussed method proposed by Nakamura (1989).

$$R(t,f) = \frac{P_{sh}\ (t,f)}{P_{sv}\ (t,f)} \tag{4.9}$$

6. Compute time histories of the modal frequency of the H- and H/V Stockwell power spectra, ${f_h}^{Mo}(t)$ and ${f_R}^{Mo}(t)$. The modal frequencies are those corresponding to the maximum value of $P_{sh}(t,f)$ or $R(t,f)$ at each time step.

$${f_h}^{Mo}(t)\ = \underset{f}{\operatorname{argmax}}\, P_{sh}(t,f) \tag{4.10}$$

$${f_R}^{Mo}(t)\ = \underset{f}{\operatorname{argmax}}\, R(t,f) \tag{4.11}$$

7. Fit a step function to each of the modal frequency functions, ${f_h}^{Mo}(t)$ and ${f_R}^{Mo}(t)$, with the step occurring at times that vary from and initial time, t_0, to a final time, t_f. The values of t_0 and t_f are set to bracket the time of liquefaction, and are taken as the first and last absolute exceedances of a threshold acceleration, nominally set at 0.04 g. The step function is defined as:

$$s(\tau) = \begin{cases} F_1 = \dfrac{1}{\tau - t_0}\displaystyle\int_{t_0}^{\tau} f^{Mo}(t)\,dt & t_0 \le t \le \tau \\ F_2 = \dfrac{1}{t_f - \tau}\displaystyle\int_{\tau}^{t_0} f^{Mo}(t)\,dt & \tau \le t \le t_f \end{cases} \tag{4.12}$$

where $f^{Mo}(t)$ is either ${f_h}^{Mo}(t)$ or ${f_R}^{Mo}(t)$ over the time interval.

8. Compute the error functions for the step function fit to both ${f_h}^{Mo}(t)$ and ${f_R}^{Mo}(t)$.

$$E(t) = \frac{2}{F_1 + F_2}\int_{t_0}^{t_f} (f^{Mo}(t) - s(t))^2\,dt \tag{4.13}$$

9. Normalize the error function so the step function fit to ${f_h}^{Mo}(t)$ and ${f_R}^{Mo}(t)$ can be compared.

$$E_n(t) = \frac{E(t)}{\min[E(t)]} \tag{4.14}$$

10. Plot both normalized error functions versus time. The time at which $E_n(t) = 1$ is the most likely time when liquefaction was triggered. The rate of increase of $E_n(t)$ at times other than when $E_n(t) = 1$ provides a measure of the confidence of the time of liquefaction, i.e. steeper values of $E_n(t)$ indicate a higher confidence in the time of liquefaction.
11. Compare the most likely times of triggering from Step 10 and examine the times relative to the horizontal time histories and the Stockwell spectrograms. If both agree, the indicated time of liquefaction is generally reliable. If the times are inconsistent, the time histories and spectrograms should be examined carefully to determine which triggering time appears more appropriate. The following "tests" should be performed:
    11.1. The cyclic stress ratio in the critical layer of the soil profile should be computed for each candidate triggering time. Using a suitable cycle-counting and magnitude scaling factor correlation (i.e., Liu and Stewart, 2001), the cyclic stress ratio (CSR) can be computed as a function of time. The computed cyclic stress ratios should be compared with those at which liquefaction of the critical layer should be

expected using an appropriate cyclic resistance ratio model (i.e., Idriss and Boulanger, 2014). Candidate triggering times that correspond to unrealistically low CSR values may be associated with frequency content changes caused by s-wave arrivals rather than liquefaction.

11.2. Compute a rotated vector ground motion in 5-degree increments from 0 to 180 degrees and, using equations (4.5) and (4.6), compute the mean horizontal frequency for one component as a function of time. Plot the time histories of mean frequency on polar coordinates and examine the consistency of the frequency shifts with the candidate times of liquefaction over the various azimuthal orientations of the rotated motion. Some motions may show a rapid decrease in frequency content due to the arrival of surface waves; such frequency shifts may show significant azimuthal variability due to surface wave polarization. Since rapid decreases in frequency content caused by elevated pore pressure, which acts equally in all direction, are azimuthally-independent, frequency shifts due to liquefaction should not show any azimuthal variability.

11.3. Examine the differences in frequencies before and after the estimated time of liquefaction. If the frequency after the estimated time of liquefaction is relatively high and close to the pre-triggering frequency, liquefaction may not have been triggered. If the frequencies before and after the time of liquefaction are relatively low and close to each other, the recorded motion may not be a good candidate for identifying the time of liquefaction triggering based on changes in frequency content. Such conditions can be found at sites where the liquefiable soil is underlain by soft clay so that the response is "soft" even before liquefaction is triggered.

The procedure described in this section can be applied consistently and objectively to any ground motion influenced by liquefaction. For many such motions, the two procedures produce consistent estimates of the time at which liquefaction was triggered. Some motions, however, are poorly suited to a procedure that relies on detection of changes in frequency content. These include sites where liquefiable soils are underlain by soft soils where the frequency transmitted by the soil is very low, regardless of the presence or absence of liquefied soils. Sites with relatively thin liquefiable zones that are bounded by highly permeable soils may not show a rapid drop in frequency content since pore pressure dissipation and drainage can occur during earthquake

shaking. Sites where relatively dense soils may also not show a rapid decrease in frequency content, even when the soils liquefy, since dense soils may soften enough to produce significant changes in frequency content. In some of these cases, the additional tests described in Step 11 can be helpful to identify the time of liquefaction. These procedures also indicate if the H- or H/V-spectra are providing reliable shift in frequency content due to liquefaction triggering.

4.4.1 *Comparison with vertical array procedure*

Before applying this procedure to sites with only ground surface motion recordings, it was evaluated at sites where the times of liquefaction were relatively well-constrained. At the Wildlife liquefaction array, the time of liquefaction was estimated to be about 13 to 14 seconds into the Superstition Hills earthquake. Normalized error functions and azimuthal variation of the mean horizontal frequency from the surface motions are shown in Figure 4.6. The error functions for the modal H- and H/V-spectral frequencies were minimized at 13.2 and 14.3 seconds, respectively. These values were consistent with the estimated time of liquefaction based on the downhole array observation and the estimated time of liquefaction inferred by others through numerical modeling (e.g. Bonilla et al., 2005; Ziotopoulou et al., 2012; Roten et al., 2014). The values of the error function for the H/V-spectrum were lower than the H-spectrum, indicating that the frequency content shifted less in the H/V-spectrum than in the H-spectrum. The azimuthal plot showed a rapid decrease in the frequency content in all directions around 13-14 seconds, which supported the hypothesis that liquefaction was triggered at this time. The frequency content increased for short periods of time between 15 and 20 seconds in the EW direction, possibly indicating dilation pulses after the soil liquefied. Thus, the results from the procedure based on the surface motion alone were consistent with those obtained using both the surface and downhole records.

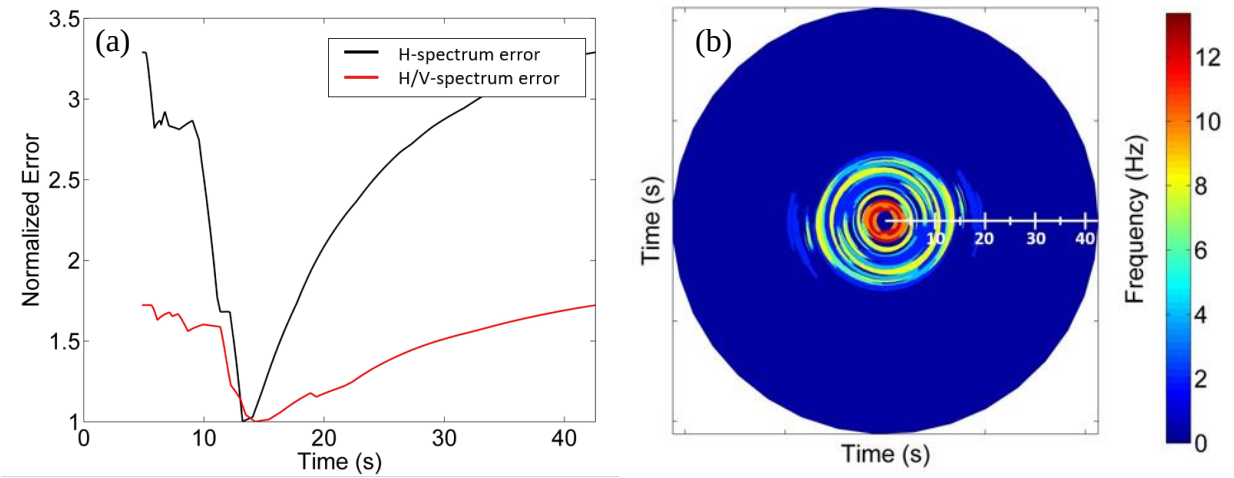

Figure 4.6: Computations for the time of liquefaction using the Stockwell-based procedure for the Superstition Hills earthquake at the Wildlife array. (a) Normalized error function (b) The azimuthal mean frequency.

At the Port Island vertical array, the time of liquefaction was estimated to be about 16 to 18 seconds into the Hyogo-Ken Nanbu earthquake. Normalized error functions of the mean horizontal frequency from the surface motions are shown in Figure 4.7. The azimuthal variation of modal frequency is shown in Figure 4.8. The most rapid decreases in frequency content occurred at 11.8 seconds and 16.7 seconds into the motion, as indicated by the H- and H/V-spectra, respectively. The rapid decrease in frequency content at 11.8 seconds was very sharp and distinct but occurred relatively early in the motion at a time when the acceleration amplitude was barely above the minimum threshold to trigger liquefaction in extraordinarily loose sands. This early drop in frequency content likely indicated the arrival of lower frequency s- or surface waves, rather than the triggering of liquefaction; Bouin et al. (2000) assigned an s-wave arrival time of 13.25 seconds to the Port Island array. The H/V spectrum showed a rapid decrease in the frequency content around 16 to 17 seconds, which was consistent with the estimated time of liquefaction from the vertical array observations and the estimated time of liquefaction inferred by others (Zeghal et al., 1996; Cubrinovski et al. 1996; and Sawada et al., 2000). Figure 4.7(b) shows the error function for the H/V ratio. The error function for the H/V ratio was very flat, indicating that the time of liquefaction included a large amount of uncertainty, especially compared to results from the Wildlife liquefaction array. The azimuthal plot in Figure 4.8 shows a rapid drop in frequency content from about 9 Hz to less than 1 Hz in the NW-SE direction between 11-12

seconds. However, the modal frequency remained above 5 Hz in the NE-SW direction until about 14 seconds. The lack of a distinct, directionally-independent shift in frequency content indicated that liquefaction probably did not occur between 11-12 seconds as the horizontal Stockwell power spectrum implied. However, the shift in frequency content seen in the H/V-spectrum at about 16 to 17 seconds was probably indicative of liquefaction, even though the modal frequencies before and after that time were similar.

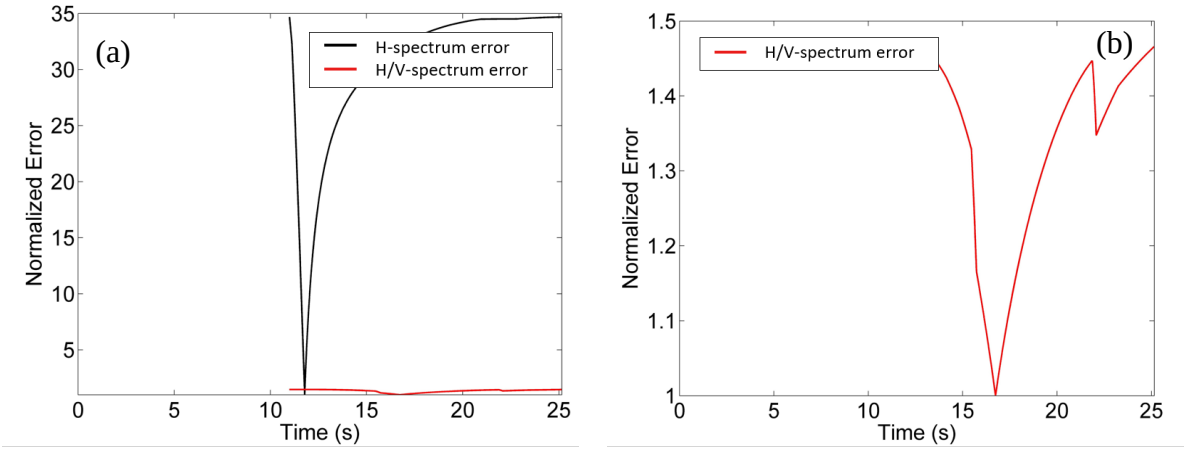

Figure 4.7: Computations for the time of liquefaction using the Stockwell-based procedure for the Hyogo-Ken Nanbu earthquake at the Port Island array. (a) Normalized error function. (b) H/V spectrum only.

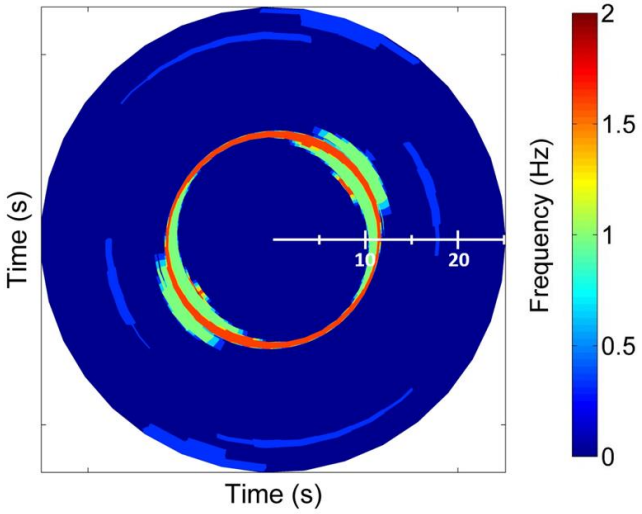

Figure 4.8: Azimuthal variation of the modal frequency using the Stockwell-based procedure for the Hyogo-Ken Nanbu earthquake at the Port Island array.

4.4.2 *Discussion*

The analyses of the Wildlife and Port Island vertical arrays illustrated a range of conditions that could be encountered with ground motions influenced by liquefaction. The Wildlife array showed significant and rapid softening upon the triggering of liquefaction and both H- and H/V-spectrum error functions produced clear and generally consistent indications of the time of liquefaction. The Port Island array, on the other hand, was located at a site that was so soft that the frequency content did not change dramatically when liquefaction was triggered. Thus, the error functions based on the surface motions alone produced inconsistent times of liquefaction. Moreover, the error function from the H/V-spectrum was very broad, which indicated a high degree of uncertainty in the estimated time of liquefaction. Despite the uncertainty of identifying the time of liquefaction at very soft sites, the procedure developed for this study has shown the ability to identify the time of liquefaction from ground surface motion records, if the site conditions are favorable.

4.5 APPLICATION TO OTHER GROUND SURFACE MOTIONS

Earthquake ground motions are complicated in both the time and frequency, and the motions become even more complicated as the soil softens due to pore pressure generation and liquefaction. The proposed procedure for estimating the time of liquefaction has shown the ability to identify the time at which the frequency content of a ground motion changed in a manner that was consistent with the effects of liquefaction-induced softening in a soil profile. When applied to ground motions from sites where evidence of liquefaction was observed, the procedure can be used to estimate the time when liquefaction was triggered in a generally consistent and objective manner. The procedure is not, however, a completely automated process that can be relied upon to accurately estimate the time of liquefaction triggering without careful examination. Some motions show evidence of severe, rapid softening and have a clear time when the frequency content of the motion decreased and liquefaction occurred. Others motions show gradual softening and the shift in frequency content is subtler. Several factors require careful consideration when using and interpreting the results of the procedure:

1. Changes in frequency content at the ground surface can result from changes in the motion below the liquefiable layer. This effect can largely be removed at sites with relatively shallow downhole instruments, as in the cases of the Wildlife and Port Island vertical arrays. However,

the non-stationary behavior of earthquake motions must be considered in the interpretation of other records. Care must be taken to avoid mistaking changes in frequency content associated with the arrival of different wave types (e.g. surface waves) as the triggering of liquefaction.

2. Relatively dense soil profiles may build up high levels of pore pressure and liquefy under strong shaking, but these soils can exhibit such strong dilative tendencies that significant changes in frequency content before and after liquefaction may be difficult to detect. Dilation pulses can occur both before and after liquefaction is triggered, and high-frequency dilation pulses may mask the rapid shift in frequency content associated with liquefaction.
3. Profiles in which a liquefiable soil layer is either underlain or overlain by soft non-liquefiable soils may have such soft site response behavior that only very low-frequency motions are transmitted through the soil, regardless of the presence or absence of liquefied soil. Such profiles may not show distinct changes in frequency content once liquefaction occurs, making the time of liquefaction difficult to identify.

4.5.1 *Case history database*

The proposed procedure for estimating the time of liquefaction has been applied to suites of ground surface motions recorded at sites where evidence of liquefaction was observed. Some of these sites showed evidence of liquefaction in the form of sand boils surrounding the recording instrument following an earthquake. Other sites exhibited other visual characteristics that suggest liquefaction occurred, such as ground cracking or lateral spreading. All the sites exhibited a rapid drop in the frequency content of motions at the ground surface, presumably due to rapid softening caused by elevated pore pressure and liquefaction.

Twenty-one case histories were selected based on the availability of subsurface information. Case histories must have sufficient subsurface information that critical layers the liquefied could be identified. Additional discussion about the subsurface properties associated with each of these cases is discussed in Chapter 5. All the sites used in this study were identified as showing evidence of liquefaction during an earthquake, showed a rapid drop in frequency content at a time that corresponded to the triggering of liquefaction, and contained sufficient information for subsequent analysis. Information about the selected sites is summarized in Table 4.1.

Table 4.1: Information for selected ground motion records

Motion	Site/Station	Earthquake	Liquefaction severity and evidence	Reference
1	Alameda Naval Air Station	M6.9 Loma Prieta (1989)	Minor. Evidence of sand boils and ground settlement	Youd and Carter (2003)
2	Amagasaki	M6.9 Hygoken-Nambu (1995)	Minor. Trace surficial evidence and strong motion recorder tilted	Sato et al. (1995)
3	Aomori (1968)	M8.3 Tokachi-Oki (1968)	Severe. Sand boils.	Yasuda and Tohno (1988)
4	Aomori (1983)	M7.7 Nihonkai-Chubu (1983)	Liquefaction in vicinity. No direct observation near recorder.	Iai et al. (1989)
5	Bond's Corner	M6.5 Imperial Valley (1975)	Strong motion recorder indicated liquefaction. Liquefaction observed nearby by Moss et al. (2005).	--
6	CHB024	M9 Tohoku (2011)	Severe. Large sand boils in vicinity and around the station.	Cox et al. (2013)
7	Hachirogata	M7.7 Nihonkai-Chubu (1983)	Widespread liquefaction in the area.	Kostadinov and Towhata (2002)
8	Higashi Kobe	M6.9 Hygoken-Nambu (1995)	Minor. Ground surface time history exhibits longer period motion than downhole time history	Ganev (1998)
9	HKD086	M8.3 Tokachi-Oki (2003)	Severe. Sand boils and accelerometer tilted	Kinoshita (2008)
10	IBR014	M9 Tohoku (2011)	Minor. Minor sand boils in the vicinity.	Cox et al. (2013)
11	Kawagishi-cho	M7.7 Niigata (1964)	Severe. Ground failure caused by liquefaction	Ishihara and Yoga (1981)
12	Kobe JIS	M6.9 Hygoken-Nambu (1995)	Severe. Lateral spreading nearby.	Kostadinov and Yamazahi (2001)
13	Kushiro Port	M7.8 Kushiro-Oki (1993)	Minor. No evidence of ground deformation. Distinct changes in time history corresponding with dilation pulses	Iai (1995)

Table 4.1: Information for selected ground motion records

Motion	Site/Station	Earthquake	Liquefaction severity and evidence	Reference
14	MYG010	M9.0 Tohoku (2011)	Severe. Tsunami inundation obscured evidence, but widespread liquefaction during aftershocks.	Cox et al. (2013)
15	MYG013	M9.0 Tohoku (2011)	Minor. Cracking in the parking lot and strong motion recorder settlement.	Ashford et al. (2011)
16	NIG018	M6.6 Niigata-Chuetsu (2007)	Minor. Strong motion recorder tilted.	Yoshida et al. (2007)
17	Onahama Port	M9.0 Tohoku (2011)	Severe. Large sand boils observed.	Rotten et al. (2013)
18	Port Island	M6.9 Hygoken-Nambu (1995)	Severe. Widespread liquefaction and major ground deformation	Zeghal et al. (1996)
19	Sakaiminato	M6.6 Western Tottori	Minor. Sand boils in the vicinity of strong motion recorder.	Mori and Sogabe (2004)
20	Treasure Island	M6.9 Loma Prieta (1989)	Severe. Sand boils and differential settlement nearby.	Cetin et al. (2004)
21	Wildlife	Superstition Hills	Severe. Sand boils, ground fissures, and lateral spreading	Youd and Holzer (1994)

The procedure to identify the time of liquefaction was applied to these twenty-one different case histories. The estimated times of liquefaction are shown with the horizontal acceleration time histories on Figure 4.9.

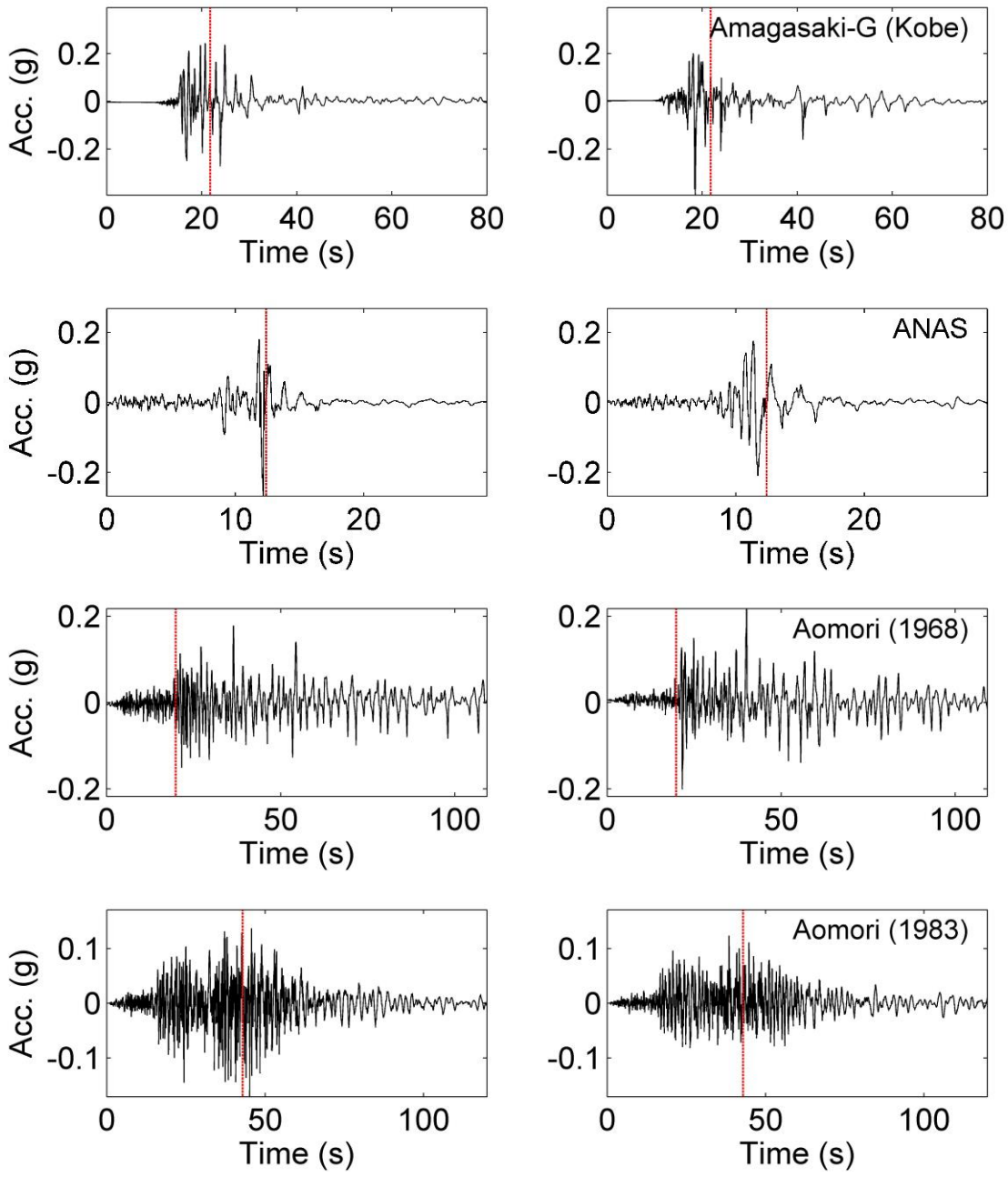

Figure 4.9: Time of liquefaction from case histories

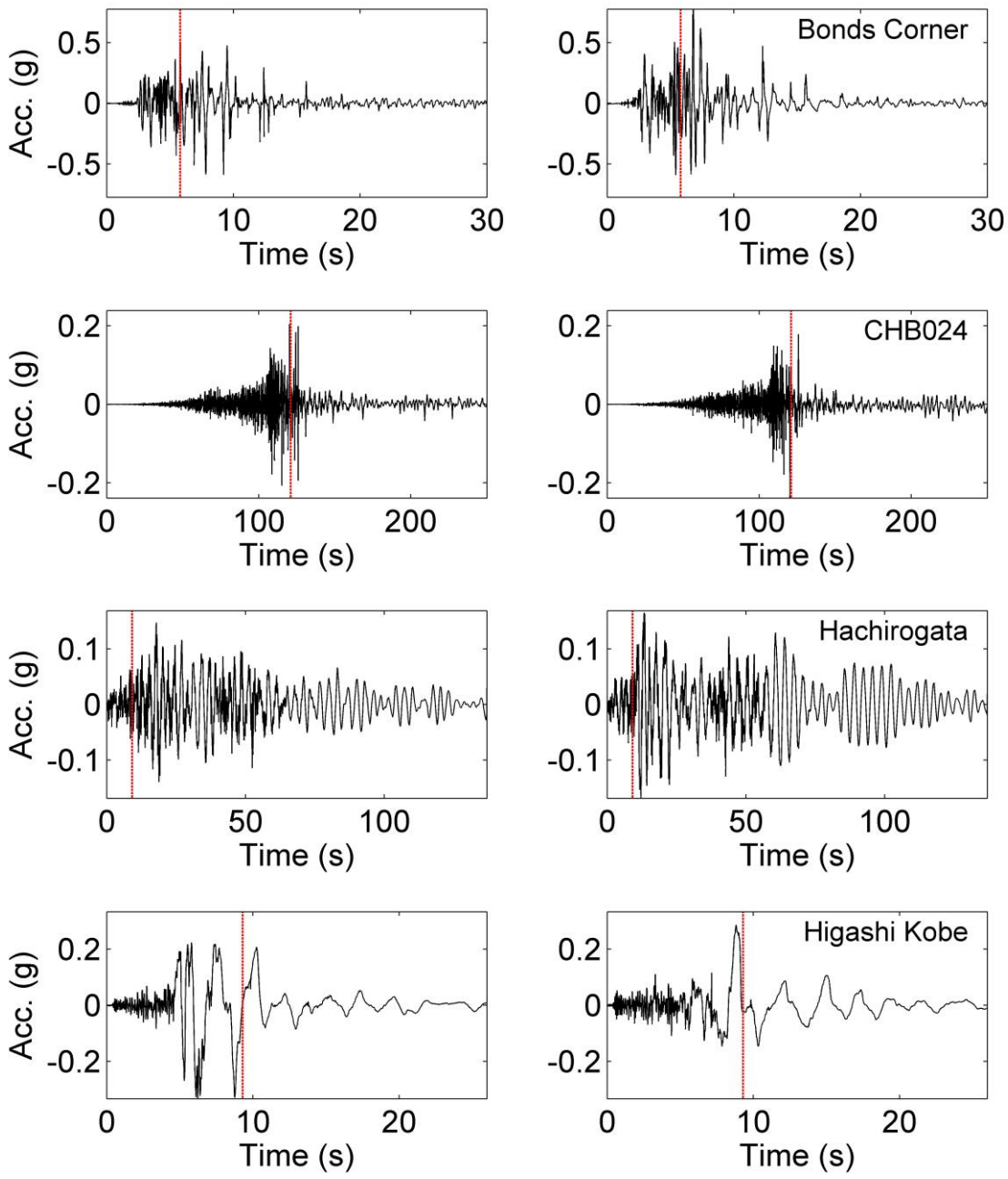

Figure 4.9: Time of liquefaction from case histories (cont.)

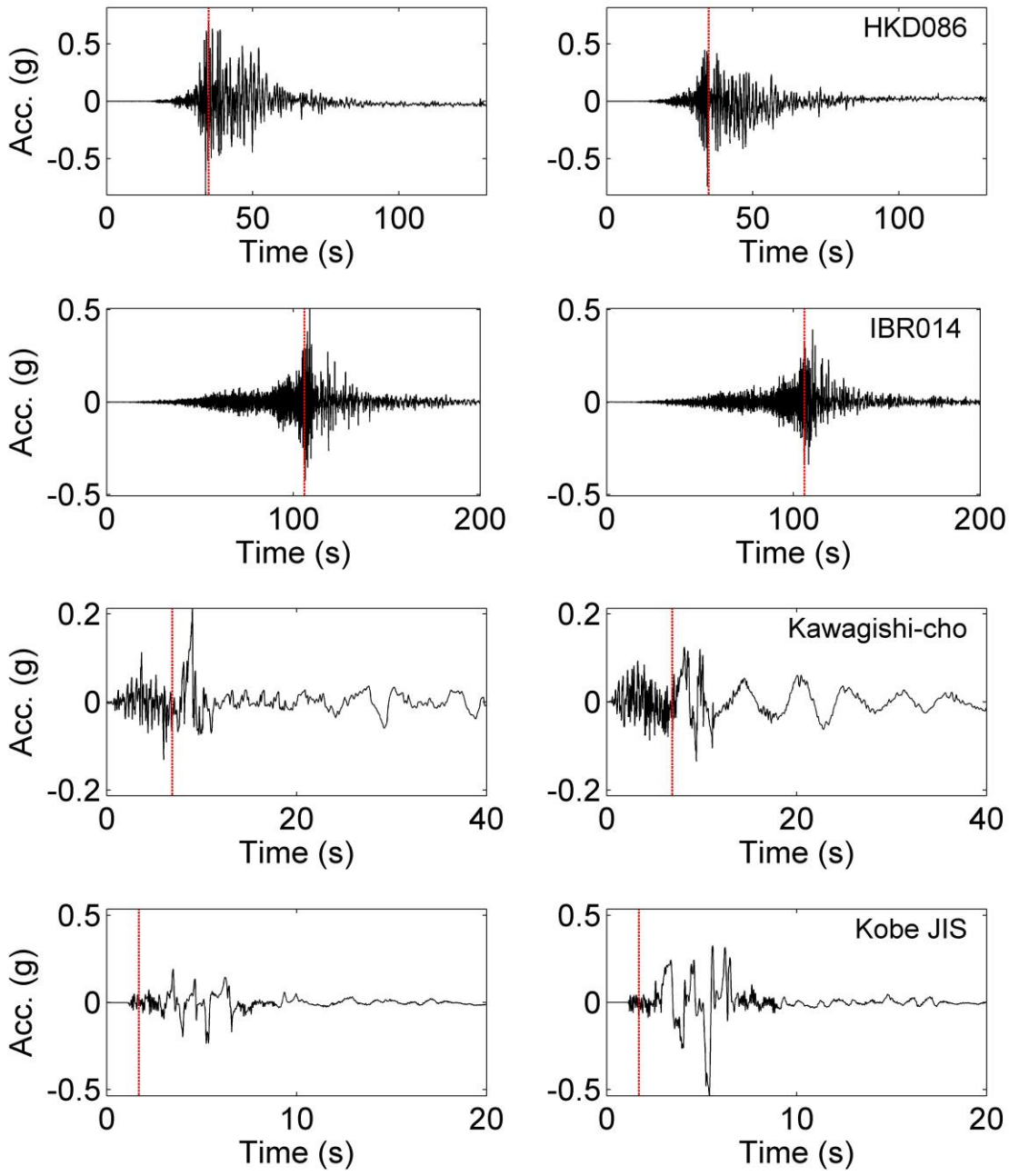

Figure 4.9: Time of liquefaction from case histories (cont.)

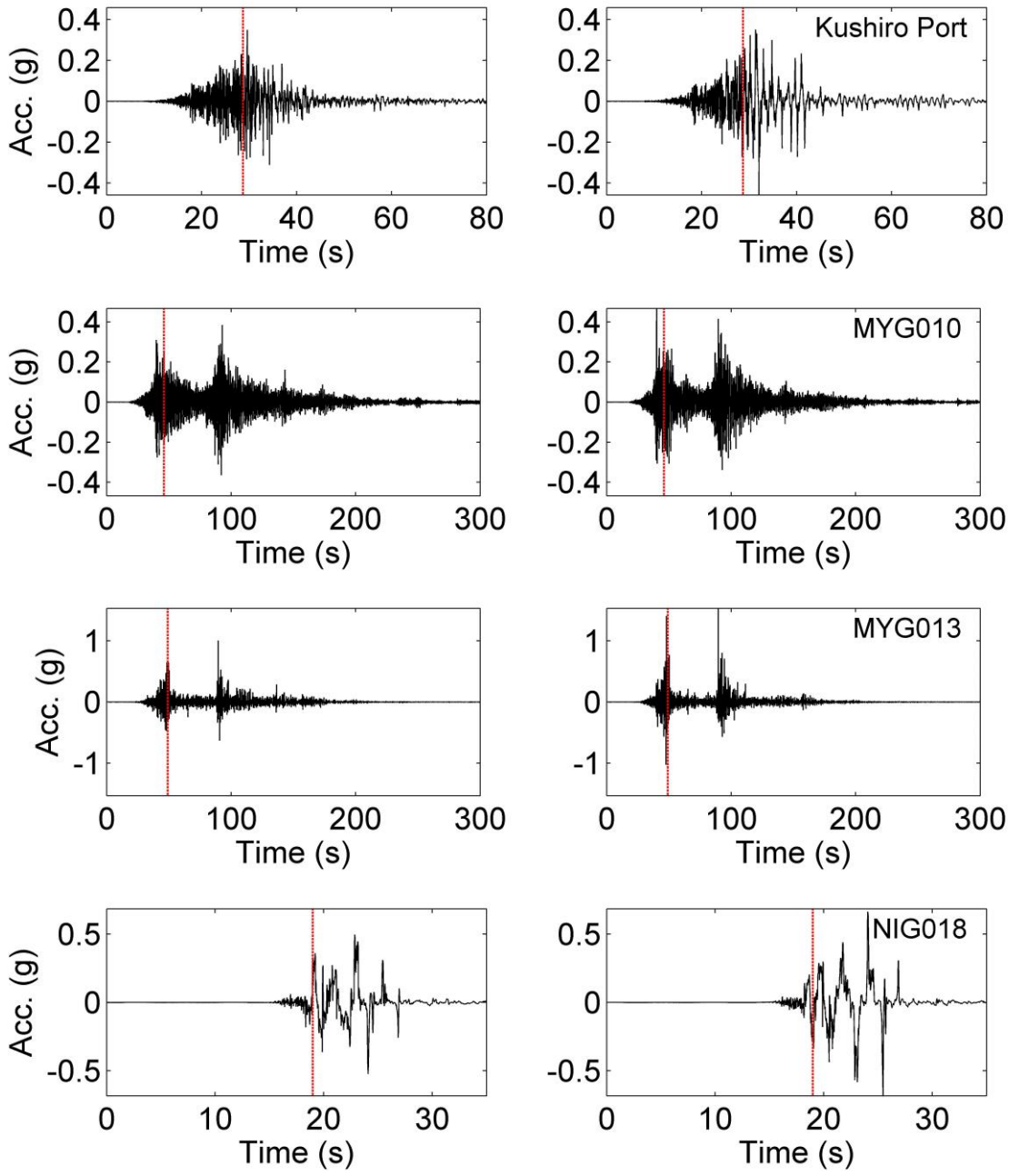

Figure 4.9: Time of liquefaction from case histories (cont.)

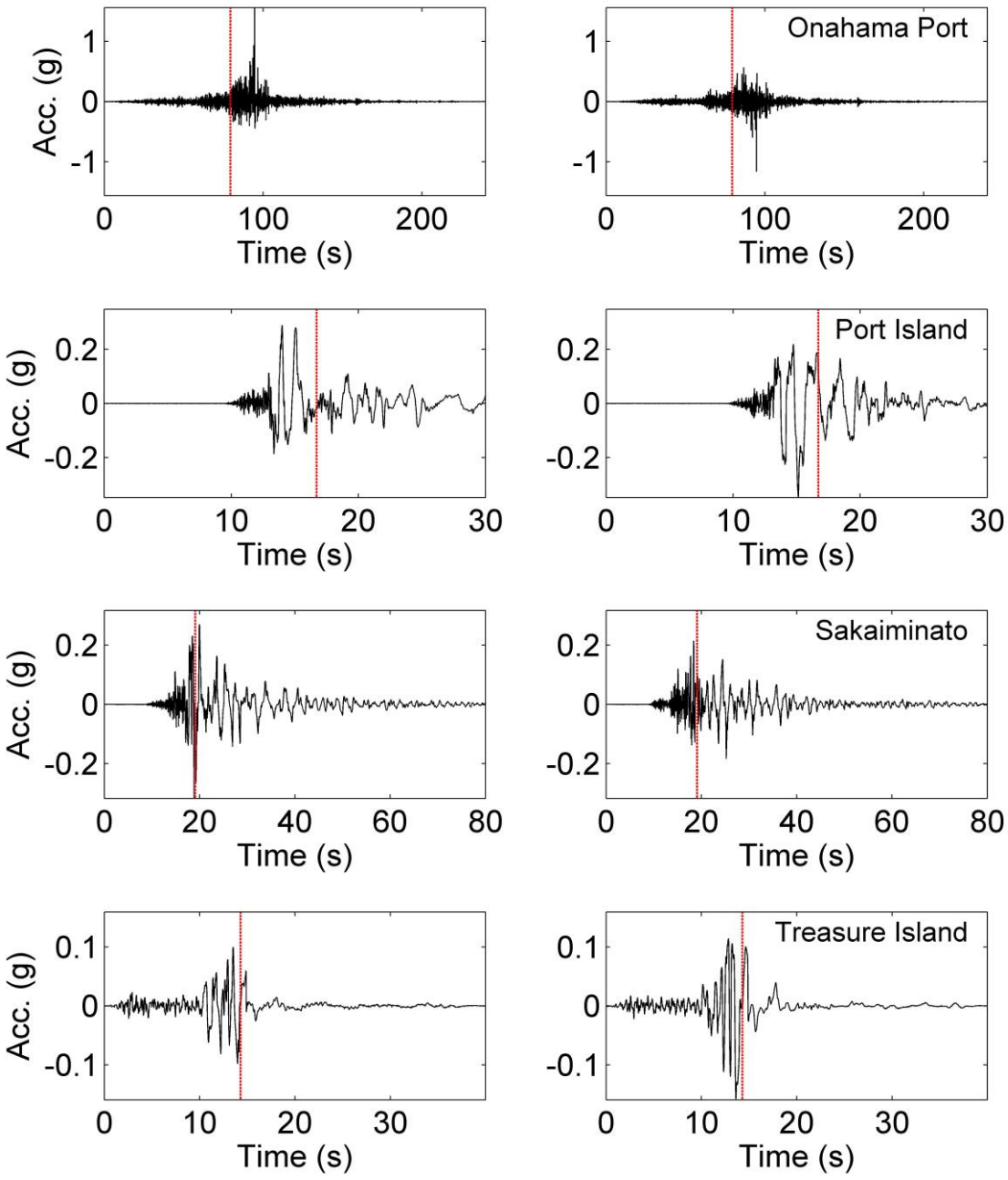

Figure 4.9: Time of liquefaction from case histories (cont.)

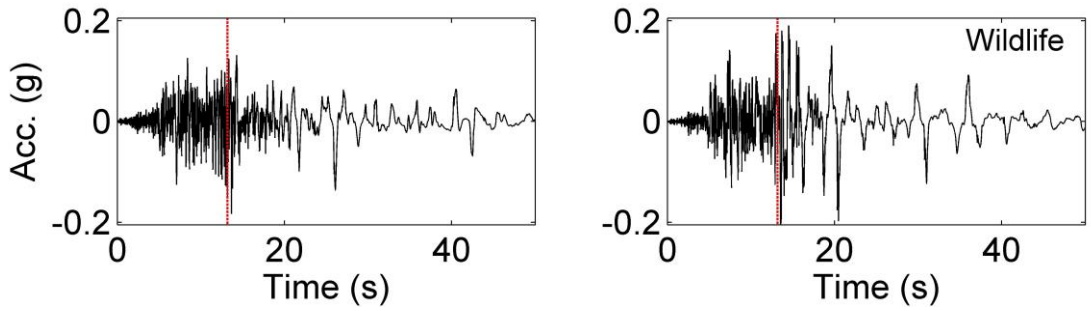

Figure 4.9: Time of liquefaction from case histories (cont.)

4.5.2 *Anomalous cases*

Detailed time-frequency analyses, such as those made possible by the Stockwell transform, can allow more detailed examination of case histories where ground motions have been recorded at sites that liquefied. Observations of the presence or absence of surficial evidence of liquefaction can be supplemented by observations of the changes in ground motion frequency content during shaking. These supplementary observations can confirm the occurrence of liquefaction, or even call into question whether liquefaction was actually triggered when surficial evidence is not conclusive. They can also aid in the interpretation of anomalous cases.

Any purely numerical procedure for identifying the triggering of a phenomenon as complex as liquefaction runs the risk of being confounded by behavior and/or observations that are not consistent with the phenomenon of interest. Such cases can lead to the occurrence of false positives, i.e., observations of surficial evidence of liquefaction where liquefaction did not actually occur, and false negatives, i.e., the occurrence of liquefaction at sites where no surficial evidence was observed. False positives can also result from changes in frequency content caused by phenomena other than liquefaction, such as the arrival of surface waves.

IBRH20

Kik-Net Station IBRH20, located in Kamisu in Ibaraki prefecture, was listed by Cox et al. (2013) as a recording station with evidence of liquefaction following the 2011 Tohoku earthquake, although sand boils were noted as being observed "in the vicinity on three sides but not directly around station." Kik-Net characterized the instrument site as being mantled with about 4 m of fill placed on quaternary sand and gravel, which extended to depths exceeding 30 m below the ground

surface. KiK-Net indicated that the upper 8 m of the soil had a shear wave velocity of about 180 m/s, which increased to about 280 m/s throughout most of the Quaternary sand and gravel. A nearby excavation showed a groundwater table depth of 4-6 m. A normalized Stockwell spectrogram for the IBRH20 motion is shown in Figure 4.10. The spectrogram does not show visual evidence of a sharp reduction in the high-frequency content motions or a sharp increase in low-frequency motions. The modal frequency shifts to lower frequencies at about 180 seconds, when the amplitude of the motion has decreased to very weak levels. This frequency content shift is likely due to low-frequency surface waves dominating the motion, rather than the triggering of liquefaction. Based on the lack of a distinctive shift in the frequency content of the ground motion, it appears that the ground motion at IBRH20 was strong enough to produce significant pore pressure in a thick layer of potentially liquefiable soil, but not strong enough to actually trigger liquefaction.

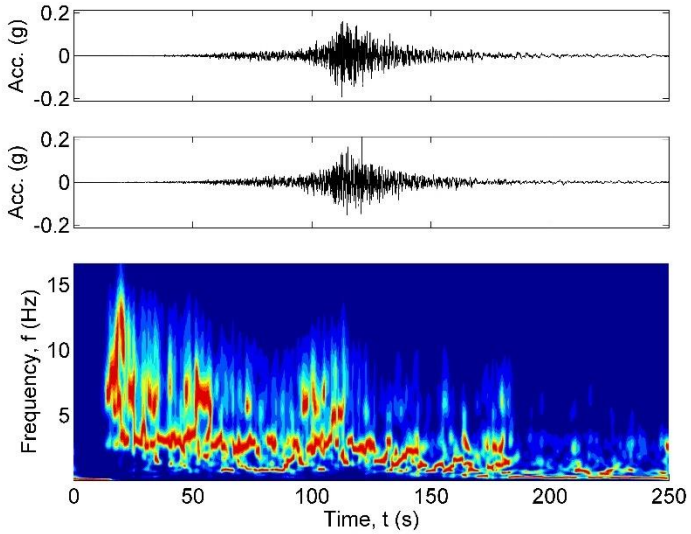

Figure 4.10: Recorded ground motion and normalized Stockwell spectrum at IBRH20 during the 2011 Tohoku earthquake

CHB008

K-Net Station CHB008 is located just north of the old coastline in Urayasu City along Tokyo Bay. Cox et al. (2013) list the site as a site underlain by recent sediments but without evidence of ground failure in the 2011 Tohoku earthquake. Tokimatsu et al. (2012) reported that no evidence of liquefaction was observed near the instrument, and presented a "normalized running spectrum"

(Figure 4.11) that showed only gradual lengthening of the period of the motion. The running spectrum is based on the STFT and is normalized "at the spectral peak of each 10-second interval." Subsurface conditions tabulated by Kik-Net at CHB008 consist of approximately 1 m of fill underlain by 1.2 m of "sandy soil" (interpreted here as silty sand), underlain by about 2.5 m of "sand" (interpreted as clean sand) over 3.4 m of sandy soil. The lower layer of sandy soil is underlain by "silt" to the base of the 20-m-deep exploration. The groundwater table was characterized by Tokimatsu et al. (2012) as being 2.4 m below the ground surface, which would be close to the top of the sand layer. The Kik-Net profile shows uncorrected SPT resistances less than 10 blows/ft in the sandy soil layers, less than 5 blows/ft in the deep silt layer, and ranging from about 10-20 in the sand layer blows/ft. Available SPT (Tokimatsu et al., 2012) data from the area around CHB008 shows somewhat higher penetration resistances in the 2-6 m depth range than observed in areas of Urayasu south of the old coastline, but the average SPT resistance is still less than 10 blows/ft down to about 4 m depth. It is likely that some component of the higher penetration resistance, and the apparently increased liquefaction resistance, of these soils is due to aging effects. Nevertheless, factor of safety calculations showed factors of safety against liquefaction being slightly below 1.0 over significant depth ranges for the CHB008 vicinity in relatively clean (FC < 15%) sands, and over much shorter depth ranges for siltier sands. Examination of time-frequency behavior using the Stockwell spectrum (Figure 4.12), which provides much greater resolution than the techniques used by Tokimatsu et al. (2012), does reveal a relatively sudden reduction in the amplitude of higher frequency motion at a time of between 116 and 118 seconds. Examination of the azimuthal variation of modal frequency shows the presence of polarized low-frequency waves prior to the estimated time of liquefaction, which may be the result of surface waves in the basin. Figure 4.13 shows the azimuthal modal frequency starting from the time of strong shaking around 80 seconds. Normalizing the horizontal frequency spectrum by the vertical frequency spectrum provides an estimate of the fundamental frequency of the site, rather than the frequency content shift due to surface waves. The azimuthal plot of the model H/V spectrum shows a relatively uniform shift in the frequency content of the motion. Modal frequencies were about 2 to 6 Hz before 116 seconds, and about 1 Hz after 118 seconds. Whether the pore pressures were high enough to produce liquefaction cannot be determined, but the shift in frequency content suggests that the amplification behavior of the profile changed quickly in all directions, a behavior typically associated with the generation of high pore pressures.

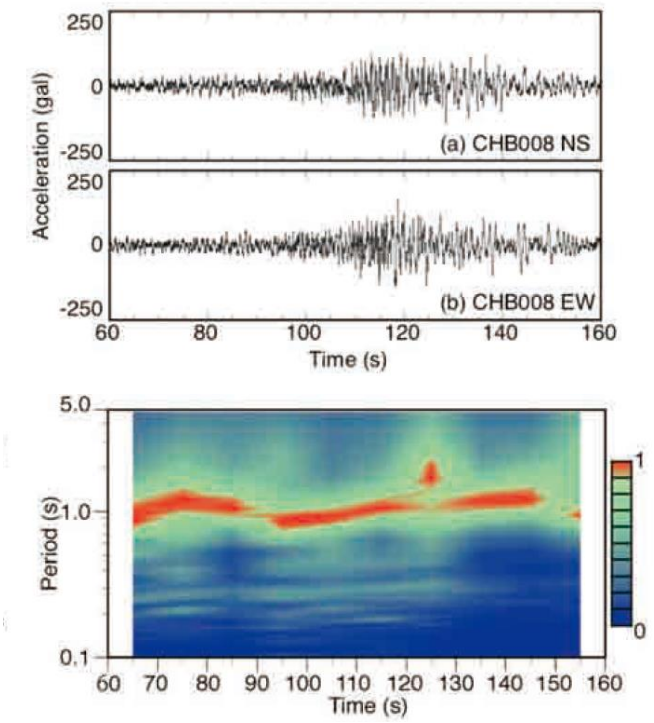

Figure 4.11: STFT-based spectrum at CHB008 during the 2011 Tohoku earthquake (from Tokimatsu et al. 2012).

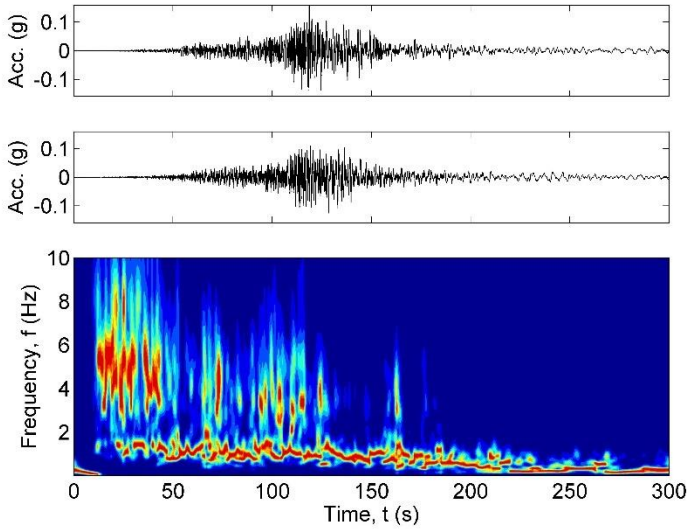

Figure 4.12: Recorded ground motion and normalized Stockwell spectrum at CHB008 during the 2011 Tohoku earthquake.

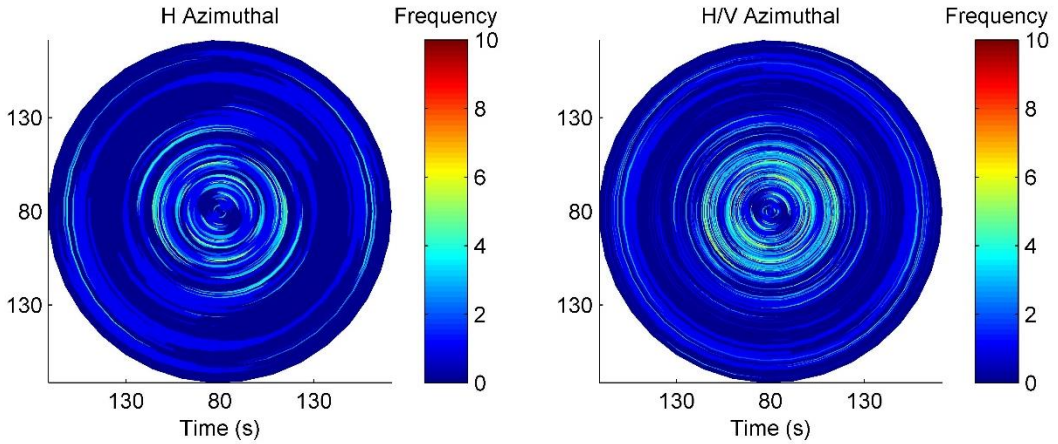

Figure 4.13: Azimuthal variation of the modal frequency using the Stockwell-based procedure for the 2011 Tohoku earthquake at CHB008.

Onahama Port

Onahama Port is located near Iwaki City in Fukushima Prefecture. During the 2011 Tohoku earthquake, Onahama Port suffered damage from settlement that displaced crane rails and other port facilities. While the port was affected by a tsunami, sand boils were observed from aftershocks. The Port and Airport Research Institute (PARI) operated a vertical array at Onahama Port. An instrument at a depth of 11 m recorded peak accelerations of 0.173 g in the EW and 0.204 g in the NS directions with corresponding ground surface accelerations of 1.560 g and 1.162 g. The PARI instrument was in an area underlain by saturated sand, but that sand was quite dense at depths below about 2.8 m. With the groundwater level at 1.2 m, the loose, saturated portion of the profile was only about 1.6 m thick and was both underlain and overlain by permeable soils. Figure 4.13 shows a Stockwell spectrogram of the Onahama Port ground surface motions. The modal frequency of the ground surface motion appears to be approximately 5 Hz at the beginning of the record. It then drops relatively slowly as the shaking progresses, reaching a minimum of about 1 Hz at about 105 sec. The modal frequency can then be seen to recover, increasing during the latter portion of the recorded motion. Eventually, around 200 seconds into the motion, the modal frequency is about equal to the initial modal frequency. The increase in modal frequency resulted from increased soil stiffness, which resulted from increased effective stress. Thus, the Onahama record appears to show evidence of pore pressure dissipation due to drainage while shaking was

taking place. While the Onahama profile softened and produced numerous strong dilation pulses (Roten et al., 2013), it never became extremely soft at any point during the record.

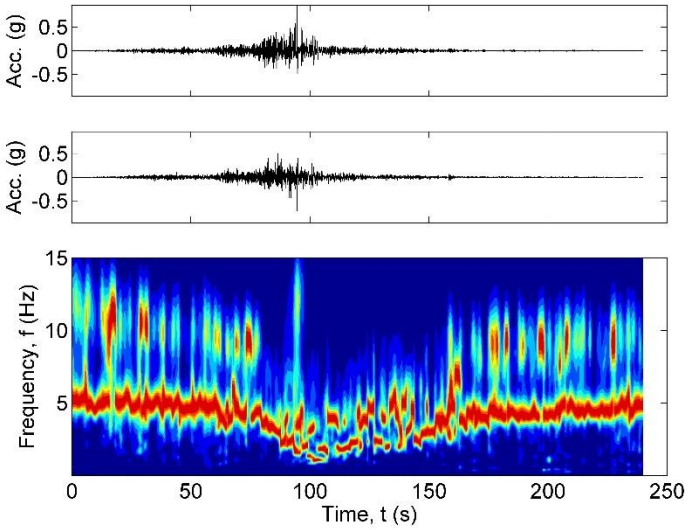

Figure 4.14: Recorded ground motion and normalized Stockwell spectrum at Onahama Port during the 2011 Tohoku earthquake

4.6 SUMMARY

Identifying the time of liquefaction has important potential benefits for predicting both liquefaction triggering and the effects of liquefaction. Case histories where the time of liquefaction can be identified are different than case histories that are based solely on the presence or absence of surficial evidence. Rather than providing binary data points of liquefied versus not liquefied for logistic regression or Bayesian updating, case histories where the time of liquefaction is identified provide data about the cumulative intensity of shaking at the time of liquefaction. Measures of the cumulative intensity of shaking, such as cycle-adjusted peak ground acceleration, Arias intensity, or cumulative absolute velocity, recorded at the time of liquefaction can be used to directly define the liquefaction triggering curve, rather than binary classifications, which are plotted above or below the liquefaction triggering curve. The current state-of-practice liquefaction trigging procedures include many case histories, but the actual decision functions that define the deterministic liquefaction triggering curves are controlled by relatively few data points with high leverage—even a slight change in these high leverage data points may affect the deterministic liquefaction triggering curve. Intensity measurements at the time of liquefaction also provide

critical information about the factors that control liquefaction triggering behavior including relative density, fines content, magnitude scaling factor, overburden effective stress, and static shear stresses. These factors are easier to distinguish and isolate in a linear regression-type framework where intensity measures are recorded at the time of liquefaction, rather than in a logistic regression-type framework based on binary classifications.

Knowledge of the frequency content shift due to liquefaction may also be used to confirm the occurrence of liquefaction in cases that are questionable or where liquefaction occurred without surficial evidence. The current liquefaction case history databases (Boulanger and Idriss, 2014; Cetin et al. 2004) are based on case histories where surficial evidence of liquefaction was observed after an earthquake. Sites where liquefaction was triggered without producing surficial evidence would be classified as non-liquefied case histories without an evaluation of the frequency content of the motion. Liquefaction does not always produce surficial expressions, and specific subsurface conditions are necessary to produce ejecta or develop evidence of ground failure, lateral spreading, bearing capacity failure, etc. However, liquefaction without surficial expression may have damaging effects to structures due to the shifts in frequency content and changes in site response behavior. A spectrally-based procedure that can identify liquefaction triggering regardless of surficial evidence is useful to identify new case histories or reclassify existing case histories. Surficial evidence of liquefaction is also available for only a relatively short time after an earthquake and the evidence may be obscured by other effects of an earthquake. For example, the devastating tsunami after the 2011 Tohoku earthquake eliminated much of the surficial evidence of liquefaction in Fukushima and Miyagi prefectures (Cox et al. 2011), but the available acceleration time histories indicated that several sites liquefied during the main shock of the earthquake.

An additional benefit of identifying the time of liquefaction is that the site-response behavior of liquefied soil can be isolated. Loose soils or soils subject to long duration earthquakes may liquefy relatively early during an earthquake, and the soil may be subject to many cycles of loading in a liquefied state. The post-triggering behavior of liquefied soil is typically limited to laboratory observations (e.g. Ishihara and Yoshimine, 1992; Kawakami et al., 1994; Wu and Seed, 2004) or empirical observations of the effects of liquefaction (Youd et al., 2002; Baska, 2002; Olson and Johnson, 2008). Identifying the site response behavior after the soil has liquefied provides details of the mechanics of liquefied soil that cannot be determined with laboratory or

empirical data alone, including the potentially competing effects of soil fabric degradation, dilation-induced stiffening, and drainage during shaking. Separating the effects and mechanics of pre- and post-triggered behavior has important design implications as well. Most of the deformation and kinematic loading occurs after liquefaction is triggered. Current design procedures (e.g. AASHTO, 2012; Allen, 2015) recommend that, in lieu of nonlinear analysis, structures subject to long duration earthquakes should be evaluated with a combination of inertial loads due to shaking from nonliquefied soil conditions coupled with the kinematic loads due to liquefied soil deformation. Combining the inertial and kinematic effects in this way may produce unrealistic results since the presence of liquefied soil affects the site response behavior and inertial loads on the structure. Especially for structures with long fundamental periods, the recommendation of combining the kinematic load with 25% of the peak inertial load appears to be unconservative in the case histories evaluated in this study. Opposite, combining the kinematic load with the peak inertial load may be excessively conservative in certain soil conditions for structures with very short fundamental periods.

[This page intentionally left blank]

Chapter 5. ANALYTICAL SOLUTION FOR DRAINAGE IN A LAYER OF LIQUEFIABLE SOIL

The relationship between pore pressure generation due to shaking in liquefiable soils and pore pressure dissipation due to drainage is not well defined by either the current methods of analyzing liquefaction susceptibility or liquefaction triggering. In principle, it is possible a layer of soil can drain so quickly that it cannot liquefy under any reasonable loading conditions. Likewise, case histories have shown that drainage during shaking may increase the soil's resistance to liquefaction. These conditions are difficult to re-create in the laboratory, and in most circumstances, computational models are necessary to evaluate the competing effects of pore pressure generation and drainage. In computational models, a system of equations is solved that includes expressions for pore pressure dissipation due to drainage and pore pressure generation due to volumetric strain. The equations of motion and the pore pressure dissipation are related through the constitutive model of the soil, and typically require nonlinear finite difference methods to solve the rate of pore pressure dissipation in time. These systems can result in many non-unique solutions for different constitutive models. So, the results of numerical models largely depend on the constitutive model and model parameters. Little validation for these types of analyses is available outside of matching the results of the computations models to field observations, and because of this, computational models are typically limited to case-by-case analyses.

An analytical solution for evaluating liquefaction resistance and susceptibility that accounts for the effects of drainage will have important practical implications. The effects of drainage during shaking are not typically considered in most practical geotechnical earthquake engineering applications, and a simple tool to identify layers whose liquefaction behavior may be affected by drainage will be beneficial for practicing engineers. The effects of drainage can be important for explaining the behavior of liquefiable soils during long duration earthquakes, since shaking may occur over a long enough period of time that pore pressures may dissipate. Identifying granular layers where drainage may have occurred during past earthquakes also reduces the uncertainty in determining which layers liquefied, and can potentially explain the

behavior observed at sites that have been used to develop empirical liquefaction triggering and lateral spreading procedures.

The analytical approach to evaluate pore pressure dissipation used by Terzaghi for consolidation settlement can be expanded to include pore pressure generated due to cyclic shear stress. The solution proposed in this study is formulated in terms of a partial differential equation with competing terms for pore pressure dissipation due to drainage and pore pressure generation due to shearing. The solution is solved for drained boundary conditions to show that under conditions where the soil drains rapidly, the soil's resistance to liquefaction increases. Under even more rapidly draining conditions, the rate of drainage exceeds the rate of pore pressure generation and the soil cannot liquefy under typical loading conditions.

5.1 PORE PRESSURE GENERATION

The rate of pore pressure generated during cyclic loading in laboratory tests can be described by the number of cycles of loading, N, relative to the number of cycles required to initiate liquefaction, N_l. DeAlba et al. (1975) developed an empirical function that relates the number of cycles of loading to the pore pressure ratio based on the results of laboratory tests.

$$r_{\mathrm{u}} = \frac{1}{2} + \frac{1}{\pi}\arcsin\left[2\left(\frac{N}{N_l}\right)^{1/\alpha} - 1\right] \tag{5.1}$$

The expression was later simplified by Booker et al. (1976). Figure 5.1 shows the pore pressure ratio, r_u, for several values of an empirical material property, α.

$$r_u = \frac{2}{\pi}\arcsin\left[\left(\frac{N}{N_l}\right)^{1/2\alpha}\right] \tag{5.2}$$

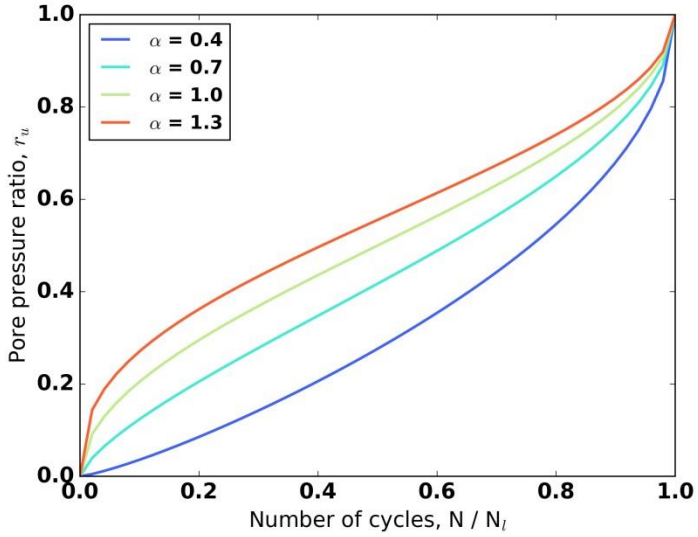

Figure 5.1: Rate of pore pressure generation (after DeAlba, 1975). The exponent α is a soil property

Defining the generation of the pore pressure as a continuous function is necessary for an analytical solution. Equations (5.1) and (5.2) are defined in terms of the number of cycles of loading, N, which is a discrete measure. For this analysis, the number of cycles of loading is assumed to be a continuous measure, which allows calculation of $\frac{\partial r_u}{\partial t}$ using the chain rule.

$$\frac{\partial r_u}{\partial t} = \frac{\partial r_u}{\partial N}\frac{\partial N}{\partial \tau}\frac{\partial \tau}{\partial t} \tag{5.3}$$

Equations (5.1) and (5.2) contain arcsines, and the expressions are undefined for values of $\frac{N}{N_l} \geq 1.0$. However, pore pressure dissipation during shaking may reduce the pore pressure ratio so that $r_u < 1.0$ even when $\frac{N}{N_l} \geq 1.0$. To account for the generation of excess pore pressure when $\frac{N}{N_l} \geq 1.0$, equations (5.1) and (5.2) must be generalized and extended for $\frac{N}{N_l} \geq 1.0$. The derivative of equation (5.2) can be modified so it is defined for all real values of $\frac{N}{N_l}$, although extrapolating above $\frac{N}{N_l} = 1.0$ may result in behavior that has not been experimentally verified. Extrapolating the DeAlba (1975) expression beyond $\frac{N}{N_l} = 1.0$ is referred to as the pore pressure potential, $r_u{}^*$ in this analysis. Equation (5.2) is first differentiated with respect to time.

$$\frac{\partial r_u}{\partial t} = \frac{\left(\frac{N}{N_l}\right)^{\frac{1}{2\alpha}}}{\left(\frac{N}{N_l}\right)\pi\alpha\left(1-\left(\frac{N}{N_l}\right)^{\frac{1}{\alpha}}\right)^{0.5}}\frac{\partial N}{\partial t} \tag{5.4}$$

The expression in the denominator of equation (5.4), $\left(1-\left(\frac{N}{N_l}\right)^{\frac{1}{\alpha}}\right)^{0.5}$, can be redefined so the expression has real values if $\frac{N}{N_l}$ is greater than 1.0. The definition does not affect the value of r_u at values of $\frac{N}{N_l}$ less than 1.0.

$$\frac{\partial {r_u}^*}{\partial t} = \frac{\left(\frac{N}{N_l}\right)^{\frac{1}{2\alpha}}}{\left(\frac{N}{N_l}\right)\pi\alpha\left|1-\left(\frac{N}{N_l}\right)^{\frac{1}{\alpha}}\right|^{0.5}}\frac{\partial N}{\partial \tau}\frac{\partial \tau}{\partial t} \tag{5.5}$$

Integrating equation (5.5) creates a continuous, smooth piecewise function for pore pressure potential.

$${r_u}^*\left(\frac{N}{N_l}\right) = \int \frac{\partial {r_u}^*}{\partial t}dt = \begin{cases} \frac{2}{\pi}\arcsin\left[\left(\frac{N}{N_l}\right)^{1/2\alpha}\right] & \left(\frac{N}{N_l}\right) < 1 \\ 1+\frac{2}{\pi}\operatorname{arccosh}\left[\left(\frac{N}{N_l}\right)^{1/2\alpha}\right] & \left(\frac{N}{N_l}\right) \geq 1 \end{cases} \tag{5.6}$$

The expression for is ${r_u}^*$ identical to Booker's expression, equation (5.2), but is defined for $\frac{N}{N_l}$ greater than 1.0. Figure 5.2 shows the pore pressure potential for values of $\frac{N}{N_l}$ up to 2.0.

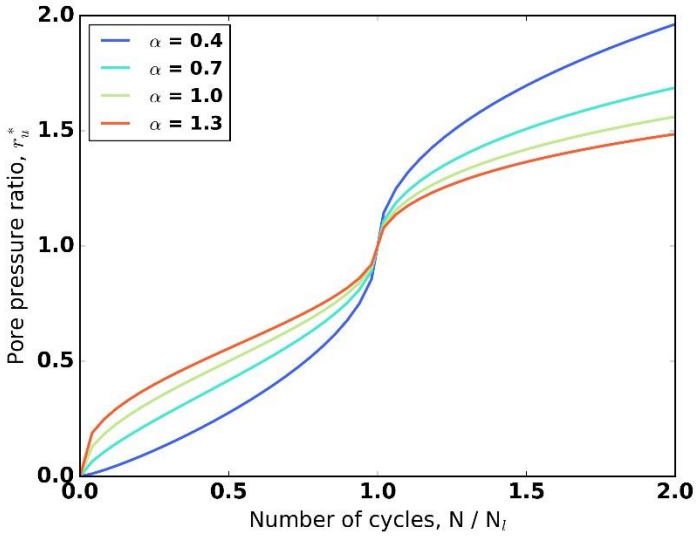

Figure 5.2: Rate of pore pressure potential, $r_u{}^*$

5.2 PORE PRESSURE DISSIPATION

The dissipation of pore pressure due to drainage requires a solution which considers the drainage regime. Terzaghi (Terzaghi and Peck, 1948) developed an analytical expression for the dissipation of pore water pressure in a layer of soil subject to constant vertical total stress. The net rate of pore water entering or leaving the layer, dq, is equal to the change in volume of the layer over time, $\frac{\partial \varepsilon}{\partial t}$.

$$dq = \frac{\partial \varepsilon}{\partial t} \tag{5.7}$$

By Darcy's law, the flow rate is equal to the hydraulic conductivity, k, times the hydraulic gradient. If the flow velocity is negligible, the hydraulic gradient is equal to the change in excess pore pressure with respect to height, $\frac{\partial u}{\partial x}$, divided by the unit weight of water, γ_w. After differentiating, the change in volume over time is equal to the change in flow rate.

$$q = -\frac{k}{\gamma_w}\frac{\partial u}{\partial x} \tag{5.8}$$

Substituting equation (5.7) into equation (5.8) yields:

$$-\frac{k}{\gamma_w}\frac{\partial^2 u}{\partial x^2} = \frac{\partial \varepsilon}{\partial t} \tag{5.9}$$

Terzaghi's solution assumed that change in volumetric strain was linearly related to the change in effective stress with a coefficient of compressibility, m_v.

$$\varepsilon = m_v p \tag{5.10}$$

where p is the mean effective stress, $p = p_{tot} - u$. The typical sign convention used in soil mechanics is compression is positive, so the rate of volumetric strain is negative with respect to the rate of pore pressure change. Taking the derivative of equation (5.10) with respect to time yields:

$$\frac{\partial \varepsilon}{\partial t} = m_v \frac{\partial p}{\partial t} \tag{5.11}$$

$$\frac{\partial \varepsilon}{\partial t} = -m_v \frac{\partial u}{\partial t} \tag{5.12}$$

The resulting expression is equivalent to the Laplace diffusion equation for excess pore pressure, u. Substituting equation (5.12) into (5.9) yields:

$$-\frac{k}{\gamma_w}\frac{\partial^2 u}{\partial x^2} = -m_v \frac{\partial u}{\partial t} \tag{5.13}$$

The hydraulic conductivity, coefficient of compressibility, and unit weight of water are all constants, and can be grouped together as the coefficient of consolidation, c_v.

$$c_v = \frac{k}{m_v \gamma_w} \tag{5.14}$$

where γ_w is the unit weight of water. Substituting equation (5.14) into equation (5.13) yields:

$$c_v \frac{\partial^2 u}{\partial x^2} = \frac{\partial u}{\partial t} \tag{5.15}$$

Solutions to this type of equation usually involve separating the dependent variable, which is excess pore pressure in equation (5.15), into independent functions of depth, $X(x)$, and time, $T(t)$.

$$u(x,t) = X(x)T(t) \tag{5.16}$$

Substituting equation (5.16) into (5.15) yields:

$$c_v \frac{\partial^2 X}{\partial x^2} T = X \frac{\partial T}{\partial t} \tag{5.17}$$

Differentials of independent functions are expressed using dots for simplicity in this analysis, i.e. $\frac{\partial T}{\partial t} = \dot{T}$, and $\frac{\partial X}{\partial t} = \dot{X}$.

$$c_v \ddot{X} T = X \dot{T} \tag{5.18}$$

The expressions for X and T are then separated into independent expressions using a separation constant, β.

$$\frac{\ddot{X}}{X} = \frac{1}{c_v} \frac{\dot{T}}{T} = -\beta^2 \tag{5.19}$$

Then the independent differential expressions for X and T are solved for the separation coefficient.

$$X(x) = c_1 \cos \beta x + c_2 \sin \beta x \tag{5.20}$$

$$T(t) = \exp(-c_v \beta^2 t) \tag{5.21}$$

Equations (5.20) and (5.21) are substituted back into equation (5.16).

$$u(x,t) = \exp(-c_v \beta^2 t)\,(c_1 \cos \beta x + c_2 \sin \beta x) \tag{5.22}$$

The coefficients β, c_1, and c_2 are solved by considering appropriate boundary conditions. The drainage regime is defined between the top of the layer, where $x = 0$, and the bottom of the layer, where $x = H$. At each boundary, the excess pore pressure is always equal to zero, i.e. $u(0,t) = 0$ and $u(H,t) = 0$. The initial conditions are set such that the excess pore pressure in the layer when $t = 0$ is equal to the applied load, $u(x,0) = p_o$. Equation (5.22) is periodic in nature, and when $u(x,t) = 0$, the separation constant has an infinite number of possible periodic values for positive integer values of n.

$$\beta = \frac{\pi n}{H} \tag{5.23}$$

The periodic components for β may be superimposed for all values of n. The final solution for Terzaghi's pore pressure dissipation equation is the sum of all periodic components.

$$u(x,t) = \sum_{n=1}^{\infty} \exp\left(-c_v \left[\frac{\pi n}{H}\right]^2 t\right)\left(c_2 \sin\left[\frac{\pi n}{H}\right] x\right) \tag{5.24}$$

5.3 DRAINAGE AND EXCESS PORE PRESSURE DUE TO SHAKING

A simple model that accounts for the effects of pore pressure generation due to shaking and the dissipation of pore pressure due to drainage would be beneficial for evaluating pore pressure in thin layers where drainage may occur. Terzaghi's solution for pore pressure dissipation can be modified to account for pore pressure generation due to cyclic shear stress. Terzaghi's original solution is based on the relationship between pore pressure dissipation and volumetric strain.

$$-\frac{k}{\gamma_w}\frac{\partial^2 u}{\partial x^2} = \dot{\varepsilon} \tag{5.25}$$

Pore pressure, u, generated during shaking is largely due to cyclic shear stresses, and expression for volumetric strain can be expanded to include a term for pore pressure generation. The amount of excess pore pressure, for liquefaction evaluation, is usually expressed as a pore pressure ratio, r_u.

$$r_u = 1 - \frac{p}{p_o} \tag{5.26}$$

$$r_u = \frac{u}{p_o} \tag{5.27}$$

where p is the mean effective stress and p_o is the initial mean effective stress. The pore pressure ratio increases during shearing up to the point where it is equal to 1.0 once liquefaction occurs. Differentiating the pore pressure ratio in equation (5.27) produces an expression that includes the rate of change in the pore pressure, $\frac{\partial u}{\partial t}$.

$$\frac{\partial r_u}{\partial t} = \frac{1}{p_o}\frac{\partial u}{\partial t} \tag{5.28}$$

Equation (5.28) is based on undrained conditions, which implies that the change in volumetric strain, $\dot{\varepsilon}$, is equal to zero. The change in volumetric strain used in the diffusion equation (5.25) should be formulated in such a way that it:

1. reduces to equation (5.28) in undrained conditions, when $\dot{\varepsilon} = 0$, and
2. reduces to Terzaghi's equation (5.24) in conditions when no additional change in pore pressure occurs due to shear stress, $\frac{\partial r_u}{\partial t} = 0$.

The relationship between volumetric strain and pore pressure, equation (5.12), is expanded to include a term for excess pore pressure generated during cyclic shearing to satisfy that these requirements.

$$\dot{\varepsilon} = -m_v \left(\frac{\partial u}{\partial t} - p_o \frac{\partial r_u}{\partial t} \right) \tag{5.29}$$

Although the expression for $\frac{\partial r_u}{\partial t}$ in equation (5.6) is complicated, a general solution can be derived for arbitrary functions of $\frac{\partial r_u}{\partial t}$ that vary only in time. This implies that the shear stress and cyclic resistance are uniform across the layer of liquefiable soil. If the pore pressure potential function is constant across the layer and does not vary with depth, equation (5.29) can be combined with the diffusion equation (5.25) and rearranged into a common form of an inhomogeneous partial differential equation.

$$-\frac{k}{\gamma_w} \frac{\partial^2 u}{\partial x^2} = m_v \left(-\frac{\partial u}{\partial t} + p_o \frac{\partial r_u}{\partial t} \right) \tag{5.30}$$

Plugging equation (5.14) into equation (5.30)

$$\frac{\partial^2 u}{\partial x^2} = \frac{1}{c_v} \left(\frac{\partial u}{\partial t} - p_o \frac{\partial r_u}{\partial t} \right) \tag{5.31}$$

and rearranging equation (5.31)

$$\frac{\partial^2 u}{\partial x^2} - \frac{1}{c_v} \frac{\partial u}{\partial t} = -\frac{p_o}{c_v} \frac{\partial r_u}{\partial t} \tag{5.32}$$

Just like Terzaghi's solution, this differential equation can be solved by separating variables, although both characteristic and particular solutions must be found for inhomogeneous partial differential equations. Partial differential equations of this type can be solved using separable solutions for independent variables such that $u(x,t) = X(x)T(t)$.

$$\ddot{X}T - \frac{1}{c_v} X\dot{T} = -\frac{p_o}{c_v} \frac{\partial r_u}{\partial t} \tag{5.33}$$

The characteristic solution to equation (5.33) is calculated when the expression on the right side of the equation equal to zero. The particular solution to equation (5.33) is calculated when the expression on the right-hand side is included. The characteristic and particular solutions are added together to develop a solution for $u(x,t)$.

$$\mathrm{u}(x,t) = X_c T_c + X_p T_p \tag{5.34}$$

For the characteristic solution, independent univariate functions are separated and set equal to a separation constant, β^2.

$$\ddot{X_c} T_c - \frac{1}{c_v} X_c \dot{T_c} = 0 \tag{5.35}$$

The characteristic solution is identical to Terzaghi's solution for pore pressure dissipation, equation (5.22).

$$X_c T_c = \exp(-c_v \beta^2 t)(c_1 \cos(\beta x) + c_2 \sin(\beta x)) \tag{5.36}$$

The inhomogeneous portion of equation (5.34) is only a function of $r_u(t)$. Since the inhomogenous expression in equation (5.33), $\frac{p_o}{c_v}\frac{\partial r_u}{\partial t}$, does not vary with depth, then $\ddot{X}_p = 0$. The particular solution for $X_p T_p$ can be simplified into a univariate expression that is only a function of t.

$$-\frac{1}{c_v} X_p \dot{T_p} = -\frac{p_o}{c_v}\left(\frac{\partial r_u}{\partial t}\right) \tag{5.37}$$

The independent variables in equation (5.37) are separated and solved.

$$X_p = p_o \tag{5.38}$$

$$\dot{T_p} = \frac{\partial r_u}{\partial t} \tag{5.39}$$

Integrating equation (5.39) yields

$$T_p = r_u + \alpha \tag{5.40}$$

where α is an integration constant. The combined characteristic and particular solution are similar to Terzaghi's solution, but with the inclusion of a term for pore pressure generation, r_u, and coefficient α. Equations (5.36), (5.38), and (5.40) are combined into equation (5.34), which is the general solution for $u(x,t)$ that includes the competing effects of pore pressure generation due to shearing and pore pressure dissipation due to drainage.

$$u(x,t) = \exp(-c_v \beta^2 t)\,(c_1 \cos(\beta x) + c_2 \sin(\beta x)) + p_o(r_u{}^*(t) + \alpha) \tag{5.41}$$

5.3.1 *Drained boundary conditions*

The expression in equation (5.41) for excess pore pressure accounts for simultaneous pore pressure dissipation due to drainage and pore pressure generation due to cyclic shear stress. The solution has four unknowns, β, c_1, c_2, and α, which can be solved using two boundary conditions and the initial and final conditions.

At a long time after the shaking has stopped, the pore pressure generated in an undrained system is equal the maximum pore pressure developed during shaking, and a variable $r_{u,\max}$ is defined such that $r_u(\infty) = r_{u,\max}$. As discussed earlier, the pore pressure potential, r_u, is defined such that it can exceed values of 1.0 if $\frac{N}{N_l} > 1$. Under partial drained conditions, the excess pore pressure generated during shaking dissipates over time. At a very long time after the end of shaking, no excess pore pressure is present, so the final condition of excess pore pressure is $u(x, \infty) = 0$. Solving equation (5.41) for the condition a very long time after shaking:

$$0 = \exp(-c_v\beta^2[\infty])\,(c_1\cos(\beta x) + c_2\sin(\beta x)) + p_o(r_u{}^*(\infty) + \alpha) \tag{5.42}$$

Since $\exp(-\infty) = 0$,

$$0 = p_o\left(r_{u,\max} + \alpha\right) \tag{5.43}$$

Then, solving for α

$$\alpha = -r_{u,\max} \tag{5.44}$$

and substituting equation (5.44) into equation (5.42)

$$u(x,t) = \exp(-c_v\beta^2 t)\,(c_1\cos(\beta x) + c_2\sin(\beta x)) + p_o\left(r_u(t) - r_{u,\max}\right) \tag{5.45}$$

Finally, solving equation (5.45) with $r_{u,\max} = 0$ results in Terzaghi's solution.

The boundaries of the problem are defined so that drainage occurs at the top of the layer, where $x = 0$, and at the bottom of the layer, where $x = H$. Drained boundary conditions, in this case, are defined such that there is no resistance to drainage across the boundary, and the change in flow rate, q, through the boundary is zero, i.e. $\frac{\partial q}{\partial x} = 0$. Defining the drainage boundary as $\frac{\partial q}{\partial x} = 0$, implies that $\frac{\partial^2 u(0,t)}{\partial x^2} = 0$. This is different than the boundary conditions used for Terzaghi's solution, which assume that $u(0,t) = 0$. However, since Terzaghi's solution is a second order periodic differential equation, assuming $\frac{\partial^2 u(0,t)}{\partial x^2} = 0$ at the drainage boundaries does not change the results

of Terzaghi's solution. For example, the boundary condition Terzaghi used in equation (5.22) yields:

$$0 = \exp(-c_v\beta^2 t)\,(c_1 \cos\beta x + c_2 \sin\beta x) \tag{5.46}$$

The boundary condition in this solution with equation (5.42) yields

$$0 = -\beta^2\exp(-c_v\beta^2 t)\,(c_1 \cos\beta x + c_2 \sin\beta x) \tag{5.47}$$

Equations (5.46) and (5.47) result in the same values of coefficients c_1 and c_2. Defining the boundary conditions as $\frac{\partial^2 u(0,t)}{\partial x^2} = 0$ is necessary for this solution because the term for excess pore pressure generated by cyclic shear stress, $r_u(t)$, is independent of depth. No solution would be possible for the boundary conditions if $u(0,t) = 0$, because $r_u(t)$ varies with time. However, since $\frac{\partial^2 r_u}{\partial x^2} = 0$, equation (5.39) can be solved with a boundary condition where $\frac{\partial^2 u}{\partial x^2} = 0$.

This boundary condition is applied at the top of a layer, where $x = 0$, and at the bottom of a layer, where $x = H$. The solution is differentiated twice in terms of x.

$$\frac{\partial^2 u}{\partial x^2} = -\beta^2\exp(-c_v\beta^2 t)\,(c_1 \cos(\beta x) + c_2 \sin(\beta x)) \tag{5.48}$$

The first boundary condition of $\frac{\partial^2 u}{\partial x^2}(0,t) = 0$ is used to solve for values of coefficient c_1. Substituting this boundary conditions into equation (5.48)

$$0 = -\beta^2\exp(-c_v\beta^2 t)\,(c_1 \cos(\beta[0]) + c_2 \sin(\beta[0])) \tag{5.49}$$

Since $\cos(0) = 1$ and $\sin(0) = 0$,

$$0 = -\beta^2\exp(-c_v\beta^2 t)\,(c_1) \tag{5.50}$$

Then, solving equation (5.50) for c_1 yields

$$c_1 = 0 \tag{5.51}$$

Substituting c_1 back into equation (5.45)

$$u(x,t) = \exp(-c_v\beta^2 t)\,(c_2 \sin(\beta x)) + p_o\big(r_u(t) - r_{u,\max}\big) \tag{5.52}$$

The second boundary condition of $\frac{\partial^2 u}{\partial x^2}(H,t) = 0$ can be used to solve for non-trivial values of β. Substituting this boundary condition into equation (5.48) with $c_1 = 0$:

$$0 = -\beta^2\exp(-c_v\beta^2 t)\,(c_2 \sin(\beta H)) \tag{5.53}$$

For non-trivial values where $\beta \neq 0$:

$$0 = \sin(\beta H) \tag{5.54}$$

The value for β is periodic for positive integer values of n.

$$\beta = \frac{\pi n}{H} \tag{5.55}$$

The periodic components for β may be superimposed for all values of n. In many applications, the drainage path length, H_{dr}, is used rather than the thickness of the layer, H. Under conditions where both the top and bottom of the layer are drained, $H = 2H_{dr}$. Coefficient c_2 is designated a coefficient c_n since it's value depends on n. Substituting equation (5.55) into equation (5.45) yields

$$u(x,t) = \sum_{n=1}^{\infty} c_n \exp\left(-c_v \left[\frac{\pi n}{H}\right]^2 t\right) \sin\left(\left[\frac{\pi n}{H}\right] x\right) + p_o\left(r_u(t) - r_{u,\max}\right) \tag{5.56}$$

The initial condition is defined by no excess pore pressure in the layer at the beginning of shaking, so $u(x,0) = 0$. Applying this initial condition to equation (5.56) can be used to solve for values of c_n.

$$0 = \sum_{n=1}^{\infty} c_n \exp\left(-c_v \left[\frac{\pi n}{H}\right]^2 [0]\right) \sin\left(\left[\frac{\pi n}{H}\right] x\right) + p_o\left(r_u(0) - r_{u,\max}\right) \tag{5.57}$$

Since $\exp(0) = 1$ and $r_u(0) = 0$, equation (5.57) reduces to

$$0 = \sum_{n=1}^{\infty} c_n \sin\left(\left[\frac{\pi n}{H}\right] x\right) - p_o r_{u,\max} \tag{5.58}$$

Rearranging equation (5.58) yields

$$p_o r_{u,\max} = \sum_{n=1}^{\infty} c_n \sin\left(\left[\frac{\pi n}{H}\right] x\right) \tag{5.59}$$

Equation (5.59) has the general form of a Fourier sine series (DuChateau and Zachmann, 1989). Fourier series are defined by an arbitrary function $f(y)$ that is periodic between $y = 0$ and $y = H$. Equations (5.60) and (5.61) show the general form of a Fourier series and Fourier series coefficient, c_n.

$$f(y) = \sum_{n=1}^{\infty} c_n \sin\left(\frac{n\pi y}{H}\right) \tag{5.60}$$

$$c_n = \frac{2}{H}\int_0^H f(y)\sin\left(\frac{n\pi y}{H}\right)dy \tag{5.61}$$

To make equation (5.59) a Fourier sine series, $f(y) = p_o r_{u,\max}$ and $y = x$. Equation (5.61) then becomes

$$c_n = \frac{2}{H}\int_0^H p_o r_{u,\max}\sin\left(\frac{n\pi x}{H}\right)dx \tag{5.62}$$

Removing the constant terms from the integral yields

$$c_n = \frac{2}{H}p_o r_{u,\max}\int_0^H \sin\left(\frac{n\pi x}{H}\right)dx \tag{5.63}$$

Integration equation (5.63) from 0 to H yields

$$c_n = \frac{2}{H}p_o r_{u,\max}\left(-\frac{H}{\pi n}\right)\cos\left(\frac{n\pi x}{H}\right)\Big]_{x=0}^{H} \tag{5.64}$$

Evaluating equation (5.64) at $x = 0$ and $x = H$ yields

$$c_n = \frac{2}{\pi n}p_o r_{u,\max}(1-\cos(n\pi)) \tag{5.65}$$

Equations (5.57) and (5.65) combine to generate the solution for $u(x,t)$. The resulting expression combines the boundary, initial, and final conditions in a transcendental expression for excess pore pressure due to competing effects of shearing and drainage.

$$\begin{aligned} u(x,t) = {} & p_o\left(r_u(t) - r_{u,\max}\right) \\ & + \sum_{n=1}\frac{2}{\pi n}p_o r_{u,\max}(1-\cos(n\pi))\exp\left(-c_v\left[\frac{\pi n}{H}\right]^2 t\right)\sin\left(\left[\frac{\pi n}{H}\right]x\right) \end{aligned} \tag{5.66}$$

5.3.2 *Liquefaction potential*

If the rate of drainage is faster than the rate of pore pressure generation, then under no circumstances can the soil liquefy. The solution in equation (5.66) can be solved to find a rate of drainage that is at least as fast as the rate of pore pressure generation due to rapid loading. If the soil does not liquefy under these conditions, it implies that the soil does not liquefy. Under extreme, rapid loading conditions, the pore pressure potential, $r_u(t)$, approaches infinity over a

short time period, Δt. In these conditions, there exists a minimum value of c_v so that the rate of pore pressure generation in the center of the layer is less than the rate of drainage.

To determine values of c_v where the rate of drainage is faster than the rate of pore pressure generation. The solution in equation (5.66) is first differentiated with respect to time.

$$\frac{\partial u}{\partial t} = p_o\left(\frac{\partial}{\partial t} r_u(t)\right) + \sum_{n=1} \frac{2}{\pi n} p_o r_{u,\max}(1 - \cos(n\pi))\left(-c_v\left[\frac{\pi n}{H}\right]^2\right)\exp\left(-c_v\left[\frac{\pi n}{H}\right]^2 t\right)\sin\left(\left[\frac{\pi n}{H}\right]x\right) \tag{5.67}$$

Pore pressure takes the longest to dissipate from the center of the layer. Evaluating equation (5.67) at the center of the layer, where $x = \frac{H}{2}$, creates an expression for the maximum rate of pore pressure generation at the center of the layer over a very short period of time, where $t = \Delta t$.

$$\frac{\partial u}{\partial t}\left(\Delta t, \frac{H}{2}\right) = p_o\left(\frac{\partial}{\partial t} r_u(\Delta t)\right) + \sum_{n=1}^{\infty} \frac{2}{\pi n} p_o r_{u,\max}(1 - \cos(n\pi))\left(-c_v\left[\frac{\pi n}{H}\right]^2\right)\exp\left(-c_v\left[\frac{\pi n}{H}\right]^2 \Delta t\right)\sin\left(\frac{\pi n}{2}\right) \tag{5.68}$$

The rate of pore pressure generation in the center of the layer should be less than or equal to zero under the conditions where the pore pressure is dissipating faster than it can be generated, i.e. $\frac{\partial u}{\partial t}\left(\Delta t, \frac{H}{2}\right) \leq 0$. A layer of soil that cannot liquefy under any loading conditions implies that $r_{u,\max}$ is infinitely large and $r_u(\Delta t) = r_{u,\max} = \infty$. If the rate of pore pressure generation is neither increasing nor decreasing, then $\frac{\partial u}{\partial t} = 0$, which provides a limit state for liquefaction potential due to drainage. Evaluating equation (5.68) for very rapid, very extreme loading conditions yields

$$0 = p_o\left(\frac{\partial}{\partial t} r_u(\Delta t)\right) + \sum_{n=1}^{\infty} \frac{2}{\pi n} p_o r_{u,\max}(1 - \cos(n\pi))\left(-c_v\left[\frac{\pi n}{H}\right]^2\right)\exp\left(-c_v\left[\frac{\pi n}{H}\right]^2 \Delta t\right)\sin\left(\frac{\pi n}{2}\right) \tag{5.69}$$

Rearranging equation (5.69) yields

$$-p_o\left(\frac{\partial}{\partial t} r_u(\Delta t)\right) = \sum_{n=1}^{\infty} \frac{2}{\pi n} p_o r_{u,\max}(1 - \cos(n\pi))\left(-c_v\left[\frac{\pi n}{H}\right]^2\right)\exp\left(-c_v\left[\frac{\pi n}{H}\right]^2 \Delta t\right)\sin\left(\frac{\pi n}{2}\right) \tag{5.70}$$

Rearranging equation (5.70) so that terms independent of n are on the left-hand side yields

$$\frac{\frac{\partial r_u}{\partial t}}{r_{u,\max}} = \sum_{n=1}^{\infty} \frac{2}{\pi n}(1 - \cos(n\pi))\left(c_v\left[\frac{\pi n}{H}\right]^2\right)\exp\left(-c_v\left[\frac{\pi n}{H}\right]^2 \Delta t\right)\sin\left(\frac{\pi n}{2}\right) \tag{5.71}$$

As the pore pressure potential approaches infinity, $r_{u,\max} = \lim_{t \to \Delta t} r_u(t) = \infty$, the left-hand side of equation (5.71) approaches zero, where $\frac{1}{r_{u,\max}} = 0$

$$0 = \sum_{n=1}^{\infty} \frac{2}{\pi n}(1 - \cos(n\pi))\left(c_v\left[\frac{\pi n}{H}\right]^2\right)\exp\left(-c_v\left[\frac{\pi n}{H}\right]^2 \Delta t\right)\sin\left(\frac{\pi n}{2}\right) \tag{5.72}$$

For positive integer values of n, $(1 - \cos(n\pi))\sin\left(\frac{n\pi}{2}\right) = 2\sin\left(\frac{n\pi}{2}\right)$. Equation (5.72) then becomes

$$0 = \sum_{n=1}^{\infty} \frac{4}{\pi n}\left(c_v\left[\frac{\pi n}{H}\right]^2\right)\exp\left(-c_v\left[\frac{\pi n}{H}\right]^2 \Delta t\right)\sin\left(\frac{\pi n}{2}\right) \tag{5.73}$$

The terms in the summation are positive for values of $n = 1,5,9$ ..., negative when $n = 3,7,11$ ..., and zero when $n = 2,4,6$ .... Values of c_v that satisfy the inequality can be approximated using the first positive and negative terms, i.e. $n = 1$ and $n = 3$.

$$0 = \frac{4}{\pi}\left(c_v\left[\frac{\pi}{H}\right]^2\right)\exp\left(-c_v\left[\frac{\pi}{H}\right]^2\Delta t\right) - \frac{4}{\pi[3]}\left(c_v\left[\frac{\pi[3]}{H}\right]^2\right)\exp\left(-c_v\left[\frac{\pi[3]}{H}\right]^2\Delta t\right) \tag{5.74}$$

Grouping like terms yields

$$\frac{4}{\pi[3]}\left(9\,c_v\left[\frac{\pi}{H}\right]^2\right)\exp\left(-9\,c_v\left[\frac{\pi}{H}\right]^2\Delta t\right) = \frac{4}{\pi}\left(c_v\left[\frac{\pi}{H}\right]^2\right)\exp\left(-c_v\left[\frac{\pi}{H}\right]^2\Delta t\right) \tag{5.75}$$

Canceling terms that are equal on the left and right-hand sides of the equation yields

$$3\exp\left(-9\,c_v\left[\frac{\pi}{H}\right]^2\Delta t\right) = \exp\left(-c_v\left[\frac{\pi}{H}\right]^2\Delta t\right) \tag{5.76}$$

Pulling all terms inside of the exponential yields

$$\exp\left(\ln 3 - 9\,c_v\left[\frac{\pi}{H}\right]^2\Delta t\right) = \exp\left(-c_v\left[\frac{\pi}{H}\right]^2\Delta t\right) \tag{5.77}$$

Taking the natural log of both sides yields

$$\ln 3 - 9\,c_v\left[\frac{\pi}{H}\right]^2\Delta t = -c_v\left[\frac{\pi}{H}\right]^2\Delta t \tag{5.78}$$

Grouping like terms together yields

$$\frac{\ln 3}{8} = c_v\left[\frac{\pi}{H}\right]^2\Delta t \tag{5.79}$$

Finally, regrouping yields

$$\frac{\ln 3}{8\,\pi^2} = \frac{c_v\,\Delta t}{H^2} \tag{5.80}$$

A layer of soil where c_v is greater than or equal to expression above drains too rapidly to liquefy under any realistic loading conditions. The expression is rearranged as an inequality.

$$\frac{\ln 3}{8\,\pi^2} \leq \frac{c_v\,\Delta t}{H^2} \tag{5.81}$$

Figure 5.3 shows this inequality graphically for a range of values of c_v and Δt, and the region where soils are not liquefiable due to rapid drainage.

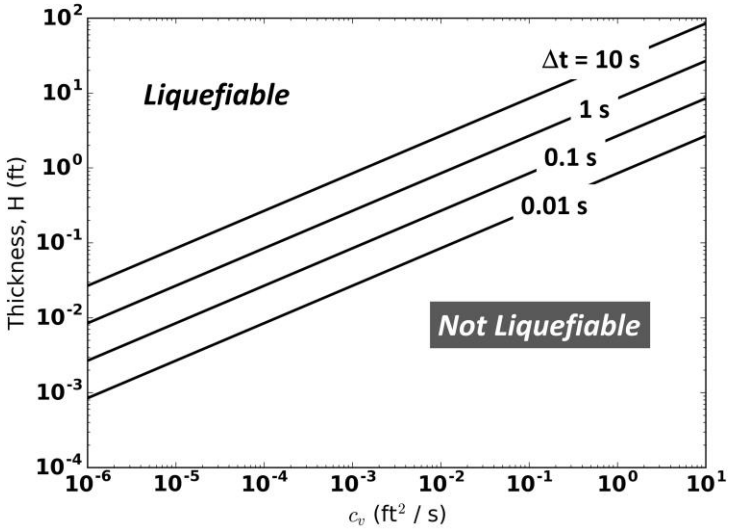

Figure 5.3: Drainage characteristics of soils that do not liquefy due to rapid drainage.

5.3.3 *Examples*

The effects of drainage on the pore pressure generation can be illustrated through several examples. In the first example, a 5 ft thick layer of liquefiable soil was subject to a 1 Hz cyclic motion. The soil had a cyclic resistance ratio such that, without drainage, liquefaction would occur after 10 cycles. Three different values of the coefficient of drainage, c_v, were selected to illustrate the effects of drainage. Figure 5.3 shows the isochrones of pore pressure ratio, r_u, in the layer after 10 cycles, where t = 10 seconds, of loading for $c_v = 0.1$, 0.01, and 0.001 ft^2/s.

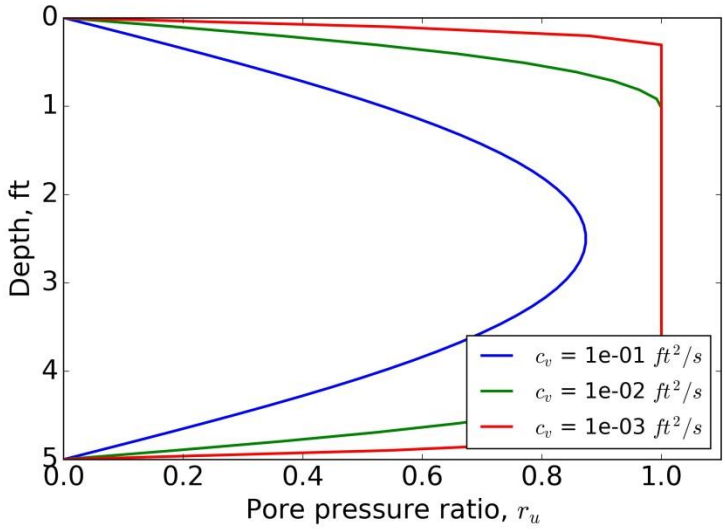

Figure 5.4: Example pore pressure ratio isochrones. Example site with a 5 ft-thick layer of liquefiable soil subjected to a 1 Hz load at t=10 seconds.

In this example, the inequality in equation (5.81) indicates that the layer would not be susceptible to liquefaction if c_v was greater than about 0.3 ft^2/s. However, even if $c_v = 0.1$ ft^2/s, the soil drained rapidly enough that r_u at center of the layer was less than 0.9 after 10 cycles of loading. The example indicates that if the soil drained at a slower rate, i.e. $c_v = 0.01$ ft^2/s or 0.001 ft^2/s, the soil at the center of the layer would liquefy, but the pore pressure ratio at the edges of the layer near the drainage boundaries would be less than 1.0. Figure 5.5 shows the development of pore pressure versus time in the center of the layer where $x = \frac{H}{2}$. The slower draining soils ($c_v =$ 0.01 ft^2/s or 0.001 ft^2/s) had nearly the same pore pressure ratio in the center of the layer after 10 cycles of loading.

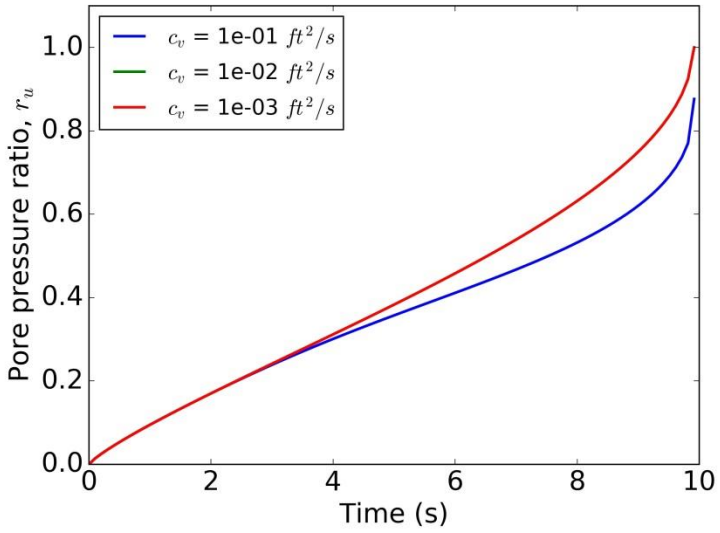

Figure 5.5: Example pore pressure ratio at 2.5 ft.

In this example, the strong shaking stopped after 10 cycles of loading (t = 10 seconds) and pore pressure began to dissipate. Figure 5.6(a) shows the pore pressure at the center of the three example profiles from 0 to 120 seconds. Figure 5.6(b) also shows pore pressure isochrones at 120 seconds. The analytical solution indicates that after 120 seconds, most of the excess pore pressure would have dissipated from the rapidly draining layer where $c_v = 0.1$ ft^2/s. Some of the excess pore pressure would have dissipated from the layer where $c_v = 0.01$ ft^2/s after 120 seconds, such that that the soil was no longer liquefied, but pore pressure at the center of the layer was still greater than 0.8. Pore pressure would not have dissipated from the center of the slowest draining layer, where $c_v = 0.001$ ft^2/s, and the pore pressure ratio would still have been 1.0 in the center of the layer after 120 seconds.

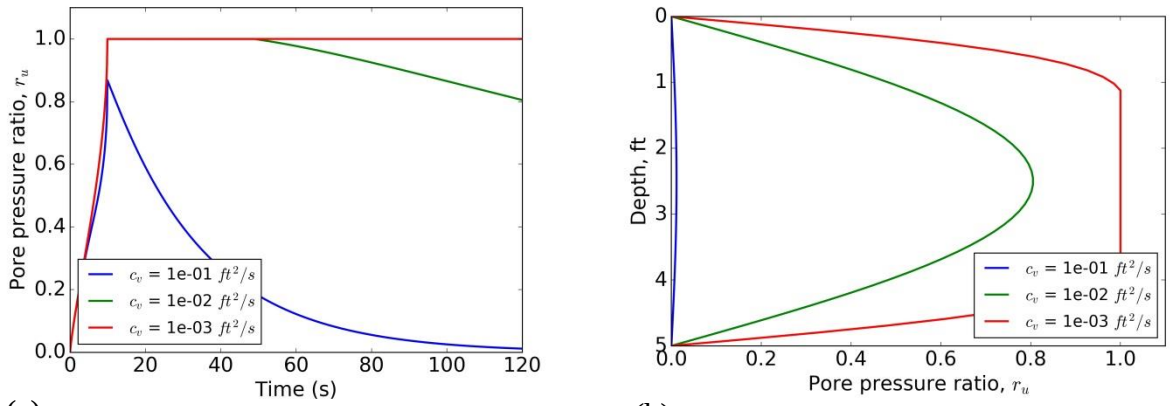

(a) (b)

Figure 5.6: Example of pore pressure dissipation after shaking. (a) Pore pressure ratio at 2.5 ft deep. Strong shaking occurs from 0 to 10 seconds and then stops. (b) Isochrones at 120 seconds.

Even if a soil layer is susceptible to liquefaction and does not satisfy the inequality in equation (5.81), drainage during shaking can increase the liquefaction resistance of a soil deposit. The competing effects of pore pressure generation due to shaking and pore pressure dissipation due to drainage ultimately result in lower pore pressure than would be generated during undrained conditions. Additional shaking may eventually liquefy the soil, but the intensity of shaking required to liquefy the soil would be greater than it would be under undrained conditions. Equation (5.6) was developed to estimate the pore pressure generation potential, $r_u{}^*$, for such conditions. A second example is based on a 5 ft thick layer of soil with a cyclic resistance ratio such that liquefaction would occur after 15 cycles of loading during undrained conditions. The example soil profile was subject to repeated cyclic loading at 10 Hz until liquefaction occurred. Figure 5.7 shows the number of cycles to trigger liquefaction for values of c_v ranging from 10^{-3} to 10^{1} ft^2/s.

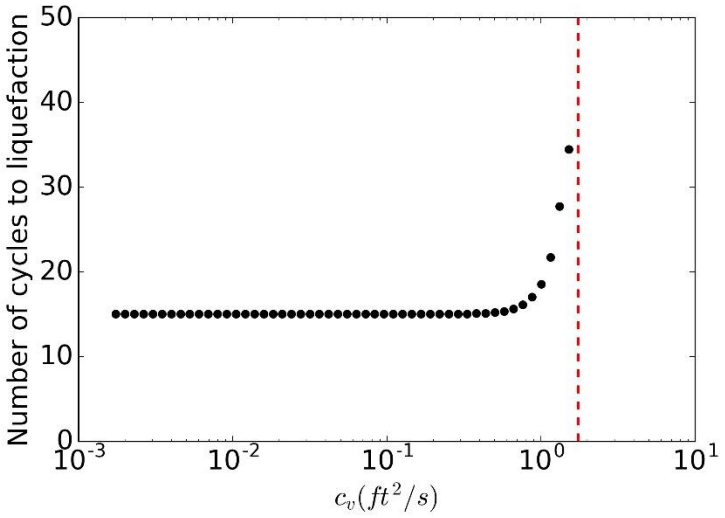

Figure 5.7: Number of cycles to trigger liquefaction with 10 Hz loading.

The number of cycles required to trigger liquefaction did not appreciably increase until $\frac{c_v \Delta t}{H^2}$ approached $\frac{\ln 3}{8\,\pi^2}$. This is in part due to the rapid rate of loading (10 Hz) in this example, which does not allow much time for drainage to occur. Under slower rates of loading the effects of drainage may be more pronounced. The same soil profile was loaded with a 1 Hz motion until liquefaction occurred. The number of cycles necessary to trigger liquefaction is shown in Figure 5.8.

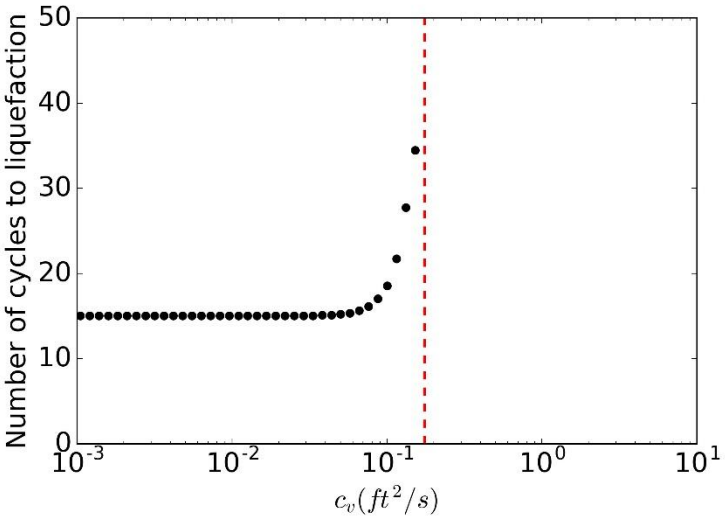

Figure 5.8: Number of cycles to trigger liquefaction with 1 Hz loading.

Under the slower loading conditions, the layer was not susceptible to liquefaction if the value of c_v was greater than 0.03 ft^2/s. The liquefaction resistance also increased at lower values of c_v. However, the effects of drainage were still not appreciable until $\frac{c_v \Delta t}{H^2}$ approached $\frac{\ln 3}{8\,\pi^2}$. This example indicates that the effects of drainage on liquefaction resistance may not become appreciable until c_v is within about 1/3 of a log cycle of the value of c_v where liquefaction cannot occur.

5.3.4 *Discussion*

The solution developed for this study is applicable for thin layers of liquefiable soils that have at least one drainage boundary. Identifying thin layers of soil that are not susceptible to liquefaction due to their drainage characteristics is very useful from a practical perspective. Very often, thin layers of loose sand are present within a thicker, dense, well-drained soil deposit that is unlikely to liquefy during the expected loading conditions. This solution implies that drainage from loose granular layers into dense well-drained layers may increase the loose layer's resistance to liquefaction, if no pore pressure is generated in the soils that make up the boundaries of the loose layer. Drainage and pore pressure generation in thick, liquefiable layers of soil, where the cyclic resistance ratio of the soil and rate of pore pressure generation are not uniform across the entire layer, are not captured with this solution.

The solution implies that soils that drain sufficiently rapidly with a value of $\frac{c_v \Delta t}{H^2}$ greater than $\frac{\ln 3}{8\,\pi^2}$ do not liquefy under any reasonable loading condition. The examples in this study imply that the rate of drainage may not have a significant effect on liquefaction resistance until $\frac{c_v \Delta t}{H^2}$ approaches $\frac{\ln 3}{8\,\pi^2}$. The liquefaction resistance and susceptibility are heavily influenced by the time increment over which very strong shaking may occur, Δt. For transient loading, Δt, is likely a function of the period of the largest pulse in the motion, although an analysis of transient motions has not been performed at this time.

[This page intentionally left blank]

Chapter 6. NUMERICAL ANALYSIS OF LIQUEFIED SOILS

Numerical analysis of liquefied soils is necessary to understand and model the complicated interaction between pore pressure, shear stress, and shear strain that occurs during dynamic loading. Despite recent advances in the analysis of liquefaction triggering (Cetin et al. 2004; Green and Lee, 2006; Boulanger and Idriss, 2014) estimates of deformations that develop after liquefaction still include a large amount of uncertainty. Much of this uncertainty stems from the lack of case history observations and the inability to directly observe transient stresses and strains that have occurred during past earthquakes. Numerical analyses provide a link from laboratory data, where stresses, strains, and pore pressures are directly observed, to field-based empirical observations of deformation. A properly calibrated numerical model provides the ability to "see inside" the soil during dynamic loading. Since only a limited number of case histories where liquefaction has been observed are available, numerical analyses can be used to complement the available empirical observations for an array of sites and loading conditions. Because earthquake ground motions inherently include uncertainty, parallel, stochastic batching of numerical models also helps to quantify the effects of uncertainty in ground motions and subsurface conditions by using Monte Carlo or similar techniques.

Although many finite element packages were available for this study, the list of desirable characteristics of a constitutive model rules out some of the modeling packages. The finite element program FLIP included the Cocktail Glass constitutive model (Iai et al., 2011), which was designed to account for the complicated nonlinear, effective stress, dynamic behavior of liquefiable soils. In this study, the Cocktail Glass model was calibrated to match existing semi-empirical behavior that has been derived from laboratory tests for pore pressure generation and post-liquefaction shear strains, and case history observations for liquefaction triggering. The calibrated Cocktail Glass model was used to provide detailed insight into the liquefaction case histories in Chapter 8 and was used to develop a database of deformation observations for various ground motion intensity measures in Chapter 9. The desirable features of a liquefied soil model are discussed, followed by a detailed description of the Cocktail Glass constitutive model, the calibration procedure, results, and a comparison with semi-empirical and laboratory-based data.

6.1 DESIRABLE FEATURES IN A LIQUEFIED SOIL MODEL

The response of liquefiable soil to dynamic loading results in a wide and complicated range of possible behaviors. Liquefiable soils exhibit nonlinear stress-strain behavior, shear and volumetric coupling, and effective stress dependence. These behavioral phenomena have a significant influence on pore pressure generation, liquefaction triggering, and post-liquefaction deformation. A soil model for liquefaction should be able to accounts for these different behaviors, and the model should be defined in such a way that it can be calibrated to empirical observations. Desirable features in a constitutive model that can account for liquefaction must include the following characteristics (Kramer and Elgamal, 2001).

Nonlinear stress-strain behavior

Under drained monotonic loading, as the shear strain increases, the tangent shear modulus decreases. At a yield state, the tangent shear modulus approaches zero (Kramer, 1996). The nonlinear stress-strain behavior is typically based on modulus reduction curves (Vucetic and Dobry, 1991; EPRI, 1993; Darendelli, 2001; etc.), that when integrated, form a nonlinear stress-strain relationship.

Hysteresis response under cyclic loading

Soil stiffness varies depending on the direction of loading. Plastic strains accumulation during the loading phase. Upon unloading, the soil initially is much stiffer than it was during loading. The dependence on the direction of loading results in hysteric stress-strain behavior, where the stress-strain curves during cyclic loading develop ellipse-like loops. The hysteresis stress-strain behavior dissipates energy through material damping, and the amount of damping can be described by the damping ratio, ξ.

$$\xi = \frac{A_{loop}}{2\pi\, G_{sec}\, {\gamma_c}^2} \tag{6.1}$$

where A_{loop} is the area of the stress-strain loop, G_{sec} is the secant modulus, and γ_c is the cyclic shear strain.

Dependence on effective confinement

The low-strain shear modulus and the shear strength of the soil depend on the effective confining stress. The low-strain shear modulus increases with increasing confining pressure. For granular soils, this rate is approximately proportional to the square root of the mean confining stress (Kramer, 1996). The strength of soil also generally increases with increasing confining stress, as soils typically derive some component of their strength due to friction.

Contraction and dilation of the soil skeleton

Soils exhibit complicated volumetric strain behavior in response to shear loading. The contraction and dilation relationship of soils is defined by a critical state, where soils that are loose of critical tend to contract, and soils that are dense of critical tend to dilate. The critical state of soils is uniquely defined by a surface based on the void ratio, e, deviator stress invariant, q, and mean effective stress, p (Scofield and Wroth, 1968).

All soils contract slightly at low shear stress ratios, and in soils that are also saturated, excess pore pressure is generated as the soil attempts to contract. The rate of contraction is important for quantifying the rate at which excess pore pressure develops during repeated cycles of loading. The amount of volumetric contraction also affects the volumetric strain that occurs after shaking stops and the excess pore pressure due to shaking dissipates. At shear stress ratios that are above the critical state line and dense of critical, soils tend to dilate, when they are sheared. If the soil is also saturated, volumetric strain cannot occur and excess pore pressure decreases as the soil attempts to dilate. Since the soil stiffness depends on the effective confining pressure, the shear stiffness of saturated soils can vary over many orders of magnitude as soil dilates and contracts due to cyclic shearing.

Degradation of soil fabric

Laboratory tests (Ishihara and Yoshimine, 1992) indicate that the shear strain amplitude incrementally increases after soil liquefies in response to constant-stress amplitude cyclic loading. This continued softening and accumulation of shear strain is due to degradation of the soil fabric. In soils with a static shear bias, the degradation of soil fabric leads to kinematic hardening, or "ratcheting", shear stress-strain behavior. The shear strains that develop in response to cyclic

loading with a constant shear stress bias can be permanent, and this phenomenon is important for lateral spreading analysis.

Drainage

Particularly during long duration earthquakes, high permeability soils in thin to moderately thick layers may have sufficient time to drain. Since the soil stiffness depends on the effective stress, dissipation of excess pore pressure due to drainage increases the soil stiffness. Pore water tends to migrate towards the ground surface pore pressure redistributes. This phenomenon can lead to greatly reduced strength and stiffness of the soil at the top of a liquefiable deposit if the deposit is capped by impervious material (Idriss and Boulanger, 2008). A constitutive model must be formulated in a way to allow the computation of pore pressure redistribution and dissipation during shaking.

Several modern constitutive models were available on multiple platforms that exhibited these characteristics. These models included PM4Sand (Boulanger and Ziotopoulou, 2014), UBCSand (Beaty and Byrne, 2011), PSNL (Kramer et al., 2013), and the Cocktail Glass model (Iai et al., 2011). The Cocktail Glass model was selected based on its availability, the characteristics of the model, and the ability of the model to account for the complicated behavior of liquefied soil described previously. The finite element program FLIP (Finite element Liquefaction Program) supports the nonlinear, effective stress Cocktail Glass model. FLIP was particularly desirable for this analysis because the program can perform 2D dynamic, nonlinear computations while accounting for pore pressure dissipation due to drainage during shaking. The finite element computations in FLIP are considerably faster than similar packages like FLAC. The FLIP program has also been compiled in such a way that parallel analysis and simultaneous batching of many simulations can be performed.

6.2 COCKTAIL GLASS MODEL

The Cocktail Glass model (Iai et al., 2011) was designed to represent the micromechanical structure of soil particles using virtual multi-dimensional mechanisms. This model provided a link between microscopic observations of soil grains and macroscopic observations of shear stress and strain behavior. The Cocktail Glass model was developed as an extension of the commonly used Multi-Spring model (Iai et al., 1992) in FLIP.

As with most constitutive models, the low-strain stiffness of the Cocktail Glass model was defined in terms of shear and bulk moduli, G and K. The low-strain stiffness values varied with the mean effective stress as a power law.

$$\mathrm{G} = \mathrm{G}_{atm}\left(\frac{p}{p_{atm}}\right)^{m} \tag{6.2}$$

$$\mathrm{K} = \mathrm{K}_{atm}\left(\frac{p}{p_{atm}}\right)^{n} \tag{6.3}$$

where p is the mean effective stress, p_{atm} is the atmospheric pressure, n and m are empirical coefficients, and G_{atm} and K_{atm} are normalized stiffness for 1 atm. The low-strain shear and compressive moduli were calculated from shear wave velocity measurements, v_s, and Poison's ratio, ν, which was estimated to be about 0.3.

$$\mathrm{G} = \rho(v_s)^2 \tag{6.4}$$

$$\mathrm{K} = \frac{2\mathrm{G}(1+\nu)}{3(1-2\nu)} \tag{6.5}$$

where ρ is the soil density. The difference in bulk modulus for drained and undrained loading was accounted for by a parameter, r_K, that was applied to the drained bulk modulus. The bulk modulus for undrained loading was used even for partially saturated soils in dynamic analysis.

$$\mathrm{K}' = r_K\mathrm{K}\left(\frac{p}{p_0}\right)^2 \tag{6.6}$$

where K' is the bulk modulus for undrained or partially drained soils and p_0 is the initial mean effective stress.

The peak shear stress in the Cocktail Glass model was enveloped by the peak friction angle, ϕ'. The residual shear strength at large shear strain was controlled by a residual friction angle through the parameter r_{tmp}. If r_{tmp} was equal to 1 the residual friction angle was equal to the peak friction angle, ϕ', and if r_{tmp} was equal to 0 the residual friction angle was equal to the phase transformation angle, ϕ_p. Steady-state undrained shear strength, s_{us}, could also be modeled in the Cocktail Glass model, although was not considered for the calibration.

A key component of the Cocktail Glass model was decoupling the parameters that controlled the soil's contractive behavior from its dilative behavior. The total volumetric strain increment in the Cocktail Glass model was broken into three separate components: strain due to

changes in isotropic pressure, $\dot{\varepsilon}'$, strain due to shear-induced dilation, $\dot{\varepsilon}_d^d$, and strain due to shear-induced contraction, $\dot{\varepsilon}_d^d$.

$$\dot{\varepsilon} = \dot{\varepsilon}' + \dot{\varepsilon}_d^d + \dot{\varepsilon}_d^c \tag{6.7}$$

The rate of strain due to changes in isotropic pressure, $\dot{\varepsilon}'$, was calculated using the undrained bulk modulus.

$$\dot{\varepsilon}' = \mathrm{K}'\dot{p} \tag{6.8}$$

The rate of strain due to dilation was controlled by a coefficient, r_{ε_d}. The expression for volumetric dilation was defined as a function of the shear strain increment, $\dot{\gamma}$, and the stress ratio, $\frac{q}{p}$.

$$\dot{\varepsilon}_d^d = -r_{\varepsilon_d}\,\dot{\gamma}\,\frac{q}{p} \tag{6.9}$$

Where p is the mean effective stress and q is the mean deviatoric stress. The rate of strain due to contraction was controlled by several parameters and material states including the stress tensor of the soil, a fabric tensor, the plastic increment of shear strain, and loading state. In this formulation, the effective stress tensor, $\boldsymbol{\sigma}'$, was defined using the normal and shear forces on virtual particles.

$$\boldsymbol{\sigma}' = -p\,\mathbf{I} + \frac{1}{4\pi}\iint q\,\langle \boldsymbol{t} \otimes \mathbf{n}\rangle\, d\omega\, d\Omega \tag{6.10}$$

where vectors $\boldsymbol{t}$ and $\boldsymbol{n}$ are virtual particle contact normal and shear force vectors, $\langle \boldsymbol{t} \otimes \boldsymbol{n}\rangle$ is the deviatoric contact force tensor, and ω and Ω represent spherical coordinates. The component of volumetric contraction was formulated through a fabric tensor, $\mathbf{I}_{\boldsymbol{d}}^{\boldsymbol{c}}$.

$$\dot{\varepsilon}_d^c = \mathbf{I}_{\boldsymbol{d}}^{\boldsymbol{c}} : \dot{\boldsymbol{\varepsilon}} \tag{6.11}$$

where $\dot{\boldsymbol{\varepsilon}}$ is the incremental strain tensor. The fabric tensor was defined as

$$\mathbf{I}_{\boldsymbol{d}}^{\boldsymbol{c}} = -r_{\varepsilon_d}\, r_{\varepsilon_d^c}\, r_{s_0} \int \mathrm{M}_v \left(1 - c_1 \left(\frac{\mathrm{G_{L/U}}}{\mathrm{G}_0}\right)\right) |\langle \boldsymbol{t} \otimes \boldsymbol{n}\rangle|^* d\omega \tag{6.12}$$

where $|\langle \boldsymbol{t} \otimes \boldsymbol{n}\rangle|^*$ is the absolute value of the deviatoric contact force tensor, and ω is an angular coordinate, $\mathrm{G_{L/U}}$ is the loading or unloading shear modulus, G_0 is the initial low-strain shear modulus, c_1 is an elastic limiting factor, and r_{s_0}, $r_{\varepsilon_d^c}$, and r_{ε_d} are defined subsequently. The coefficient r_{ε_d} was defined for volumetric dilation, and was also applied for volumetric contraction. The coefficient $r_{\varepsilon_d^c}$ was introduced in the calculation of volumetric contraction to

decouple the rates of contraction and dilation. The coefficient r_{s_0} was calculated from the soil's stress state, $s_0 = \frac{p''}{p_0}$, where p'' is the virtual effective stress. Additional details about the calculation of the virtual effective stress are provided in Iai et al. (2011). The coefficient r_{s_0} defined a liquefaction front, where soils contracted more rapidly once their stress state crossed the liquefaction front.

$$r_{s_0} = \begin{cases} s_0{}^{q_2} & s_0 < 0.8 \\ s_0{}^{q_2}\,[(s_0 - 0.8)q_1 + 0.2] & s_0 \geq 0.8 \end{cases} \tag{6.13}$$

where q_1 and q_2 are curve fitting parameters. The two curve fitting parameters, q_1 and q_2, controlled the rate of contraction at low and high pore pressure ratios, respectively, through r_{s_0}. The parameter q_2 influenced the liquefaction resistance of the soil, and larger values of q_2 tended to increase the liquefaction resistance of the soil.

Equation (6.12) included a parameter M_v that was defined as

$$M_v = \frac{1}{2}\left(1 + \frac{\varepsilon_d^c}{\varepsilon_d^{cm}}\right)\sin\phi_p \tag{6.14}$$

where ε_d^{cm} was the maximum contractive volumetric strain and ϕ_p was the phase transformation angle. The phase transformation angle, ϕ_p, defined a surface where soils at a stress states below the phase transformation line contracted, and soils at a stress states above the phase transformation line dilated. The maximum contractive volumetric strain, ε_d^{cm}, placed a limit on the maximum volumetric strain that could occur after excess pore pressure had dissipated. The complicated interaction between shear strain and volumetric strain in the Cocktail Glass model caused the value of ε_d^{cm} to also affect the rate of contraction and pore pressure generation at very large cyclic shear strains. Low values of ε_d^{cm} resulted in an upper bound limit of shear strain during cyclic loading. A limiting shear strain after liquefaction had occurred has been proposed by several research groups (Seed et al., 1985; Idriss and Boulanger, 2008).

To develop hysteresis cycles, the shear stiffness in the Cocktail Glass modeled varied between loading and unloading states. The term for shear stiffness, $G_{L/U}$, in equation (6.12) was defined using a hyperbolic backbone curve. In Figure 6.1, both the shear strain, γ, and the shear stress, p, were normalized by reference values, γ_v and p_v. The sample was loaded from the origin to point 1 along the hyperbolic backbone curve. The sample was then unloaded from point 1 to 2, along an unloading curve that was defined by the stress and strain values at point 1. If unloading

had continued such that the shear stress at point 2 was equal to the negative value of the shear stress at point 1, the unloading curve would have rejoined the backbone curve. After the sample was loaded to point 2, it was reloaded to point 3, which had a lower shear stress than point 1, and then was unloaded until it rejoined the backbone curve. This figure illustrates the unloading and reloading stress-strain curves that were used in the Cocktail Glass model.

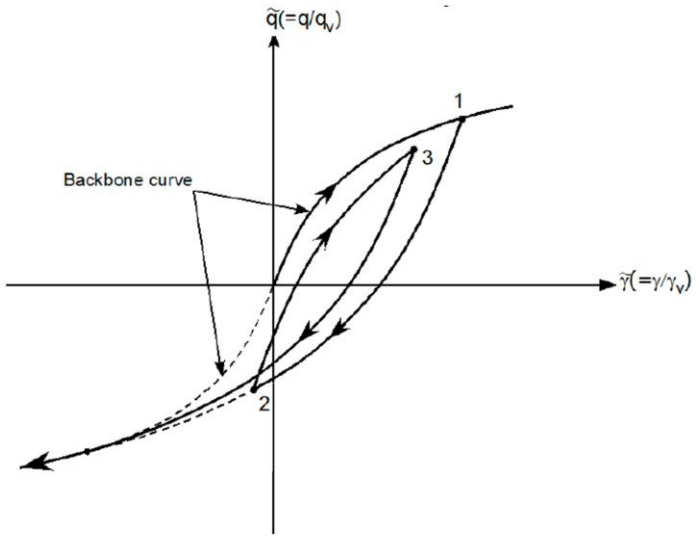

Figure 6.1: Stress-strain path for loading and unloading (from Iai et al., 1992)

A threshold for the elastic limit of shear strain was defined using the parameter, c_1. The term $c_1 \left(\frac{G_{L/U}}{G_0}\right)$ in equation was limited to a maximum value of 1, so that no plastic shear strain occurred when $c_1 \left(\frac{G_{L/U}}{G_0}\right) > 1$. Larger values of c_1 tended to decrease the liquefaction triggering resistance of the soil at low cycles shear stresses.

The Cocktail Glass model also included a parameter to limit the maximum hysteretic damping, H_{max}. The value of H_{max} affected the shape of the stress-strain curve, particularly after liquefaction was triggered. Larger values of H_{max} tended to allow wider hysteresis loops.

Additional details about the calculation of $\dot{\varepsilon}_d^c$ were described by Iai et al. (2011). The Cocktail Glass model was created such that, during drained loading, contraction caused a decrease in the void ratio, e, and dilation caused an increase in void ratio. The interaction between volumetric dilation and contraction resulted in volumetric strain versus the shear strain relationship that had a "cocktail glass" shape. Figure 6.2 shows the change in void ratio due to a partial cycle of loading in drained conditions. The sample in Figure 6.2 was initially consolidated to the void

ratio at point "A." As the sample was sheared, it dilated and the void ratio at point "B" was greater than at point "A". Once the loading was reversed and the sample was returned to zero shear strain, the volumetric strain due to dilation, ε_d^d, decreased, such that the void ratio at zero shear strain (point "C") was less than the void ratio at point "A" or "B".

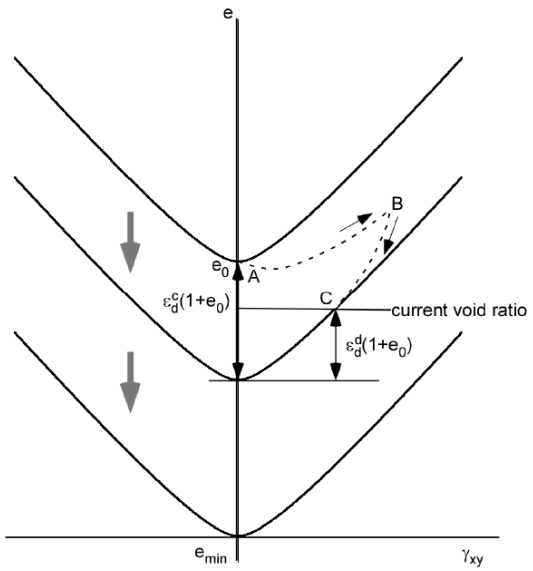

Figure 6.2: Strain path for Cocktail Glass model (from Iai et al. 2011)

Table 6.1 summarizes the input parameters for the Cocktail Glass model and their effect on liquefaction resistance and post-liquefaction shear strain.

Table 6.1: Cocktail Glass model parameters

Parameter	Symbol	Effect on liquefaction resistance	Effect on post-liquefaction shear strain
Soil density	ρ		
Shear wave velocity	v_s	Increased v_s increased liquefaction resistance	Increased v_s decreases post-liquefaction shear strain
Poisson's ratio	ν	Increased ν decreased liquefaction resistance	
Shear modulus exponent	m		
Bulk modulus exponent	n		
Reference stress	p_0		

Table 6.1: Cocktail Glass model parameters

Parameter	Symbol	Effect on liquefaction resistance	Effect on post-liquefaction shear strain
Effective stress bulk modulus reduction	r_K	Increased r_K decreased liquefaction resistance and increased excess pore pressure	
Friction angle	ϕ'	Increased ϕ' increased liquefaction resistance	
Residual friction angle ratio	r_{tmp}		
Steady-state undrained shear strength	s_{us}		
Coefficient of dilation	r_{ε_d}	Increased r_{ε_d} decreased liquefaction resistance	
Coefficient of contraction	$r_{\varepsilon_d^c}$	Increased $r_{\varepsilon_d^c}$ decreased liquefaction resistance	
Phase transformation angle	ϕ_p	Increased ϕ_p decreased liquefaction resistance	
Low pore pressure ratio curve fitting parameter	q_1	Increased q_1 increased rate of pore pressure generation	Increased q_1 increased post-liquefaction shear strain
High pore pressure ratio curve fitting parameter	q_2	Increased q_2 increased liquefaction resistance	Increased q_2 decreased post-liquefaction shear strain
Elastic shear strain coefficient	c_1	Increased c_1 decreased liquefaction resistance at a large number of cycles	Increased c_1 increased post-liquefaction shear strain
Maximum hysteretic damping	H_{max}		Increased H_{max} increased the width of the stress-strain hysteresis
Maximum contractive volumetric strain	ε_d^{cm}		Decreased ε_d^{cm} decreased the limiting shear strain, but only at small values of ε_d^{cm}

The Cocktail Glass constitutive model was designed to consider softening due to pore pressure generation, stiffening due to dilation and pore pressure reduction, and stiffness

degradation that occurred after repeated cycles of loading. Nonliquefiable soils, such as clay or moderate and higher plasticity silts, could also be modeled using the Cocktail Glass model by placing a lower-bound limit on the stress state, s_0, so that liquefaction could not occur. Figure 7.3 shows example stress and strain behavior of a simulated cyclic simple shear test was modeled as either (a) a soil that was susceptible to liquefaction or (b) a soil that was not susceptible to liquefaction. Both samples had the same initial stiffness and monotonic shear strength, but the liquefiable soil in simulation (a) generated pore pressure and liquefied after several cycles of loading, while the nonliquefiable soil in simulation (b) generated pore pressure, softened, and exhibited cyclic mobility, but did not liquefy. Note that the strain scales on the two plots are different, and the liquefied soil developed much larger shear strains than the nonliquefiable soil.

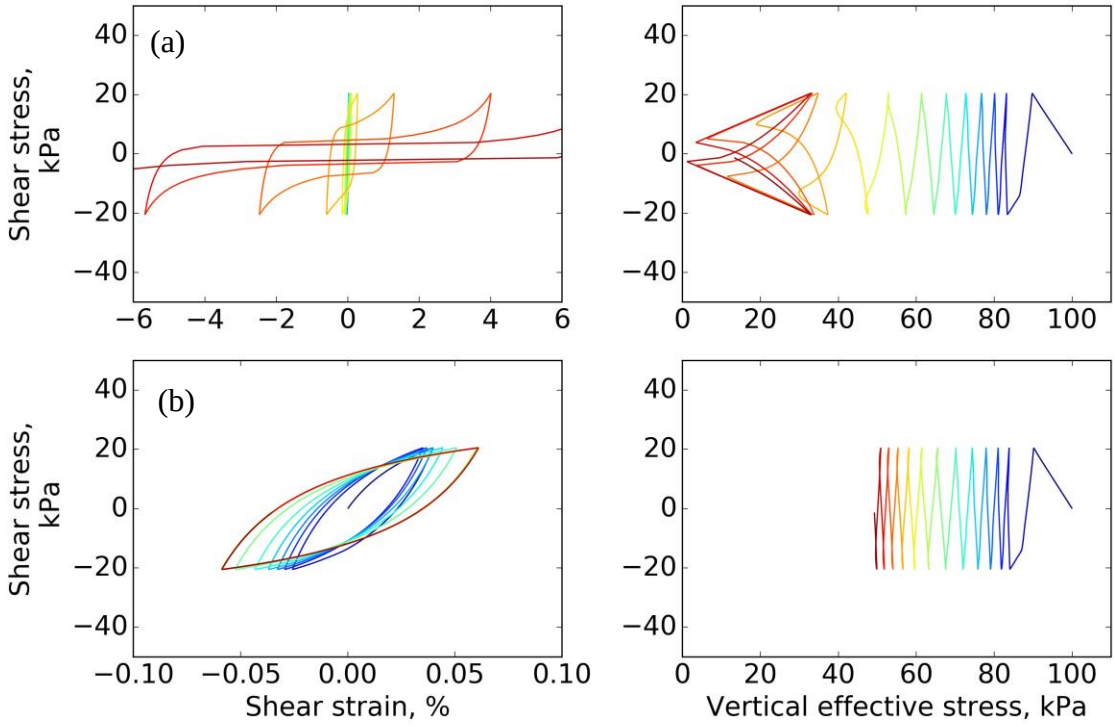

Figure 6.3: Example stress-strain and stress path from Cocktail Glass model. A layer of soil in the same profile modeled two different ways: (a) soil was susceptible to liquefaction modeled using the Cocktail Glass model and (b) a soil that was not susceptible to liquefaction. Note that the strain scales on the two plots are different.

This example showed that both liquefied and non-liquefied soils could be modeled in FLIP using the Cocktail Glass model. Individual properties, such as shear strength, shear stiffness, the monotonic rate of contraction or dilation, and the damping ratio can be adjusted as necessary for

modeling. Alternatively, nonliquefiable soils can also be modeled using the well-documented Multi-Spring model (Iai et al. 1992) in FLIP.

The pore pressure within individual layers of soil may be affected by the redistribution of excess pore pressure from adjacent layers of soil, particularly in thick, variably dense, liquefiable soil deposits. During shaking, pore water tends to flow from layers with high total head into layers with low total head. The redistribution of pore pressure changes the effective stress within each layer of soil, and during long duration shaking, redistribution of pore pressure could affect the soil stiffness, site response, and ground surface deformation. In a deposit of uniform relative density, excess pore pressure generated during shaking tends to migrate from the bottom of the deposit towards the top of the deposit due to differences in the total head. However, the relative density and hydraulic conductivity typically vary within a deposit. The redistribution of pore pressure can be considered in FLIP by solving the pore pressure diffusion equation simultaneously with the equations of motion. Including the pore pressure diffusion equations increases the computational complexity of the analysis, but only requires estimating the hydraulic conductivity in each layer of soil.

A typical site in Seattle was modeled with two different values of hydraulic conductivity to show the effects of drainage with respect to pore pressure and the frequency content of the ground surface motion. The typical site consisted of 1.5 m of dense gravel fill underlain by 2 m of liquefiable sand, followed by dense till. The water table at the site was 1.5 m deep. The hydraulic conductivity of the liquefiable sand was assumed to be within a range of $1x10^{-5}$ and $1x10^{-6}$ m/s. This range corresponded to typical values for clean, fine to medium sand. Parametric FLIP analyses were performed with values of hydraulic conductivity within this range, and the EW component of the Constitucion record from the Maule earthquake was applied to the base of the profile. The variations of pore pressure ratio versus depth and time from the two parametric models are shown in Figure 6.4. FLIP captured changes in soil behavior that occurred due to pore pressure dissipation, and the models with different values of hydraulic conductivity responded very differently. Liquefaction occurred in both models at about 20 seconds. However, the ground surface acceleration of the model with the higher hydraulic conductivity contained much more high-frequency content after pore pressure dissipated later in the motion. In addition to dissipating much faster, the excess pore pressure in the model with high hydraulic conductivity tended to

migrate towards the ground surface at a faster rate than the excess pore pressure in the model with low hydraulic conductivity.

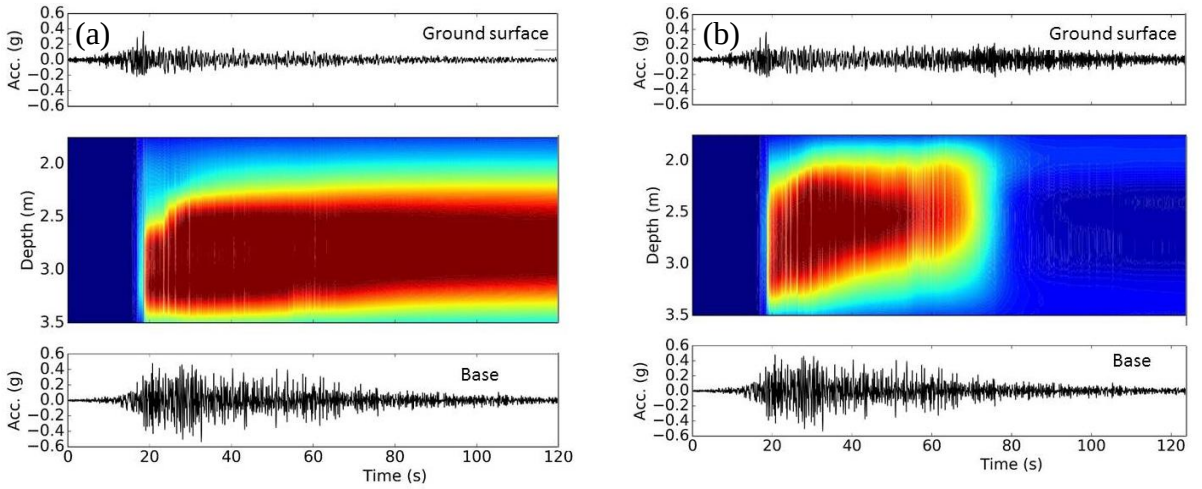

Figure 6.4: Effect of hydraulic conductivity on post-triggering behavior in Cocktail Glass model. Hydraulic conductivity of the soil was equal to (a) $1x10^{-6}$ m/s and (b) $1x10^{-5}$ m/s

The drainage and pore pressure redistribution analyses were also compared to the analytical solution presented in Chapter 4. Pore pressure dissipation in the analytical solution was based on the coefficient of consolidation in the vertical direction, c_v. To correspond with the hydraulic conductivities in Figure 6.5, c_v was calculated to be about $3x10^{-3}$ m^2/s and $1x10^{-2}$ m^2/s.

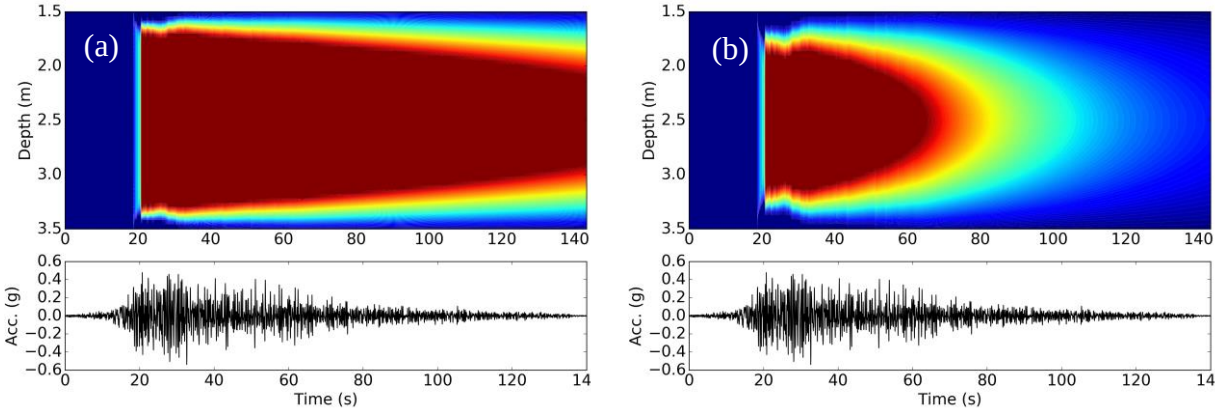

Figure 6.5: Effect of hydraulic conductivity on post-triggering behavior in analytical solution. Coefficient of vertical drainage was equal to (a) $3x10^{-3}$ m^2/s and (b) $1x10^{-2}$ m^2/s.

The analysis of pore pressure redistribution and dissipation in FLIP reflects the trends of the pore pressure dissipation in the analytical solution. Both results show that, over a relatively

narrow range of hydraulic conductivity or c_v, the excess pore pressure could dissipate from the layer of liquefied soil or could remain relatively high after the end of shaking, depending on the hydraulic conductivity. The value of excess pore pressure could have significant implications for site response or deformation behavior, particularly for long duration motions.

To show how much the dissipation of pore water during shaking can impact the site response behavior, the FLIP analyses were performed for the typical Seattle site with values of hydraulic conductivity ranging from $1x10^{-3}$ and $1x10^{-8}$ m/s in the liquefiable sand. The low end of this range corresponded to well-drained, clean, coarse sand, and the high end corresponded to poorly draining silty sand. The EW component of the Constitucion record from the Maule earthquake was again applied to the base of the profile. The variation of spectral acceleration from the analyses between these models is shown in Figure 6.6. The variability of the hydraulic conductivity affected the spectral acceleration at the ground surface significantly, and the profiles that were well-drained ($1x10^{-3}$ to $1x10^{-4}$ m/s) did not liquefy and exhibited very strong dilation pulses, resulting in high spectral acceleration across a range of periods.

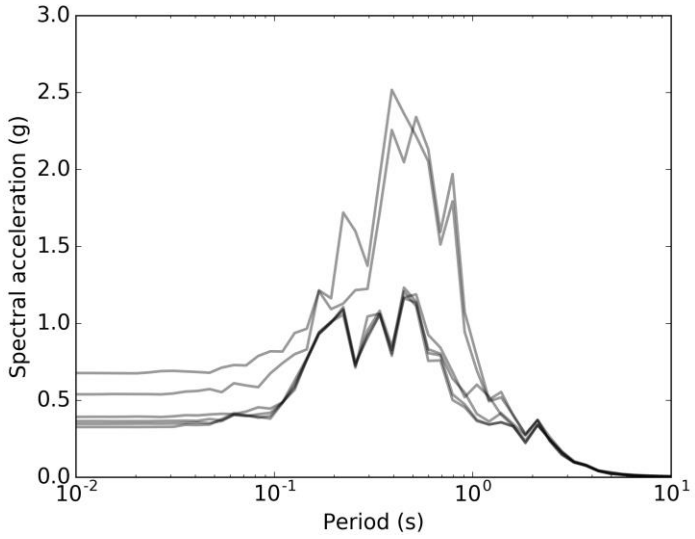

Figure 6.6: Effect of hydraulic conductivity on spectral acceleration. Coefficient of vertical drainage ranged from $1x10^{-3}$ m/s to $1x10^{-8}$ m/s.

Likewise, the dissipation of pore water can affect the lateral spreading deformation of gently sloping sites. The typical Seattle profile with 2 m of liquefiable sand was analyzed with a gently sloping ground surface grade of 2%. The post-triggering lateral spreading deformation

depended on the shear stiffness of the soil, which was very sensitive to excess pore pressure and effective stress. The variation of lateral deformation from the analyses is shown in Figure 6.7.

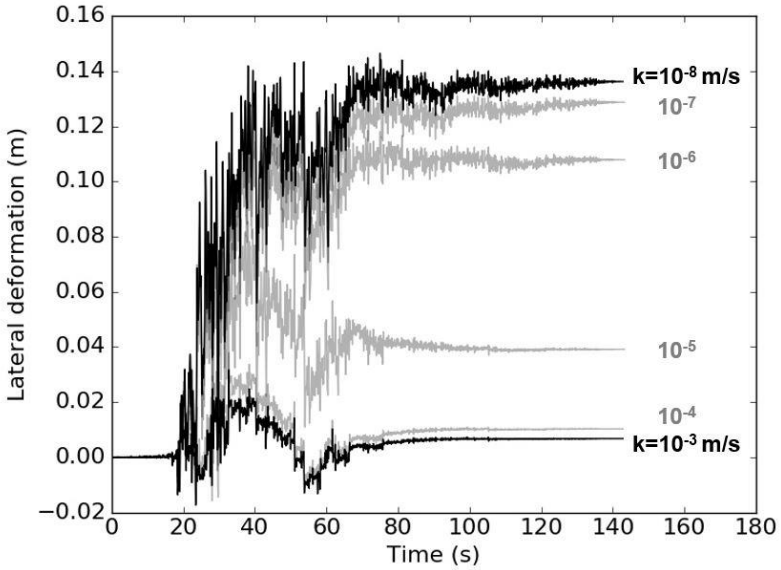

Figure 6.7: Effect of hydraulic conductivity on lateral spreading deformation. Coefficient of vertical drainage ranged from $1x10^{-3}$ m/s to $1x10^{-8}$ m/s.

6.3 CALIBRATION

The Cocktail Glass model has all of the desirable features of a liquefaction soil model that were described in Section 6.1. The model can be calibrated to semi-empirical or laboratory-based observations for pore pressure generation, liquefaction triggering, overburden correction, and shear strain development. Table 6.2 lists the material behaviors that should be captured by a properly calibrated constitutive model for liquefaction.

Table 6.2: Material behavior for a calibrated constitutive model

▪ Pore pressure should be generated at a rate that is consistent with laboratory observations (DeAlba et al., 1976)
▪ Liquefaction should trigger after an appropriate cyclic stress ratio and number of cycles of loading (Boulanger and Idriss, 2014)
▪ Shear strains should increase under constant amplitude cyclic loading at a rate consistent with laboratory observations (Ishihara and Yoshimine, 1992)
▪ Liquefaction should trigger at an appropriate cyclic stress ratio at different overburden pressures (Boulanger and Idriss, 2014)

Details for each of the behaviors were described in Chapter 2. The references in Table 6.2 can be used to describe the material behavior for pore pressure generation, liquefaction triggering, overburden correction, and shear strain as a function of the intensity of shaking and soil properties that can be determined from typical geotechnical investigations. Commonly recorded properties from field investigations include the soil's SPT penetration resistance, CPT penetration resistance, and shear wave velocity. These properties can be related to the soil's relative density, D_r. Empirical correlations for the relative density of clean sand have been developed for normalized SPT $(N_1)_{60}$ values and CPT q_{c1N} values (Idriss and Boulanger 2008).

$$D_r = \sqrt{\frac{(N_1)_{60}}{46}} \tag{6.15}$$

$$D_r = 0.478\,(q_{c1N})^{0.264} - 1.063 \tag{6.16}$$

Equations (6.15) and (6.16) can be used to convert CPT tip resistance values into equivalent SPT penetration resistance values and vice versa. Likewise, shear wave velocity can be converted into equivalent SPT penetration resistance (Wair et al., 2012), which can then be converted into $(N_1)_{60}$ or relative density.

$$v_s = 30\,N_{60}\,(\sigma_v')^{0.25} \tag{6.17}$$

Pore pressure generation and the behavior of liquefied soil were modeled in FLIP using effective stress analysis, and a brief description of the parameters necessary to control the complicated interaction between stresses and strains was provided in Table 6.1. The Cocktail glass

model's volumetric strain parameters were developed from a soil model with 14 different parameters that controlled the strain behavior of the soil. A wide range of soil behavior was possible depending on the values selected for these parameters. For practical use, the parameters in the Cocktail Glass model should be calibrated to match well-established behavior that has been observed during field or laboratory testing. Calibration for this behavior should be based on properties that are typically recorded or can be estimated during typical geotechnical investigations. These properties include the soil's density, ρ, shear wave velocity, v_s, penetration resistance $(N_1)_{60}$ values, friction angle, ϕ, and hydraulic conductivity, k.

The values of the Cocktail Glass model were calibrated to match the observed behavior listed in Table 6.2. For specific values of $(N_1)_{60}$, these target functions were used to calculate values of pore pressure, the number of cycles necessary to trigger liquefaction, an overburden correction factor, and the post-liquefaction shear strain amplitude for a range of cyclic stress ratios and number of cycles of loading. These tests were then simulated in FLIP, and the results from FLIP were compared to the target functions. Residuals from each target function were calculated, and a normalized objective function, L, was developed to quantify the goodness-of-fit between the FLIP simulations and the target functions. Equation (6.18) shows the form of the objective function for an arbitrary target.

$$L = \sum_i \left(\frac{y_i - \hat{y}_i}{\hat{\sigma}/w} \right)^2 \tag{6.18}$$

where y_i is the resulting value from FLIP, $\hat{y}_i$ is the target function based on empirical observations, $\hat{\sigma}$ is the standard deviation of $\hat{y}$, and w is the parameter weight. Weight values were assigned to each target function based on the goodness-of-fit following several iterations, the sensitivity of the analyses to the weight values, and engineering judgement. Table 6.3 shows the weight used in equation (6.18) for the optimization analysis.

Table 6.3: Variables used in the Cocktail Glass model calibration

Variable	Symbol	Weight, w
Excess pore pressure ratio	r_u	2
Number of cycles to trigger liquefaction	n	4
Overburden stress correction	K_σ	2
Shear strain amplitude	γ	1

The residuals from each target function were standardized and weighted so that functions of pore pressure, liquefaction triggering, and post-liquefaction shear strain could be combined in a single objective function. Adding each standardized and weighted residual resulted in a general objective function in equation (6.19).

$$L = \sum_i \left(\frac{r_{u_i} - \widehat{r_{u_i}}}{\hat{\sigma}_{r_u}/w_{r_u}} \right)^2 + \sum_i \left(\frac{\ln n_i - \ln \hat{n}_i}{\hat{\sigma}_n/w_n} \right)^2 + \sum_i \left(\frac{\mathrm{K}_{\sigma i} - \widehat{\mathrm{K}}_{\sigma i}}{\hat{\sigma}_{\mathrm{K}_\sigma}/w_{\mathrm{K}_\sigma}} \right)^2 + \sum_i \left(\frac{\ln \gamma_i - \ln \hat{\gamma}_i}{\hat{\sigma}_\gamma/w_\gamma} \right)^2 \tag{6.19}$$

where r_u is the excess pore pressure, n is the number of cycles of loading to trigger liquefaction, K_σ is the overburden correction factor, and γ is the shear strain. This scaler objective function could then be minimized with consideration for four different target variables. Tests were simulated for three different relative densities corresponding to $(\mathrm{N}_1)_{60}$ values of 5, 15, and 25, five different cyclic stress ratios corresponding to liquefaction triggering after 3, 7, 15, 25, and 50 cycles of loading, and initial overburden stresses of 25, 50, 100, 200, and 400 kPa. The friction angle and shear wave velocity of the soil layers was estimated using well-documented correlations (Allen, 2015; Holtz et al., 2011; Wair et al., 2012) with the $(\mathrm{N}_1)_{60}$ values. The maximum contractive shear strain, ε_d^{cm}, was set based on values from the recommendation provided by Yoshimine et al. (2006). The objective function in equation (6.19) was minimized using the SciPy package in Python 2.7 with 14 variables from Table 6.1.

Figure 6.8 shows the final calibrated model results for $(\mathrm{N}_1)_{60}$ values of 5, 15, and 25. The solid lines in Figure 6.8 represent the target functions, and the data points represent the simulation results. Figure 6.8(a) shows the range of estimated pore pressure ratios (DeAlba et al., 1976) for typical soils with α ranging from 0.3 to 1.0. Figure 6.8(b) shows the number of cycles required to trigger liquefaction for different cyclic stress ratios (Boulanger and Idriss, 2014). Figure 6.8(c) shows the overburden stress correction factor (Boulanger and Idriss, 2014) for different initial overburden stresses. Figure 6.8(d) shows the accumulation of shear strain amplitude for soils that were expected to liquefy after 15 cycles of loading. The parameters that minimized the objective function are summarized in Table 6.4.

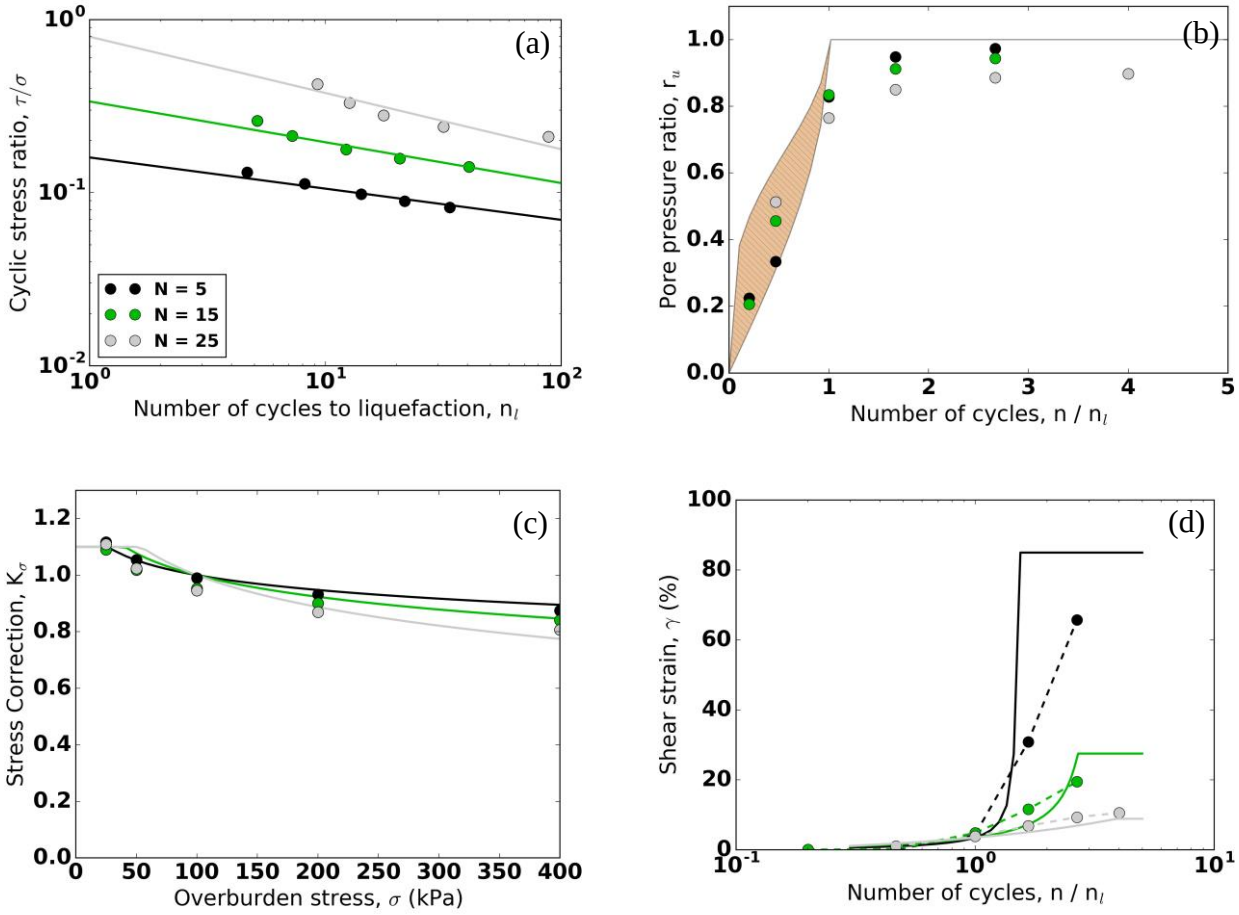

Figure 6.8: Calibration results for Cocktail Glass model. (a) Liquefaction triggering, (b) Pore pressure generation, (c) Overburden stress correction, (d) Shear strain amplitude.

Table 6.4: Cocktail Glass model calibration

		Penetration resistance, $(N_1)_{60}$		
Parameter	**Symbol**	**5**	**15**	**25**
Shear modulus exponent	m	0.11	0.15	0.24
Bulk modulus exponent	n	0.54	0.47	0.43
Reference stress (kPa)	p_0	240	90	30
Poisson's ratio	ν	0.3	0.3	0.3
Effective stress bulk modulus reduction	r_K	0.94	0.65	0.47
Coefficient of dilation	r_{ε_d}	0.54	0.34	0.20

Table 6.4: Cocktail Glass model calibration

		Penetration resistance, $(N_1)_{60}$		
Parameter	**Symbol**	**5**	**15**	**25**
Coefficient of contraction	$r_{\varepsilon_d^c}$	1.68	0.77	0.29
Phase transformation angle	ϕ_p	29.0	35.1	38.6
Low pore pressure ratio curve fitting parameter	q_1	6.79	3.09	2.65
High pore pressure ratio curve fitting parameter	q_2	1.21	1.13	0.89
Reference strain curve fitting parameter	q_4	1.0	1.06	1.19
Elastic shear strain coefficient	c_1	1.46	2.21	3.82
Maximum contractive volumetric strain	ε_d^{cm}	0.060	0.028	0.010
Residual friction angle ratio	r_γ	0.10	0.14	0.23

These parameters were calculated using a routine to minimize the objective function in Equation (6.19), which captured the pore pressure generation, liquefaction triggering, overburden correction, and post-liquefaction shear strain behavior. Most of the desired behavior in a liquefaction model was captured using these functions, although the hysteresis, contraction and dilation, and degradation behavior were not explicitly considered. No empirically or laboratory-based expressions relating these trends have been developed, so these trends could not be explicitly considered in the minimization analysis. However, the stress-strain curves and stress paths in FLIP should qualitatively reflect aspects of these trends. Figure 6.9 shows stress-strain and stress paths for $(N_1)_{60}$ values of 5, 15, and 25 with cyclic stress ratios that were expected to trigger liquefaction after 15 cycles. The tests were simulated until the absolute values of shear strain exceeded 6%.

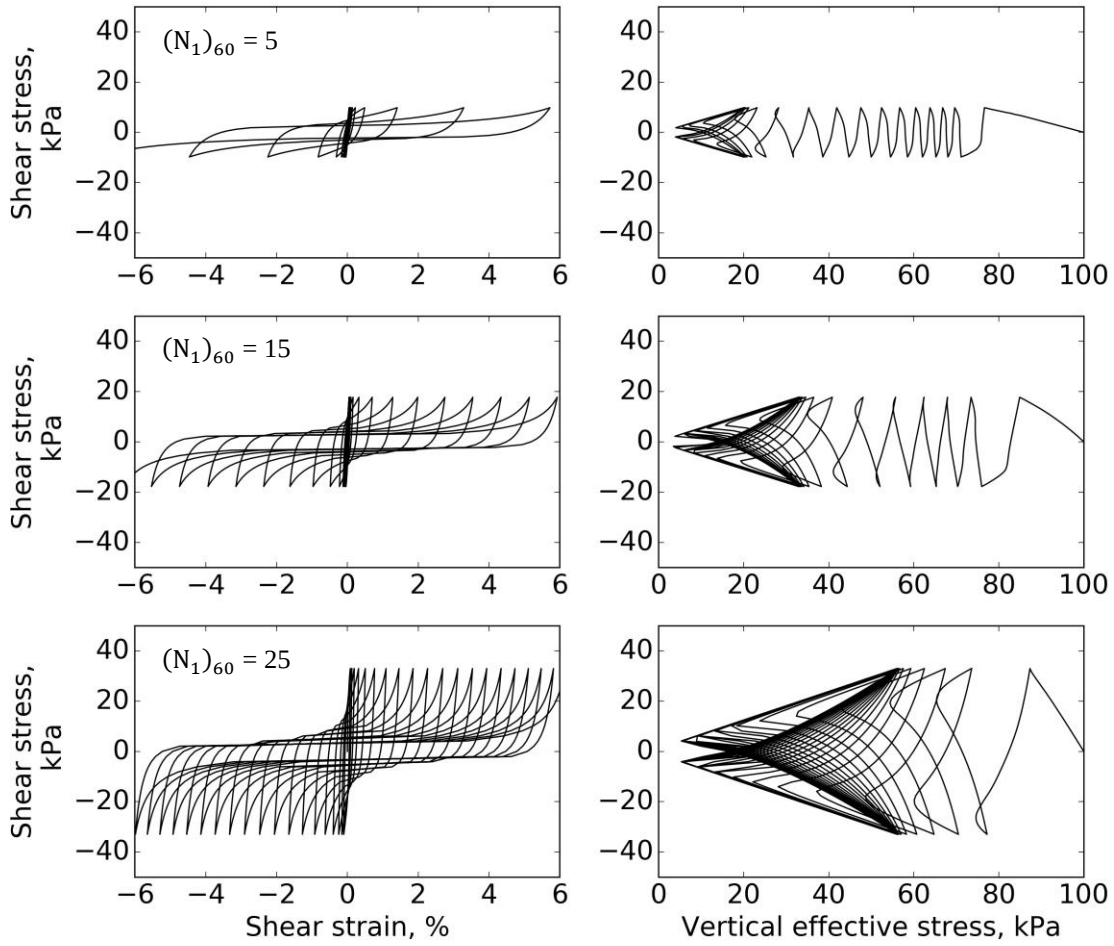

Figure 6.9: Stress-strain and stress paths from calibrated Cocktail Glass model

In addition to matching the explicitly described targets for pore pressure generation, liquefaction triggering, overburden correction, and post-liquefaction shear strain, the stress-strain and stress paths shown in Figure 6.9 generally reflected the desired behavior in a liquefaction model. These figures show that the soil exhibited a hysteretic response under cyclic loading and that the stiffness depended on the direction of loading. As the soil went through cycles of dilation and contraction in the simulations, the effective confining pressure changed and the stiffness of the soil also changed. The simulations show that excess pore pressure initially developed rapidly during the first few cycles of loading, but then the rate of excess pore pressure generation slowed down. As the soil crossed the phase transformation line, the rate of contraction and excess pore pressure generation increased until the soil liquefied and the stress path converged. After the soil liquefied, additional cycles of loading caused the soil to dilate and contract, forming "banana-like"

hysteresis loops. Denser ($(N_1)_{60}$ = 25) soils exhibited stronger dilation than looser ($(N_1)_{60}$ = 5) soils. As additional cycles of loading occurred after liquefaction, additional shear strain continued to accumulate, and looser soils developed more shear strain than denser soils.

Comparison with laboratory tests

The calibration of the Cocktail Glass model was designed to represent the behavior of "typical" sands. The values of the model parameters were based on conditions that could be collected during a typical subsurface investigation, and the values of the parameters listed in Table 6.4 have all been calibrated as a function of $(N_1)_{60}$. However, when laboratory tests are available, the behavior observed in these tests can provide additional insight into the pore pressure generation, liquefaction triggering, and post-trigger behavior of soils. The relative density of samples prepared in the laboratory provides a measure of the liquefaction resistance of the soil, but other effects such as preparation methods, the rate of transient loading, and the type of test all affect the soil's liquefaction resistance. The Cocktail Glass model has been calibrated so that it is flexible and the properties listed in Table 6.4 can be adjusted very simply when laboratory tests are available. In this section, the "typical" properties based on semi-empirical observations are shown to provide a good reference point for the parameters that control volumetric strain in the model, even when laboratory tests are available.

Over 100 cyclic direct simple shear (CSS) tests were performed (Kwan et al., 2014) with transient shear stress histories. During transient loading, individual cycles of loading may affect the response of the soil differently. In addition to relative density, the excess pore pressure, past strain history, and direction of loading all affect the soil behavior. These transient load tests are very useful for evaluating the effectiveness of numerical models that capture these effects. Many of these CSS tests were performed with modulated sine waves, where the frequency of the wave remained constant while the amplitude of the wave varied with time. Several of these modulated sine wave CSS tests were simulated in FLIP by applying the boundary conditions of a direct simple shear test and subjecting the soil to the transient shear stresses. In the FLIP model, the relative density and friction angles were adjusted until a good match with the laboratory tests was observed, indicating that the calibration results are applicable beyond just the "typical" values based on empirical observations. Figures 6.10 through 6.12 show three comparisons of CSS test results

with the FLIP simulations. The penetration resistance and friction angle that was selected for each test are shown on each of the figures.

The first simulation, in Figure 6.10, shows the stress path and stress-strain curve for a medium dense sand that was subject to a constant amplitude harmonic load. FLIP captured the pore pressure generation, number of cycles necessary to trigger liquefaction, and the large shear strains that developed after liquefaction was triggered. The second simulation, in Figure 6.11, shows the results for a medium dense soil where the amplitude of the shear stress was not constant for the duration of the test, but rather decreased towards the end of the test. FLIP again captured the number of cycles necessary to trigger liquefaction and the shear strain amplitude that continued to increase after the soil liquefied, even though the shear stress amplitude decreased. This result shows that FLIP accurately captures the degradation of soil fabric, not just the triggering of liquefaction. The third simulation, in Figure 6.12, shows the results for a dense sand where the amplitude of the shear stress was modulated up, then down, then up again. The Cocktail Glass model captured the rate of pore pressure generation, the number of cycles necessary to trigger liquefaction, and the shear strain after liquefaction very well in this test, even though the loading history was very complicated. The results of these tests further indicate that the Cocktail Glass model is suitable to simulate the behavior of liquefiable soils during transient shear stress loading and that the method which the model was calibrated is flexible and can be adapted to many different soil conditions.

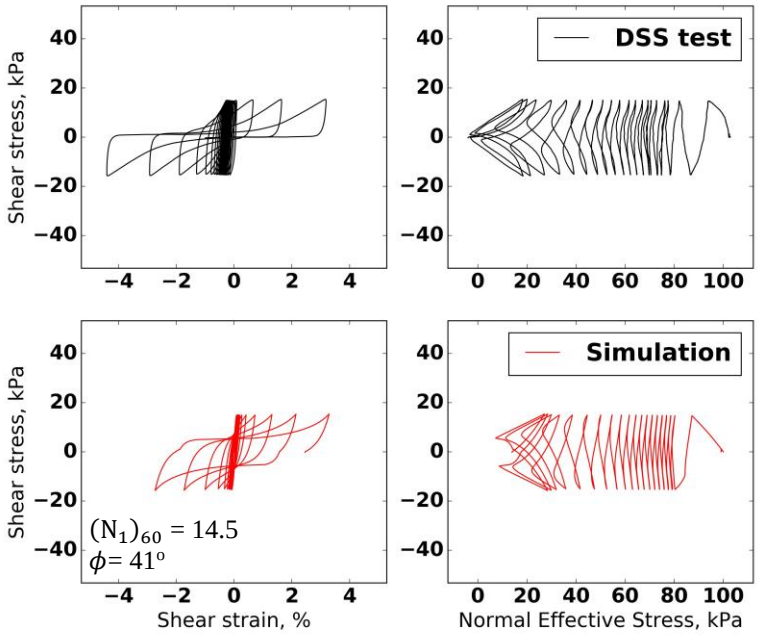

Figure 6.10: Simulation of test 2013-0524_CSS_NV_Modulated-Baseline_CSR=0.15_ru=1.00_Dr=55. Data from Kwan et al. (2014).

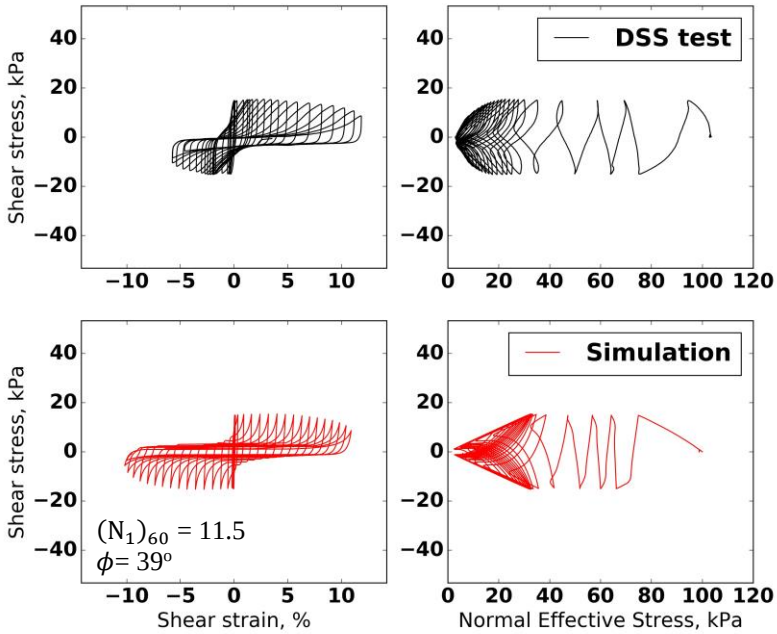

Figure 6.11: Simulation of test 2013-0716_CSS_NV_Modulated-down0.2_CSR=0.15_ru=0.97_Dr=39. Data from Kwan et al. (2014).

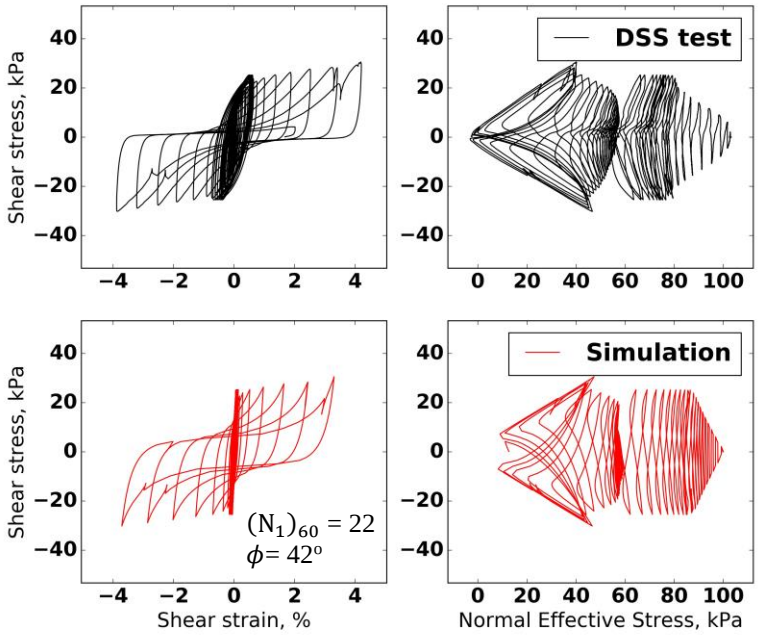

Figure 6.12: Simulation of test 2013-0805_CSS_ NV_Modulated-up0.25_CSR=0.25_ru=0.48_0.2HzTaperUp_ Dr=77. Data from Kwan et al. (2014).

6.4 SUMMARY

The complicated interaction between volumetric and shear strain in soils can only be realistically evaluated using numerical methods. The nonlinear, effective stress Cocktail Glass model (Iai et al., 2011), which was designed to account for phase transformation behavior and the large shear strains that can develop in liquefied soils. The Cocktail Glass model can capture the complicated shear and volumetric strain coupling that is necessary to evaluate the behavior of liquefied soils. The model was calibrated to empirical and semi-empirically observed rates of pore pressure generation, liquefaction triggering, and shear strain development. The calibrated model then predicted these same behaviors that were observed in laboratory tests.

[This page intentionally left blank]

Chapter 7. CHARACTERIZATION OF JAPANESE LIQUEFACTION CASE HISTORIES

Liquefaction triggering and effects analyses require complete and accurate characterization of subsurface conditions. Observations of liquefaction near strong motion recorders are especially valuable for developing liquefaction models because the uncertainty in the seismic loading is low and intensity measures can be directly calculated. The strong motion recording network in Japan is very dense, and many observations of liquefaction near strong motion stations following earthquakes are now available (Iai et al., 1995; Ganev et al., 1998; Sato et al., 1998; Kinoshita, 2008; Cox et al., 2013). Unfortunately, many of these stations have limited, incomplete, or no subsurface information. Additional investigation at key sites could improve the liquefaction case history database and provide observations for unique or infrequently observed conditions, such as sites subjected to many cycles of loading, sites where liquefaction may have occurred at relatively large depths, and sites where dense soils liquefied.

From the available literature, 21 sites where liquefaction appears to have occurred beneath strong motion recording instruments were identified as potential candidates for additional subsurface investigation. The sites were evaluated and ranked for based on several criteria that reflected their unique value to the liquefaction case history database. Specifically, additional investigation at sites where liquefaction was observed in relatively dense soils, occurred relatively deep, or where long-duration ground motions triggered liquefaction would provide important contributions to the liquefaction case history database. Case histories where the time of liquefaction could be clearly identified from the recorded ground motion also provide important contributions to the database. Sites with recordings from downhole as well as surface instruments would be particularly valuable for their potential to improve understanding of the material behavior of liquefied soil. Table 7.1 shows the list of considerations that were used as ranking criteria for selecting sites for additional investigation.

Table 7.1: Consideration for site investigations

- Confidence in time of liquefaction, t_L – higher confidence is preferred
- Number of cycles at t_L – large number of cycles preferable for long duration study
- Minimum $(N_1)_{60cs}$ – dense soils are underrepresented in the case history database and are preferred
- Fines content – information on soils with a high fines content and the plasticity of the fines are important considerations
- Depth of critical layer – deep is preferable to shallow
- Undrained conditions – drainage during shaking may affect behavior
- Depth of downhole instrument (if any)

From the 21 identified sites, seven were identified as potentially providing unique value to the liquefaction case history database. Table 8.2 shows a list of the preferred sites for possible investigation. Three sites, IBR014, MYG013, and MYG010, showed exceptional promise for additional investigation. All three sites showed evidence of liquefaction during the Tohoku earthquake. IBR014 was considered uniquely valuable since liquefaction appeared to have occurred at relatively large depths. MYG010 was considered attractive since dense sand appeared to have liquefied, and MYG013 was considered valuable since a well-confined layer of medium dense gravel appeared to have liquefied. All three sites were owned and maintained by the Kyoshin strong motion network (K-net). Permission was requested and granted to investigate these three sites, and the investigations were performed in the fall of 2015.

Table 7.2: Preferred sites for possible investigation

Station	Earthquake	Primary Reconnaissance Source	Station Owner
IBR014	Tohoku	Cox et al. 2013	K-net
HKD086	Tokachi-Oki	Kinoshita 2008	K-net
PARI: amagasaki-g	Kobe	Sato et al. 1998	PARI
Higashi-Kobe Bridge	Kobe	Ganev et al. 1998	Hanshin Expressway Corporation
MYG013	Tohoku	Cox et al. 2013	K-net
PARI: kushiro	Kushiro-Oki	Iai et al. 1995	PARI
MYG010	Tohoku	Cox et al. 2013	K-net

7.1 TOHOKU EARTHQUAKE

The M9.0 Tohoku earthquake occurred on March 11, 2011 on the subduction zone off the eastern shore of Honshu, Japan. The shaking along much of the coast was very strong, and the most intense shaking occurred in Fukushima and Miyagi prefectures. Recorded peak ground acceleration (PGA) exceeded 1.0 g (981 cm/s^2) at many locations, and shaking near Sendai in Miyagi prefecture was exceptionally strong, with recorded PGA values exceeding 2.0 g at some locations. Figure 7.1 shows contours of peak acceleration from the Tohoku earthquake on Honshu.

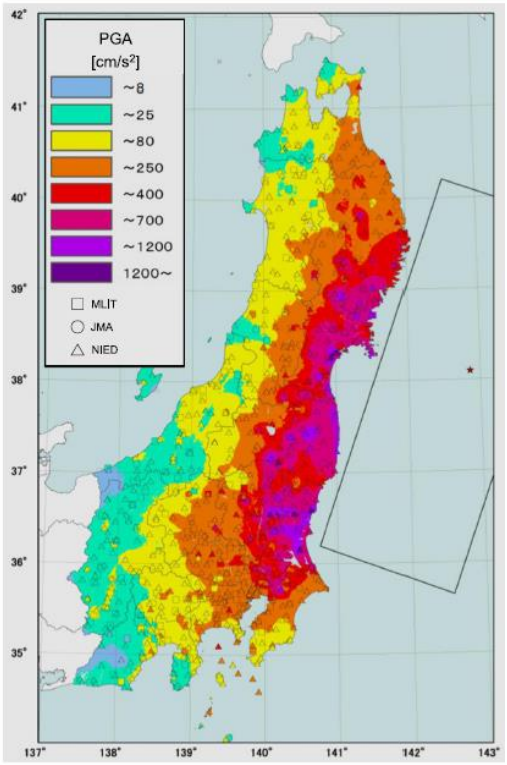

Figure 7.1: Peak ground acceleration during the 2011 Tohoku earthquake (from Unjoh et al., 2012)

Large magnitude subduction zone events like the Tohoku earthquake tend to produce very long duration ground motions. The fault rupture of the Tohoku earthquake included multiple subevents that each released bursts of energy and the arrival of high-frequency, high-amplitude acceleration waves from the subevents were separated in some areas by over 100 seconds. Figure 3.2 showed time histories from the Tohoku earthquake at many recording stations along the coast of Honshu. Ground motions from at least three subevent ruptures can easily be seen in the figure where high frequency, high amplitude acceleration waves arrived at several sites within a region at similar times.

Severe liquefaction occurred at many locations on the eastern side of Honshu after the Tohoku earthquake. In a tragic sequence, much of the evidence of liquefaction along the coast in Fukushima and Miyagi prefectures was obscured by the tsunami that devastated much of the area. Coastal areas that were inundated by the tsunami later showed widespread evidence of liquefaction during subsequent aftershocks, in particular, during the $M_w = 7.1$ aftershock that occurred on April 7, 2011. Liquefaction was observed inland from the area of tsunami inundation during the main

shock and subsequent aftershocks. Hata et al. (2013) indicated that liquefaction was observed at distances of up to 192 km from the fault rupture.

The shaking was generally less intense near Tokyo than in Fukushima and Miyagi prefectures, but widespread liquefaction was observed near Tokyo in areas constructed on man-made fill, such as Urayasu City and Chiba. Very little liquefaction was observed in the vicinity of Tsuchiura, which is located inland and to the north of Tokyo, where the surficial soils were predominately composed of clay soils.

Recorded ground motions

Japan had a dense array of recording stations in place at the time of the Tohoku earthquake. Over 1,000 ground surface recording stations were spaced about every 20 km as part of the Kyoshin strong motion network (K-net). An additional 700 surface and downhole recording arrays were established as part of the Kiban Kyoshin strong motion network (KiK-net). Recording stations from both K-net and KiK-net have been operational since 1996.

This study was aimed at gathering data from sites where liquefaction occurred near strong motion recording instruments. Because these recorded ground motions were affected by liquefied soils, they could not be directly used for liquefaction analysis. Instead, the spectral acceleration, S_a, if liquefaction did not occur was estimated using Ground Motion Prediction Equations (GMPEs). GMPEs have been developed to estimate ground motions with consideration for source, path, and site effects. The BCHydro GMPE has a general form that accounts for source, path, and site effects.

$$\ln S_{a,GMPE} = f(M,R) + f_{site}(M,R,v_{s30}) \tag{7.1}$$

where $S_{a,GMPE}$ is the geometric average of the 2-component spectral acceleration. The term for source and path effects, $f(M,R)$, in the GMPE was based on the earthquake magnitude, M, and distance to the fault rupture, R. The term for site amplification or deamplification effects, f_{site}, was based on the average shear wave velocity in the upper 30 m of the site, v_{s30}.

The BCHydro GMPE was used to estimate $S_{a,GMPE}$ using records from many earthquakes. The GMPE can be adjusted to provide more accurate estimates of S_a for a specific earthquake in the data set by applying an event term, f_{event}.

$$\ln S_{a,event} = \ln S_{a,\mathrm{GMPE}} + f_{event} \tag{7.2}$$

Abrahamson et al. (2015) calculated event terms for the Tohoku earthquake, which are shown in Figure 7.2 for periods ranging from 0.01 to 10 s. Tabulated values of the Tohoku event terms are shown in Table 7.3.

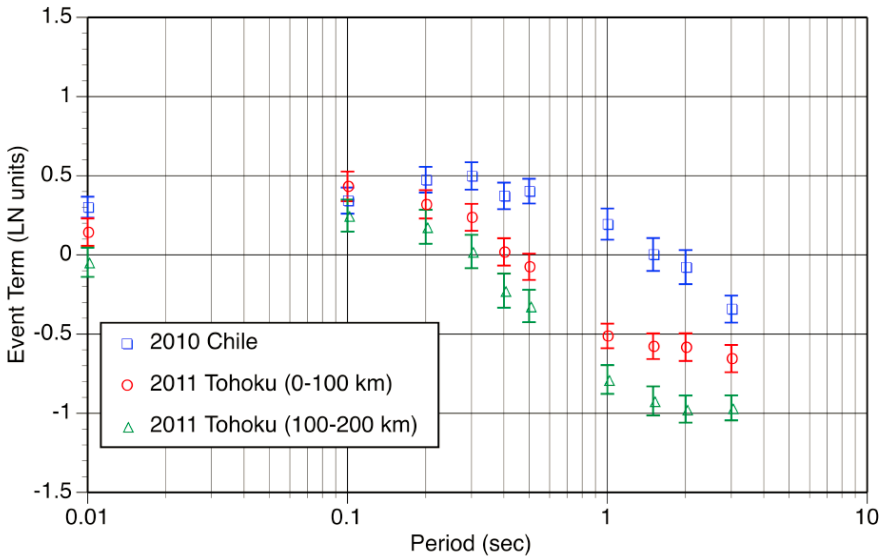

Figure 7.2: BCHydro GMPE event terms (from Abrahamson et al., 2015)

Table 7.3: Recommended event term for the BCHydro GMPE for the 2011 Tohoku earthquake

Period, T (s)	Event Term
0.01	0.14
0.1	0.43
0.2	0.31
0.3	0.23
0.4	0.02
0.5	-0.08
1.0	-0.51
1.5	-0.58
2.0	-0.59
3.0	-0.66

The event term indicated that the Tohoku earthquake generally produced larger values of S_a at short periods than the median recorded data from the earthquakes used to develop the GMPE.

However, at longer periods, the S_a values from the Tohoku earthquake were generally less than the GMPE median values. The event term for the Tohoku earthquake was applied to the BCHydro GMPE using equation (7.2) to provide more accurate estimates of the ground motions for the Tohoku earthquake.

Individual ground motions recorded during the Tohoku earthquake may have deviated from $S_{a,event}$ due to factors that were not included in the source, path, site, or event terms in the BCHydro GMPE. Figure 7.3 illustrates the difference between an example motion recorded during the Tohoku earthquake, the GMPE median estimated spectral acceleration, $S_{a,GMPE}$, and the GMPE-estimated spectral acceleration adjusted for the Tohoku earthquake, $S_{a,event}$. The BCHydro GMPE was developed using the geometric mean of the spectral acceleration calculated from 2-component ground motions, and so the spectral acceleration for each horizontal component of motion was calculated, and then the geometric mean of these components was compared to the event-adjusted GMPE estimate.

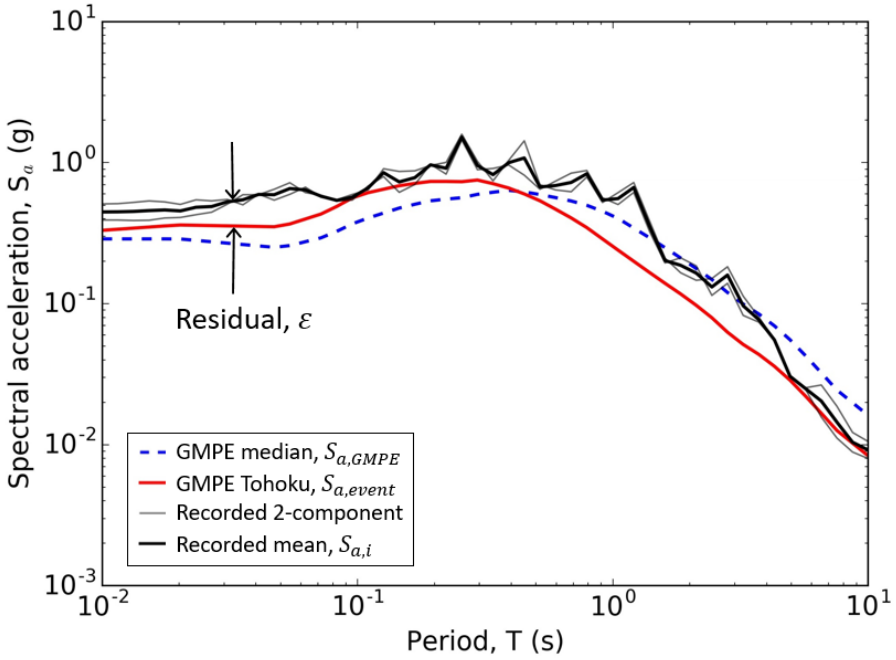

Figure 7.3: Example residual calculation

The residual, ε, is defined by the difference between $S_{a,event}$ and the recorded geometric mean $S_{a,i}$.

$$\varepsilon = \ln S_{a,i} - \ln S_{a,event} \tag{7.3}$$

Residuals tend to reflect random, aleatory variation between ground motions, but may also indicate that there are deviations due to regional path and source effects from $S_{a,event}$. If the residuals within a specific region show consistent, nonzero trends, additional source and path effects that were not included in the GMPE may have affected the ground motions. A regional, within-event residual can be calculated and applied to the GMPE to provide a more accurate estimate of ground motions.

$$\ln S_{a,region} = \ln S_{a,event} + \varepsilon_{region} \tag{7.4}$$

Regional residuals were calculated using the inverse distance-weighted average from ground motions recorded near a location of interest.

$$\varepsilon_{region} = \frac{\sum_i \frac{1}{r_i}\varepsilon_i}{\sum_i \frac{1}{r_i}} \tag{7.5}$$

where r_i represents the distance from the location of interest to the station where $S_{a,i}$ was recorded.

To appropriately estimate ground motions at a site without a strong motion recording, the ground motions from nearby recording stations, $S_{a,\mathrm{i}}$, were first corrected to standard rupture distance and site conditions. The source term, f, was recalculated using a reference rupture distance, R^*. The site term, f_{site}, was recalculated using a reference shear wave velocity, ${v_{s,30}}^*$. Both R^* and ${v_{s,30}}^*$ were selected to represent the conditions at the target site of interest. In this case, the target sites of interests were nearby locations with strong motion recording instruments that were affected by liquefaction. Correction for the reference rupture distance and site conditions can be used to estimate what the ground motions would have been at the sites investigated in this study if liquefaction had not occurred. Equations (7.1) through (7.4) were rearranged to calculate adjusted values of spectral acceleration, ${S_{a,i}}^*$, at a target site.

$$\ln {S_{a,\mathrm{i}}}^* = \ln S_{a,\mathrm{i}} - f(M,R) - f_{site}\left(v_{s,30}\right) + f(M,R^*) + f_{site}\left({v_{s,30}}^*\right) \tag{7.6}$$

Estimates of ${S_{a,i}}^*$ include deviations that may have occurred due to regional source and path effects, since $S_{a,i}$ was calculated from ground motions near the target site. The values of ${S_{a,i}}^*$ varied from record-to-record, since each recorded ground motion, $S_{a,i}$, also included some amount of aleatory uncertainty. Estimated value of spectral acceleration at a target location, ${S_{a,\mathrm{target}}}^*$,

were calculated using median values of $S_{a,i}{}^{*}$ from nearby recorded motions with inverse distance weighting.

$$\ln S_{a,\text{target}}{}^{*} = \frac{\sum_i \frac{1}{r_i} \ln S_{a,i}{}^{*}}{\sum_i \frac{1}{r_i}} \tag{7.7}$$

Equation (7.7) provides estimates of spectral acceleration at sites without strong motion recorders. As discussed, liquefaction affected the ground motions at the sites investigated for this study, and the BCHydro GMPE was not developed to account for the effects of liquefaction. However, the BCHydro GMPE can be used to provide estimates of spectral acceleration at a target site if liquefaction had not occurred. The liquefaction triggering analyses presented in Chapter 2 are based on values of peak ground acceleration (PGA) if liquefaction had not occurred. The PGA at a target site, if liquefaction did not occur, would have been equal to the value of $S_{a,\text{target}}{}^{*}$ at a period of 0 seconds. This PGA was estimated using a reference $v_{s,30}{}^{*}$ based on the shear wave velocity information collected during the subsurface investigations for this study.

Finite element analyses were also used to model the behavior of the soil and to provide insight into which layers of soil liquefied. Ground motions were input into the base of the finite element model at a linear halfspace, which had a shear wave velocity that was representative of stiff soil or rock, $v_{s,30}{}^{*}$. Equation (7.7) was then used to create a target spectrum for selecting ground motions representative of a stiff soil site that were input into the base of the finite element model.

7.2 IBR014

The strong motion recorder IBR014 was located approximately 60 km north of Tokyo on the west side of Kasumigaura Lake in the city of Tsuchiura. Figure 7.4 shows the area in the vicinity of the recording station, and Figure 7.5 shows a site plan. The strong motion recording station was in a parking lot about 400 m south of a river running into the west side of Kasumigaura Lake. The ASTER 10 m DEM indicated that the parking lot was about 8 m above the elevation of the river. The parking lot was constructed on the side of a slope which rose to the west at about 3H:1V. On the other side of the site, the parking lot sloped gently towards the southeast. A lower parking lot and apartment complex on the southeast side of the site were separated from the upper parking lot by an approximately 0.3 m-tall retaining wall. The parking lots and apartment complex appear to

have been constructed on a series of terraced cuts and fills that followed the natural grade of the hillside, which slopes towards the southeast. The natural grade of the hillside was apparent in the street and adjacent properties and appeared to be flatter than about 30H:1V, on average. Standing water and wet spots were observed on the west side of the parking lot, although the site reconnaissance and subsurface investigation were performed after a prolonged period of intense rainfall. Figure 7.5 shows the location of the recording station relative to the upper and lower parking lots.

Figure 7.4: Vicinity of IBR014 recording station. Image courtesy of Google Earth, Zenrin.

Figure 7.5: Site plan for IBR014. Image courtesy of Google Earth, Zenrin. Imagery date March 14, 2014.

The strong motion recorder at IBR014 was a standard K-net surface instrument installed on a stiff spread footing. The instrument recorded motions at a rate of 100 samples per second. A photo of the recording stations is provided in Figure 7.6.

Figure 7.6: IBR014 strong motion recording station

7.2.1 *Subsurface conditions*

Previous investigations at the site included a boring drilled to a depth of 20 m during installation of the K-net recording station. The K-net log included Standard Penetration Test (SPT) N-values, P- and S-wave velocity measurements, and general soil classifications. Figure 7.7 shows the K-net log at IBR014. The velocity profiles were processed by K-net, and only coarse representations of the depth-varying velocities were provided.

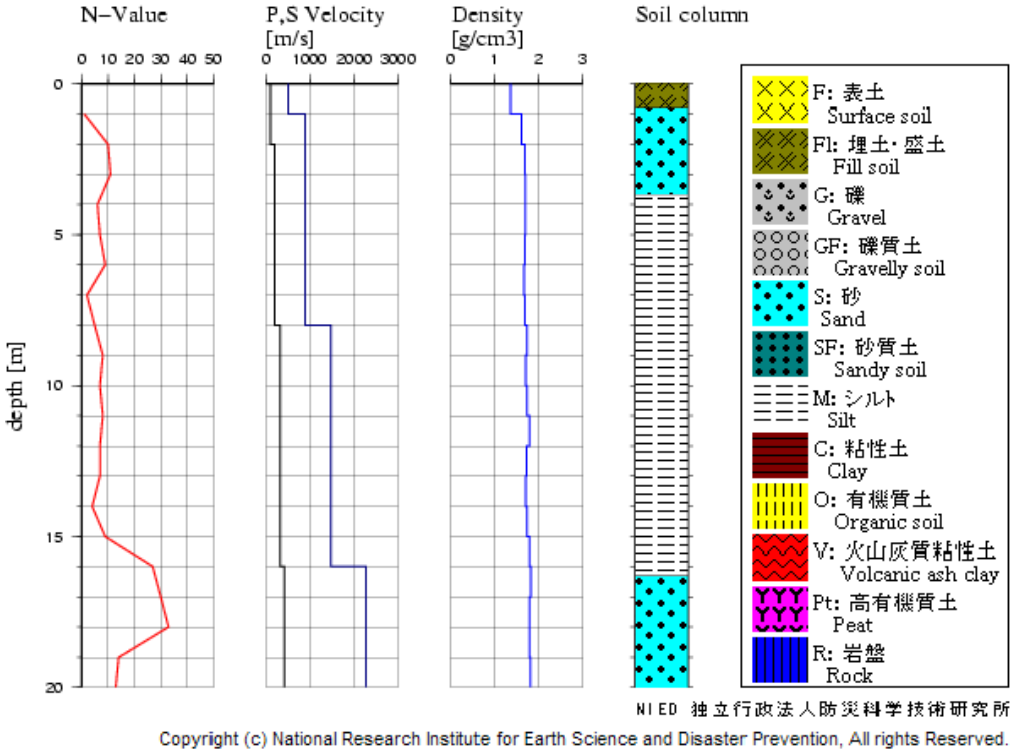

Figure 7.7: K-net boring log for IBR014

The subsurface conditions at IBR014 were investigated in September 2015 by Tokyo Soil Research and the author. The investigation included a mud rotary boring to a depth of 30.3 m, a cone penetration test (CPT) probe to a depth of 27.2 m and seismic cone shear and compressive wave velocity measurements. Pilot holes for both the boring and the CPT probe were hand-augured to a depth of about 2 m before drilling and probing to collect grab samples. Groundwater was encountered at a depth of about 1.3 m in the pilot holes. The hydrostatic pore pressure was measured with the CPT piezometer after excess pore pressure dissipated, and the piezometric surface of the groundwater was about 1.3 m deep at the time of the investigation. An increase in

compressive wave velocity to over 1,500 m/s was observed at a depth of about 1.3 m, further confirming the presence of saturated soil.

During drilling, Standard Penetration Tests (SPT) were performed at about 1 m intervals. An automatic trip hammer with a cathead and rope was used to drive the sampler. An SPT Analyzer from PDI, Inc. indicated that the hammer delivered between 72 to 82% of the theoretical maximum energy. Figure 7.8 shows a schematic of the soil profile with values of overburden and energy-corrected SPT $(N_1)_{60}$ resistance, overburden-corrected cone tip resistance, q_{c1}, and shear wave velocity, v_s.

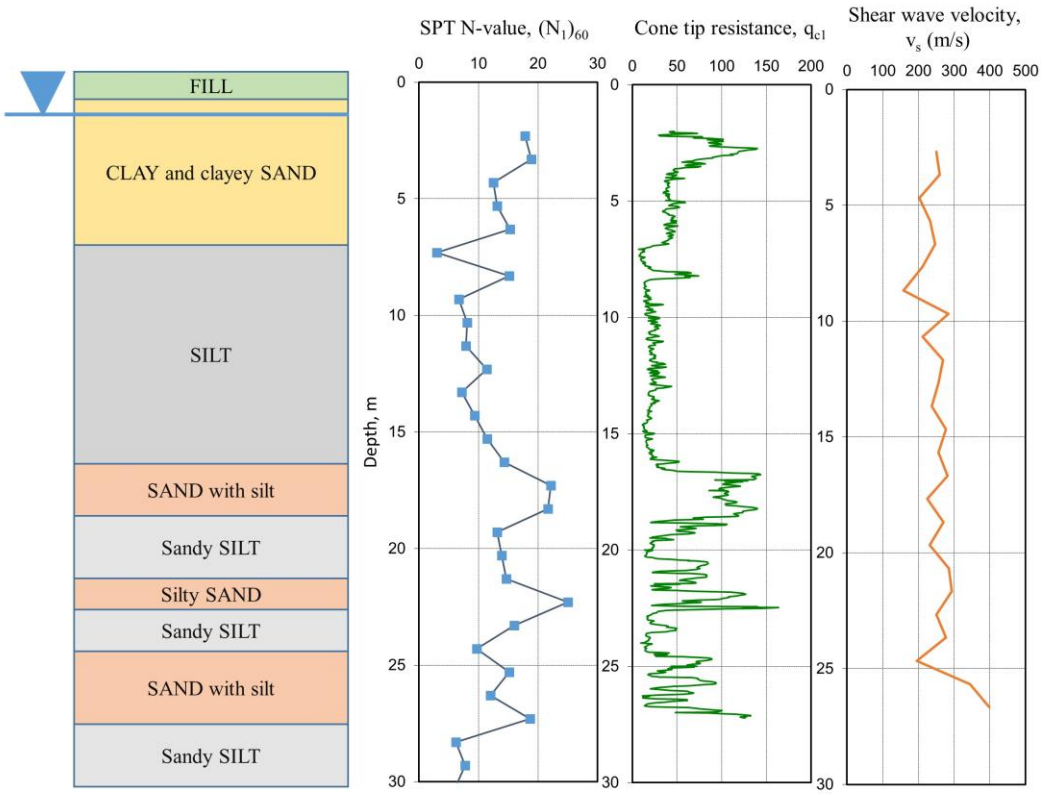

Figure 7.8: IBR014 soil profile

The soils encountered during the investigation were classified and logged per the methods in the WSDOT Geotechnical Design Manual (Allen, 2015). Summary logs of the boring and CPT probes are provided in the Appendix. The subsurface conditions encountered during the investigation were described according to their engineering properties: fill, clay and clayey sand, silt, and sand.

Fill

Fill consisting of a thin layer of organic silt (OL) mantled the ground surface at the site and extended to a depth of about 0.5 m. The organic silt fill was typically brown and included a 0.15 m-thick heavily rooted zone at the ground surface.

Clay and clayey sand

Clay (CL) and clayey sand (SC) were encountered below the fill. The clay and clayey sand extended between depths of about 0.5 to 7 m. Between a depth of about 0.5 and 2 m, the soil appeared to be composed of brown clay with moderate plasticity. Loose to medium dense, orange-brown clayey fine sand was encountered below the brown clay and extended from about 2 to 6 m deep. Gradations indicated that the fines content of the clayey sand ranged from 33 to 39%, and Atterberg limits indicated that the clayey sand had moderate plasticity with Plasticity Index (PI) ranging from 17 to 22. The clayey sand transitioned to stiff, sandy clay at a depth of about 6 m. The shear wave velocity of the clayey sand and sandy clay ranged from about 200 to 260 m/s.

Silt

Gray silt with sand and sandy silt (ML) were encountered below the clay and clayey sand at a depth of about 7 m. The silt was soft at a depth of 7 m and then transitioned to medium stiff or stiff below a depth of about 8 m. The silt typically exhibited moderate plasticity with a PI of about 20. The sand content of the silt ranged from some sand to sandy, and gradations indicated that the silt contained between 22 and 43% sand-sized particles. The shear wave velocity of the silt ranged from about 160 to 280 m/s.

Sand

Medium dense to dense fine sand (SP and SM) was encountered interbedded with the silt unit below a depth of about 17 m. The sand was nonplastic. The interbedded layers of sand ranged from about 1 to 3 m-thick. The sand contained varying amounts of silt which ranged from some silt to silty. The shear wave velocity of the sand ranged from about 220 to 400 m/s. The interlayered silt and sand units extended to maximum depth explored of 30.3 m.

7.2.2 *Observations at IBR014 site*

Surficial evidence of liquefaction was observed near IBR014 during the GEER reconnaissance after the Tohoku earthquake (Ashford et al., 2011). Photographs taken during the reconnaissance are shown in Figure 7.9. Figure 7.9 (a) was taken shortly after the earthquake and showed ejecta in the lower parking lot at the site. No description of the ejecta was provided, but the photos appear to show brown sand or silty sand. The photographs in Figures 7.9 (b) through (d) were taken by Jon Stewart during the GEER reconnaissance on March 31, 2011. The caption for Figure 7.9 (b) noted "limited evidence of liquefaction on day of visit" in the lower parking lot, and the photograph shows cracking and ejecta in the lower parking lot below to the strong motion recorder. The caption for Figure 7.9 (c) noted a "small retaining wall with minor tilt" in the lower parking lot, and an approximately 0.3 m-tall retaining wall between the lower parking lot and the apartment complex appeared to have tilted and failed during the earthquake. The caption for Figure 7.9 (d) noted an "unaffected parking lot above area in previous picture," and the photograph showed cracks in the upper parking lot, but not the ejecta that was observed in the other photographs of the lower parking lot. Since no ejecta was observed in the upper parking lot, even though the cracks in the pavement would have allowed the liquefied soil to be ejected at the surface, the near surface soil in the upper parking lot may not have liquefied.

Figure 7.9: Photos showing surficial evidence of liquefaction at IBR014. (a) Ejecta in the lower parking lot shortly after the Tohoku earthquake. Image courtesy of Yoshiya Hata. (b) Photograph of surface ejecta in the lower parking lot. (c) Photograph of minor retaining wall failure. (d) Photograph of cracks without ejecta in the upper parking lot. Images courtesy of Jon Stewart, GEER taken on March 31, 2011.

An aerial photograph taken on March 28, 2011, 17 days after the Tohoku main shock, is shown in Figure 8.9. The photograph also showed the presence of ejecta in the lower parking lot, but no evidence of liquefaction could be seen in the immediate vicinity of the strong motion recorder. Dr. Akio Abe, of Tokyo Soil Research, indicated that the extent of liquefaction was very limited in the Tsuchiura area. He was generally unaware of any other sites near Tsuchiura that exhibited surficial evidence of liquefaction. He indicated that clay soils generally mantled the ground surface around Tsuchiura.

Figure 7.10: Aerial photo showing the location of ejecta after Tohoku earthquake. Aerial photo of the site taken on March 28, 2011, showing the extent of ejecta in the lower parking lot. Image courtesy of Google Earth, GeoEye.

7.2.3 *Ground motions at IBR014 site*

The strong shaking at IBR014 from the Tohoku earthquake lasted for over two minutes as defined by 0.05 g bracketed duration, and over 70 seconds as defined by 5-95 significant duration. The peak ground accelerations were 0.51 and 0.39 g in the EW and NS directions, respectively, and the peak ground velocities were 0.34 and 0.26 m/s in the EW and NS directions. The geometric mean of the PGA from the two horizontal components was 0.45 g. The peak vertical ground acceleration was 0.25 g, and the peak vertical ground velocity was 0.10 m/s. The acceleration amplitude of the horizontal ground motion increased gradually from the beginning of the earthquake up to about 110 seconds, when the peak ground acceleration of 0.51 g occurred in the EW direction. After about 110 seconds, the frequency content of the motion decreased rapidly, although the acceleration amplitude of the motion remained relatively high. Around 120 seconds, the acceleration amplitude of the motion began to decrease. Figure 7.11 shows the horizontal and vertical acceleration time histories. Figures 7.12 and 7.13 show the velocity and displacement time histories, which were baseline-corrected by detrending the waveform, filtering out frequencies above 35 Hz and below 0.1 Hz, and removing a high-order polynomial from to the

data to reduce drift. The baseline correction process was similar to the approach by Boore et al. (2002). The spectral accelerations in the NS and EW directions are shown in Figure 7.14.

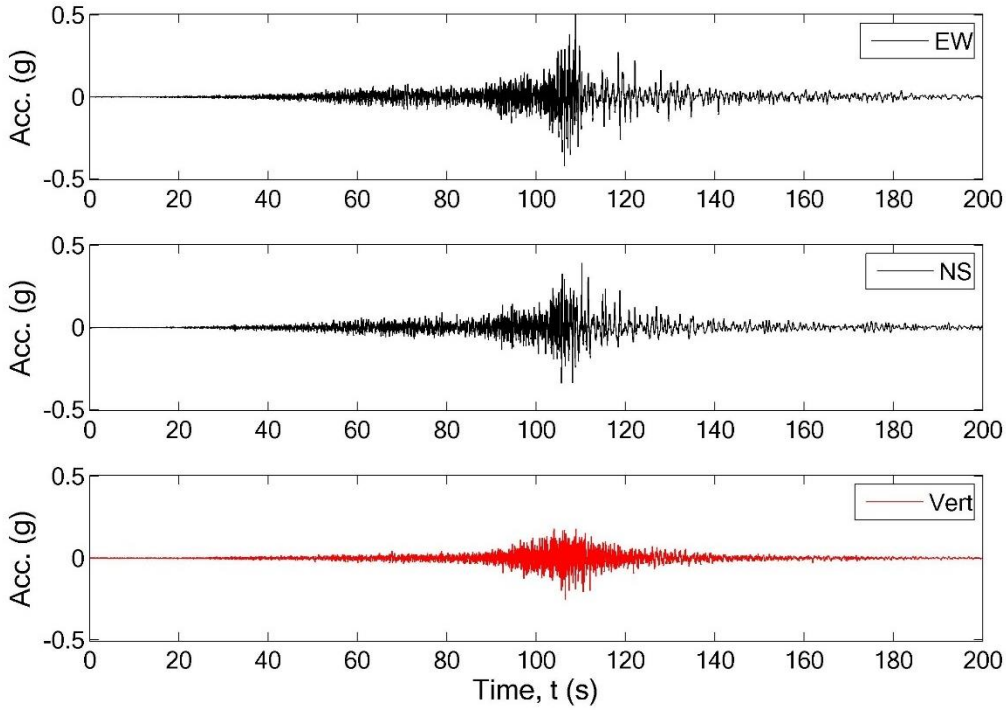

Figure 7.11: Baseline-corrected acceleration time histories at IBR014

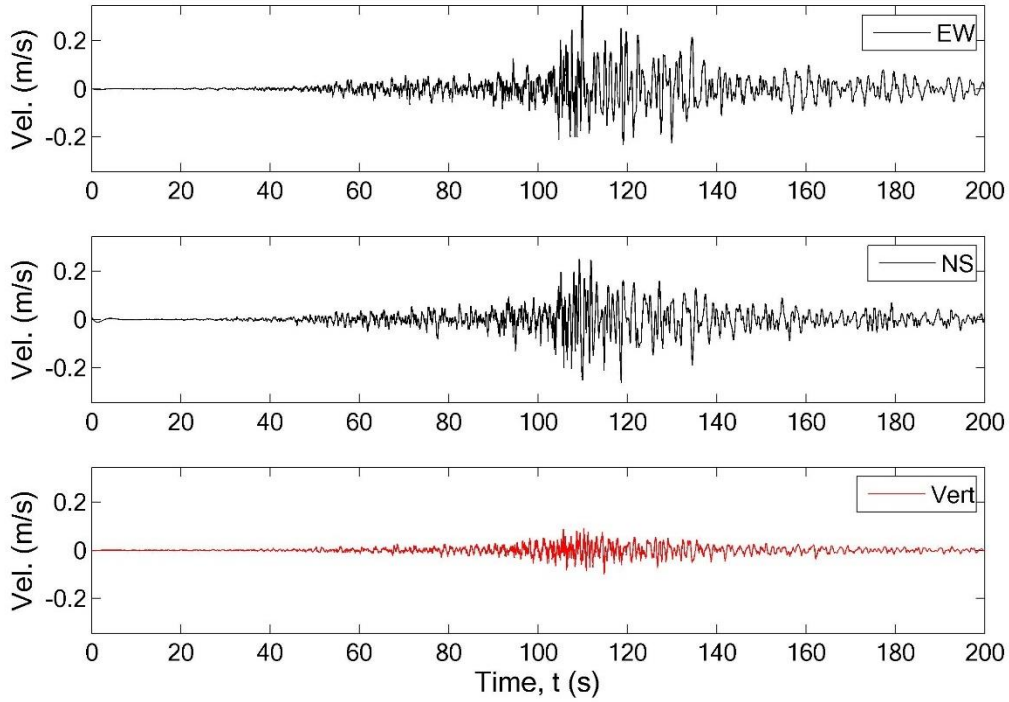

Figure 7.12: Baseline-corrected velocity time histories at IBR014

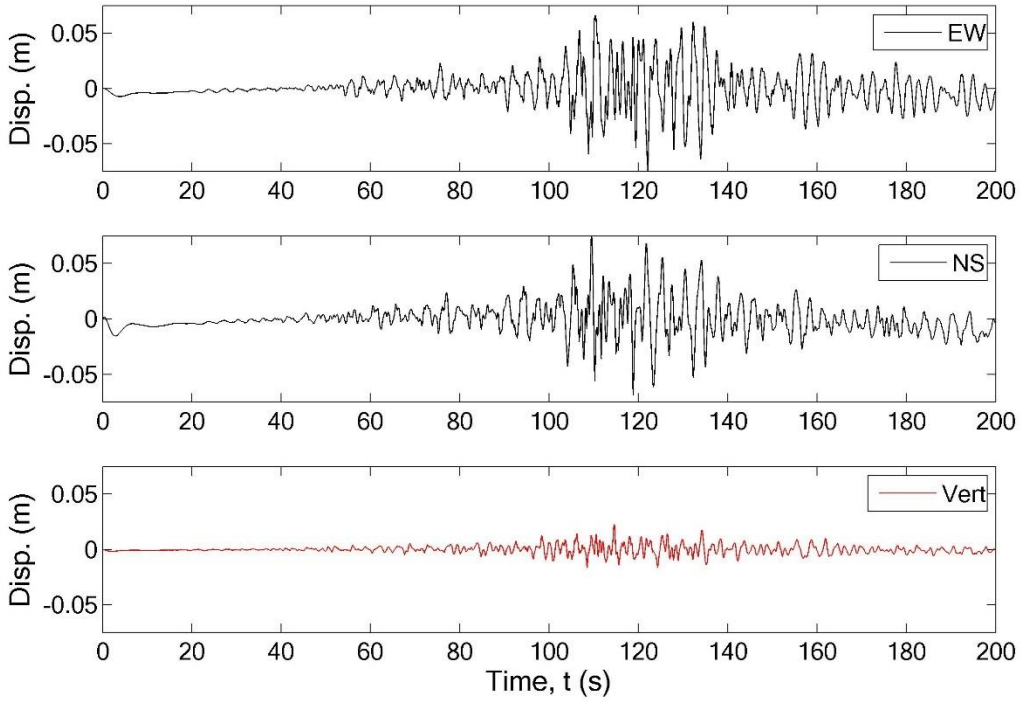

Figure 7.13: Baseline-corrected displacement time histories at IBR014

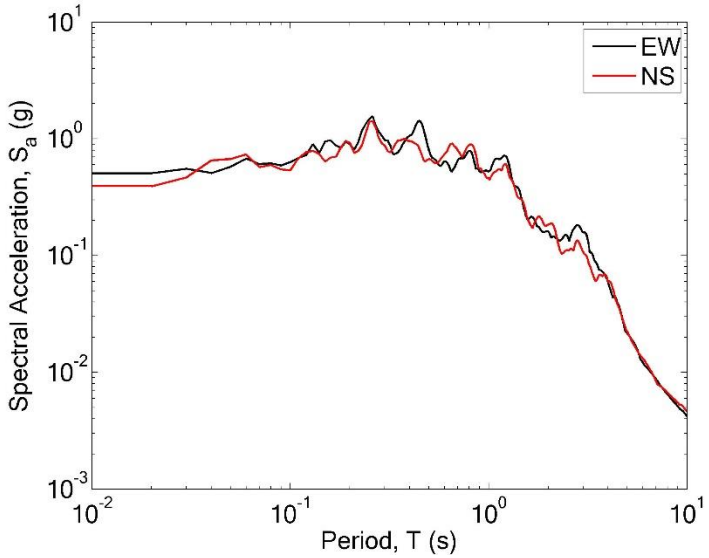

Figure 7.14: Spectral acceleration for IBR014

The PGA occurred during a very high-frequency spike in acceleration in the EW direction at about 106 seconds, which was approximately the time when the frequency content of the motion shifted from higher to lower frequencies. Although the peak acceleration in the EW direction was higher than in the NS direction, the spectral accelerations at periods longer than about 0.03 sec were similar in both directions.

The Stockwell power spectrum was used to isolate changes in frequency content that occurred at various times during shaking. As pore pressure increased in the liquefiable soils during shaking, the stiffness of the soil decreased. Once liquefaction occurred, the soil became extremely soft and could only transmit very low-frequency motions from the bedrock to the ground surface. If the frequency content of the bedrock motion remained stationary while liquefaction occurred, a rapid drop in frequency content at the ground surface would occur once the soil liquefied. An apparent drop in frequency content was identified in the recorded motion using a procedure based on the Stockwell time-frequency spectrum which corresponded with the time at which liquefaction occurred. Additional discussion regarding the identification of the time of liquefaction was provided in Chapter 4. Figure 7.15 shows the horizontal times histories and the normalized Stockwell power spectrum at IBR014.

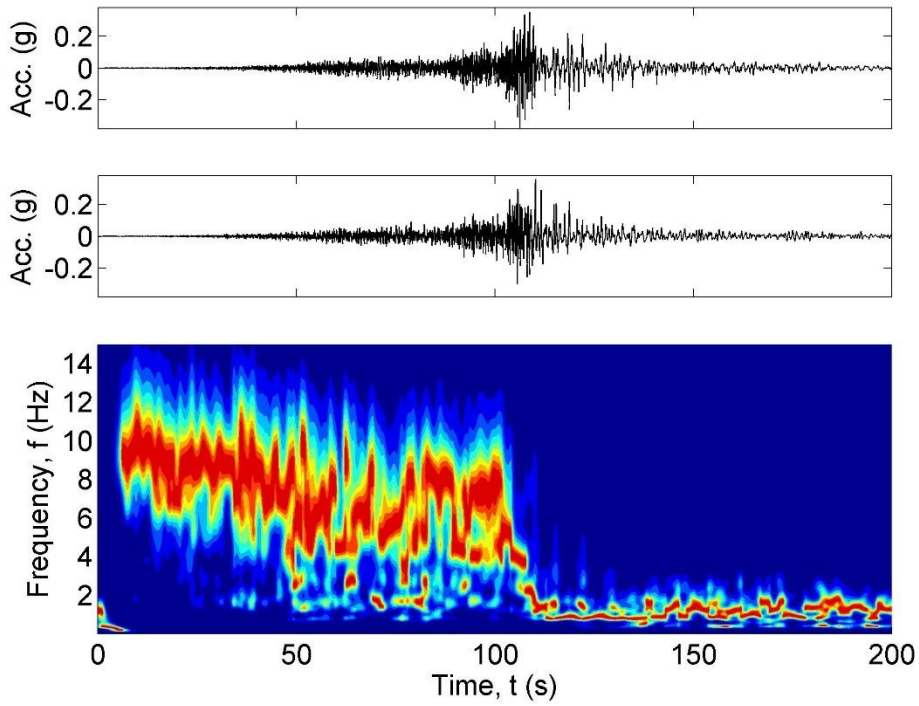

Figure 7.15: Acceleration time histories and normalized Stockwell power spectrum at IBR014

The Stockwell spectrum in Figure 7.14 indicated that a rapid shift in frequency content occurred between about 100 and 110 seconds. Figure 7.15 shows the Stockwell time-frequency spectrum zoomed in between 90 and 130 seconds. The modal frequency of the motion decreased from about 6 Hz to 4 Hz at approximately 104 seconds, and then from 4 Hz down to about 1.5 Hz at about 110 seconds. The acceleration amplitude of the ground motion increased immediately before the frequency content began to decrease. Since the frequency content shifted rapidly in response to increased acceleration, and the high-frequency content of the motion did not return later in the motion, it was presumed that the soil liquefied sometime between 100 and 110 seconds and could no longer transmit high-frequency motions to the ground surface. A step function was fit to the modal frequencies of the Stockwell spectrum and the average frequency content before and the time of liquefaction was estimated. The best-fit step function indicated that liquefaction likely occurred at about 110 seconds.

Strong, "spiky" acceleration pulses were recorded after the rapid drop in frequency content. These spiky acceleration pulses were presumably caused by the liquefied soil dilating in response

to large shear strains as the strong shaking continued. The effect of soil dilation on shear stiffness and ground motion frequency content was discussed in Chapter 2. One of these dilation pulses, which occurred at about 110 seconds, produced the PGA recorded at the site. Since dilation pulses are spiky in shape, rather than sinusoidal, they produced obvious bands of high-frequency amplitude over a short duration of time in the normalized Stockwell time-frequency spectrum. Dilation pulses can be seen in Figure 7.16 as thin bands of high frequency, high amplitude motion in the Stockwell spectrum at approximately 110, 115, and 122 seconds.

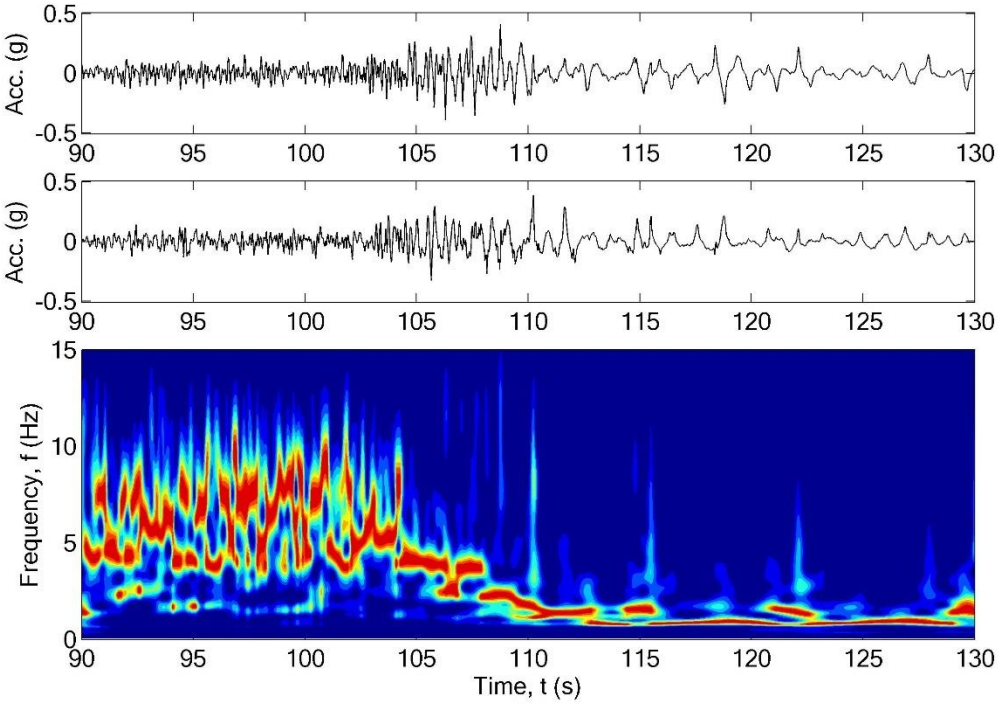

Figure 7.16: Acceleration time histories and normalized Stockwell power spectrum at IBR014 in the vicinity of the rapid frequency content shift.

The recorded PGA at the site was 0.51 g. The empirical procedures for evaluating liquefaction presented in Chapter 2 are based on inferred values of peak ground acceleration from non-liquefied sites. Because the recorded acceleration time history at IBR014 was affected by liquefied soils, it could not be directly used for liquefaction analysis. Seven stations from the K-net and KiK-net arrays were located within 20 km of the site and recorded data during the Tohoku earthquake. However, these sites were too far away from IBR014 to reliably use the recorded

ground motions for liquefaction analysis. Figure 7.17 shows the locations of the nearby strong motion recording stations.

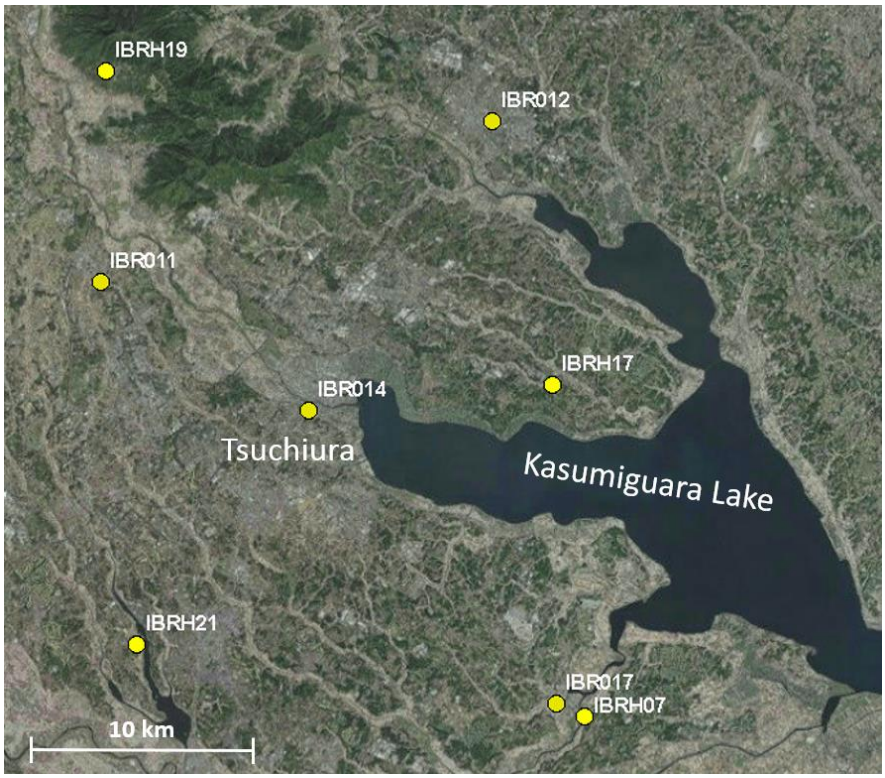

Figure 7.17: Recording stations in the vicinity of IBR014

Estimated ground motions if liquefaction had not occurred

The PGA that would have occurred at IBR014 if the ground motion was not affected by was estimated using the BCHydro GMPE, which provided a median estimate of the ground shaking at a site with consideration for the source, path, and site effects. GMPE estimates required values of distance to the fault rupture, R_{rup}, earthquake magnitude, and shear wave velocities in the upper 30 m of the site, v_{s30}. Distances to the fault rupture were documented for Kik-net stations (Dawood et al., 2015) and were inferred for the K-net stations. Shear wave velocities in the upper 30 m were documented in the K-net and Kik-net metadata.

Although seven recording stations were located relatively close to IBR014, three of these recording stations had site conditions that could not be corrected and could not be used to estimate within-event residuals. No subsurface information or ground motions were available from the KiK-net database for IBRH21. The recorded value of v_{s30} at IBRH07 was less than 130 m/s, which

was outside of the range of the data used to develop the BCHydro model. The recording station IBRH19 was located on a slope, and topographic effects, which were not considered in the BCHydro GMPE, many have affected the recorded ground motion. Sufficient data, however, was available from recording stations IBR012, IBR011, IBR017, and IBRH17 to estimate $S_{a,event}$. The PGA, or $S_{a,event}$ at a period of 0 sec, was first calculated using the event-adjusted GMPE for liquefaction triggering analysis. Table 7.4 shows the recorded data from the Tohoku earthquake at stations near IBR014.

Table 7.4: Ground motion records from the 2011 Tohoku earthquake near IBR014

Station	v_{s30} (m/s)	R_{rup} (km)	Geometric mean PGA (g)	Arias Intensity (m/s)	Significant duration (s)	Distance to IBR014 (km)	Notes
IBR014 (target)	270	71	0.45	4.6	68.2	0	Liquefied
IBR012	190	64	0.30	4.6	68.3	15	No liquefaction
IBR011	240	81	0.35	4.5	54.3	11	No liquefaction
IBR017	260	59	0.42	4.7	51.9	17	No liquefaction
IBRH17	300	60	0.40	5.9	48.3	11	No liquefaction
IBRH19	692	73	0.21	0.83	36.2	17	Site may have topographic effects
IBRH21	--	81	0.36	--	--	13	No ground motion data
IBRH07	107	58	0.19	3.0	130.4	19	v_{s30} too low for GMPE

The stations IBR012, IBR011, IBR017, and IBRH17 all had similar durations intensity measures during the Tohoku earthquake. Figure 7.18 shows plots of Arias Intensity evolving with time for these four stations and IBR014. The time when the PGA occurred at each station is also included in the figure. The shape of the Arias Intensity and timing of the PGA were similar at all of recording stations near IBR014. The PGA at IBR014 occurred slightly earlier and at a slightly larger Arias Intensity that the other nearby stations. The increased intensity of shaking during the early part of the motions was due to the amplification caused by elevated pore pressure in the liquefaction susceptible soils. The time-frequency analysis indicated that liquefaction occurred at

approximately 110 seconds at IBR014, and the PGA occurred after the soil liquefied during a dilation pulse.

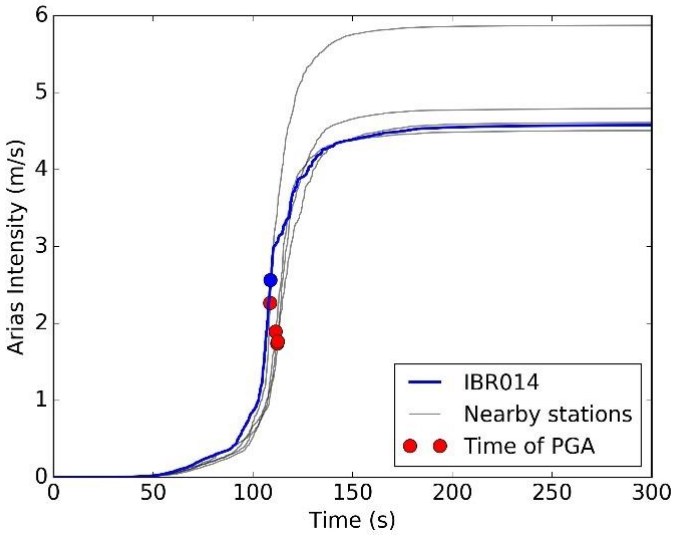

Figure 7.18: Arias intensity recorded at stations near IBR014

The GMPEs predicted that the PGA at IBR014 would have been 0.33 g if liquefaction had not occurred. However, this value did not include regional source and path effects, and the PGA used for liquefaction triggering analyses should reflect any regional variation that would have also affected the nearby recording stations. A procedure for calculating regionally adjusted PGA values was described in detail in Section 7.1.1. This procedure uses recorded ground motions from nearby stations to calculate a PGA value that is representative of the intensity of shaking if liquefaction had not occurred. The recorded PGA at each site near IBR014 was first adjusted using equation (7.6) to reference shear wave velocity, $v_{s,30}{}^{*}$, and distance, R^{*}, conditions. Representative values of $v_{s,30}{}^{*}$ = 270 m/s and R^{*} = 71 km were used in this analysis. Then, a regionally adjusted PGA was calculated using equation (7.7). Table 7.5 shows the PGA recorded at each site, as well as the PGA adjusted to the target site conditions.

Table 7.5: Event residuals for the recorded PGA at stations near IBR014

Station	v_{s30} (m/s)	R_{rup} (km)	Distance to IBR014 (km)	Geometric mean PGA (g)	PGA adjusted to target site (g)
IBR014 (target)	270	71	0	0.45	0.45
IBR012	190	64	15	0.30	0.29
IBR011	240	81	11	0.35	0.38
IBR017	260	59	17	0.42	0.38
IBRH17	300	60	11	0.40	0.36

These adjusted PGA values ranged from 0.29 to 0.38 g and combined with inverse distance weighting, resulted in an estimated regionally adjusted PGA of 0.35 g at IBR014. This value indicated that the path and source effects likely amplified the PGA in the region of IBR014 by a factor of approximately 1.06 relative to the event-adjusted GMPE prediction. However, this regionally adjusted PGA was significantly lower than the recorded PGA of 0.45 g. Since the PGA occurred after liquefaction was triggered, the recorded PGA at IBR014 was likely affected by the presence of elevated pore water pressure and liquefied soil. Site response effects and amplification due to liquefaction cannot be accounted for in the GMPE, but the peak acceleration before the time of liquefaction was more reflective of soil conditions that are appropriate for GMPEs. The recorded peak ground acceleration before liquefaction occurred was 0.34 g, which was very close to the estimated PGA at the site based on the event and region-corrected GMPE.

The process described in Section 7.1.1 was also used to develop a target spectrum. Ground motions that reasonably match this target spectrum can be input into a finite element model. The shear wave velocity of the halfspace in the finite element model was selected as 400 m/s based on the shear wave velocity of the deepest layer in the exploration. Recorded spectral accelerations from nearby stations were adjusted to a reference shear wave velocity, $v_{s,30}{}^{*}$, of 400 m/s, and reference distance, R^{*}, of 71 km using equation (7.6). The target spectral acceleration from the event-adjusted GMPE was then calculated using equation (7.7). Figure 7.19 shows the response spectra from each of the four stations near IBR014 corrected to the reference conditions.

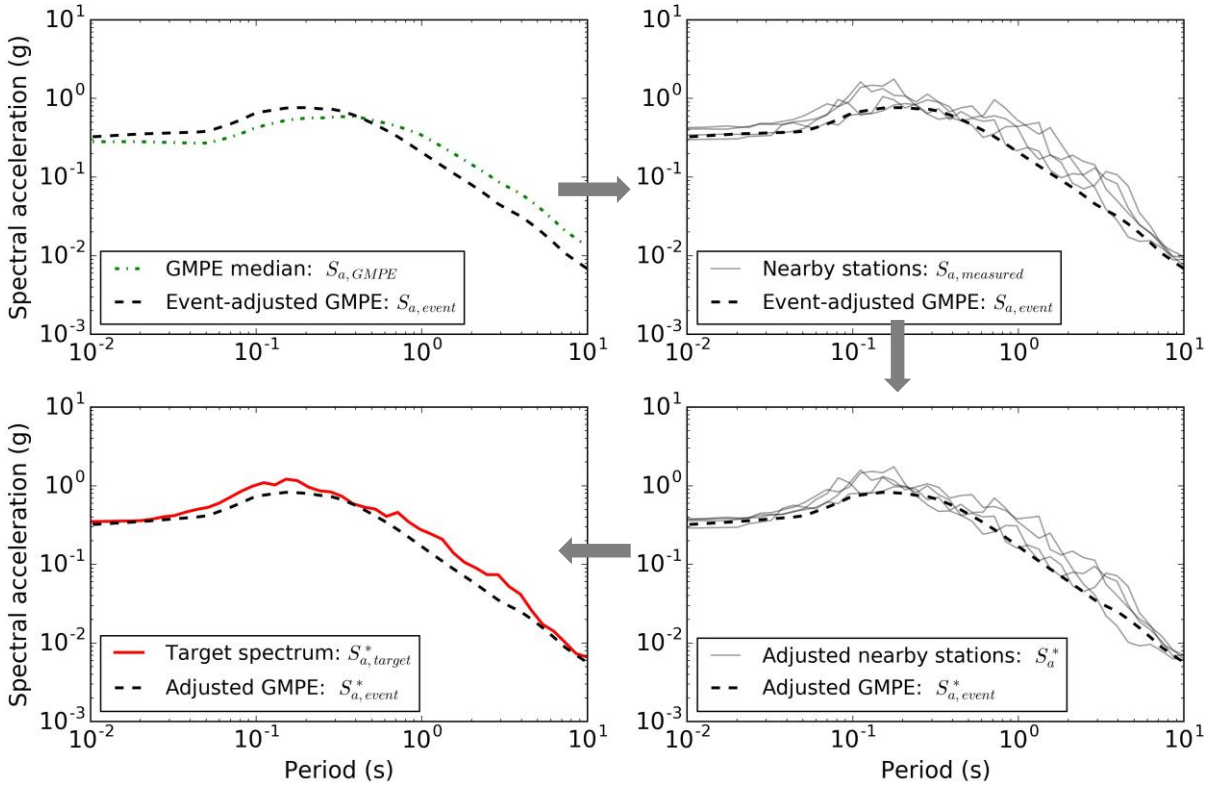

Figure 7.19: Calculation of target spectrum for IBR014 motions

The adjusted spectral acceleration from the nearby stations was greater than $S^*_{a,event}$ at all periods. This implied that the spectral acceleration in the vicinity of IBR014 was greater than the median spectral acceleration recorded during the Tohoku earthquake. Motions selected to represent the shaking at IBR014 should reflect this regional variation, and the inverse distance-weighted average values of $S_a{}^*$ were used as a target spectrum for selecting ground motions.

Over 1,500 records from Tohoku, Maule, Kushiro-Oki and several other long-duration earthquakes were compared to the target spectrum developed in Figure 7.19. The motions were first screened so that only motions with similar durations as the recorded motions near IBR014 were selected. The selected ground motions were then scaled to minimize the sum of squared residuals (SSR) between the target spectrum and the recorded spectral acceleration. The scaling factors were limited to a maximum of 3 times the original spectral acceleration values, and the SSR from each motion was calculated over periods ranging from 0.01 to 10 seconds. The motions with the smallest SSR were selected to represent time histories for the shaking at a stiff soil outcrop at IBR014. Recent design guidelines (FEMA, 2015) recommend selecting a minimum of 11

ground motions that matched a target spectrum for site response analysis. Figure 7.20 shows the target spectral acceleration for a stiff soil outcrop near IBR014 and the 11 records that best fit the target spectrum. The calculated scaling factor that was used to minimize the SSR for each motion is also listed in Figure 7.20.

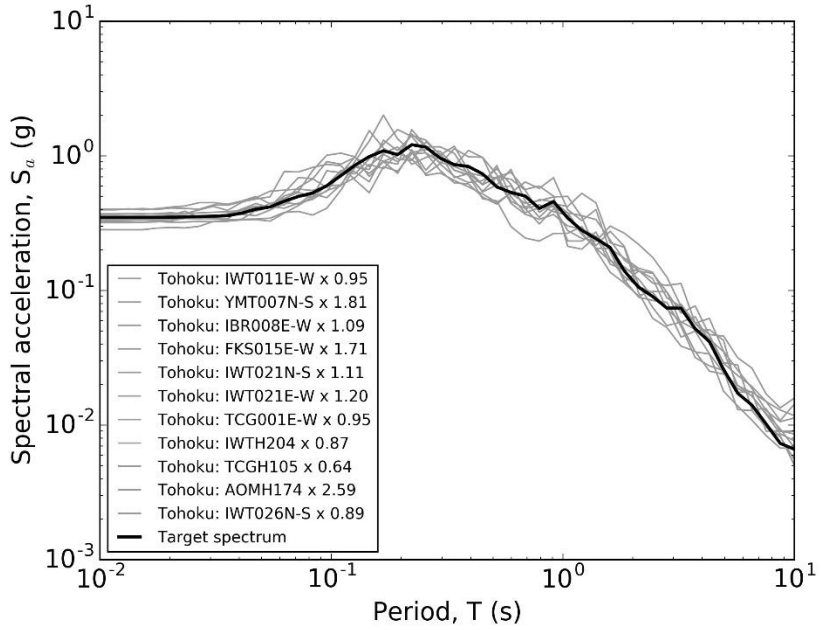

Figure 7.20: Spectral acceleration of ground motions selected to represent shaking at IBR014

In addition to matching the target spectral acceleration in Figure 7.19, motions that were representative of the shaking at IBR014 should have a relatively long duration and many cycles of loading. Figure 7.21 shows the Arias Intensity and Husid Parameter values of the 11 selected ground motions.

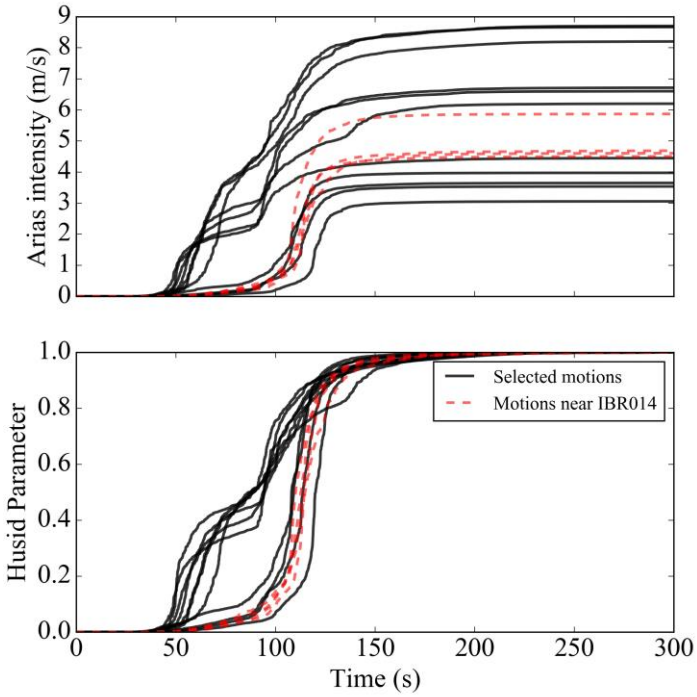

Figure 7.21: Arias and Husid Parameter of ground motions selected to represent shaking at IBR014

7.2.4 *Liquefaction*

The liquefaction susceptibility of saturated soils was influenced by their plasticity characteristics. Soils that had low plasticity or were non-plastic were the most susceptible to liquefaction, while soils with moderate or high plasticity were generally not susceptible to liquefaction. The Plasticity Index (PI) and the water content to liquid limit ratio (w/LL) of the soils were used as simple criteria to assess the liquefaction susceptibility of the soils at IBR014. The near-surface clayey sand that extended from the ground surface to a depth of about 6 m had a PI that ranged from 17 to 22 and a w/LL of about 0.9 to 1.0. The silt that extended from the bottom of the clayey sand to a depth of about 17 m had a PI of about 20 with a w/LL of about 1.0. The layers of medium dense to dense sand encountered below a depth of 17 m were nonplastic, with a PI of 0.

Liquefaction susceptibility

As presented in Chapter 2, two major studies by Boulanger and Idriss (2006) and Bray and Sancio (2006) proposed criteria for evaluating the liquefaction susceptibility of fine-grained soils based on plasticity index. A critical issue at IBR014 was the liquefaction susceptibility of all sandy soils below the water table and a depth of 6 m. Table 7.6 shows the result of the Atterberg limits performed for this study, and Figure 7.22 shows the results plotted on axes used for the Boulanger and Idriss (2006) and the Bray and Sancio (2006) analyses. The samples were grouped into the soil units described in the subsurface conditions section. The Idriss and Boulanger (2006) criterion indicated that the clayey sand should clearly not be susceptible to liquefaction. However, the Bray and Sancio (2006) criteria indicated that the clayey sand may have been moderately susceptible to liquefaction. Both susceptibility criteria are considered plausible, and both criteria were used to evaluate the liquefaction susceptibility of the soils at IBR014. The test results indicated that the silt unit below a depth of 6 m was not susceptible to liquefaction, and the sand unit below a depth of 17 m was susceptible to liquefaction.

Table 7.6: Liquefaction susceptibility for IBR014

Soil unit	Depth (m)	Water Content, w	Liquid Limit, LL	Plasticity Index, PI	Susceptibility (I&B)[1]	Susceptibility (B&S)[2]
clayey sand	4	44	44	17	No	Moderate
clayey sand	6	44	44	22	No	No
silt	9	47	48	20	No	No
sand	19	39		0	Yes	Yes

[1] Susceptibility criterion according to Idriss and Boulanger (2006)

[2] Susceptibility criteria according to Bray and Sancio (2006)

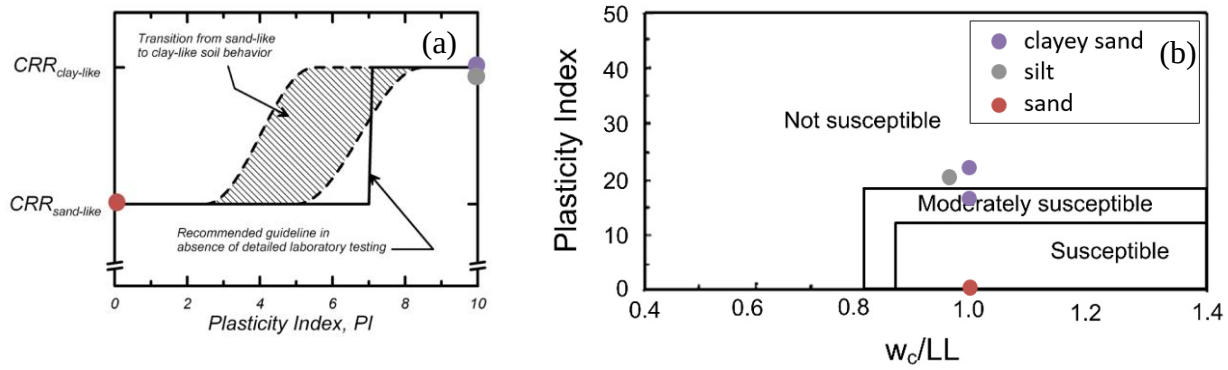

Figure 7.22: Liquefaction susceptibility of soils at IBR014. (a) Liquefaction susceptibility based on plasticity index from Boulanger and Idriss (2006). (b) Liquefaction susceptibility based on plasticity index and water content from Bray and Sancio (2006).

Since the Boulanger and Idriss (2006) and Bray and Sancio (2006) susceptibility criteria produced inconsistent indications of liquefaction susceptibility of the shallow clayey sand between the water table and a depth of 6 m, two susceptibility scenarios were investigated using empirical procedures. One case assumed that the clayey sand was not susceptible to liquefaction (Model NS) and the other analysis it was susceptible to liquefaction (Model S).

Empirical liquefaction triggering analysis

Soils susceptible to liquefaction liquefy if the cyclic resistance ratio, CRR, in a soil is less than the cyclic stress ratio, CSR. The empirically-derived CRR values of the soils at IBR014 were estimated using the corrected SPT N-values, $(N_1)_{60cs}$ (Idriss and Boulanger, 2010) or corrected CPT tip resistances, q_{c1Ncs} (Boulanger and Idriss, 2014). The $(N_1)_{60cs}$ values of potentially liquefiable soils ranged from 15 to 31 blows per foot. The q_{c1Ncs} values of these soils ranged from 90 to 250. The layer of soil with the lowest adjusted penetration resistance was the medium dense sand at a depth of 26 m. Table 7.7 shows the calculation of $(N_1)_{60cs}$ values.

Table 7.7: SPT correction for IBR014

Depth (m)	Susceptibility	N	Fines	Ce	Cr	σ_v (kPa)	σ_v' (kPa)	N_{60}	$(N_1)_{60}$	$(N_1)_{60\text{-cs}}$
2	Moderate?[1]	11	33%	1.27	0.8	37	27	10	18	23
3	Moderate?[1]	12	33%	1.27	0.8	58	38	12	19	24
4	Moderate?[1]	8	39%	1.20	0.9	74	45	8	13	17
5	Moderate?[1]	9	39%	1.20	0.9	90	51	9	13	18
17	Susceptible	20	20%	1.27	1.0	297	139	25	22	27
18	Susceptible	20	20%	1.27	1.0	313	146	25	22	26
22	Susceptible	25	30%	1.27	1.0	389	183	32	25	31
25	Susceptible	17	15%	1.27	1.0	444	208	22	15	18
26	Susceptible	14	15%	1.27	1.0	460	215	18	12	15
27	Susceptible	21	15%	1.27	1.0	476	221	27	19	22

[1] Moderate susceptibility based on Bray and Sancio (2006). Clay-like behavior based on Idriss and Boulanger (2006)

The CSR values for the empirical liquefaction triggering methods were based on the 0.35 g peak ground acceleration value inferred from recordings at non-liquefied sites. The inferred PGA was used to calculate the CSR values at IBR014 using the simplified methods for liquefaction triggering analysis presented in Chapter 2. Figure 7.23 shows the results of the liquefaction triggering analyses from both cases.

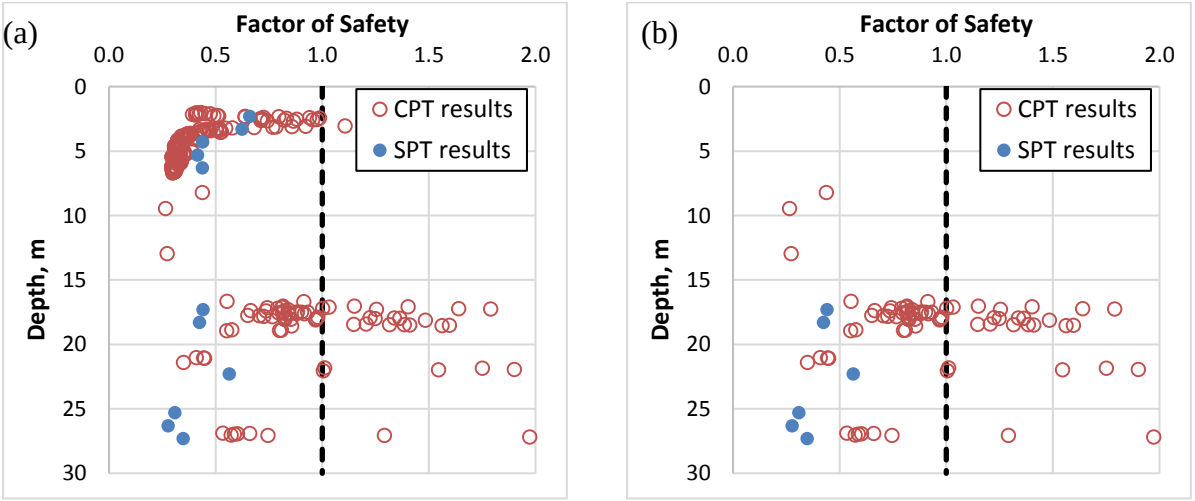

Figure 7.23: Factor of safety against liquefaction at IBR014. (a) Clayey sand above 6 m was assumed not susceptible to liquefaction. (b) Clayey sand above 6 m was assumed susceptible to liquefaction.

Liquefaction triggering analysis indicated that the layers that were susceptible to liquefaction likely liquefied during the strong shaking of the Tohoku earthquake, and the shallow layer of clayey sand would have liquefied if it were susceptible to liquefaction. The cyclic behavior of the clayey sand could not be fully assessed without advanced cyclic testing, but several lines of evidence suggest that the clayey sand was not susceptible to liquefaction.

1. The Japanese drilling contractor used for this investigation indicated that the near surface soils in the Tsuchiura area were predominately composed of clayey soils, and this observation was consistent with the near-surface soils encountered at IBR014. If these soils were susceptible to liquefaction, the low factors of safety (less than 0.5) computed at IBR014 suggest that widespread evidence of liquefaction would have existed across much of Tsuchiura. However, the Japanese drilling contractor was unaware of any other sites in Tsuchiura where surficial evidence of liquefaction was observed after the Tohoku earthquake.
2. Surficial evidence of liquefaction in the form of sand ejecta was observed in the parking lot below the strong motion recorder. While the plasticity of the ejecta was not noted, the ejecta would have significant fines content and moderate plasticity if it had been produced by the clayey sand. Based on the surrounding topography, the lower parking lot may have been constructed with a thin layer of fill placed over the original ground surface to grade the lower parking lot. The high groundwater at the site may have saturated the fill, which may have liquefied during the Tohoku earthquake and produced the ejecta observed during the reconnaissance. The photographs in Figure 7.8 showed evidence of the ejecta in the lower, but not the upper, parking lot. Reconnaissance by the GEER team (Ashford et al. 2011), which visited the site 17 days after than earthquake, noted that the upper parking lot immediately adjacent to the strong motion recorder appeared to be unaffected by the earthquake, while the ejecta was observed in the lower parking lot.
3. Cracks were observed in the upper parking lot, which would have allowed liquefied sand to easily eject to the ground surface if the near-surface soils had liquefied. A thick layer of liquefied soil would have produced sand boils according to the sand boil screening criteria proposed by Ishihara (1985). However, ejecta was only seen in the lower parking lot, and not in the upper parking lot where the recording station was located and where the subsurface investigation was performed.

4. Since the site had very high groundwater and was gently sloping towards the river, severe liquefaction of the clayey sand near the ground surface would cause lateral spreading. Estimates of lateral spreading using the Youd et al. (2002) equations indicated that 0.5 to 1.5 m of lateral spreading would have occurred if the near surface layers of saturated clayey sand with $(N_1)_{60}$ less than 15 liquefied at the site. Figure 7.8(d) shows approximately 5 cm-wide cracks oriented NNE to SSW. The orientation of the cracks was perpendicular to the general slope at the site, indicating the cracks may have resulted from downslope deformation at the site, but not the large deformations predicted by the lateral spreading equations.

Although Bray and Sancio (2006) indicated that soils with PI less than 18 and w/LL greater 0.8 were moderately susceptible to liquefaction, the circumstances of liquefaction at the site indicated that the clayey sand extending from the water table to a depth of 6 m did not liquefy. The low relative density (penetration resistance) of those soils suggests that they should have undergone extensive liquefaction if they were susceptible. The fact that they did not suggest that those soils were not susceptible to liquefaction. Table 7.8 summarizes the lines of evidence that the clayey sand was not susceptible to liquefaction.

Table 7.8: Evidence that shallow clayey sand at IBR014 did not liquefy during the 2011 Tohoku earthquake

- Boulanger and Idriss (2006) criterion indicated PI = 17 materials should exhibit clearly "clay-like" behavior.
- Bray and Sancio (2006) indicated PI = 17 with w/LL = 1.0 exhibited only "moderate susceptibility" to liquefaction. A second sample in the clayey sand with PI = 22 with w/LL = 1.0 indicated the clayey sand was "not susceptible" to liquefaction.
- Near-surface clay-like soils were common in Tsuchiura, but liquefaction was not observed in areas other than the lower parking lot near IBR014.
- The lower parking lot near IBR014 may have been constructed on imported fill, which could have liquefied and produced the ejecta seen at that location in the reconnaissance.
- If the clayey sand was susceptible to liquefaction, it's thickness combined with the thin overlying crust would have been expected to cause severe sand boils. However, no sand boils were observed in the direct vicinity of IBR014.
- Lateral spreading would have been expected in the upper parking lot and other nearby sites if the near surface soils liquefied. Very little damage was observed.

Even though the near-surface clayey sand was unlikely to have liquefied, the ground motion recorded during the Tohoku earthquake showed a rapid and significant drop in the high-frequency content of the motion at about 110 seconds. This rapid decrease in high-frequency content occurred immediately after an increase in acceleration amplitude and indicated that liquefaction very likely occurred at that time. The subsurface investigation and liquefaction analysis indicated that the soils between depths of 6 to 17 m were clearly not susceptible to liquefaction. It also indicated, however, that the layers of medium dense sand below a depth of 17 m were susceptible to liquefaction. The estimated factor of safety of these soils was significantly less than 1.0 during the Tohoku earthquake. Thus, it appears that these soils likely liquefied and produced the changes in frequency content observed in the recorded ground motion.

7.2.5 *Numerical analysis*

To gain additional insight into the characteristics of the IBR014 profile, a series of nonlinear effective stress site response analyses were performed with the computer program FLIP. The 11

time histories that best matched the estimated non-liquefied target spectrum at IBR014 were used as input motions in the analysis. Since one liquefaction susceptibility criterion indicated that the clayey sand between the water table and a depth of 6 m at IBR014 was not susceptible, and the other indicated it was marginally susceptible to liquefaction, parallel analyses were performed considering the clayey sand as susceptible in one case (Model S) and not susceptible (Model NS) in the other. Material properties for the finite element analyses were estimated using the data collected from the subsurface investigations at IBR014. Table 7.9 shows the input parameters that were used to model the 1D effective stress site response of IBR014. The water table was modeled at a depth of about 1 m as indicated by the subsurface investigation.

The site response analyses were performed using the finite element program, FLIP (FLIP Consortium, 2011). The Cocktail glass model in FLIP was developed to predict softening due to pore pressure generation, soil fabric degradation during intense shaking, and strong dilation pulses after liquefaction was triggered. The analyses for IBR014 predicted that much of the soil that was susceptible to liquefaction would have liquefied during the Tohoku earthquake. The analyses also showed that the spectral acceleration at the ground surface was very sensitive to the thickness of liquefied soil. Thicker layers of liquefied soil resulted in a softer site with a longer fundamental period, which amplified longer period ground motions. The thickness of liquefiable soil was very different in Model S that in Model NS, and the parametric analyses resulted in very different predictions of ground surface spectral acceleration. The parametric FLIP models used the acceleration time histories that matched the target spectrum that was developed using the BCHydro GMPE with corrections based on nearby recorded ground motions. The predicted spectral acceleration showed marked differences compared to the recorded spectral acceleration at IBR014 (Figure 7.24). These deviations were assumed to be caused by liquefaction, and were not captured in the GMPE estimates but can be captured in FLIP. The FLIP model that best matched the recorded spectral acceleration indicated which model appropriately captured the behavior of the shallow clayey sand at the site.

Table 7.9: Material properties for modeling site response at IBR014

Depth (m)	Model	Soil description	ρ (kg/cm^3)	v_s (m/s)	$(N_1)_{60}$	ϕ
1	Cocktail glass	Clayey sand	1.6	90	23	38º
2	Cocktail glass	Clayey sand[1]	1.6	250	23	38º
3	Cocktail glass	Clayey sand[1]	1.7	260	24	38º
4	Cocktail glass	Clayey sand[1]	1.7	200	18	38º
5	Cocktail glass	Clayey sand[1]	1.7	230	18	38º
6	Cocktail glass	Clayey sand[1]	1.7	250	21	38º
7	Cocktail glass	Silt	1.7	210	8	34º
8	Cocktail glass	Silt	1.7	160	21	34º
9	Cocktail glass	Silt	1.7	280	12	34º
10	Cocktail glass	Silt	1.7	210	14	34º
11	Cocktail glass	Silt	1.7	270	13	34º
12	Cocktail glass	Silt	1.7	260	17	34º
13	Cocktail glass	Silt	1.7	240	13	34º
14	Cocktail glass	Silt	1.7	230	15	34º
15	Cocktail glass	Silt	1.7	280	17	34º
16	Cocktail glass	Silt	1.7	220	20	34º
17	Cocktail glass	Sand[2]	1.8	270	27	38º
18	Cocktail glass	Sand[2]	1.8	230	26	38º
19	Cocktail glass	Silt	1.8	280	18	34º
20	Cocktail glass	Sand[2]	1.8	290	20	34º
21	Cocktail glass	Sand[2]	1.8	250	20	34º
22	Cocktail glass	Sand[2]	1.8	280	30	38º
23	Cocktail glass	Silt	1.8	200	22	34º
24	Cocktail glass	Silt	1.8	340	15	34º
25	Cocktail glass	Sand[2]	1.8	400	18	38º
26	Cocktail glass	Sand[2]	1.8	400	15	38º
27	Cocktail glass	Sand[2]	1.8	400	22	38º
28	Cocktail glass	Silt	1.8	400	12	34º
29	Cocktail glass	Silt	1.8	400	13	34º
30	Linear Halfspace		2.0	400		

[1] Modeled in two separate analyses. One analysis was performed where the soil is not susceptible to liquefaction and the other where the soil is susceptible to liquefaction

[2] The sand below a depth of 17 m is susceptible to liquefaction

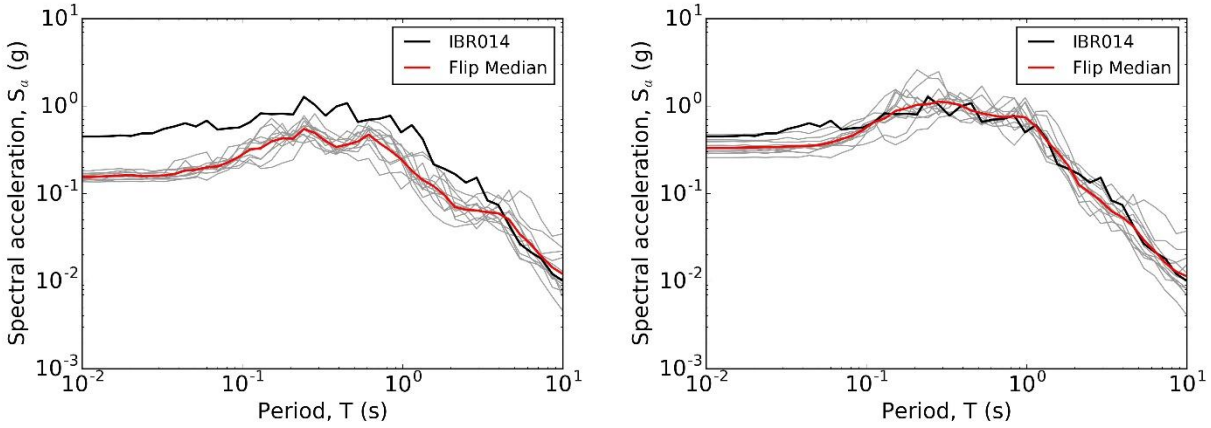

Figure 7.24: Computed and recorded spectral acceleration at IBR014. (a) Shallow clayey sand was susceptible to liquefaction, Model S. (b) Shallow clayey sand was not susceptible to liquefaction, Model NS.

Since the shallow clayey sand would have liquefied and become very soft, the overall response of the Model S soil deposit would have been softer and the higher frequency motions would have been deamplified compared to Model NS. The results of the Model S analyses did indeed predict spectral accelerations that were much lower than the spectral acceleration estimated in Model NS and were much lower than the recorded spectral accelerations at short periods. The spectral acceleration predicted by Model NS matched the recorded spectral accelerations at IBR014 quite well. This comparison provides further evidence that the shallow clayey sand did not liquefy during the Tohoku earthquake.

Model NS predicted that layers of medium dense sand between depths of 24 to 26 m, which had the lowest relative density of any layers in the sand deposit, liquefied first. The model then indicated that the other layers of medium dense and dense sand below 17 m deep liquefied as the strong shaking continued. Once liquefaction occurred, the soil profile became very soft and the high-frequency content of the ground surface motion decreased dramatically. Figure 7.25 shows a profile of the pore pressure versus time in the liquefiable sand deposit below 17 m for one of the motions selected to represent the Tohoku earthquake at IBR014. Figure 7.26 shows a profile of excess pore pressure versus cycle-adjusted PGA.

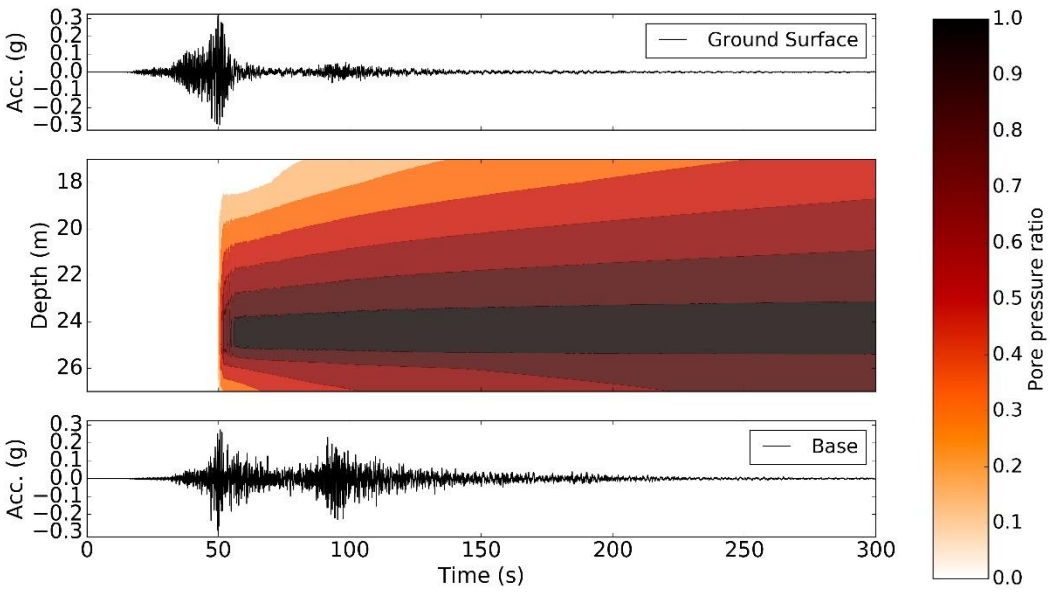

Figure 7.25: Pore pressure generation at IBR014. Input motion IWT011E-W.

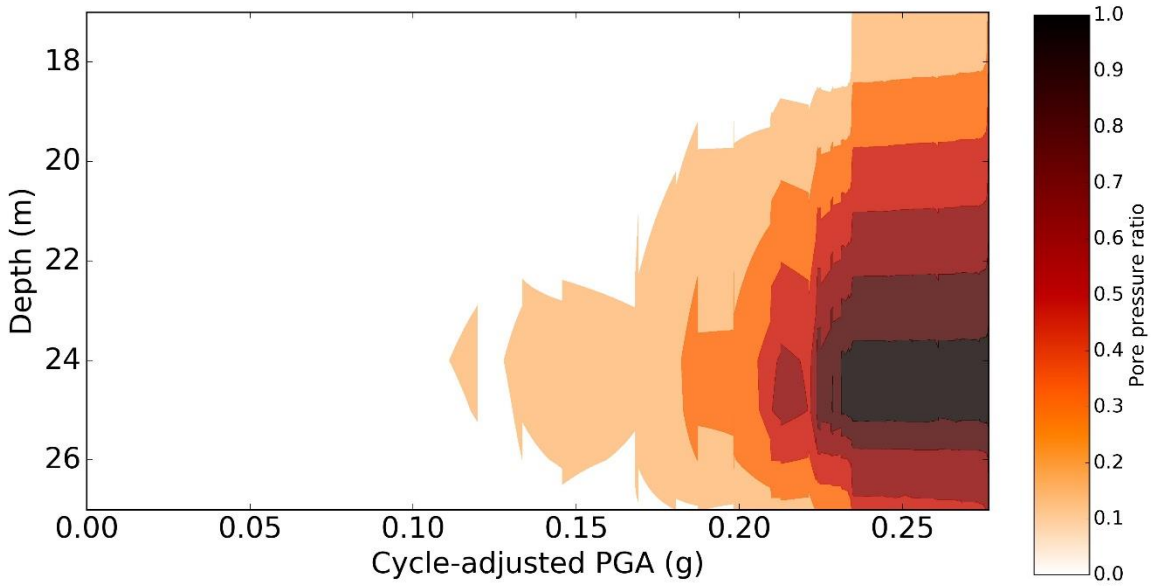

Figure 7.26: Pore pressure versus magnitude-adjusted PGA at IBR014. Input motion IWT011E-W.

The ability of FLIP to capture the liquefaction triggering behavior was further examined by comparing the recorded intensity measures at the time of liquefaction to the estimated intensity measures from the numerical model. If the model was accurately predicting liquefaction triggering, the intensity measures from the numerical model should have been similar to the

recorded intensity measures. Table 7.10 shows the median values and standard deviations of three intensity measures at the time when liquefaction was triggered. Figure 7.27 shows histograms of the cycle-adjusted PGA, Arias intensity, and cumulative absolute velocity (CAV) at the time of liquefaction.

Table 7.10: Intensity measures at the time of liquefaction at IBR014

Intensity Measure	Recorded	Median	Standard deviation, $\sigma_{\ln IM}$
Magnitude-adjusted PGA	0.32 g	0.34 g	0.28
Arias Intensity	2.5 m/s	5.3 m/s	0.41
Cumulative Absolute Velocity	21.7 m/s	30.6 m/s	0.35

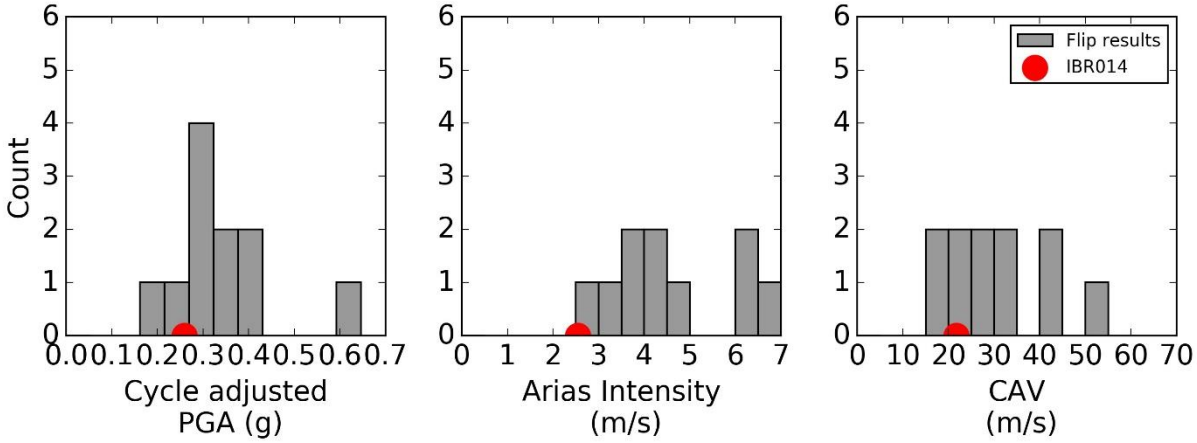

Figure 7.27: Intensity measure at the time of liquefaction

The median cycle-adjusted PGA from the FLIP model was very close to the recorded intensity measures at the time of liquefaction and exhibited relatively modest variance, indicating that FLIP reasonably estimated the cumulative intensity of shaking that triggered liquefaction. Even though the Arias intensity and cumulative absolute velocity from the model were generally higher than the recorded values, the predicted intensity measures at the time of liquefaction were within the range of recorded values.

7.2.6 *Conclusions*

Surficial evidence of liquefaction was observed near, but not at, the location of the IBR014 strong motion instrument. The IBR014 record shows clear evidence of rapid and pronounced changes in

frequency content that are normally associated with liquefaction. Liquefaction at IBR014 appears to have occurred in one of the relatively deep layers of medium dense to dense sand and silty sand below a depth of 17 m. Although the groundwater was very shallow at this site, laboratory testing and subsequent parametric analyses indicated that the near-surface clayey sand and silt were not susceptible to liquefaction and did not liquefy. The surficial ejecta observed in the parking lot below IBR014 was likely due to liquefaction of a thin layer of saturated fill placed to grade the lower parking lot, rather than from the deep layers of medium dense to dense sand that liquefied during the Tohoku earthquake. Stockwell time-frequency analysis indicated that a rapid change in frequency content occurred at about 110 seconds, which was likely the time when liquefaction first occurred. The behavior recorded at the site was reasonably reproduced by using nonlinear, effective stress site response analyses with the computer program FLIP. These analyses showed good agreement with the recorded motion when the shallow clayey sand was assumed to be not susceptible to liquefaction, and poor agreement with it was assumed to be susceptible to liquefaction. When the shallow clayey sand was modeled as not susceptible to liquefaction, the clayey sand between the water table and a depth of 6 m degraded during shaking and developed large shear strains but did not liquefy. This response was consistent with the observation of cracks in the upper parking lot without the ejecta associated with liquefaction. If the shallow clayey sand was susceptible to liquefaction, ejecta should have been observed in the upper parking lot, and the results predicted by nonlinear, effective stress analyses would have been very different than the recorded motions.

7.3 MYG010

The K-net strong motion recorder MYG010 was located in central Ishinomaki, approximately 40 km northeast of Sendai, in the prefecture of Miyagi. Figure 7.28 shows an aerial photograph from the vicinity of the recording station, and Figure 7.29 shows a site plan. The strong motion recording station was in a densely-populated area about 1 km north of the Port of Ishinomaki waterfront. The site was not visited by a UW representative, but according to the coordinates of the recording station provided by K-net, the station was located on the grounds of the Okaido Elementary School next to a swimming pool on the northwest side of the property. The Google Earth DEM indicated that the recording station was about 3 m above sea level. The area surrounding the site appeared to be relatively flat, and the site was located about 2-3 m above the

Port of Ishinomaki waterfront to the south, and inland channels and waterways to the north and west.

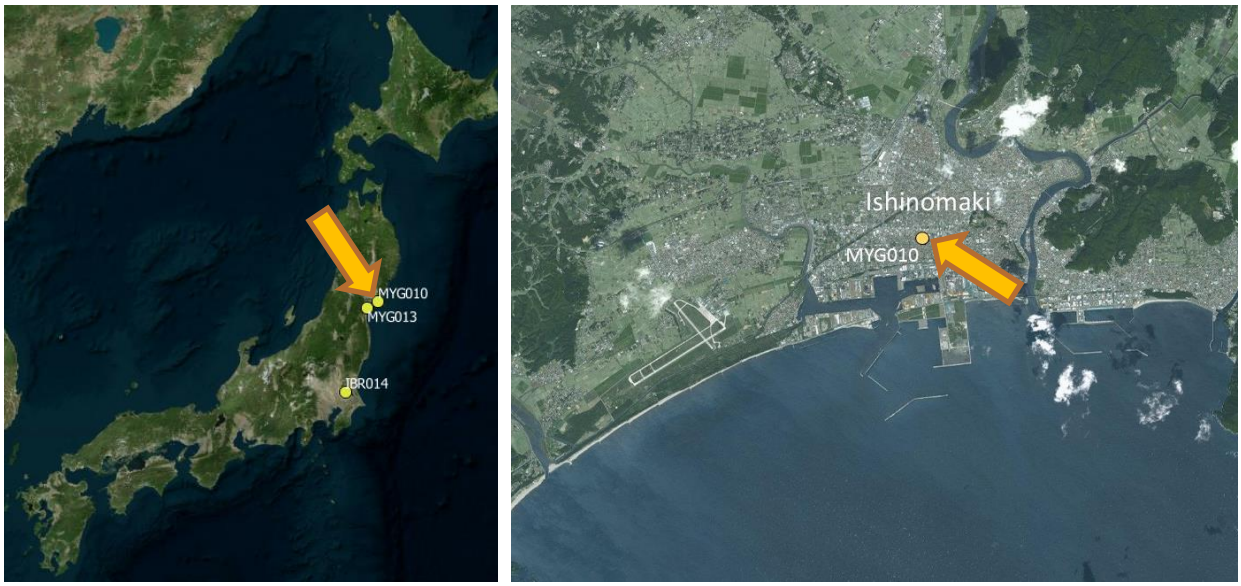

Figure 7.28: Vicinity of MYG010 recording station. Image courtesy of Google Earth, TerraMetrics.

The strong motion recorder was a standard 3-component K-net surface recorder. The instrument was installed in 1996 and recorded ground motions at a rate of 100 samples per second. The recorder was likely damaged or destroyed by the tsunami following the 2011 M_w = 9 Tohoku earthquake, and the station was later rebuilt in August 2012.

Figure 7.29: Site plan for MYG010. Image courtesy of Google Earth.

7.3.1 *Subsurface conditions*

Previous investigations at the site included a boring that was drilled to a depth of 20 m during the initial installation of the K-net recording station. The K-net log included Standard Penetration Test (SPT) N-values, compression and shear wave-velocity measurements, and general soil classifications. Figure 7.30 shows the K-net log at MYG010. The velocity profiles were processed by K-net, and only provided a coarse representation of the depth-varying velocities.

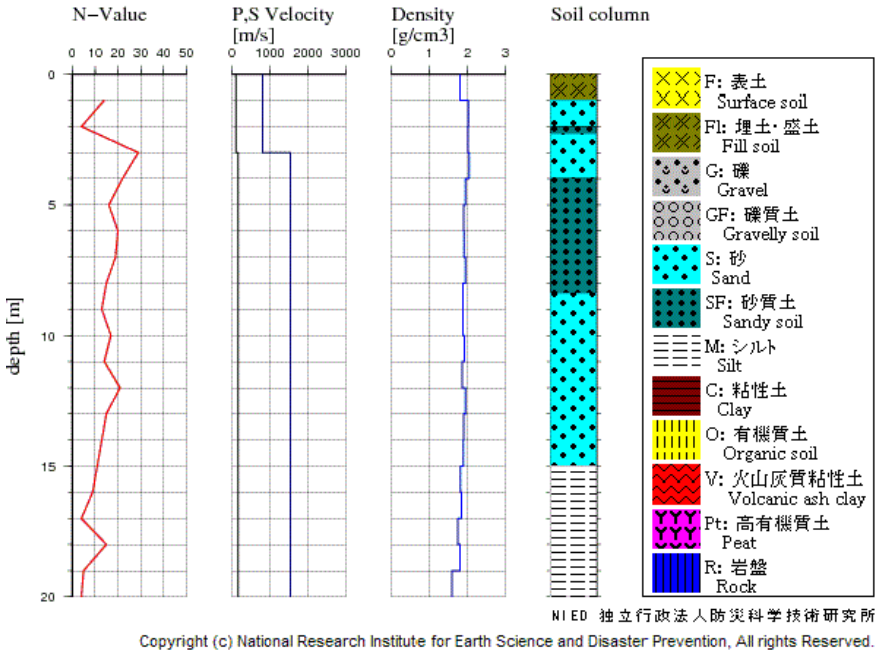

Figure 7.30: K-net boring log for MYG010

The subsurface conditions at MYG010 were investigated in October 2015 by Tokyo Soil Research. The investigation included a cone penetration test (CPT) probe to a depth of 8.0 m, where practical refusal was encountered. The subsurface seismic shear and compressive wave velocities were measured as part of the CPT investigation. Soil samples were collected at about 1.0 m intervals using a CPT-based piston sampler. Hydrostatic pore pressures were measured with the CPT piezometer after excess pore pressure dissipated. The results of the piezometric measurements indicated that the piezometric surface of the groundwater was about 2.1 m deep at the time of the investigation, which was consistent with elevations of nearby bodies of water, which were about 2-3 m below the elevation of the site. An increase in compressive wave velocity to 1,300 m/s was also observed at a depth of about 2.6 m, which was consistent with the presence

of saturated soil. Figure 7.31 shows a schematic of the soil profile with overburden-corrected CPT q_{c1} values.

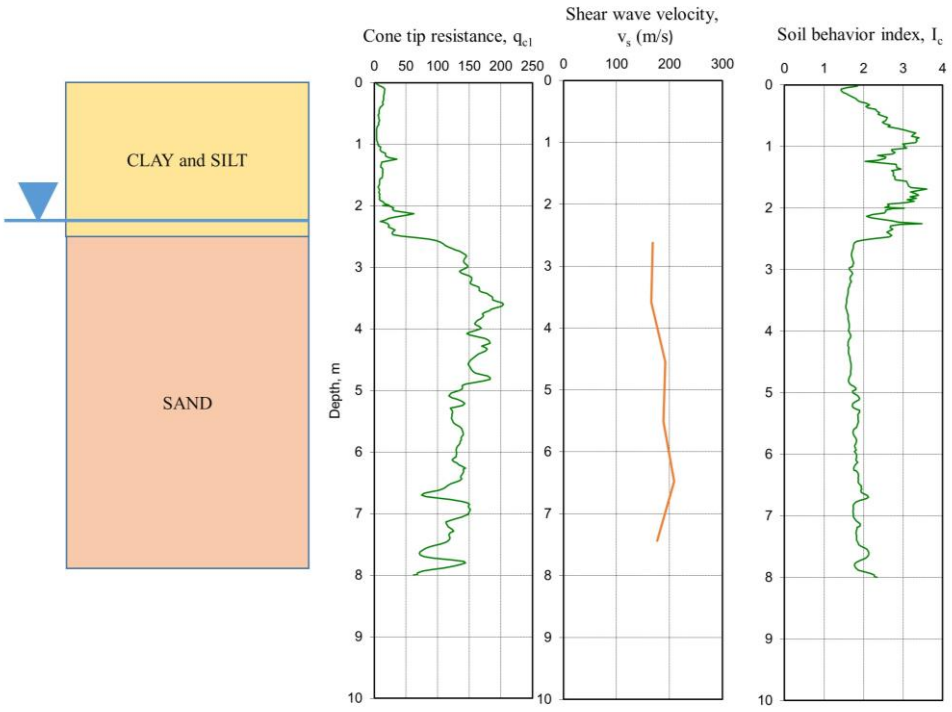

Figure 7.31: MYG010 profile

The soils encountered during the investigation were classified and logged by Tokyo Soil Research. A summary log of the probe is included in the Appendix. The subsurface conditions encountered during this investigation were described according to their engineering properties. Two distinct units were encountered: clayey sand (SC) and sand (SW and SM). The K-net log indicated that fill mantled the ground surface to a depth of about 1 m, but the presence of fill could not be confirmed by the CPT probe alone.

Clayey sand

Clayey sand with gravel (SC) was present from the ground surface and extended to a depth of about 2.6 m. The clayey sand was very loose to loose with q_c values ranging from about 0.2 to 3.7 MPa. A sample at 2 m indicated that the fines content of the clayey sand was about 23%. One Atterberg limit test from a sample at from a depth of 2 m indicated that the clayey sand had moderate plasticity with a Plasticity Index (PI) of about 17. A gradation analysis of the sample

collected at a depth of about 2 m indicated that the clayey sand contains about 27% gravel-sized particles. The average shear wave velocity in the clayey sand was about 133 m/s.

Sand

Fine to medium sand (SW and SM) extended from the bottom of the clayey sand to the maximum depth explored of 8 m. The sand was medium dense to dense with q_c values ranging from about 5.9 to 16.3 MPa. The sand tended to be dense in the upper part of the deposit between 2.6 and 5 m and then transitioned to medium dense below a depth of 5 m. Gradation tests indicated that the sand was fine to medium with D_{50} values ranging from 0.19 to 0.30 mm. The fines content of the sand ranged from 8 to 19%, and the sand was classified as well-graded sand to silty sand. Laboratory testing of a sample collected at a depth of 6 m indicated the water content of the sand was about 23%. The shear wave velocity of the sand ranged from about 158 to 211 m/s. Practical refusal with the CPT probe was encountered at a depth of 8 m.

The K-net log indicated that the medium dense to dense sand extended to a depth of about 15 m, where medium stiff to stiff silt was encountered. The silt extended to the maximum depth explored of 20 m.

7.3.2 *Observations at MYG010 site*

The bay and surrounding areas of Ishinomaki were heavily damaged by the tsunami caused by the main shock of the Tohoku earthquake on March 11, 2011. Extensive liquefaction was reported around Ishinomaki, although much of the liquefaction damage was obscured by the tsunami (Cox et al. 2013). Figure 7.27 shows an aerial photo of the area surrounding the MYG010 site taken on March 29, 2011, 18 days after the earthquake. Significant amounts of debris were seen near the site, which indicated that the tsunami likely inundated the area. If the tsunami inundated the location where the station was established, it would have completely obscured surficial evidence of liquefaction. The strong motion recorder was not visible in aerial photographs taken shortly after the earthquake. A new strong motion recorder was later installed at the location indicated in Figure 7.32. The photo taken shortly after the Tohoku earthquake showed circular features in the field adjacent to the site, which may have been sand boils caused by aftershocks. Surficial evidence of liquefaction at nearby waterfront sites was later observed during a strong M_w = 7.1

aftershock on April 7 (Ashford et al. 2011). Since the soil liquefied due to M_w = 7.1 aftershocks, it very likely liquefied due to the M_w = 9.0 main shock.

Figure 7.32: Aerial photo showing debris and damage at MYG010 after Tohoku earthquake. Aerial photo of the site taken on March 28, 2011. Image courtesy of Google Earth.

7.3.3 *Ground motions at MYG010 site*

The strong shaking at MYG010 from the Tohoku earthquake lasted 149 seconds, as defined by 0.05 g bracketed duration and 110 seconds as defined by 5-95 significant duration. The peak ground accelerations were 0.38 and 0.47 g in the EW and NS directions, respectively, and the peak ground velocities were 0.55 and 0.50 m/s in the EW and NS directions. The geometric mean of the PGA from the two horizontal components was 0.42 g. The peak vertical ground acceleration was 0.34 g, and the peak vertical ground velocity was 0.22 m/s. As shown in Figure 7.33, the acceleration amplitudes of the horizontal ground of motion increased rapidly about 37 seconds into the earthquake record. The peak ground acceleration of 0.47 g occurred in the NS direction shortly thereafter, at about 40 seconds, after which the amplitude of the motion began to diminish. A second rapid increase in acceleration amplitude occurred at about 92 seconds, which was

characteristic of the multiple subevents associated with the Tohoku earthquake in the Miyagi region. The horizontal acceleration amplitude during the second period of strong shaking was as large as 0.38 g and produced the peak acceleration in the EW direction. Figure 7.33 shows the horizontal and vertical acceleration time histories. Figures 7.34 and 7.35 show the velocity and displacement time histories, which were baseline-corrected by detrending the waveform, filtering out frequencies above 35 Hz and below 0.1 Hz, and removing a high-order polynomial from to the data to remove drift. The baseline correction method was similar to the approach described by Boore et al. (2002). The spectral accelerations of the detrended motions in the NS and EW directions are shown in Figure 7.36.

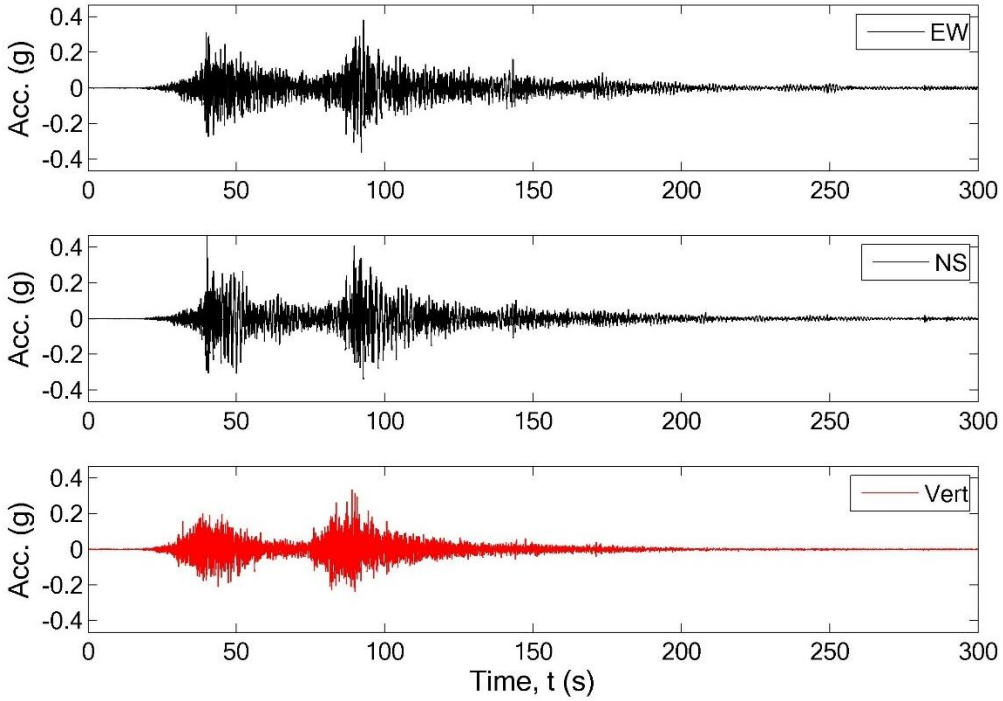

Figure 7.33: Baseline-corrected acceleration time histories at MYG010.

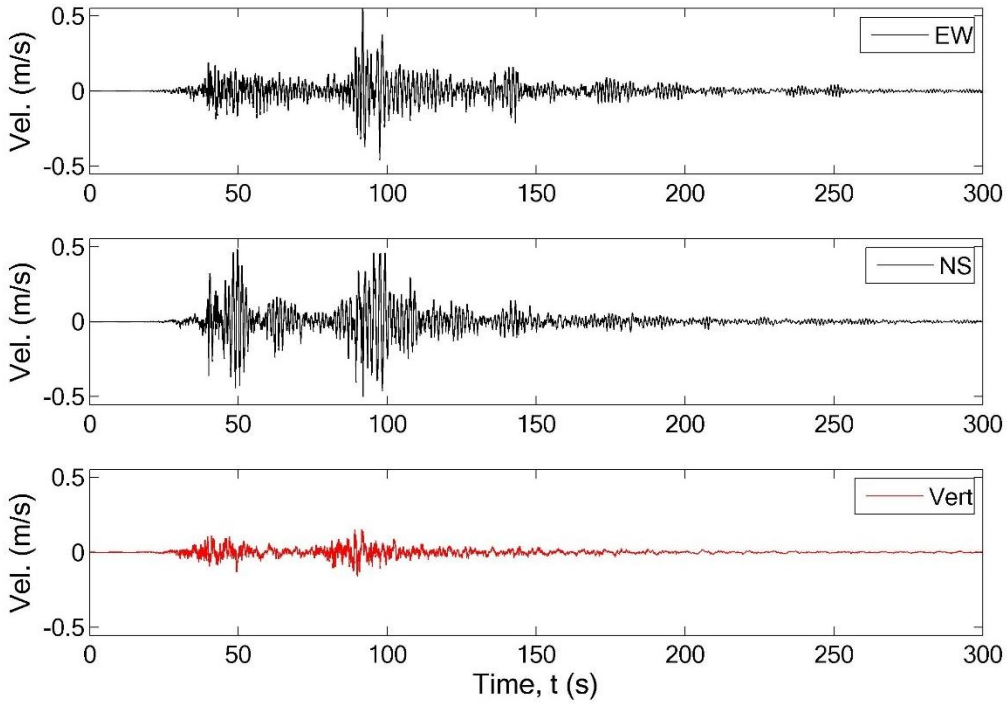

Figure 7.34: Baseline-corrected velocity time histories at MYG010

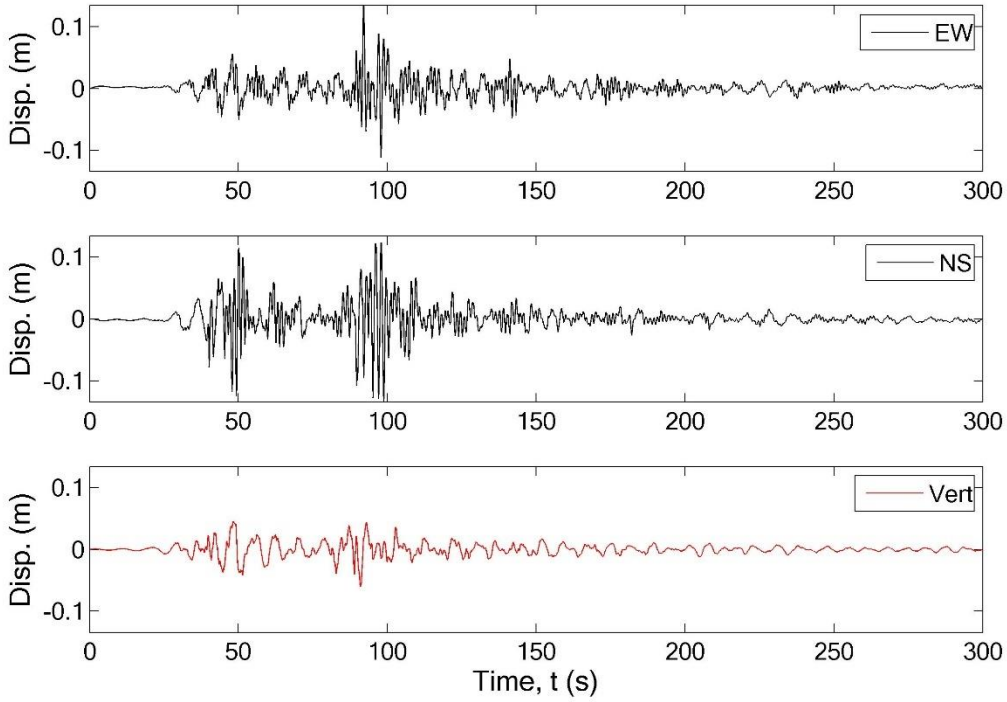

Figure 7.35: Baseline-corrected displacement time histories at MYG010

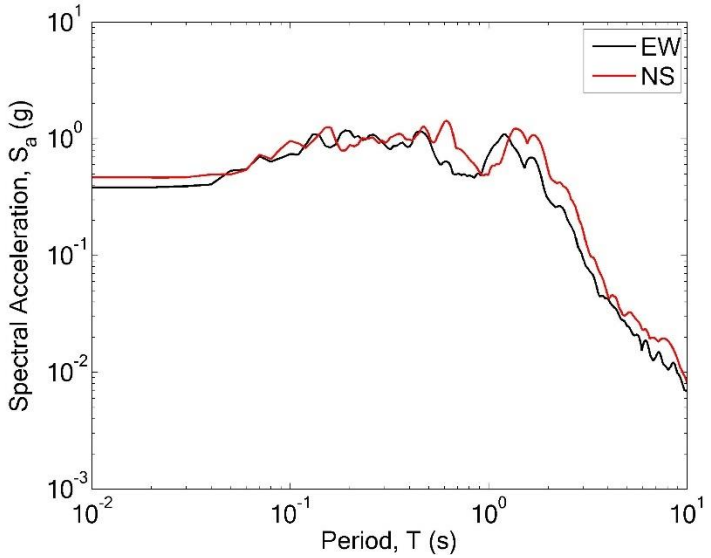

Figure 7.36: Spectral acceleration at MYG010

Although the PGA in the NS direction was higher than in the EW direction, the spectral accelerations at periods longer than about 0.05 seconds were similar in both directions. An increase in spectral acceleration occurred at periods of about 2 seconds in both horizontal directions. Fairly regular acceleration pulses with periods of about 2 seconds were observed in the recorded motion between about 40 to 50 seconds which produced the peak spectral acceleration of a single degree of freedom oscillator with a period of 2 seconds.

The Stockwell power spectrum was used to isolate changes in frequency content that occurred at various times during shaking. As pore pressure increased in the liquefiable soils, the stiffness of the soil decreased. Once the soil liquefied, it became extremely soft and could only transmit very low-frequency motions from the bedrock to the ground surface. The time at which the frequency content decreased rapidly due to liquefaction was identified using a procedure based on the Stockwell time-frequency spectrum (Kramer et al., 2016). Using the approach described in Section 4.3, a rapid drop in frequency content was observed at the ground surface between 40 and 50 seconds, which occurred once the soil liquefied. Figure 7.37 shows the horizontal acceleration times histories and the normalized Stockwell power spectrum at MYG013.

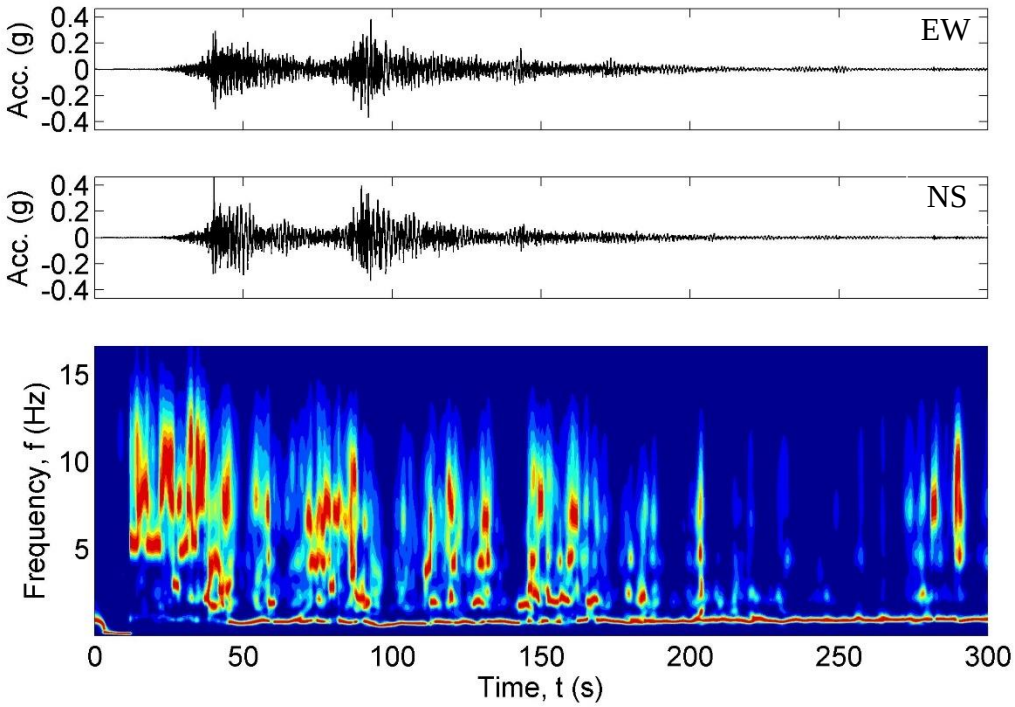

Figure 7.37: Acceleration time histories and normalized Stockwell power spectrum at MYG010.

The Stockwell spectrum in Figure 7.37 showed several distinct shifts in frequency content that corresponded with increases or decreases in the acceleration amplitude. During the initial part of the earthquake, while the amplitude of the motion was low, the frequency content of the motion remained relatively constant. Around 39 seconds, the acceleration amplitude began to increase rapidly, and then at about 46 seconds, the high-frequency content of the motion dramatically decreased. Figure 7.38 shows the horizontal time histories and Stockwell spectrum zoomed in around 46 seconds.

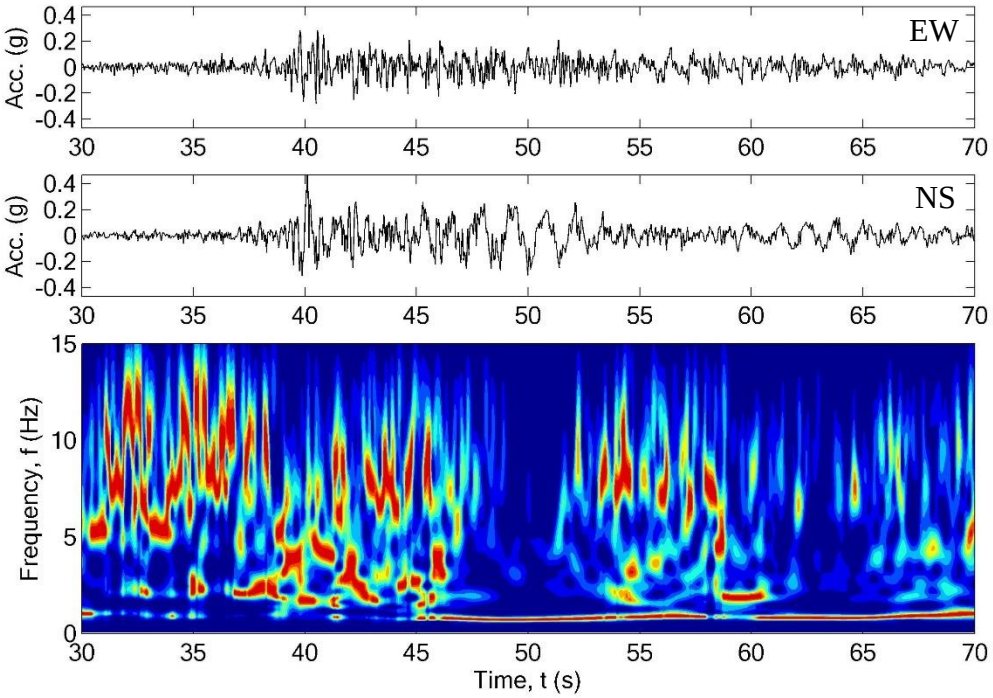

Figure 7.38: Acceleration time histories and normalized Stockwell power spectrum at MYG010 in the vicinity of initial liquefaction triggering.

The modal frequency of the motion remained relatively low after 46 seconds except for occasional short duration high-frequency pulses. After the initial period of strong shaking, the amplitude of the ground motion decreased at about 53 seconds. As the amplitude of the motion decreased, the modal frequency of the motion began to increase. Additional strong shaking occurred around 92 seconds, and the modal frequency of the motion again decreased very rapidly once the strong shaking resumed. Figures 7.39 shows the horizontal time histories and Stockwell spectrum zoomed in around 92 seconds. Once the second period of strong shaking subsided, short duration, high-frequency pulses were again observed in the Stockwell spectrum.

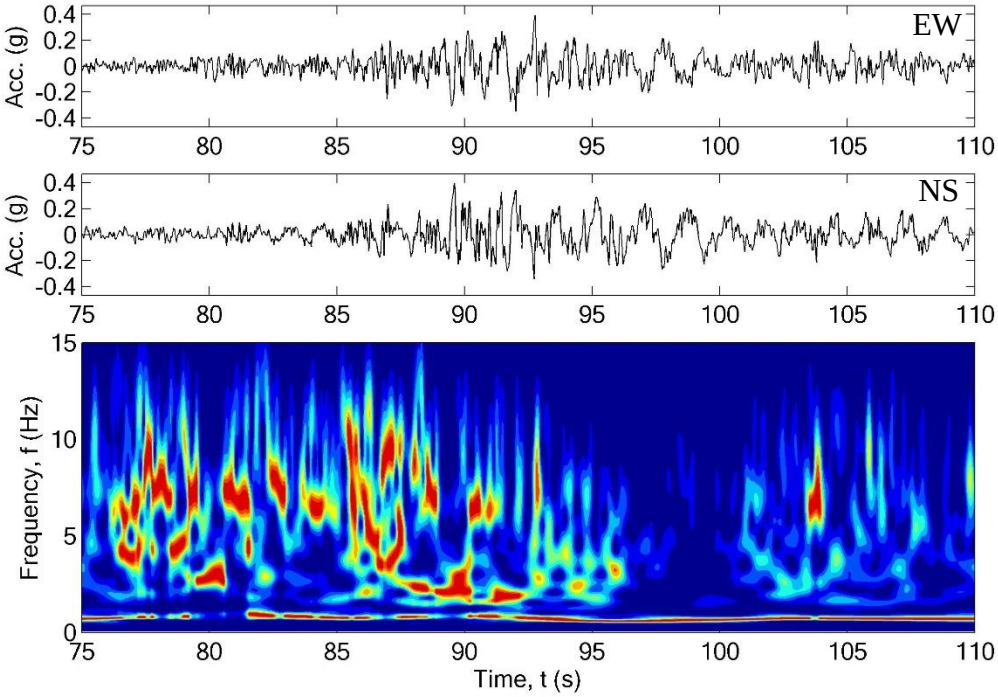

Figure 7.39: Time histories and normalized Stockwell power spectrum at MYG010 in the vicinity of the second frequency content shift.

A step function was fit to the modal frequencies of the Stockwell spectrum and the average frequency content before and the time of liquefaction triggering was estimated. The best-fit step function indicated that liquefaction was likely triggered at about 46 seconds. The medium dense to dense sand had strong dilative tendencies and could transmit high-frequency content motions to the ground surface even in a liquefied state. After the soil initially liquefied, occasional short duration, high-frequency pulses were observed in the Stockwell spectrum during periods of strong shaking. Large and significant shifts in the modal frequency were also observed in the Stockwell spectrum after the soil initially liquefied. The modal frequency increased for short durations, and then returned to its original post-triggering modal frequency. These shifts in frequency content were likely due to dilation, pore pressure dissipation, and additional layers of soil liquefying as the strong shaking continued. The complicated interactions of liquefied soil cannot be determined solely from ground surface recordings. However, the observed behavior can be explained by finite element site response modeling, which is discussed later in this section.

The peak recorded acceleration at the site was 0.47 g and occurred in the NS direction. The empirical procedures for evaluating liquefaction presented in Section 2.3 were based on inferred values of peak ground acceleration at sites where liquefaction did not occur. Because the recorded acceleration time history at MYG010 was affected by liquefied soils, it could not be directly used for liquefaction analysis. Nine stations from the K-net and KiK-net arrays were located within 35 km of the site. However, even the closest station was over 17 km away, which was too far from MYG010 to directly use the recorded ground motions for liquefaction analysis. Figure 7.40 shows a map of the nearby strong motion recording stations.

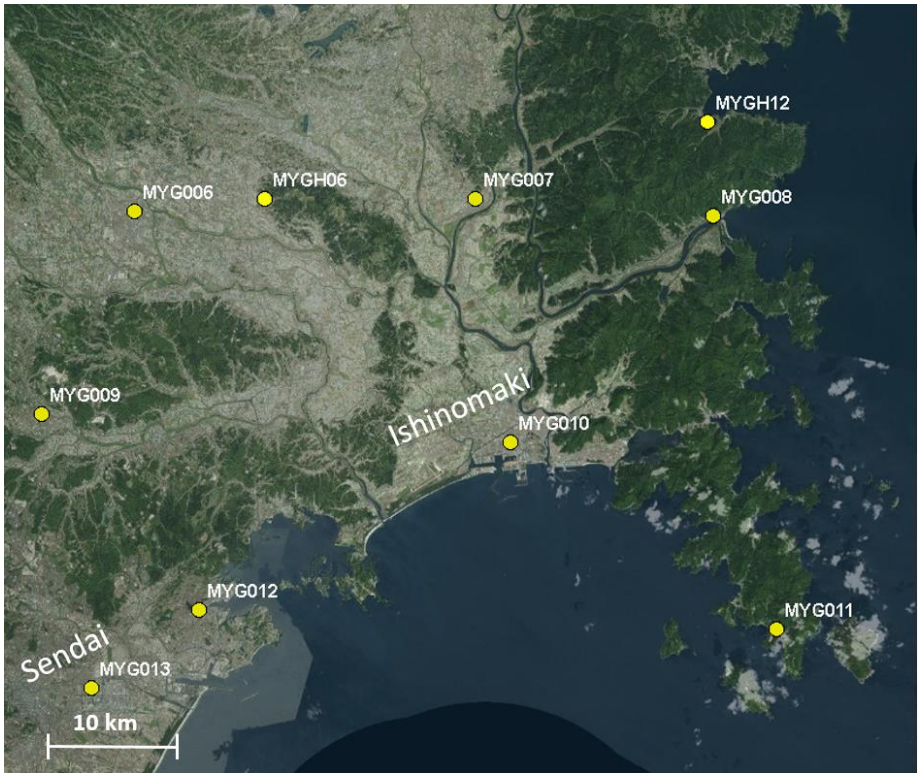

Figure 7.40: Recording stations in the vicinity of MYG010.

Estimated ground motions if liquefaction had not occurred

The PGA that would have been recorded at MYG010 if liquefaction had not occurred can be estimated using ground motion prediction equations (GMPE). GMPE estimates required values of distance to the fault rupture, Rrup, earthquake magnitude, and shear wave velocities in the upper 30 m of the site, v_{s30}. Distances to the fault rupture were documented for Kik-net stations

(Dawood et al., 2015) and were inferred for the K-net stations. Shear wave velocities in the upper 30 m were documented in the K-net and Kik-net metadata.

Two of the nine recording stations were founded on sites with conditions that could not be accounted for in the GMPE and, therefore, could not be used to estimate within-event residuals. The recording station MYG013 showed evidence of liquefaction, and the effects of liquefaction on ground motions were not considered in the GMPE. The recorded value of v_{s30} at MYG007 was less than 95 m/s, which was outside of the range of the data used to develop the BCHydro GMPE. Sufficient data, however, was available from recording stations MYG006, MYG008, MYG009, MYG011, MYGH06, MYG012, and MYGH12 to estimate $S_{a,event}$. Table 7.11 shows the recorded data from the Tohoku earthquake at stations near MYG010.

Table 7.11: Ground motion records from the 2011 Tohoku earthquake near MYG010

Station	v_{s30} (m/s)	R_{rup} (km)	Geometric mean PGA (g)	Geometric mean I_a (m/s)	Significant duration (s)	Distance to MYG010 (km)	Notes
MYG010 (target)	160	45	0.42	8.5	98.7		Liquefied
MYG006	160	64	0.51	12.4	115.1	32	No liquefaction
MYG007	95	52	0.62	9.1	102.3	18	v_{s30} too low for GMPE
MYG008	630	52	0.34	6.2	80.7	22	No liquefaction
MYG009	220	73	0.51	5.0	101.7	35	No liquefaction
MYG011	1680	22	0.82	33.3	75.2	24	No liquefaction
MYGH06	590	64	0.26	3.0	85.5	25	No liquefaction
MYG012	660	58	1.26	22.8	103.1	26	No liquefaction
MYG013	220	64	1.25	12.4	89.4	35	Liquefied
MYGH12	750	54	0.50	11.1	82.2	27	No liquefaction

Although the seven recording stations were in the same region, the durations and amplitudes of the recorded motions varied significantly. Figure 7.41 shows plots of Arias Intensity evolving with time for these seven stations and MYG013, and includes the time at which the PGA occurred at each station. The Arias Intensity in all seven motions increased rapidly during the shaking from the first sub-event between about 40 to 50 seconds. Shaking from the second sub-event caused the Arias Intensity again to increase rapidly between about 85 to 90 seconds. The magnitude of Arias Intensity varied quite significantly from 3.0 m/s at MYGH06 to over 30 m/s at MYG012. The PGA at MYG010 occurred during the first sub-event, as did the PGA at MYG008 and MYGH12. The PGA occurred during the second sub-event at the other stations. Based on the wide distribution of Arias Intensity, the timing of the PGA, and the overall long duration of these motions, no motions showed evidence of unique behavior that precluded its use from assessing the regional effects of shaking near MYG010.

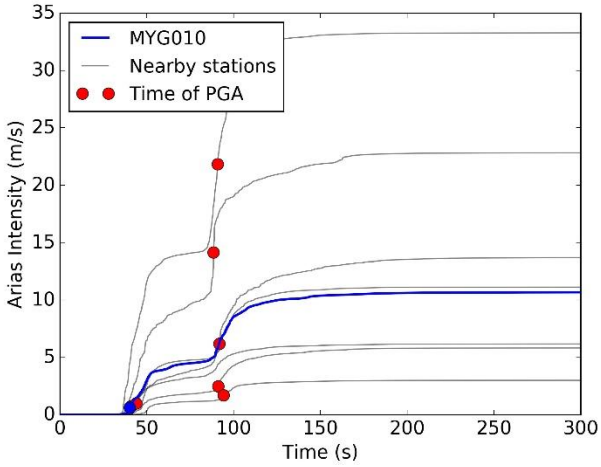

Figure 7.41: Arias intensity recorded at stations near MYG010.

The GMPEs predicted that the PGA at MYG010 would have been 0.38 g if liquefaction had not occurred. However, this value did not include regional source and path effects, and the PGA used for liquefaction triggering analyses should reflect any regional variation that would have also affected the nearby recording stations. A procedure for calculating regionally adjusted PGA values was described in detail in Section 7.1.1. This procedure uses recorded ground motions from nearby stations to calculate a PGA value that is representative of the intensity of shaking if liquefaction had not occurred. The recorded PGA at each site near MYG010 was first adjusted using equation (7.6) to reference shear wave velocity, $v_{s,30}{}^{*}$, and distance, R^{*}, conditions.

Representative values of $v_{s,30}{}^{*}$ = 160 m/s and R^{*} = 45 km were used in this analysis. Then, a regionally adjusted PGA was calculated using equation (7.7). Table 7.12 shows the PGA recorded at each site, as well as the PGA adjusted to the target site conditions.

Table 7.12: Event residuals for the recorded PGA at stations near MYG010

Station	v_{s30} (m/s)	R_{rup} (km)	Distance to MYG010 (km)	Geometric mean PGA (g)	PGA adjusted to target site (g)
MYG010 (target)	160	45	0	0.42	0.42
MYG006	160	64	32	0.51	0.64
MYG008	630	52	22	0.34	0.32
MYG009	220	73	35	0.51	0.60
MYG011	1680	22	24	0.82	0.50
MYGH06	590	64	25	0.26	0.29
MYG012	660	58	26	1.26	1.33
MYGH12	750	54	27	0.50	0.51

These adjusted PGA values ranged from 0.29 to 1.33 g and combined with inverse distance weighting, resulted in an estimated regionally adjusted PGA of 0.52 g at MYG010. This value indicated that the path and source effects likely amplified the PGA in the region of MYG010 by a factor of approximately 1.37 relative to the event-adjusted GMPE prediction. However, this regionally adjusted PGA was significantly higher than the recorded PGA of 0.42 g. The PGAs at five of the nearby recording stations occurred during the second sub-event, while the PGA at MYG010 occurred during the first sub-event before the soil liquefied. The ground motion at MYG010 was likely affected by the presence of elevated pore water pressure and liquefied soil. The effects of elevated pore pressure and liquefaction at MYG010 may have caused the PGA to occur much earlier than it otherwise would have, and diminish the acceleration amplitude during the shaking from the second sub-event.

The process described in Section 7.1.1 was also used to develop a target spectrum. Ground motions that reasonably match this target spectrum can be input into a finite element model. The shear wave velocity of a stiff soil outcrop, which was used to model a halfspace in the finite element model, was assumed to be 290 m/s. Recorded spectral accelerations from nearby stations were adjusted to a reference shear wave velocity, $v_{s,30}{}^{*}$, of 290 m/s, and reference distance, R^{*}, of

45 km using equation (7.6). The target spectral acceleration from the event-adjusted GMPE was then calculated using equation (7.7). Figure 7.42 shows the response spectra from each of the seven stations near MYG010 corrected to the reference conditions.

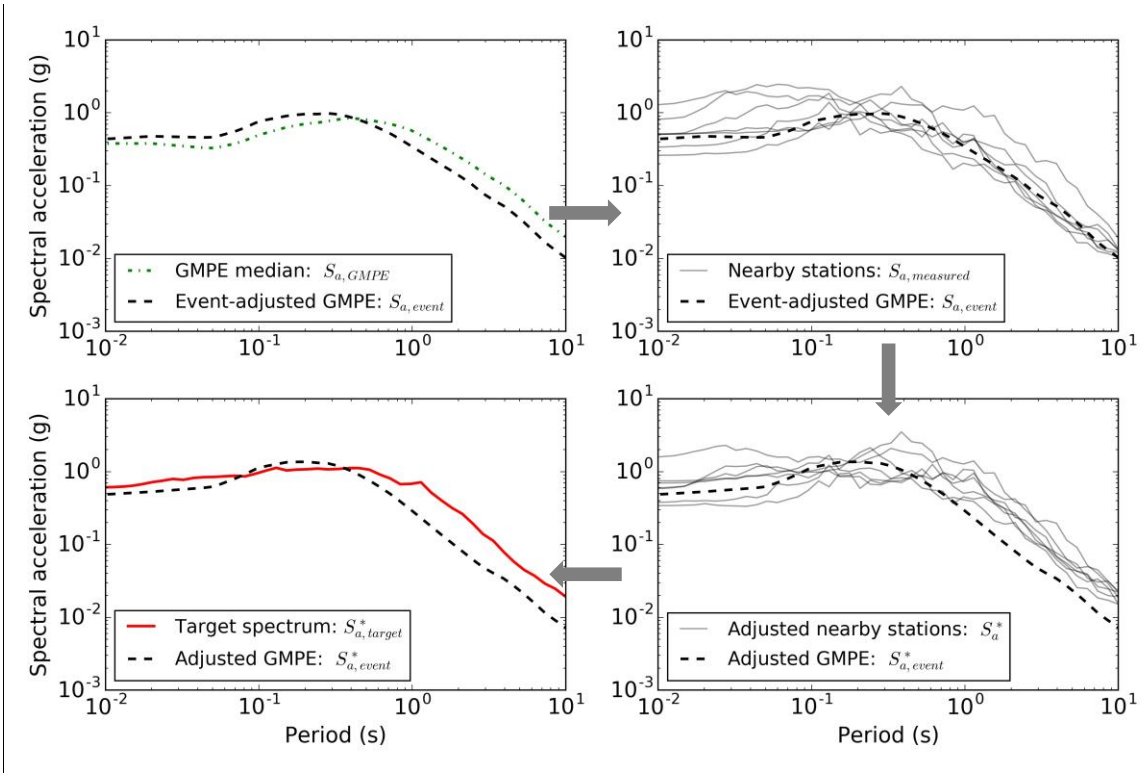

Figure 7.42: Calculation of target spectrum for MYG010 motions.

The adjusted response spectra from the nearby stations were similar to the GMPE-estimated event-adjusted spectra at periods less than about 0.4 seconds. At periods greater than 0.4 seconds, the spectral accelerations from nearby stations had positive residuals, which implied that the spectral accelerations near MYG010 were greater than the event-adjusted spectral accelerations. Motions selected to represent the shaking near MYG010 should reflect this regional variation and the inverse distance-weighted average values of $S_a{}^*$ were used to develop a target spectrum for selecting ground motions.

Over 1,500 records from Tohoku, Maule, Kushiro-Oki and several other long-duration earthquakes were compared to the target spectrum. The motions were first screened so that the durations of the selected motions were similar to the recorded motions near MYG010. The remaining ground motions were then scaled to minimize the sum of squared residuals (SSR) between the target spectrum and the recorded motions. Scaling factors for minimizing the SSR

were limited to a maximum of 3 times the original spectral acceleration values, and the SSR was calculated over periods ranging from 0.01 to 10 seconds. The motions with the smallest SSR were selected to represent the ground motion at stiff soil outcrop near MYG010. Recent design guidelines (FEMA, 2015) recommend selecting a minimum of 11 ground motions that match a target spectrum for site response analysis. Figure 7.43 shows the target spectral acceleration for a stiff soil outcrop near MYG010 and the 11 records that best fit the target spectrum. The scaling factor that was used to minimize the SSR for each motion is also listed in Figure 7.43.

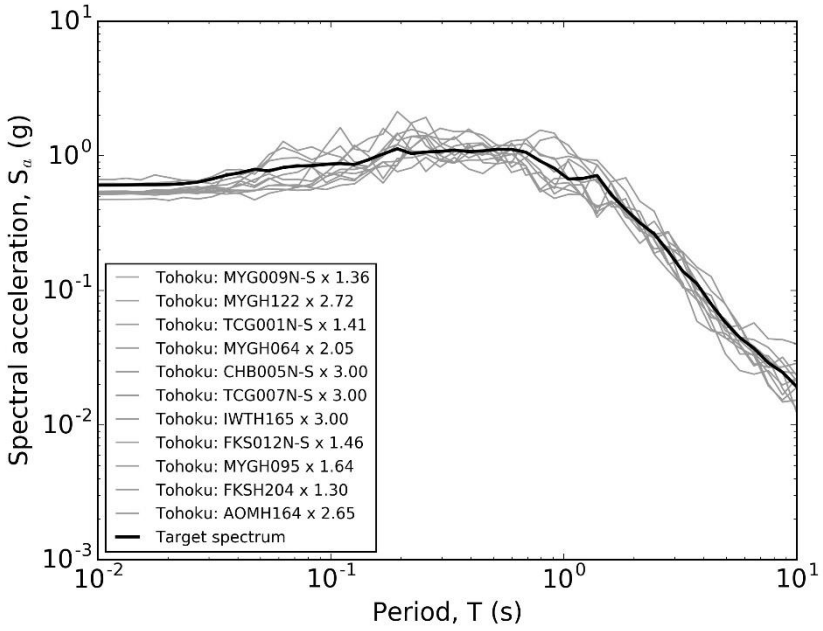

Figure 7.43: Spectral acceleration of ground motions selected to represent shaking at MYG010.

In addition to matching the target spectral acceleration in Figure 7.39, motions that were representative of the shaking at MYG010 should have a relatively long duration and many cycles of loading. Figure 7.44 shows the Arias Intensity and Husid Parameter values for the 11 selected motions selected to represent a stiff soil outcrop near MYG010. The selected motions were all recorded during the Tohoku earthquake, and some of the motions show evidence of multiple sub-events, which was observed in the recorded motions near MYG010.

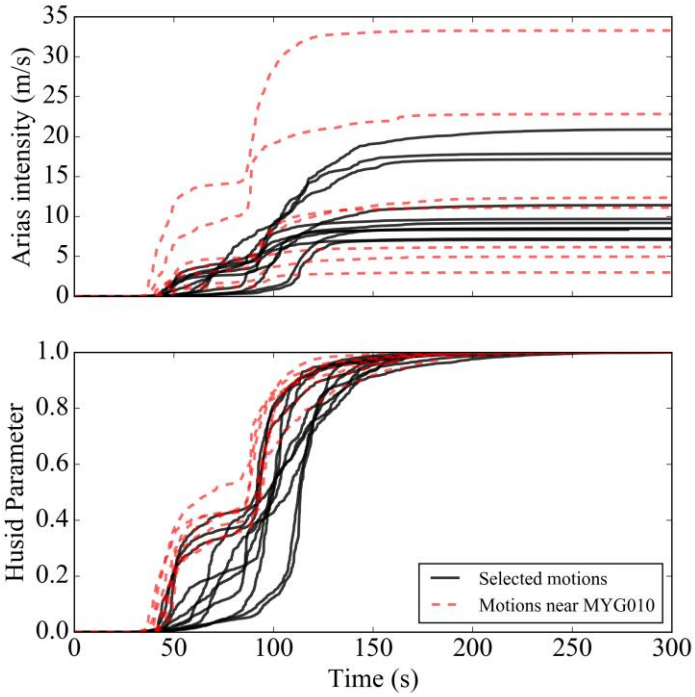

Figure 7.44: Arias Intensity and Husid Parameter of ground motions selected to represent shaking at MYG010.

7.3.4 *Liquefaction*

The clayey sand encountered from the ground surface to a depth of about 2.5 m was above the water table, not saturated, and therefore not susceptible to liquefaction. Saturated sand that was susceptible to liquefaction was encountered at the bottom of the clayey sand and extended to the maximum depth explored during this investigation (8 m). The K-net log indicated that the saturated sand layer extended to a depth of about 15 m. Medium stiff to stiff silt was encountered below the sand layer. Although no description of the sand was provided in the K-net log, it was assumed that the sand between the bottom of the CPT sounding and a depth of 15 m was susceptible to liquefaction. This assumption is necessarily conservative, and the properties of this layer are evaluated in a sensitivity analysis, which is discussed later in this section.

Empirical liquefaction triggering analysis

Soils susceptible to liquefaction will liquefy if the cyclic resistance ratio, CRR, of the soil is less than the cyclic stress ratio, CSR. The empirically-derived CRR values of the soils at MYG010 were estimated using corrected CPT tip resistances, q_{c1Ncs} (Boulanger and Idriss, 2014). The q_{c1Ncs} values of the liquefiable soils ranged from 90 to 240. The lowest adjusted q_{c1Ncs} values were in the medium dense sand between depths of 7.5 to 8 m. Over 200 CPT measurements were taken in liquefaction-susceptible soils, so calculations for individual layers are not shown here.

The CSR values for the empirical liquefaction triggering methods were based a PGA of 0.52 g inferred from recordings at non-liquefied sites. The inferred value of PGA was used to calculate the CSR at MYG010 using the simplified method for liquefaction triggering analysis presented in Chapter 2. Figure 7.45 shows the results of the liquefaction triggering analyses from both cases.

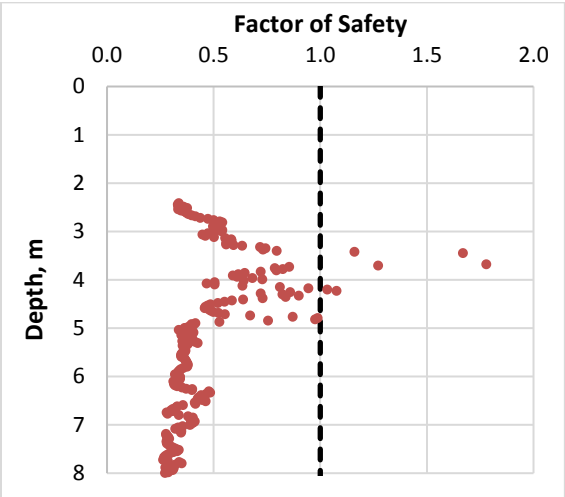

Figure 7.45: Factor of safety against liquefaction at MYG010.

Liquefaction triggering analysis indicated that the susceptible layers likely liquefied during the Tohoku earthquake. Even though direct visual evidence of liquefaction would have been obscured by the tsunami, several lines of evidence indicate that liquefaction likely occurred at the site.

1. The liquefaction susceptibility and triggering analyses indicated that the saturated sand below a depth of 2.5 m had a factor of safety well below 1.0 and likely liquefied during the very strong shaking of the Tohoku earthquake.

2. The crust overlying the liquefiable layer of sand was relatively thin compared to the thickness of the liquefiable layer, and empirically-based procedures for predicting the occurrence of sand boils (Ishihara, 1985) indicated that sand boils likely occurred during the strong shaking. Possible evidence of sand boils could be seen in the aerial photographs taken several days after a M_w = 7.1 aftershock, further indicating that liquefaction was likely to have occurred.
3. The time history recorded during the Tohoku earthquake showed a rapid and significant drop in the high-frequency content of the motion at about 46 seconds. This rapid decrease in high-frequency content occurred immediately after an increase in acceleration amplitude and was likely due to the triggering of liquefaction. Once the medium dense sand below 2.5 m deep liquefied, the deposit could no longer transmit high-frequency motions to the ground surface, resulting in the rapid decrease in high-frequency content observed at the ground surface.
4. Extensive liquefaction-induced damage was reported in similar soils around Ishinomaki at locations that were not inundated by the tsunami.

7.3.5 *Numerical analysis*

To gain additional insight into the behavior of the soil and recorded ground motion at MYG010, a series of nonlinear effective stress site response analyses were performed with the computer program FLIP. The 11 time histories that best matched the estimated non-liquefied target spectrum at MYG010 were used as input motions in the analyses. Material properties were estimated from the results of the subsurface investigations to model the soils at MYG010. The investigation at this site was terminated at a depth of 8 m in the medium dense sand, but the K-net boring logs indicated that the medium dense sand extended to a depth of about 15 m. The data from the K-net investigation provided information about the general classification, shear wave velocity, and relative density of the soil, but did not include important details of the soil, such as soil consistency, fines content, and hammer energy, for liquefaction susceptibility and triggering analyses. The K-net log, however, did provide sufficient evidence to indicate that the shallow sand (between 2.5 and 8 m deep) had similar characteristics as the deep sand (between 8 and 15 m deep).

1. The course soil descriptions (sand and sandy soil) were the same for the deep sand as for the shallow sand.

2. The shear wave velocity profile did not change between the shallow and deep sand.
3. Penetration resistance $(N_1)_{60}$ values ranged from 15 to 29 blows/ft in the shallow sand and 11 to 21 blows/ft in the deep sand. The shallow sand was densest in the upper part of the deposit and transitioned from dense to medium dense below a depth of 5 m. This trend of decreasing relative density in the shallow sand matched the relative density observations in the deep sand.

Without additional information, the plasticity, fines content, and hammer energy of the sand encountered during the K-net investigation were assumed to have similar characteristics as the sand encountered during this investigation. For numerical analysis, the sand between a depth of about 8 m and 15 m was assumed to be susceptible to liquefaction and contain about 10% fine-grained particles. The SPT hammer used during the K-net investigation was assumed to apply 72% of the theoretical maximum energy. A sensitivity analysis was performed to evaluate the effects of these assumed properties, the results of which are presented in the next section. Shear wave velocities recorded during the K-net investigation were also measured in a relatively coarse manner, and the sensitivity of the model to different shear wave velocity profiles was also evaluated.

Soft silt was encountered below the medium dense to dense sand and extended to the maximum depth explored during the K-net investigation. The shear wave velocity of the silt at the bottom of the boring was too low to model as a linear halfspace and could potentially exhibit nonlinear behavior. Since detailed shear wave velocity information below a depth of 20 m was not available, median values from the Toro (1995) generic site class D profile were used to estimate the shear wave velocity below the maximum depth explored. At a depth of 44 m, the shear wave velocity in a generic site class D profile was estimated to be nearly 300 m/s, which was sufficiently stiff to model a linear halfspace.

Table 7.13 shows the input parameters that were used for the 1D effective stress site response model of MYG010. The water table was modeled at the top of the liquefiable sand deposit at a depth of 2.5 m.

The site response analyses were performed using the finite element program, FLIP (FLIP Consortium, 2011). Additional discussion about finite element modeling of liquefiable soils was provided in Chapter 5. The FLIP model can predict softening due to pore pressure generation, soil fabric degradation during the intense shaking, and the dilation and contraction of liquefiable soils.

The analyses predicted that much of the soil that was susceptible to liquefaction would be likely to have liquefied during the Tohoku earthquake. The analysis also showed that the spectral acceleration at the ground surface was very sensitive to the thickness of liquefied soil. The spectral acceleration from the recorded motion showed marked differences compared to the target spectrum that was estimated using GMPE predictions that included within-event residuals. These deviations were assumed to be caused by liquefaction, the effects of which were not captured in the GMPE estimates. The ground motions estimated by FLIP were based on acceleration time histories that were matched to the target spectrum, which was based on regionally adjusted values of $S_a{}^*$. The estimated spectral acceleration at the ground surface should be similar to the recorded ground motion if the liquefiable soil was properly modeled. Figure 7.46 shows a comparison of the recorded spectral acceleration and the spectral acceleration from the FLIP analysis.

Table 7.13: Material properties for modeling site response at MYG010

Depth (m)	Model	Soil description	ρ (kg/cm^3)	v_s (m/s)	$(N_1)_{60}$	ϕ	s_u (kPa)	k (m/s)
1	Multi-spring	sandy Clay	1.5	130	4	--	25	1E-08
2	Multi-spring	sandy Clay	1.6	160	7	--	50	1E-08
2.5	Multi-spring	sandy Clay	1.6	160	11	--	50	1E-08
3	Cocktail glass	Sand[2]	2.1	210	29	39º	--	3E-06
4	Cocktail glass	Sand[2]	2.1	210	29	39º	--	3E-06
5	Cocktail glass	Sand[2]	2.1	190	27	39º	--	3E-06
6	Cocktail glass	Sand[2]	2.1	190	22	39º	--	3E-06
7	Cocktail glass	Sand[2]	2.1	180	23	39º	--	3E-06
8	Cocktail glass	Sand[2]	2.1	180	21	39º	--	3E-06
9	Cocktail glass	Sand[2]	2.1	180	22	39º	--	3E-06
10	Cocktail glass	Sand[2]	2.1	180	16	39º	--	3E-06
11	Cocktail glass	Sand[2]	2.1	180	21	39º	--	3E-06
12	Cocktail glass	Sand[2]	2.1	180	17	39º	--	3E-06
13	Cocktail glass	Sand[2]	2.1	180	24	39º	--	3E-06
14	Cocktail glass	Sand[2]	2.1	180	17	39º	--	3E-06
15	Cocktail glass	Sand[2]	2.1	180	14	39º	--	3E-06
16	Multi-spring	Silt	2.0	170	16	35º	--	1E-08
17	Multi-spring	Silt	2.0	170	14	35º	--	1E-08
18	Multi-spring	Silt	2.0	170	10	35º	--	1E-08
19	Multi-spring	Silt	2.0	170	19	35º	--	1E-08
20	Multi-spring	Silt	2.0	170	10	35º	--	1E-08
30	Multi-spring[1]		2.0	210	10	35º	--	1E-08
44	Multi-spring[1]		2.0	250	10	35º	--	1E-08
	Linear Halfspace[1]		2.0	290				

[1] Shear wave velocity estimated using Toro (1995) median values for site class D.

[2] Sand was susceptible to liquefaction.

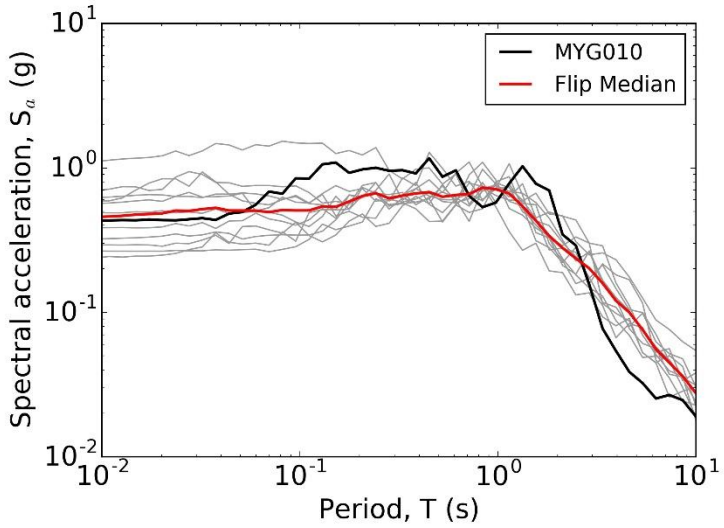

Figure 7.46: Computed and recorded spectral acceleration at MYG010.

The median spectral acceleration predicted by FLIP matched the recorded motion relatively well, although the variance between the individual simulations at short periods was relatively large. Although the input motions were carefully selected to match the target spectrum, the actual motion at the bottom of the profile was not recorded. Differences between the target motions and the actual motion could result in the large short-period variance in Figure 7.46. Likewise, the spectral acceleration at short periods was greatly influenced by the complicated interaction between pore pressure redistribution during shaking and dilation of the medium dense sand, which can produce very high-frequency pulses. The liquefiable sand deposit at MYG010 was relatively thick and ranged from medium dense to dense in relative density. The medium dense sand exhibited strong dilative tendencies even in a liquefied state. The combination of strong dilative tendencies and redistribution of pore pressure caused very strong dilation pulses to occur in the medium dense sand after it initially liquefied. In some cases, these strong dilation pulses produced the PGA of the simulated motion. The post-triggering amplitudes of the ground motions were very sensitive to the characteristics of the input motion. Motions with intense shaking later in the record produced a different PGA than those with intense shaking earlier in the record. Figure 7.47 shows a profile of the pore pressure versus time in the sand deposit for one of the motions selected to represent the Tohoku earthquake at MYG010. Figure 7.48 shows a profile of excess pore pressure versus cycle-adjusted PGA. The layer of soil at a depth of 10 m had the lowest relative density in the deposit and liquefied first. After the soil at a depth of 10 m initially liquefied, pore pressure

redistributed from layers with high total head into layers with low total head over the long duration of the motion. The strong shaking due to a second sub-event caused very strong dilation pulses and produced the PGA after the soil liquefied in this example.

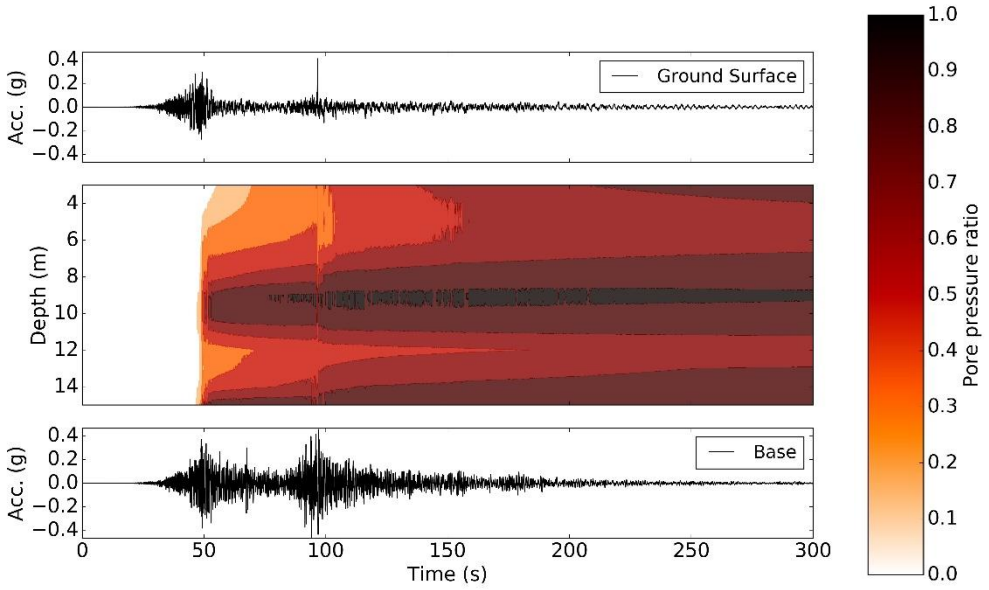

Figure 7.47: Pore pressure generation at MYG010. Input motion MYGH064.

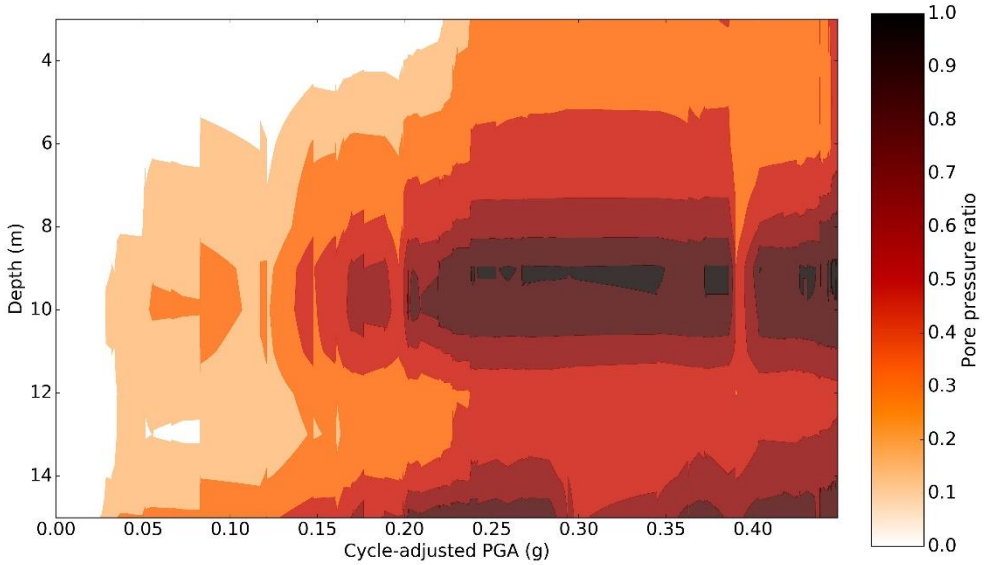

Figure 7.48: Pore pressure generation versus magnitude-adjusted PGA at MYG010. Input motion MYGH064.

The ability of FLIP to capture the liquefaction triggering behavior was further examined by comparing the recorded intensity measures at the time of liquefaction to the estimated intensity measures from the numerical model. If the model was accurately predicting liquefaction triggering, the intensity measures from the numerical model should be similar to the recorded intensity measures. Table 7.14 shows the median values and standard deviation of the estimated intensity measures. Figure 7.49 shows histograms of the cycle-adjusted PGA, Arias intensity, and cumulative absolute velocity at the time of liquefaction.

Table 7.14: Intensity measures at the time of liquefaction at MYG010

Intensity Measure	Recorded	Median	Standard deviation, $\sigma_{\ln IM}$
Magnitude-adjusted PGA	0.22 g	0.22 g	0.16
Arias Intensity	2.0 m/s	3.8 m/s	0.30
Cumulative Absolute Velocity	12.9 m/s	31.3 m/s	0.33

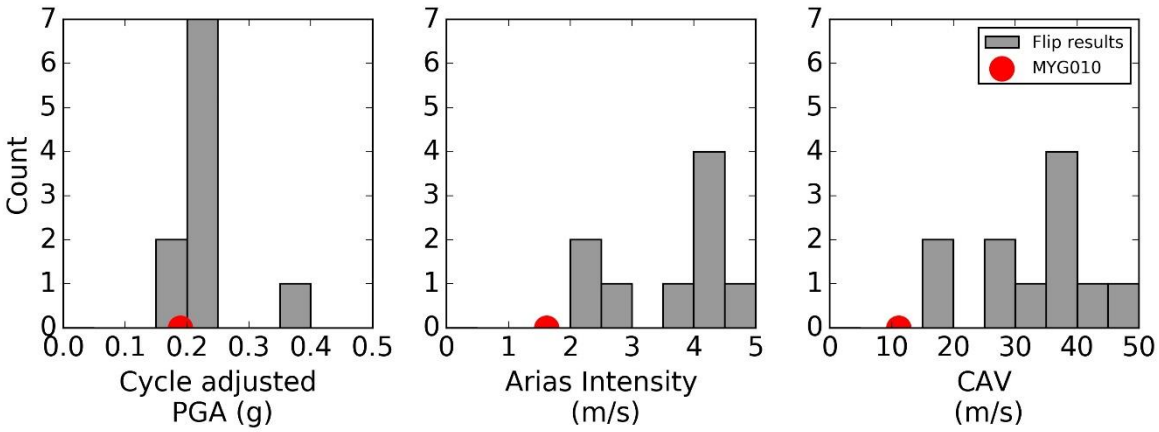

Figure 7.49: Intensity measures at the time of liquefaction at MYG010.

The median cycle-adjusted PGA from the FLIP model was very close to the recorded intensity measures at the time of liquefaction and exhibited relatively modest variance, indicating that FLIP reasonably estimated the cumulative intensity of shaking required to trigger liquefaction. The Arias intensity and cumulative absolute velocity estimated by the FLIP model generally had a relatively large variance and did not provide a good estimate of the intensity of shaking at the time of liquefaction. These intensity measures were more strongly affected by the frequency content of the selected ground motion than cycle-adjusted PGA, which is usually associated with liquefaction triggering. Despite efforts to select ground motions that matched the estimated

spectral acceleration and evolution of Arias Intensity at MYG010, the motions near MYG010 exhibited a wide range of Arias Intensity values and evolutionary patterns.

Figure 7.39 shows the evolution of Arias Intensity at stations near MYG010. Since the recorded ground motion at MYG010 was affected by the presence of liquefied soils, and the intensity of shaking at nearby stations exhibited a wide range of evolutionary intensity measures, selecting ground motions that were representative of the evolution of intensity measures at MYG010, like Arias Intensity and cumulative absolute velocity, may not be feasible with the available data. Despite the difficulty of selecting motions that represented the evolution of shaking intensity at MYG010, the selected ground motions that were used in the FLIP analyses appeared to provide good estimates of the cycle-adjusted PGA at the time of liquefaction.

7.3.6 *Sensitivity analysis*

The investigation performed for this study encountered practical refusal at a depth of 8 m, and limited information was available for the liquefiable soils between depths of 8 to 15 m (deep sand). In the preceding analysis, the fines content, hammer energy, and shear wave velocity values of the deep sand were selected based on properties of the sand between depths of 2.5 and 8 m (shallow sand). The K-net log indicated that the deep sand and shallow sand indeed had similar soil classifications, shear wave velocities, and relative densities. However, due to the coarse information provided in the K-net log, these assumptions should be validated.

To understand the effect of the soil properties for the numerical analyses had on the computed response, sensitivity analyses were performed by varying the shear wave velocity and penetration resistance of the liquefiable soil between 8 and 15 m. Fines content and hammer energy were not recorded during the K-net investigation and based on a reasonable range of fines content and hammer energy, it was possible that the actual $(N_1)_{60}$ values could deviate by about 3 blowcounts from the assumed values. The average shear wave velocity in the shallow sand was 185 m/s, and individual records deviated by a maximum of 25 m/s. Although the shear wave velocity of the deep sand was provided in the K-net logs, the logs provide a relatively coarse interpretation of the shear wave velocity profile. It is reasonable to believe that the shear wave velocity in the deep sand could have deviated by as much as 25 m/s from the reported values.

Four additional FLIP analyses were performed with lower and higher than assumed penetration resistances and shear wave velocities. In each of these analyses, a property was

independently varied, while the other properties were set at the values listed in Table 7.13. Table 7.15 provides the results of the sensitivity analyses, including the median values and standard deviation of the intensity measures at the time of liquefaction. Figure 7.50 shows the median response spectra from the sensitivity analyses.

Table 7.15: Sensitivity of intensity measures at the time of liquefaction to subsurface properties at MYG010

Model	Magnitude-adjusted PGA (g)	Arias Intensity (m/s)	Cumulative Absolute Velocity (m/s)
Recorded	0.22	2.0	12.9
Assumed v_s and $(N_1)_{60}$ values	0.22	3.8	31.3
Low v_s	0.20	4.0	34.3
High v_s	0.21	3.8	34.7
Low $(N_1)_{60}$	0.16	1.9	19.4
High $(N_1)_{60}$	0.29	4.0	25.3

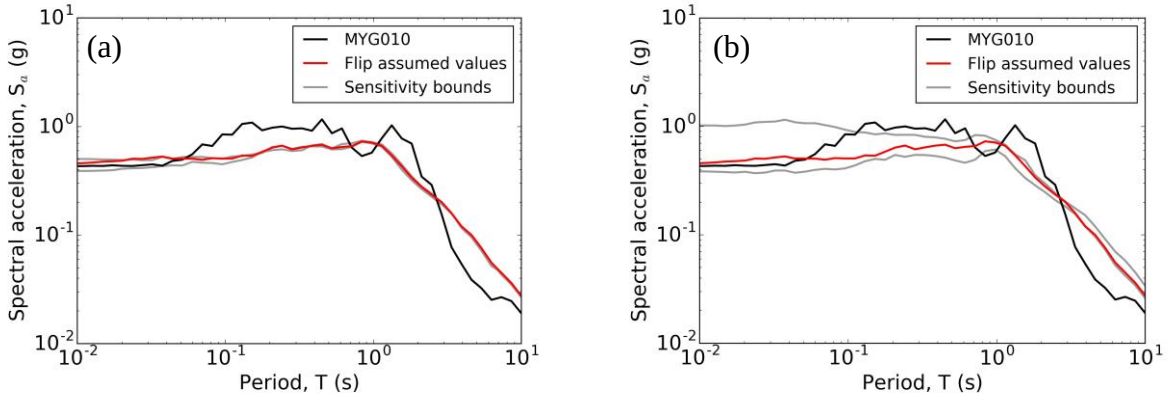

Figure 7.50: Median spectral acceleration from sensitivity analysis at MYG010. (a) Sensitivity to v_s, (b) Sensitivity to $(N_1)_{60}$.

The results of the sensitivity analyses indicated that the uncertainty in the shear wave velocity in the deep sand had only a limited effect on the intensity of shaking necessary to trigger liquefaction and the computed spectral acceleration. Even though the shear wave velocity in the deep sand was uncertain, the variation in the sensitivity analysis was relatively minor compared to the shear wave velocity of the entire profile. The range of possible shear wave velocities in the

deep sand produced $v_{s,30}$ values between 178 and 191 m/s. With respect to site amplification, this difference is relatively minor and only resulted in modest variations in spectral acceleration. Calculation using an event-adjusted GMPEs (Abrahamson et al., 2015) indicated that this range of $v_{s,30}$ values produced PGA value that only varied between 0.46 and 0.48 g.

However, changes in penetration resistance had a relatively large effect on the intensity of shaking required to trigger liquefaction and the computed spectral acceleration. The parameters that affected liquefaction triggering and phase transformation in FLIP have been calibrated based on the penetration resistance of the soil. So, the intensity of shaking necessary to trigger liquefaction and the dilative response after liquefaction is triggered varied significantly with changes in penetration resistance. If the penetration resistances were lower than the assumed values, the liquefiable soil between 8 and 15 m would become too soft once excess pore pressure developed. The soil would have liquefied at a lower intensity of shaking, and the spectral acceleration would have been less than values that were recorded. Likewise, if the penetration resistances were higher than the assumed values, the soil between 8 and 15 m would have liquefied at a higher shaking intensity and would have produced dilation pulses that were much stronger than the observed ground motion. Selected penetration resistances that were much higher than the assumed values would have resulted in short period spectral accelerations that would have been too large. However, the penetration resistance that was assumed for the initial analysis reasonably modeled spectral acceleration and the intensity of shaking necessary to trigger liquefaction. The sensitivity analysis, therefore, indicated that the assumed penetration resistance of the deep sand was appropriate to model the liquefaction triggering and post-triggering response.

7.3.7 *Conclusions*

The thick, saturated layers of medium dense to dense sand between depths of about 2.5 and 15 m likely liquefied during the Tohoku earthquake, although direct surficial evidence of liquefaction was obscured by the tsunami. The Stockwell power spectrum showed a very rapid shift in frequency content around 46 seconds, which indicated that liquefaction likely occurred at that time. Possible evidence of sand boils can be seen in aerial photographs taken following large aftershocks. Evidence of liquefaction was also observed at nearby sites with similar soils that were not inundated by the tsunami.

The Stockwell spectrum showed rapid shifts from high to low-frequency content several times through the duration of shaking. Rapid decreases in frequency content occurred as the soil became very soft during periods of elevated pore pressure. Even though the deposit was relatively thick, the duration of the Tohoku earthquake was sufficiently long that pore pressures likely had time to redistribute within the mass of medium dense to dense sand during shaking. As pore pressures redistributed, excess pore pressure in the layers of liquefied sand may have dissipated, and the liquefied soil layers may have stiffened. Likewise, the medium dense to dense sand exhibited strong dilative tendencies and even in a liquefied state, these layers could transmit high-frequency motions to the ground surface.

Simulations using nonlinear, effective stress analyses indicated that the intensity of shaking could have been sufficient to trigger liquefaction at 46 seconds. The simulations indicated that the amplitude and frequency content of the ground motion after liquefaction was initially triggered were affected by the redistribution of pore pressure within the thick, variably dense sand deposit. The simulations predicted strong dilation pulses after liquefaction was initially triggered, which reasonably matched the spectral acceleration from the recorded motion. However, the behavior of dilation pulses in the liquefied soil depended not only on the relative density and drainage characteristics of the soil but also on the loading history. Since the actual motion at the base of the profile was not available, the post-triggering behavior of the medium dense to dense sand was difficult to infer. Differences in the input ground motions and post-triggering behavior resulted in a wide range of possible short period spectral accelerations. Although important properties for liquefaction analysis were not recorded during the K-net investigation, a sensitivity study showed that the assumed values of these properties were appropriate to model the soil behavior.

7.4 MYG013

The K-net station MYG013 was located on the east side of Sendai in the Miyagino Ward in the prefecture of Miyagi. Figure 7.51 shows the area near the recording station, and Figure 7.52 shows a site plan. UW representatives did not visit the site but, according to the coordinates of the recording station provided by K-net, the K-net recording station was located on the western side of the Sendaishi Miyagino Fire Department property. A slough was located about 600 m to the north of the recording station, and the slough connected to a larger river about 3 km east of the site, which eventually ran into the Pacific Ocean about 7 km east of the site. The Google Earth

DEM indicated the recording station was about 7 m above sea level and about 2 m above the slough elevation. The area surrounding the site appeared to slope gently toward the east.

The strong motion recorder was a standard digital 3-component K-net surface recorder. The station was first installed in 1996 and the recorder was upgraded in 2004 to a K-net 2 recording station. The station recorded ground motions at a rate of 100 samples per second.

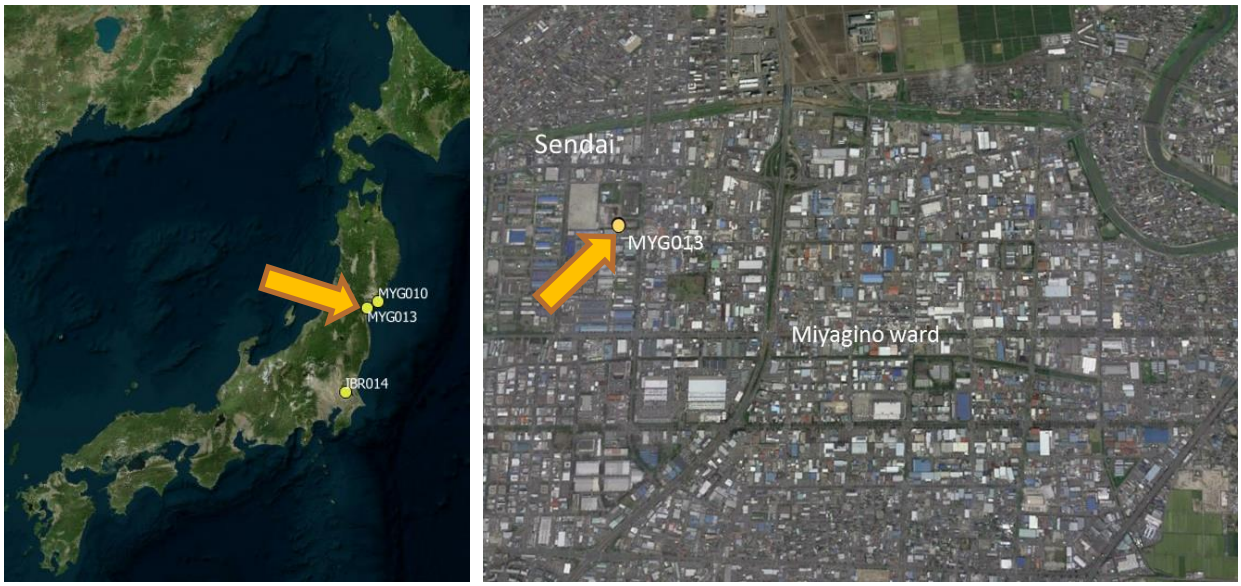

Figure 7.51: Vicinity of MYG013 recording station. Image courtesy of Google Earth, Zenrin.

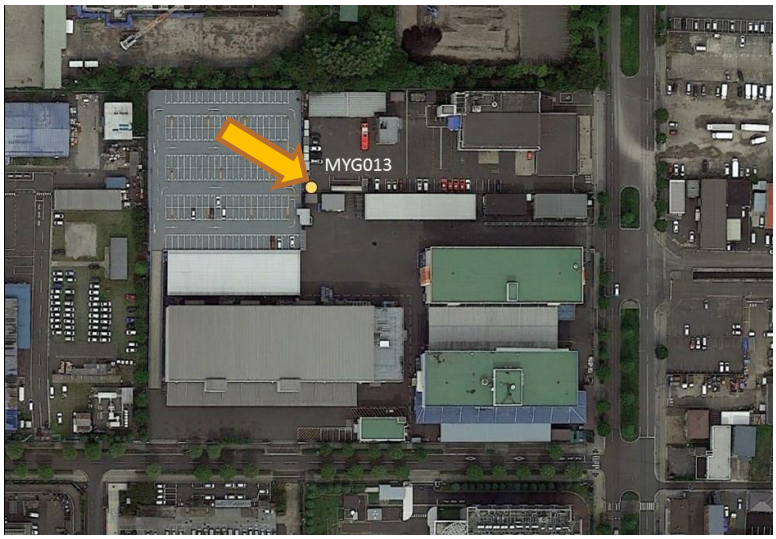

Figure 7.52: Site plan for MYG013. Image courtesy of Google Earth.

7.4.1 *Subsurface conditions*

Previous investigations at the site included a boring that was drilled to a depth of 15 m during the initial installation of the K-net recording station. The K-net log included Standard Penetration Test (SPT) N-values, P- and S-wave velocity measurements, and general soil classifications. Figure 7.53 shows the K-net log at MYG013. The velocity profiles were processed by K-net, and only coarse representations of the depth-varying velocities were provided.

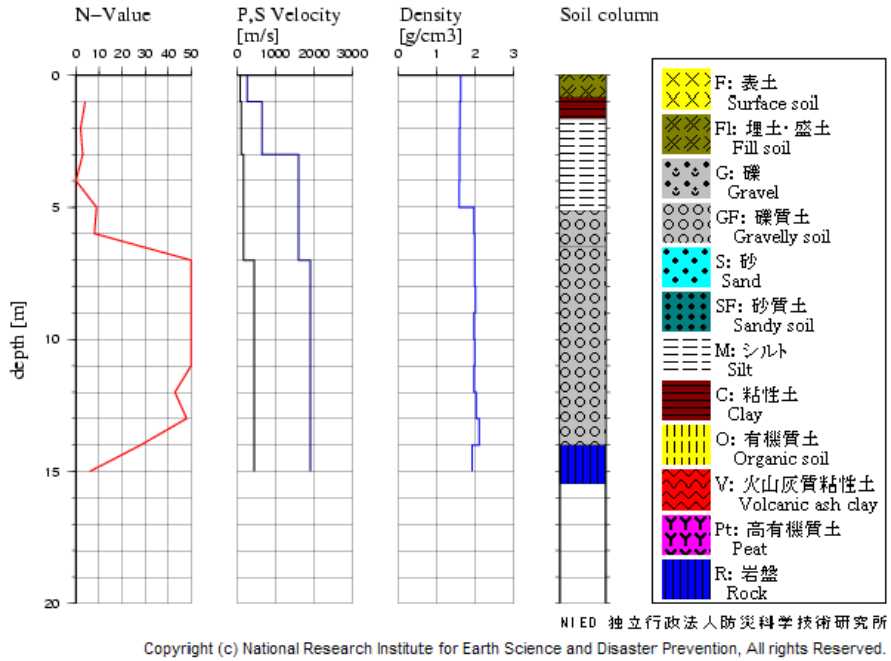

Figure 7.53: K-net boring log for MYG013.

The subsurface conditions at MYG013 were investigated in October 2015 by Tokyo Soil Research (TSR). The investigation included a mud rotary boring to a depth of 8.3 m and a cone penetration test (CPT) probe to a depth of 5.5 m with seismic shear and compressive wave velocity measurements. The hydrostatic pore pressure was measured with the CPT piezometer after pore pressure dissipated tests were performed, and the piezometric surface of the groundwater was found to be about 0.9 m deep at the time of the investigation. This depth was consistent with the elevation of the site relative to the elevation of nearby bodies of water. An increased in compressive wave velocity was also observed at a depth of about 1 m, which was consistent with the presence of saturated soil. During drilling, Standard Penetration Tests (SPT) were performed at about 1 m intervals. A PDI SPT Analyzer indicated that the hammer delivered between 76 to

83% of the theoretical maximum energy. Figure 7.54 shows a schematic of the soil profile with overburden and energy-corrected SPT $(N_1)_{60}$ values, overburden-corrected cone tip resistance, q_{c1}, and shear wave velocity, v_s, values.

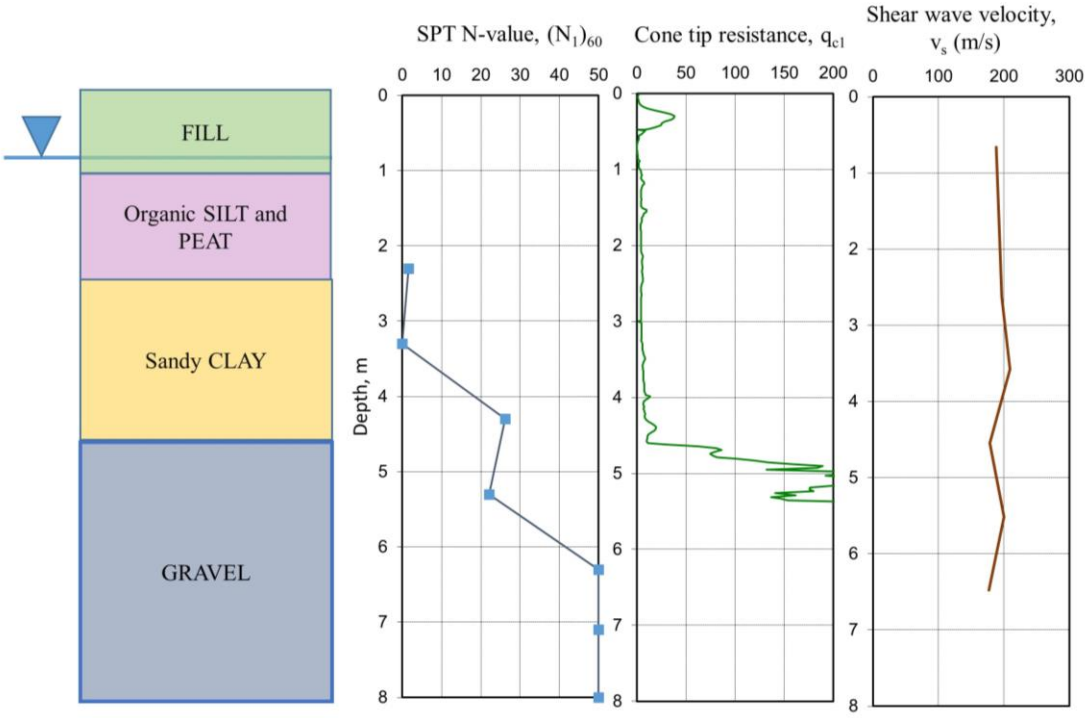

Figure 7.54: MYG013 profile.

The soils encountered during the investigation were classified and logged by Tokyo Soil Research. Summary logs of the boring and CPT probes are included in Appendix A. The subsurface conditions encountered during the investigation were described according to their engineering properties: fill, organic silt and peat, sandy clay, and gravel.

Fill

Fill mantled the ground surface and extended to a depth of about 1 m. No samples were taken in the fill, but representatives from TSR described the fill as sand with gravel and scattered concrete debris in the upper 0.5 m. The relative density of the sand fill was very loose to loose with cone tip penetration q_c values ranging from 0.1 up to 2.2 MPa. Cone tip I_c values indicate the fill consisted of very soft organic soils between depths of 0.5 to about 1 m.

Organic silt and peat

Organic silt and peat (OL) was encountered below the fill, and extended to a depth of about 2.4 m. The consistency of the organic silt and peat was very soft with an SPT N-value of 1 and q_c values ranging from about 0.2 to 0.6 MPa. CPT-based I_c values ranged from 2.7 to 3.8, which indicated the presence of clay and organic material. Field descriptions from TSR representatives indicated that the organic silt exhibited high plasticity. The shear wave velocity of the organic silt and peat ranged from about 190 to 200 m/s based measurements performed during the CPT investigation.

Sandy clay

Sandy clay (CH) was encountered below the organic silt and peat and extended to a depth of about 4.6 m. The sandy clay was very soft from the ground surface to a depth of about 4 m with a measured SPT N-value of 0 and q_c values ranging from about 0.2 to 0.6 MPa. The sandy clay became stiff between 4 and 4.6 m with an SPT N-value of 15 and q_c values ranging from about 0.4 to 1.1 MPa. CPT-based I_c values ranged from 2.6 to 3.2, which indicated the presence of silt and clay. The sand content of the sandy clay ranged from 21 to 39% based on gradation analysis of samples at 3 and 4 m. An Atterberg Limit test at a depth of 3 m indicated the sandy clay had a plasticity index of 32. Traces organic debris was observed in the sandy clay. Shear wave velocity measurements performed during the CPT probe indicated the shear wave velocity of the organic silt and peat ranged from about 180 to 200 m/s.

Gravel

Gravel with sand and silt (GW) was encountered below the sandy clay, and extended to maximum depth explored of 8 m. The relative density of the gravel was medium dense between the bottom of the sandy clay and a depth of about 6 m and had an SPT N-value of 15. The relative density of the gravel transitioned to very dense below 6 m with SPT N-values greater than 50 blows/30 cm. The gravel was of sub-angular shape. A gradation analysis performed on a sample at a depth of 5 m indicated the sand content of the gravel was 23% and the fines content of the gravel was 12%. The gradation analysis also indicated that the median diameter (D50) of the gravel was about 5.4 mm and the 10th percentile diameter (D10) was about 0.046 mm. Practical refusal was encountered during the CPT test in the gravel at a depth of 5.5 m, and the boring was terminated

in the gravel at a depth of 8 m. The K-net log indicated the shear wave velocity of the gravel was about 440 m/s.

The K-net log provided in Figure 7.53 indicated that the gravel extended to a depth of 14 m, where extremely weak to very weak rock was encountered. The extremely weak to very weak rock extended to the maximum depth explored of 15 m.

7.4.2 *Observations at MYG013 site*

Unlike MYG010, the tsunami did not appear to inundate the area surrounding MYG013. An aerial photo taken on March 27, 2011, 12 days after the Tohoku earthquake, showed evidence of possible sand ejecta and ponded water in the parking lot where the recording station was located. Figure 7.55 shows the aerial photo. The thin layer of sand in the parking lot was identified as surficial evidence of liquefaction during the GEER reconnaissance (Ashford et al. 2011). Figure 7.56 shows photos from the GEER reconnaissance, including the presumed sand ejecta. No description of the thin layer of sand was provided, but the photos appeared to show tan-brown fine sand.

Figure 7.55: Aerial photo showing possible ejecta near MYG013 after Tohoku earthquake. Aerial photo of the site taken on March 23, 2011. Image courtesy of Google Earth, Digital Globe.

Figure 7.56: Photos showing surficial evidence of liquefaction at MYG013. (a) Cracking in nearby parking lot. Ejecta was swept away before photo. (b) Ejecta surrounding MYG013 instrument (c) Possible evidence of instrument pad settlement. Images courtesy of Steve Kramer, GEER, taken on April 12, 2011.

The caption for Figure 7.56(a) noted "cracking in parking lot adjacent to MYG013 instrument," and the photograph showed cracks in the upper parking lot, but no ejecta. The cracks appeared to be about 5 cm wide and the parking lot appeared to have deformed downslope slightly. The caption for Figure 7.56(b) noted "extensive liquefaction surrounding instrument," and showed evidence of ejecta surrounding the MYG013 instrument. A pile of sand was located next to the strong motion recorder, and reports from the reconnaissance indicated that the pile may have been ejecta swept into the pile under the blue tarp. The caption for Figure 7.56(c) noted "possible settlement at MYG013 instrument pad."

7.4.3 *Ground motions at MYG013 site*

The strong shaking at MYG013 from the Tohoku earthquake lasted for nearly three minutes, as defined by 0.05 g bracketed duration, and nearly 90 s as defined by 5-95 significant duration. The peak ground accelerations were 1.00 and 1.53 g in the EW and NS directions, respectively, and

the geometric mean of the PGA from the two horizontal components was 1.25 g. The peak vertical acceleration was 0.30 g, and the peak vertical velocity was 0.21 m/s at the ground surface. The peak velocities were 0.37 and 0.73 m/s in the EW and NS directions.

The acceleration amplitude of the horizontal components of motion increased gradually from the beginning of the ground motion up to about 50 seconds. A large acceleration pulse of more than 1.4 g occurred at this time. After the large pulse, the acceleration amplitude and frequency content of the motion decreased rapidly. The acceleration amplitude of the motion remained relatively low until about 80 seconds, when strong ground motions from a second sub-event began. Ground motions from multiple sub-events were commonly observed in the Miyagi region during the Tohoku earthquake. The acceleration amplitude of the second sub-event was very large, and the PGA was 1.53 g. The acceleration amplitude began to diminish around 98 seconds, although the acceleration amplitude remained over 0.05 g well past 160 seconds. Figure 7.57 shows the horizontal and vertical acceleration time histories. Figures 7.58 and 7.59 show the velocity and displacement time histories, which were baseline-corrected by detrending the waveform, filtering out frequencies above 35 Hz and below 0.1 Hz, and removing a high-order polynomial from to the data. The baseline correction was similar to the approach by Boore et al. (2002). Figure 7.60 shows the response spectra of the baseline corrected motions. The motion was generally much stronger in the NS direction than in the EW direction, and the spectral acceleration was much larger in the NS direction than in the EW direction for nearly all periods.

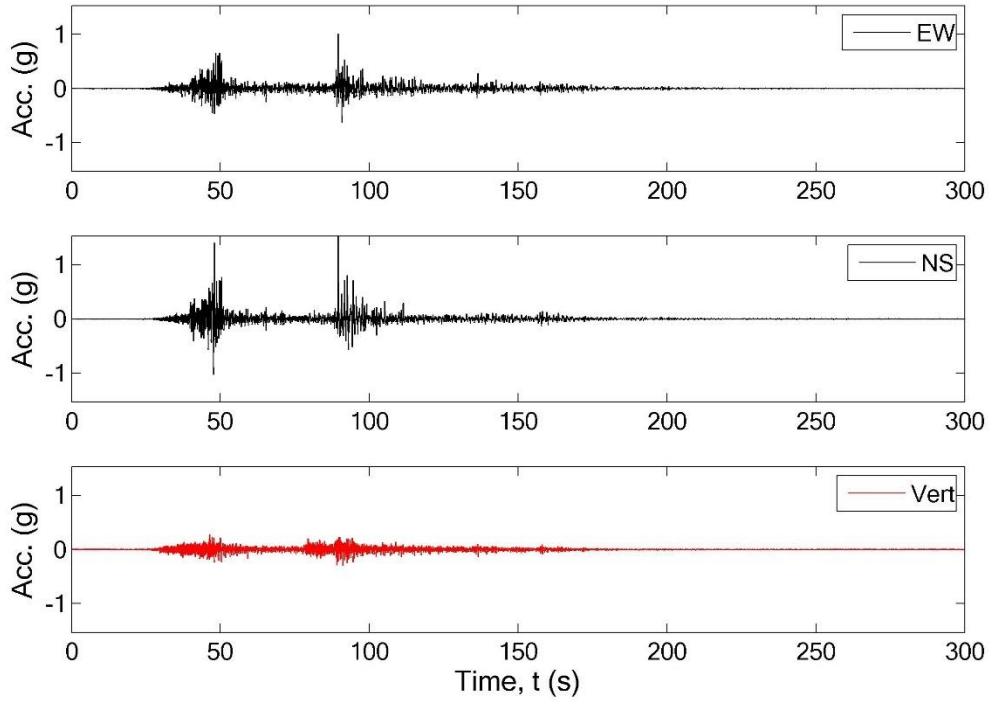

Figure 7.53: Baseline-corrected acceleration time histories at MYG013.

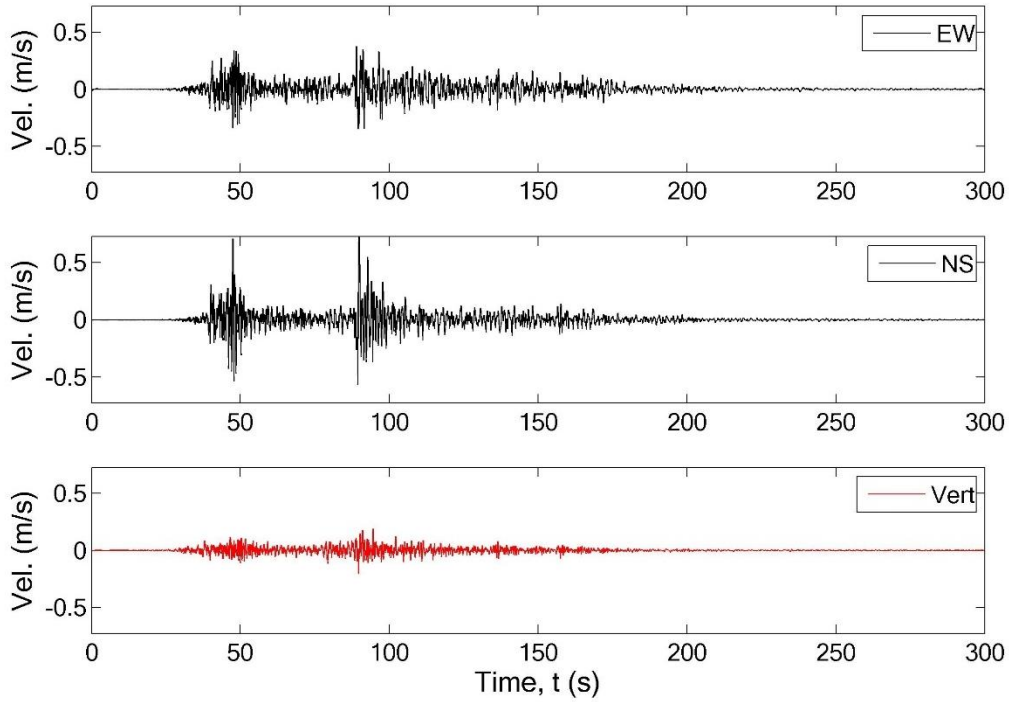

Figure 7.58: Baseline-corrected velocity time histories at MYG013.

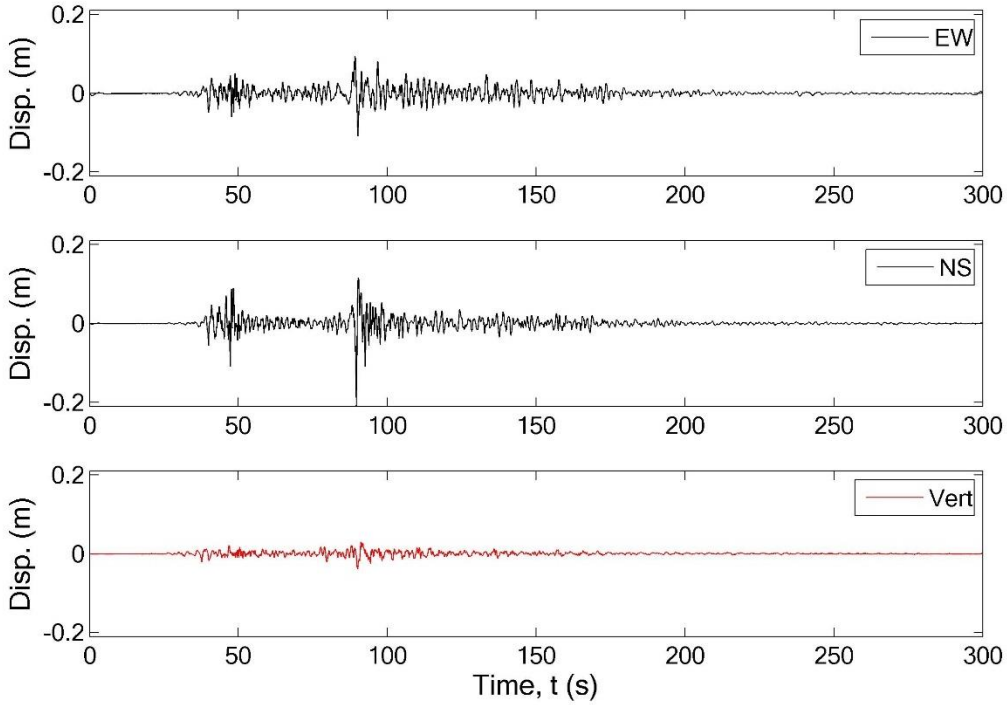

Figure 7.59: Baseline-corrected displacement time histories at MYG013.

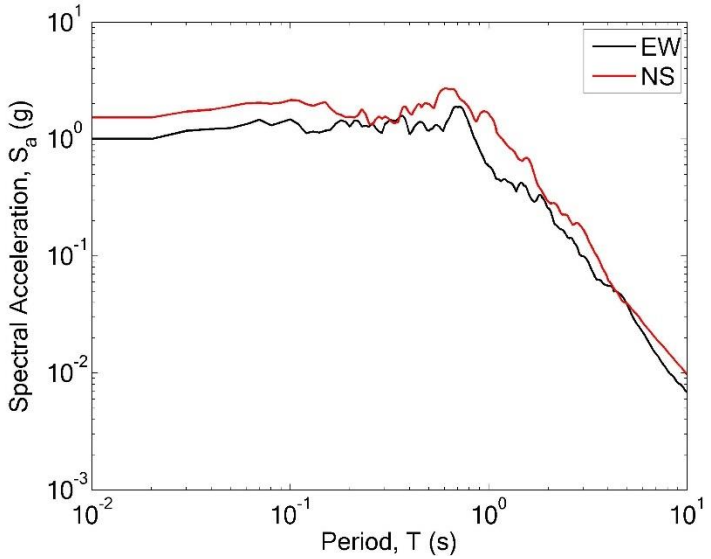

Figure 7.60: Spectral acceleration at MYG013.

The Stockwell power spectrum was used to identify changes in frequency content that occurred at various times during shaking. As excess pore pressure developed during shaking, the stiffness of liquefiable soils decreased. Once the soils liquefied, they became extremely soft and could only transmit very low-frequency motions from the bedrock to the ground surface. If the

frequency content of the bedrock motion remained stationary while liquefaction occurred, a rapid shift in frequency content at the ground surface should occur once the soils liquefy. An apparent shift in frequency content due to liquefaction was identified in the MYG013 motion using a procedure based on the Stockwell time-frequency spectrum (Kramer et al., 2016). Section 4.4 provides additional discussion about identifying the time of liquefaction using the Stockwell time-frequency spectrum. Figure 7.61 shows the horizontal times histories and the normalized Stockwell power spectrum at MYG013.

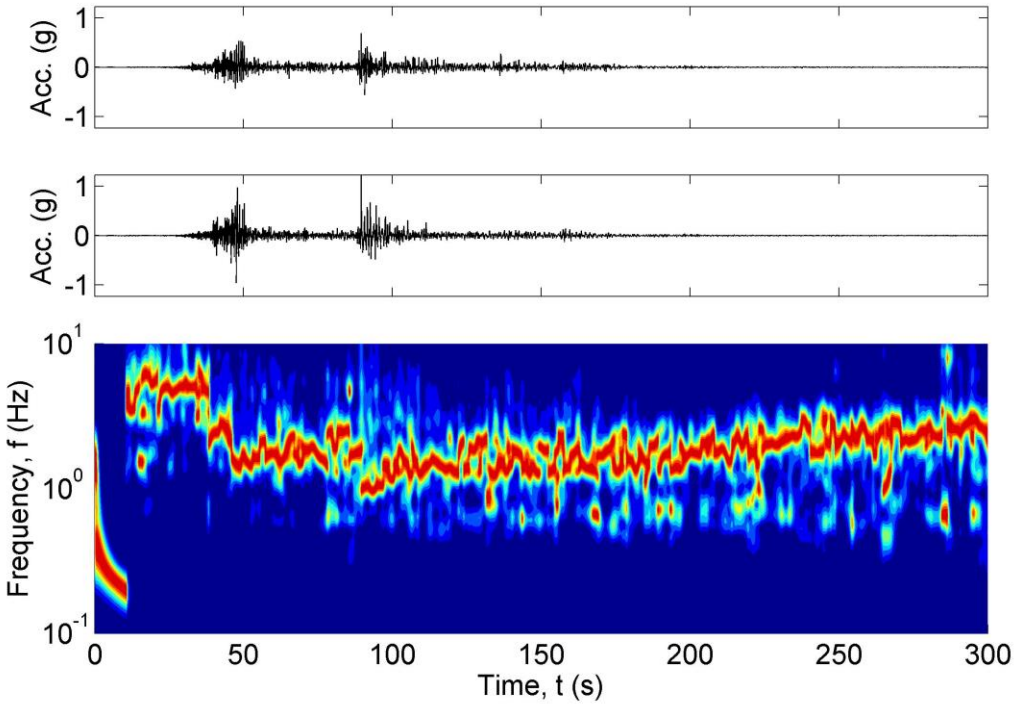

Figure 7.61: Acceleration time histories and normalized Stockwell power spectrum at MYG013.

The Stockwell spectrum in Figure 7.61 showed rapid shifts in frequency content at two times: 39 and 47 seconds. Figure 7.62 shows the Stockwell spectrum zoomed in around these times. The first rapid shift in frequency content occurred relatively early in the ground motion when the acceleration amplitude was low. The PGA prior to 39 seconds was 0.15 g. Accounting for the number of cycles of loading at that time, the CSR was about 0.09, which was much too low to trigger liquefaction in the layer of medium dense gravel. Based on the liquefaction triggering procedure from Idriss and Boulanger (2010), the probability of triggering liquefaction in the gravel

at that level of shaking was less than 0.01%. The arrival of s-waves at the site likely caused this shift in frequency content. A second rapid shift in frequency content occurred around 47 seconds as the acceleration amplitude increased. The PGA prior to 47 seconds was 0.58 g, and the CSR at this time was 0.71. Based on the liquefaction triggering analysis results, the probability of liquefaction triggering at this level of shaking was over 99.9%. So, the rapid shift in frequency content at 47 seconds was much more likely to be the time when liquefaction was first triggered than the shift in frequency content at 39 seconds.

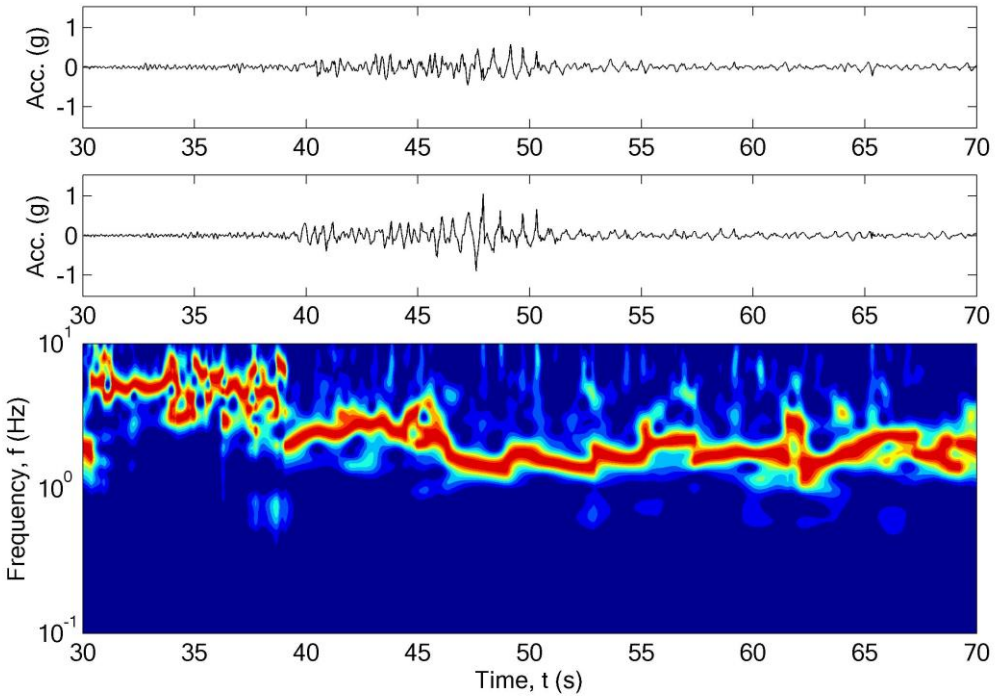

Figure 7.62: Acceleration time histories and normalized Stockwell power spectrum at MYG013 in the vicinity of the rapid frequency content shifts.

The ground motion showed very strong pulse-like behavior after 47 seconds. These pulses were spiky in shape and were presumably caused by the liquefied soil dilating in response to large shear strains as strong shaking continued. Very strong shaking occurred after liquefaction was first triggered, and a dilation pulse produced the PGA at MYG013 at about 89 seconds. Figure 7.63 shows the horizontal Stockwell power spectrum zoomed in between 70 and 130 seconds. Since dilation pulses are spiky in shape, rather than sinusoidal, they create obvious bands of high-frequency amplitude over a short duration. These dilation pulses also created pulses at regular

intervals that can excite single degree-of-freedom oscillators at longer periods. Figure 7.64 shows the acceleration of single-degree of freedom oscillators at periods of 0.5, 1, and 2 seconds. The strong dilation pulses between 89 and 100 seconds not only produced PGA, but also the peak spectral accelerations at these periods.

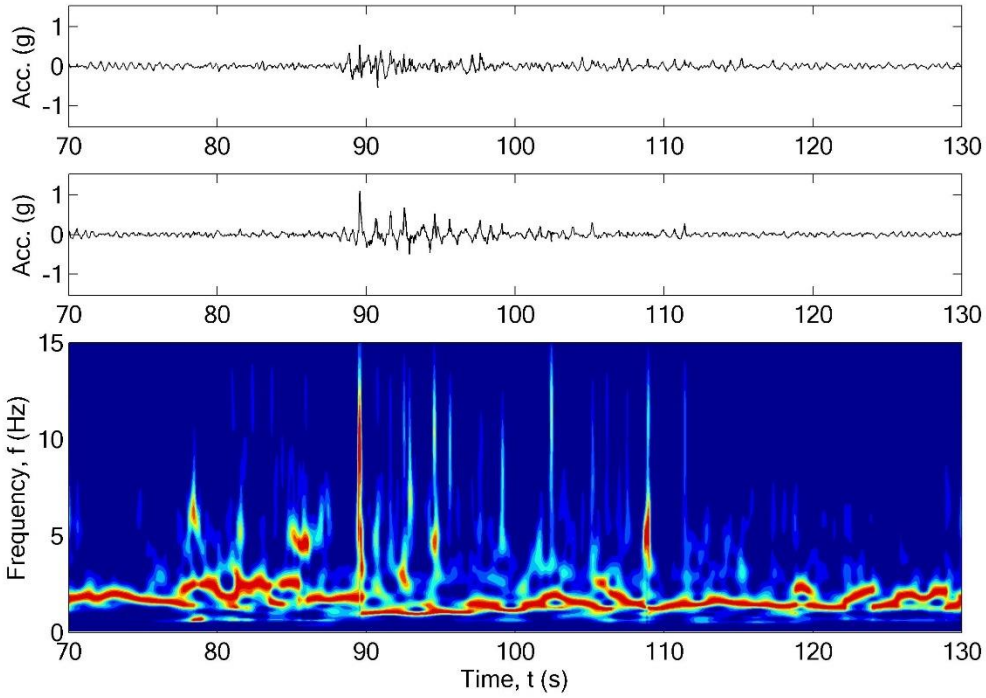

Figure 7.63: Acceleration time histories and normalized Stockwell power spectrum for MYG013 in the vicinity of very large dilation pulses.

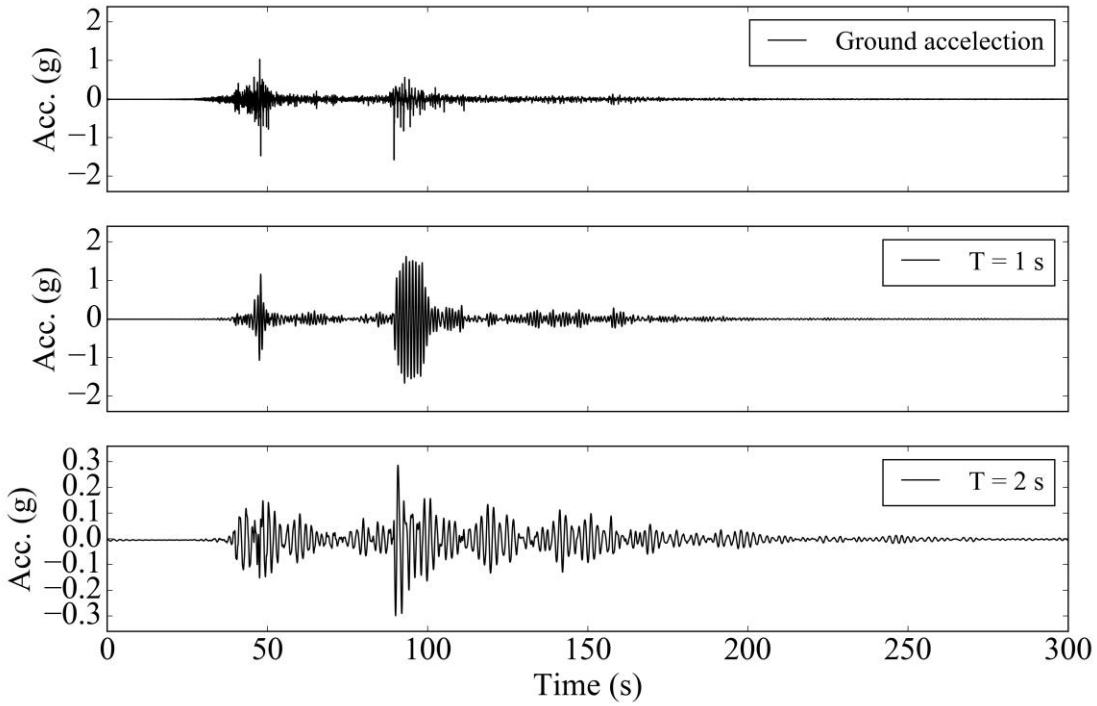

Figure 7.64: Time history response of single degree-of-freedom oscillators from MYG013 ground motion.

As the amplitude of the motion diminished after about 120 seconds, the modal frequency of the motion began to increase. Figure 7.64 shows the horizontal time histories and the Stockwell spectrum between 120 and 300 seconds. The consistent, steady increase in modal frequency may indicate that the liquefied soils drained and stiffened as the amplitude of the shaking diminished. As the soils drained and pore pressure dissipated, the stiffer soil could transmit higher frequency motions to the ground surface. Additional discussion about drainage during shaking was provided in Section 5.3.

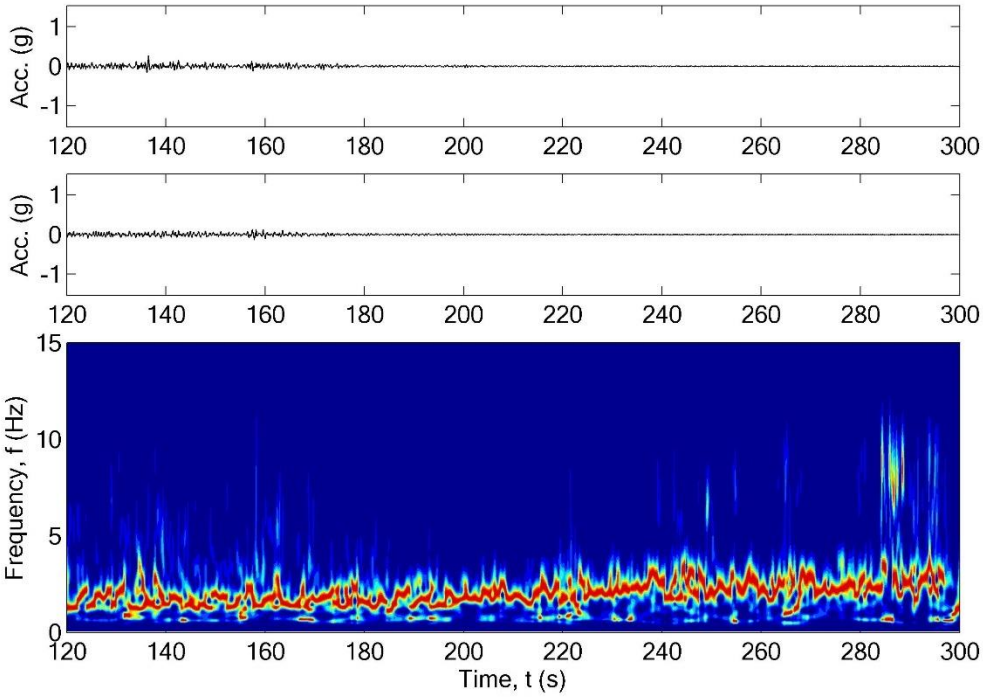

Figure 7.65: Acceleration time histories and normalized Stockwell power spectrum for MYG013 in the vicinity of the modal frequency increase.

The recorded PGA of 1.53 g occurred in the NS direction at about 89 seconds, which was after the time when liquefaction occurred. The empirical procedures for evaluating liquefaction presented in Chapter 2 were based on inferred values of peak ground acceleration from non-liquefied sites. Because the recorded acceleration time history at MYG013 was affected by liquefied soils, it could not be directly used for liquefaction analysis. Five recording stations from the K-net and KiK-net arrays were located within 25 km of the site and recorded motions during the Tohoku earthquake. However, these sites were located too far away from MYG013 to reliably use the recorded ground motions for liquefaction analysis. Figure 7.66 shows the locations of the nearby strong motion recording stations.

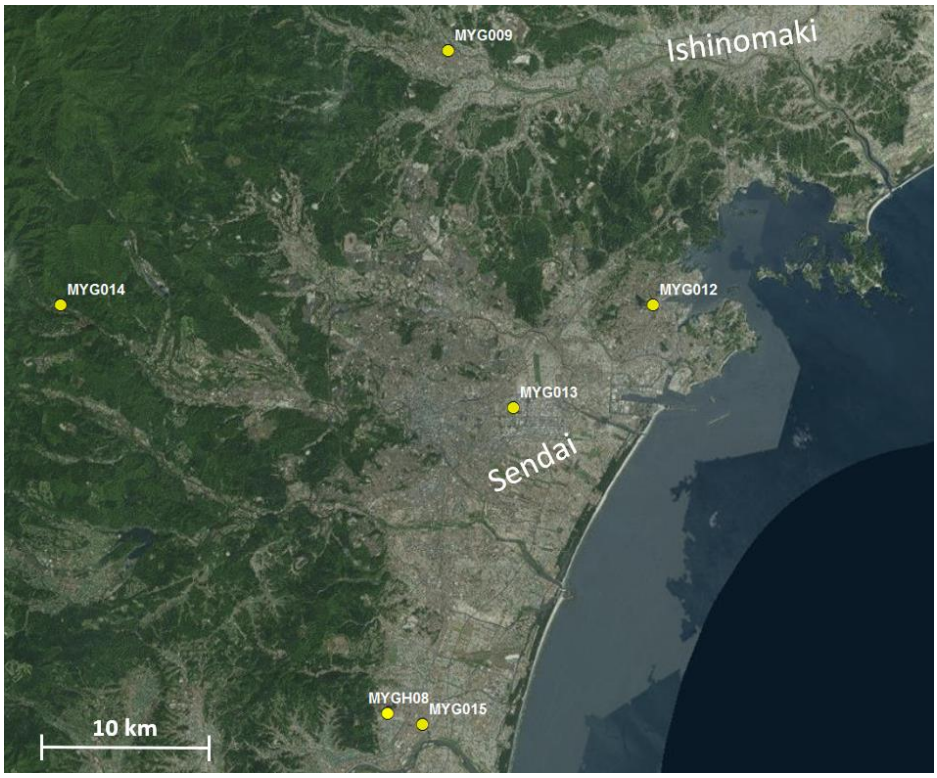

Figure 7.66: Recording stations in the vicinity of MYG013.

The PGA that would have been recorded at MYG013 if liquefaction had not occurred can be estimated using ground motion prediction equations (GMPE). GMPEs provide a median estimate of the ground shaking at a site with consideration for the source, path, and site effects. GMPE estimates require values of distance to the fault rupture, R_{rup}, earthquake magnitude, M_w, and shear wave velocities in the upper 30 m of the site, v_{s30}. Dawood et al. (2015) documented distances from the stations to the fault rupture or KiK-net stations. The distances to the fault rupture were inferred for the K-net stations. Shear wave velocities in the upper 30 m were documented in the K-net and Kik-net metadata.

The five recording stations closest to MYG013 had sufficient data to estimate $S_{a,event}$ with the BCHydro GMPE. For liquefaction triggering analysis, the PGA, or $S_{a,event}$ at a period of 0 seconds, was first calculated using the event-adjusted GMPE. Table 7.16 shows the recorded data from the Tohoku earthquake at stations near MYG013.

Table 7.16: Ground motion records from the 2011 Tohoku earthquake near MYG013

Station	v_{s30} (m/s)	R_{rup} (km)	Geometric mean PGA (g)	Geometric mean I_a (m/s)	Significant duration (s)	Distance to MYG013 (km)	Notes
MYG013 (target)	220	64	1.25	18.2	89.4		Liquefied
MYG012 (K-net)	660	58	1.26	22.8	103.1	10	No liquefaction
MYG009 (K-net)	220	73	0.51	5.82	101.7	20	No liquefaction
MYG014 (K-net)	140	90	0.46	9.7	111.8	26	No liquefaction
MYGH08 (KiK-net)	200	67	0.27	3.8	112.4	19	No liquefaction
MYG015 (K-net)	230	65	0.39	14.4	115.8	19	No liquefaction

The stations near MYG013 exhibited a wide range of shaking intensities, including a range of Arias Intensity from 3.8 to 22.8 m/s. Figure 7.67 shows plots of Arias Intensity evolving with time at these five stations and at MYG013. Large variability in the intensity of shaking between nearby recording stations was common in the Miyagi Prefecture during the Tohoku earthquake. This large variation was also observed at MYG010. However, despite the large range of Arias Intensities, the durations of shaking were very similar in the recorded motions near MYG013. The significant duration of the nearby motions only varied between 103 and 115 seconds. The time at which the PGA occurred was also fairly uniform, and Figure 7.67 also indicates the time of the PGA in each motion. Even though the PGAs and Arias Intensities of the motions near MYG013 varied significantly, no discernable trends or outliers indicated individual stations had different source or path effects than MYG013. The shape of the evolution of Arias Intensity and timing of the PGA were similar at all of recording stations, although the PGA at MYG013 occurred at a slightly larger Arias Intensity than most of the other nearby stations. The time-frequency analysis indicated that liquefaction occurred at approximately 47 seconds at MYG013, and the PGA occurred due to a very strong dilation pulse at 89 seconds after the soil had liquefied. The presence of elevated pore pressure and liquefied soils likely affected the evolution of Arias intensity at

MYG013. As shown in Figure 7.67, the Arias Intensity at MYG013 increased more rapidly during the initial shaking than the other stations.

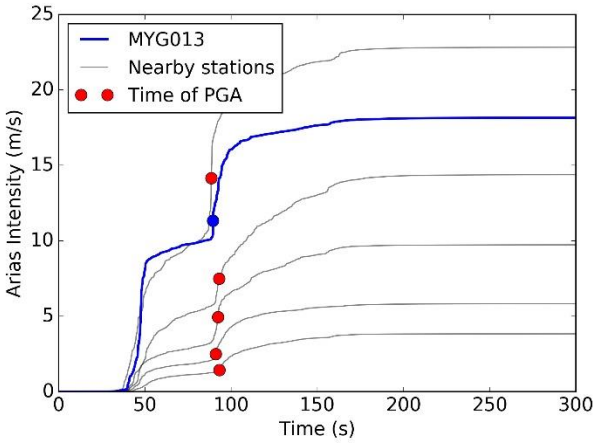

Figure 7.67: Arias intensity recorded at stations near MYG013.

Estimated ground motions if liquefaction had not occurred

The GMPEs predicted that the PGA at MYG013 would have been 0.34 g if liquefaction had not occurred. However, this value did not include regional source and path effects, and the PGA used for liquefaction triggering analyses should reflect any regional variation that would have also affected the nearby recording stations. A procedure for calculating regionally adjusted PGA values was described in detail in Section 7.1.1. This procedure uses recorded ground motions from nearby stations to calculate a PGA value that is representative of the intensity of shaking if liquefaction had not occurred. The recorded PGA at each site near MYG013 was first adjusted using equation (7.6) to reference shear wave velocity, $v_{s,30}{}^{*}$, and distance, R^{*}, conditions. Representative values of $v_{s,30}{}^{*}$ = 220 m/s and R^{*} = 64 km were used in this analysis. Then, a regionally adjusted PGA was calculated using equation (7.7). Table 7.17 shows the PGA recorded at each site, as well as the PGA adjusted to the target site conditions.

Table 7.17: Event residuals for the recorded PGA at stations near MYG013

Station	v_{s30} (m/s)	R_{rup} (km)	Distance to MYG013 (km)	Geometric mean PGA (g)	PGA adjusted to target site (g)
MYG013 (target)	220	64	0	1.25	1.25
MYG012	660	58	10	1.26	1.22
MYG009	220	73	20	0.51	0.54
MYG014	140	90	26	0.46	0.58
MYGH08	200	67	19	0.27	0.29
MYG015	230	65	19	0.39	0.39

These adjusted PGA values ranged from 0.29 to 1.22 g. The estimated regionally adjusted PGA at MYG013 was 0.60 g, based on inverse-distance weighting. This value was significantly greater than the 0.34 g PGA estimated without regional adjustment and the path and source effects likely amplified the PGA in the region of MYG013. However, this regionally adjusted PGA was significantly lower than the recorded geometric mean PGA of 1.25 g. Since the PGA occurred after the soil liquefied, the PGA at MYG013 was likely affected by the presence of elevated pore water pressure and liquefied soil. Site response effects and amplification due to liquefied soil cannot be accounted for in the GMPE.

The process described in Section 7.1.1 was also used to develop a target spectrum. Ground motions that reasonably match this target spectrum can be input into a finite element model. The shear wave velocity of the halfspace in the finite element model was 400 m/s. The recorded spectral accelerations from nearby stations were adjusted to a reference shear wave velocity, $v_{s,30}{}^{*}$, of 400 m/s, and reference distance, R^{*}, of 64 km using equation (7.6). The target spectral acceleration was then calculated using equation (7.7). Figure 7.68 shows the response spectra from each of the five stations near MYG013 corrected to the reference conditions.

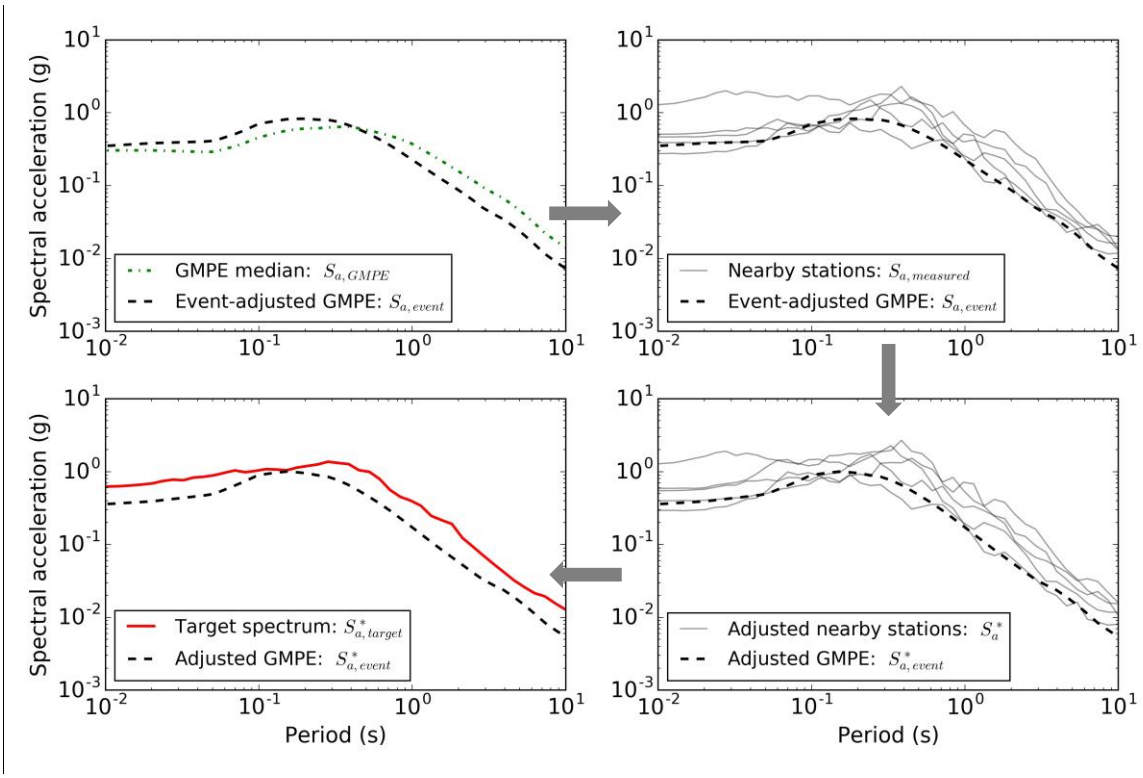

Figure 7.68: Calculation of target spectrum for MYG013 motions.

The adjusted response spectra from the nearby stations had positive residuals at all periods. These positive residuals implied that the source and path effects amplified the spectral acceleration at MYG013 at all periods. Motions selected to represent the shaking in the vicinity of MYG013 should reflect this regional variation. The inverse distance-weighted average values of $S_a{}^*$ shown in Figure 7.68 were used to develop a target spectrum for selecting ground motions.

Over 1,500 records from Tohoku, Maule, Kushiro-Oki and several other long-duration earthquakes were compared to the target spectrum. The motions were first screened so that the duration of the selected motions was similar to the recorded motions near MYG013. The remaining ground motions were then scaled to minimize the sum of squared residuals (SSR) between the target spectrum and the recorded spectral acceleration. The scaling factors were limited to a maximum of 3 times the original spectral acceleration values, and the SSR was calculated over periods ranging from 0.01 to 10 seconds. The motions with the smallest SSR were selected to represent the ground shaking at a stiff soil outcrop at MYG013. Recent design guidelines (FEMA, 2015) recommend selecting a minimum of 11 ground motions that match a target spectrum for site response analysis. Figure 7.69 shows the target spectral acceleration for a

stiff soil outcrop near MYG013 and the 11 records that best fit the target spectrum. The calculated scaling factors that minimized the SSR for each motion are also listed in Figure 7.69.

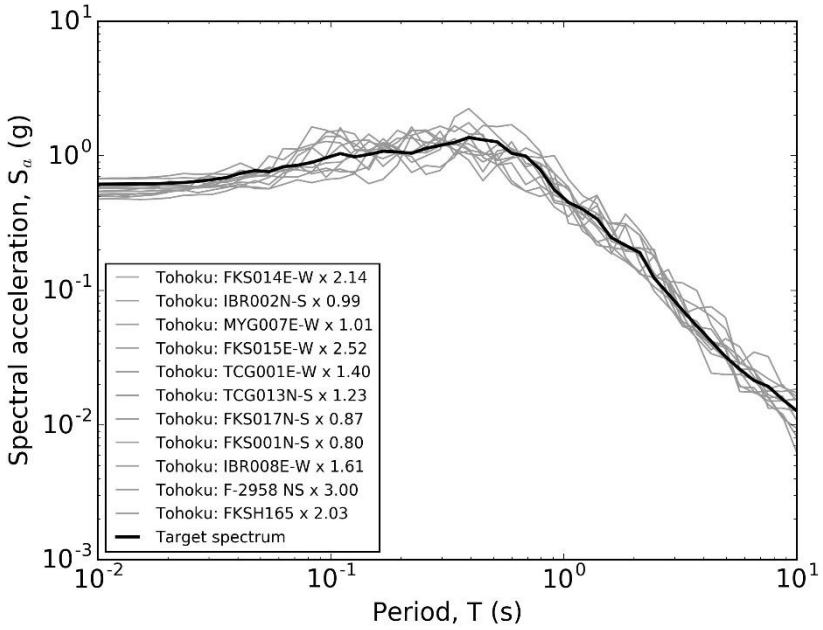

Figure 7.69: Spectral acceleration of ground motions selected to represent shaking at MYG013.

In addition to matching the target spectral acceleration in Figure 7.69, motions that were representative of the shaking at MYG013 should have a relatively long duration and many cycles of loading. Figure 7.70 shows the Arias Intensity and Husid Parameter values for the 11 selected motions.

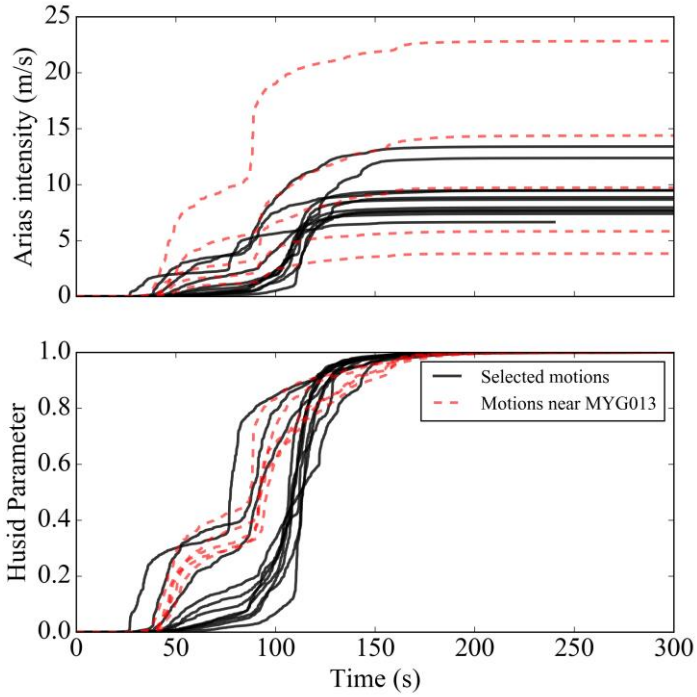

Figure 7.70: Arias Intensity and Husid Parameter of ground motions selected to represent shaking at MYG013.

7.4.4 *Liquefaction*

Based on field plasticity descriptions and CPT-based I_c values, the organic silt and peat and sandy clay were not susceptible to liquefaction. The organic silt and peat and sandy clay extended to a depth of 4.6 m, where medium dense gravel was encountered. The gradation of the gravel was 65% gravel, 23% sand, and 12% fine-grained particles, indicating that gravel was well-graded and the gravel was in a matrix of sand and silt. The gravel was susceptible to liquefaction, although the gravel became very dense below a depth of 6 m. The very dense gravel was unlikely to liquefy even during the extremely strong shaking of the Tohoku earthquake. Therefore, the medium dense gravel between 4.6 and 6 m deep was the only soil encountered in the subsurface investigation that was susceptible to liquefaction and was likely to have liquefied.

Empirical liquefaction triggering analysis

Soils that were susceptible to liquefaction liquefy if the cyclic resistance ratio, CRR, in the layer was less than the cyclic stress ratio, CSR. The empirically derived CRR of the soil at MYG013 was estimated using depth and fines content-adjusted SPT N-values, $(N_1)_{60cs}$ (Idriss and Boulanger, 2010) or depth and friction ratio-corrected CPT tip resistance, q_{c1Ncs} (Boulanger and Idriss, 2014). One SPT test was performed in the medium dense gravel and the resulting $(N_1)_{60cs}$ value was 24 blows/ft. Tokyo Soil Research performed the SPT tests at 4-inch intervals and they recovered full-length samples. Even in the samples with N-values greater than 50 blows/ft, at no interval did the field N-values increase rapidly, indicating that gravel particles did not become lodged in the driving shoe. CPT tests in the layer of medium dense gravel resulting in q_{c1Ncs} values ranging from 87 to over 300. The CRR values was encountered about 5 m deep. Table 7.18 shows the calculation of $(N_1)_{60cs}$ values. The calculation of q_{c1Ncs} values was similar, but over 40 CPT measurements were taken in this soil deposit, so calculations for individual layers are not shown here.

Table 7.18: SPT correction for MYG013

Depth (m)	Susceptibility	N	Fines	Ce	Cr	σ_v (kPa)	σ_v' (kPa)	N_{60}	$(N_1)_{60}$	$(N_1)_{60\text{-cs}}$
5	Susceptible	15	12%	1.26	0.9	90	42	16	22	24

The CSR values for the empirical liquefaction triggering analyses were based on the 0.60 g peak ground acceleration value inferred from recordings at nearby non-liquefied sites. This PGA was used to calculate the factor of safety against liquefaction using the simplified method for liquefaction triggering analysis presented in Chapter 2. Figure 7.71 shows the results of the liquefaction triggering analysis.

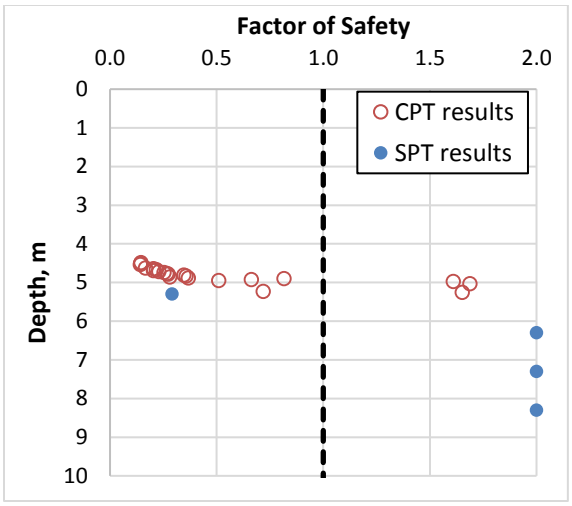

Figure 7.71: Factor of safety against liquefaction at MYG013.

The liquefaction susceptibility and triggering analyses indicated the saturated gravel between a depth of 4.6 and 6 m had a factor of safety much lower than 1.0 and likely liquefied during the Tohoku earthquake. Although ejecta was observed after the earthquake, the crust overlying the liquefiable layer was relatively thick compared to the thickness of the liquefiable layer. Empirically-based procedures for evaluating the likelihood of sand boils (Ishihara, 1985) extend to levels of shaking up to about 0.5 g. Based on the thickness of the non-liquefied crust and liquefied soil, ejecta would have been unlikely during an earthquake with a PGA of 0.5 g. However, the shaking at MYG013 was much stronger than 0.5 g and the duration of shaking was much longer than the ground motions used in Ishihara's analysis. The overlying non-liquefiable crust consisted of primarily very soft sandy clay and organic soils. These soils exhibited high plasticity, could crack easily, and the organic soil may have had existing root holes and pathways for water. Since the shaking at the site was extremely intense and the non-liquefied crust consisted of soils that could easily crack, it was possible that the ejecta observed at the ground surface was produced by the liquefied medium dense gravel between 4.6 and 6 m deep.

7.4.5 *Spectral amplification*

Based on differences between the estimated regionally adjusted spectral acceleration and the recorded ground motion, the presence of liquefied soil amplified the long period spectral acceleration at MYG013. Spectral amplification at long periods is common at sites with liquefied soil since the fundamental period of such sites become very low due to the extremely soft nature

of the liquefied soil. However, because of the low thickness, strong dilative tendencies, and redistribution of pore pressure during the long duration of the Tohoku earthquake, the liquefied medium dense gravel at MYG013 also appears to have amplified the short period spectral acceleration. The recorded geometric mean PGA at MYG013 was 1.25 g, while the PGA based on the regionally adjusted GMPE estimates was 0.60 g. These differences imply that the peak ground acceleration at MYG013 was amplified by a factor of about 2.1 by the liquefied soil. The short period spectral acceleration was largely influenced by dilation pulses that occurred after the medium dense gravel liquefied. These dilatational pulses produced the PGA, and the pulses also occurred in regular 0.7 to 2-second intervals. The regular intervals of the acceleration pulses produced the peak spectral acceleration of a single degree-of-freedom oscillator at periods of 0.7 to 2 seconds. Figure 7.72 shows the spectral amplification ratio, SAR, based on the recorded spectral acceleration and estimated non-liquefied spectral acceleration.

$$\text{SAR} = \frac{S_{a,\text{liquefied}}}{S_{a,\text{non-liquefied}}} \tag{7.8}$$

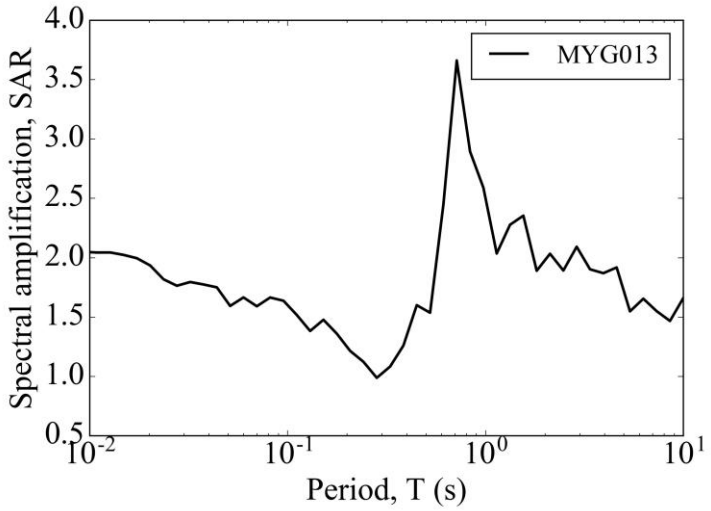

Figure 7.72: Spectral amplification due to liquefied soil at MYG013.

7.4.6 *Numerical analysis*

To gain additional insight into the characteristics of the MYG013 profile, nonlinear effective stress site response analyses were performed. The 11 time histories that best matched the estimated non-

liquefied target spectrum at MYG013 were used as input motions in the analyses. Material properties were estimated using the results of the subsurface investigations to model the soils at MYG013. Table 7.19 shows the input parameters that were used for the 1D effective stress site response model of MYG013. The water table was modeled at a depth of about 0.9 m, as indicated by the subsurface investigation.

Table 7.19: Material properties for modeling liquefaction at MYG013

Depth (m)	Model	Soil description	ρ (kg/cm^3)	v_s (m/s)	$(N_1)_{60}$	ϕ	s_u (kPa)	k (m/s)
0.9	Multi-spring	organic Silt	1.6	190	4	--	30	1E-10
1.0	Multi-spring	organic Silt	1.6	190	4	--	30	1E-10
2	Multi-spring	organic Silt	1.6	190	6	--	30	1E-10
3	Multi-spring	sandy Clay	1.8	200	6	--	80	1E-10
4	Multi-spring	sandy Clay	1.8	210	6	--	80	1E-10
4.6	Multi-spring	sandy Clay	1.8	210	32	--	80	1E-10
6	Cocktail	Gravel[1]	2.1	180	24	42^o	--	5E-05
7	Cocktail	Gravel[1]	2.1	200	50	42^o	--	5E-05
8	Cocktail	Gravel[1]	2.1	400	50	42^o	--	5E-05
9	Cocktail	Gravel[1]	2.1	400	50	42^o	--	5E-05
10	Cocktail	Gravel[1]	2.1	400	50	42^o	--	5E-05
11	Cocktail	Gravel[1]	2.1	400	50	42^o	--	5E-05
12	Cocktail	Gravel[1]	2.1	400	50	42^o	--	5E-05
13	Cocktail	Gravel[1]	2.1	400	50	42^o	--	5E-05
14	Cocktail	Gravel[1]	2.1	400	50	42^o	--	5E-05
	Linear Halfspace		1.9	400				

[1] Susceptible to liquefaction

Site response analyses were performed using the finite element program, FLIP (FLIP Consortium, 2011). The Cocktail glass model in FLIP was developed to predict softening due to pore pressure generation, phase transformation behavior during cyclic loading, and soil fabric degradation during intense shaking. The layer of medium dense gravel between 4.6 m and 6 m deep was sufficiently permeable that pore pressure could dissipate during shaking, which was captured in FLIP by solving the pore pressure diffusion equation simultaneously with the equations of motion. Figure 7.73 shows a simulated profile of the excess pore pressure ratio versus time in the gravel deposit for one of the motions selected to represent the Tohoku earthquake. The

analyses for MYG013 predicted that the medium dense gravel between depths of 4.6 and 6 m liquefied during the Tohoku earthquake. The medium dense gravel was capped by a relatively impermeable layer of sandy clay, but the elevated pore pressure in the medium dense gravel could dissipate into the underlying layer of very dense gravel. As the amplitude of shaking diminished, excess pore pressure dissipated from the medium dense gravel, which allowed the medium dense gravel to stiffen and the modal frequency of the ground motion to increase.

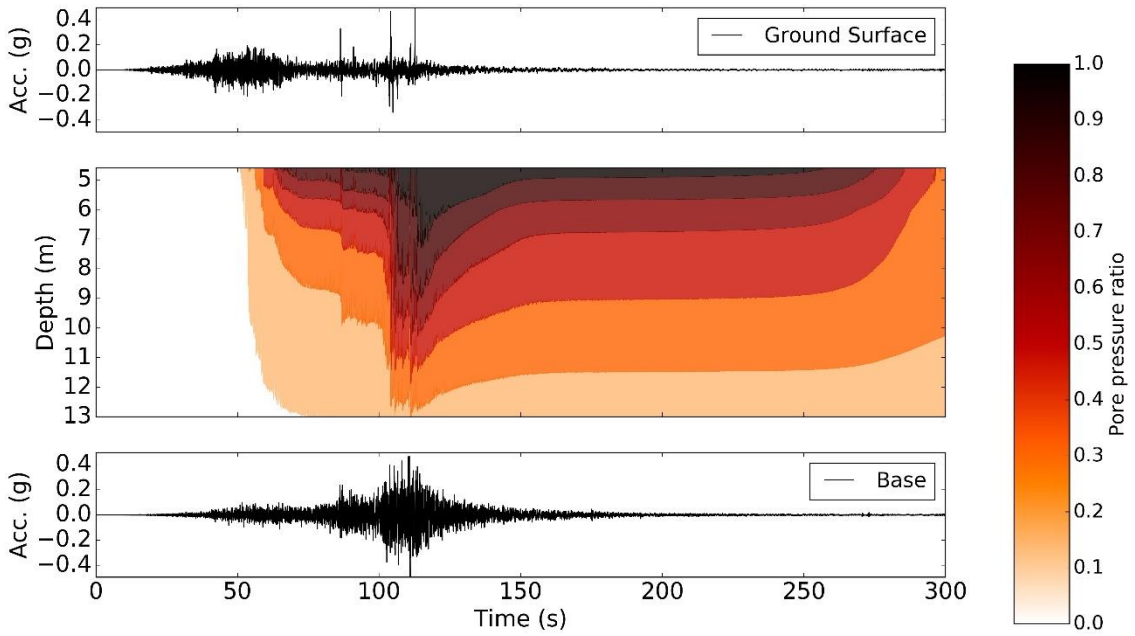

Figure 7.73: Pore pressure generation at MYG013. Input motion FKS014E-W.

Furthermore, the results of the FLIP model indicated that strong dilation pulses produced the peak ground acceleration after the medium dense gravel liquefied. This observation was consistent with the estimated time of liquefaction using Stockwell time frequency analysis, which also indicated that the PGA occurred after the soil initially liquefied. The amplitudes and periods of the dilation pulses were very sensitive to the site conditions, modeling parameters, and the input motions. As the layer of medium dense gravel became stiffer once pore pressure dissipated, it then transmitted higher frequency motions to the ground surface. The interaction between pore pressures generated during shaking, dilation of the medium dense gravel at large shear strains, and pore pressure dissipation due to drainage contributed to the pulse-like behavior of the ground motions. Predicting the period and amplitude of such dilation pulses presents very difficult modeling challenges, especially when the motion at the base of the profile is not known.

If the FLIP model is accurately representing the soil behavior at MYG013, it should capture the general trends of the response spectrum, the intensity of shaking required to trigger liquefaction, and the post-triggering liquefied soil behavior. Figure 7.74 shows the spectral acceleration from the FLIP analyses compared to the recorded response spectrum. The median PGA was about 1.24 g, which was very close to the recorded value was 1.25 g. However, Figure 7.74 shows significant variation in the PGA of individual ground motions. These variations arise due to the complicated interactions between shear strains, excess pore pressure, and drainage. The PGA occurred during strong dilation pulses after liquefaction was triggered in some of the simulations, and occurred before liquefaction was triggered in others. The PGA and spectral amplification was, therefore, very strongly dependent on the ground motion selected to represent the motion at the base of the profile.

The median estimated spectral acceleration shown in Figure 7.74 deviated from the recorded spectral acceleration at periods greater than 0.4 seconds. The event-adjusted GMPE also showed marked differences compared to the recorded spectral acceleration at MYG013 at these periods (Figure 7.68). These deviations were due, in part, to the effects of liquefaction. Figure 7.63 shows very strong, regular-interval dilation pulses produced the peak 1- and 2-second spectral accelerations. While the FLIP model reasonably predicting the median amplitude of the dilation pulses, the period of these pulses was much more difficult to predict. The ground motions at MYG013 were particularly difficult to model or recreate from existing ground motions since the recorded motions were exceptionally strong and were dominated by two very large sub-events that produced periods of very strong shaking that were separated by over 30 seconds.

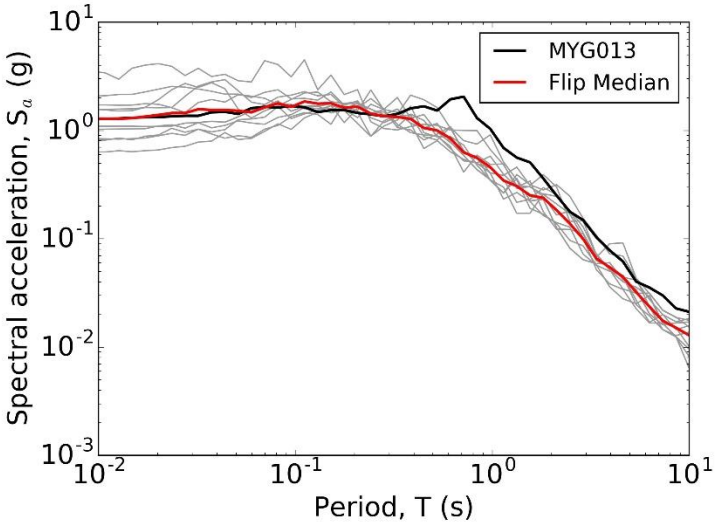

Figure 7.74: Computed and recorded spectral acceleration at MYG013.

The FLIP model has been calibrated to predict liquefaction triggering at the intensity of shaking that is consistent with current conventional practice. Table 7.20 shows the median values and standard deviation of the intensity measures at the time of liquefaction estimated by the FLIP. Figure 7.75 shows histograms of the magnitude-adjusted PGA, Arias intensity, and cumulative absolute velocity (CAV) at the time of liquefaction. The median magnitude-adjusted PGA was very close to the recorded magnitude-adjusted PGA at the time of liquefaction, indicating that FLIP reasonably estimated the cumulative intensity of shaking that triggered liquefaction. However, the intensity of shaking at the time of liquefaction exhibited a relatively large variance, particularly compared to the variances of the estimated intensities necessary to trigger liquefaction at IBR014 and MYG010. The dissipation of excess pore pressure during shaking likely influenced the intensity of shaking necessary to trigger liquefaction at MYG013. In conditions where drainage can occur relatively rapidly, excess pore pressure depends very strongly on the selected input motion. While the input motions were selected to represent the evolution of Arias Intensity at MYG013, the actual motion at the base of the profile was not recorded.

The estimated Arias Intensity at the time liquefaction was triggered was generally higher than the recorded value. The estimated cumulative absolute velocity generally had a relatively large variance and did not provide a good estimate of the intensity of shaking at the time of liquefaction. Both Arias Intensity and cumulative absolute velocity are more strongly affected by the frequency content of the selected ground motion than cycle-adjusted PGA. Despite efforts to

select ground motions that matched the estimated spectral acceleration and evolution of Arias Intensity at MYG010, the motions near MYG010 exhibited a wide range of Arias Intensity values and evolutionary patterns.

Table 7.20: Intensity measures at the time of liquefaction at MYG013

Intensity Measure	Recorded	Median	Standard deviation, $\sigma_{\ln IM}$
Magnitude-adjusted PGA	0.34 g	0.35 g	0.53
Arias Intensity	3.0 m/s	7.4 m/s	0.79
Cumulative Absolute Velocity	13.9 m/s	48.0 m/s	0.61

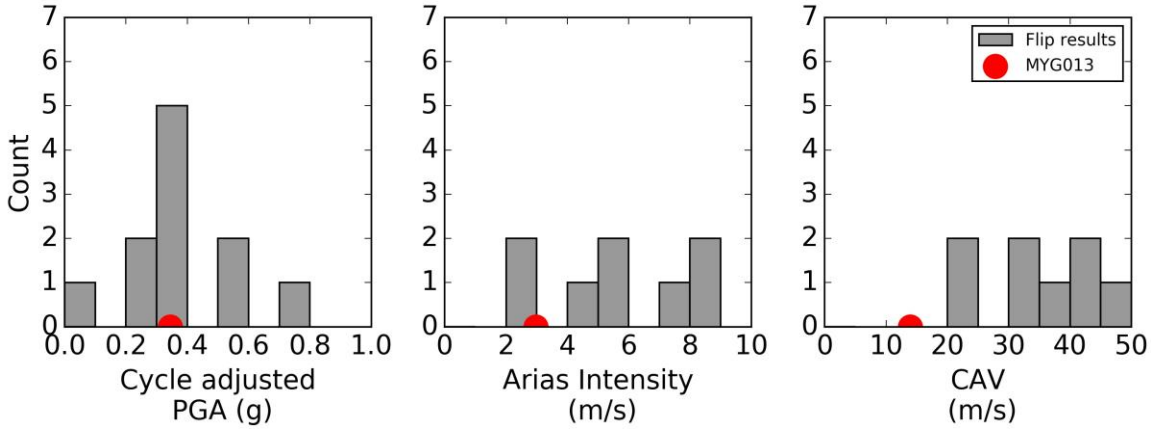

Figure 7.75: Intensity measure at the time of liquefaction at MYG013.

7.4.7 *Conclusions*

The layer of medium dense gravel between 4.6 and 6 m likely liquefied during the Tohoku earthquake, and produced the ejecta seen near the strong motion recording instrument. Once the soil liquefied, rapid and pronounced changes were observed in the frequency content of the recorded ground motion. Both conventional liquefaction analysis and finite element analyses indicated that the saturated layer of medium dense gravel between depths of about 4.6 and 6 m likely liquefied during the Tohoku earthquake. Although the medium dense gravel was relatively deep and was capped by poorly draining, non-liquefiable sandy clay and organic silt, the overlying non-liquefiable soil was very soft, highly plastic, and likely cracked during the Tohoku earthquake. Cracks in the soil would have allowed pore water to flow to the ground surface, resulting in the ejecta observed during the GEER reconnaissance.

The layer of medium dense gravel had strong dilatational tendencies even when it was liquefied and could transmit high-frequency content motions to the ground surface. High-frequency dilation pulses were evident in the horizontal Stockwell spectrum after the estimated time when liquefaction was triggered. After the strong shaking began to diminish, excess pore pressure in the gravel could have dissipated from the layer of medium dense gravel into the underlying layers of dense gravel. The dissipation of pore pressure after strong shaking explains the gradual increase in frequency content observed in the Stockwell spectrum between 120 and 300 seconds.

[This page intentionally left blank]

Chapter 8. EFFECTS OF LIQUEFACTION ON GROUND DEFORMATION

Knowledge of the timing of liquefaction can aid in the estimation of the effects of liquefaction (Kramer et al., 2016; Kramer and Greenfield, 2017). Laboratory testing and field observations have both shown that cyclic and permanent shear strains are small before liquefaction is triggered and potentially quite large afterward. In the field, the static shear stresses that exist under sloping ground can lead to permanent shear strains during earthquake loading. In non-liquefiable soils, these strains are usually small and cause only small amounts of lateral ground surface displacements. Once the soil liquefies, shear strains can become quite large and lead to significant ground surface deformation, which is referred to as lateral spreading. Numerical simulations and physical modeling (e.g. centrifuge) tests indicate that the lateral spreading deformations on gently sloping ground tend to be small before liquefaction is triggered but then can potentially become very large afterwards.

Because lateral spreading deformations do not begin to develop until after liquefaction is triggered, they are "driven" by the ground motions that occur after that time. The shear stiffness of liquefied soil is extremely low, which causes the frequency content of ground motions to change dramatically once liquefaction is triggered. This results in very low-frequency ground motions after liquefaction is triggered. Since lateral spreading deformations occur primarily after liquefaction, the deformations are therefore driven by the low-frequency components of ground motions. Two conclusions can be drawn about the relationship between lateral spreading and ground motion frequency content:

1. Lateral spreading deformations should be related to the portion of the ground motion that remains after liquefaction has been triggered, rather than to the entire ground motion, and
2. Lateral spreading deformation should be related to a measure of the amplitude and duration of low-frequency ground motions.

These conclusions can be used advantageously in a lateral spreading prediction model that accounts for the timing of liquefaction.

8.1 FRAMEWORK FOR ESTIMATING DEFORMATION BASED ON POST-TRIGGERING INTENSITY MEASURES

Since permanent deformations develop primarily after liquefaction has been triggered, the ground motions for liquefaction-induced deformation analysis should ideally be partitioned into the intensities of shaking before and after the soil liquefies. The portion of the loading that occurs after liquefaction is triggered then drives the permanent deformations. Figure 2.9 shows the results of a cyclic direct simple shear laboratory tests that was cyclically shear until liquefaction was triggered. The shear strain amplitude was relatively modest early in the test, when the pore pressure ratio was near 0, but then grew very rapidly as the pore pressure ratio approached 1. It is reasonable to expect that the level of deformation should be most closely related to the post-triggering intensity of shaking. Figure 8.1 shows the results of a numerical simulation where lateral deformation occurred at a site with a gently sloping ground surface. The profile on the left side of the figure shows the subsurface conditions, which consist of

- 1.5 m of dense, granular fill mantling the ground surface, underlain by
- 2 m of saturated, medium dense sand that was susceptible to liquefaction, underlain by
- at least 30 m of very dense alluvial gravel,

This hypothetical example site was subjected to a ground motion from a $M_w = 9$ earthquake with a PGA of about 0.22 g. The right side of the figure shows time histories of the base and ground surface acceleration. Liquefaction was triggered by the intense ground shaking, and the time at which liquefaction was triggered is shown as a dashed vertical line. Once the saturated, medium dense sand liquefied, permanent shear strains were driven down the slope by the intense shaking that continued after the soil liquefied. Figure 8.1 also shows that nearly all of the lateral deformation occurred after liquefaction was triggered.

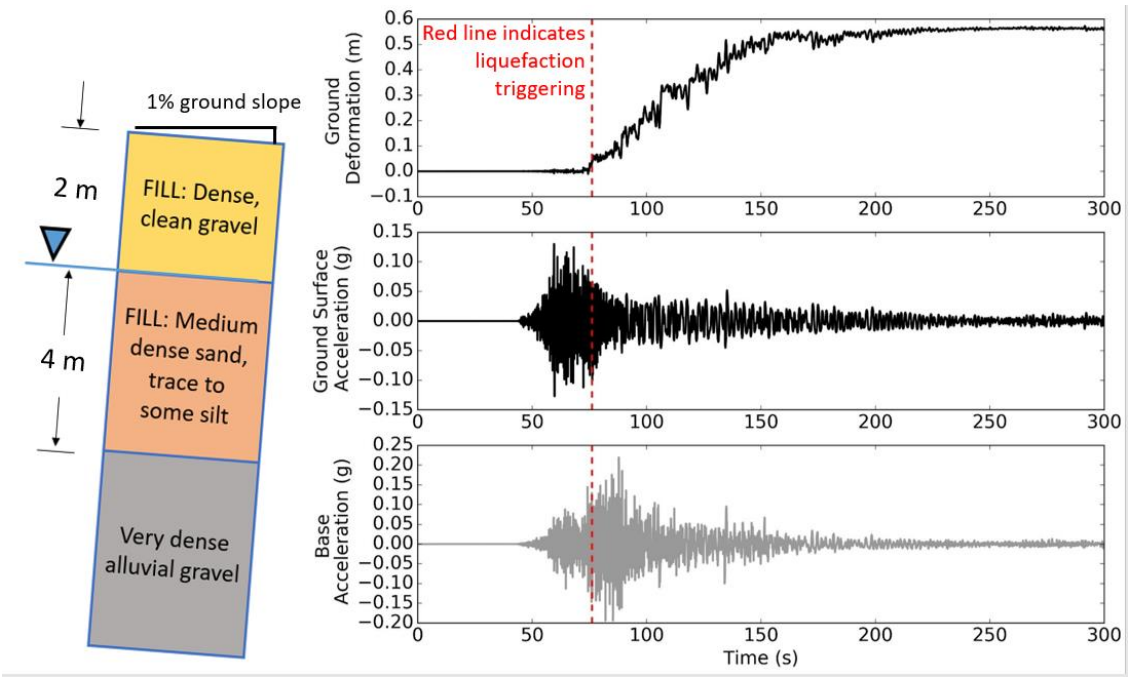

Figure 8.1: Estimated deformation at an example site with a gently sloping ground surface.

Separating ground motions before and after the time of liquefaction can be advantageously used to calculate pre- and post-triggering intensity measures. The pre-triggering intensity measure is associated with the intensity of shaking necessary to trigger liquefaction. The post-triggering intensity measure is then associated with effects of liquefaction. Partitioning the ground motion in this way is referred to as a timing-based framework since it takes advantage of the timing of liquefaction to estimate the remaining intensity of shaking after liquefaction is triggered. The timing-based framework is fundamentally different than conventional procedures used to predict deformation, which rely solely on the intensity measures for the entire duration of shaking. This total *IM* framework refers to the class of conventional procedures that do not distinguish between intensity measures associated with the triggering and effects of liquefaction.

The different *IM*s used in either framework should first be clearly defined. The intensity measure for the prediction of liquefaction triggering, IM^{trig}, can be obtained from an empirical triggering model. In conventional analyses, IM^{trig} is typically a combination of PGA and a magnitude scaling factor. Knowing the value of IM^{trig} necessary to trigger liquefaction, $IM_{\text{L}}^{\text{trig}}$, a plot of the evolutionary time history of IM^{trig} can be used to determine the time of liquefaction triggering, t_{L}, for an individual motion. The time of liquefaction triggering can then be used to

determine the intensity of shaking that remains after liquefaction is triggered, IM^{eff}. This post-triggering intensity measure can then be used to predict the effects of liquefaction on ground surface deformation including lateral spreading and reconsolidation settlement. Table 8.1 lists the different *IM*s that are used in each of these analyses, the function of each *IM*, and the most common way the *IM* is calculated. Some of these *IM*s are used in both the timing-based and total *IM* frameworks, while some *IM*s are exclusive to the timing-based framework.

Table 8.1: Definition of *IM*s used in timing-based and total *IM* frameworks

IM	**Description**
IM^{trig}:	An evolutionary intensity measure for liquefaction triggering and a function of time. Typically, IM^{trig} = PGA_{M}, since most liquefaction triggering procedures are defined using PGA and MSF.
$IM_{\text{L}}^{\text{trig}}$:	A static value of IM^{trig} at the moment when liquefaction is triggered. $IM_{\text{L}}^{\text{trig}}$ can be calculated using liquefaction triggering procedures, and in the timing-based framework, is primarily a function of penetration resistance.
IM^{eff}:	An evolutionary intensity measure for the intensity of shaking after liquefaction has been triggered. IM^{eff} is a necessary variable in the timing-based framework. It can be calculated using values of $IM_{\text{tot}}^{\text{eff}}$ (a static variable) and α_2 (an evolutionary variable).
$IM_{\text{tot}}^{\text{eff}}$:	A static value of IM^{eff} that represents the shaking for the entire ground motion. $IM_{\text{tot}}^{\text{eff}}$ is necessary for the total *IM* framework, which is similar in form to the conventional procedures used to estimate lateral spreading or reconsolidation settlement. $IM_{\text{tot}}^{\text{eff}}$ is also used to calculate IM^{eff} in the timing-based framework. $IM_{\text{tot}}^{\text{eff}}$ is typically calculated using GMPEs.

The steps of the timing-based framework lend themselves to a convenient graphical representation. Figure 8.2 shows a schematic of the timing-based framework for a single ground motion.

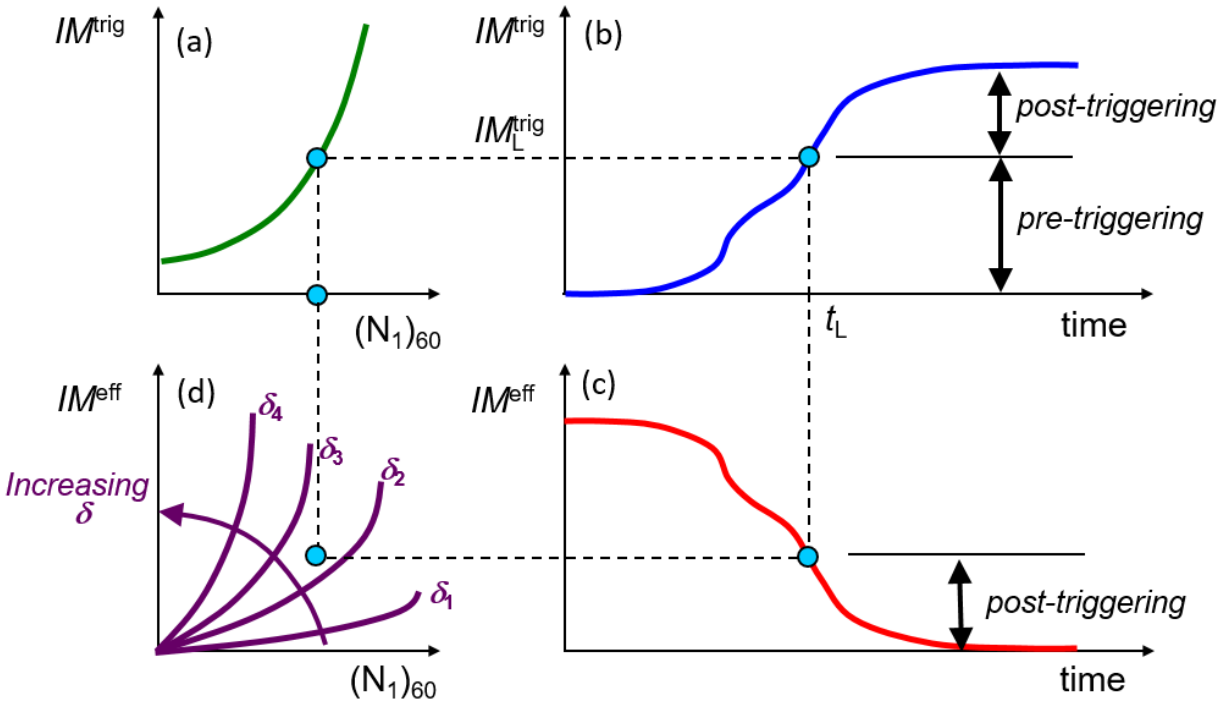

Figure 8.2: Framework for estimating deformation using post-triggering intensity measures in a timing-based framework (from Kramer et al. 2016).

The time history of IM^{eff}, plotted in Figure 8.2(c), is graphically equivalent to the time history of IM^{trig} flipped vertically when the same intensity measures are used for both IM^{trig} and IM^{eff}. Note that the value of IM^{trig} increases with time, while the value of IM^{eff} decreases with time. The empirical models typically correlate liquefaction resistance to penetration resistance, and the liquefaction triggering model in Figure 8.2 is based on $(N_1)_{60}$. Once t_L is identified through a liquefaction triggering procedure, the value of IM^{eff} is defined as the remaining intensity of shaking that can influence the effects of liquefaction.

One benefit of the timing-based framework is that deformations calculated using IM^{eff} should have less uncertainty than conventional methods, which almost exclusively rely on $IM_{\text{tot}}^{\text{eff}}$, or a proxy thereof. Values of $IM_{\text{tot}}^{\text{eff}}$ include not only the intensity of shaking after liquefaction is triggered but also the intensity of shaking before liquefaction is triggered. Since deformations are relatively small before liquefaction is triggered, a method to predict deformation based on $IM_{\text{tot}}^{\text{eff}}$, would most likely result in greater uncertainty than estimates using the timing-based framework.

For discussion in this chapter, conventional procedures that rely on $IM_{\text{tot}}^{\text{eff}}$ for the prediction of the effects of liquefaction are referred to as the total *IM* framework.

A second benefit of the timing-based framework is that the intensity measure for estimating liquefaction triggering, IM^{trig}, does not need to be the same as the intensity measure for estimating the deformation after liquefaction is triggered, IM^{eff}. Because the characteristics of a soil profile change very significantly after liquefaction is triggered, there is no reason to assume that an intensity measure that efficiently predicts liquefaction triggering should also efficiently predict the effects of liquefaction. By identifying and using optimal intensity measures for each case, uncertainty in the predicted effects can be reduced.

Each step of the process of calculating deformations using the timing-based framework can be completed with known, contemporary procedures that are commonly used in practice. The exception is the contours of δ based on $(N_1)_{60}$ and IM^{eff} shown in Figure 8.2(d). Conventional procedures for estimating δ are empirical and based on penetration resistance and $IM_{\text{tot}}^{\text{trig}}$. Reported values of IM^{eff} from liquefaction case histories do not currently exist, but could be developed from careful examination of the case histories. Such a study is beyond the scope of this project. Without empirical data or procedures, contours of δ versus $(N_1)_{60}$ and IM^{eff} can be calculated on a site-by-site basis using numerical analysis.

In the following sections, each step necessary for the timing-based framework is described in detail, starting with the calculation of $IM_{\text{L}}^{\text{trig}}$ at the time of liquefaction based on $(N_1)_{60}$, then the calculation of IM^{eff} using values of IM^{trig}, and then finally the calculation of δ based on $(N_1)_{60}$ and IM^{eff}. These steps are defined in such a way that the probability of exceeding δ can be calculated for given conditions, with the objective of reducing the total uncertainty in estimating δ.

8.2 INTENSITY OF SHAKING AT THE TIME OF LIQUEFACTION

The calculation of $IM_{\text{L}}^{\text{trig}}$ based on $(N_1)_{60}$ has been well-established through the liquefaction triggering procedures described in Chapters 2 and 3. These procedures are typically based on CSR, which is a function of PGA, the effective and total stress on the soil, a depth reduction factor, and earthquake magnitude. For contemporary liquefaction triggering analysis, Idriss and

Boulanger (2004, 2010) have included a magnitude scaling factor, MSF, as part of the calculation of CSR. A reference CSR was defined for a $M_w = 7.5$ earthquake as,

$$\mathrm{CSR}_{\mathrm{M_w=7.5}} = 0.65 \frac{\mathrm{PGA}\ \sigma_v\ r_d}{\sigma_v'} \frac{1}{\mathrm{MSF}} \tag{8.1}$$

where $\mathrm{CSR}_{\mathrm{M_w=7.5}}$ is the CSR normalized for a $M_w = 7.5$ earthquake. Since PGA and MSF are both included in the calculation of a reference CSR, an intensity measure for liquefaction triggering, $IM^{\mathrm{trig}} = \mathrm{PGA_M}$, can be extracted from the liquefaction triggering procedures.

$$\mathrm{CSR}_{\mathrm{M}_w=7.5} = 0.65 \frac{\sigma_v\ r_d}{\sigma_v'} \mathrm{PGA_M} \tag{8.2}$$

where $\mathrm{PGA_M} = \mathrm{PGA/MSF}$. The value of $IM_{\mathrm{L}}^{\mathrm{trig}}$ can be calculated when $\mathrm{CSR}_{\mathrm{M}_w=7.5} = \mathrm{CRR}_{\mathrm{M}_w=7.5}$. The normalized cyclic resistance ratio, $\mathrm{CRR}_{\mathrm{M}_w=7.5}$, is based on an energy and overburden-corrected penetration resistance, $(N_1)_{60}$. For a given soil deposit, the value of $(N_1)_{60}$ contains a significant amount of uncertainty due to uncertainty in the depositional environment, correction factors, and other conditions. The penetration resistance should therefore be considered as a random variable, *N* (random variables denoted in *italics*). Even if the uncertainty in $(N_1)_{60}$ itself is not considered, the correlation between $(N_1)_{60}$ and $\mathrm{CRR}_{\mathrm{M}_w=7.5}$ is also uncertain, so $IM_{\mathrm{L}}^{\mathrm{trig}}$ should also be considered as a random variable.

These uncertainties in *N* and $IM_{\mathrm{L}}^{\mathrm{trig}}$ propagate through the timing-based procedure. The uncertainty in *N* causes uncertainty in $IM_{\mathrm{L}}^{\mathrm{trig}}$, which leads to uncertainty in $IM_{\mathrm{L}}^{\mathrm{eff}}$, IM^{eff}, and ultimately δ. Fortunately, the distribution of *N* and the conditional distribution of $IM_{\mathrm{L}}^{\mathrm{trig}}$ given *N* have both been calculated as part of the contemporary liquefaction triggering procedures (Cetin et al. 2004; Boulanger and Idriss, 2010, 2014). Idriss and Boulanger assumed that *N* was a normally distributed random variable.

$$N = \mathrm{E}[N] + \sigma_N \varepsilon_N \tag{8.3}$$

where $\mathrm{E}[N]$ is the expected value of *N*, σ_N is the standard deviation of *N*, and ε_N is a standard normally distributed random variable (zero mean and unit standard deviation). The value of σ_N varies with *N*, but was assumed by Idriss and Boulanger to have a relatively constant coefficient of variation, $\mathrm{COV_N}$, equal to about 0.15.

$$\sigma_N = \mathrm{COV}_N \, N \tag{8.4}$$

Idriss and Boulanger further assumed that $\mathrm{CRR}_{\mathrm{M}_w=7.5,\, \sigma_v'=1\ \mathrm{atm}}$ and $\mathrm{CSR}_{\mathrm{M}_w=7.5,\, \sigma_v'=1\ \mathrm{atm}}$ were log-normally distributed random variables, denoted as *R* and *S*. These random variables could be defined by their expected (natural logarithm) values, standard deviations, and standard normally distributed random variables

$$\ln R = \mathrm{E}[\ln R] + \sigma_{\ln R}\varepsilon_{\ln R} \tag{8.5}$$

$$\ln S = \mathrm{E}[\ln S] + \sigma_{\ln S}\varepsilon_{\ln S} \tag{8.6}$$

where $\sigma_{\ln R}$ and $\sigma_{\ln S}$ are the standard deviations of $\ln R$ and $\ln S$, and $\varepsilon_{\ln R}$ and $\varepsilon_{\ln S}$ are independent, identically distributed standard normal random variables. Idriss and Boulanger combined the random variables *N*, *R*, and *S* to calculate a limit state function, g, where positive values of g indicated that liquefaction was not likely and negative values of g indicated that liquefaction was likely. For the timing-based framework, the limit state function can be used to estimate the uncertainty in IM^{trig} when *N* is given. The limit state function, g, was defined as

$$g = \ln R - \ln S \tag{8.7}$$

The $\mathrm{E}[\ln S] = \ln\left(\mathrm{CSR}_{\mathrm{M}_w=7.5,\, \sigma_v'=1\ \mathrm{atm}}\right)$, so equation (8.6) can be rearranged as

$$\ln S = \ln[\mathrm{PGA}_M] + \ln\left[0.65\ \frac{\sigma_v\ r_d}{\sigma_v{}'}\ \frac{1}{\mathrm{K}_\sigma}\right] + \sigma_{\ln S}\varepsilon_{\ln S} \tag{8.8}$$

Substituting equations (8.5) and (8.8) into equation (8.7) results in

$$g = \mathrm{E}[\ln R] + \sigma_{\ln R}\varepsilon_{\ln R} - \ln[\mathrm{PGA}_M] - \ln\left[0.65\ \frac{\sigma_v\ r_d}{\sigma_v{}'}\ \frac{1}{\mathrm{K}_\sigma}\right] - \sigma_{\ln S}\varepsilon_{\ln S} \tag{8.9}$$

At the moment when liquefaction occurs, the limit state is 0. When g = 0, equation (8.9) can then be solved for $\mathrm{PGA_M}$.

$$\ln[\mathrm{PGA}_M] = \mathrm{E}[\ln R] + \ln\left[0.65\ \frac{\sigma_v\ r_d}{\sigma_v{}'}\ \frac{1}{\mathrm{K}_\sigma}\right] + \sigma_{\ln R}\varepsilon_{\ln R} - \sigma_{\ln S}\varepsilon_{\ln S} \tag{8.10}$$

where, at the time of liquefaction, the median value of $\mathrm{PGA_M}$ is

$$\mathrm{E}[\ln \mathrm{PGA}_M] = \mathrm{E}[\ln R] + \ln\left[0.65\ \frac{\sigma_v\ r_d}{\sigma_v{}'}\ \frac{1}{\mathrm{K}_\sigma}\right] \tag{8.11}$$

The calculation of $\ln[\mathrm{PGA}_M]$ includes a linear combination of two random variables, $\sigma_{\ln R}\varepsilon_{\ln R} - \sigma_{\ln S}\varepsilon_{\ln S}$. The variance of a linear combination of two independent, normally distributed random variables is the sum of the variance of each random variable (Goldberger, 1991). So, the variance of $\ln \mathrm{PGA}_M$ is

$$\sigma_{\ln \mathrm{PGA}_M}{}^2 = \sigma_{\ln R}{}^2 + \sigma_{\ln S}{}^2 \tag{8.12}$$

$\mathrm{PGA_M}$ at the time of liquefaction is a log-normally distributed random variable. It is a function of the $\mathrm{CRR}_{\mathrm{M}_w=7.5,\ \sigma_v'=1\ \mathrm{atm}}$, denoted as random variable *R*, which in the sequence of calculations, is a function of *N*. Calculations of $\mathrm{PGA_M}$ at the time of liquefaction in equation (8.10) are therefore conditional upon *N*. The data in Idriss and Boulanger's analysis did not necessarily constrain the relationship between *N*, *S*, and *R* and the values of σ_N, $\sigma_{\ln R}$, and $\sigma_{\ln S}$. The total uncertainty was quantified, but the uncertainty in each variable was not characterized. Additional discussion of the assumptions and analysis in calculating the limit state function is provided by Idriss and Boulanger (2010). However, they found that values of $\mathrm{COV_N} = 0.15$, $\sigma_{\ln S} = 0.20$, and $\sigma_{\ln R} = 0.15$ maximized the likelihood that their model fit the data. These values of COV, $\sigma_{\ln S}$, and $\sigma_{\ln R}$ provided reasonable estimates of the uncertainty in *N*, *S*, and *R*, and are used in further calculations for the timing-based framework. σ_N can be calculated using equation (8.4) with values of $\mathrm{COV_N} = 0.15$. Given $\sigma_{\ln S}$ and $\sigma_{\ln R}$, the conditional standard deviation of $\mathrm{PGA_M}$ given *N*, $\sigma_{\ln \mathrm{PGA}_M|\ N}$, is 0.25.

8.3 CORRELATION OF PRE- AND POST-TRIGGERING INTENSITY MEASURES

For the timing-based framework, the correlation between IM^{trig} and IM^{eff} can be used to calculate the conditional value of IM^{eff} given IM^{trig}, with some level of uncertainty. Knowledge of one *IM* reduces the uncertainty in other *IM*s through their conditional probability. In general, the conditional probability of an arbitrary intensity measure, IM_2, given another intensity measures, IM_1, is less than or equal to the marginal probability of IM_2. This can be shown through the definition of marginal probability.

$$\mathrm{P}[IM_2] = \sum_{IM_1} \mathrm{P}[IM_2|IM_1]\,\mathrm{P}[IM_1] \tag{8.13}$$

where $\mathrm{P}[IM_2|IM_1]$ is the conditional probability of IM_2 given IM_1.

Many of the intensity measures investigated in this study capture different aspects of the amplitude, frequency content, or duration of a ground motion. Since these intensity measures are not necessarily completely independent of all aspects of the ground motion (amplitude, frequency content, or duration), they are inherently correlated with each other to some degree. For example, the analysis in Section 3.3 suggests that significant duration is nearly independent of ground motion amplitude. Conversely, bracketed duration, while primarily capturing the duration of ground motions, captures some aspects of ground motion amplitude, due to its reliance upon an amplitude threshold. Because bracketed duration captures even a slight amount of the ground motion amplitude, it is strongly correlated with both magnitude-adjusted PGA, which is an intensity measure primarily associated with ground motion amplitude, and significant duration, which is primarily associated with ground motion duration.

Intensity measures typically associated with liquefaction triggering and the effects of liquefaction—magnitude-adjusted PGA, Arias intensity, and cumulative absolute velocity—all capture some aspect of the ground motion amplitude, frequency content, and duration. As shown in Chapter 3, many of these intensity measures are somewhat correlated with each other, and these correlations can be advantageously used to reduce the uncertainty in IM^{eff} given IM^{trig}. Many ground motion prediction equations (GMPEs) have been developed to predict intensity measures such as PGA, Arias intensity, and cumulative absolute velocity. Some of these GMPEs (Campbell and Bozorgnia, 2010; 2012) also include estimates of the correlation between these *IM*s. The most recent GMPEs from the NGA West-2 database (Bozorgnia et al., 2014) were based on crustal ground motion, and as such, were typically limited to earthquakes with $M_w < 7.8$. Despite their limitations, these GMPEs provide vital information for the timing base-framework, including the variance and correlation between intensity measures. This information can be extended to calculate the conditional probability of IM^{eff} given IM^{trig} with three additional steps.

1) Develop equations to estimate the conditional distribution of IM^{eff} given IM^{trig} when the correlation between the two *IM*s is known,

2) Estimate the correlation between two *IM*s using available ground motion data when the correlation between *IM*s is not known, and
3) Develop evolutionary *IM*s and correlations to estimate the rate at which different intensity measures evolve.

The details of each of these steps are discussed subsequently.

8.3.1 *Conditional distribution of intensity measures*

The correlation coefficient, $\rho_{IM_2|IM_1}$, quantifies the amount of variance of IM_2 that is explained by the variance of IM_1 (Bradley, 2010). For normal distributions with two random variables, x and y, the conditional mean, $\mu_{y|x}$, and the conditional variance, $\sigma^2_{y|x}$, are given by

$$\mu_{y|x} = \mu_y + \rho_{x,y}\frac{\sigma_y}{\sigma_x}(x - \mu_x) \tag{8.14}$$

$$\sigma^2_{y|x} = \sigma^2_y\left(1 - \rho^2_{x,y}\right) \tag{8.15}$$

These relationships can be used in the timing-based framework to predict the mean and variance of IM^{eff} given IM^{trig} when $\rho_{IM^{\text{eff}}|IM^{\text{trig}}}$ is known. Campbell and Bozorgnia (2012) developed a GMPE for PGA and calculated correlations coefficients between PGA, Arias intensity, and cumulative absolute velocity. These correlation coefficients can be used with equations (8.15) and (8.15) to calculate the uncertainty in IM^{eff} given IM^{trig}.

For liquefaction triggering analysis, IM^{trig} = PGA_M, however, specific GMPEs have not been developed to estimate PGA_M. GMPEs (Liu et al. 2001; Kishida and Tsai, 2014) have, however, been developed to estimate the number of cycles of loading, n, based on earthquake metadata. Through the definitions of PGA_M and MSF, values of PGA and n can be used to calculate PGA_M with consideration of the uncertainty in each *IM*. Taking the logarithm of PGA_M

$$\ln \text{PGA}_M = \ln \text{PGA} - \ln \text{MSF} \tag{8.16}$$

The magnitude scaling factor can be calculated using the equivalent number of cycles of loading.

$$\text{MSF} = \left(\frac{n}{n_{ref}}\right)^{-b} \tag{8.17}$$

where b is an exponent based on material properties that is described in Section 2.3, and n_{ref} is the reference number of cycles corresponding to an $M_w = 7.5$ earthquake. Taking the logarithm of both sides of equation (8.17), the magnitude scaling factor can be expressed as

$$\ln \text{MSF} = -b \ln n + b \ln n_{ref} \tag{8.18}$$

Equation (8.18) can then be substituted into equation (8.16).

$$\ln \text{PGA}_M = \ln \text{PGA} + b \ln n - b \ln n_{ref} \tag{8.19}$$

To quantify the uncertainty in PGA_M, both the uncertainty in PGA and n must be considered. PGA can be defined as a random variable, such that

$$\ln \text{PGA} = \text{E}[\ln \text{PGA}] + \sigma_{\ln \text{PGA}} \varepsilon_{\ln \text{PGA}} \tag{8.20}$$

where $\text{E}[\ln \text{PGA}]$ is the expected value of ln PGA calculated using a GMPE, $\sigma_{\ln \text{PGA}}$ is the standard deviation, and $\varepsilon_{\ln \text{PGA}}$ is a standard normally distributed random variable. The random variable for the number of cycles of loading, n, is also assumed to be log-normally distributed.

$$\ln n = \text{E}[\ln n] + \sigma_{\ln n} \varepsilon_{\ln n} \tag{8.21}$$

where $\text{E}[\ln n]$ is the expected value of $\ln n$, $\sigma_{\ln n}$ is the standard deviation, and $\varepsilon_{\ln \text{PGA}}$ is a standard normally distributed random variable. The uncertainty in n implies that there is also uncertainty in the magnitude scaling factor. Substituting equation (8.21) into equation (8.18)

$$\ln \text{MSF} = -b(\text{E}[\ln n] + \sigma_{\ln n} \varepsilon_{\ln n}) + b \ln n_{ref} \tag{8.22}$$

and then separating the random variables

$$\ln \text{MSF} = b\big(\ln n_{ref} - \text{E}[\ln n]\big) - b \sigma_{\ln n} \varepsilon_{\ln n} \tag{8.23}$$

The uncertainty in MSF is therefore related to $b\sigma_{\ln n}$. Equations (8.19) and (8.23) can be combined to estimate values of PGA_M with consideration of the uncertainties in PGA and n. Since the PGA and n are inherently correlated, the uncertainty in n is conditional on PGA with standard deviation $\sigma_{\ln n \mid \ln \text{PGA}}$.

$$\begin{aligned} \ln \text{PGA}_M = \ln \text{E}[\text{PGA}] + b\big(\text{E}[\ln n] - \ln n_{ref}\big) + \sigma_{\ln PGA} \varepsilon_{\ln \text{PGA}} \\ + b \sigma_{\ln n \mid \ln \text{PGA}} \varepsilon_{\ln n \mid \ln \text{PGA}} \end{aligned} \tag{8.24}$$

The conditional standard deviation $\sigma_{\ln n \mid \ln \mathrm{PGA}}$ can be calculated using equation (8.15) by substituting ln PGA and ln n for x and y.

$$\sigma^2_{\ln n \mid \ln \mathrm{PGA}} = \sigma^2_{\ln n}\left(1 - \rho^2_{\ln \mathrm{PGA},\ln n}\right) \tag{8.25}$$

where $\rho_{\ln \mathrm{PGA},\ln n}$ is the correlation between ln PGA and ln n. The expected value of $\mathrm{PGA_M}$ is therefore a function of E[ln PGA] and E[ln n], and the standard deviation of $\mathrm{PGA_M}$ is calculated as the sum of two random variables $\sigma_{\ln \mathrm{PGA}}\varepsilon_{\ln \mathrm{PGA}} + b\sigma_{\ln n \mid \ln \mathrm{PGA}}\varepsilon_{\ln n \mid \ln \mathrm{PGA}}$. The variance of the sum of two independent normally distributed random variables is the sum of the variance of each random variable (Goldberger, 1991). The variance of $\mathrm{PGA_M}$ is given by

$$\sigma^2_{\ln \mathrm{PGA}_M} = \sigma^2_{\ln \mathrm{PGA}} + \left(b\,\sigma_{\ln n \mid \ln \mathrm{PGA}}\right)^2 \tag{8.26}$$

Kishida and Tsai indicated that the log-normal standard deviation of n, $\sigma_{\ln n}$, was 0.41 for typical values of b, and the correlation coefficient between ln PGA and ln n, $\rho_{\ln \mathrm{PGA},\ln n}$, was -0.22. The conditional standard deviation of ln n given ln PGA was calculated using equation (8.15) as $\sigma_{\ln n \mid \ln \mathrm{PGA}}$ = 0.40. The conditional standard deviation of ln n is not very significantly smaller than the marginal standard deviation of n, $\sigma_{\ln n}$. The correlation coefficient $\rho_{\ln \mathrm{PGA},\ln n}$ = -0.22 indicated that these two *IM*s are not well correlated, and therefore the reduction in variance of ln n when ln PGA is given is small.

The most recent magnitude scaling factors (Boulanger and Idriss, 2014) include variables for relative density. A value of $(N_1)_{60}$ = 15 blows/ft was used to standardize $\mathrm{PGA_M}$, which implied that the value of b was about 0.24. The product of b and $\sigma_{\ln n \mid \ln \mathrm{PGA}}$ was then equal to about 0.096. Campbell and Bozorgnia (2012) indicated that the log-normal standard deviation of PGA, $\sigma_{\ln \mathrm{PGA}}$, was 0.53 for crustal events. Since the value of $b\sigma_{\ln n \mid \ln \mathrm{PGA}}$ was much smaller than $\sigma_{\ln \mathrm{PGA}}$, the uncertainty in n represents a relatively small contribution to the total uncertainty in $\mathrm{PGA_M}$. With these values, equation (8.26) indicates that the standard deviation of $\mathrm{PGA_M}$, $\sigma_{\ln \mathrm{PGA}_M}$, is about 0.54.

8.3.2 *Intensity measures without known correlations*

The preceding analysis requires known values of $\rho_{x,y}$, which is the case for I_a given PGA and CAV given PGA (Campbell and Bozorgnia, 2012) for crustal events, but not for subduction-zone events.

Correlations between other *IM*s can be calculated using data from the suites of ground motions developed in Section 3.3. Figure 8.3 shows scatterplots of PGA_M, I_a, and CAV and the correlation coefficient between these *IM*s. PGA_M and I_a exhibit a very strong correlation, with $\rho_{\ln I_a,\ln PGA_M}$ = 0.94. The correlation between CAV and I_a is also very strong with $\rho_{\ln I_a,\ln CAV}$ = 0.92. The correlation between PGA_M and CAV is relatively strong with $\rho_{\ln CAV,\ln PGA_M}$ = 0.77, but not as strong as $\rho_{\ln I_a,\ln PGA_M}$ or $\rho_{\ln I_a,\ln CAV}$. The strength of correlation between these *IM*s can be explained by the relative frequency contents that each *IM* captures. PGA_M captures the highest frequency ground motions, and is well-correlated with I_a, which captures moderate frequency ground motions. PGA_M is not as well correlated with CAV, which is more strongly influenced by the lower frequency components of ground motions. Since the frequencies captured by I_a are between the range of frequencies captured by PGA_M and CAV, I_a is well-correlated with both.

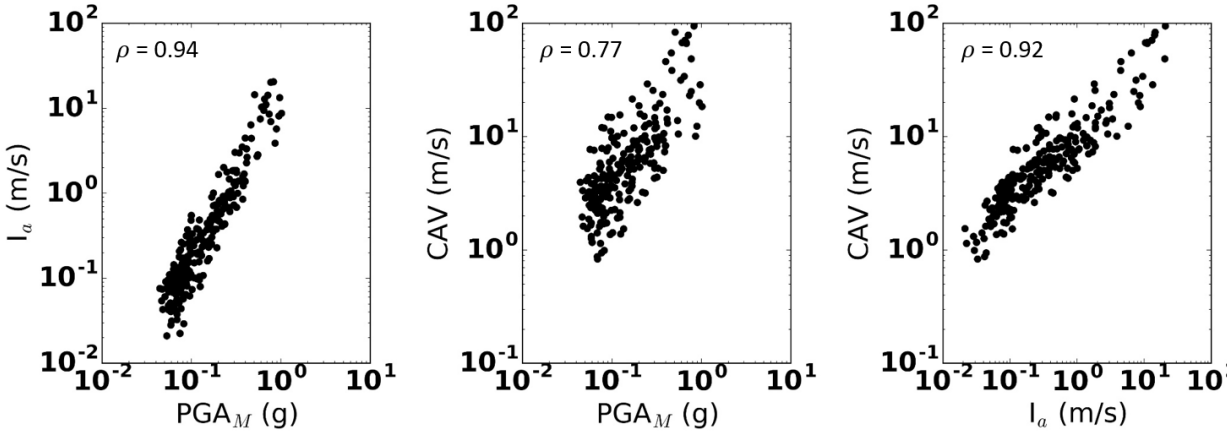

Figure 8.3: Correlation between *IM*s. Ground motions from the CS-dataset.

The previous analysis indicates that $\sigma_{\ln PGA_M}$ was about 0.54. Campbell and Bozorgnia (2012) indicated the value of $\sigma_{\ln I_a}$ was about 0.83 and $\sigma_{\ln CAV}$ was about 0.42. With the correlation coefficients in Figure 8.3, equation (8.16) can be used to calculate the conditional standard deviation, $\sigma_{\ln IM_2|\ln IM_1}$, for any combination of these *IM*s. These values are listed in Table 8.2. In this table, when $IM_1 = IM_2$, the marginal standard deviation, $\sigma_{\ln IM}$, is shown.

Table 8.2: Conditional standard deviation of *IM*s, $\sigma_{IM_2|IM_1}$

	IM_1		
IM_2	ln PGA_M	ln I_a	ln CAV
ln PGA_M	0.54	0.18	0.34
ln I_a	0.28	0.83	0.32
ln CAV	0.27	0.16	0.42

Table 8.2 indicates that ln CAV given ln I_a has the lowest conditional uncertainty of any of the combinations. These two *IM*s are very well correlated, as shown in Figure 8.3, and ln CAV has the lowest marginal uncertainty of any of the *IM*s. The *IM* most commonly associated with liquefaction triggering is PGA_M, while the effects of liquefaction should be associated with lower-frequency intensity measures, like I_a or CAV. Both ln I_a given ln PGA and ln CAV given ln PGA have about the same conditional standard deviation, leading to the conclusion that, from a predictability perspective, both I_a and CAV are good candidates for IM^{eff} in the timing-based framework.

To use equation (8.14), expected values of ln IM_2 must also be calculated. The CS-dataset in Chapter 3.3 includes observations from crustal as well as subduction-zone earthquakes. While GMPEs have been developed using data from crustal earthquakes for *n*, I_a, and CAV, GMPEs have not been widely developed for these *IM*s based on large-magnitude subduction-zone earthquakes. However, a GMPE has been developed to estimate PGA for subduction zone events (Abrahamson et al., 2015). The correlations between PGA_M, I_a, and CAV are sufficiently strong that conditional values of I_a and CAV can be estimated when PGA_M is known. Equations for estimating I_a and CAV based regression to values of PGA_M in the CS-dataset are provided in Section 3.3. Despite the inclusion of subduction-zone earthquakes in the CS-dataset, *IM* estimated using these correlations may not be appropriate for some conditions. Rather, these correlations should serve as a guideline for estimating the conditional distribution when only one *IM* is known. The conditional standard deviations of ln I_a and ln CAV given ln PGA_M are both very large compared to the conditional standard deviation based on Campbell and Bozorgnia's GMPEs. Equations (3.35) and (3.36) both indicate the conditional standard deviations using the CS-dataset are 0.51 for ln I_a given PGA_M and 0.58 for ln CAV given ln PGA_M. These same conditional standard deviations are equal to 0.28 and 0.27 using Campbell and Bozorgnia's GMPEs. These large

uncertainties stem from the simplicity of equations (3.35) and (3.36), which are not fully-developed GMPEs. However, for large magnitude subduction-zone earthquakes, the correlations in equation (3.35) and (3.36) may be more accurate than the crustal earthquake-based GMPEs.

In addition, the data in the CS-dataset only includes ground motions on very stiff soil or rock. The correlations are therefore not directly applicable to conditions where site amplification by softer soils might occur. Amplification may not occur uniformly between the two *IM*s. Amplification factors from existing GMPEs could be used to calculate the ground surface values of these *IM*s, but these amplification factors also included some amount of uncertainty.

8.3.3 *Evolutionary intensity measures*

Figure 8.2 shows the evolution of IM^{trig} and IM^{eff} for a single ground motion. The timing-based framework requires estimates of evolutionary values of IM^{eff} given IM^{trig} as a function of time. These estimates should also account for the uncertainty in IM^{eff} given IM^{trig}. Although values of PGA_M, I_a, and CAV are well correlated, they all capture different bands of frequency content and evolve differently with respect to time. Ground motions produced by earthquakes are nonstationary processes, and the frequency contents of these motions tend to shift from high frequencies early in the motion to low frequencies later in the motion. The PGA_M captures the highest frequency components of ground motions, and therefore increases very rapidly early in the ground motion when the frequency is the highest. I_a and CAV are both based on the integral of the ground motion and are therefore much more affected by the duration and lower frequency content motions than PGA_M. Since I_a is calculated using the square of acceleration, it is more sensitive to high amplitude acceleration pulses than CAV. As such, I_a tends to increase more rapidly in the early part of the ground motion than CAV, but still less rapidly that PGA_M. Each of these *IM*s has a unique rate of evolution with respect to individual ground motions. Figure 8.4 shows an example ground motion and these three different *IM*s as they evolve with time.

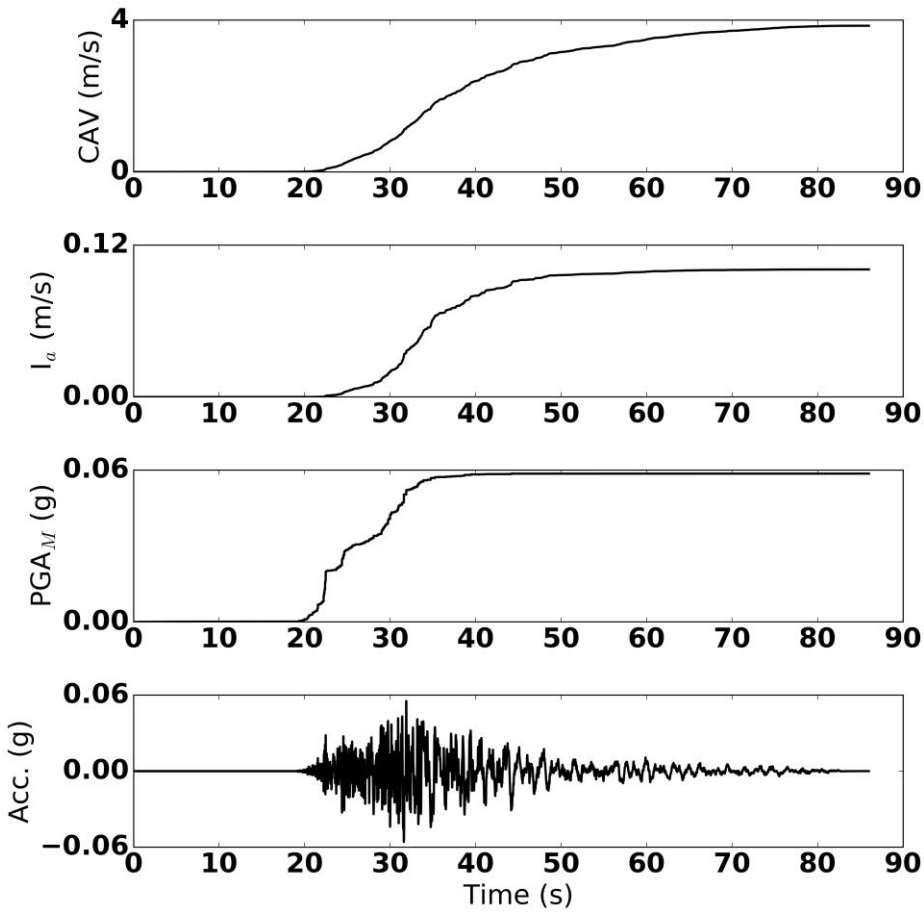

Figure 8.4: Evolution of *IM*s with time. Ground motion from TCU138 during the 1999 Chi-Chi earthquake.

The relative evolution of these intensity measures with respect to time can be normalized and compared by defining two normalized evolutionary intensity measure, α_1 and α_2.

$$\alpha_1 = \frac{IM^{\text{trig}}}{IM_{\text{tot}}^{\text{trig}}} \tag{8.27}$$

$$\alpha_2 = 1 - \frac{IM^{\text{eff}}}{IM_{\text{tot}}^{\text{eff}}} \tag{8.28}$$

where IM^{trig} and IM^{eff} are evolutionary IM as that change with time, and $IM_{\text{tot}}^{\text{trig}}$ and $IM_{\text{tot}}^{\text{eff}}$ are these *IM*s for the entire duration of shaking. The example ground motion shown in Figure 8.4 was used to calculate α_1 and α_2, and the evolution of these *IM*s is shown in Figure 8.5. PGA_M was

used as IM^{trig} to calculate α_1, and PGA_M, I_a, and CAV were all used as IM^{eff} to calculate α_2. This figure also shows the relative evolutions of α_1 and α_2. When $IM^{\text{eff}} = IM^{\text{trig}} = PGA_M$, the function of α_2 given α_1 forms a straight line. When $IM^{\text{eff}} = I_a$ or CAV, α_1 evolves much more rapidly than α_2 in the early stages of the motion.

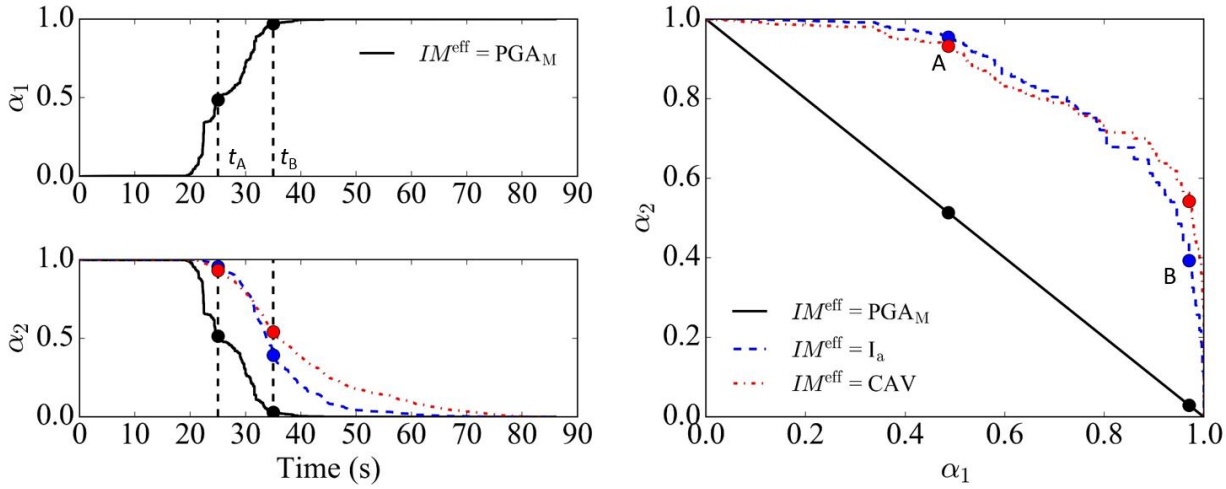

Figure 8.5: Evolution of α_1 and α_2 for a single ground motion. Ground motion from TCU138 during the 1999 Chi-Chi earthquake.

The values of α_1 and α_2 were calculated using the suite of crustal and subduction-zone motions (CS-dataset) from stiff soil and rock sites. Additional details about this suite of motions are described in Section 3.3. Figure 8.6 provides calculated values of α_2 evolving with α_1 in the CS-dataset. Since PGA_M is typically associated with liquefaction triggering, $IM^{\text{trig}} = PGA_M$ was used to calculate α_1. $IM^{\text{eff}} = I_a$ was used to calculate α_2 in Figure 8.6, but CAV was also considered as a candidate for IM^{eff}.

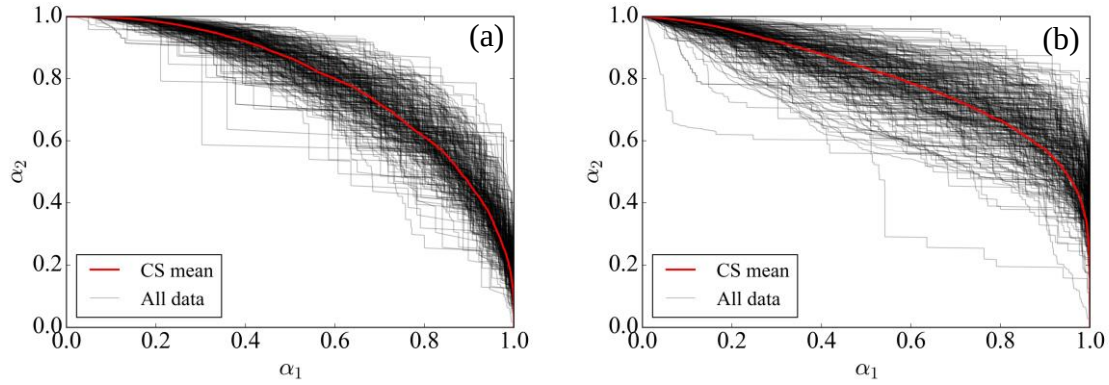

Figure 8.6: Evolution of α_1 and α_2 in CS data set. (a) IM^{trig} = PGA_M and IM^{eff} = I_a (b) IM^{trig} = PGA_M and IM^{eff} = CAV.

Figure 8.6 also shows the mean of α_2 evolving with α_1. Residuals from the mean were calculated for each ground motions with given values of α_1 = 0.25, 0.5, and 0.75. These residuals can help identify any source or path effects that affect the evolutionary relationship between α_2 and α_1. Figures 8.7 and 8.8 show the residuals of α_2 plotted against M_w and R_{rup}. Linear trendlines were fitted to the residuals in these figures. Very little bias or trend with respect to M_w or R_{rup} was observed in the residuals of α_2 given α_1, indicating that α_2 is independent of M_w and R_{rup} for practical purposes. Based on the results of this analysis with the CS dataset, the function of α_2 versus α_1 was assumed to be uncorrelated with M_w or R_{rup} for further analysis.

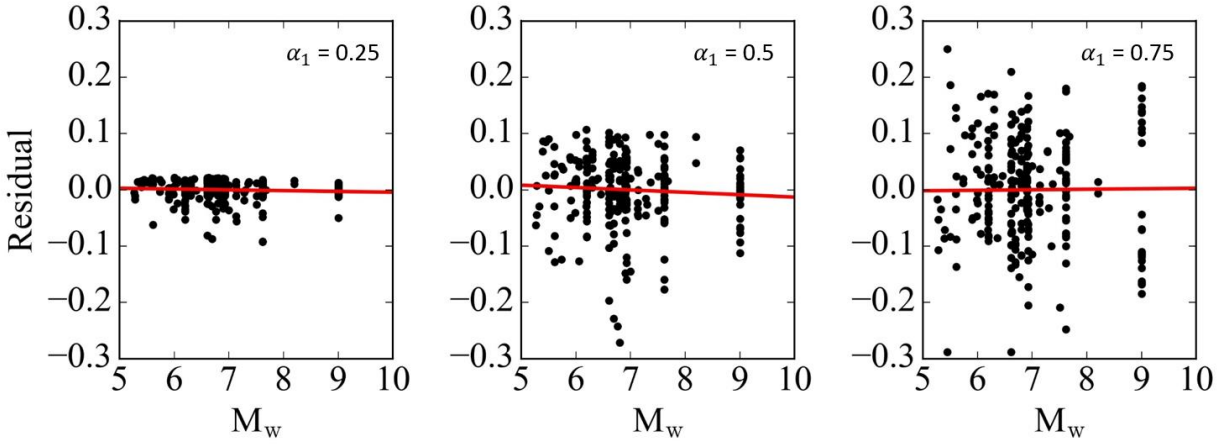

Figure 8.7: Residuals of α_2 versus M_w.

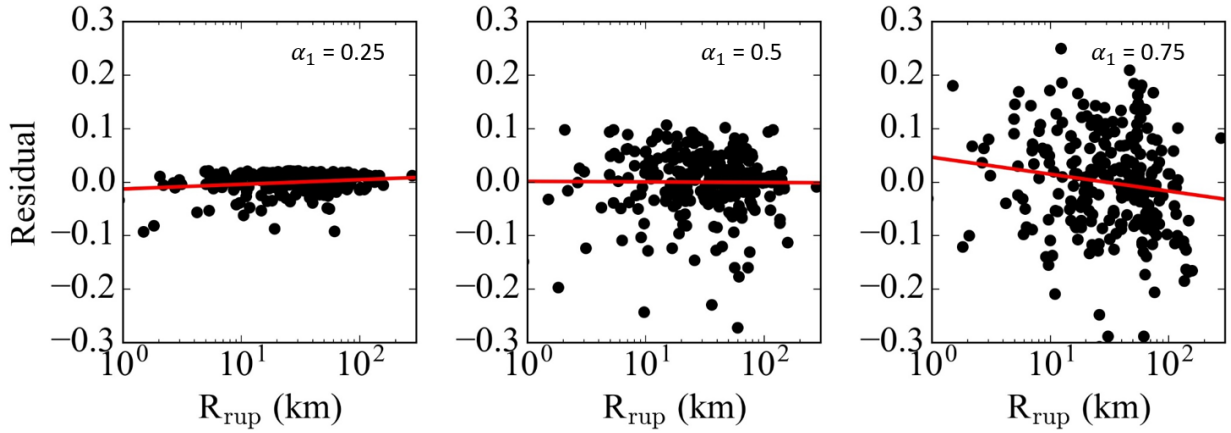

Figure 8.8: Residuals of α_2 versus R_{rup}.

To further investigate the effects of earthquake source, path, and site conditions, the relationship between α_2 and α_1 was plotted for the Japanese suite of motions (J-dataset). In addition to contain ground motions with a large range of earthquake magnitude and rupture distance, this dataset included ground motions from sites located on soft soil and within basins. Additional details about the J-dataset are provided in Section 3.3. Figure 8.8 shows the evolutionary *IM*s from the J-dataset. The mean value of α_2 evolving with α_1 from the CS-dataset in also shown in this figure. The shape of the mean curves from the J-dataset was very similar to that for the CS-dataset, and the difference in α_2 between the curves was on average, about 2.5%.

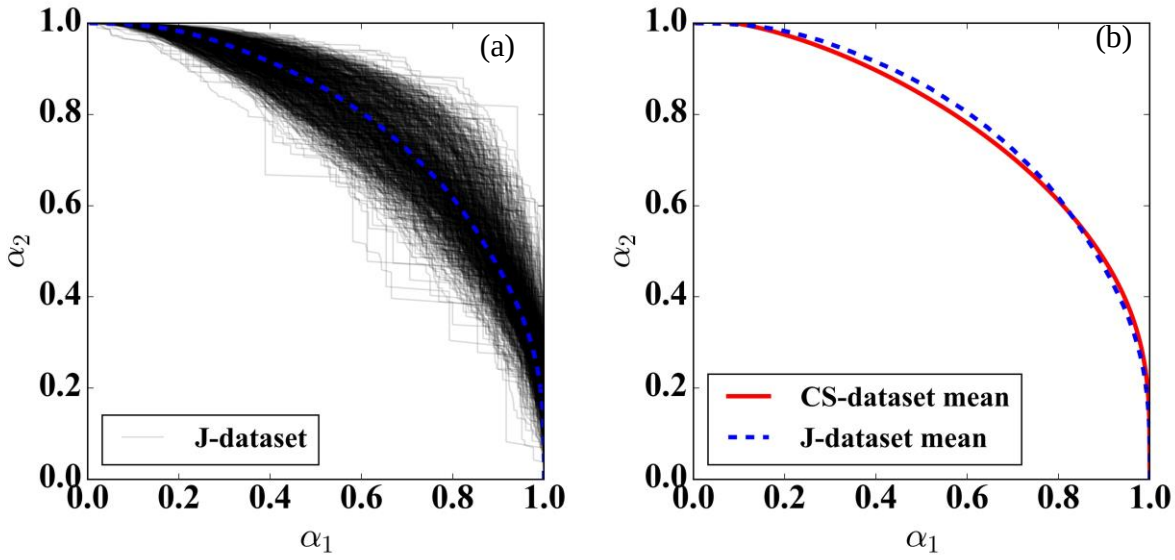

Figure 8.9: Evolution of Arias Intensity versus magnitude-adjusted PGA in CS and J-datasets. (a) All motions in the J-dataset. (b) Comparison of mean values of the J-dataset with the mean values of CS-dataset.

For the timing-based procedure, the uncertainty between values of α_2 given α_1 must also be known. The variance of the evolution of α_2 given α_1 was calculated using the motions in the CS-dataset, and Figure 8.10 shows mean, 16th, and 84th percentile ground motions for both IM^{eff} = I_a and CAV. When IM^{eff} = I_a, α_2 evolves at a more consistent rate and has smaller variance than when IM^{eff} = CAV. I_a is better correlated with PGA_M than CAV, so a smaller variance of α_2 given α_1 should be expected when IM^{eff} = I_a. Likewise, since I_a and PGA_M both capture a similar range of frequency contents, they should evolve at a more similar rate than CAV and PGA_M. Because of the different ranges of frequency content that PGA_M and CAV capture, when IM^{eff} = CAV, the plot of α_2 given α_1 shows a large variance and the shape of the mean exhibits a large curvature.

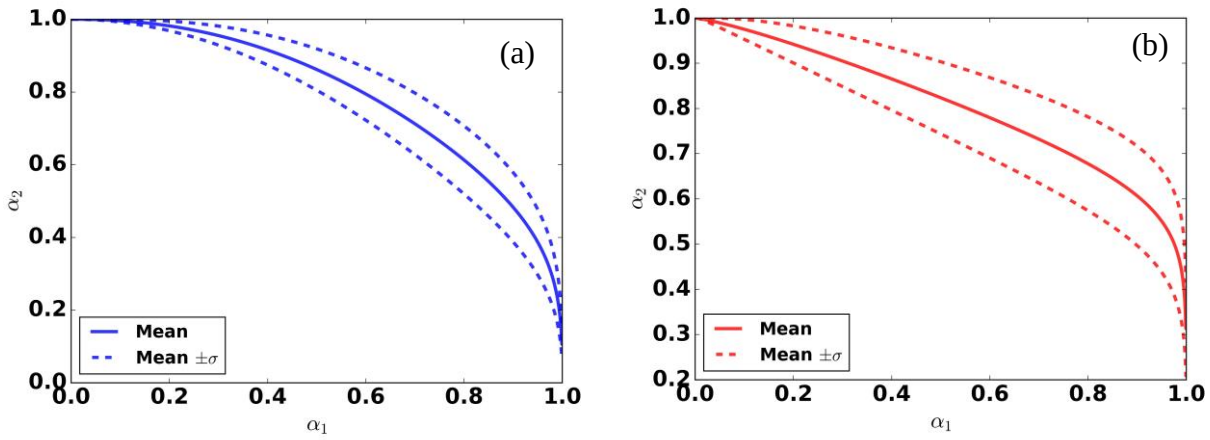

Figure 8.10: Evolution of normalized intensity measures. (a) α_2 as a function of Arias intensity. (b) α_2 as a function of cumulative absolute velocity

Both plots in Figure 8.10 show that the conditional variance of α_2 increases very rapidly as α_1 increases. When α_1 = 0, the variance of α_2 is 0. However, the conditional variance of α_2 given α_1 increases very rapidly until α_1 = 0.2. At values of α_1 > 0.2, the variance of α_2 given α_1 increases less rapidly, but remains relatively large. The domain of α_2 is limited to values between 0 to 1, so the distribution of α_2 given α_1 should also be bounded by 0 and 1. The beta distribution is bounded by values of 0 and 1, is very flexible, and can be fit to many different distributions of data. The probability density function of the beta distribution for a random variable, x, is given by

$$p(a,b) = \frac{\Gamma(a)\Gamma(b)}{\Gamma(a+b)}\, x^{a-1}(1-x)^{b-1} \tag{8.29}$$

where a and b are beta distribution coefficients, and Γ is the gamma function. The coefficients a and b in the beta distribution can be calculated from the expected value, $\mathrm{E}[x]$, and variance, $\mathrm{V}[x]$, of the data (Murphy, 2012).

$$a = \left(\frac{1-\mathrm{E}[x]}{\mathrm{V}[x]} - \frac{1}{\mathrm{E}[x]}\right)(\mathrm{E}[x])^2 \tag{8.30}$$

$$b = \left(\frac{1}{\mathrm{E}[x]} - 1\right) a \tag{8.31}$$

The beta distribution fits the very narrow, but bounded, distribution of α_2 when α_1 approaches 0, and also fits the broader distribution of α_2 when the variance is much larger. Figure 8.11 shows

histograms of α_2 when α_1 = 0.25, 0.5, and 0.75 with a beta distribution probability density function fit to the data.

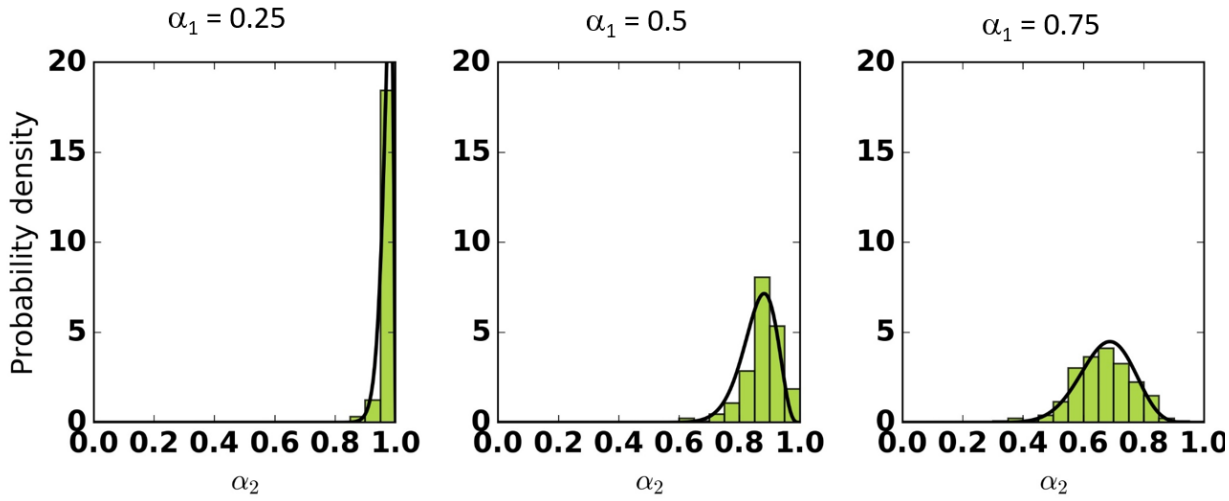

Figure 8.11: Histograms of α_2 conditional upon α_1.

Since the conditional distribution of α_2 given α_1 can be calculated using $E[\alpha_2|\alpha_1]$ and $V[\alpha_2|\alpha_1]$, simplifying equations were developed to estimate parameters a and b for given values of α_1. A simple function was developed to fit to these conditional values.

$$\ln w = c_0 + c_1 \ln \alpha_1 + c_2 \ln(1 - \alpha_1) \tag{8.32}$$

where w is a general parameter that could be either a or b, and c_0, c_1, and c_2 are coefficients determined through regression. The values of c_0, c_1, and c_2 depend on which parameter is used for w, and which IM^{eff} is used to calculate α_2. The coefficients c_0, c_1, and c_2 were estimated using ordinary least squares regression with the ground motions in the CS-dataset. Since the variance of α_2 is essentially 0 as α_1 approaches 0, and since very low values of α_1 are not of interest for prediction of liquefaction effects, the regression was only performed for values of α_1 > 0.1. Figure 8.12 shows the values a and b calculated for both IM^{eff} = I_a and CAV. The estimated values of a and b using the simple fitting function in equation (8.32) are also included in Figure 8.12 represent. Table 8.3 provides the values of c_0, c_1, and c_2.

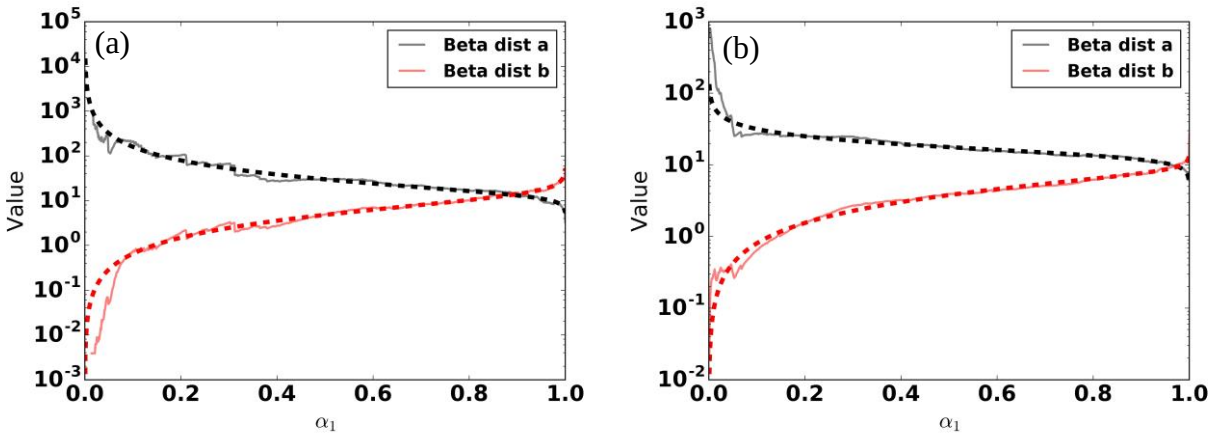

Figure 8.12: Calculated and fitted conditional beta distribution parameters. (a) α_2 based on Arias intensity. (b) α_2 based on cumulative absolute velocity. The solid lines represent the values calculated from the ground motion data, and the dashed lines represent the values estimated using equation (8.32).

Table 8.3: Coefficients in equation (8.32)

α_2 function	Beta distribution parameter	c_0	c_1	c_2
Arias intensity	a	2.82	-0.98	0.16
	b	2.20	1.15	-0.24
Cumulative absolute velocity	a	2.75	-0.31	0.14
	b	1.91	0.93	-0.10

Equation (8.32) and the coefficients in Table 8.3 provide a simple but robust method to calculate the probability of α_2 for given values of α_1. This calculation can then be used to estimate the probability of IM^{eff} given IM^{trig}, which is a necessary step for calculating liquefaction-induced deformation using the timing-based framework.

8.4 POST-TRIGGERING DEFORMATION USING NUMERICAL SIMULATIONS

Despite the intuitive correlation between deformation and the post-triggering intensity of shaking, no procedures currently exist to estimate deformation in this way. One reason is that insufficient data from case histories are available to develop predictive relationships. Case histories that could provide insight into this framework require a detailed understanding of the subsurface conditions, a detailed record of the intensity of shaking required to trigger liquefaction, the intensity of shaking after liquefaction is triggered, and detailed measurements of ground surface deformation. Only

two case histories have this amount of information, Port Island and Wildlife, so other means are necessary to develop a database of deformation versus post-triggering shaking intensity.

Determining an intensity measure that sufficiently predicts post-triggering deformation is an important step in the post-triggering framework. The curves shown in Figure 8.2(d) require a relationship between subsurface conditions, the intensity of shaking after liquefaction is triggered, and the resulting ground surface deformation. The amount of deformation can, therefore, be described as functions of $(N_1)_{60}$ and IM^{eff}. In the absence of field observations, deformation can be estimated using numerical analyses with a model that has been calibrated to match empirical field observations. The Cocktail Glass model in the finite element program FLIP has been calibrated to current procedures for predicting liquefaction triggering and post-triggering behavior. Details about this calibration and the Cocktail Glass model are provided in Section 6.3. Pre-processing software has been written to rapidly batch FLIP in one-dimensional analyses with consideration of liquefaction, lateral deformation at gently-sloping sites, and post-liquefaction reconsolidation settlement. To investigate which *IM*s provide the best prediction of deformation, a general equation was developed to account for the effects of $(N_1)_{60}$ and IM^{eff} on the post-triggering ground surface deformation.

$$\ln \delta = d_0 + d_1 f_1[(N_1)_{60}] + d_2 f_2\left[IM^{\text{eff}}\right] \tag{8.33}$$

where $f_1[(N_1)_{60}]$ and $f_2\left[IM^{\text{eff}}\right]$ are univariate functions of $(N_1)_{60}$ and IM^{eff}, and d_0, d_1, and d_2 are coefficients determined through regression.

An important premise of the timing-based procedure is that different *IM*s can be used for analyzing liquefaction triggering and post-triggering deformation. Lower-frequency *IM*s are more closely associated with the ground motions that drive deformation in liquefied soils, whereas higher-frequency *IM*s are typically associated with liquefaction triggering. In the timing-based framework, IM^{eff} does not need to be, and should not be, the same intensity measure as IM^{trig}. Accounting for the uncertainty in the relationships between IM^{trig} and IM^{eff}, the combination of IM^{trig} and IM^{eff} that produce the lowest uncertainty in predicting δ can be identified.

Another major premise of the timing-based framework is that knowledge of the timing of liquefaction and the intensity of shaking after liquefaction is triggered reduces the uncertainty in predicting δ. To show the effectiveness of the timing-based framework, values of δ estimated

using equation (8.33) can be compared to separate analyses where the intensity of the entire ground motion, $IM_{\text{tot}}^{\text{eff}}$, is used to predict $\ln \delta$. This analysis is referred to as the total *IM* framework, and analyses using $IM_{\text{tot}}^{\text{eff}}$, or a proxy of $IM_{\text{tot}}^{\text{eff}}$, are almost exclusively used in conventional practice. The functional form of the total *IM* framework is similar to equation (8.33), but $IM_{\text{tot}}^{\text{eff}}$ is substituted for IM^{eff}.

$$\ln \delta = d_0 + d_1 f_1[(\text{N}_1)_{60}] + d_2 f_3\left[IM_{\text{tot}}^{\text{eff}}\right] \tag{8.34}$$

where $f_3\left[IM_{\text{tot}}^{\text{eff}}\right]$ is a univariate function of $IM_{\text{tot}}^{\text{eff}}$. Since $IM_{\text{tot}}^{\text{eff}}$ includes the intensity of shaking both before and after liquefaction is triggering, the uncertainty in estimates of δ using the total *IM* framework should be larger than the timing-based framework. The total *IM* framework uses the same information as the timing-based framework, since the evolution between IM^{trig} and IM^{eff} can be calculated using the information in the previous sections.

The expressions in equations (8.33) and (8.34) are limited to a particular site, and they include no variables for the thickness and depth of liquefiable soils, static shear stresses, the ground surface slope, or other properties of the surface or subsurface conditions that are known to affect ground surface deformation. Rather, these analyses show the effects of varying the intensity of shaking and penetration resistance. This information provides the basis for future studies where additional geometry and subsurface conditions could be more rigorously considered in general equations for lateral spreading and settlement prediction.

An example profile was modeled based on a site near a liquid fuel storage facility in Portland, Oregon. The site sloped gently towards the river at a grade of about 2%. The subsurface profile consisted of

- 3-m of unsaturated, loose to medium dense sand fill mantling the ground surface, underlain by
- 5-m of saturated sand with trace to some silt, that was susceptible to liquefaction, underlain by
- 7-m of stiff clayey silt, underlain by
- moderately weathered basalt at a depth of 15 m.

The water table was located at the bottom of the fill at a depth of 3 m. The soil and shear wave velocity profiles of the example site are shown in Figure 8.13.

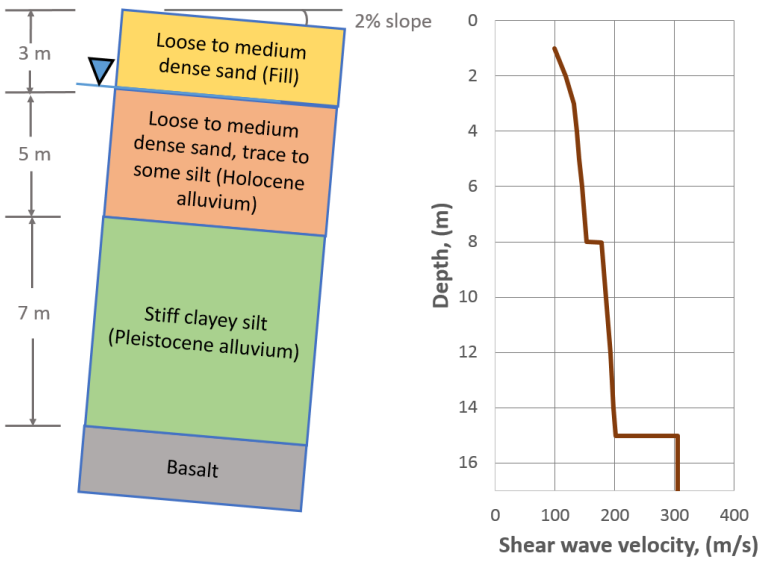

Figure 8.13: Example site profile.

If liquefaction was triggered in the saturated sand between 3 and 8 m deep, large permanent shear strains could develop during shaking due to the gently sloping ground surface. These permanent shear strain would result in lateral spreading deformation at the ground surface. Likewise, as the saturated sand expels excess pore pressure and reconsolidates after liquefaction is triggered, the ground surface would settle.

A limited numerical study was performed using FLIP with the Cocktail Glass model. From the CS-dataset 258 motions were applied to the soil profile, which represented a wide range of possible loading conditions with varying amplitude, duration, and frequency content. The analysis was performed with values of $(N_1)_{60}$ = 4,8,12,16, and 20 blows/ft to represent a range of possible relative densities of the saturated sand. The combination of the CS-data set with the five different values of $(N_1)_{60}$ resulted in over 1,200 simulations, each with a unique combination of IM^{eff}, $(N_1)_{60}$ and values of δ. Regression was performed with these results to estimate the coefficients in equations (8.33) and (8.34). Since equation (8.33) was based on values of IM^{eff}, ground motions that were not strong enough to cause liquefaction (IM^{eff} = 0) were ignored.

8.4.1 *Lateral spreading*

The analysis was first performed to assess lateral spreading deformation assuming that the site sloped gently towards the river at a grade of 2%. Many of the strong ground motions in the CS

data set caused the loose to medium dense sand layer to liquefy, and lateral spreading deformations resulted as the liquefied soil developed permanent shear strains due to the sloping ground. An analysis using the total *IM* framework was first performed to show that lower frequency *IM*s, like I_a and CAV, are more closely associated with deformation than higher-frequency *IM*s, like PGA_M. The values of $IM_{\text{tot}}^{\text{eff}}$ and $(N_1)_{60}$ in the data set were normalized by the constant reference values, IM_{ref}, to create dimensionless quantities. Results from the Box-Cox transformation (Box and Cox, 1964; Weisberg, 2012) indicated that the normalized variables were approximately normally distributed as $\ln\left[\frac{(N_1)_{60}}{15\text{ blows/ft}}\right]$ and $\ln\left[\frac{IM_{\text{tot}}^{\text{eff}}}{IM_{\text{ref}}}\right]$. These terms were substituted into equation (8.34).

$$\ln\delta = d_0 + d_1 \ln\left[\frac{(N_1)_{60}}{15\text{ blows/ft}}\right] + d_2 \ln\left[\frac{IM_{\text{tot}}^{\text{eff}}}{IM_{\text{ref}}}\right] + \sigma_{\ln\delta|N}\varepsilon_{\ln\delta|N} \tag{8.35}$$

where δ is the estimated values of deformation and d_0, d_1, d_2 are constants estimated using regression, and IM_{ref} is a reference normalizing value. In equation (8.35) δ is log-normally distributed with standard deviation $\sigma_{\ln\delta|N}$, that is conditional upon given values of $(N_1)_{60}$. $\varepsilon_{\ln\delta|N}$ is a standard normally distributed random variable. Regression was performed to estimate the coefficients in equation (8.35) using $IM_{\text{tot}}^{\text{eff}}$ = PGA_M, I_a, and CAV. An analysis of the regression results indicated that $IM_{\text{tot}}^{\text{eff}}$ = CAV produced the lowest uncertainty in ln δ, followed by $IM_{\text{tot}}^{\text{eff}}$ = I_a. $IM_{\text{tot}}^{\text{eff}}$ = PGA produced estimates of ln δ with relatively large uncertainty. These results show that, when only $IM_{\text{tot}}^{\text{eff}}$ was considered, *IM*s associated with lower-frequency ground motions generally produced less uncertain estimates of ln δ. This supports the notion that deformations should be more closely related to ground motion intensity measures that correlate well to lower frequencies. Figure 8.15 shows the distributions of ln δ with the median value of δ = 1 m. The values of d_0, d_1, d_2 and $\sigma_{\ln\delta|N}$ from the regression analyses are provided on Table 8.4.

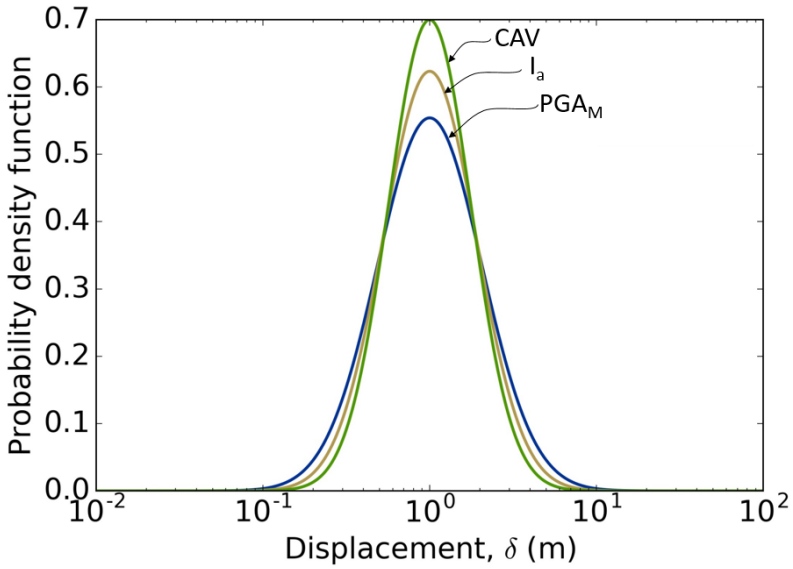

Figure 8.15: Distribution of lateral spreading deformation estimated using the total *IM* framework.

Table 8.4: Coefficients and uncertainties for lateral spreading estimates using the total *IM* framework

Framework	Intensity measures	Reference value for normalizing, IM_{ref}	d_0	d_1	d_2	$\sigma_{\ln \delta \mid N}$
Total IM	$IM_{tot}^{eff} = PGA_M$	0.20 g	-0.59	-1.54	0.63	0.72
Total IM	$IM_{tot}^{eff} = I_a$	1 m/s	-1.22	-1.68	0.45	0.64
Total IM	$IM_{tot}^{eff} = CAV$	5 m/s	-1.85	-1.62	0.77	0.57

In accordance with the timing-based framework, the uncertainty in ln δ should be reduced with IM^{eff} is used instead of IM_{tot}^{eff}. A value of IM_L^{trig} was calculated for each analysis using a conventional liquefaction triggering procedure (Boulanger and Idriss, 2014) with $IM^{trig} = PGA_M$. In each ground motion, the time when $IM^{trig} = IM_L^{trig}$ was identified, and then the evolutionary value of IM^{eff} was calculated in accordance with Section 8.1. Although IM^{trig} and IM^{eff} do not need to be the same intensity measure, the timing-based framework analysis was first performed with $IM^{eff} = PGA_M$ to show that the timing-based framework reduced the uncertainty in estimating δ even when the same intensity measures are used. The contours of δ versus IM^{eff} and $(N_1)_{60}$ were calculated as

$$\ln \delta = d_0 + d_1 \ln\left[\frac{(\mathrm{N}_1)_{60}}{15\ \mathrm{blows/ft}}\right] + d_2 \ln\left[\frac{IM^{\mathrm{eff}}}{IM_{\mathrm{ref}}}\right] + \sigma_{\ln\delta|N}\varepsilon_{\ln\delta|N} \tag{8.36}$$

Coefficients d_0, d_1, and d_2 were then estimated using least squares regression with IM^{eff} = $\mathrm{PGA_M}$. The regression results indicate that, when IM^{eff} = $\mathrm{PGA_M}$, $\sigma_{\ln\delta|N}$ = 0.53. This value of $\sigma_{\ln\delta|N}$ was significantly lower than the corresponding value of $\sigma_{\ln\delta|N}$ calculated using the total *IM* framework with $IM_{\mathrm{tot}}^{\mathrm{eff}}$ = $\mathrm{PGA_M}$, $\sigma_{\ln\delta|N}$ = 0.72. Even though the total *IM* and timing-based frameworks used the same data set, as is typical in contemporary practice, the total *IM* framework did not take advantage of the knowledge that most of the deformation occurred after liquefaction was triggered. The timing-based framework, however, did take advantage of this knowledge, and the uncertainty in estimates of $\ln\delta$ were reduced as a result. Figure 8.15 shows the distributions of $\ln\delta$ for both the total *IM* framework with $IM_{\mathrm{tot}}^{\mathrm{eff}}$ = $\mathrm{PGA_M}$ and the timing based framework with IM^{eff} = $\mathrm{PGA_M}$.

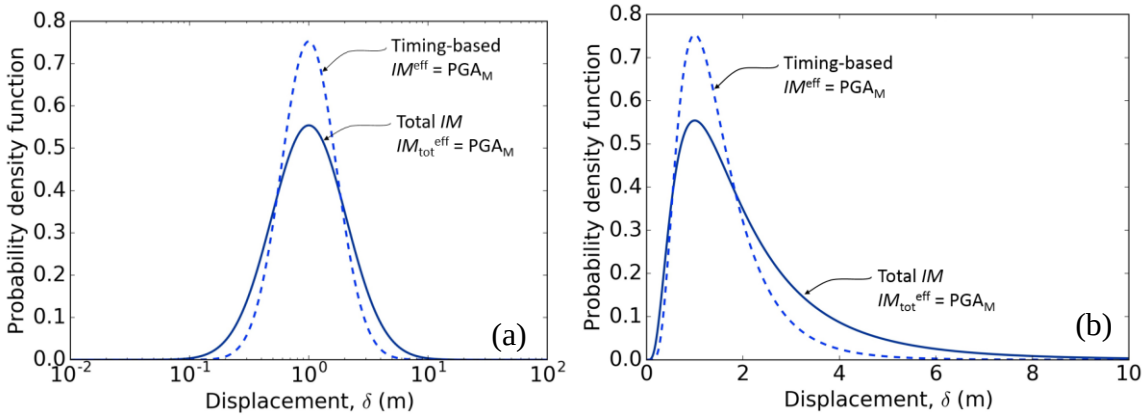

Figure 8.15: Comparison of the distribution of lateral spreading deformation estimated using total *IM* and timing-based frameworks with IM^{eff} = $\mathrm{PGA_M}$. (a) Logarithmic scale. (b) Linear scale.

Additional analyses were then performed using the timing-based procedure to show that the uncertainty in $\ln\delta$ decreased (1) by using an *IM* that is more closely associated with lower-frequency ground motions, and (2) by using the post-triggering intensity of shaking, IM^{eff}, as opposed to the intensity of shaking for the entire ground motion, $IM_{\mathrm{tot}}^{\mathrm{eff}}$. Values IM^{eff} = $\mathrm{PGA_M}$, $\mathrm{I_a}$ and CAV were calculated using the curves described in Figure 8.2. Coefficients d_0, d_1, and d_2 and $\sigma_{\ln\delta|N}$ were then calculated using least squares regression with equation (8.37) and the ground motions in the CS-dataset. The regression analyses indicated that the timing-based framework

consistently reduced the uncertainty in $\ln \delta$ compared to the total *IM* framework. IM^{eff} = CAV yielded the lowest uncertainty, followed by IM^{eff} = I_a, and IM^{eff} = PGA_M yielded the highest uncertainty. The results of the regression analyses are provided in Table 8.5.

Table 8.5: Coefficients for lateral spreading estimates timing-based framework

Framework	Intensity measures	Reference value for normalizing, IM_{ref}	d_0	d_1	d_2	$\sigma_{\ln \delta \mid N}$
Timing-based	IM^{trig} = PGA_M IM^{eff} = PGA_M	0.20 g	-0.07	-1.31	0.30	0.53
Timing-based	IM^{trig} = PGA_M IM^{eff} = I_a	1 m/s	-0.97	-1.58	0.40	0.45
Timing-based	IM^{trig} = PGA_M IM^{eff} = CAV	5 m/s	-1.44	-1.53	0.68	0.40

In the timing-based framework, both IM^{eff} = I_a and CAV showed relatively low uncertainty in $\ln \delta$. Simply using the total *IM* framework with IM^{trig} = PGA_M resulted in a large amount of uncertainty and $\sigma_{\ln \delta \mid N}$ was equal to 0.72. The timing-based framework reduced this uncertainty even when the same *IM* was used to estimate triggering and the effects of liquefaction; when IM^{eff} = PGA_M, $\sigma_{\ln \delta \mid N}$ was equal to 0.53. Optimally selecting an intensity measure to estimate the effects of liquefaction further reduced the uncertainty. The timing-based framework with IM^{eff} = CAV resulted in the lowest uncertainty and $\sigma_{\ln \delta \mid N}$ was equal to 0.40. Figure 8.16 shows distributions of ln δ calculated using the total *IM* framework with $IM_{\text{tot}}^{\text{eff}}$ = PGA_M, and the timing based framework with IM^{eff} = PGA_M, and the timing based framework with IM^{eff} = CAV.

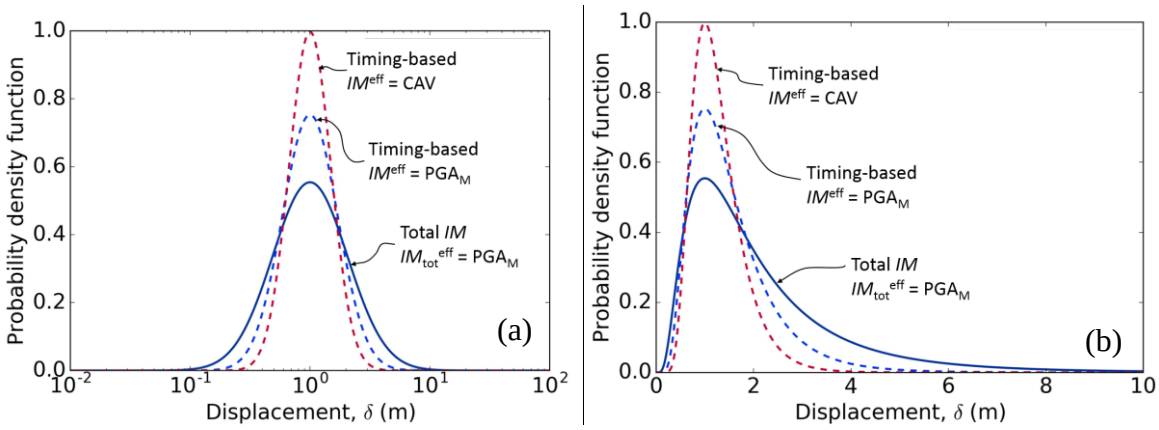

Figure 8.16: Comparison of the distribution of lateral spreading deformation estimated using total *IM* and timing-based frameworks with IM^{eff} = PGA_M and IM^{eff} = CAV. (a) Logarithmic scale. (b) Linear scale.

These results show that I_a and CAV are good potential candidates for IM^{eff} in the timing-based framework. The coefficients listed in Table 8.5 were substituted into equation (8.36) to calculate contours of δ as functions of $(N_1)_{60}$ and IM^{eff}. These contours provide the final link to estimate lateral spreading deformation using the timing-based procedure, where previously, no methods were available to complete the sequence shown in Figure 8.2(d) to estimate δ. Figure 8.17 shows the contours of δ for both IM^{eff} = I_a and CAV.

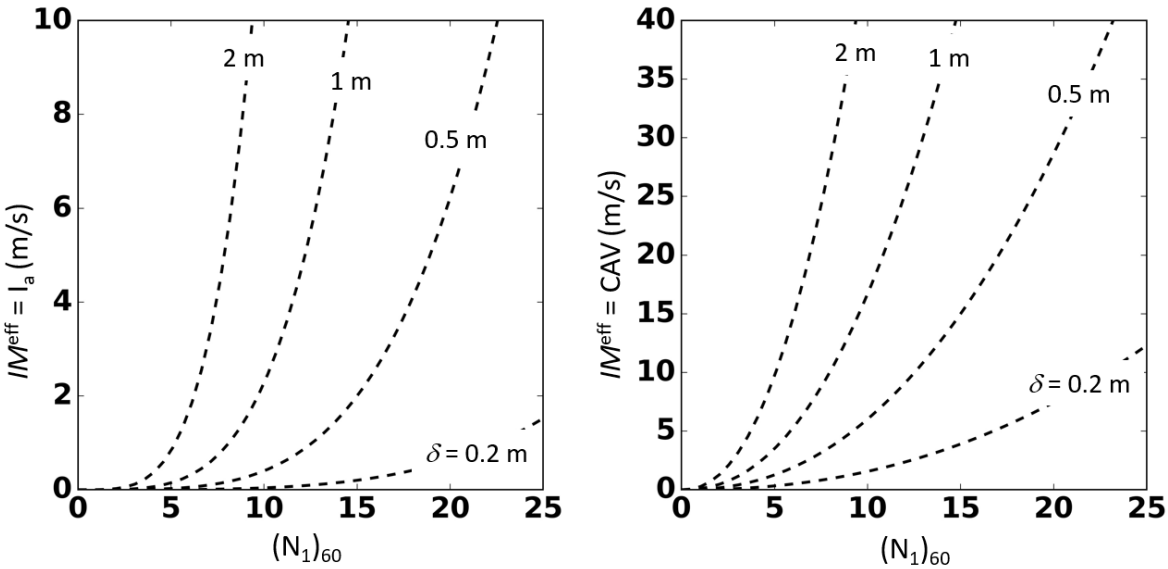

Figure 8.17: Estimated lateral spreading deformation for the example site profile.

8.4.2 *Settlement*

The post-triggering and total *IM* analyses were repeated for liquefaction-induced reconsolidation settlement. It should be acknowledged that reconsolidation is not the only mechanism that can lead to liquefaction-induced settlement, but reconsolidation settlement can be a large contributor to free-field settlement after liquefaction is triggered in many conditions.

The decrease in uncertainty by using the timing-based framework rather than the total *IM* framework is not as effective for estimating reconsolidation settlement as it is for estimating lateral spreading. Reconsolidation settlement occurs due to the dissipation of excess pore pressure after the end of shaking. Even before the soil liquefies, excess pore pressure could be relatively high, which could result in significant amounts of settlement, but not liquefaction. Based on the research by Ishihara and Yoshimine (1992), even if $IM^{\text{eff}} = 0$ and the factor of safety against liquefaction is exactly 1.0, the reconsolidation volumetric strain of the soil ranges from about 0.5-1%, depending on the relative density of the soil. For the example profile, these strains would result in a minimum settlement of about 0.025 to 0.05 m when $IM^{\text{eff}} = 0$. Likewise, an upper limit of 1.5 to 5.5% reconsolidation volumetric strain has been observed in laboratory tests, regardless of the intensity of shaking after liquefaction. These upper-bound limits would result in maximum settlements of about 0.08 to 0.27 m for the example.

Despite the dependence of reconsolidation settlement on factors other than IM^{eff}, the timing-based framework can still be used to reduce the uncertainty in estimated settlement compared to the total *IM* framework. Over 1,200 simulations were again performed using FLIP for a site with the same profile to the one shown in Figure (8.14), but with flat ground. The amount of reconsolidation settlement, *s*, a long time after the end of shaking after excess pore pressure dissipated was calculated. The total *IM* framework was first used to identify which *IM*s are likely to be associated with reconsolidation settlement. The Box-Cox transform indicated that $\ln\left[\frac{(\mathrm{N}_1)_{60}}{15\ \text{blows/ft}}\right]$ and $\ln\left[\frac{IM_{\text{tot}}^{\text{eff}}}{IM_{\text{ref}}}\right]$ both produced approximately normal distributions of the data, and coefficients d_0, d_1, and d_2 were estimated using least squares regression.

$$\ln s = d_0 + d_1 \ln\left[\frac{(\mathrm{N}_1)_{60}}{15\ \text{blows/ft}}\right] + d_2 \ln\left[\frac{IM_{\text{tot}}^{\text{eff}}}{IM_{\text{ref}}}\right] + \sigma_{\ln s|N}\varepsilon_{\ln s|N} \tag{8.37}$$

where s is the estimated values of reconsolidation settlement, d_0, d_1, d_2, $\sigma_{\ln s|N}$ are constants estimated using regression, and IM_{ref} is a reference normalizing value. $\varepsilon_{\ln s|N}$ is a standard normally distributed random variable. Regression was performed to estimate the coefficients in equation (8.37) using $IM_{\text{tot}}^{\text{eff}}$ = PGA_M, I_a, and CAV. An analysis of the regression results indicated that $IM_{\text{tot}}^{\text{eff}}$ = CAV produced the lowest uncertainty in ln s, although the uncertainty using $IM_{\text{tot}}^{\text{eff}}$ = I_a was very similar. $IM_{\text{tot}}^{\text{eff}}$ = PGA_M produced estimates of ln s with the largest uncertainty. These results show that, when the total *IM* framework is used, *IM*s associated with lower-frequency ground motions generally produced estimates of ln s with lower uncertainty. Figure 8.18 shows the distributions of ln s with a median value of δ = 0.1 m. The values of d_0, d_1, d_2 and $\sigma_{\ln s|N}$ from the regression analyses are provided on Table 8.6.

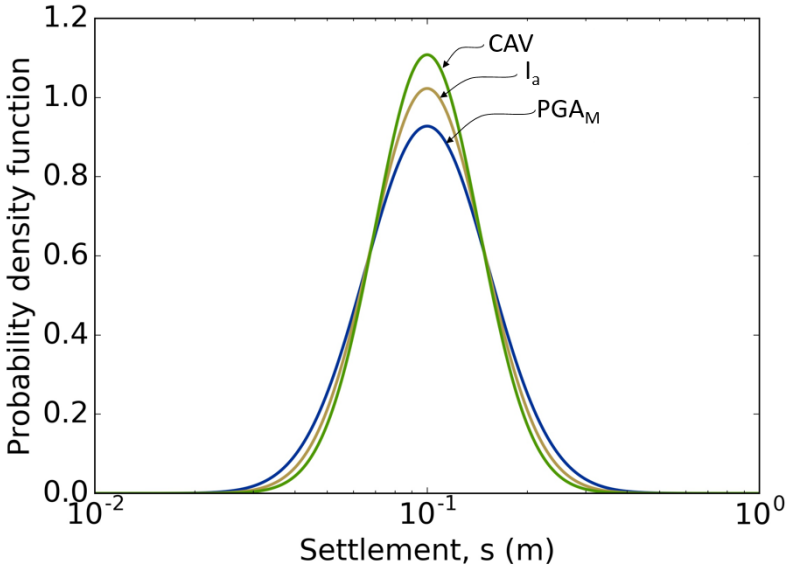

Figure 8.18: Distribution of reconsolidation settlement estimated using total *IM* framework.

Table 8.6: Coefficients for reconsolidation settlement estimates using the total *IM* framework

Framework	Intensity measures	Reference value for normalizing, IM_{ref}	d_0	d_1	d_2	$\sigma_{\ln s|N}$
Total IM	$IM_{\text{tot}}^{\text{eff}}$ = PGA_M	0.20 g	-3.07	-0.78	0.159	0.43
Total IM	$IM_{\text{tot}}^{\text{eff}}$ = I_a	1 m/s	-3.25	-0.87	0.187	0.39
Total IM	$IM_{\text{tot}}^{\text{eff}}$ = CAV	5 m/s	-3.50	-0.91	0.371	0.36

As with the lateral spreading analysis, the uncertainty in ln δ should be reduced by using the timing-based framework with IM^{eff} instead of the total *IM* framework with $IM_{\text{tot}}^{\text{eff}}$. Values of $IM_{\text{L}}^{\text{trig}}$ were calculated using a conventional liquefaction triggering procedure (Boulanger and Idriss, 2014) with $IM_{\text{L}}^{\text{trig}}$ = PGA_{M}. The process described in Section 8.1 was then used to calculate IM^{eff}. Like the lateral spreading analyses, the timing-based framework was first analyzed with IIM^{eff} = PGA_{M}. This analysis isolates the reduction in uncertainty that is just from the timing-based framework. The uncertainty can be further reduced by considering separate *IM*s for the triggering and effects of liquefaction. Both $(\text{N}_1)_{60}$ and IM^{eff} were used as variables for predicting ln s.

$$\ln s = d_0 + d_1 \ln\left[\frac{(\text{N}_1)_{60}}{15\ \text{blows/ft}}\right] + d_2 \ln\left[\frac{IM^{\text{eff}}}{IM_{\text{ref}}}\right] + \sigma_{\ln s|N}\varepsilon_{\ln s|N} \tag{8.38}$$

Coefficients d_0, d_1, and d_2 were then estimated using least squares regression with IM^{eff} = PGA_{M}. The regression results indicate that, when IM^{eff} = PGA_{M}, the value of $\sigma_{\ln s|N}$ = 0.42. This value was only slightly less than the value of $\sigma_{\ln s|N}$ calculated using the total *IM* framework with $IM_{\text{tot}}^{\text{eff}}$ = PGA_{M}, $\sigma_{\ln s|N}$ = 0.43. The relatively insignificant improvement using the timing-base framework stems from (1) the nature of reconsolidation settlement, which depends on many factors, not just the intensity of shaking after liquefaction is triggered, and (2) the *IM* selected for IM^{eff}, which may not be a good predictor of reconsolidation settlement.

Repeating this analysis with IM^{eff} = I_{a} and CAV did, however, produce substantial reductions in the uncertainty of predicting ln s relative to the total *IM* framework. Values IM^{eff} = I_{a} and CAV were calculated in accordance with Section 8.1, and coefficients d_0, d_1, and d_2 and $\sigma_{\ln s|N}$ were estimated using least squares regression with equation (8.38). The regression analyses indicated that IM^{eff} = CAV yielded the lowest uncertainty in estimates of ln s, followed by IM^{eff} = I_{a}. The results of the regression analyses are provided in Table 8.7.

Table 8.7: Coefficients for settlement estimates the timing-based framework

Framework	Intensity measures	Reference value for normalizing, IM_{ref}	d_0	d_1	d_2	$\sigma_{\ln s\|N}$
Timing-based	IM^{trig} = PGA_M IM^{eff}= PGA_M	0.20 g	-2.83	-0.71	0.062	0.42
Timing-based	IM^{trig} = PGA_M IM^{eff} = I_a	1 m/s	-3.05	-0.80	0.151	0.35
Timing-based	IM^{trig} = PGA_M IM^{eff} = CAV	5 m/s	-3.23	-0.82	0.322	0.28

In the timing-based framework, both IM^{eff} = I_a and IM^{eff} = CAV showed lower uncertainty in $\ln s$ compared to IM^{eff} = PGA_M. Simply using the total *IM* framework with IM^{trig} = PGA_M resulted in a large amount of uncertainty and $\sigma_{\ln \delta|N}$ was equal to 0.43. The timing-based framework did not reduce the uncertainty as significantly for reconsolidation settlement as it did for lateral spreading. When IM^{eff} = PGA_M, $\sigma_{\ln \delta|N}$ was only reduced to 0.42. However, the timing-based framework allows different *IM*s to be used for the triggering and effects of liquefaction. Optimally selecting IM^{eff} = CAV to estimate the effects of liquefaction reduced the uncertainty and $\sigma_{\ln s|N}$ was equal to 0.28. Figure 8.19 shows distributions of $\ln \delta$ calculated using the total *IM* framework with IM_{tot}^{eff} = PGA_M, the timing based framework with IM^{eff} = PGA_M, and the timing based framework with IM^{eff} = CAV.

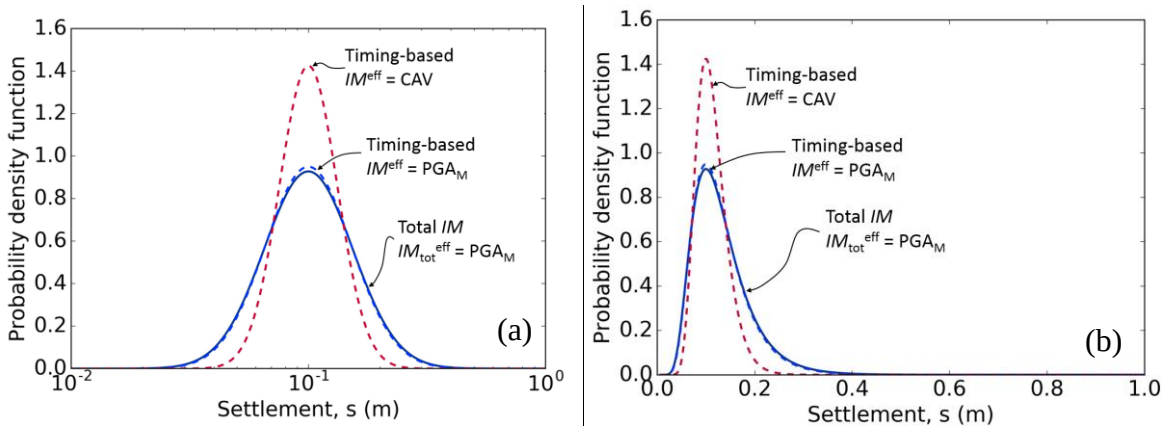

Figure 8.19: Comparison of the distribution of reconsolidation settlement estimated using total *IM* and timing-based frameworks with IM^{eff} = PGA_M and IM^{eff} = CAV. (a) Logarithmic scale. (b) Linear scale.

Based on the results of the regression analyses, CAV is the best potential candidates for IM^{eff} in the timing-based framework to calculate reconsolidation settlement. The data from Table 8.6 was substituted into equation (8.38) to calculate contours of s versus $(N_1)_{60}$ and IM^{eff}. These contours are shown in Figure 8.20 for both IM^{eff} = I_a and CAV. This figure provides the final link to estimate reconsolidation settlement using the timing-based procedure, where previously, no methods were available to complete the sequence shown in Figure 8.2(d) to estimate s.

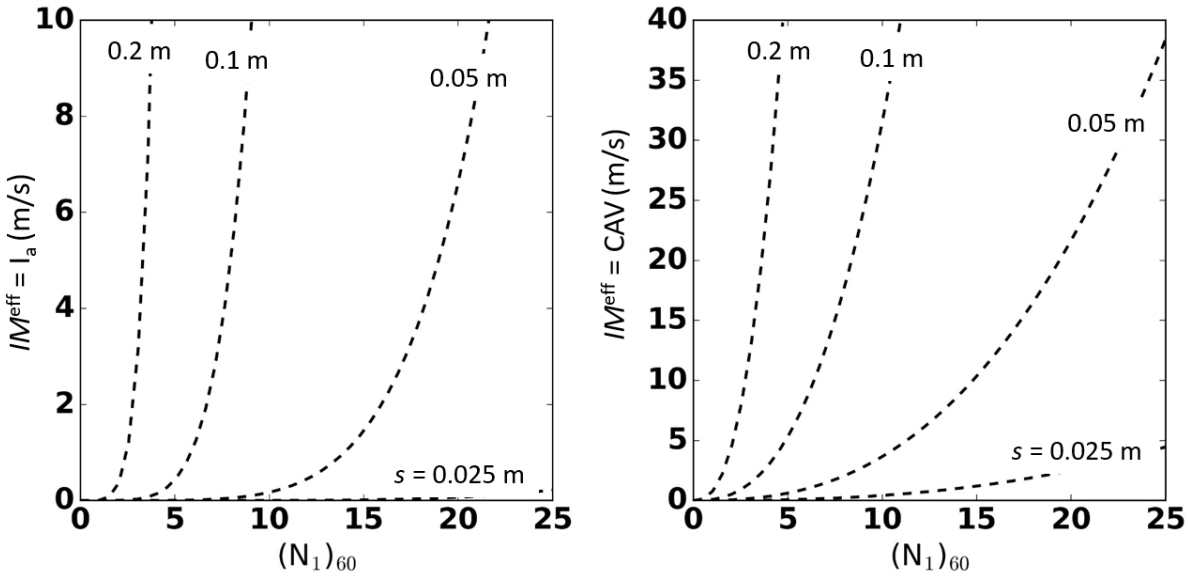

Figure 8.20: Estimated reconsolidation settlement for the example site profile

8.4.3 *Relationship to factor of safety*

Many of the existing laboratory-based observations of post-triggering shear strain are based on the relative density of the soil and the factor of safety against liquefaction. Semi-empirical procedures to predict lateral spreading based on strain potential (Zhang et al., 2004; Khoshnevisan et al., 2015) use these observations to estimate ground surface deformation as a function of the factor of safety against liquefaction. Since the factor of safety is typically based on $\mathrm{PGA_M}$, separate *IM*s for liquefaction triggering and post-triggering deformation are not advantageously used in these procedures. In this context, the factor of safety can be defined as

$$\mathrm{FS} = \frac{IM_{\mathrm{L}}^{\mathrm{trig}}}{IM_{\mathrm{tot}}^{\mathrm{trig}}} \tag{8.39}$$

where $IM_{\mathrm{L}}^{\mathrm{trig}}$ = $\mathrm{PGA_M}$ at the moment liquefaction is triggered, and $IM_{\mathrm{tot}}^{\mathrm{trig}}$ = $\mathrm{PGA_M}$ at the end of the ground motion. Both of these *IM*s are "static" in that they do not evolve with time. To show that the factor of safety against liquefaction is more closely related to the total *IM* framework than the timing-based framework, a simple expression for predicting $\ln \delta$ can be written using $(\mathrm{N_1})_{60}$ and FS.

$$\ln \delta = d_0 + d_1 \ln\left[\frac{(\mathrm{N_1})_{60}}{15\ \mathrm{blows/ft}}\right] + d_2 \ln[\mathrm{FS}] + \sigma_{\ln \delta|N}\varepsilon_{\ln \delta|N} \tag{8.40}$$

Substituting equation (8.39) into equation (8.4) yields an equation that includes $IM_{\mathrm{tot}}^{\mathrm{trig}}$ and $IM_{\mathrm{L}}^{\mathrm{trig}}$.

$$\ln \delta = d_0 + d_1 \ln\left[\frac{(\mathrm{N_1})_{60}}{15\ \mathrm{blows/ft}}\right] + d_2 \ln\left[\frac{IM_{\mathrm{L}}^{\mathrm{trig}}}{IM_{\mathrm{tot}}^{\mathrm{trig}}}\right] + \sigma_{\ln \delta|N}\varepsilon_{\ln \delta|N} \tag{8.41}$$

Then, expanding $\ln\left[\frac{IM_{\mathrm{L}}^{\mathrm{trig}}}{IM_{\mathrm{tot}}^{\mathrm{trig}}}\right]$,

$$\ln \delta = d_0 + d_1 \ln\left[\frac{(\mathrm{N_1})_{60}}{15\ \mathrm{blows/ft}}\right] + d_2\left(\ln\left[IM_{\mathrm{L}}^{\mathrm{trig}}\right] - \ln\left[IM_{\mathrm{tot}}^{\mathrm{trig}}\right]\right) + \sigma_{\ln \delta|N}\varepsilon_{\ln \delta|N} \tag{8.42}$$

Equation (8.42) does not include any intensity measure that captures the intensity of shaking after liquefaction has been triggered. It is similar in form to the total *IM* framework in equation (8.34), since $IM_{\mathrm{L}}^{\mathrm{trig}}$ can be calculated using $(\mathrm{N_1})_{60}$, and $IM_{\mathrm{tot}}^{\mathrm{trig}}$ only provides a measure of the intensity of the ground motion for the total duration of shaking. Equation (8.42) also does not advantageously

use different *IM*s for liquefaction triggering and post-triggering deformation, since $IM_{\mathrm{L}}^{\mathrm{trig}}$ is the *IM* associated with liquefaction triggering. Performing regression with the numerical lateral spreading data resulted in a value of $\sigma_{\ln\delta|N}$ = 0.71. The uncertainty obtained using FS is nearly identical to that obtained using the total *IM* framework with $IM_{\mathrm{tot}}^{\mathrm{eff}}$ = $\mathrm{PGA_M}$. These uncertainties are significantly greater than the uncertainties when the total *IM* framework is used with $IM_{\mathrm{tot}}^{\mathrm{eff}}$ = $\mathrm{I_a}$ or CAV. This suggests that FS does not capture the lower frequency ground motions that are associated with deformation, and may not be a good *IM* for predicting the effects of liquefaction. The value of $\sigma_{\ln\delta|N}$ calculated using equation (8.42) is also much greater than when the value of $\sigma_{\ln\delta|N}$ calculated using the timing-based framework with IM^{eff} = $\mathrm{PGA_M}$, suggesting that the functional form of FS in equations (8.40) through (8.42) may not even result in the lowest uncertainty with the given data. While smaller values of FS frequently could imply that liquefaction was triggered early in the motion, which would result in a large value of IM^{eff}, the functional form of FS could be improved by using it to calculate IM^{eff} to use in the timing-based framework.

$$IM^{\mathrm{eff}} = \max\begin{Bmatrix} IM_{\mathrm{tot}}^{\mathrm{eff}}(1-\mathrm{FS}) \\ 0 \end{Bmatrix} \tag{8.43}$$

As shown in Table 8.5, the timing-based framework with IM^{eff} = $\mathrm{PGA_M}$ produced a value of $\sigma_{\ln\delta|N}$ = 0.53. This value is dramatically less than the value of $\sigma_{\ln\delta|N}$ = 0.71 calculated using FS in equation (8.42). This observation indicates that using FS as a predictor of deformation could be improved by calculating IM^{eff}, which would require no additional information to be collected.

8.5 PROBABILITY OF EXCEEDING LEVELS OF DEFORMATION

The framework outlined in Section 8.1 and shown graphically in Figure 8.2 can be implemented to estimate the probabilities of exceeding specific levels of deformation. The previous discussions indicate that, in the steps of the timing-based framework, uncertainty exists in the calculation of

- field penetration resistance,
- the relationship between $IM_{\mathrm{L}}^{\mathrm{trig}}$ and $(\mathrm{N_1})_{60}$,
- the relationship between IM^{eff} and IM^{trig}, and
- the relationship between δ given IM^{eff} and *N*.

Total uncertainty in δ therefore depends on the conditional uncertainty and relationships between each of these steps. However, even when the uncertainty between each step is known, combining the uncertainties into the timing-based framework is not trivial. In a deterministic earthquake scenario, when $IM_{\text{tot}}^{\text{eff}}$ is known, the uncertainty in *N* and IM^{eff} must still be considered. In a probabilistic calculation, intensity measures $IM_{\text{tot}}^{\text{trig}}$ and $IM_{\text{tot}}^{\text{eff}}$ are also random variables, which add to complexity of the calculation. Fortunately, in a probabilistic seismic hazard analysis (PSHA) or probabilistic liquefaction hazard analysis, values of $IM_{\text{tot}}^{\text{trig}}$ are calculated for a particular return period. Even though it is acknowledged that $IM_{\text{tot}}^{\text{trig}}$ could contain uncertainty, the objective of this section is to show that the timing-based framework reduces the uncertainty in estimating deformation compared to the total *IM* framework. Incorporating the uncertainty in $IM_{\text{tot}}^{\text{trig}}$ could be accomplished using the performance-based techniques established by Kramer and Mayfield (2007). For subsequent analyses, the value of $IM_{\text{tot}}^{\text{trig}}$ at a particular design return period is assumed to be known through PSHA. Even when values of $IM_{\text{tot}}^{\text{trig}}$ are known, the correlations of $IM_{\text{tot}}^{\text{eff}}$ given $IM_{\text{tot}}^{\text{trig}}$ contain some amount of uncertainty, which must be considered in the timing-based framework.

The combination of random variables in this analysis must first be discussed in the context of the total probability theorem, which provides the basis for linking the uncertainties in each step of the timing-based framework. Equations for estimating the probability of exceeding δ are then described for the total *IM* framework, and are then discussed for the timing-based framework.

8.5.1 *Total probability theorem*

The analysis of the probability of exceeding levels of δ is an extension of conditional probability, where in a multivariable distribution, the joint probability of events *A* and *B*, can be defined by the conditional probability of *A* given *B*.

$$\mathrm{P}[A \cap B] = \mathrm{P}[A|B]\mathrm{P}[B] \tag{8.44}$$

where ∩ is the "and" (or intersection) operator. For a set of events, B_i, that are mutually exclusive and occupy the entire sample space, the probability of event *A* can be expressed as

$$\mathrm{P}[A] = \sum_{i=1}^{\infty} \mathrm{P}[A \cap B_i] \tag{8.45}$$

Substitution equation (8.45) into equation (8.46) result in

$$\mathrm{P}[A] = \sum_{i=1}^{\infty} \mathrm{P}[A|B_i]\mathrm{P}[B_i] \tag{8.46}$$

which defines the total probability theorem. An example of total probability theorem is shown in Figure 8.21. In this figure, the events B_1 through B_6 occupy the entire sample space and are mutually exclusive. The sum of conditional probabilities of A given B_1 through B_6 is equal to the total probability of A.

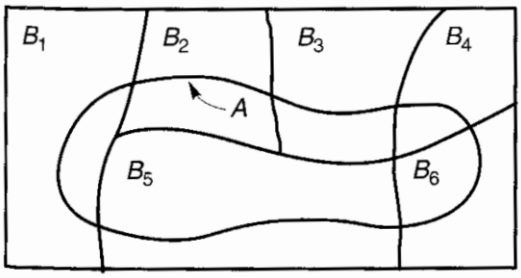

Figure 8.21: Venn diagram example showing the total probability theorem using events *A* and *B* (from Kramer 1996).

Thus, the concept of conditional probability is a powerful tool to calculate the joint probability of an event with many different variables. The probability of exceeding a particular displacement level, $\mathrm{P}[D > \delta]$ where D is a random variable and δ is an amount of deformation, is the primary focus of this analysis.

8.5.2 *Total IM framework*

Equation (8.35) can be used to estimate δ given $IM_{\mathrm{tot}}^{\mathrm{eff}}$ and N. Each one of these terms, δ, $IM_{\mathrm{tot}}^{\mathrm{eff}}$, and N, is a random variable, and has some uncertainty associated with it. The total probability theorem can be used to calculate the probability of exceeding δ by considering the uncertainty in $IM_{\mathrm{tot}}^{\mathrm{eff}}$ and N.

$$\mathrm{P}[D > \delta] = \sum_{IM_{\mathrm{tot}}^{\mathrm{eff}},N} \mathrm{P}\left[D > \delta \middle| IM_{\mathrm{tot}}^{\mathrm{eff}}, N\right] \mathrm{P}\left[IM_{\mathrm{tot}}^{\mathrm{eff}}, N\right] \tag{8.47}$$

where $\mathrm{P}\left[IM_{\mathrm{tot}}^{\mathrm{eff}}, N\right]$ is a joint probability distribution. If N and $IM_{\mathrm{tot}}^{\mathrm{eff}}$ are independent, then

$$\mathrm{P}[D > \delta] = \sum_{N} \sum_{IM_{\mathrm{tot}}^{\mathrm{eff}}} \mathrm{P}\left[D > \delta \middle| IM_{\mathrm{tot}}^{\mathrm{eff}}, N\right] \mathrm{P}\left[IM_{\mathrm{tot}}^{\mathrm{eff}}\right] \mathrm{P}[N] \tag{8.48}$$

The probability of exceeding levels of deformation, therefore, required multiple summations over N and $IM_{\mathrm{tot}}^{\mathrm{eff}}$. The term $\mathrm{P}\left[D > \delta \middle| IM_{\mathrm{tot}}^{\mathrm{eff}}, N\right]$ can be calculated using equation (8.35), which defines δ given N and $IM_{\mathrm{tot}}^{\mathrm{eff}}$ as a log-normal distribution with constant standard deviation, $\sigma_{\ln \delta|N}$. $IM_{\mathrm{tot}}^{\mathrm{eff}}$ is typically assumed to be log-normally distributed, and $\sigma_{IM_{\mathrm{tot}}^{\mathrm{eff}}}$ can be calculated using GMPEs or correlations with $IM_{\mathrm{tot}}^{\mathrm{trig}}$. Details of the uncertainty in N are discussed in Section 8.2, and for this analysis, N is assumed to be normally distributed with a standard deviation, σ_N, that varies with E[N], but is based on a constant coefficient of variation.

8.5.3 *Timing-based framework*

In the timing-based framework, the distribution of D depends on penetration resistance and post-triggering intensity of shaking, denoted as random variables IM^{eff} and N. Using the total probability theorem,

$$\mathrm{P}[D > \delta] = \sum_{IM^{\mathrm{eff}},N} \mathrm{P}\left[D > \delta \middle| IM^{\mathrm{eff}}, N\right] \mathrm{P}\left[IM^{\mathrm{eff}}, N\right] \tag{8.49}$$

The term $\mathrm{P}\left[D > \delta \middle| IM^{\mathrm{eff}}, N\right]$ can be calculated using equation (8.36), which defines δ given N and IM^{eff} as a log-normal distribution with constant standard deviation, $\sigma_{\ln \delta|N}$. Unlike the total IM framework, in the timing-based framework IM^{eff} depends on N, so these random variables are not independent. However, the expression $\mathrm{P}\left[IM^{\mathrm{eff}}, N\right]$ can be expanded using the total probability theorem. Using the normalized intensity measures, α_1 and α_2, equation (8.28) can be rearranged to solve IM^{eff} as a function of α_2 and $IM_{\mathrm{tot}}^{\mathrm{eff}}$.

$$IM^{\mathrm{eff}} = \alpha_2 IM_{\mathrm{tot}}^{\mathrm{eff}} \tag{8.50}$$

where α_2 is a function of α_1, and $\alpha_1 = IM_{\mathrm{L}}^{\mathrm{trig}}/IM_{\mathrm{tot}}^{\mathrm{trig}}$. Equation (8.50) is the product of two random variables. The probability of the product of two random variables, x and y, can be calculated using the product distribution (Goldberger, 1991).

$$\mathrm{P}[xy] = \sum_i \mathrm{P}\left[y = \frac{xy}{x_i} | x_i\right] \mathrm{P}[x_i] \tag{8.51}$$

Substituting α_2 for *x* and $IM_{\mathrm{tot}}^{\mathrm{eff}}$ for *y* yields

$$\mathrm{P}\left[IM^{\mathrm{eff}}\right] = \mathrm{P}\left[\alpha_2 IM_{\mathrm{tot}}^{\mathrm{eff}}\right] = \sum_{IM_{\mathrm{tot}}^{\mathrm{eff}}} \mathrm{P}\left[\alpha_2 | IM_{\mathrm{tot}}^{\mathrm{eff}}\right] \mathrm{P}\left[IM_{\mathrm{tot}}^{\mathrm{eff}}\right] \tag{8.52}$$

The total intensity of shaking associated with liquefaction-induced deformation, $IM_{\mathrm{tot}}^{\mathrm{eff}}$, depends on the total intensity of shaking associated with liquefaction triggering, $IM_{\mathrm{tot}}^{\mathrm{trig}}$, which is known prior to this analysis. However, the calculation of α_2 also depends on α_1, which is a function of $IM_{\mathrm{L}}^{\mathrm{trig}}$, and ultimately *N*. Using the total probability theorem once again, $\mathrm{P}\left[\alpha_2 | IM_{\mathrm{tot}}^{\mathrm{eff}}\right]$ can be rewritten as

$$\mathrm{P}\left[\alpha_2 | IM_{\mathrm{tot}}^{\mathrm{eff}}\right] = \sum_{IM_{\mathrm{L}}^{\mathrm{trig}}} \mathrm{P}\left[\alpha_2 | IM_{\mathrm{tot}}^{\mathrm{eff}}, IM_{\mathrm{L}}^{\mathrm{trig}}\right] \mathrm{P}\left[IM_{\mathrm{L}}^{\mathrm{trig}}\right] \tag{8.53}$$

Substituting equation (8.53) back into equation (8.52) result in

$$\mathrm{P}\left[IM^{\mathrm{eff}}\right] = \mathrm{P}\left[\alpha_2 IM_{\mathrm{tot}}^{\mathrm{eff}}\right] = \sum_{IM_{\mathrm{tot}}^{\mathrm{eff}}} \sum_{IM_{\mathrm{L}}^{\mathrm{trig}}} \mathrm{P}\left[\alpha_2 | IM_{\mathrm{tot}}^{\mathrm{eff}}, IM_{\mathrm{L}}^{\mathrm{trig}}\right] \mathrm{P}\left[IM_{\mathrm{tot}}^{\mathrm{eff}}\right] \mathrm{P}\left[IM_{\mathrm{L}}^{\mathrm{trig}}\right] \tag{8.54}$$

$IM_{\mathrm{L}}^{\mathrm{trig}}$ depends on *N*, so $\mathrm{P}\left[IM_{\mathrm{L}}^{\mathrm{trig}}\right]$ can be expanded using the total probability theorem.

$$\mathrm{P}\left[IM_{\mathrm{L}}^{\mathrm{trig}}\right] = \sum_N \mathrm{P}\left[IM_{\mathrm{L}}^{\mathrm{trig}} | N\right] \mathrm{P}[N] \tag{8.55}$$

Substituting equation (8.55) back into equation (8.54) results in

$$\mathrm{P}\left[IM^{\mathrm{eff}}\right] = \mathrm{P}\left[\alpha_2 IM_{\mathrm{tot}}^{\mathrm{eff}}\right] = \sum_{IM_{\mathrm{tot}}^{\mathrm{eff}}} \sum_{IM_{\mathrm{L}}^{\mathrm{trig}}} \sum_N \mathrm{P}\left[\alpha_2 | IM_{\mathrm{tot}}^{\mathrm{eff}}, IM_{\mathrm{L}}^{\mathrm{trig}}\right] \mathrm{P}\left[IM_{\mathrm{tot}}^{\mathrm{eff}}\right] \mathrm{P}\left[IM_{\mathrm{L}}^{\mathrm{trig}} | N\right] \mathrm{P}[N] \tag{8.56}$$

Substituting equation (8.56) back into equation (8.49) results in the final equation for calculating the probability of exceeding δ.

$$\mathrm{P}[D > \delta] = \sum_{IM^{\mathrm{eff}}} \sum_{IM_{\mathrm{tot}}^{\mathrm{eff}}} \sum_{IM_{\mathrm{L}}^{\mathrm{trig}}} \sum_{N} \mathrm{P}\left[D > \delta | N, IM^{\mathrm{eff}}\right] \mathrm{P}\left[\alpha_2 | IM_{\mathrm{tot}}^{\mathrm{eff}}, IM_{\mathrm{L}}^{\mathrm{trig}}\right] \mathrm{P}\left[IM_{\mathrm{tot}}^{\mathrm{eff}}\right] \mathrm{P}\left[IM_{\mathrm{L}}^{\mathrm{trig}} | N\right] \mathrm{P}[N] \tag{8.57}$$

Each of the distributions necessary to calculate the individual terms in equation (8.57) have been discussed in previous sections. The distributions *N* and $IM_{\mathrm{L}}^{\mathrm{trig}}$ were discussed in Section 8.2. The conditional distributions of $IM_{\mathrm{tot}}^{\mathrm{eff}}$ and $IM_{\mathrm{tot}}^{\mathrm{trig}}$, and α_2 given α_1 were discussed in Section 8.3. The distribution of δ given IM^{eff} and *N* was discussed in Section 8.4. However, equation (8.57) cannot be solved as a closed form expression, since it requires summation over multiple distributions and types of distributions (normal, log-normal, and beta). It can be solved numerically when specific values of $IM_{\mathrm{tot}}^{\mathrm{trig}}$ and $(\mathrm{N}_1)_{60}$ are provided. The following pseudocode describes a numerical algorithm to calculate $\mathrm{P}[D > \delta]$ with the distributions discussed previously.

Pseudocode for calculating P$[D > \delta]$ using the timing-based framework

Given $(N_1)_{60}$ and $IM_{\text{tot}}^{\text{trig}}$

Calculate distribution of N given $(N_1)_{60}$ and σ_N

Calculate distribution of $IM_{\text{tot}}^{\text{eff}}$ given $IM_{\text{tot}}^{\text{trig}}$ and $\sigma_{\ln IM_{\text{tot}}^{\text{eff}} | \ln IM_{\text{tot}}^{\text{trig}}}$ using equations (8.14) and (8.15)

Set P = 0

For i in N:

Calculate distribution $IM_{\text{L}}^{\text{trig}}$ given N_i and $\sigma_{IM_{\text{L}}^{\text{trig}}|N}$ using equation (8.10)

For j in $IM_{\text{L}}^{\text{trig}}$:

Calculate α_1 given $IM_{\text{L}}^{\text{trig}}{}_j$ using equation (8.27)

Calculate distribution of α_2 given α_1 using equations (8.30) through (8.32)

For k in α_2:

For m in $IM_{\text{tot}}^{\text{eff}}$:

Calculate $IM^{\text{eff}}{}_{km}$ given $\alpha_{2,k}$ and $IM_{\text{tot}}^{\text{eff}}{}_m$ using equation (8.50)

Calculate distribution of D_{ijkm} given N_i and IM^{eff} using equation (8.36)

$$\text{P} = \text{P} + \text{P}\left[D_{ijkp} > \delta\right]\text{P}\left[IM^{\text{eff}} = IM^{\text{eff}}{}_{kp}\right]\text{P}\left[IM_{\text{tot}}^{\text{eff}} = IM_{\text{tot}}^{\text{eff}}{}_p\right]$$
$$\text{P}\left[IM_{\text{L}}^{\text{trig}} = IM_{\text{L}}^{\text{trig}}{}_j\right]\text{P}[N = N_i]$$

Ideally, in the timing-based framework, variables for IM^{trig} and IM^{eff} would both be selected to minimize the total uncertainty in in post-triggering deformation. IM^{trig} = PGA_{M} is most commonly used in practice, and contemporary liquefaction triggering procedures almost exclusively rely on PGA_{M} with few exceptions. The regression analysis results described in Section 8.4 show that IM^{eff} = CAV had the lowest uncertainty in predicting post-triggering deformation, defined by $\sigma_{\ln \delta|N}$, when N and IM^{eff} are given. However, in the timing-based framework, the uncertainties in the evolutionary relationships between PGA_{M}, I_a, and CAV all contribute to the total uncertainty in predictions of $\ln \delta$. These uncertainties must also be considered in selecting IM^{trig} and IM^{eff}. Figure 8.10 shows that the uncertainty in α_2 given α_1 is

larger when IM^{eff} = CAV than when IM^{eff} = I_a. So, even though the value of $\sigma_{\ln\delta|N}$ is less when IM^{eff} = CAV, the uncertainty in α_2 given α_1 may reduce the effectiveness of CAV as a predictor of post-triggering deformation in a probabilistic calculation. IM^{eff} = I_a produced larger values of $\sigma_{\ln\delta|N}$, but has a lower uncertainty in calculation of α_2 given α_1, indicating that IM^{eff} = I_a may be as efficient of a predictor of post-triggering deformation as CAV in a probabilistic calculation. Since equation (8.57) can only be realistically calculated using numerical computations, no analytical solution is available to determine which *IM* minimizes the uncertainty in δ. Both IM^{eff} = CAV and I_a should be considered as plausible candidates for IM^{eff} in the timing-based framework.

8.5.4 *Estimates of the total uncertainty in deformation*

The $\text{P}[D > \delta]$ is calculated using equation (8.48) using the total *IM* framework and equation (8.57) using the timing-based framework. Each of these equations require multiple summations over nested conditional distributions, and calculations of $\text{P}[D > \delta]$ therefore must be performed numerically. If an array of values of δ are used to calculate $\text{P}[D > \delta]$, a complementary cumulative density function (CDF) is produced. This CDF is not necessarily representative of an established distribution, but it can be used to calculate a probability density function (PDF) of δ using numerical derivatives.

$$f_D(\delta_i) = \frac{\text{P}[D > \delta_{i-1}] - \text{P}[D > \delta_i]}{\delta_i - \delta_{i-1}} \tag{8.58}$$

where $f_D(\delta)$ is the PDF of δ. Assuming the PDF is approximately log-normally distributed, the variance of the distribution, ${\sigma_{\ln\delta}}^2$, can be calculated as

$${\sigma_{\ln\delta}}^2 = \sum_{\delta} (\ln\delta - \text{E}[\ln\delta])^2 f_D(\ln\delta) \tag{8.59}$$

where $\text{E}[\ln\delta]$ is the expected value of $\ln\delta$, and $\sigma_{\ln\delta}$ is the estimated standard deviation of $\ln\delta$. The assumption that δ is log-normally distributed should be verified by comparing the PDF calculated using equation (8.58) to a log-normal PDF calculated using $\text{E}[\ln\delta]$ and $\sigma_{\ln\delta}$. Note that the value of $\sigma_{\ln\delta}$ calculated with equation (8.59) includes the uncertainty in *N*, $IM_{\text{L}}^{\text{trig}}$, and $IM_{\text{tot}}^{\text{eff}}$ and is typically greater than the values of $\sigma_{\ln\delta|N}$ calculated in Section 8.4. Including these

uncertainties provides a means to directly compare values of $\sigma_{\ln \delta}$ to determine if IM^{eff} = I_a or CAV provides the more efficient estimator of post-triggering deformation. While only I_a and CAV were considered as candidate *IM*s for this analysis, the sets to calculate $\sigma_{\ln \delta}$ could be applied with any *IM*.

8.5.5 *Probability of liquefaction triggering*

The procedures to estimate log-normal or approximately log-normal distributions of δ all assume that liquefaction has been triggered. These distributions are defined by $\mathrm{E}[\ln \delta]$ and $\sigma_{\ln \delta}$. However, when liquefaction is not triggered, $\delta = 0$. If this probability is considered, δ becomes a mixed random variable with a partitional of δ as a log-normally distributed random variable, and a partition of δ equal to 0.

Khoshnevisan et al. (2015) described equations to estimate lateral spreading deformation with consideration of the probability of liquefaction. The expected value of deformation, $\mathrm{E}[\delta]$, can be calculated to include the probability that liquefaction is triggered.

$$\mathrm{E}[\delta] = \mathrm{E}[\delta|L]\ \mathrm{P}[L] \tag{8.60}$$

where L is an event indicating that liquefaction is triggered, and $\mathrm{P}[L]$ is the probability of liquefaction. The preceding analyses have largely been performed for δ based on a log-normal distribution. The $\mathrm{E}[\delta]$ can be calculated (Goldberger, 1991) from a log-normal distribution as

$$\mathrm{E}[\delta|L] = \exp\left(\mathrm{E}[\ln \delta\,|L] + \frac{1}{2}\mathrm{V}[\ln \delta\,|L]\right) \tag{8.61}$$

where $\mathrm{V}[\ln \delta\,|L]$ is the variance of $\ln \delta$, assuming that liquefaction has been triggered. This quantity has been described previously as ${\sigma_{\ln \delta}}^2$. Introducing a term for the median deformation when liquefaction is triggered, $\mathrm{M}[\delta|L]$,

$$\mathrm{M}[\delta|L] = \exp(\mathrm{E}[\ln \delta\,|L]) \tag{8.62}$$

equation (8.61) can be simplified

$$\mathrm{E}[\delta|L] = \mathrm{M}[\delta|\mathrm{L}] \exp\left(\frac{1}{2}{\sigma_{\ln \delta}}^2\right) \tag{8.63}$$

Equation (8.63) can then be substituted into equation (8.60), resulting in

$$\mathrm{E}[\delta] = \mathrm{P}[L]\ \mathrm{M}[\delta|\mathrm{L}] \exp\left(\frac{1}{2}{\sigma_{\ln\delta}}^2\right) \tag{8.64}$$

Thus, the expected value of deformation, $\mathrm{E}[\delta]$, is a function of the probability that liquefaction is triggered and the expected value of variance of $\ln\delta$.

The variance of δ when the probability of liquefaction is considered can be calculated using a similar approach. Defining the variance of δ as

$$\mathrm{V}[\delta] = \mathrm{E}[\delta^2] - (\mathrm{E}[\delta])^2 \tag{8.65}$$

Then, expanding $\mathrm{E}[\delta^2]$ using the conditional probability of liquefaction results in

$$\mathrm{E}[\delta^2] = \mathrm{E}[\delta^2|L]\ \mathrm{P}[L] \tag{8.66}$$

which, along with equation (8.60), can be substituted into equation (8.65).

$$\mathrm{V}[\delta] = \mathrm{E}[\delta^2|L]\ \mathrm{P}[L] - (\mathrm{E}[\delta|L]\ \mathrm{P}[L])^2 \tag{8.67}$$

Equation (8.67) can be rewritten in terms of $\mathrm{V}[\delta|L]$

$$\mathrm{V}[\delta] = \mathrm{P}[L]\ \mathrm{V}[\delta|L] + \mathrm{P}[L](1 - \mathrm{P}[L])(\mathrm{E}[\delta|L])^2 \tag{8.68}$$

where $\mathrm{V}[\delta|L] = {\sigma_{\ln\delta}}^2$. Substituting equation (8.63) into equation (8.68) results in

$$\mathrm{V}[\delta] = \mathrm{P}[L]\ {\sigma_{\ln\delta}}^2 + \mathrm{P}[L](1 - \mathrm{P}[L])(\mathrm{M}[\delta|\mathrm{L}]^2 \exp({\sigma_{\ln\delta}}^2)) \tag{8.69}$$

Equation (8.69) indicates that when liquefaction is very likely and $\mathrm{P}[L] = 1$, $\mathrm{V}[\delta] = {\sigma_{\ln\delta}}^2$. When liquefaction is very unlikely, $\mathrm{P}[L] = 0$ and $\mathrm{V}[\delta] = 0$.

While many of the analyses performed in this document are conditional upon liquefaction being triggered, these equations can be used to calculate the expected value and variance of δ when the probability of liquefaction is considered. These expressions do not necessary constrain the distribution of δ, but merely assume that when liquefaction is triggered, δ is log-normally distributed. Consideration of the probability of liquefaction affects both the total *IM* and timing-based frameworks.

8.5.6 *Sensitivity to relative density*

Obviously, the estimated values of δ should change with $(N_1)_{60}$. As $(N_1)_{60}$ increases, the estimated value of δ should decrease, and vice-versa. In probabilistic calculations, both the expected value of δ and the variance of δ are affected by the value of $(N_1)_{60}$.

First, the probability of liquefaction changes with $(N_1)_{60}$, as the probability that the soil liquefies affects both the expected value and variance of δ. Soils with larger $(N_1)_{60}$ values are less likely to liquefy under a given loading conditions. If liquefaction is less likely to trigger, then the expected value of δ should decrease. The variance of δ is also affected by the probability of liquefaction. When $(N_1)_{60}$ is sufficiently large that the probability of liquefaction approaches 0, the uncertainty in δ also approaches 0 because no liquefaction-induced deformation occurs. These considerations affect both the total *IM* and timing-based frameworks.

Second, after liquefaction is triggered, the magnitude of post-triggering shear strain decreases with increasing relative density and $(N_1)_{60}$. This effect is reflected in the equations used to predict δ when $(N_1)_{60}$ is given. Equation (8.36) for the total *IM* framework and equation (8.37) for the timing-based framework both have negative coefficients for $(N_1)_{60}$. As $(N_1)_{60}$ increases, these equations indicate that δ should decrease.

Third, larger values of $(N_1)_{60}$ cause liquefaction to be triggered later in the ground motion, resulting in less intense shaking after liquefaction is triggered, IM^{eff}. This effect is directly considered in the timing-based framework. In equation (8.37), the coefficient on IM^{eff} is positive, indicating that decreased values of IM^{eff} result in decreased estimates of δ.

Fourth, the uncertainty in N increases with $(N_1)_{60}$, since the COV_N was assumed to be constant. So, if the uncertainty in N increases as $(N_1)_{60}$ increases, so too should the uncertainty in estimates of δ.

Fifth, changes in $(N_1)_{60}$ affect the value of $IM_{\text{L}}^{\text{trig}}$, which in turn, affect the value of α_1. The uncertainty in α_2 given α_1 is not constant. Figure 8.10 shows that the uncertainty in α_2 increases as α_1 increases. At sites with very loose soils, liquefaction is triggered at relatively low values of $IM_{\text{L}}^{\text{trig}}$ with correspondingly low values of α_1. The uncertainty in α_2 given α_1 is therefore relatively low in these conditions. However, at relatively dense sites where $IM_{\text{L}}^{\text{trig}}$ approaches

$IM_{\text{tot}}^{\text{trig}}$, α_1 approaches 1.0 and the uncertainty in α_2 becomes relatively large. The timing-based framework is subject to the uncertainty between α_2 given α_1, but the total *IM* framework is not.

Both the total *IM* and timing-based frameworks were developed using the same set of data, and estimated values of deformation when liquefaction is triggered, E[ln δ], should not vary significantly between the frameworks. Variations may occur due to the simplicity of the equations used to predict ln δ, but these variations should be slight. Changes in $(N_1)_{60}$, however, affect the uncertainty in the prediction of δ, and these effects are not equal between the two frameworks. The effects of these influences depend on the values of $(N_1)_{60}$, the uncertainties in each of the *IM*s, and the framework used to estimate δ. These influences can only be properly compared through analysis with specific examples.

8.5.7 *Sensitivity to IM_{tot}*

The deformations estimated using either the timing-based or total *IM* frameworks also depend on the total intensity of shaking. $IM_{\text{tot}}^{\text{trig}}$ is correlated with $IM_{\text{tot}}^{\text{eff}}$, so increases in one of these *IM*s causes a corresponding increase the other. In general, more intense shaking should increase deformation and increase the expected value of δ. In probabilistic calculations, both the expected value of δ and the variance of δ are influenced by $IM_{\text{tot}}^{\text{trig}}$ and $IM_{\text{tot}}^{\text{eff}}$.

First, the probability of liquefaction changes with $IM_{\text{tot}}^{\text{trig}}$. Soils with a given cyclic resistance are more likely to liquefy when shaking is stronger. As discussed in Section 8.5.5, if probability of liquefaction is greater, then the expected value of δ should increase. The variance of δ is also affected by the probability of liquefaction. When $IM_{\text{tot}}^{\text{trig}}$ is sufficiently small and the probability of liquefaction approaches 0, the uncertainty in δ also approaches 0 because no liquefaction-induced deformation can occur. These considerations affect both the total *IM* and timing-based frameworks.

Second, after liquefaction is triggered, the magnitude of deformation increases with more intense shaking, as described by $IM_{\text{tot}}^{\text{eff}}$. This effect is reflected in the equations used to predict δ. In the total *IM* framework, equation (8.36) has a positive coefficient for $IM_{\text{tot}}^{\text{eff}}$, indicating that as $IM_{\text{tot}}^{\text{eff}}$ increases, estimated values of δ increase. In the timing-based framework, $IM_{\text{tot}}^{\text{eff}}$ is used to

calculate IM^{eff}, which in equation (8.37), also has a positive coefficient for the predictions of δ. As IM^{eff} increases, so too does the estimated value of δ.

Third, changes in $IM_{\text{tot}}^{\text{trig}}$ affect the value of α_1. The uncertainty in α_2 given α_1 is not constant. Larger values of $IM_{\text{tot}}^{\text{trig}}$ that increase α_1 also increase the uncertainty in α_2 given α_1, ultimately increasing the uncertainty in estimates of δ. The timing-based framework is subject to the uncertainty between α_2 given α_1, while the total *IM* framework is not.

The influences of $IM_{\text{tot}}^{\text{trig}}$ and $IM_{\text{tot}}^{\text{eff}}$ affect the uncertainty in the prediction of δ differently between the total *IM* framework and the timing-based framework. These effects are not equal between the two frameworks, and depend on the values of $(N_1)_{60}$ and the uncertainties in each of the *IM*s. The influence of $IM_{\text{tot}}^{\text{trig}}$ and $IM_{\text{tot}}^{\text{eff}}$ on the prediction of δ can only be properly compared through analysis with specific examples.

8.6 EXAMPLE ANALYSIS

An example site was selected based on a liquid fuel storage facility on the west bank of the Willamette River in Portland, Oregon. The site was located about 81 km from the down-dip edge of the Cascadia Subduction Zone, on the eastern edge of the Tualatin/Portland Basin. The depth to rock with a shear wave velocity greater than 2.5 km/s was about 2.5 km. The average shear wave velocity in the upper 30 m of the site was about 250 m/s. Figure 8.14 shows a typical profile of the soils at the site. This profile includes a layer of liquefiable sand between 3 and 8 m deep with an average $(N_1)_{60}$ of about 14 blows/ft.

8.6.1 *Estimated IMs*

Several different approaches could be used to estimate *IM*s for liquefaction deformation analysis. The most commonly used method is to use GMPEs. This option was considered, and while GMPEs have been developed to estimate PGA for large-magnitude subduction zone earthquakes, they have not been developed to estimate I_a or CAV for such events. Known correlations between PGA and other *IM*s could also be considered to estimate I_a or CAV, but these correlations include a large amount of uncertainty. Synthetic ground motions have been produced by the University of Washington's M9 project for a potential M_w = 9 Cascadia Subduction Zone rupture. Ground motions from the M9 project at several key locations, including the location of the example site,

are discussed in Chapter 3. These simulations predicted a range of ground motions from multiple rupture scenarios, and probably provide the best estimate of *IM*s due to a CSZ rupture.

However, the CSZ simulations were representative of a stiff soil profile with $v_{s,30}$ = 550 m/s. To account for site amplification, equivalent linear site response analyses were performed using the computer program SHAKE. Figure 8.14 shows the profile and shear wave velocity used for this analysis, and Table 8.8 provides the details of the soil profile that was input into SHAKE.

Table 8.8: Subsurface properties of the example profile for site response analysis

Soil Type	Thickness, m	Unit Weight (kN/m^3)	Shear wave velocity (m/s)
EPRI 0-20 ft	1	2.0	100
EPRI 0-20 ft	1	2.0	118
EPRI 0-20 ft	1	2.0	131
EPRI 0-20 ft	1	1.9	136
EPRI 0-20 ft	1	1.9	141
EPRI 0-20 ft	1	1.9	145
EPRI 21-50 ft	1	1.9	149
EPRI 21-50 ft	1	1.9	153
EPRI 21-50 ft	1	1.9	182
EPRI 21-50 ft	1	1.9	186
EPRI 21-50 ft	1	1.9	189
EPRI 21-50 ft	1	1.9	192
EPRI 21-50 ft	1	1.9	196
EPRI 21-50 ft	1	1.9	199
EPRI 21-50 ft	1	1.9	201
Rock	3	2.1	305
Rock	3	2.1	391
Rock	3	2.1	477
Rock	(Halfspace)	2.1	550

SHAKE analyses were performed for each of the 18 simulated ground motions in the M9 suite and intensity measures at the ground surface were calculated. Table 8.9 shows the resulting *IM*s, the correlation between *IM*s, and the log-normal standard deviation from the CSZ simulations after site response analysis was performed.

Table 8.9: CSZ scenario intensity measures for example site

Intensity measures, IM	Median value	$\sigma_{\ln IM}$	$\rho_{\ln IM,\ln \mathrm{PGA}_M}$	$\sigma_{\ln IM \mid \ln \mathrm{PGA}_M}$
PGA	0.24 g	0.24	0.58	0.11
Number of cycles	21.4	0.72	0.20	0.64
Magnitude-adjusted PGA	0.26 g	0.18	1.00	0.00
Arias intensity	0.49 m/s	0.37	0.92	0.11
Cumulative absolute velocity	6.9 m/s	0.21	0.68	0.12

8.6.2 *Liquefaction triggering*

The median value of PGA_M listed in Table 8.9 was used to estimate a deterministic factor of safety against liquefaction. The liquefiable sand between depths of 3 and 8 m had an average $(N_1)_{60}$ value of 14 blows/ft. Idriss and Boulanger (2010) discuss details about calculating representative parameters for their liquefaction triggering procedure. They indicate representative values should be calculated by averaging the depth, $(N_1)_{60}$, σ_v' and σ_v values from the liquefiable layers, and then $CRR_{7.5,1\ atm}$ and $CSR_{7.5,1\ atm}$ values should be calculated for the average values. Table 8.10 shows the tabulated values necessary for liquefaction triggering analysis. The factor of safety in the liquefiable sand deposit was about 0.77, indicating that liquefaction would be likely during a M_w = 9 CSZ rupture.

Table 8.10: Liquefaction triggering parameters for example site

Average depth	Average σ_v	Average σ_v'	$(N_1)_{60}$	$CRR_{7.5,1\ atm}$	$CSR_{7.5,1\ atm}$	Factor of safety
3.3 m	106 kPa	82 kPa	14	0.17	0.22	0.77

A deterministic value of IM_L^{trig} was calculated by varying the values of PGA_M in the liquefaction triggering analysis until FS = 1.0. Based on $(N_1)_{60}$ = 14 blows/ft, a value of IM_L^{trig} = 0.20 g would trigger liquefaction at the example site. This analysis was repeated for a range of $(N_1)_{60}$ values to generate a liquefaction triggering curve for $IM^{trig} = PGA_M$. Figure 8.23 shows the liquefaction triggering curve for the example site.

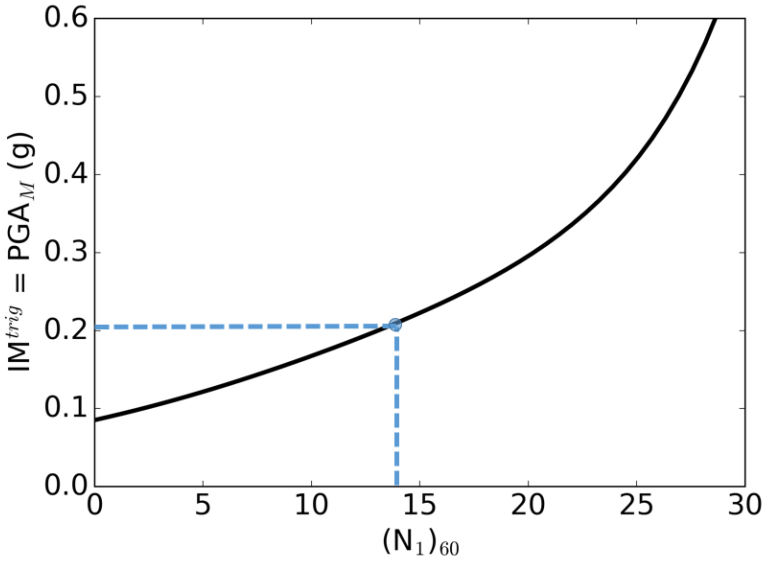

Figure 8.23: Liquefaction triggering curve for example site.

The conventional liquefaction triggering procedures also provide information to calculate the probability of liquefaction triggering. Based on the recommendations by Idriss and Boulanger (2012), the penetration resistance, *N*, was taken to be normally distributed with σ_N = 2.1 when $(N_1)_{60}$ = 14 blows/ft. IM^{trig} is log-normally distributed with a conditional log-normal standard deviation of $\sigma_{\ln \text{PGA}_M|N}$ = 0.25. The total standard deviation for liquefaction triggering, σ_T, was calculated as 0.27 using the equations described by Idriss and Boulanger, which resulted in a probability of liquefaction of 84% when $IM_{\text{tot}}^{\text{trig}}$ = 0.26 g.

8.6.3 *Lateral spreading analysis with deterministic seismic hazard*

In a deterministic analysis, the *IM*s for the entire duration of the motion, $IM_{\text{tot}}^{\text{trig}}$ and $IM_{\text{tot}}^{\text{eff}}$, are assumed to be known. Values of $IM_{\text{tot}}^{\text{eff}}$ and *N* can be input directly into equation (8.35) to calculate δ using the total *IM* framework. In this example, deterministic values of $IM_{\text{tot}}^{\text{eff}}$ 0.49 m/s for I_a and 6.9 m/s for CAV. Substituting these values into equation (8.35) resulted in estimates of δ = 0.26 m when IM^{eff} = I_a and δ = 0.25 m when IM^{eff} = CAV.

Given values of $IM_{\text{tot}}^{\text{eff}}$ and $(N_1)_{60}$, the timing-based procedure can also be used to calculate δ. However, the timing-based framework requires the additional complexity of calculating α_2 to arrive at values of IM^{eff}. Equation (8.36) can then be used to estimate δ when $(N_1)_{60}$ and IM^{eff}

are given. In this example scenario, the PGA_M necessary to trigger liquefaction, IM_L^{trig}, was 0.20 g, and the PGA_M for the entire duration of the ground motion, IM_{tot}^{trig}, was 0.26 g. These values were used to calculate $\alpha_1 = 0.77$. The equations relating α_2 and α_1 yielded a value of $\alpha_2 = 0.64$ when $IM^{eff} = I_a$. These calculations implied that 77% of the PGA_M had evolved by the time liquefaction was triggered, but 64% of the I_a occurred after liquefaction was triggered. The remaining value of I_a after liquefaction was triggered (IM^{eff}) was 0.31 m/s. This deterministic analysis indicated that a $M_w = 9.0$ Cascadia Subduction Zone earthquake would produce about 0.26 m of lateral spreading at the site.

The analysis was repeated using the timing-based framework with IM^{eff} = CAV. A value of $\alpha_2 = 0.69$ was calculated for the example site, indicating that 69% of the CAV occurred after liquefaction was triggered. Based on this value of α_2 and the *IM*s from the CSZ scenario, the remaining values of CAV after liquefaction was triggered was 4.8 m/s. Substituting this value into equation (8.36) indicated that a $M_w = 9.0$ Cascadia Subduction Zone earthquake would produce about 0.25 m of lateral spreading at the site.

It should be acknowledged that the major benefit of the timing-based framework is that the uncertainty in estimates of δ are greatly reduced compared to the total *IM* framework. However, since these two frameworks use the same data to predict deformations, deterministically calculated estimates of δ should not vary significantly between the two. The differences in deterministically calculated values of δ in this example analysis (0.26 m for the total *IM* framework, and 0.26 and 0.25 m for the timing-based framework with I_a and CAV, respectively) were indeed relatively insignificant. The timing-based framework requires additional complexity and assumptions relative to the total *IM* framework. Median values of α_2 given α_1 were assumed for the deterministic calculation, but the uncertainty in α_2 given α_1 could result in differences between the two frameworks. Within each framework, the relatively simple equations used to predict δ could also result in different values of δ.

8.6.4 *Probability of exceeding levels of lateral spreading deformation*

The preceding section showed that the timing-based framework produced estimates of deformation which were similar to estimates using the total *IM* framework in a deterministic analysis. The true benefit of the timing-based framework, however, is that the uncertainty in these estimates is

dramatically reduced, even though no additional data is required. The total *IM* and timing-based frameworks can be compared by calculating the probability of exceeding levels of deformation ($P[D > \delta]$). All the information necessary to perform these calculations is discussed in previous sections or is provided in Table 8.9.

The $P[D > \delta]$ was first calculated using the total *IM* framework with an array of δ values. Calculation of $P[D > \delta]$ was performed using the nested summation in equation (8.48). Figure 8.24 shows the complementary CDF of $P[D > \delta]$ for both IM_{tot}^{eff} = I_a and CAV. Note that the probability of exceeding very low levels of deformation could not exceed the probability of triggering liquefaction, which was about 84%.

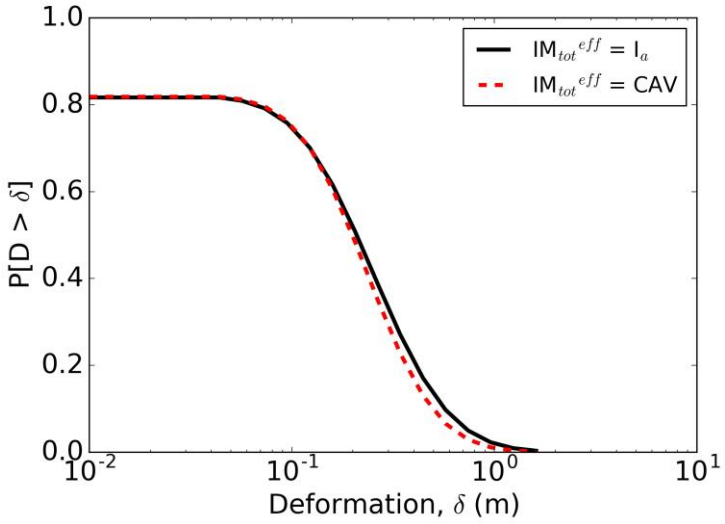

Figure 8.24: Probability of exceeding levels of deformation at the example site using the total *IM* framework.

The CDFs in Figure 8.24 were then used with equation (8.58) to calculate PDFs of deformation. These PDFs were conditional upon the triggering of liquefaction, such that the integrals of the PDFs were equal to 1.0. Even though calculations for $P[D > \delta]$ required summation over multiple distributions and types of distribution, the calculated PDFs were remarkably close to log-normal PDFs. Histograms of PDFs for both IM_{tot}^{eff} = I_a and CAV are provided in Figure 8.25. The median and log-normal standard deviations were calculated using equation (8.59), and $\sigma_{\ln \delta}$ = 0.67 when IM_{tot}^{eff} = I_a, and $\sigma_{\ln \delta}$ = 0.62 when IM_{tot}^{eff} = CAV. Log-normal approximations using these values are also shown in Figure 8.25.

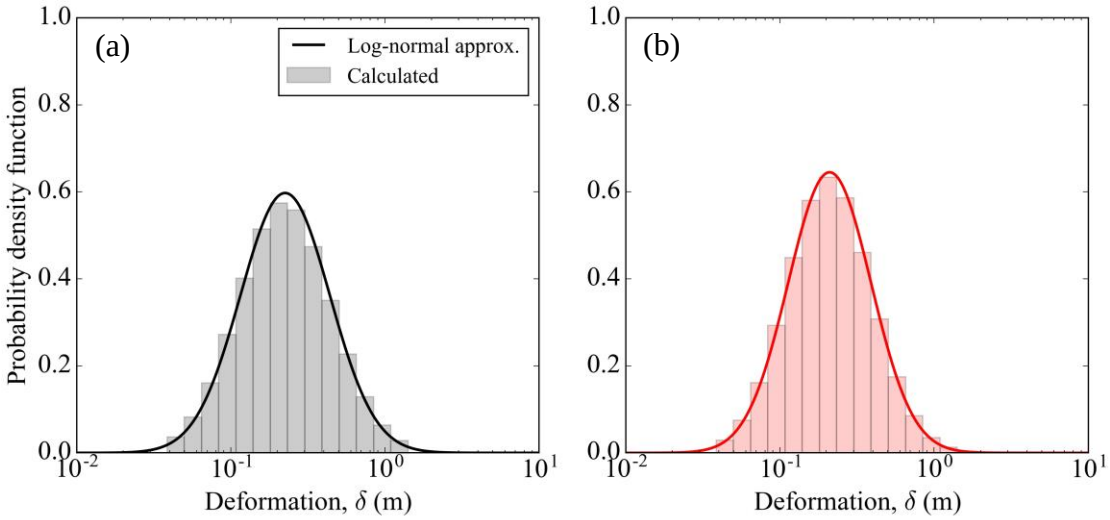

Figure 8.25: Probability density function of deformation at the example site using total *IM* framework. (a) $IM_{\text{tot}}^{\text{eff}}$ = I_a (b) $IM_{\text{tot}}^{\text{eff}}$ = CAV.

The reduction in uncertainty using the timing-based framework is evident when similar analyses were performed to calculate $\sigma_{\ln \delta}$. The probabilities of exceeding levels of deformation were calculated using equation (8.57) with the pseudocode provided in Section 8.5. Figure 8.26 shows the complementary CDFs calculated using the timing-based framework with both IM^{eff} = I_a and CAV.

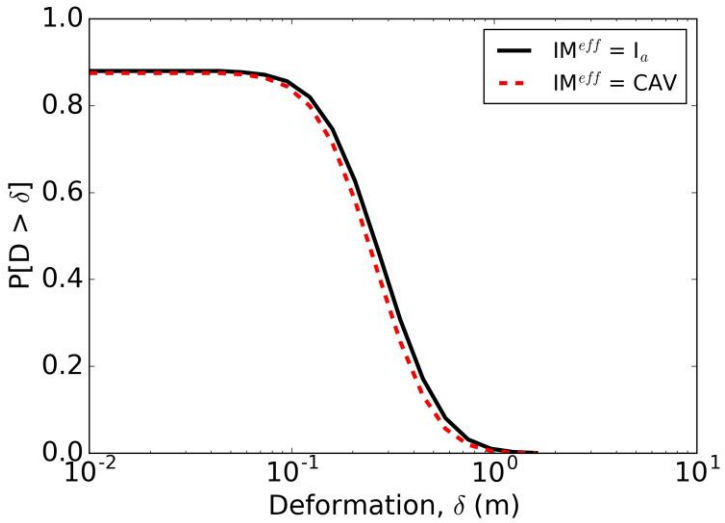

Figure 8.26: Probability of exceeding levels of deformation at the example site using the timing-based framework.

Following the approach used for the total *IM* framework, the PDF of δ was calculated using numerical derivatives. These PDFs were also approximately log-normally distributed, and a value of $\sigma_{\ln \delta}$ = 0.55 was calculated when IM^{eff} = I_a and $\sigma_{\ln \delta}$ = 0.54 when IM^{eff} = CAV. Figure 8.27 shows the PDFs calculated using the timing-based framework and their log-normal approximations. The values of $\sigma_{\ln \delta}$ calculated using the timing-based framework were significantly less that the values calculated using the total *IM* framework, even though the same data was used. Figure 8.28 shows a comparison of the log-normal approximations from the timing-based and total *IM* frameworks.

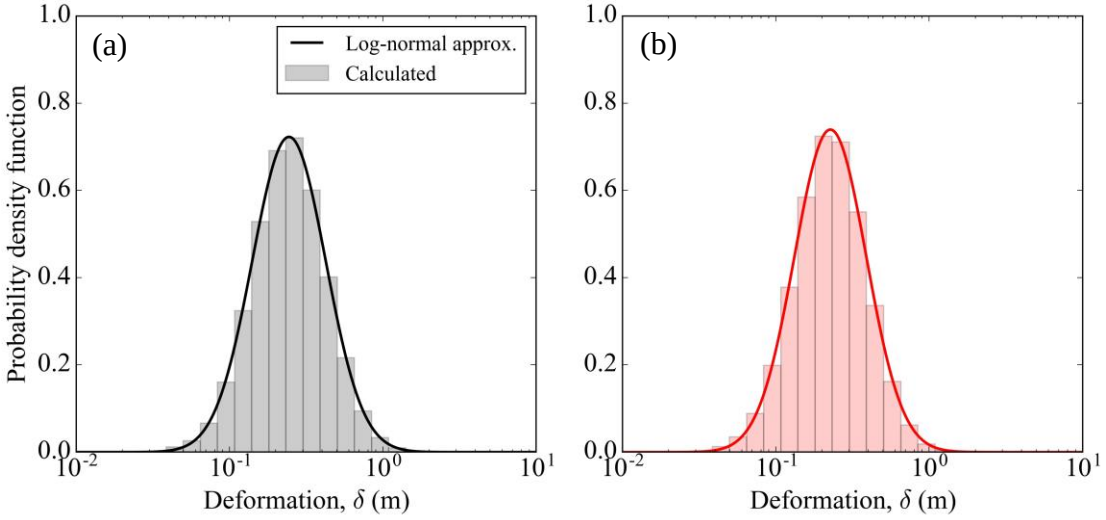

Figure 8.27: Probability density function of deformation at the example site using the timing-based framework. (a) IM^{eff} = I_a (b) IM^{eff} = CAV.

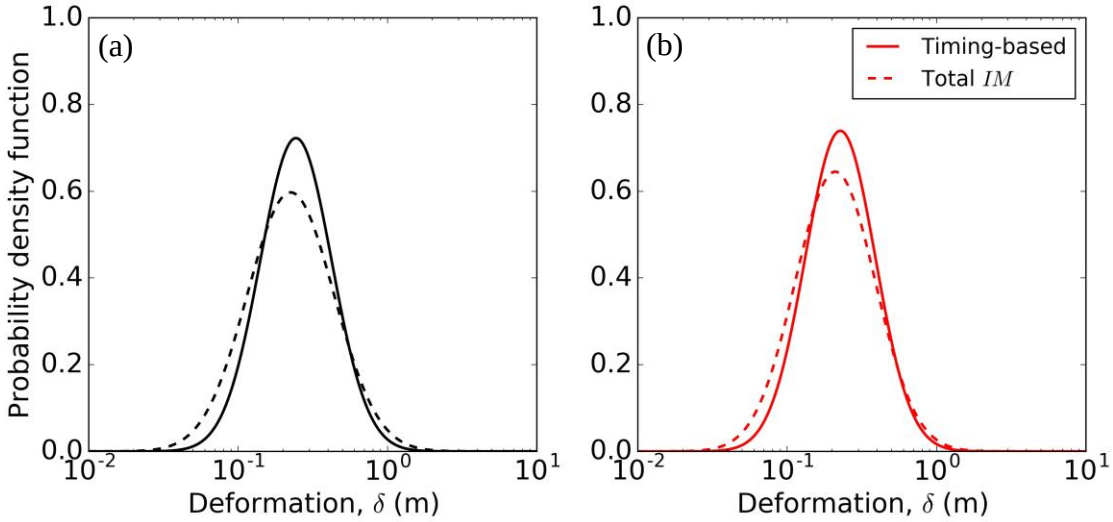

Figure 8.28: Comparison of log-normal probability density function calculated using the timing-based and total *IM* frameworks. (a) $IM^{\text{eff}} = I_a$ (b) $IM^{\text{eff}} = \text{CAV}$.

8.6.5 *Sensitivity to relative density*

The process of calculating E[ln δ] and $\sigma_{\ln \delta}$ when $(N_1)_{60}$ = 14 blows/ft was repeated for a range of $(N_1)_{60}$ values. In this analysis, $IM_{\text{tot}}^{\text{trig}} = \text{PGA}_M$ was held constant at 0.26 g and $(N_1)_{60}$ was varied between 5 and 25 blows/ft. These calculations provide a basis to evaluate the influence of $(N_1)_{60}$ on both the estimated values and uncertainty in deformation estimates.

As described in Section 8.5.5, the probability of liquefaction triggering affects both the expected value and variance of deformation. The probability of liquefaction is very sensitive to $(N_1)_{60}$. In conditions where $(N_1)_{60}$ values are very large, P[L] approaches 0. Conversely, in conditions where $(N_1)_{60}$ is very small, P[L] approaches 1. Figure 8.29 shows the probability of liquefaction for the example site as a function of $(N_1)_{60}$.

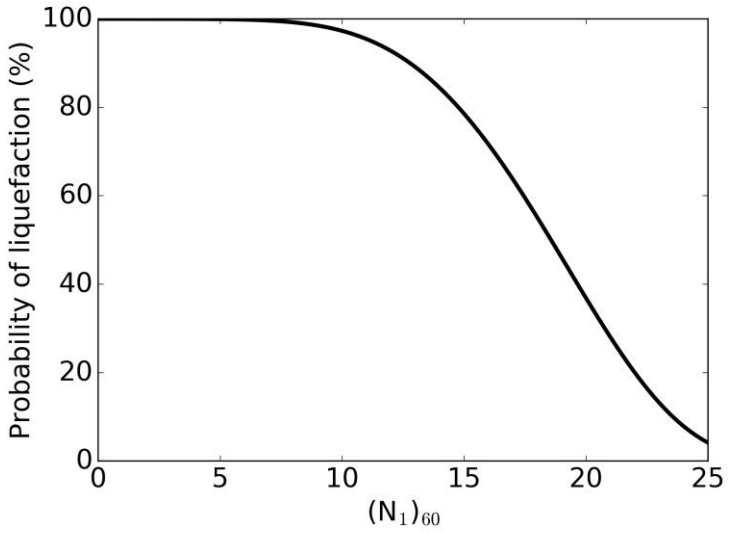

Figure 8.29: Probability of liquefaction versus $(N_1)_{60}$ values.

The expected values of deformation, E[δ], were then calculated for the range of $(N_1)_{60}$ values. The expected values of deformation should be largely independent of the framework and the intensity measure used, since the equations for both the total *IM* and timing-based frameworks were developed using the same finite element deformation results. In general, as $(N_1)_{60}$ increases, E[δ] should decrease. In conditions where $(N_1)_{60}$ values are very large, P[L] should approach 0 and E[δ] should also approach 0. In conditions where $(N_1)_{60}$ values are very small, liquefaction is triggered at a lower intensity of shaking and the post triggering intensity of shaking, IM^{eff}, becomes relatively large. Large values of IM^{eff} should result in large values of E[δ]. Figure 8.30 shows the expected values of deformation for both the total *IM* and timing-based frameworks as a function of $(N_1)_{60}$. These plots indicate that, indeed, the E[δ] was relatively independent of the framework and *IM* used for these analyses.

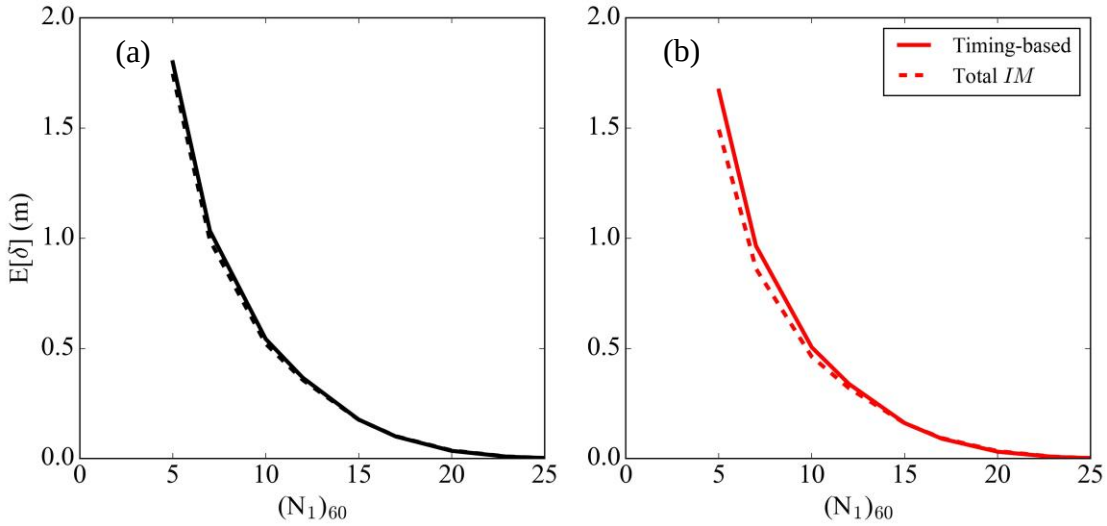

Figure 8.30: Comparison of estimated deformation as a function of $(N_1)_{60}$ with total *IM* and timing-based frameworks. (a) $IM^{\text{eff}} = I_a$ (b) $IM^{\text{eff}} = \text{CAV}$.

Next, the variance of deformation, $V[\delta]$, was calculated for the range of $(N_1)_{60}$ values. Based on the results in Section 8.6.4, when $(N_1)_{60}$ = 14 blows/ft, the timing-based framework should show a large improvement in the uncertainty in deformation estimates relative to the total *IM* framework. However, the variance of deformation is very sensitive to the probability of liquefaction triggering. In conditions where $(N_1)_{60}$ values are large and $P[L]$ approaches 0, $V[\delta]$ should also approach 0. Conversely, in conditions where $(N_1)_{60}$ values are small and $P[L]$ approaches 1, $V[\delta]$ should approach $\sigma_{\ln \delta}{}^2$. The results of the $V[\delta]$ calculations for the example site are plotted in Figure 8.31. The timing-based framework showed lower values of $V[\delta]$ than the total *IM* framework for the range of $(N_1)_{60}$ values, indicating that the timing-based framework did indeed reduce the uncertainty in δ. The timing-based framework is subject to the uncertainty in the relationship of α_2 given α_1, which increases at larger values of $(N_1)_{60}$. However, for the example site, this variation appeared to be relatively minor and only produced a small local maximum in $V[\delta]$ between $(N_1)_{60}$ values of 10 to 15 blows/ft.

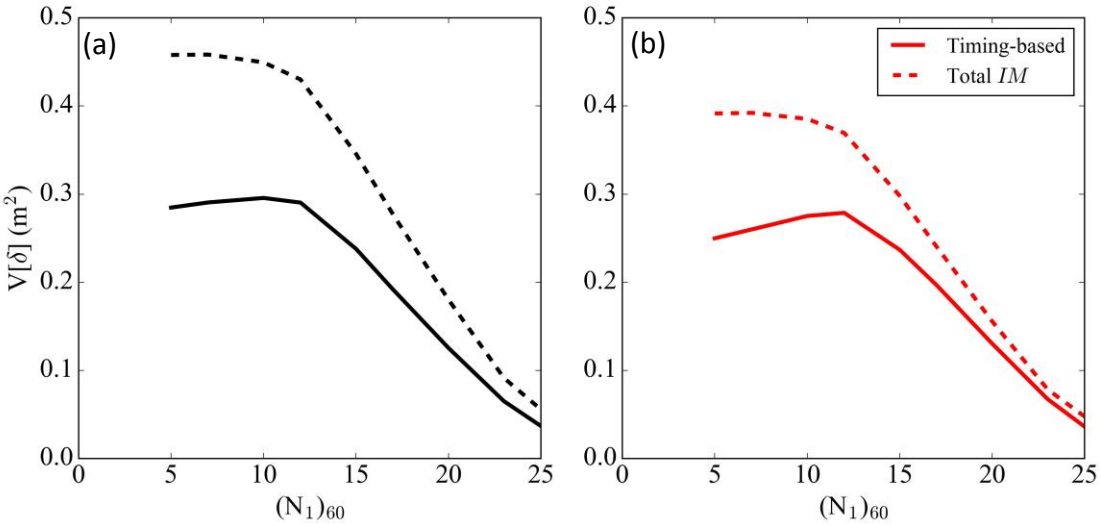

Figure 8.31: Comparison of $\sigma_{\ln \delta}$ as a function of $(N_1)_{60}$ with total *IM* and timing-based frameworks. (a) $IM^{\text{eff}} = I_a$ (b) $IM^{\text{eff}} = \text{CAV}$.

8.6.6 *Sensitivity to IM_{tot}*

The process of calculating the expected value and variance of deformation was repeated for a range of PGA_M values. In this analysis, $(N_1)_{60}$ was held constant at 14 blows/ft and $IM_{\text{tot}}^{\text{trig}}$ was varied. These calculations provide a basis for evaluating the influence of $IM_{\text{tot}}^{\text{trig}}$ on both the estimated values and uncertainties in deformation estimates.

As described in Section 8.5.5, the probability of liquefaction triggering affects both the expected value and variance of deformation. The probability of liquefaction triggering is very sensitive to $IM_{\text{tot}}^{\text{trig}}$, and at low values of $IM_{\text{tot}}^{\text{trig}}$, $P[L]$ approaches 0. Conversely, at high values of $IM_{\text{tot}}^{\text{trig}}$, $P[L]$ approaches 1. Figure 8.32 shows the probability of liquefaction as a function of $IM_{\text{tot}}^{\text{trig}}$.

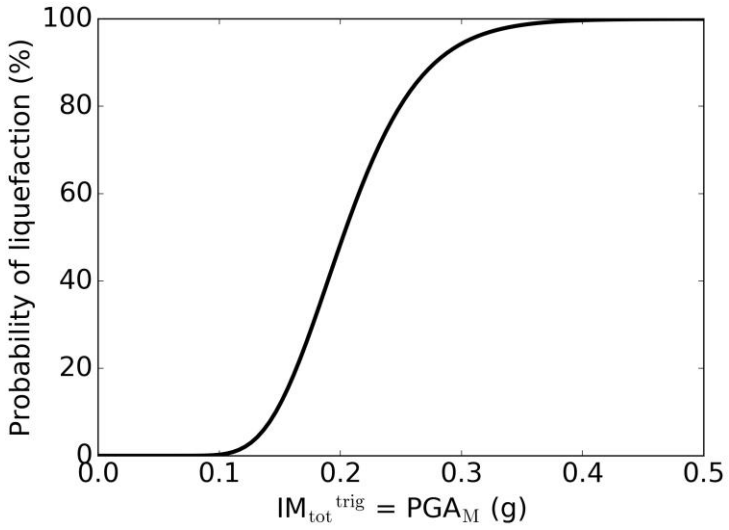

Figure 8.32: Probability of liquefaction versus $IM_{\mathbf{tot}}^{\mathbf{trig}}$ values.

The expected value of deformation, E[δ], should be largely independent of the framework and the intensity measures used in this analysis, since the equations for both the total *IM* and timing-based frameworks were developed using the same finite element deformations results. The equations in Section 8.5.5 were used to calculate E[δ] with consideration for the probability of liquefaction, P[L]. In conditions where $IM_{\mathrm{tot}}^{\mathrm{trig}}$ values are small, and P[L] approaches 0 and E[δ] should also approach 0. Conversely, in conditions where is $IM_{\mathrm{tot}}^{\mathrm{trig}}$ values are large, IM^{eff} should also be large which, in turn, results in large values of E[δ]. Figure 8.33 shows the expected values of deformation for both the total *IM* and timing-based frameworks as a function of $IM_{\mathrm{tot}}^{\mathrm{trig}}$. The plots in this figure indicate that the expected value of deformation is largely independent of the framework and intensity measure used.

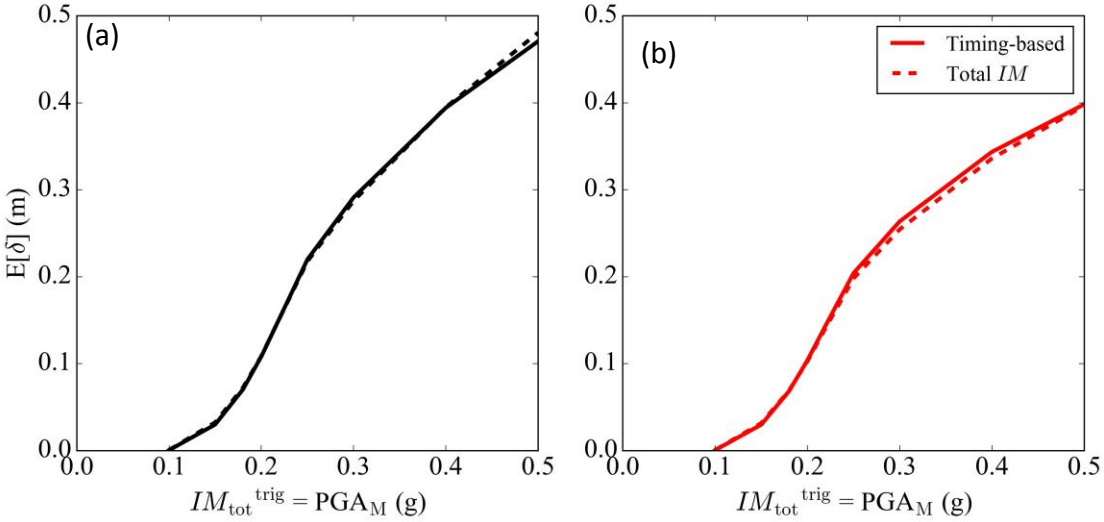

Figure 8.33: Comparison of estimated deformation as a function of $IM_{\mathbf{tot}}^{\mathbf{trig}}$ with total *IM* and timing-based frameworks. (a) IM^{eff} = I_a (b) IM^{eff} = CAV.

Next, the variance of deformation, V[δ], was calculated for the range of $IM_{\text{tot}}^{\text{trig}}$ values. Based on the results for the example site when PGA_M = 0.26 g, the timing-based framework should show a large improvement in V[δ] compared to the total *IM* framework. The equations in Section 8.5.5 were used to calculate V[δ] with consideration for the probability of liquefaction, P[L]. In conditions where $IM_{\text{tot}}^{\text{trig}}$ is small and P[L] approaches 0, V[δ] should also approach 0. In conditions where $IM_{\text{tot}}^{\text{trig}}$ is large and P[L] approaches 1, V[δ] should approach $\sigma_{\ln \delta}{}^2$. The results of these calculations are shown on Figure 8.34. The timing-based framework had lower values of V[δ] than the total *IM* framework for the entire range of $IM_{\text{tot}}^{\text{trig}}$ evaluated, indicating that the timing-based framework did indeed reduce the uncertainty in estimates of δ. The timing-based framework is subject to the uncertainty in the relationship of α_2 given α_1, but this variation in uncertainty appears to be relatively minor for the conditions at the example site.

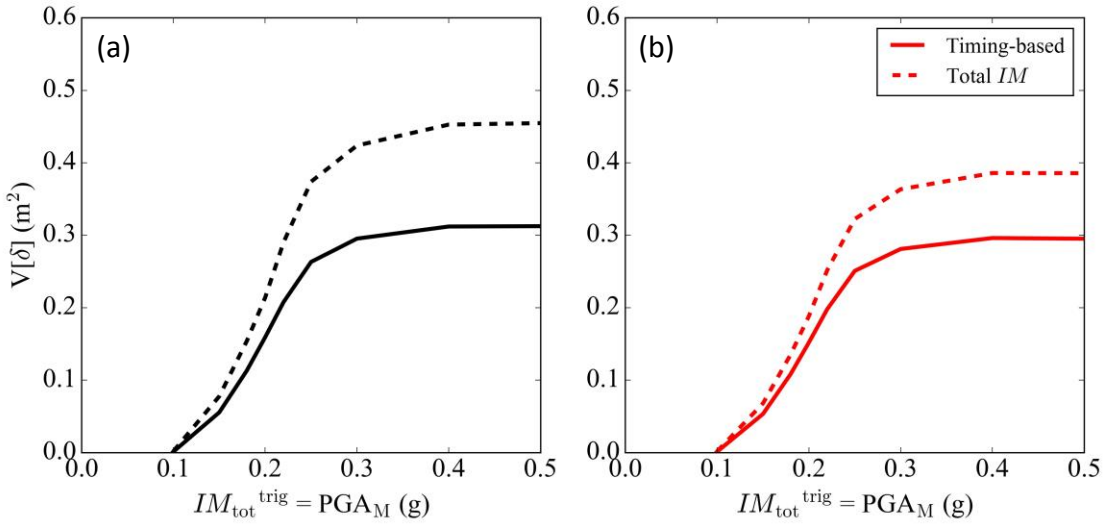

Figure 8.34: Comparison of V[δ] as a function of IM_{tot}^{trig} with timing-based framework and total *IM* framework. (a) IM^{eff} = I_a (b) IM^{eff} = CAV.

8.7 CONCLUSIONS

The intensity measures typically associated with liquefaction triggering, PGA and the number of cycles of loading, are not necessarily the same intensity measures that correspond best to post-triggering deformation, such as I_a and CAV. These *IM*s correspond to different frequencies and, since earthquakes are nonstationary processes, *IM*s associated with the high-frequency components of a ground motion, like PGA_M, arrive earlier in the motion than *IM*s associated with the low-frequency components of a ground motion, like I_a and CAV. When liquefaction is triggered, the shift from high to low-frequency ground motions occurs very rapidly, and low-frequency ground motions control the post-triggering deformations.

Decoupling the intensity of shaking necessary to trigger liquefaction from the intensity of shaking that produces post-triggering ground surface deformation has important implications for reducing the uncertainty in lateral spreading deformation estimates. The timing-based framework proposed in this chapter has the potential to significantly reduce the uncertainty in estimating deformations. This procedure advantageously uses different *IM*s to predict liquefaction triggering, IM^{trig}, and the post-triggering effects of liquefaction, IM^{eff}. Even after accounting for the uncertainty in liquefaction triggering parameters and in the uncertainty in the evolution between

triggering and effects *IM*s, the deformations predicted by the timing-based framework have lower uncertainty than deformations predicted using a similar framework based on the entire ground motion.

However, limited data exist to develop relationships between deformation and post-triggering intensity measures. In this study, numerical analyses were used in place of empirical observations to approximate the relationship between post-trigging intensity measures and deformations. Additional studies are recommended to supplement the timing-based framework. These studies should be designed to better describe the correlation between *IM*s for long-duration earthquakes, reduce the uncertainty in IM^{eff} given IM^{trig}, and provide estimates of the post-triggering deformation as a function of general subsurface and site conditions.

Chapter 9. EVOLUTIONARY RESPONSE OF CASE HISTORIES AFTER LIQEUFACTION TRIGGERING

Liquefaction causes a rapid and significant shift in the frequency content of a ground surface motion. The modal frequency of ground motions tends to shift from higher frequencies early in the motion to lower frequencies once liquefaction has been triggered. This shift is usually very rapid, and structures founded on sites with liquefiable soils may experience ground motions with very different characteristics before and after liquefaction has been triggered. These characteristics require structures founded on liquefiable soils to be designed for two different site conditions—one that amplifies high-frequency motions during the period of shaking before liquefaction is triggered, and one that amplifies low-frequency motions during the period of shaking after liquefaction is triggered. Indeed, some design guidelines recommend evaluating structures founded on liquefiable soil with two completely separate analyses: one analysis where the soil does not liquefy during the entire duration of the motion, which represents the characteristics of the motion before liquefaction is triggered, and another analysis in which the soil is assumed to be liquefied for the entire duration of the motion, which represents the characteristics of the motion after liquefaction is triggered. The guidelines recommend enveloping the results of these two analyses for design (Allen, 2013), but such a procedure does not really capture the rapid shift in frequency content that occurs once soils liquefy. Enveloping the two analyses may be extremely conservative in some cases and possibly unconservative in others. The timing of peak kinematic and inertial demands on structures depends on the ground motion, the rate of the intensity of loading, and the behavior of the soil after liquefaction has been triggered. All of these aspects need to be considered when evaluating the effects of liquefaction.

Since the rapid shift in ground motion frequency content has important implications for structures founded on liquefiable soils, it is important to understand what mechanisms cause these changes. Liquefaction causes a rapid change in the shear stiffness of the soil as the effective stress approaches the overburden pressure. As the stiffness and shear wave velocity of the liquefiable layer change, so does the characteristic frequency of the profile. The characteristic frequency, $\tilde{f}$, of a single layer of soil on a rigid base is defined as

$$\tilde{f} = \frac{v_s}{4\mathrm{H}} \tag{9.1}$$

where v_s is the shear wave velocity of the layer of soil and H is the thickness. Details provided in Section 2.4 illustrate the mechanics by which soil layers become extremely soft as the pore pressure approaches the overburden pressure. Figure 2.10 (from Zhang et al., 2004) indicates that the amplitude of shear strain after liquefaction is triggered depends on the relative density of the soil and the intensity of loading. Dense soils develop smaller shear strains after they liquefy, therefore, their secant stiffnesses are greater than those of loose soils. In fact, it may be possible that liquefaction can occur in relatively thin layers of dense soils such that the shear strain is minimal, the secant stiffness of the layer is only slightly reduced, and changes in ground motion frequency content at the ground surface are relatively minor.

Changes in effective stress also affect the stiffness of the soil. During periods of high shear strain, dilation can temporarily decrease the excess pore pressure and increase the stiffness of the soil. Likewise, during long-duration ground motions, excess pore pressure may have sufficient time to dissipate and thereby increase the stiffness of the soil. While continued softening due to pore pressure generation and soil fabric degradation tend to decrease the characteristic frequency of a layer of liquefied soil, the effects of dilation and drainage tend to increase it. These mechanisms have competing effects, and their interaction is complicated.

The procedure developed in Section 4.4 can be used to identify the time at which liquefaction is triggered at sites where ground surface motions have been recorded. This procedure identifies the rapid shift in frequency content that occurs once the soil liquefies by using the Stockwell time-frequency spectrum. The normalized Stockwell spectrum is used to calculate the modal frequency of the ground motion over the entire duration of shaking, and the resolution of the Stockwell spectrum is sufficient that the evolving frequency content after liquefaction is triggered can also be analyzed. Figure 9.1 shows the normalized Stockwell spectrum from the IBR014 ground motion during the Tohoku earthquake. Liquefaction was triggered about 110 seconds into the motion, where a rapid and significant decrease in frequency content can be seen. Before the soil liquefied, the modal frequency of the motion range of about 5 to 8 Hz, then after the soil liquefied, the modal frequency of the motion ranged from about 0.5 Hz to 2 Hz. Plotting the frequencies on a log scale highlights the low-frequency ground motions that dominated the spectrum after liquefaction was triggered.

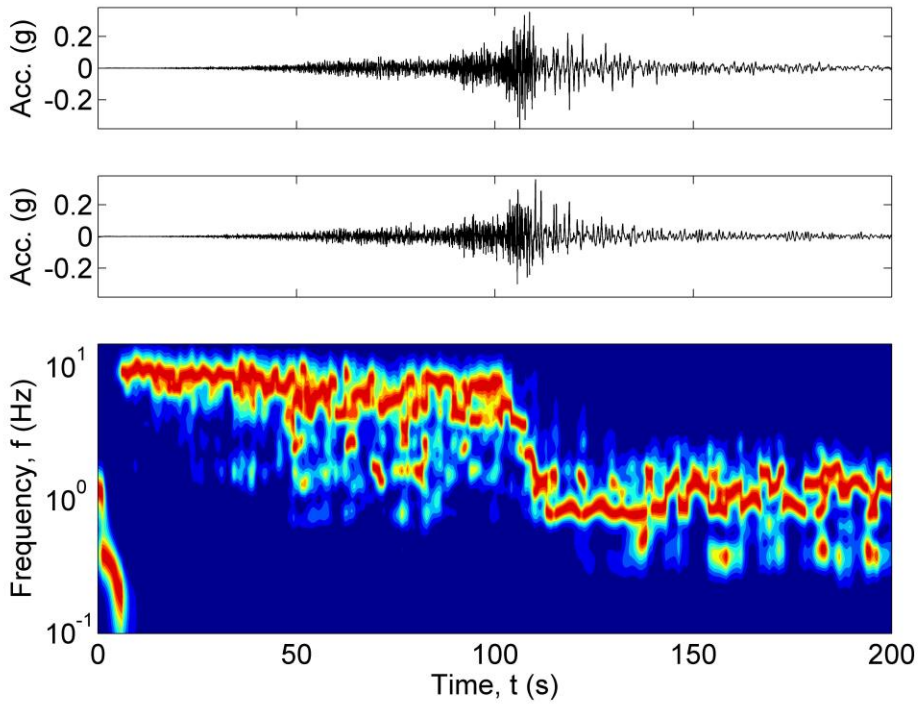

Figure 9.1: Stockwell spectrum at IBR014

Because the frequency content of the ground motion shifted so dramatically at the time liquefaction was triggered, the peak spectral acceleration of single degree-of-freedom oscillators with various periods would occur at very different times. The recorded ground motion at IBR014 was dominated by high-frequency components during the early part of the motion before liquefaction was triggered, and the PGA and peak short period spectral acceleration occurred prior to the time liquefaction was triggered. The later part of the ground motion, after liquefaction was triggered, was dominated by lower frequency motions. The peak spectral acceleration at a period of 1 seconds occurred well after liquefaction was triggered. Figure 9.2 shows the spectral acceleration partitioned into ground motions before and after liquefaction was triggered.

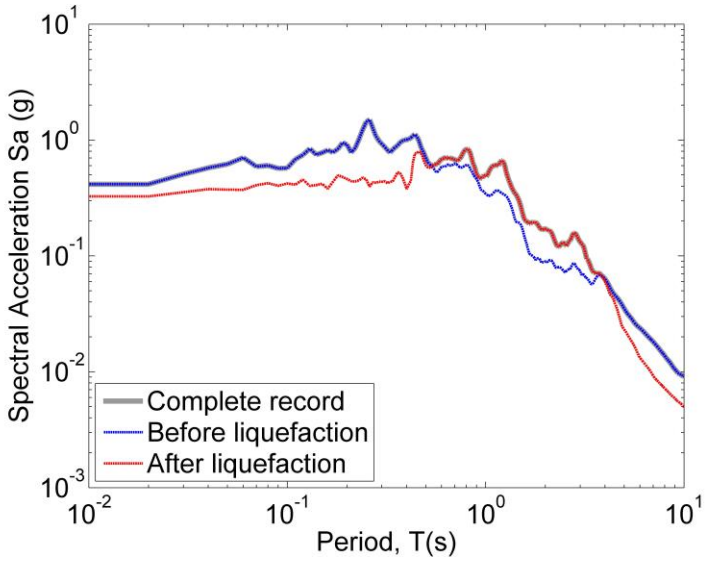

Figure 9.2: Spectral acceleration at IBR014 before and after liquefaction was triggered

This shift in frequency content due to liquefaction and the relative timing of the peak spectral acceleration has important implications for the seismic demands on structures at the site. The peak spectral acceleration at periods between 0.5 and 4 seconds was likely amplified by the presence of liquefied soil. Before liquefaction occurred, the Stockwell spectrum in Figure 9.1 was dominated by frequencies in the 4 to 6 Hz (0.17 to 0.25 second period) range, and the maximum spectral acceleration occurred at a period of about 0.25 seconds. The modal frequency after liquefaction was triggered was in the 0.8 to 2 Hz range (0.5 to 1.2 second period), and the maximum spectral acceleration occurred at a period of about 0.8 seconds. The inverse of the modal frequency provides a very simple approximation of the period that the maximum spectral acceleration occurred—0.25 seconds before liquefaction was triggered and 0.8 seconds after liquefaction was triggered. Based on this observation, the modal frequency of the Stockwell spectrum can provide important insight into which frequencies have the strongest spectral acceleration.

The relative timing of the peak spectral acceleration is also important for evaluating the combined effects of inertial and kinematic loading on structures. Spectral acceleration and the fundamental period of the structure control the inertial loading demand, while soil deformation can control kinematic loading. The magnitude of soil deformation increases substantially after liquefaction is triggered, but may not necessarily coincide with the peak inertial loading, particularly if the peak spectral acceleration occurs before the soil liquefies. If lateral spreading

had been an issue near IBR014, the peak kinematic loading due to lateral spreading would have coincided with the 0.5-second spectral acceleration, but not the 0.1-second spectral acceleration.

Possibly the most important aspect of the shift in frequency content due to liquefaction is the association between frequency content and intensity measures that drive deformation. As discussed in Section 8.3, the intensity measures that are best associated with post-triggering deformation, IM^{eff} are not necessarily the same as the intensity measures associated with liquefaction triggering, IM^{trig}. Knowledge of the frequency content of the ground motion after liquefaction has been triggered provides key information to help determine which intensity measures are appropriate for estimating post-triggering deformation. Even though Arias intensity and cumulative absolute velocity are both associated with post-triggering deformation, they capture different bands of frequency content. Identifying the most common ranges of modal frequency after liquefaction has been triggered could indicate if one of these intensity measures is more appropriate than the other. Likewise, intensity measures associated with spectral acceleration may provide good estimators for predicting of lateral spreading deformation. These types of intensity measures are associated with a fundamental period, which could be approximated by the inverse of the modal frequency of a ground motion.

9.1 CASE HISTORY DATA

Twenty-one sites with ground surface accelerometers were identified as potentially providing important case history information where the changes in ground motion frequency content could be correlated with site and loading conditions. All of these sites showed evidence of liquefaction during an earthquake and had previously been investigated with sufficient subsurface information for subsequent analyses. The shift in ground motion frequency content due to liquefaction depended on the thickness and relative density of the liquefiable layer, the intensity of shaking after liquefaction was triggered, and the potential for drainage during shaking. Parameters important for liquefaction analysis, such as $(N_1)_{60}$, fines content, and drainage path length, were recorded from subsurface data when it was available or were estimated from soil classification and boring log descriptions when sufficient data were not available. The critical layer of soil that likely liquefied was first identified in each case history. Values of $(N_1)_{60}$, overburden pressure, and the fines content from these critical layers are provided in Table 9.1.

Table 9.1: Case history subsurface data

Motion	Site/Station	Depth to critical layer (m)	Shear wave velocity, $v_{s,0}$ (m/s)	Critical layer $(N_1)_{60}$	Fines content (%)	Overburden pressure (kPa)	Reference
1	Alameda Naval Air Station	2.5	87	4	13	42	Youd and Carter (2003)
2	Amagasaki	3.3	109	12	50	37	Sato et al. (1995)
3	Aomori (1968)	15.3	200	6	30	165	Yasuda and Tohno (1988), PARI
4	Aomori (1983)	15.3	200	6	30	165	Iai et al. (1989), PARI
5	Bond's Corner	4.5	167	13	17	81	Bonilla et al. (1995)
6	CHB024	20.3	199	5	5	185	Cox et al. (2013)
7	Hachirogata	7.3	148	5	5	89	Kostadinov and Towhata (2002)
8	Higashi Kobe	15.3	183	13	10	130	Ganev (1998)
9	HKD086	4.3	135	26	15	59	Kinoshita (2008)
10	IBR014	26.3	400	12	15	221	Cox et al. (2013), this study
11	Kawagishi-cho	4.3	129	5	5	52	Ishihara and Yoga (1981)

Table 9.1: Case history subsurface data

Motion	Site/Station	Depth to critical layer (m)	Shear wave velocity, $v_{s,0}$ (m/s)	Critical layer $(N_1)_{60}$	Fines content (%)	Overburden pressure (kPa)	Reference
12	Kobe JIS	6.3	109	7	5	71	Kostadinov and Yamazahi (2001)
13	Kushiro Port	2.3	91	7	5	35	Iai (1995)
14	MYG010	9.3	190	15	10	98	Cox et al. (2013), this study
15	MYG013	5.3	180	22	15	48	Ashford et al. (2011), this study
16	NIG018	5.3	210	21	15	74	Yoshida et al. (2007)
17	Onahama Port	2.3	99	12	6	31	Rotten et al. (2013)
18	Port Island	8.3	210	6	20	87	Zeghal et al. (1996)
19	Sakaiminato	4.3	90	10	30	52	Mori and Sogabe (2004)
20	Treasure Island	9.0	125	4	20	96	Cetin et al. (2004), Idriss and Boulanger (2010)
21	Wildlife	3.4	103	7	40	46	Youd and Holzer (1994)

Each of the sites listed in Table 9.1 was subject to strong shaking from a large earthquake that triggered liquefaction. Metadata of the earthquake magnitude, rupture distance, and shear wave velocity was collected from the references listed in Table 9.1. Table 9.2 lists this metadata

information, including the earthquake magnitude, rupture distance, and the site shear wave velocity.

Table 9.2: Case history earthquake metadata

Motion	Site/Station	Earthquake and Year	Earthquake magnitude, M_w	Rupture distance, R_{rup} (km)	Site shear wave velocity, v_{s30} (m/s)
1	Alameda Naval Air Station	Loma Prieta (1989)	6.9	71	190
2	Amagasaki	Hygoken-Nambu (1995)	6.9	11.6	180
3	Aomori (1968)	Tokachi-Oki (1968)	8.3	140	185
4	Aomori (1983)	Nihonkai-Chubu (1983)	7.8	120	185
5	Bond's Corner	Imperial Valley (1975)	6.5	2.7	223
6	CHB024	Tohoku (2011)	9.0	52	298
7	Hachirogata	Nihonkai-Chubu (1983)	7.7	74	86
8	Higashi Kobe	Hygoken-Nambu (1995)	6.9	4.1	235
9	HKD086	Tokachi-Oki (2003)	8.3	59	230
10	IBR014	Tohoku (2011)	9.0	71	270
11	Kawagishi-cho	Niigata (1964)	7.7	14.6	220
12	Kobe JIS	Hygoken-Nambu (1995)	6.9	1.9	220
13	Kushiro Port	Kushiro-Oki (1993)	7.8	100	279
14	MYG010	Tohoku (2011)	9.0	45	160
15	MYG013	Tohoku (2011)	9.0	64	220
16	NIG018	Niigata-Chuetsu (2007)	6.8	1.5	189
17	Onahama Port	Tohoku (2011)	9.0	43	537
18	Port Island	Hygoken-Nambu (1995)	6.9	3.3	198

Table 9.2: Case history earthquake metadata

Motion	Site/Station	Earthquake and Year	Earthquake magnitude, M_w	Rupture distance, R_{rup} (km)	Site shear wave velocity, v_{s30} (m/s)
19	Sakaiminato	Western Tottori	6.6	20.1	154
20	Treasure Island	Loma Prieta (1989)	6.9	77.4	155
21	Wildlife	Superstition Hills (1977)	6.5	23.8	179

The metadata in Table 9.2 was then used to calculate intensity measures associated with liquefaction triggering, IM^{trig}, and the effects of liquefaction, IM^{eff}. For crustal ground motions, GMPEs (Campbell and Bozorgnia, 2010; 2012) produced as part of the NGA West-2 project were used to estimate PGA, I_a, and CAV. When available, these values were adjusted to match any regional variation observed in the USGS Shakemaps. For subduction-zone ground motions, the PGA was estimated using the BCHydro GMPE (Abrahamson et al. 2015). However, as discussed in Section 8.3, subduction zone GMPEs for I_a and CAV have not been developed. When GMPEs were not available, correlations based on a large suite of subduction and crustal ground motions (CS-dataset) were used to estimate I_a and CAV based on PGA. Equations (3.35) and (3.36) provided these correlations. The stations IBR014, MYG010, and MYG013 were investigated in-detail for this study, and *IM*s at these stations were estimated based on nearby recorded ground motions adjusted to match the conditions at these sites. Table 9.3 shows the estimated *IM* values for each of the 21 case histories. These values represent *IM*s for the total duration of shaking, $IM_{\text{tot}}^{\text{trig}}$ and $IM_{\text{tot}}^{\text{eff}}$.

Table 9.3: Estimated intensity measures for the case histories

Motion	Site/Station	Earthquake magnitude, M_w	PGA (g)	I_a (m/s)	CAV (m/s)	Source
1	Alameda Naval Air Station	6.9	0.20	0.49	8.0	Shakemap
2	Amagasaki	6.9	0.23	0.94	10.1	GMPE, Shakemap rupture distance
3	Aomori (1968)	8.3	0.13	0.22	8.3	GMPE
4	Aomori (1983)	7.8	0.11	0.14	6.1	GMPE
5	Bond's Corner	6.5	0.37	1.91	9.9	GMPE
6	CHB024	9.0	0.35	0.78	17.1	GMPE
7	Hachirogata	7.7	0.20	0.92	14.9	Shakemap
8	Higashi Kobe	6.9	0.35	2.04	12.4	GMPE
9	HKD086	8.3	0.72	1.88	20.9	Shakemap
10	IBR014	9.0	0.35	2.37	14.8	This study
11	Kawagishi-cho	7.7	0.23	1.22	15.2	GMPE
12	Kobe JIS	6.9	0.38	2.28	12.5	GMPE
13	Kushiro Port	7.8	0.60	5.38	22.1	Shakemap
14	MYG010	9.0	0.52	5.05	21.4	This study
15	MYG013	9.0	0.60	6.64	24.4	This study
16	NIG018	6.8	0.64	4.95	21.2	Shakemap
17	Onahama Port	9.0	0.40	3.06	16.8	GMPE
18	Port Island	6.9	0.34	1.91	11.9	GMPE
19	Sakaiminato	6.6	0.32	1.26	10.9	Shakemap
20	Treasure Island	6.9	0.20	0.51	8.4	Shakemap
21	Wildlife	6.5	0.21	0.62	7.6	GMPE, Shakemap

Additional shaking after liquefaction was triggered could cause continued degradation of the soil fabric and further reduce the modal frequency of the ground motion. The details of the timing-based procedure in Section 8.3 provide a link between intensity measures associated with liquefaction triggering, IM^{trig}, and intensity measures associated with the effects of liquefaction, IM^{eff}. Given the values of $IM_{\text{tot}}^{\text{trig}}$ and $IM_{\text{tot}}^{\text{eff}}$ in Table 9.3, *IM*s associated with the post-triggering effects of liquefaction can be calculated. The relative density, fines content, and overburden pressure data in Table 9.1 can be used to calculate a value of PGA_M that would trigger liquefaction,

$IM_{\mathrm{L}}^{\mathrm{trig}}$. The relative evolutionary parameter, α_1, was then calculated with values of $IM_{\mathrm{L}}^{\mathrm{trig}}$ and the data in Table 9.3.

$$\alpha_1 = \frac{IM_{\mathrm{L}}^{\mathrm{trig}}}{IM_{\mathrm{tot}}^{\mathrm{trig}}} \tag{9.2}$$

α_2 is the evolutionary parameter associated with the effects of liquefaction, IM^{eff}. The procedures in Chapter 8 describe a correlation between α_2 and α_1 that is largely independent of earthquake source, path, and site effects. α_2 is defined as

$$\alpha_2 = \frac{IM^{\mathrm{eff}}}{IM_{\mathrm{tot}}^{\mathrm{eff}}} \tag{9.3}$$

Once α_2 is calculated, IM^{eff} can be calculated using equation (9.3) to estimate a measure of the intensity of shaking after liquefaction has been triggered.

$IM_{\mathrm{tot}}^{\mathrm{trig}}$ = $\mathrm{PGA_M}$ was first calculated using the values listed in Tables 9.1 and 9.3. Then, $IM_{\mathrm{L}}^{\mathrm{trig}}$ = $\mathrm{PGA_M}$ was calculated using the properties listed in Table 9.2. Values of IM^{eff} = $\mathrm{I_a}$ and CAV were finally calculated using equations (9.2) and (9.3). Table 9.4 lists the values of these *IM*s.

Table 9.4: Post-triggering intensity measures for the case histories

Motion	Site/Station	$IM_{\mathrm{L}}^{\mathrm{trig}}$ = $\mathrm{PGA_M}$ (g)	$IM_{\mathrm{tot}}^{\mathrm{trig}}$ = $\mathrm{PGA_M}$ (g)	IM^{eff} = $\mathrm{I_a}$ (m/s)	IM^{eff} = CAV (m/s)
1	Alameda Naval Air Station	0.16	0.19	0.30	5.3
2	Amagasaki	0.22	0.23	0.41	5.7
3	Aomori (1968)	0.10	0.14	0.16	6.1
4	Aomori (1983)	0.10	0.11	0.08	3.8
5	Bond's Corner	0.33	0.33	0.50	4.4
6	CHB024	0.07	0.40	0.77	16.3
7	Hachirogata	0.20	0.20	0.28	7.2
8	Higashi Kobe	0.17	0.33	1.77	10.2
9	HKD086	0.70	0.78	0.97	12.7
10	IBR014	0.13	0.40	2.26	13.3
11	Kawagishi-cho	0.11	0.23	1.08	12.7
12	Kobe JIS	0.11	0.36	2.18	11.3
13	Kushiro Port	0.17	0.62	5.20	20.2

Table 9.4: Post-triggering intensity measures for the case histories

Motion	Site/Station	IM_L^{trig} = PGA_M (g)	IM_{tot}^{trig} = PGA_M (g)	IM^{eff} = I_a (m/s)	IM^{eff} = CAV (m/s)
14	MYG010	0.17	0.60	4.87	19.5
15	MYG013	0.29	0.69	6.07	20.9
16	NIG018	0.42	0.59	3.59	15.4
17	Onahama Port	0.19	0.46	2.81	14.5
18	Port Island	0.15	0.32	1.70	10
19	Sakaiminato	0.22	0.29	0.87	7.7
20	Treasure Island	0.13	0.20	0.40	6.4
21	Wildlife	0.19	0.19	0.19	3.7

Any drainage that could have occurred during shaking would reduce excess pore pressure and increase the stiffness of the soil. This effect must be accounted for when considering the changes in the frequency content of the ground motion after liquefaction has been triggered, particularly if the layer of liquefiable soil is relatively thin and free-draining. Finite element analyses of IBR014, MYG010, and MYG013 indicated that liquefaction tended to occur in the loosest layer of the soil deposit first, and then pore water drained from these layers into adjacent, denser layers of soil during shaking. As the pore water drained, pore pressure dissipated, and the stiffness of the critical layer of soil increased.

The analytical solution in Chapter 5 provides a basis for estimating the competing effects of pore pressure generation due to shaking and pore pressure dissipation during drainage. Two parameters are necessary for the analytical solution, the drainage path length, H_{dr}, and the vertical coefficient of consolidation, c_v. For each case history, the soil layers above and below the critical layer of liquefied soil were identified as either free-draining or impervious. The drainage path length was then calculated as the longest path pore water would have to travel to reach a free-draining boundary. When both the top and bottom boundaries were relatively impermeable, drainage was assumed to not occur during shaking.

Estimates of c_v are usually obtained through laboratory tests, however, c_v can also be calculated based on the hydraulic conductivity, k, and vertical compressibility, m_v, of the soil. Terzaghi (1943) defined c_v as

$$c_v = \frac{k}{m_v \gamma_w} \tag{9.4}$$

where γ_w is the unit weight of water. Order-of-magnitude values of k were estimated based on well-established charts (Casagrande, 1938; Schwartz and Zhang, 2003; Holtz et al. 2011) that provided a range of hydraulic conductivity values for various soil types. The vertical compressibility is difficult to calculate for liquefied soil, since it depends on many factors including the relative density of the soil, load increment, stress path, etc. Terzaghi's definition of m_v is

$$m_v = \frac{\Delta e}{\Delta \sigma'(1+e)} \tag{9.5}$$

where is Δe the change in void ratio and $\Delta \sigma'$ is the change in effective stress. For this analysis, Δe and $\Delta \sigma'$ were approximated by the reconsolidation volumetric strain that would occur as excess pore pressure dissipates after the soil has liquefied. After shaking has stopped, the effective stress of the liquefied soil eventually returns from $\sigma_v{}' = 0$ back to the initial effective stress, $\sigma_{v,o}{}'$. This change in effective stress causes the soil to consolidate, and $\frac{\Delta e}{(1+e)}$ was estimated using conventional procedures to predict reconsolidation settlement (Ishihara and Yoshimine, 1992; Idriss and Boulanger, 2008).

Even under carefully controlled laboratory tests, the value of c_v can vary over several orders of magnitude. Estimates using equations (9.4) and (9.5) should be considered as order of magnitude approximations. Table 9.5 provides information about derived estimates of c_v and the drainage path length for each case history.

Table 9.5: Case history depth and drainage data

Motion	Site/Station	Depth to critical layer, H (m)	Drainage path length, H_{dr} (m)	k (m/s)	m_v (1/kPa)	c_v (m^2/s)
1	Alameda Naval Air Station	2.5	0.5	$1x10^{-4}$	$1x10^{-3}$	$1x10^{-5}$
2	Amagasaki	3.3	1	$3x10^{-5}$	$4x10^{-4}$	$8x10^{-6}$
3	Aomori (1968)	15.3	2	$3x10^{-5}$	$2x10^{-4}$	$2x10^{-5}$
4	Aomori (1983)	15.3	2	$3x10^{-5}$	$2x10^{-4}$	$2x10^{-5}$
5	Bond's Corner	1.5	1.8	$3x10^{-3}$	$1x10^{-3}$	$3x10^{-4}$

Table 9.5: Case history depth and drainage data

Motion	Site/Station	Depth to critical layer, H (m)	Drainage path length, H_{dr} (m)	k (m/s)	m_v (1/kPa)	c_v (m^2/s)
6	CHB024	20.3	2	$3x10^{-5}$	$3x10^{-4}$	$1x10^{-5}$
7	Hachirogata	7.3	2	$3x10^{-5}$	$3x10^{-4}$	$1x10^{-5}$
8	Higashi Kobe	15.3	--[1]	$1x10^{-4}$	$2x10^{-4}$	$5x10^{-5}$
9	HKD086	4.3	0.5	$1x10^{-5}$	$1x10^{-4}$	$1x10^{-5}$
10	IBR014	26.3	2	$1x10^{-5}$	$1x10^{-4}$	$1x10^{-5}$
11	Kawagishi-cho	4.3	3	$1x10^{-4}$	$1x10^{-3}$	$1x10^{-5}$
12	Kobe JIS	6.3	5.1	$1x10^{-5}$	$2x10^{-4}$	$5x10^{-6}$
13	Kushiro Port	2.3	1	$1x10^{-7}$	$6x10^{-4}$	$2x10^{-8}$
14	MYG010	9.3	6	$3x10^{-6}$	$2x10^{-4}$	$2x10^{-5}$
15	MYG013	5.3	1.4	$3x10^{-5}$	$1x10^{-4}$	$3x10^{-5}$
16	NIG018	5.3	1.5	$3x10^{-5}$	$2x10^{-4}$	$2x10^{-5}$
17	Onahama Port	2.3	0.6	$3x10^{-3}$	$1x10^{-3}$	$3x10^{-4}$
18	Port Island	8.3	--[1]	$3x10^{-5}$	$4x10^{-4}$	$8x10^{-6}$
19	Sakaiminato	4.3	1	$3x10^{-5}$	$5x10^{-4}$	$6x10^{-6}$
20	Treasure Island	9.0	1	$1x10^{-4}$	$4x10^{-4}$	$3x10^{-5}$
21	Wildlife	3.4	--[1]	$3x10^{-6}$	$3x10^{-4}$	$1x10^{-6}$

[1] The layer of liquefied soil was bounded by relatively impervious layers, and no drainage occurred during shaking.

9.2 FREQUENCY CONTENT SHIFT

The Stockwell spectra developed from the 21 case histories in Chapter 4 showed rapid and significant changes in the modal frequency of the ground motions as the soil liquefied. Continued changes in modal frequency were then observed following triggering as additional shaking caused the soil fabric to degrade and/or as pore pressure dissipated from the liquefied layer. The time of liquefaction was identified in each of these case histories using the horizontal, H/V, and azimuthal Stockwell spectra. The modal frequencies of the ground motions were then calculated after the soil had liquefied. For example, Figure 9.3 shows the modal frequency of the ground motion recorded at IBR014 as it evolved with time. The procedure for estimating the time of liquefaction indicated that liquefaction occurred at about 110 seconds, where an obvious shift in the frequency content can be seen in the Stockwell spectrum. After liquefaction was triggered, the modal frequency of the ground motion remained relatively constant at about 1 Hz. Occasional short

duration increases in model frequency, which were presumably due to dilation pulses, can be seen at various times. Horizontal Stockwell spectra and the modal frequencies for all 21 of the case histories are provided in Appendix B.

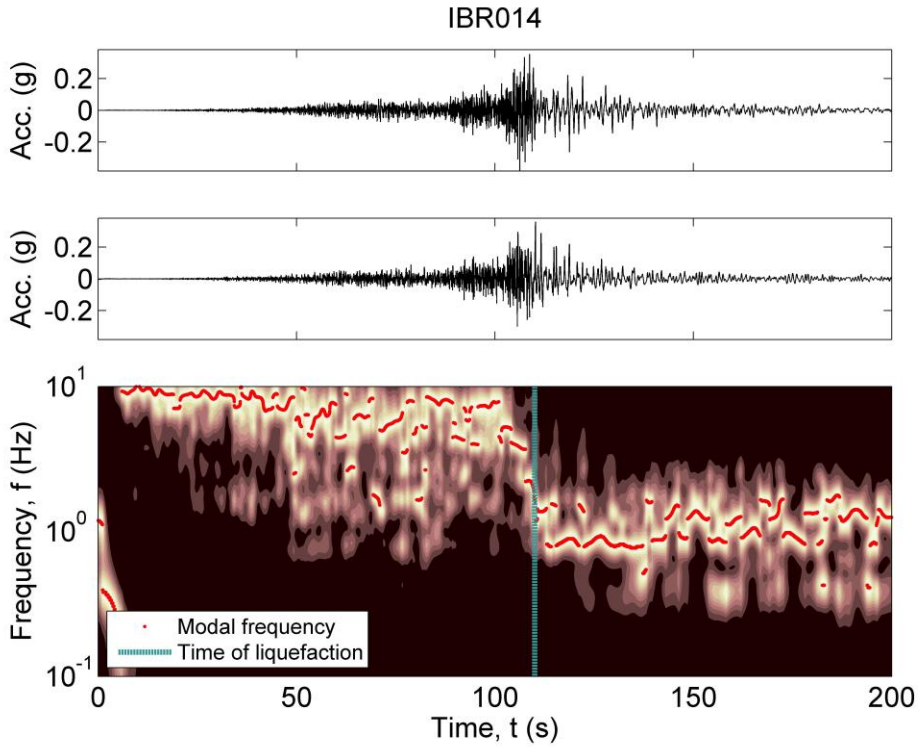

Figure 9.3: Shift in modal frequency at IBR014

The shift in the ground motion's modal frequency can be explained by the rapid softening of the layer of liquefiable soil. Changes in soil stiffness, especially the dramatic changes associated with liquefaction, also change the characteristic frequency of the site. In conditions where the liquefiable soil is much softer than the underlying non-liquefied soil, the modal frequency of the ground motion begins to approach the characteristic frequency of the site.

9.2.1 *Characteristic frequency*

The relationship between the soil stiffness and the shift in characteristic frequency due to liquefaction can be explained through a simple soil model based on a single layer of soil on a rigid base. The characteristic frequency of a single layer of soil, $\tilde{f}$, is a function of the thickness, H, stiffness, G, and density, ρ, of the soil layer.

$$\tilde{f}(t) = \frac{\sqrt{\mathrm{G}}}{4\mathrm{H}\sqrt{\rho}} \tag{9.6}$$

The value of G in equation (9.6) represents the secant stiffness of the soil. Rearranging equation (9.6) as a function of G,

$$\mathrm{G} = 16\mathrm{H}^2\rho\left(\tilde{f}(t)\right)^2 \tag{9.7}$$

Particularly for conditions where the effective stress may be extremely low or near zero, the stiffness of the soil is assumed to be composed of two components: one that depends on the effective stress of the soil, G', and the other that is independent of the effective stress and represents the minimum stiffness of the soil when $\sigma_v{}' = 0$, $\mathrm{G}_{\mathrm{min}}$.

$$\mathrm{G} = \mathrm{G}'\left(\frac{\sigma_v{}'}{p_{\mathrm{atm}}}\right)^{0.5} + \mathrm{G}_{\mathrm{min}} \tag{9.8}$$

where p_{atm} is the atmospheric pressure. Initially, before liquefaction is triggered, the stiffness of the soil is relatively constant. However, as excess pore pressure increases and $\sigma_v{}'$ approaches 0, G drops very quickly to $\mathrm{G}_{\mathrm{min}}$. The characteristic frequency, $\tilde{f}$, of the layer of soil evolves with time as $\sigma_v{}'$ and G decrease. Eventually, when liquefaction is triggered and $\sigma_v{}' = 0$, the characteristic frequency reaches a limiting value, $\tilde{f}_{\mathrm{min}}$.

$$\tilde{f}_{\mathrm{min}} = \frac{\sqrt{\mathrm{G}_{\mathrm{min}}}}{4\mathrm{H}\sqrt{\rho}} \tag{9.9}$$

The shear stiffness of the soil can change many orders of magnitude between initial and liquefied states. As such, it is appropriate to apply a log-transformation to G in equation (9.7).

$$\ln \mathrm{G} = 2\ln\left(4\mathrm{H}\tilde{f}(t)\sqrt{\rho}\right) \tag{9.10}$$

The rate at which ln G decreases is motion-specific, but generally, has the form of

$$\ln \mathrm{G} = g_0 - \Delta g\left(\frac{1}{1+\left(\frac{t}{a_1}\right)^{b_1}}\right) \tag{9.11}$$

where g_0 is the initial value of ln G before liquefaction is triggered, Δg is the shift from the initial value of ln G to $\ln G_{min}$ due to liquefaction, and a_1 and b_1 are motion-specific curve fitting parameters. A long time after the transition from the soil's initial stiffness to the liquefied stiffness, when $t \gg a_1$,

$$\ln G_{min} = g_0 - \Delta g \tag{9.12}$$

The stiffness of liquefied soil can increase due to pore pressure dissipation even while strong shaking continues. The competing effects of pore pressure dissipation due to drainage and pore pressure generation due to shaking can be calculated using the analytical solution described in Section 5.3. This solution indicates that the excess pore pressure ratio varies with depth, time, drainage boundary conditions, and the intensity of shaking that occurs simultaneously with drainage. For this analysis, equation (9.11) can be extended to include terms for the increased soil stiffness due to pore pressure dissipation as σ_v' returns back to its initial value of $\sigma_{v,0}'$.

$$\ln G = g_0 - \Delta g \left(\frac{1}{1 + \left(\frac{t}{a_1}\right)^{-b_1}} - \frac{c_2}{1 + \left(\frac{t}{a_2}\right)^{-b_2}} \right) \tag{9.13}$$

where a_2, b_2, and c_2 are motion-specific curve fitting parameters. The resulting expression for ln G is very flexible and can be fit to any modal frequency time histories that decreases very rapidly when $t = a_1$, and then increases once $t = a_2$. The parameter c_2 defines the dimensionless fraction of ln G that returns as the intensity of shaking diminishes and pore pressure dissipates. If excess pore pressure does not dissipate significantly, the shear stiffness of the liquefied soil remains near G_{min} for the duration of the motion and c_2 = 0. Conversely, if liquefaction is triggered in a thin, well-drained layer of soil, but excess pore pressure dissipates as shaking diminishes, the shear stiffness of the liquefied soil may return to its pre-triggering value and c_2 = 1.0.

9.2.2 *Modal frequency*

The modal frequency of a ground motion, f, differs from the characteristic frequency of the site, $\tilde{f}$. The modal frequency is a property of a ground motion, while the characteristic frequency is a measure of the response of a soil profile. However, in a very simple layered model with a single layer of soil on an elastic base, the modal frequency and the characteristic frequency are similar in conditions where the overlying layer of soil is very soft relative to the stiffness of the elastic base.

This situation arises when soils liquefy, since the secant stiffness of the soil becomes very low. Figure (9.4) shows a schematic of a single layer of soil on an elastic base. The transfer function, $F(\omega)$, of this layered system can be expressed (Kramer, 1996) as

$$F(\omega) = \frac{1}{\cos k_s^* H + \alpha^* \sin k_s^* H} \tag{9.14}$$

where ω is frequency in radians, $\omega = 2\pi f$, $k_s^* = \frac{\omega}{v_{s,s}^*}$, and α^* is the complex impedance ratio, which is defined as

$$\alpha = \frac{\rho_s v_{s,s}^*}{\rho_r v_{s,r}^*} \tag{9.15}$$

where ρ_s and ρ_r are the densities of the soil and base, respectively, and $v_{s,s}^*$ and $v_{s,r}^*$ are the complex shear wave velocities of the soil and base, respectively. The complex shear wave velocity is

$$v_s^* = v_s(1 + i\xi) \tag{9.16}$$

where ξ is the damping ratio and i is the imaginary unit.

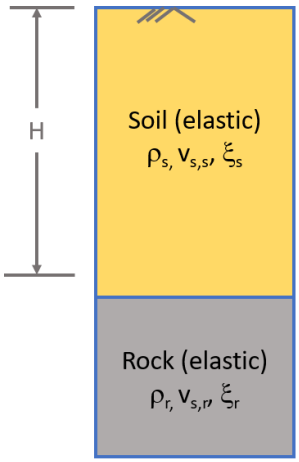

Figure 9.4: Schematic profile for elastic, damped soil on an elastic base

When the layer of soil becomes very soft relative to the base, α approaches 0 and $|F(\omega)|$ approaches $\frac{1}{\cos k_s^* H}$. If damping is minimal, the transfer function is then maximized at frequencies $\frac{\omega}{2\pi} = \frac{v_{s,s}}{4H}$, which defines the characteristic frequency of a layer of soil on a rigid base, $\tilde{f}$. While this does not necessarily mean that the modal frequency of a ground motion is equal to the characteristic frequency of the site, it does imply that the characteristic frequency is likely to be

greatly amplified. As an example, the ground motions in the CS dataset were input into a transfer function that was representative of IBR014 after liquefaction was triggered. Figure 9.5(a) shows the example profile, which has a characteristic frequency of about 1 Hz with an impedance ratio of about 0.2. Figure 9.5(b) shows a histogram of the modal frequencies of the ground motions in the CS-dataset, and Figure 9.5(c) shows a histogram of the modal frequencies of the motions after the transfer function was applied. The motions in the CS-dataset, shown in Figure 9.5(b), exhibited a wide range of modal frequencies, ranging over two orders of magnitude. However, after the motions were convolved with the transfer function, the modal frequencies converged to values very close to the characteristic frequency of the site. This observation indicates that once a ground motion is convolved through a layered system, such as the one shown in Figure 9.5, the modal frequency of a ground motion approaches the characteristic frequency of a soil layer, especially when $v_{s,s}$ is low relative to $v_{s,r}$.

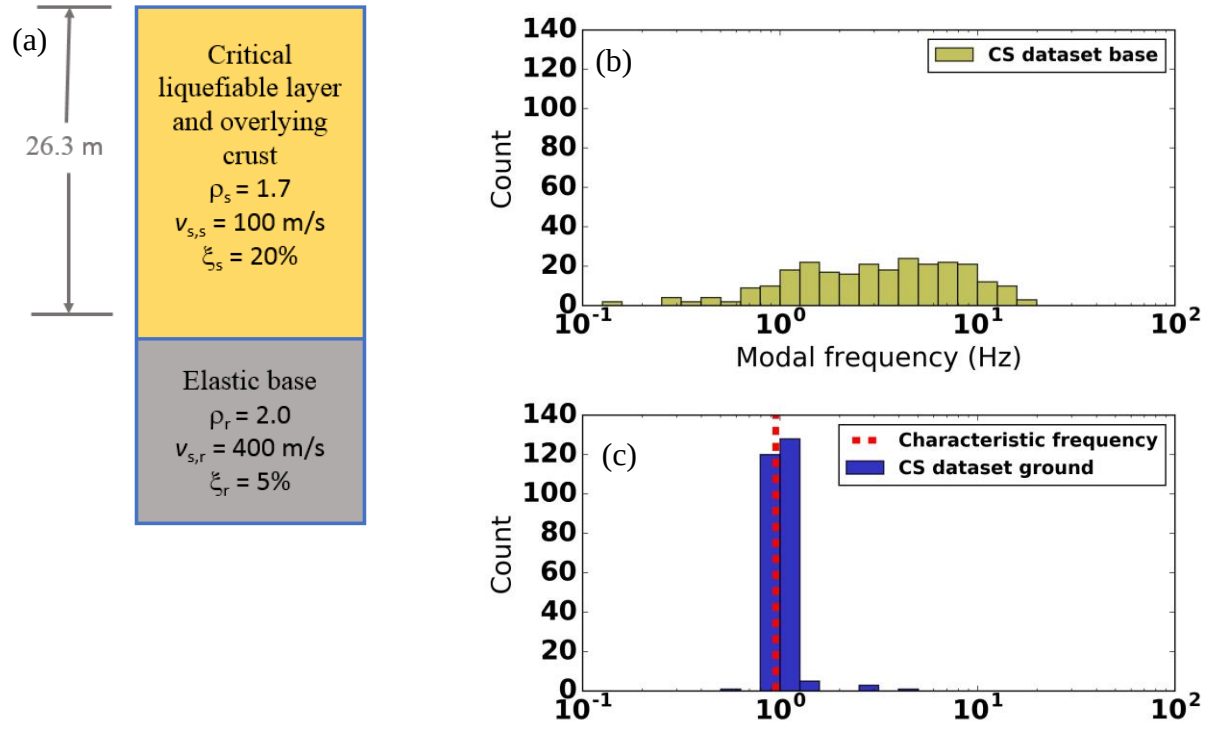

Figure 9.5: Modal frequencies of ground motions in CS-dataset. (a) Example profile. (b) Modal frequency of CS dataset. (c) Modal frequency of CS dataset with transfer function from example profile.

It should be acknowledged that, while the characteristic frequency of the site and the modal frequency of the ground motion become similar under these specific conditions, they may not be

equal under all conditions. However, after liquefaction has been triggered these differences are typically relatively small, as illustrated by the histogram in Figure 9.5(c). For the following analysis, the modal frequency of a ground motion propagated through liquefied soil is assumed to be equal to the characteristic frequency of a site.

9.2.3 *Recorded ground motions*

Equation (9.10) provides an expression to calculate the secant shear stiffness, $\ln \mathrm{G}$, as a function of the depth, H, density, $\sqrt{\rho}$, and characteristic frequency $\tilde{f}$, of a layer of liquefied soil overlying a rigid base. Once the soil has liquefied, the characteristic frequency of the layer approaches the modal frequency of the ground motion, f. If the post-triggering characteristic frequency and modal frequency of the ground motion are assumed to be equal, the evolutionary time history of $\ln \mathrm{G}$, which is referred to as g, is calculated as

$$g = 2\ln\left(4\mathrm{H}f(t)\sqrt{\rho}\right) \tag{9.17}$$

The evolution of g can be calculated from the modal frequency of a recorded ground motion.

Equation (9.13) provides a smooth function to model the evolution of $\ln \mathrm{G}$. This smooth model, which is referred to as $\hat{g}$, is defined as

$$\hat{g} = g_0 - \Delta g\left(\frac{1}{1+\left(\frac{t}{a_1}\right)^{-b_1}} - \frac{c_2}{1+\left(\frac{t}{a_2}\right)^{-b_2}}\right) \tag{9.18}$$

The right-hand side of equation (9.18) has seven parameters that control the shape of the function. Values of these parameters can be selected so that $\hat{g}$ fits g. The relative misfit between these two functions is defined by the sum of square residuals.

$$r = \sum_{t=t_0}^{t_f} (g - \hat{g})^2 \tag{9.19}$$

where t_0 and t_f are the first and last times when the ground surface acceleration exceeds 0.005 g. Nonlinear optimization can be performed to fit $\hat{g}$ to g by minimizing the sum of square residuals, r. The resulting parameters g_0, Δg, a_1, b_1, a_2, b_2, and c_2 describe a smooth model for the evolving

stiffness of the soil, g. The estimated modal frequency of the ground motion, $\hat{f}$, can be calculated as

$$\hat{f}(t) = \frac{\exp\left(\frac{1}{2}\hat{g}\right)}{4\mathrm{H}\sqrt{\rho}} \tag{9.20}$$

An example of the nonlinear optimization and fitting of $\hat{g}$ was first performed using the data from the Wildlife liquefaction case history. The log of the post-triggering shear modulus, g, was first calculated using equation (9.17). The seven curve fitting parameters were then estimated using nonlinear optimization and time histories of $\hat{g}$ and $\hat{f}$ were calculated. Both the calculated modal frequency, f, and the estimated modal frequency, $\hat{f}$, are shown in Figure 9.6. The coefficient of determination, R^2, between the calculated and estimated modal frequency was 0.71.

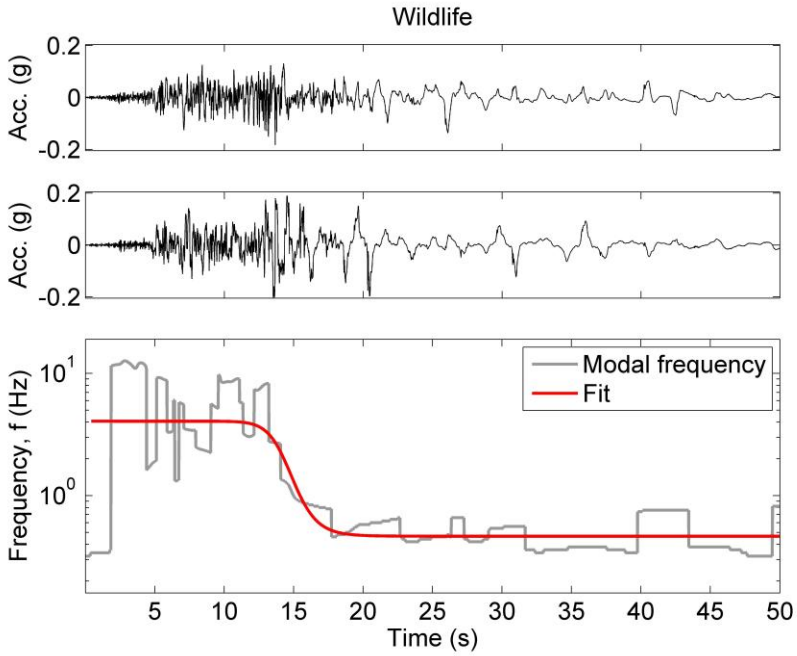

Figure 9.6: Fit of equation (9.18) to modal frequencies of the Superstition Hills Earthquake at Wildlife

The function $\hat{g}$ provided an estimate of the evolving shear stiffness of the soil as pore pressure was generated and liquefaction was triggered. The minimum shear modulus, G_{min}, can be calculated from the parameters that control the shape $\hat{g}$ using equation (9.12). The curve-fitting values from the nonlinear optimization results resulted in an estimated value of G_{min} = 72 kPa

after liquefaction was triggered. Based on the average, secant stiffness of the soil, the estimated minimum post-triggering shear wave velocity, $\hat{v}_{s,\min}$, was calculated as

$$\hat{v}_{s,\min} = \sqrt{\frac{G_{\min}}{\rho}} \tag{9.21}$$

Substituting $G_{\min}$ into equation (9.21) resulted in an estimated minimum post-triggering shear wave velocity of about 6.3 m/s.

The Wildlife liquefaction case history is one of two unique case histories where liquefaction was triggered at a site with a downhole accelerometer array. When downhole acceleration records are available, the estimated values of post-triggering shear wave velocity, $\hat{v}_{s,\min}$, can be validated by the reported travel time between the downhole and surface accelerometers. The downhole accelerometer at the Wildlife site was established 7.5 m below the ground surface. Zeghal and Elgamal (1994) reported that the travel time between the surface and downhole accelerometers corresponded to shear wave velocities between 5 to 40 m/s after liquefaction was triggered. The layer of liquefiable soil was about 3.4 m deep, which was much shallower than the downhole accelerometer. The reported shear wave velocities therefore include contributions from both liquefied and non-liquefied layers of soil, and must be adjusted for the shear wave velocity of the non-liquefied layer of soil. Based on subsurface data, the non-liquefied soil was about 3.6 m-thick and had a shear wave velocity of about 116 m/s. The shear wave velocity of the liquefied soil was back-calculated as a range between 2.3 and 22 m/s. This range of shear wave velocities was consistent with the shear wave velocity estimated using the modal frequency of the ground motion, $\hat{v}_{s,\min}$ = 6.3 m/s.

Port Island is the other case history where liquefaction was triggered at a site with a downhole accelerometer array. Nonlinear optimization was again performed using the case history data, and time histories of both $\hat{g}$ and $\hat{f}$ were calculated. Plots of the calculated modal frequency, f, and the estimated modal frequency, $\hat{f}$, are provided in Figure 9.7. The shift in modal frequency due to liquefaction was subtler at Port Island than at the Wildlife array. Port Island was founded on relatively soft soils, and initial modal frequency of the ground motion was much closer to the modal frequency of the motion after liquefaction was triggered. Because the shift in modal frequency was not as clear, the coefficient of determination, R^2, between the calculated and estimated modal frequency was only 0.18. Nonetheless, a shift in the frequency content can be

seen in Figure 9.7, and minimum values of the post-triggering secant shear modulus can be calculated.

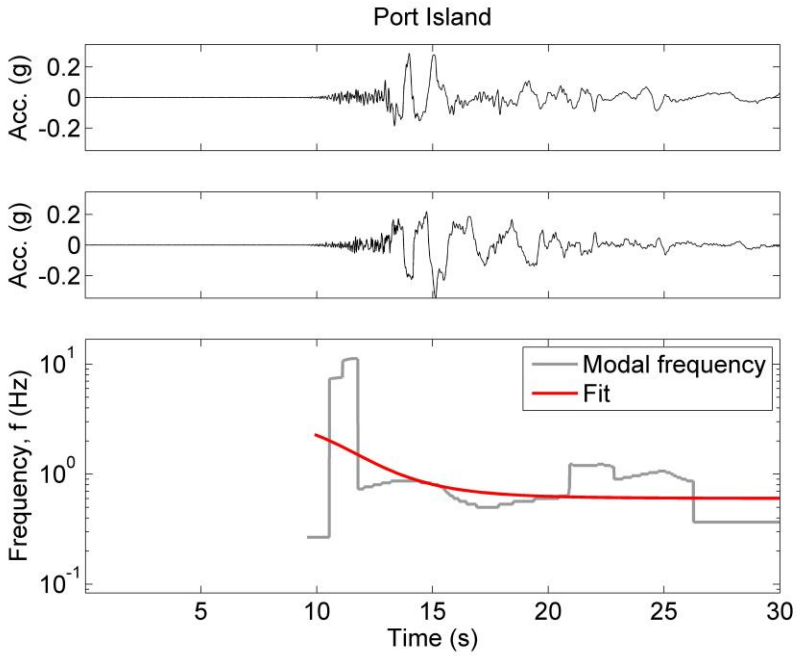

Figure 9.7: Fit of equation (9.18) to modal frequencies of the Hygoken-Nambu earthquake at Port Island.

The nonlinear regression results indicated that G_{min} was about 674 kPa after liquefaction was triggered. This corresponded to a minimum post-triggering shear wave velocity, $\hat{v}_{s,\min}$, of about 19.4 m/s. The Port Island site contained downhole accelerometers at depths of 16, 32, and 83 m. The critical layer of soil that liquefied was about 8.3 m deep and was between the ground surface and the downhole accelerometer at a depth of 16 m. Elgamal et al. (1996) used the difference in travel time between the surface and the downhole motion at a depth of 16 m to estimate a range of shear wave velocities between 20 to 120 m/s after liquefaction was triggered. The reported shear wave velocities included both the shear wave velocities of liquefied and non-liquefied layers of soil. Based on subsurface data, the non-liquefied soil was about 7.7 m-thick and had a shear wave velocity of about 210 m/s. The shear wave velocity of the liquefied soil was the back-calculated as a range between 10.9 and 86 m/s. This range of shear wave velocity values was consistent with the shear wave velocities estimated using the modal frequency of the ground motion, $\hat{v}_{s,\min}$ = 19.4 m/s.

The ground motions at both Wildlife and Port Island showed rapid decreases in modal frequency once liquefaction was triggered. The modal frequencies then remained relatively constant and showed little indication of increased stiffness due to drainage. The nonlinear optimization resulted in values of c_2 = 0 for both of these cases. However, other case histories do show indication that drainage and pore pressure dissipation occurred after liquefaction was triggered, where g increased as the amplitude of shaking diminished. The smooth function used to estimate $\hat{g}$ can model these changes. The Onahama Port case history provides an example where the modal frequency of the ground motion decreased rapidly as liquefaction was triggered, but then the modal frequency gradually increased as the amplitude of the ground motion diminished. Eventually, the modal frequency of the ground motion returned to its pre-triggering level. Both the calculated modal frequency, f, and the estimated modal frequency, $\hat{f}$, are shown in Figure 9.8. The coefficient of determination, R^2, between the calculated and estimated modal frequency was 0.45.

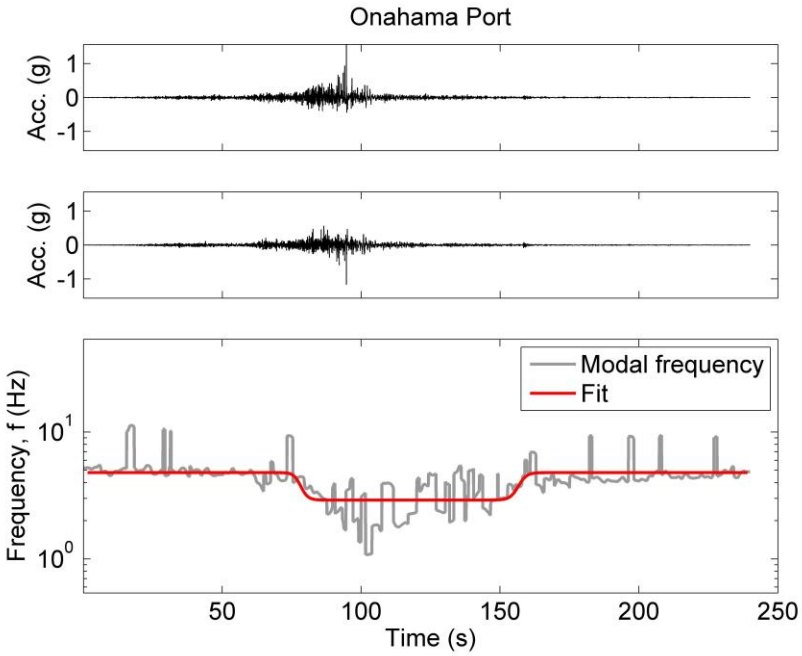

Figure 9.8: Fit of equation (9.18) to modal frequencies of the Tohoku earthquake at Onahama Port.

The plot of $\hat{f}$ captured both the decrease in modal frequency due to liquefaction and the increase in modal frequency due to pore pressure dissipation. The nonlinear regression results indicated that G_{min} was about 1,360 kPa after liquefaction was triggered, which corresponded to a minimum

post-triggering shear wave velocity, $\hat{v}_{s,\min}$, of about 26.8 m/s. At about 160 seconds, the amplitude of the ground motion diminished and the modal frequency of the ground motion increased. The model of $\hat{g}$ captured this transition, and c_2 = 1.0. This value implied that the post-triggering modal frequency of the ground motion eventually returned to the modal frequency at the beginning of the motion.

The evolving modal frequencies were estimated for all 21 of the case histories by fitting $\hat{g}$ to g using nonlinear optimization. Figures showing these results are provided in Appendix B. While the coefficients in equation (9.18) were developed as curve-fitting parameters that match the observed trends in the ground motions, the resulting parameters include a minimum post-triggering stiffness, $G_{\min}$, and the fraction of the shear stiffness that returns due to pore pressure dissipation, c_2. These values of $G_{\min}$ and c_2 are provided in Table 9.6.

Table 9.6: Estimated post-triggering liquefied layer stiffness parameters

Motion	Site/Station	$G_{\min}$ (kPa)	c_2
1	Alameda Naval Air Station	55	0.08
2	Amagasaki	40	0.33
3	Aomori (1968)	1,040	0.06
4	Aomori (1983)	377	0.17
5	Bond's Corner	104	0.86
6	CHB024	1,610	0.00
7	Hachirogata	190	0.00
8	Higashi Kobe	1,500	0.00
9	HKD086	296	0.46
10	IBR014	17,600	0.46
11	Kawagishi-cho	33	0.01
12	Kobe JIS	460	0.00
13	Kushiro Port	48	0.15
14	MYG010	527	0.33
15	MYG013	2,380	1.00
16	NIG018	121	1.00
17	Onahama Port	1,360	1.00
18	Port Island	674	0.00
19	Sakaiminato	144	0.16
20	Treasure Island	240	0.28
21	Wildlife	72	0.00

9.3 PREDICTION OF CHANGES IN FREQUENCY CONTENT

The response of soil is sensitive to not only the amplitude and duration of ground motion but also the frequency content. Liquefied soils become very soft, and soft soils respond most strongly to low-frequency motions. The ability to predict the post-triggering modal frequency of ground motions would be beneficial for identifying (or developing) intensity measures that are specific to estimating permanent deformations that result from liquefaction. Intensity measures typically associated with the consequences of liquefaction, such as Arias intensity and cumulative absolute velocity, are sensitive to the frequency content of the ground motions. For such intensity measures, it is important to identify the conditions that can cause changes in frequency content, including the magnitude of shifts in the frequency content and the evolving changes in frequency content that can occur after liquefaction has been triggered.

Using current approaches, estimating the changes in frequency content due to liquefaction include a significant amount of uncertainty. Hartvigsen (2007) performed many nonlinear effective and total stress analyses using an advanced nonlinear finite difference model. The ratios of the spectral accelerations from the effective and total stress analyses were used to calculate a response spectrum ratio, which provided an estimate of the changes in frequency content due to liquefaction. Plots of the response spectrum ratio versus the factor of safety against liquefaction showed a large degree of uncertainty. Gingery (2014) analyzed recorded ground motions that had been affected by liquefied soil. He also found that the presence of liquefied soil affected the spectral acceleration relative to the spectral acceleration that would have been predicted using GMPEs. An amplification factor due to liquefaction, AF_{liq}, was calculated as the ratio of between the spectral acceleration from the recorded ground motion and the spectral acceleration predicted using GMPEs. A value of AF_{liq} greater than 1.0 indicated that the presence of liquefied soil amplified the spectral acceleration, and vice versa, values of AF_{liq} less than 1.0 indicated that the liquefied soil deamplified the spectral acceleration. For the ground motions used in this analysis, the values of AF_{liq} were found to be equal to or slightly larger than 1.0 at short periods but were often much greater than 1.0 at longer periods. Figure 9.9 shows values of AF_{liq} calculated using four of the NGA West-2 GMPEs.

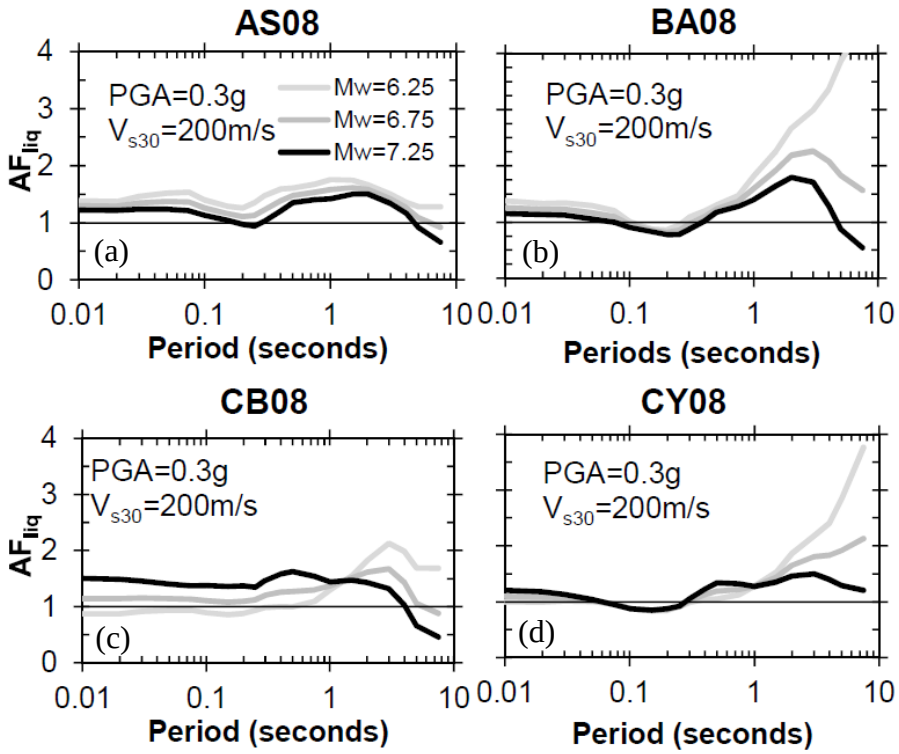

Figure 9.9: Spectral acceleration amplification factors due to liquefaction (from Gingery, 2014). (a) Abrahamson and Silva (2008) GMPE, (b) Boore and Atkinson (2008) GMPE, (c) Campbell and Bozorgnia (2008) GMPE, and (d) Chiou and Youngs (2008) GMPE.

This finding indicated that liquefaction did indeed amplify the ground motions across a broad range of frequencies. Particularly, the low-frequency components of motions were amplified. The intra-event standard deviation of the liquefied ground motions was also compared to the intra-event standard deviation predicted by the GMPEs. The liquefied ground motion standard deviation was similar to the GMPE-based standard deviation at short periods, but the liquefied ground motion standard deviation was greater than the GMPE-based standard deviation at longer periods. This indicated that liquefaction not only increased the spectral acceleration at longer periods, it also increased the uncertainty in predicting spectral acceleration.

The preceding sections suggested that equation (9.18) can be used to describe the variation in modal frequency with time after liquefaction has been triggered. The ability to predict modal frequencies would be beneficial for validating site response analyses when liquefiable soils are present (i.e. Hartvigsen, 2007; Gingery, 2014) and for developing intensity measures that are tuned to the frequency content of ground motions that are influenced by liquefied soils. The objective of collecting data from the case histories in this study is to determine which subsurface conditions

and earthquake loading properties influence the observed changes in frequency content. The characteristic frequency of a site shifts rapidly when liquefaction is triggered due to the extreme softening of the layer of liquefied soil. The model for estimating ln G is defined such that the shear stiffness of the soil approaches a minimum value, G_{min}, after liquefaction is triggered. The model also captures the increase in shear stiffness that can occur as excess pore pressure dissipates. If no pore pressure dissipates during shaking, $c_2 = 0$. Likewise, if pore pressure dissipates rapidly and the modal frequency of the ground motion returns to its initial value, $c_2 = 1.0$. Values of G_{min} and c_2 for each of 21 case histories have been calculated and are provided in Table 9.6.

Although the amount of data is small, the values of G_{min} and c_2 can be predicted, to some degree, by the site conditions and the intensity of loading. The simple mechanics used to define G_{min} assume that it represents the secant shear modulus of the liquefied soil. The stiffness of liquefied soil can vary several orders of magnitude throughout each cycle of loading, but laboratory results (Ishihara and Yoshimine, 1992; Kwan et al., 2014) show that the peak post-triggering shear strains depend on the relative density of the soil and intensity of shaking. Kramer and Wang (2015) describe the residual strength of soil as both a function of the relative density of the soil and the initial effective stress. Intuitively, the liquefied soil stiffness may also depend on the relative density and initial effective stress of the soil. Based on these observations, regression was performed to estimate values of $\ln G_{min}$ with $(N_1)_{60}$, $\sigma'_{v,o}$, and the post-triggering intensity of shaking, IM^{eff}. Values of $(N_1)_{60}$ and $\sigma'_{v,o}$ are provided in Table 9.1, and values of IM^{eff} were calculated using GMPEs and the results are provided in Table 9.4. The data in Table 9.6 indicate that G_{min} varies over several orders of magnitude, so transformation to $\ln G_{min}$ was appropriate for regression analysis. A simple expression was developed to estimate $\ln G_{min}$ based on $(N_1)_{60}$, $\sigma_{v,0}{}'$, and IM^{eff}.

$$\ln \frac{G_{min}}{p_{atm}} = d_0 + d_1 \left[\frac{(N_1)_{60}}{15 \text{ blows/ft}}\right] + d_2 \ln\left[\frac{\sigma_{v,0}{}'}{p_{atm}}\right] + d_3 \ln\left[\frac{IM^{\text{eff}}}{IM_{ref}}\right] + \sigma_{\ln G_{min}} \varepsilon_{\ln G_{min}} \qquad (9.22)$$

where p_{atm} is the atmospheric pressure, d_0, d_1, d_2, and d_3 are constants estimated using regression, IM_{ref} is a reference normalizing value selected based on the mean of the data, and $\varepsilon_{\ln G_{liq}}$ is a standard normally distributed random variable. Post-triggering intensity measures, IM^{eff}, of PGA_M, Arias Intensity, and cumulative absolute velocity were all considered as candidate

*IM*s for estimating G_{min}. The values of d_0, d_1, d_2 and $\sigma_{\ln G_{min}}$ from the regression analyses with each of these *IM*s are provided on Table 9.7.

Table 9.7: Coefficients for estimating G_{min} using equation (9.22)

Intensity measures	Reference value for normalizing, IM_{ref}	d_0	d_1	d_2	d_3	$\sigma_{\ln G_{min}}$
$IM^{eff} = PGA_M$	0.20 g	1.54	0.77	1.65	0.38	1.00
$IM^{eff} = I_a$	1 m/s	1.46	0.53	1.90	0.47	1.02
$IM^{eff} = CAV$	5 m/s	0.75	0.70	1.70	0.80	1.07

The regression analyses indicated that predictions of $\ln G_{min}$ contained a significant amount of uncertainty, regardless of the intensity measure used as IM^{eff}. $IM^{eff} = PGA_M$ produced the lowest value of $\sigma_{\ln G_{min}}$, although $IM^{eff} = I_a$ produced a similar value. The differences in $\sigma_{\ln G_{min}}$ between each of the *IM*s were not very large, indicating that any of the three *IM*s are appropriate to calculate $\ln G_{min}$. A plot of the calculated and estimated values of G_{min} is provided in Figure 9.10. This plot shows that the values of G_{min} did indeed vary over several orders of magnitude, and the relatively large values of $\sigma_{\ln G_{min}}$ are due in part to this variation.

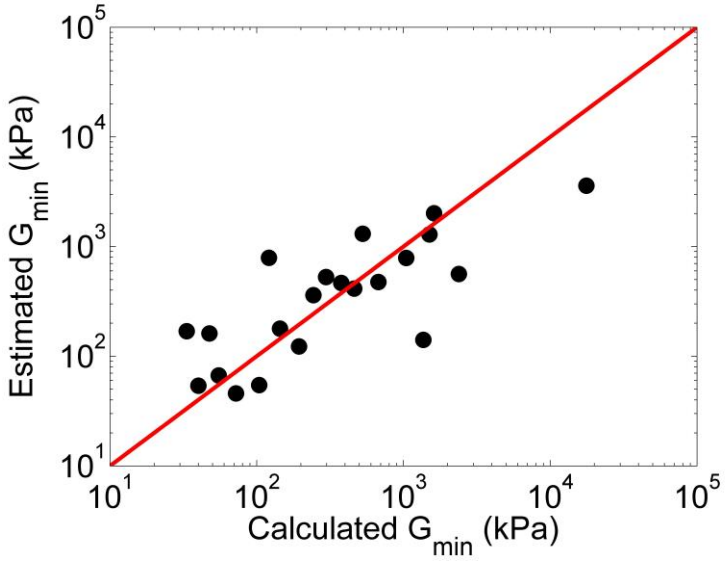

Figure 9.10: Estimated versus calculated values of G_{min}.

Estimates of the minimum modal frequency, $\hat{f}_{min}$, can be derived from the minimum post-triggering shear stiffness. Substituting equation (9.7) into equation (9.22),

$$\ln\left(\frac{16\mathrm{H}^2 \hat{f}_{\min}{}^2 \rho}{p_{\mathrm{atm}}}\right) = d_0 + d_1\left[\frac{(\mathrm{N}_1)_{60}}{15\ \mathrm{blows/ft}}\right] + d_2 \ln\left[\frac{\sigma_{v,0}{}'}{p_{\mathrm{atm}}}\right] + d_3 \ln\left[\frac{IM^{\mathrm{eff}}}{IM_{\mathrm{ref}}}\right] + \sigma_{\ln \mathrm{G}_{\min}} \varepsilon_{\ln \mathrm{G}_{\min}} \tag{9.23}$$

which can be rearranged as

$$\ln\left(\hat{f}_{\min}{}^2\right) = d_0 + d_1\left[\frac{(\mathrm{N}_1)_{60}}{15\ \mathrm{blows/ft}}\right] + d_2 \ln\left[\frac{\sigma_{v,0}{}'}{p_{\mathrm{atm}}}\right] + d_3 \ln\left[\frac{IM^{\mathrm{eff}}}{IM_{\mathrm{ref}}}\right] - \ln\left(\frac{16\mathrm{H}^2\rho}{p_{\mathrm{atm}}}\right) + \sigma_{\ln \mathrm{G}_{\min}} \varepsilon_{\ln \mathrm{G}_{\min}} \tag{9.24}$$

which can be further rearranged as

$$\ln\left(\hat{f}_{\min}\right) = \frac{1}{2}d_0 + \frac{1}{2}d_1\left[\frac{(\mathrm{N}_1)_{60}}{15\ \mathrm{blows/ft}}\right] + \frac{1}{2}d_2 \ln\left[\frac{\sigma_{v,0}{}'}{p_{\mathrm{atm}}}\right] + \frac{1}{2}d_3 \ln\left[\frac{IM^{\mathrm{eff}}}{IM_{\mathrm{ref}}}\right] - \frac{1}{2}\ln\left(\frac{16\mathrm{H}^2\rho}{p_{\mathrm{atm}}}\right) + \frac{1}{2}\sigma_{\ln \mathrm{G}_{\min}} \varepsilon_{\ln \mathrm{G}_{\min}} \tag{9.25}$$

as long as $\tilde{f}_{\min}$ is not greater than $\frac{v_{s,o}}{4\mathrm{H}}$. So, despite the large value of $\sigma_{\ln \mathrm{G}_{\min}}$, the log-normal standard deviation of the minimum modal frequency, $\hat{f}_{\min}$, is equal to $\frac{1}{2}\sigma_{\ln \mathrm{G}_{\min}}$. When IM^{eff} = $\mathrm{PGA_M}$, $\frac{1}{2}\sigma_{\ln \mathrm{G}_{\min}}$ = 0.50. While the uncertainty in $\hat{f}_{\min}$ is still relatively large, it is consistent with other studies (Hartvigsen, 2007; Gingery, 2014) that investigated the uncertainty in spectral acceleration due to liquefaction. Equation (9.24) can be used to estimate order-of-magnitude values of $\hat{f}_{\min}$. The results of the regression analyses indicated that both the penetration resistance, $(\mathrm{N_1})_{60}$, and initial effective stress, $\sigma_{v,0}{}'$, had a very strong influence on $\mathrm{G}_{\min}$. Figure 9.11 shows contours of $\mathrm{G}_{\min}$ versus $(\mathrm{N_1})_{60}$ for several values of $\sigma_{v,0}{}'$ and post-triggering values of $\mathrm{PGA_M}$ = 0.05 g.

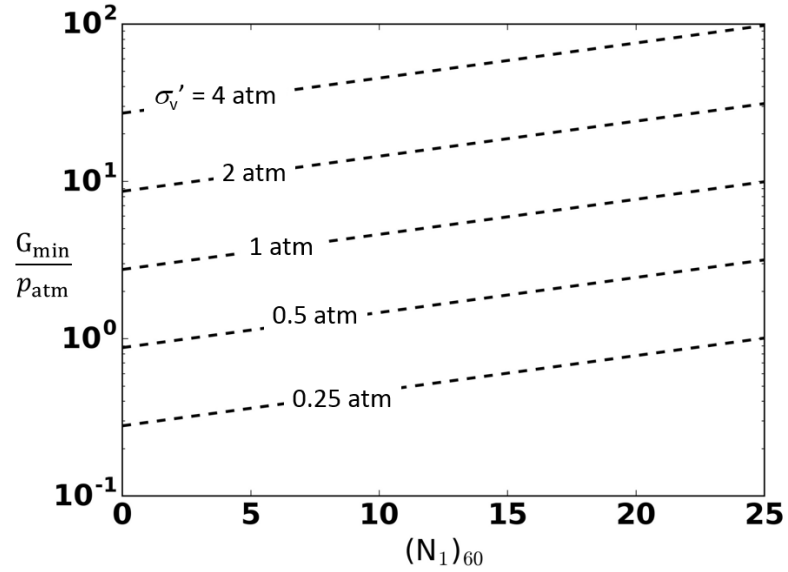

Figure 9.11: Estimated values of G_{min} based on $(N_1)_{60}$ and $\sigma_{v,0}'$.

The value of c_2 indicates whether the post-triggering shear modulus remains at G_{min} following liquefaction or increases as pore pressures dissipate. Both the rate at which pore pressure dissipates and the rate at which pore pressures are generated affect the value of c_2. The analytical solution for the competing effects of pore pressure dissipation and generation in Section 5.3 requires two parameters to calculate the dissipation of excess pore pressure: the vertical coefficient of consolidation, c_v, and the drainage path length, H_{dr}. These two parameters are grouped together as a single term, $\frac{c_v}{{H_{dr}}^2}$. The competing effect of pore pressure generation is calculated by a post-triggering intensity measure, IM^{eff}, and the resistance of the soil to pore pressure generation, which is typically a function of penetration resistance, $(N_1)_{60}$. The value of c_2 is bounded by 0 and 1, so transformation to a logistic expression, $\ln\left(\frac{1}{c_2}-1\right)$, is appropriate for regression analysis. A simple expression was developed to estimate c_2 based on $\frac{c_v}{{H_{dr}}^2}$, IM^{eff}, and $(N_1)_{60}$.

$$\ln\left(\frac{1}{c_2}-1\right) = q_0 + q_1 \ln\left[\frac{c_v}{{H_{dr}}^2}\right] + q_2\left[\frac{IM^{\text{eff}}}{IM_{\text{ref}}}\right] + q_3 \ln\left[\frac{(N_1)_{60}}{IM_{\text{ref}}}\right] + \sigma_{\ln y}\varepsilon_{\ln y} \qquad (9.26)$$

where q_0, q_1, and q_2 are constants estimated using regression, and IM_{ref} is a reference normalizing value. ε_y is a standard normally distributed random variable, where $y = \ln\left(\frac{1}{c_2}-1\right)$. Post-triggering intensity measures, IM^{eff}, of PGA_M, Arias Intensity, and cumulative absolute velocity

were all considered as candidate *IM*s for estimating c_2. The values of q_0, q_1, and q_2 and $\sigma_{\ln y}$ from the regression analyses are provided on Table 9.8.

Table 9.8: Coefficients for estimating c_2 using Equation (9.26)

Intensity measures	**Reference value for normalizing, IM_{ref}**	q_0	q_1	q_2	q_3	σ_y
IM^{eff} = PGA_M	0.20 g	-7.65	-0.59	-0.85	-3.34	2.18
IM^{eff} = I_a	1 m/s	-6.65	-0.62	-0.85	-2.18	1.88
IM^{eff} = CAV	5 m/s	-7.06	-0.57	-0.46	-3.29	2.21

The regression analyses indicated that IM^{eff} = I_a produced the lowest value of σ_y. A plot of the calculated and estimated values of c_2 is provided in Figure 9.12. Note that the regression analysis was performed for the logistic expression $y = \ln\left(\frac{1}{c_2} - 1\right)$ so that conditions where c_2 was clearly 0 or 1 could be identified. The plot in Figure 9.12 shows that equation (9.26) appropriately calculated values of c_2 when conditions clearly implied that pore pressure dissipation should not have occurred and c_2 = 0, or when the liquefied soil is relatively well-drained and c_2 = 1. The coefficient of determination, R^2, based on the residuals of the transformed variable, y, was about 0.78.

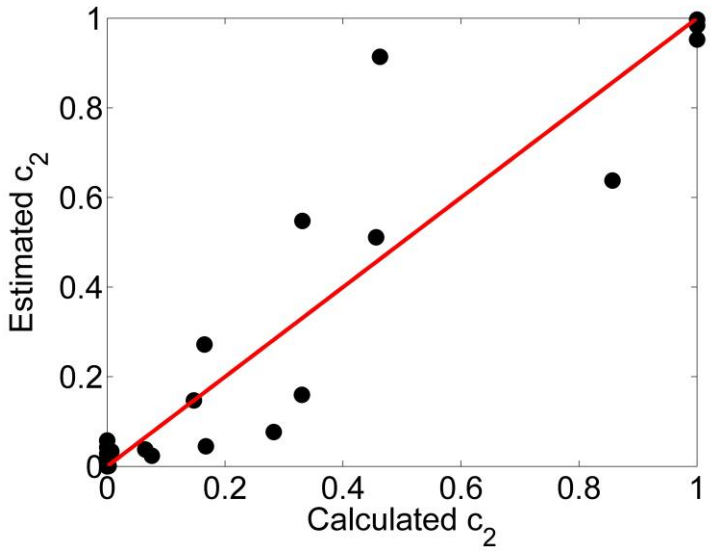

Figure 9.12: Estimated versus calculated values of c_2.

Both of the terms that represented the pore pressure dissipation, $\frac{c_v}{H_{dr}{}^2}$, and the penetration resistance, $(N_1)_{60}$, had a strong influence on c_2. Figure 9.13 shows contours of c_2 versus $\frac{c_v}{H_{dr}{}^2}$ for several values of $(N_1)_{60}$. IM^{eff} was assumed to be I_a, with a post-triggering value of 1 m/s.

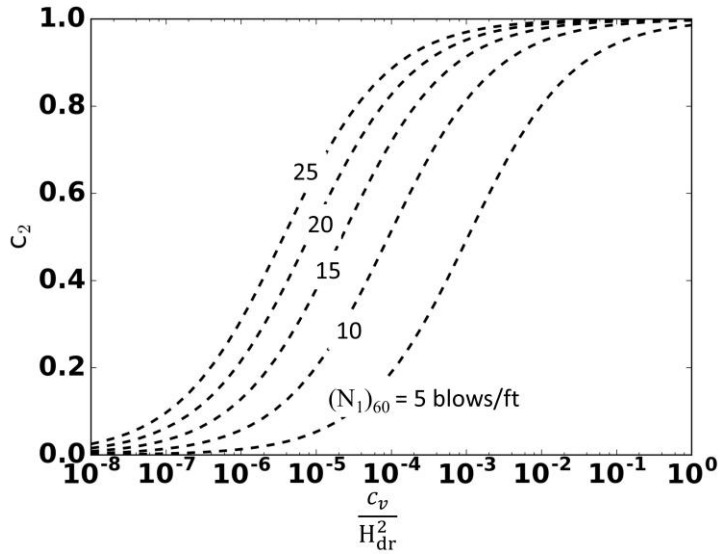

Figure 9.13: Estimated values of c_2 based on $(N_1)_{60}$ and $\frac{c_v}{H_{dr}{}^2}$

The results of the regression analysis can be used to identify situations where the post-triggering secant shear modulus remains constant after liquefaction is triggered or increases due to pore pressure dissipation. In conditions when c_2 is significantly greater than 0, the pore pressure dissipation should be considered as part of the post-triggering frequency content analysis.

9.4 POST-TRIGGERING INTENSITY MEASURES

Intensity measures associated with the effects of liquefaction, IM^{eff}, should capture the appropriate aspects of the ground motion amplitude, duration, and frequency content after liquefaction has been triggered. The frequency content of ground motions shift from high to low frequency once liquefaction is triggered, and the low-frequency components of motions tend to drive deformation. Once liquefaction is triggered, these low-frequency components of motion often have lower acceleration amplitude than the high-frequency motions. As such, intensity measures that are highly sensitive to acceleration amplitude, like PGA_M, do not necessarily capture the low-

frequency, low-amplitude ground motions that can result in large liquefaction-induced deformations. Intensity measures that are based on the integral of acceleration amplitude, like I_a and CAV, are less sensitive to the high-frequency components of motion, but are still sensitive to acceleration amplitude.

Knowledge of the post-triggering modal frequency can be used to tune intensity measures that capture the effects of liquefaction, IM^{eff}. For example, the estimated post-triggering minimum model frequency, $\hat{f}_{\min}$, at IBR014 was 0.40 Hz. The fundamental period of the site, after liquefaction was triggered, was approximately $\frac{1}{\hat{f}_{\min}}$, or 2.5 seconds. Figure 9.14(a) shows a plot of the acceleration time history recorded at IBR014 and Figure 9.14(b) the acceleration time history of a single degree of freedom oscillator (SDOF) with a fundamental period of 2.5 seconds. The number of cycles of each of these motions was calculated and a magnitude scaling factor, MSF, was applied.

$$\text{MSF} = \left(\frac{n}{n_{\text{ref}}}\right)^{-b} \tag{9.27}$$

For this example, n_{ref} = 15 cycles and b = 0.235. n was calculated based on the equivalent number of cycles of loading at 0.65 of the peak value of IM^{eff} for the time histories in both Figure 9.14(a) and (b). Figure 9.14(c) shows normalized intensity measures for magnitude-adjusted PGA and magnitude-adjusted SDOF acceleration.

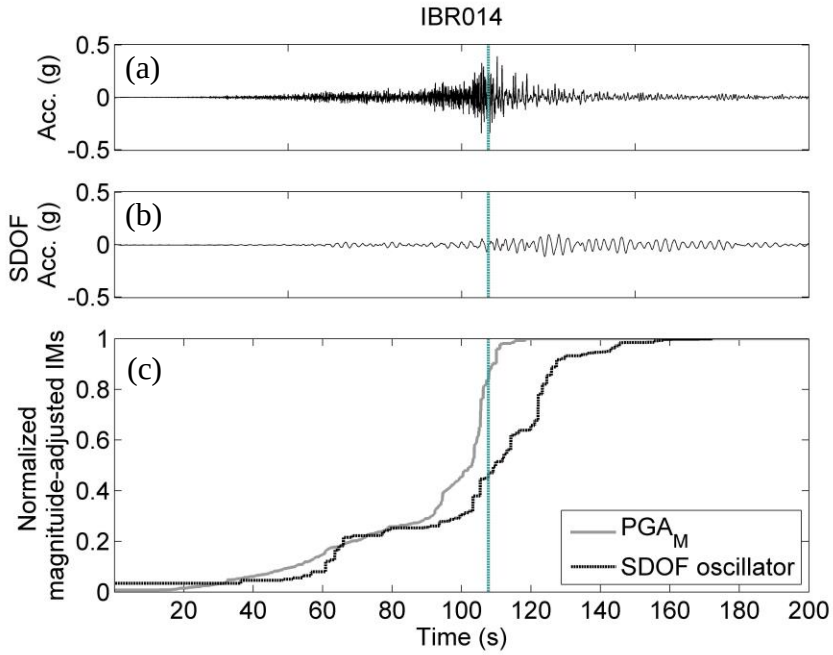

Figure 9.14: Magnitude-adjusted intensity measures. (a) Acceleration time history. (b) Single degree-of-freedom oscillator with a period of 2.5 seconds. (c) Normalized, magnitude-adjusted intensity measures.

Figure 9.13 shows that most of the *IM* associated with high-frequency components of motion, PGA_M, had evolved by the time liquefaction was triggered. However, the normalized *IM* based on a tuned SDOF evolved primarily after liquefaction was triggered. An *IM* tuned to the appropriate frequency should, intuitively, be more closely correlated with the shear stress in a layer of very soft, liquefied soil. Based on the simple mechanics of a shear wave propagating through an elastic layer of soil on a rigid base, the shear strain, γ, in the layer is

$$\gamma = -2\mathrm{A}k\sin(kz)\exp(i\omega t) \tag{9.28}$$

where A is the wave amplitude, $k = \frac{\omega}{v_s}$, z is depth, and $\omega = 2\pi f$. The transient shear strain in equation (9.28) is maximized when $kz = \frac{\pi n}{2}$. At the depth of the liquefied soil, z = H, and

$$f = \frac{v_s n}{4\mathrm{H}} \tag{9.29}$$

when n = 1, the shear strain is maximized at a frequency equal to the characteristic frequency of the layer of liquefied soil, $\hat{f}$. In the case of IBR014, the post-triggering characteristic frequency was 0.40 Hz. The tuned SDOF intensity measure would likely provide a better measure of the

transient shear strains in the layer of liquefied soil than the peak acceleration amplitude of the ground motion. Section 8.4 also indicated that the intensity measures that drive deformation tend to be lower frequency than the intensity measures associated with liquefaction triggering. In addition to capturing the wave mechanics, empirically, the intensity measures that account for the post-triggering low frequency ground motions are better correlated with deformation than high-frequency intensity measures. Three *IM*s were evaluated in detail in this study: PGA_M, I_a, and CAV. These intensity measures have not necessarily been tuned or optimized for liquefaction-induced deformation analysis, but the analyses do indicate that lower-frequency *IM*s are better predictors of liquefaction-induced deformation than higher-frequency *IM*s. Investigation of additional intensity measure other than these three *IM*s is, however, beyond the scope of this study.

9.5 CONCLUSIONS

The available data from twenty-one ground motion recording stations where liquefaction was observed showed a rapid and significant decrease in the frequency content of the ground motions once liquefaction was triggered. Some of these recorded ground motions showed relatively constant modal frequencies after liquefaction was triggered, while other motions showed a gradual increase in the modal frequency, presumably due to pore pressure dissipation.

The changes in modal frequency can be explained by a simple, linear transfer function based on a single layer of soil overlying an elastic base. Analyses using this simple model indicated that, as the stiffness of the liquefiable soil decreased, the modal frequencies of the ground motion approached the characteristic frequency of the soil layer. This observation was supported by analyses with several hundred ground motions convolved through a soil profile with a layer of soft soil overlying a stiff, elastic base. A soil model was developed to estimate the average secant shear modulus of the soil overlying the elastic base. This model was then used to calculate the evolving characteristic frequency of the layer as liquefaction was triggered. The soil model included terms for the minimum shear stiffness after liquefaction was triggered, G_{min}, and the relative increase in stiffness due to pore pressure dissipation, c_2. Based on the case history data, the minimum liquefied soil stiffness, G_{min}, can be explained, with some uncertainty, by the relative density and overburden pressure of the critical layer of liquefied soil, along with the intensity of shaking after liquefaction was triggered. The term for the increased stiffness due to pore pressure dissipation, c_2, can be explained by the coefficient of consolidation, drainage path length and the

relative density of the layer of liquefied soil, along with the post-triggering intensity of shaking. Multi-linear regression was performed to create predictive models for G_{min} and c_2. The resulting equations can be used to estimate an order-of-magnitude post-triggering secant stiffness of the soil, which can then be used to estimate the post-triggering characteristic frequency of the site. Since the characteristic frequency of the site is related to the modal frequency of the ground motion, these results can be used to validate site response analyses or to define intensity measures that capture the appropriate frequency content of ground motions after liquefaction was triggered.

[This page intentionally left blank]

Chapter 10. SUMMARY, CONCLUSIONS, AND RECOMMENDATIONS FOR FUTURE RESEARCH

Methods to evaluate the triggering and effects of liquefaction rely heavily on empirical observations from past earthquakes. The data used to develop these empirical methods include relatively few sites subjected to long-duration ground motions. As such, these methods may not fully capture the fundamental differences between long-duration ground motions, which are often produced by subduction zone earthquakes, and short-duration motions from crustal earthquakes. Because the data sets are so limited, deformation predictions using the current state-of-practice methods include a large amount of uncertainty. These methods also tend to be inaccurate when compared to observations from recent earthquakes, such as the 2011 Christchurch and 2011 Tohoku earthquakes.

The objective of this research was to use case history observations with available laboratory results, theoretical analyses, and numerical analyses to develop insight into the triggering and effects of liquefaction caused by long-duration ground motions. Several new case histories were collected to supplement the available data with respect to long-duration ground motions. Liquefied soils affected the recorded ground motions in these case histories. Observations from these case histories and from numerical simulations inspired a framework to decouple the intensity of shaking that triggers liquefaction from the intensity of shaking that drives deformations. This timing-based framework promises to reduce the uncertainty in liquefaction-induced deformation estimates.

10.1 SUMMARY

Each chapter in this dissertation presented specific aspects of research related to the evaluation of liquefaction hazards from long-duration ground motions. Both triggering and effects of liquefaction are discussed in detail.

Chapter 2 presented a review of the basic concepts of soil liquefaction, including the mechanics of liquefied soils, the dependence of the soil stiffness and strength on effective stress,

and the behavior of soil after liquefaction has been triggered. Laboratory test results indicate that pore pressures are generated during cyclic undrained shearing, which causes the stiffness of the soil to decrease and the shear strain amplitude to increases. Once the effective stress between the soil grains reaches zero, the soil has liquefied. In this state, the stiffness of the soil is extremely low and shear strain amplitudes increase rapidly. Additional cycles of loading after the soil has liquefied cause additional soil fabric degradation, the stiffness of the soil to further decrease, and the shear strain amplitude to increase.

Liquefaction analyses are usually performed by addressing the susceptibility of soil to liquefaction, liquefaction triggering potential, and effects of liquefaction. Each step in this sequence contains a significant amount of uncertainty. This uncertainty is coupled with the lack of empirical observations from long-duration ground motions. Research over the past 40+ years has sought to understand the mechanisms behind liquefaction and reduce the uncertainty associated with the liquefaction. The research summarized in Chapter 2 provided the fundamental building blocks of subsequent analyses in this dissertation.

Chapter 3 presented suites of recorded ground motions that isolated the ground motion duration in different ways. Since current methods for evaluating liquefaction hazards are based primarily on short-duration ground motions, the relevant differences between long- and short-duration ground motions had to be identified using these suites of ground motions. Several factors, including earthquake magnitude, rupture distance, site amplification, and basin effects, are known to affect ground motion duration. Statistical analyses were performed to quantify the correlation between ground motion duration and the intensity measures that are typically associated with liquefaction triggering and post-triggering deformation. The suites of motions compiled for this study showed that commonly used intensity measures for liquefaction triggering analyses capture the duration of ground motions, but are also influenced by aspects of the amplitude and frequency content of the ground motion.

Chapter 4 presented a procedure that uses the Stockwell transform (Stockwell et al., 1996) to identify the time of liquefaction triggering. After triggering, liquefiable soils can become extremely soft and primarily transmit only low-frequency motions to the ground surface. Ground motions affected by liquefied soils show a characteristic shift from being dominated by high frequencies prior to liquefaction to low frequencies afterward. This procedure was validated using data from the Port Island and Wildlife vertical array sites, where the recorded downhole motions

supported the estimated times of liquefaction. Twenty-one case histories where ground motions show the effects of liquefaction are now available. The procedure developed for this study identified the times of triggering in these case histories.

Chapter 5 presented an analytical solution to illustrate the competing effects of pore pressure generation due to shaking and pore pressure dissipation due to drainage. In some cases, pore pressure dissipation and drainage can affect ground motions after liquefaction has been triggered. The effect of pore pressure dissipation could be particularly important during very long-duration ground motions. This solution showed that pore pressure dissipation and drainage during long-duration motions could explain changes in post-triggering frequency content in some of the case histories. The solution underscored the need to consider the potential for pore pressure dissipation or redistribution during shaking, particularly during long-duration ground motions. The solution also provided a basis for comparing the results of numerical simulations, which depend on the constitutive model and user-defined model parameters. Simple recommendations were provided to identify situations where drainage could cause the pore pressure in layers of liquefiable soil to deviate from those estimated using undrained solutions, indicating more rigorous analyses are necessary.

Chapter 6 presented details of the nonlinear, effective stress Cocktail Glass model (Iai et al., 2011), which was designed to account for phase transformation behavior and the large shear strains that can develop in liquefied soils. The complicated interaction between volumetric and shear strain in soils can only be realistically evaluated using numerical methods. The Cocktail Glass model was calibrated to match empirical and semi-empirical observations that are commonly used in U.S.-based practice. The calibrated model captured the rate of pore pressure generation, liquefaction triggering, and shear strain development observed in laboratory tests.

Chapter 7 presented supplemental investigations at three locations in Japan where surficial evidence of liquefaction was observed at strong motion recording stations following the 2011 M_w = 9.0 Tohoku earthquake. Liquefaction at each of these sites occurred in unique conditions, especially since limited liquefaction observations were available from very large magnitude, long-duration earthquakes. A field investigation was performed to collect subsurface data, and the results were analyzed to identify the critical layers of soil that liquefied. The resulting analyses provided data about three new case histories that were subjected to long-duration ground motions.

These case histories were not only unique in that liquefaction was triggered by the very long-duration Tohoku earthquakes, but

- at IBR014 liquefaction was triggered in a deep layer soil,
- at MYG010 dense sand liquefied, and
- at MYG013 gravel liquefied and drained during shaking

The inferred behavior of the recorded ground motions at each site was supported by field and laboratory evidence and the results of one-dimensional site response analyses with FLIP.

Chapter 8 presented a new framework that decoupled the intensity of shaking necessary to trigger liquefaction from the post-triggering intensity of shaking that drives permanent deformations. A key objective of this study was to develop predictive models that reduced the uncertainty in estimating liquefaction-induced deformation. Laboratory data and numerical analyses indicate that deformation amplitudes increased dramatically once liquefaction has been triggered. The numerical analyses also indicated that low-frequency ground motions tended to drive the post-triggering deformations. Conventional procedures do not decouple the post-triggering intensity of shaking from the entire ground motion, rather they base deformation predictions of the total intensity measures, or *IM*s. This type of analysis is referred to as the total *IM* framework. The framework is referred to as the timing-based framework because the time of liquefaction is first identified, and then the remaining intensity of shaking is used to estimate deformations. Chapter 8 also described correlations between triggering and effects *IM*s. With these correlations, the timing-based framework requires no additional information compared to the total *IM* framework, and examples based on numerical analyses showed that it reduced the uncertainty in predicting deformations. Because the ground motion frequency content shifts so dramatically once liquefaction triggers, different intensity measures should be used to analyze triggering and the effects of liquefaction. However, the total *IM* framework inherently relies on the same intensity measures to predict liquefaction triggering and the effects of liquefaction. Different intensity measures can be used to predict liquefaction triggering and post-triggering deformations with the timing-based framework, resulting in an additional reduction of uncertainty.

Chapter 9 presented a case history database with 21 recorded ground motions that contained sufficient subsurface information to predict the post-triggering behavior of soil. As excess pore pressure is generated, the frequency content of the motion shifts towards lower frequencies as the pore pressure increases and the soil fabric degrades. The soil generally becomes

very soft after liquefaction is triggered, but if liquefaction occurs in high permeability layers that can drain as the intensity of shaking decreases, the soil profile can become stiffer over time. The stiffer soil profile can then transmit high-frequency motions through the liquefied soil to the ground surface. Multi-linear regression was performed to develop relationships intended to predict the evolving stiffness and frequency content changes following the triggering of liquefaction. While the uncertainties in post-triggering stiffness and modal frequency of the predicted ground motions are relatively large, these equations provide a basis to (1) estimate the frequencies that could be amplified the most by liquefied soils, and (2) identify intensity measures that are sensitive to the post-triggering frequency content of the ground motions. Such intensity measures would be promising candidates for prediction of liquefaction-induced permanent deformations.

10.2 CONCLUSIONS

The studies performed as part of this dissertation provided unique insight into the effects of long-duration ground motions on liquefaction hazards. Several primary conclusions can be drawn from this study.

- Liquefaction is a complex phenomenon, which is affected by many factors that are difficult to characterize. The difficulty in characterizing the soil properties for liquefaction leads to uncertainty in the prediction of liquefaction triggering and its effects.
- The geotechnical profession's understanding of the mechanics of liquefaction has advanced considerably in recent decades with the aid of modern laboratory testing equipment. Testing has confirmed that the cyclic loading of saturated soils causes pore pressure generation and reduction of effective stresses under both harmonic and transient loading.
- The triggering of liquefaction occurs at relatively low strain levels, where soil retains most of its initial stiffness. Strains are generally low prior to triggering, but laboratory tests show that they increase rapidly after triggering.
- The extreme reduction in effective stress upon the triggering of liquefaction leads to an extensive reduction of stiffness. The stiffness of the soil continues to degrade as the soil fabric is "damaged" by increased strain in the liquefied state.

- The high degree of softening of liquefied soils leads to rapid and significant changes in the frequency content of ground surface motions. Prior to triggering, the soil is relatively stiff and the profile can transmit high-frequency components of motion to the ground surface. After triggering, the soil is much softer and can only transmit low frequencies to the ground surface.
- Time-frequency analyses can be used to characterize the evolving frequency content of ground motions that have been affected by liquefaction. The Stockwell transform spectrograms are particularly useful for identifying the time at which liquefaction is triggered. These spectrograms also highlight the frequencies that dominate the ground motion.
- Since large strains, and hence deformations, develop after triggering, the post-triggering portion of loading drives the deformations. However, identifying the portion of loading that occurs after triggering first requires the ability to determine the time of liquefaction triggering.
- Since the soil profile is highly softened after triggering, the response of liquefied soil should be most sensitive to low-frequency components of motion. Improved prediction of the effects of liquefaction requires identification of intensity measures that reflect the characteristics of these low-frequency components of earthquake ground motions.
- Current procedures for evaluating liquefaction triggering and the effects of liquefaction are empirical in nature, so their reliability is related to characteristics of case history databases upon which they are based. Current liquefaction case history databases are deficient in terms of large magnitude earthquakes and the long-duration ground motions they produce.
- Ground motion duration affects the number of cycles of loading applied to the soil. The level of pore pressure generation depends on the ground motion amplitude and the number of cycles of applied loading. Pore pressures, therefore, increase for a given cycles stress amplitude with increasing ground motion duration.
- Long-duration ground motions are typically associated with large magnitude earthquakes, which are often produced in subduction-zone environments. Large magnitude earthquakes also have low corner frequencies, which makes them particularly rich in the low-frequency

amplitudes that drive post-triggering ground deformations. The long duration of shaking can lead to a liquefied soil profile being subjected to many cycles of low-frequency input motion.

- The long duration of shaking can allow time for significant pore pressure dissipation, particularly in a relatively thin layer of liquefiable soil. Such dissipation can lead to stiffening of the soil and a reduction of post-triggering deformation. Understanding the competing effects of fabric degradation-induced softening and pore pressure dissipation-induced stiffening is important for the development of improved procedures for predicting the effects of liquefaction.
- In the absence of case history data, a well-calibrated and capable constitutive model can be used to gain insight into the mechanical/hydraulic behavior of liquefiable soils under both short- and long-duration loading.
- The calibrated constitutive model can also be used, in the context of site response analysis, to investigate well-instrumented case histories. Nonlinear, effective stress analyses can help confirm the identification of critical layers of liquefiable soil.
- A logical and efficient framework can be developed to make use of timing information in prediction of the effects of liquefaction. The framework makes uses of evolutionary intensity measures for both the triggering and effects of liquefaction.
- An evolutionary version of the peak ground acceleration adjusted for the number of cycles of loading, PGA_M, appears to be an efficient predictor of the triggering of liquefaction. This intensity measure can be used with existing empirical procedures for evaluating liquefaction triggering.
- The evolutionary nature of PGA_M allows determination of the time at which liquefaction would be triggered in a given ground motion. The time of liquefaction can then be used to determine the remaining level of loading (i.e. the shaking after triggering) of a different, post-triggering intensity measure.
- Cumulative absolute velocity and Arias intensity appear, based on numerical analyses, to be good candidates for intensity measures used to predict permanent deformations of liquefiable soil profiles.

- A numerical investigation showed that the timing-based frameworks could produce estimates of permanent deformations that are significantly less uncertain than conventional procedures based on the total value of the intensity measures used for triggering. The reduced uncertainty is due to the use of a low-frequency intensity measure for predicting the effects of liquefaction and the use of only the post-triggering portion of that intensity measures for prediction of ground deformations.

10.3 RECOMMENDATIONS FOR FUTURE RESEARCH

This study relied very heavily on previous liquefaction and ground motion research. General research into liquefaction susceptibility, triggering, and effects of liquefaction should absolutely continue. Likewise, research into the understanding and prediction of ground motions should continue. Several specific studies that would improve the understanding of long-duration ground motions on liquefaction hazards are summarized here.

- Additional investigations should focus on sites where liquefaction was triggered near strong motion recorders. The case history database in Section 9.1 lists many of these sites. Some of these sites only have coarse subsurface information but have detailed records of the ground surface motions. Such case histories provide information that cannot be realistically collected in any other way. Studies of these sites should include,
    1. Additional subsurface investigation with high-quality in-situ and laboratory testing, and
    2. Numerical site response or deformation analyses.
- Additional recording instruments should be installed at locations that are potentially prone to liquefaction. Downhole arrays, such as the Wildlife liquefaction and Port Island arrays are extremely useful.
- Studies should focus on reducing the uncertainty associated with the effects of liquefaction. Such studies should include, but are not necessarily limited to:
    1. Investigations into which intensity measures are best at predicting post-triggering deformations, and
    2. Implementation of large datasets from recent events, such as the 2011 Christchurch or the 2011 Tohoku earthquakes, into rigorous, mechanics-based analyses for predicting liquefaction-induced deformation. These analyses should not be limited

to single events or types of data (i.e. only Lidar) but should incorporate the available datasets.

- The uncertainties in the timing-based framework are subject to the uncertainties in correlation between IM^{trig} and IM^{eff} and the relationship between α_1 and α_2. Limited studies were performed in this dissertation to assess these correlations. Additional research should be performed to define these relationships, particularly for subduction-zone motions, and to identify factors that potentially influence those relationships.
- The timing-based framework requires additional information before it can be implemented for practical purposes. The examples presented in the study required many hundreds to thousands of numerical simulations to develop the curves of post-triggering deformation for just a single site. Existing lateral spreading databases (i.e. Youd et al., 2001; Zhang et al., 2004; etc.) could be implemented into the timing-based framework without significant additional effort.

[This page intentionally left blank]

REFERENCES

Abrahamson, N., Gregor, N., and Addo, K. (2015). BC Hydro ground motion prediction equations for subduction events. *Earthquake Spectra*, preprint.

Aderkristi, A. and Eartherton, M. R. (2015). Time-domain spectral matching of earthquake ground motions using Broyden updating. *Journal of Earthquake Engineering*.

Ambraseys, N. N. (1988). Engineering seismology. *Earthquake Engineering and Structural Dynamics*. **17**(1).

Allen, T. (2015). Geotechnical design manual. Washington Department of Transportation, M 46-03.

Arango, I. (1996), Magnitude scaling factors for soil liquefaction evaluations. *Journal of Geotechnical Engineering*, **122**(11).

Ashford, S. A., Boulanger, R. W., Donahue, J. L., and Stewart, J. P. (2011). Geotechnical quick report on the Kanto plain region during the March 11, 2011 off Pacific coast of Tohoku earthquake, Japan. Geotechnical Extreme Events Reconnaissance (GEER).

Beaty, M. H. and Byrne, P. M. (2011). UBCSAND constitutive model, Version 904aR. Itasca, www.itascacg.com.

Been, K., Jefferies, M. G., and Hachey, J. (1991). The critical state of sands. *Géotechnique*, **41**(3).

Bommer, J. J. and Martinez-Pereira, A. (1999). The effective duration of strong ground motion. *Journal of Earthquake Engineering*, **3**(2).

Booker, J. R., Rahman, M. S., and Seed, H. B. (1976). GADFLEA – A computer program for the analysis of pore pressure generation and dissipation during cyclic or earthquake loading. EERC 76-24. University of California, Berkeley.

Boore, D. M. (1983). Stochastic simulation of high-frequency ground motions based on seismological models of the radiated spectra. *Bulletin of the Seismological Society of America*, **73**(6).

Boore, D. M., Stephens, C. D., and Joyner, W. B. (2002). Comments on baseline correction of digital strong-motion data: examples from the 1999 Hector Mine, California, earthquake. *Bulletin of the Seismological Society of America*, **92**(4).

Boore, D. M., Stewart, J. P., Seyhan, E., Atkinson, G. M. (2014). NGA-West2 equations for predicting PGA, PGV, and 5% damped PGA for shallow crustal earthquakes. *Earthquake Spectra*, **30**(3).

Boulanger, R. W. and Idriss, I. M. (2006). Liquefaction susceptibility criteria for silts and clays. *ASCE Journal of Geotechnical and Geoenvironmental Engineering*, **132**(11).

Boulanger, R. W. and Idriss, I. M. (2014). CPT and SPT based liquefaction triggering procedures. Report No. UCD/CGM-14/01, Center for Geotechnical Modeling, University of California at Davis.

Boulanger, R. W. and Ziotopoulou, K. (2015). PM4SAND (Version 3): A sand plasticity model for earthquake engineering applications. Report No. UCD/CGM-15/01, Center for Geotechnical Modeling, University of California at Davis.

Bowen, H. J., Jacka, M. E., van Ballegooy, S., and Sinclair, T. J. E. (2012), Lateral spreading in the Canterbury earthquakes – Observations and empirical prediction methods. *Proc. 15th World Conference on Earthquake Engineering*, Lisboa.

Bozorgnia, Y., Abrahamson, N. A., Al Atik, L., Achenta, T. D., Atkinson, G. M., Baker, J. W., Baltay, A., Boore, D. M., Campbell, K. W., Chiou, B. S.-J., Darragh, R., Day, S., Donahue, J., Graves, R. W., Gregor, N., Hanks, T., Idriss, I. M., Kamai, R., Kishinda, T., Kottke, A., Mahin, S. A., Shahi, S., Shantz, T., Silva, W., Spudich, P., Stewart, J. P., Watson-Lamprey, J., Woodell, K., and Youngs, R. (2014). NGA-West2 research project. *Earthquake Spectra*, **30**(3).

Bradley, B. A. (2010). A generalized conditional intensity measure approach and holistic ground-motion selection. *Earthquake Engineering and Structural Dynamics*, **39**.

Bray, J.D. and Sancio, R.B. (2006). Assessment of the liquefaction susceptibility of fine-grained soils. *Journal of Geotechnical and Geoenvironmental Engineering*, **132**(9).

Bray, J. D., O'Rourke, T. D., Cubrinovski, M., Zupan, J. D., Jeon, S-S., Taylor, M., Toprak, S., Hughes, M., van Balleooy, S., and Bouzio, D. (2013). Liquefaction impact on critical infrastructure in Christchurch. USGS, Final Technical Report G12AP20034.

Brune, J. N. (1970). Techtonic stress and the spectra of seismic waves from earthquakes. *Journal of Geophysical Research*, **75**.

Campbell, K. W. and Bozorgnia, Y. (2014). NGA-West2 ground motion model for the average horizontal components of PGA, PGV, and 5% damped linear acceleration response spectra. *Earthquake Spectra*, **30**(3).

Campbell, K. W. and Bozorgnia, Y. (2012). A comparison of ground motion prediction equations for Arias intensity and cumulative absolute velocity developed using a consistent database and functional form. *Earthquake Spectra*, **28**(3).

Campbell, K. W. and Bozorgnia, Y. (2010). A ground motion prediction equation for the horizontal component of cumulative absolute velocity (CAV) based on the PEER_NGA strong motion database. *Earthquake Spectra*, **26**(3).

Casagrade, A. (1938). Notes on soil mechanics—First semester. Harvard University. Unpublished.

Cetin, K. O. and Bilge, H. T. (2012). Performance-based assessment of magnitude (duration) scaling factors. *ASCE Journal of Geotechnical and Geoenvironmental Engineering*, **138**(3).

Cetin, K. O., Seed, R. B., Der Kiureghian, A. K., Tokimatsu, K., Harder, L. F., Kayen, R. E., and Moss, R. E. S. (2004). Standard penetration test-based probabilistic and deterministic assessment of seismic soil liquefaction potential. *ASCE Journal of Geotechnical and Geoenvironmental Engineering*, **130**(12).

Choi, Y. (2004). *Probabilistic models for effects of site conditions on strong ground motion*. PhD dissertation, University of California Los Angeles.

Chu, D. B., Stewart, J. P., Youd, T. L., and Chule, B. L. (2006). Liquefaction-induced lateral spreading in near-fault regions during the 1999 Chi-Chi, Taiwan earthquake. *ASCE Journal of Geotechnical and Geoenvironmental Engineering*, **132**(12).

Cox, B. R., Boulanger, R. W., Tokimatsu, K., Wood, C. M., Abe, A., Ashford, S., Donahue, J., Ishihara, K., Kayen, R., Katsumata, K., Kishida, T., Kokusho, T., Mason, H. B., Moss, R., Stewart, J. P., Tohyama, K., and Zekkos, D. (2013). Liquefaction at strong motion stations and in Urayasu City during the 2011 Tohoku-Oki earthquake. *Earthquake Spectra*, **29**(S1).

Cubrinovski, M., Green, R. A., and Wotherspoon, L. (2011). Geotechnical reconnaissance of the 2011 Christchurch, New Zealand earthquake. Geotechnical Extreme Event Reconnaissance (GEER), www.geerassociation.org, GEER-027.

Darendeli, M. (2001). *Development of a New Family of Normalized Modulus Reduction and Material Damping Curves*. Ph. D. Dissertation. University of Texas, Austin.

Dobry, R., Taboada, V., and Liu, L. (1995). Centrifuge modeling of liquefaction effects during earthquakes. *Proc. 1st International Conference on Earthquake Geotechnical Engineering*, Tokyo.

Dawood, H. M., Rodriguez-Marek, A., Bayless, J., Goulet, C., and Thompson, E. (2015). A flatfile for the KiK-net database processed using an automated protocol. *Earthquake Spectra*, preprint.

DeAlba, P., Seed, H. B., and Chan, C. K. (1976). Sand liquefaction in large scale simple shear tests. *Journal of Geotechnical Engineering Division*, ASCE, **102**(GT9).

Dowling, N. E. (1999). *Mechanical behavior of materials: engineering methods for deformation, fracture, and fatigue.* Prentice-Hall, New Jersey.

Dowling, N. E. (1972). Fatigue failure prediction for complicated stress-strain histories. *Journal of Materials*, **7**(1).

DuChateau, P. and Zachmann, D. (1989). *Applied partial differential equations*. Harper & Row, Publishers, Inc. New York.

Electric Power Research Institute (1993). *Guidelines for site specific ground motions*. TR-102293.

Federal Emergency Management Agency (2015), *NEHRP recommended seismic provisions for new buildings and other structures*, FEMA P-1050-1.

FLIP Consortium (2011). *FLIP (ver. 7.2.3).* August 2011.

Frankel, A. (2009). A constant stress-drop model for producing broadband synthetic seismograms: Comparison with the Next Generation Attenuation results. *Bulletin of the Seismological Society of America*, **99**(2A).

Franke, K. W. and Kramer, S. L. (2014), Procedure for Empirical Evaluation of Lateral Spreading Displacement Hazard Curves. *ASCE Journal of Geotechnical and Geoenvironmental Engineering*, **140**(1).

Ganev, T., Yamazaki, F., Ishizaki, H., and Kitazawa, M. (1998). Response analysis of the Higashi-Kobe Bridge and surrounding soil in the 1995 Hyogoken-Nanbu earthquake. *Earthquake Engineering and Structural Dynamics*, **27**.

Gingery, J. R. (2014). *Effects of liquefaction on earthquake ground motions*. PhD Dissertation, University of California, San Diego.

Green, R. A. and Terri, G. A. (2005). Number of equivalent cycles concept for liquefaction evaluations—revisited. *ASCE Journal of Geotechnical and Geoenvironmental Engineering*, **131**(4).

Green, R. A. and Lee, J. (2006). Computation of number of equivalent strain cycles: a theoretical framework. *Geomechanics II*, ASCE.

Hancock, J. and Bommer, J. J. (2004). The effective number of cycles of earthquake ground motion. *Earthquake Engineering Structural Dynamics*,

Hanks, T. C. and Kanamori, H. (1979). A moment magnitude scale. *Journal of Geophysical Research*, **84.**

Hartvigsen, A. J. (2007). *Influence of pore pressure in liquefiable soils on elastic response spectra.* Master's thesis, University of Washington.

Holtz, R.D., Kovacs, W. D., and Sheahan, T. C. (2011). *An Introduction to Geotechnical Engineering*. Second edition, Pearson Education, New Jersey.

Iai, S., Matsunage, W., and Kameoka, T. (1992). Strain space model for cyclic mobility. *Soils and Foundations*, **32**(2).

Iai, S., Morita, T., Kameoka, T., Matsunaga, Y., and Kazuyuki, A. (1995). Response of a dense sand deposit during 1993 Kushiro-Oki earthquake. *Soils and Foundations*, Japanese Society of Soil Mechanics and Foundation Engineering, **35**(1).

Iai, S., Tobita, T., Ozutsumi, O., and Ueda, K. (2011). Dilatancy of granular materials in a strain space multiple mechanism model. *International Journal for Numerical and Analytical Methods in Geomechanics*, **35**.

Idriss, I.M. and Boulanger, R.W. (2004). Semi-empirical procedures for evaluating liquefaction potential during earthquakes. *Proceedings of the 11th International Conference on Soil Dynamics & Earthquake Engineering and the 3rd International Conference on Earthquake Geotechnical Engineering.*

Idriss, I. M. and Boulanger, R. W. (2008). *Soil liquefaction during earthquakes.* Earthquake Engineering Research Institute, MNO-12.

Idriss, I. M. and Boulanger, R. W. (2010). SPT-based liquefaction triggering procedures. Report No. UCD/CGM-10/02, Center for Geotechnical Modeling, University of California at Davis.

Ishihara, K. (1985). Stability of natural deposits during earthquakes. *Proc. 11th International conference on soil mechanics and foundation engineering*, San Francisco.

Ishihara, K. and Yoshimine, M. (1992). Evaluation of settlement in sand deposits following liquefaction during earthquakes. *Soils and Foundations*, **32**(1).

Kawakami, T. Suemasa, N., Hamada, H., Sato, H., and Katada, T. (1994). Experimental study on mechanical properties of liquefied sand. *Proc. 5th US-Japan workshop on earthquake resistant design of lifeline facilities and countermeasures against soil liquefaction*, Technical report NCEER-94-0026, Salt Lake City, USA.

Kayen, R., Moss, R. E. S., Thompson, E. M., Seed, R. B., Cetin, K. O., Der Kiureghian, A., Tanaka, Y., and Tokimatsu, K. (2013). Shear-wave velocity-based probabilistic and deterministic assessment of seismic soil liquefaction potential. *ASCE Journal of Geotechnical and Geoenvironmental Engineering*, **139**.

Kinoshita, S. (2008). Tilt measurement using broadband velocity seismograms. *Bulletin of the Seismological Society of America*, **98**(4).

Kishida, T. and Tsai, C. (2014). Seismic demand of the liquefaction potential with equivalent number of cycles for probabilistic seismic hazard analysis. *ASCE Journal of Geotechnical and Geoenvironmental Engineering*, **140**(3).

Kramer, S. L. and Elgamal, A. W. (2001). Modeling soil liquefaction hazards for performance-based earthquake engineering. PEER Report 2001/13, Pacific Earthquake Engineering Research Center, University of California, Berkeley.

Kramer, S. L. and Greenfield, M. W. (2017). Effects of long-duration motions of soil liquefaction hazards. *Proc. 16th World Conference on Earthquake Engineering*. Santiago, Chile.

Kramer, S.L., Asl, B.A, Özener, P, and Sideras, S.S. (2013). Effects of liquefaction on ground surface motions. *Proc. ICEGE Istanbul 2013-From Case History to Practice, In honour of Prof. Kenji Ishihara*, June 17-19, Boğaziçi University, İstanbul.

Kramer, S. L. (2008). *Evaluation of Liquefaction Hazards in Washington State.* Washington DOT, WA-RD 668.1.

Kramer, S. L. (1996). *Geotechnical Earthquake Engineering*. Prentice-Hall, New Jersey.

Kramer, S.L., Huang, Y., and Greenfield, M. W. (2014). Performance-based assessment of liquefaction hazards. *International conference on Geotechnical Engineering for Disaster mitigation and Rehabilitations*, Kyoto, Japan, Sept. 16-18, 2014.

Kramer, S.L., Mayfield, R., and Mitchell, R. (2005). Ground motion and liquefaction – the loading part of the equation. Unpublished.

Kramer, S. L., Sideras, S. S., and Greenfield, M. W. (2016), The timing of liquefaction and its utility in liquefaction hazard evaluation. *Soil Dynamics and Earthquake Engineering*, **91**.

Khoshnevisan, S., Juang, H., Zhou, Y., and Gong, W. (2015), Probabilistic assessment of liquefaction-induced lateral spreads using CPT – Focusing on the 2010-2011 Canterbury earthquake sequence. *Engineering Geology*, **192**.

Kwan, W. Sideras, S., El Mohtar, C., and Kramer, S. (2014), Cyclic simple shear tests under transient loadings. Network for Earthquake Engineering Simulation (NEES). Data set.

Liu, A. H., Stewart, J. P., Abrahamson, N. A., and Moriwaki, Y. (2001). Equivalent Number of Uniform Stress Cycles for Soil Liquefaction Analysis. *ASCE Journal of Geotechnical and Geoenvironmental Engineering*, **127**(12).

Madariage, R. (1976). Dynamics of an expanding circular fault. *Bulletin of the Seismological Society of America*, **66**.

Marafi, N. A., Eberhard, M. O., Berman, J. W., Wirth, E. A., Frankel, A. D. (2017). Effects of deep basins on structural collapse during large subduction earthquakes. *Earthquake Spectra*, in review.

Maurer, B. W., Green, R. A., and Taylor, O. S. (2015). Moving towards an improved index for assessing liquefaction hazards: Lessons from historical data. *Soils and Foundations*, **55**(4).

Mikami, T., Ichii, K., Uemura, K., and Nishina, H. (2017). Modeling of pre/post-liquefaction strain increase under cyclic loading. Unpublished.

Murphy, K. (2012). *Machine Learning: A probabilistic perspective*. Massachusetts Institute of Technology.

National Academy of Science, Engineering, and Medicine. (2016). State of the art and practice in the assessment of earthquake-induced soil liquefaction and its consequences. *National Academies of Sciences, Engineering, and Medicine*. Prepublication.

National Information Service for Earthquake Engineering (2016). Pacific Earthquake Engineering Research Center, University of California, Berkeley. Accessed May 23, 2016.

Noguchi, S. and Fumumura, T. (2011). The rupture process of the earthquake found directly on the distribution of the seismic ground motion. outreach.eri.u-tokyo.ac.jp/eqvolc/201103_tohoku/end

Olson, S. M., and Stark, T. D. (2002). Liquefied strength ratio from liquefaction flow failure case histories. *Canadian Geotechnical Journal*, **39.**

Saragoni, G. R. and Hart, G. C. (1973). Simulation of artificial earthquakes. *Earthquake Engineering and Structural Dynamics*, **2**.

Sato, Y., Ichii, K., Hoshino, Y., Sato, Y., Miyata, M., Morita, T., and Iai, S. (1998). Strong-motion earthquake records on the 1995 Hyogo-Ken Nanbu earthquake in port areas. Technical Note of the Port and Harbour, research Institute Ministry of Transportation, Japan, No. 907.

Schofield, A., and Wroth, P. (1968). *Critical state soil mechanics*. Cambridge University.

Schwartz, F. W., and Zhang, J. (2003). *Fundamentals of Groundwater*. John Wiley & Sons.

Seed, H. B. and Idriss, I. M. (1971). Simplified procedure for evaluating soil liquefaction potential. *Journal of the Soil Mechanics and Foundations Division*, ASCE **93**(3).

Seed, H. B., Idriss, I. M., and Arango, I. (1983). Evaluation of Liquefaction Potential Using Field Performance Data. *ASCE Journal of Geotechnical Engineering*, **109**(3).

Seed, H. B., Idriss, I. M., Makdisi, F., and Banerjee, N. (1975). Representation of irregular stress time histories by equivalent uniform stress series in liquefaction analysis. Earthquake Engineering Research Center, EERC 75-29.

Seed, H. B., Tokimatsu, K., Harder, L. F., and Chung, R. (1985). Influence of SPT procedures in soil liquefaction resistance evaluations. *Journal of Geotechnical Engineering*, ASCE, **111**(12).

Sideras, S. S. and Kramer, S. L. (2012). Potential implications of long duration ground motions of the response of liquefiable soil deposits. *Joint proceedings of the 9th International Conference of Urban Earthquake Engineering and the 4th Asia Conference on Earthquake Engineering*. Tokyo Institute of Technology.

Stewart, J. P., Kramer, S. L., Kwak, D. Y., Greenfield, M. W., Kayen, R. E., Tokimatsu, J., Bray, D., Beyzaei, C. Z., Cubrinovski, M., Sekiguchi, T., Nakai, S., and Bozorgnia, Y. (2016). PEER-NGL project: open source global database and model development for the Next-Generation of Liquefaction Assessment Procedures. *Soil Dynamics and Earthquake Engineering*.

Stockwell, R. G., Mansinha, L., and Lowe., R. P. (1996). Localization of the complex spectrum: The S Transform. *IEEE Trans. Signal Processing.* **44**(4).

Terzaghi, K. (1943). *Theoretical soil mechanics*, John Wiley and Sons.

Terzaghi, K. and Peck, R. B. (1948). *Soil mechanics in engineering practice*. 1st edition. John Wiley and Sons, New York.

Toro, G. R. (1995). Probabilistic models of site velocity profiles for generic and site-specific ground-motion amplification studies. Brookhaven Nation Laboratory, Upton, NY. Second Draft.

Unjoh, S., Kaneko, M., Kataoka, S., Nagaya, K., and Matsuoka, K. (2012). Effect of earthquake ground motions on soil liquefaction. *Soils and Foundations*, **52**(5).

Youd, T L. (1998). *Screening Guide for Rapid Assessment of Liquefaction Hazard at Highway Bridge Sites*, Technical Report MCEER-98-0005, Multidisciplinary Center for Earthquake Engineering Research, Buffalo, NY.

Youd, T. L. and Idriss, I. M. (2001). Liquefaction Resistance of Soils: Summary Report from the 1996 NCEER and 1998 NCEER/NSF Workshop on Evaluation of Liquefaction Resistance of Soils. *ASCE Journal of Geotechnical and Geoenvironmental Engineering*, **127**(4).

Wair, B. R., DeJong, J. T., Shantz, T. (2012). Guidelines for estimation of shear wave velocity profiles. Pacific Earthquake Engineering Research Center, PEER 2012/08.

Wirth, E. A., Frankel, A. D., and Marafi, N. A. (2017). Synthetic ground motions from an M_w = 9.0 Cascadia Subduction Zone Rupture. Pre-release.

Zhang, G., Robertson, P. K., and Brachman R. W. I. (2004). Estimating liquefaction-induced lateral displacements using the standard penetration test or cone penetration tests. *ASCE Journal of Geotechnical and Geoenvironmental Engineering*, **130**(8).

APPENDIX A: BORING AND PROBE LOGS

NGL Project, PEER Center

Boring Network	UW Investigations	Operator	Tokyo Soil Research, LTD
TSN	IBR014 B−1	Field Log by	Mike Greenfield / Hiroshio Suzuki
Location	Tsuchiura, Ibaraki	Drilling Equipment	Geoprobe 6610DT
Latitude	36.0728	SPT system	Cathead and rope with auto trip
Longitude	140.1948	Drilling Method	Mud rotary
GWT (m)	1.3	Hammer Type	140 lb
Elevation (m)	12.4	Hole Diameter (cm)	15
Borehole Depth (m)	30.45	Date	9/24/2015
Notes			

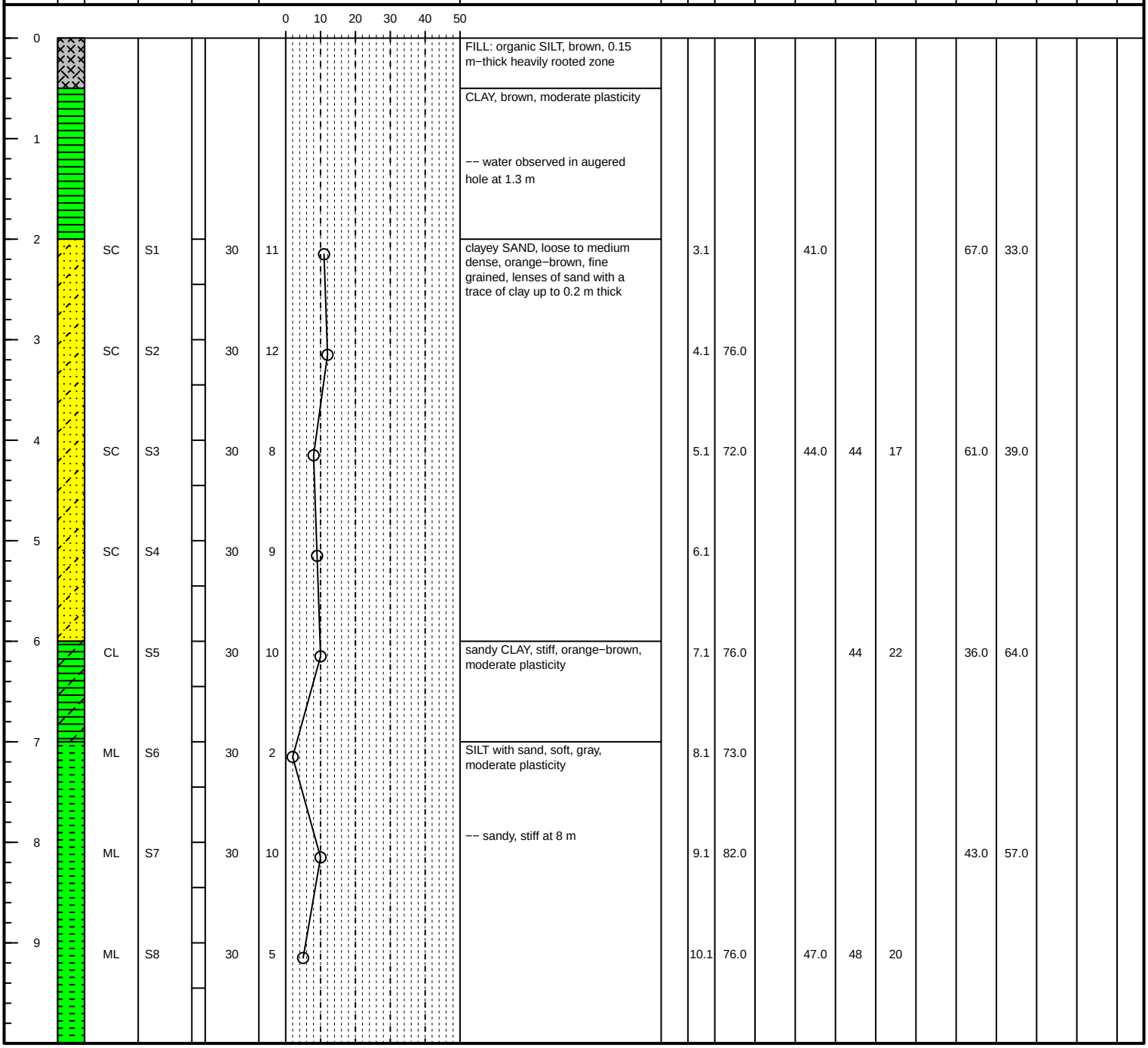

Depth (m)	Lithology	Soil Classification	Sample Type and No. (P:SPT, T:Tube)	Penetrate Depth (cm)	SPT Blows	Description	Casing Depth (m)	Rod Length (m)	Energy Ratio (%)	Specific Gravity	Water Content (%)	Liquid Limit	Plasticity Index	%gravel	%sand (2 mm − 75 µm)	%fines < 75 µm	D50 (mm)	D10 (mm)	Remark Mark
0						FILL: organic SILT, brown, 0.15 m−thick heavily rooted zone													
1						CLAY, brown, moderate plasticity −− water observed in augered hole at 1.3 m													
2		SC	S1	30	11	clayey SAND, loose to medium dense, orange−brown, fine grained, lenses of sand with a trace of clay up to 0.2 m thick		3.1			41.0				67.0	33.0			
3		SC	S2	30	12			4.1	76.0										
4		SC	S3	30	8			5.1	72.0		44.0	44	17		61.0	39.0			
5		SC	S4	30	9			6.1											
6		CL	S5	30	10	sandy CLAY, stiff, orange−brown, moderate plasticity		7.1	76.0			44	22		36.0	64.0			
7		ML	S6	30	2	SILT with sand, soft, gray, moderate plasticity		8.1	73.0										
8		ML	S7	30	10	−− sandy, stiff at 8 m		9.1	82.0						43.0	57.0			
9		ML	S8	30	5			10.1	76.0		47.0	48	20						

Footnote

Lithology Legend

- Fill soil
- Organic soil
- Gravel w/o fines
- Gravel w/ fines
- Sand w/o fines
- Sand w/ fines
- Silt w/o coarse
- Silt w/ coarse
- Clay w/o coarse
- Clay w/ coarse

NGL Project, PEER Center				
Boring Network	UW Investigations	Operator	Tokyo Soil Research, LTD
TSN	IBR014 B−1	Field Log by	Mike Greenfield / Hiroshio Suzuki
Location	Tsuchiura, Ibaraki	Drilling Equipment	Geoprobe 6610DT
Latitude	36.0728	SPT system	Cathead and rope with auto trip
Longitude	140.1948	Drilling Method	Mud rotary
GWT (m)	1.3	Hammer Type	140 lb
Elevation (m)	12.4	Hole Diameter (cm)	15
Borehole Depth (m)	30.45	Date	9/24/2015
Notes			

Depth (m)	Lithology	Soil Classification	Sample Type and No. (P:SPT, T:Tube)	Penetrate Depth (cm)	SPT Blows	Description	Casing Depth (m)	Rod Length (m)	Energy Ratio (%)	Specific Gravity	Water Content (%)	Liquid Limit	Plasticity Index	%gravel	%sand (2 mm – 75 µm)	%fines < 75 µm	D50 (mm)	D10 (mm)	Remark Mark
10		ML	S9	30	6			11.1	77.0		47.0								
11		ML	S10	30	6			12.1											
12		ML	S11	30	9			13.1											
13		ML	S12	30	6			14.1							23.0	77.0			
14		ML	S13	30	8			15.1											
15		ML	S14	30	10			16.1							22.0	78.0			
16		ML	S15	30	14			17.1											
17		SW	S16	30	20	SAND with silt, medium dense, gray, fine grained		18.1											
18		SW	S17	30	20			19.1											
19		ML	S18	30	13	sandy SILT, medium dense, gray, moderate plasticity		20.1			39.0				41.0	59.0			

SPT Blows axis: 0, 10, 20, 30, 40, 50

Footnote

Lithology Legend

- Fill soil
- Organic soil
- Gravel w/o fines
- Gravel w/ fines
- Sand w/o fines
- Sand w/ fines
- Silt w/o coarse
- Silt w/ coarse
- Clay w/o coarse
- Clay w/ coarse

NGL Project, PEER Center

Boring Network	UW Investigations	Operator	Tokyo Soil Research, LTD
TSN	IBR014 B−1	Field Log by	Mike Greenfield / Hiroshio Suzuki
Location	Tsuchiura, Ibaraki	Drilling Equipment	Geoprobe 6610DT
Latitude	36.0728	SPT system	Cathead and rope with auto trip
Longitude	140.1948	Drilling Method	Mud rotary
GWT (m)	1.3	Hammer Type	140 lb
Elevation (m)	12.4	Hole Diameter (cm)	15
Borehole Depth (m)	30.45	Date	9/24/2015
Notes			

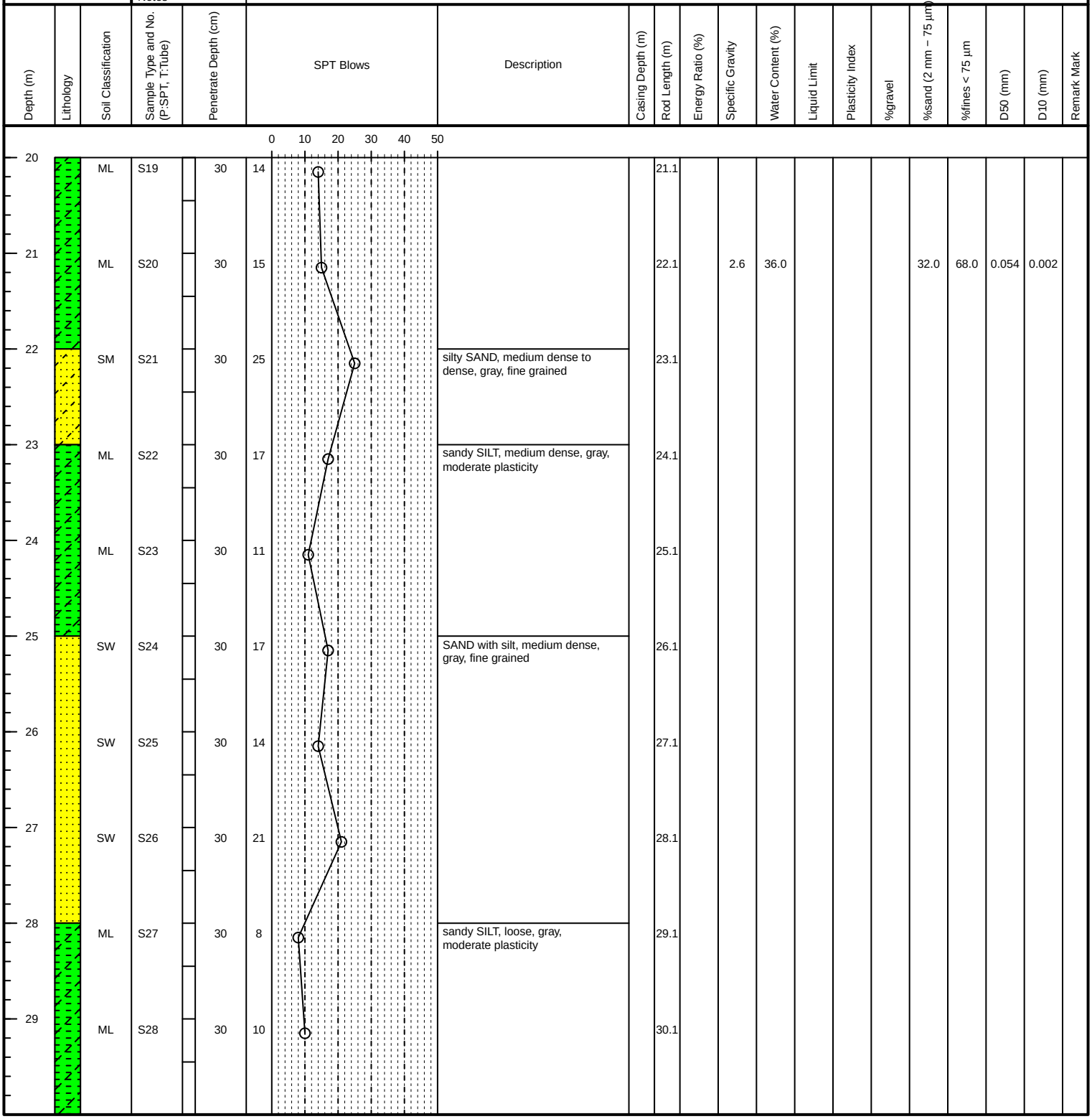

Depth (m)	Lithology	Soil Classification	Sample Type and No. (P:SPT, T:Tube)	Penetrate Depth (cm)	SPT Blows	Description	Casing Depth (m)	Rod Length (m)	Energy Ratio (%)	Specific Gravity	Water Content (%)	Liquid Limit	Plasticity Index	%gravel	%sand (2 mm – 75 µm)	%fines < 75 µm	D50 (mm)	D10 (mm)	Remark Mark
20		ML	S19	30	14			21.1											
21		ML	S20	30	15			22.1		2.6	36.0				32.0	68.0	0.054	0.002	
22		SM	S21	30	25	silty SAND, medium dense to dense, gray, fine grained		23.1											
23		ML	S22	30	17	sandy SILT, medium dense, gray, moderate plasticity		24.1											
24		ML	S23	30	11			25.1											
25		SW	S24	30	17	SAND with silt, medium dense, gray, fine grained		26.1											
26		SW	S25	30	14			27.1											
27		SW	S26	30	21			28.1											
28		ML	S27	30	8	sandy SILT, loose, gray, moderate plasticity		29.1											
29		ML	S28	30	10			30.1											

Footnote

Lithology Legend

- Fill soil
- Organic soil
- Gravel w/o fines
- Gravel w/ fines
- Sand w/o fines
- Sand w/ fines
- Silt w/o coarse
- Silt w/ coarse
- Clay w/o coarse
- Clay w/ coarse

NGL Project, PEER Center				
	Boring Network	UW Investigations	Operator	Tokyo Soil Research, LTD
	TSN	IBR014 B−1	Field Log by	Mike Greenfield / Hiroshio Suzuki
	Location	Tsuchiura, Ibaraki	Drilling Equipment	Geoprobe 6610DT
	Latitude	36.0728	SPT system	Cathead and rope with auto trip
	Longitude	140.1948	Drilling Method	Mud rotary
	GWT (m)	1.3	Hammer Type	140 lb
	Elevation (m)	12.4	Hole Diameter (cm)	15
	Borehole Depth (m)	30.45	Date	9/24/2015
	Notes			

Depth (m)	Lithology	Soil Classification	Sample Type and No. (P:SPT, T:Tube)	Penetrate Depth (cm)	SPT Blows	Description	Casing Depth (m)	Rod Length (m)	Energy Ratio (%)	Specific Gravity	Water Content (%)	Liquid Limit	Plasticity Index	%gravel	%sand (2 mm – 75 µm)	%fines < 75 µm	D50 (mm)	D10 (mm)	Remark Mark
30		ML	S29	30	8	0 10 20 30 40 50		31.1											

Footnote

Lithology Legend

- Fill soil
- Organic soil
- Gravel w/o fines
- Gravel w/ fines
- Sand w/o fines
- Sand w/ fines
- Silt w/o coarse
- Silt w/ coarse
- Clay w/o coarse
- Clay w/ coarse

NGL Project, PEER Center

Project Name	UW Investigations	Elevation (m)*	12.4
TSN	IBR014 P−1	Sounding Depth (m)	27.2
Location	Tsuchiura, Ibaraki	Operator	Tokyo Soil Research, LTD
Latitude	36.0728	CPT system	10 cm^2 cone
Longitude	140.1948	Sounding Equipment	Geoprobe 6610DT
		Sounding Method	
GWT (m)	1.3	Date	9/24/2015

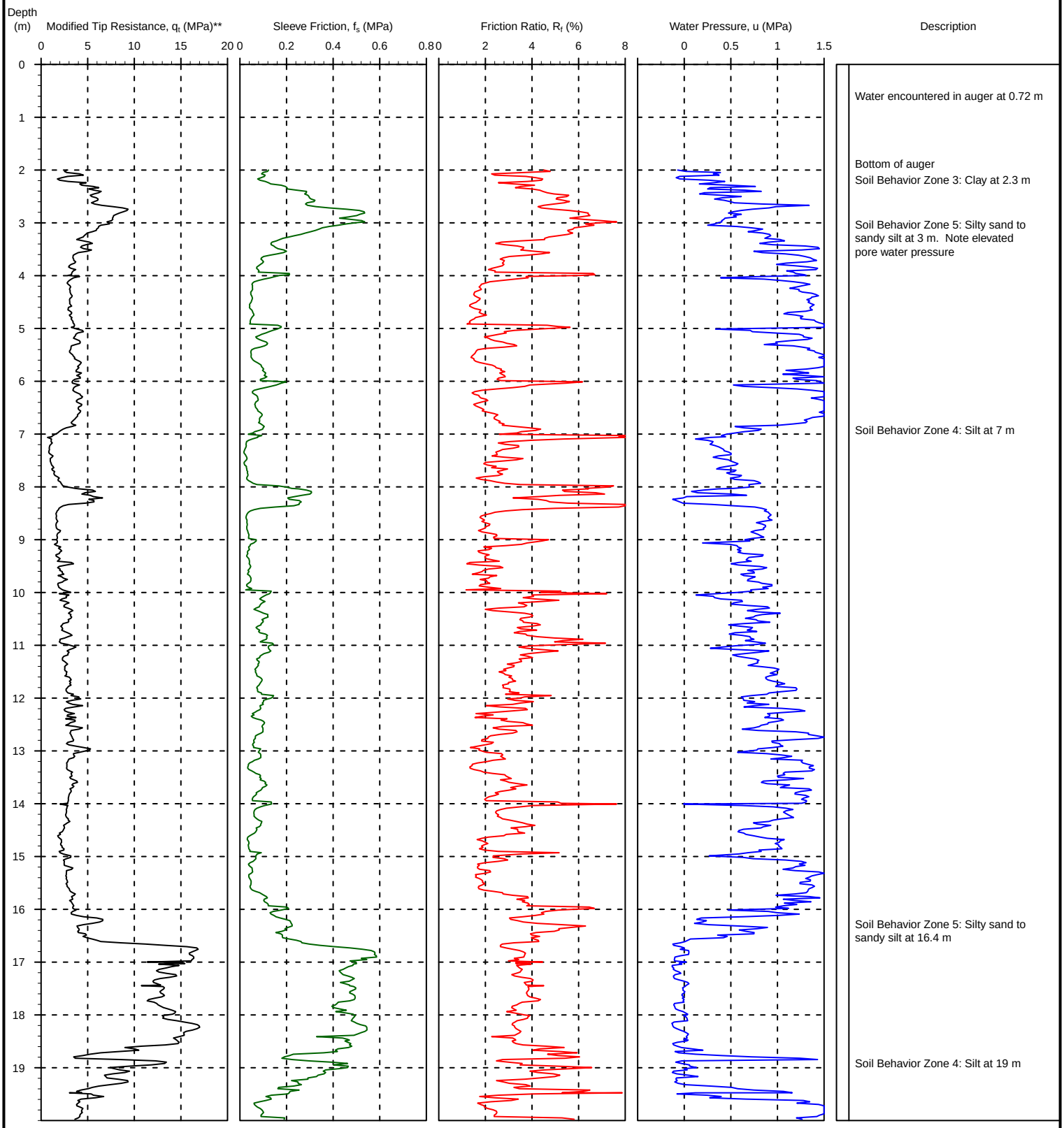

CPT Soil Classification based on Roberstson (1990)

NGL Project, PEER Center				
	Project Name	UW Investigations	Elevation (m)*	12.4
	TSN	IBR014 P−1	Sounding Depth (m)	27.2
	Location	Tsuchiura, Ibaraki	Operator	Tokyo Soil Research, LTD
	Latitude	36.0728	CPT system	10 cm^2 cone
	Longitude	140.1948	Sounding Equipment	Geoprobe 6610DT
			Sounding Method	
	GWT (m)	1.3	Date	9/24/2015

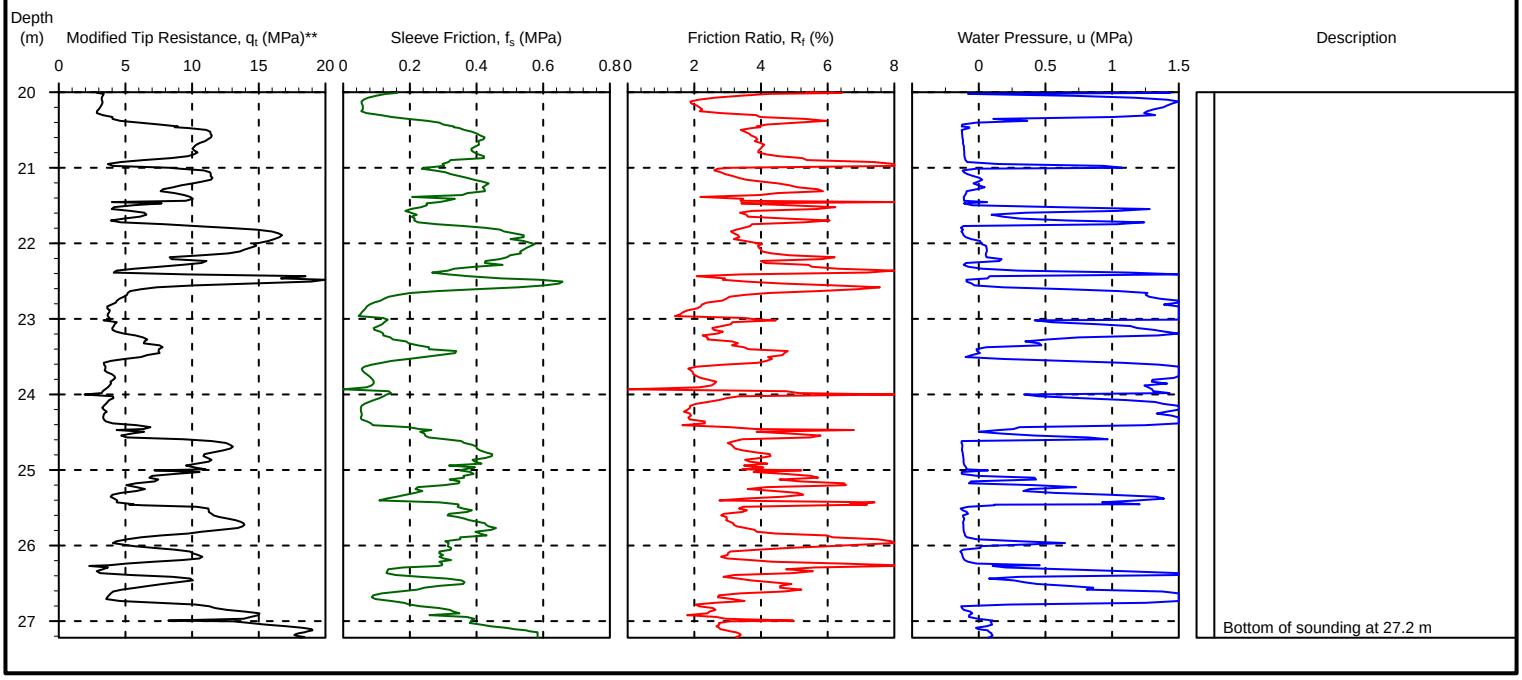

CPT Soil Classification based on Roberstson (1990)

NGL Project, PEER Center				
	Project Name	UW Investigations	Elevation (m)*	4
	TSN	MYG010 P−1	Sounding Depth (m)	8.0
	Location	Ishinomaki	Operator	Tokyo Soil Research, LTD
	Latitude	38.428	CPT system	10 cm^2 cone
	Longitude	141.281	Sounding Equipment	
			Sounding Method	
	GWT (m)	2.07	Date	10/17/2015

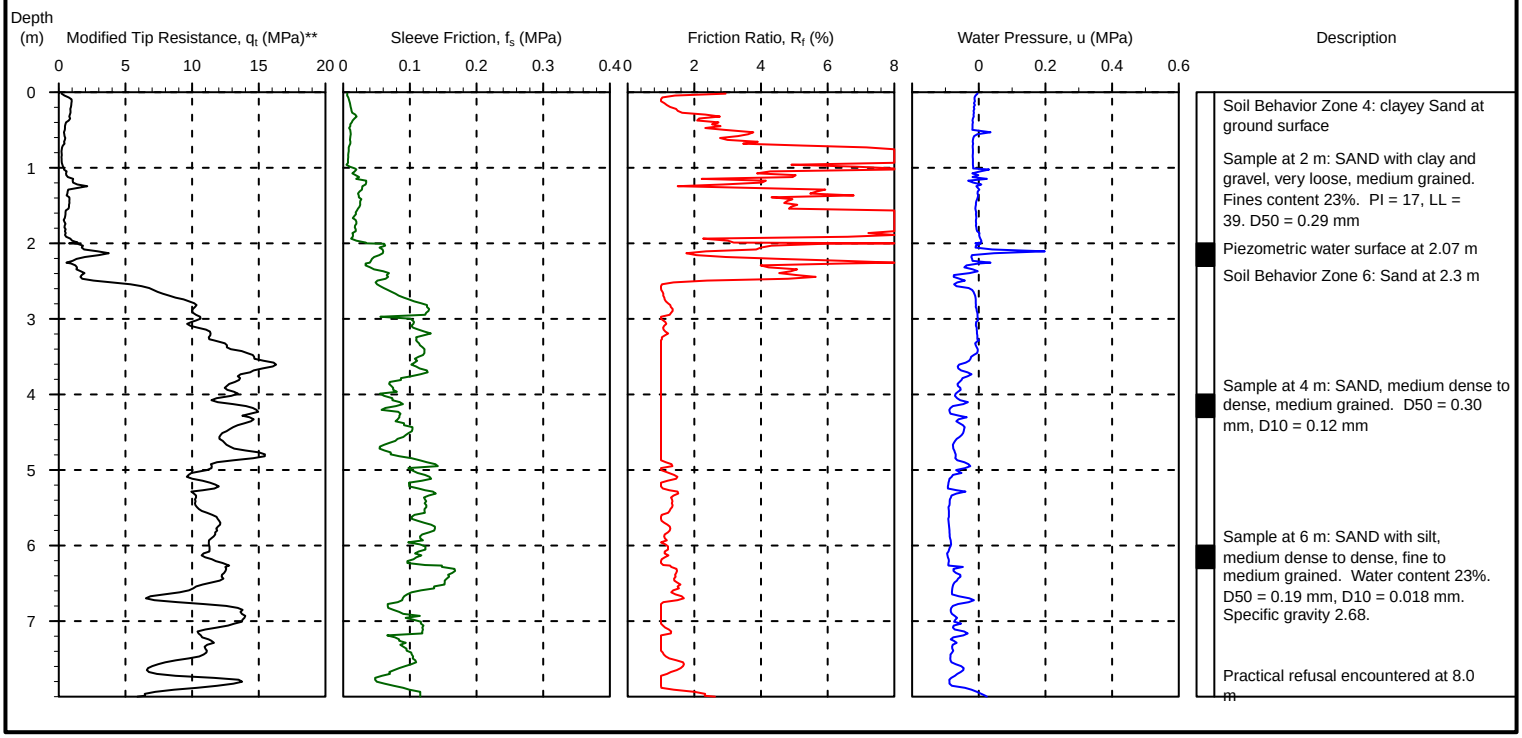

CPT Soil Classification based on Roberstson (1990)

NGL Project, PEER Center

Boring Network	UW Investigations	Operator	Tokyo Soil Research, LTD
TSN	MYG013	Field Log by	Hiroshio Suzuki
Location	Sendai	Drilling Equipment	Geoprobe 6610DT
Latitude	38.266	SPT system	Cathead and rope with auto trip
Longitude	140.929	Drilling Method	Mud rotary
GWT (m)	0.9	Hammer Type	140 lb
Elevation (m)	4	Hole Diameter (cm)	15
Borehole Depth (m)	8.31	Date	10/15/2015
Notes			

Depth (m)	Lithology	Soil Classification	Sample Type and No. (P:SPT, T:Tube)	Penetrate Depth (cm)	SPT Blows	Description	Casing Depth (m)	Rod Length (m)	Energy Ratio (%)	Specific Gravity	Water Content (%)	Liquid Limit	Plasticity Index	%gravel	%sand (2 mm – 75 µm)	%fines < 75 µm	D50 (mm)	D10 (mm)	Remark Mark
0					0 10 20 30 40 50	FILL: SAND with gravel, scattered concrete debris													
1						ORGANIC SILT and PEAT, very soft, high plasticity													
2		OL	S1	30	1			3.1											
3		CH	S2	30	0	sandy CLAY, very soft, high plasticity, trace organics		4.1				61	32		21.0	79.0			
4		CH	S3	30	15	–– stiff below 4 m		5.1	83.0	2.6					39.0	61.0	0.032		
5		GW	S4	30	15	Gravel with sand and silt, sub−angular, medium dense		6.1	76.0	2.6				65.0	23.0	12.0	5.400	0.046	
6		GW	S5	30	50	–– very dense below 6 m		7.1	83.0										
7		GW	S6	30	50			8.1											
8		GW	S7	30	50			9.1											

Footnote

Lithology Legend

- Fill soil
- Organic soil
- Gravel w/o fines
- Gravel w/ fines
- Sand w/o fines
- Sand w/ fines
- Silt w/o coarse
- Silt w/ coarse
- Clay w/o coarse
- Clay w/ coarse

NGL Project, PEER Center				
	Project Name	UW Investigations	Elevation (m)	4
	TSN	MYG013 P−1	Sounding Depth (m)	5.5
	Location	Sendai	Operator	Tokyo Soil Research, LTD
	Latitude	38.266	CPT system	10 cm^2 cone
	Longitude	140.929	Sounding Equipment	Geoprobe 6610DT
			Sounding Method	
	GWT (m)	0.88	Date	10/17/2015

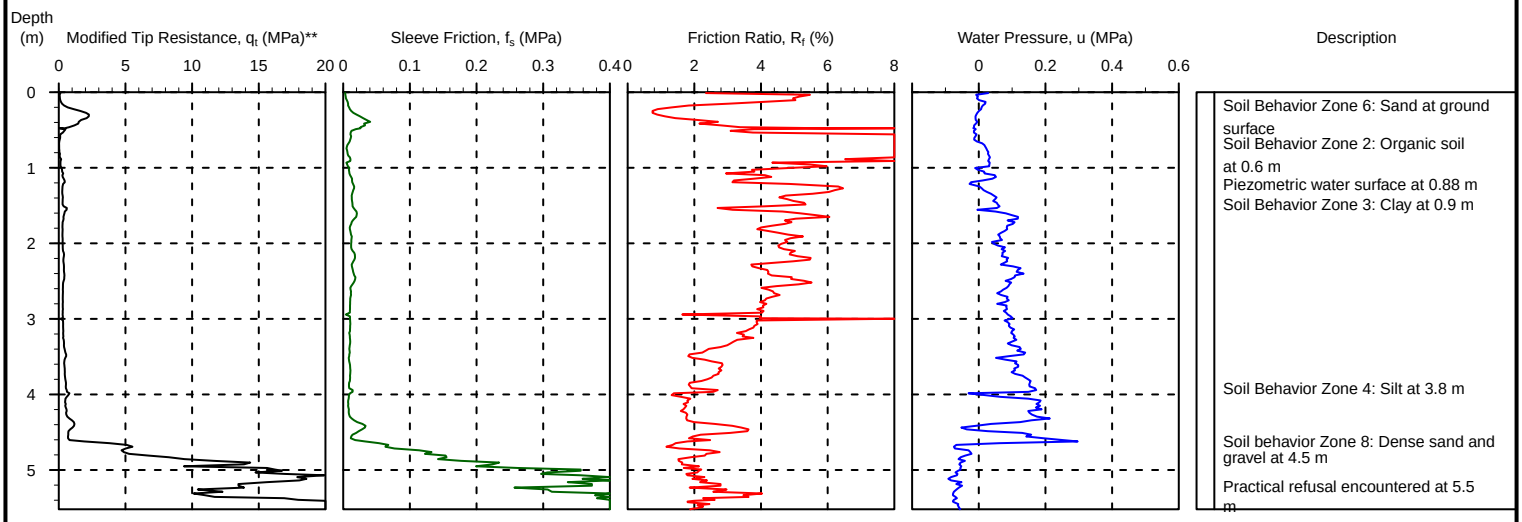

CPT Soil Classification based on Roberstson (1990)

APPENDIX B: TIME-FREQUENCY ANALYSIS OF SELECTED CASE HISTORIES

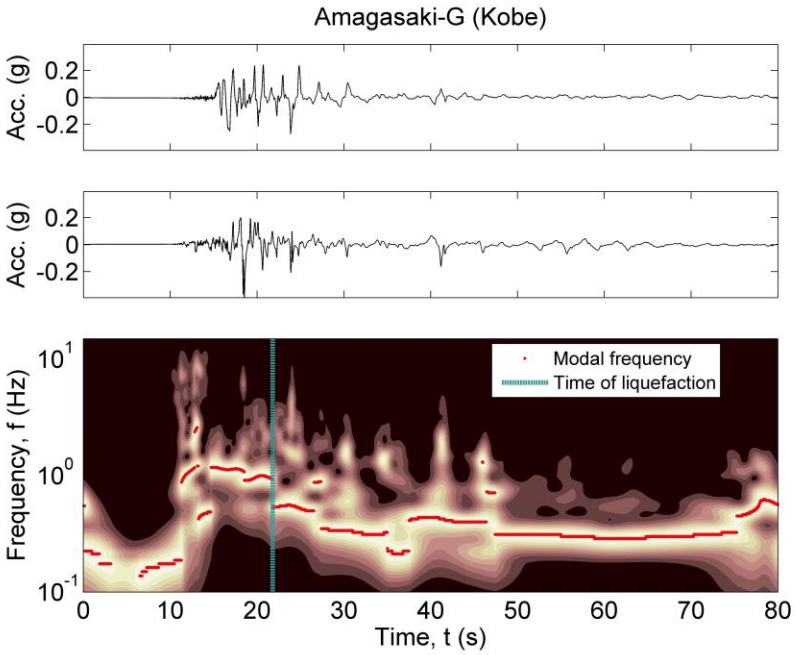

Figure B.1: Time of liquefaction at Amagasaki-G

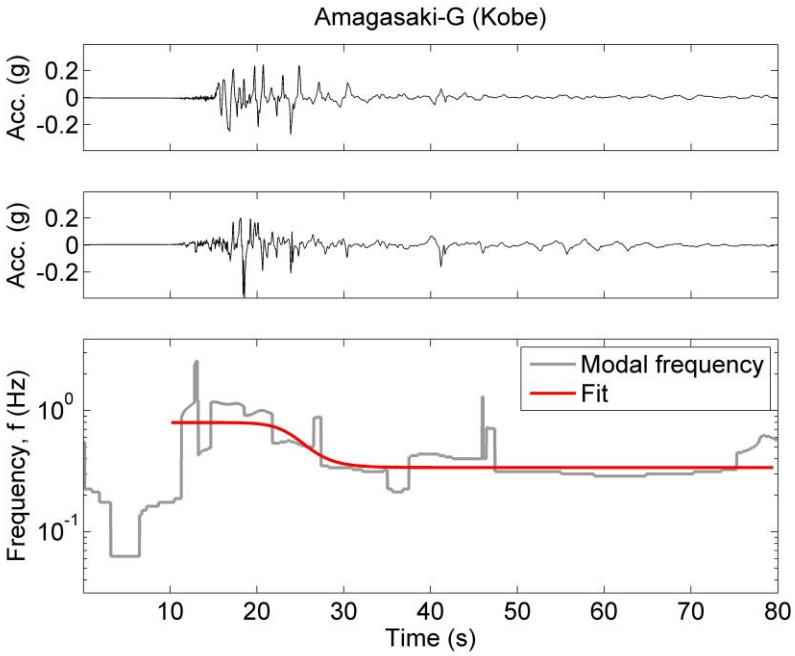

Figure B.2: Shift in modal frequency at Amagasaki-G

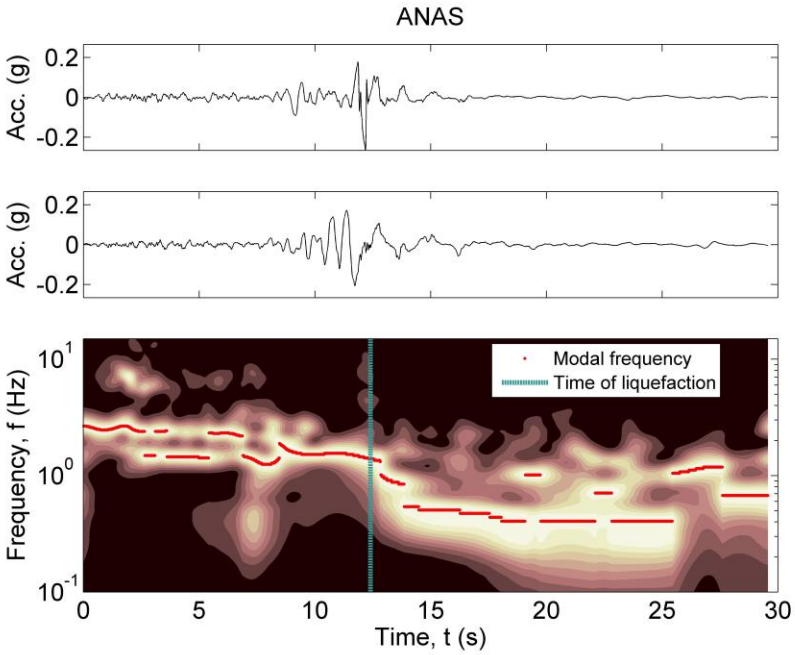

Figure B.3: Time of liquefaction at ANAS

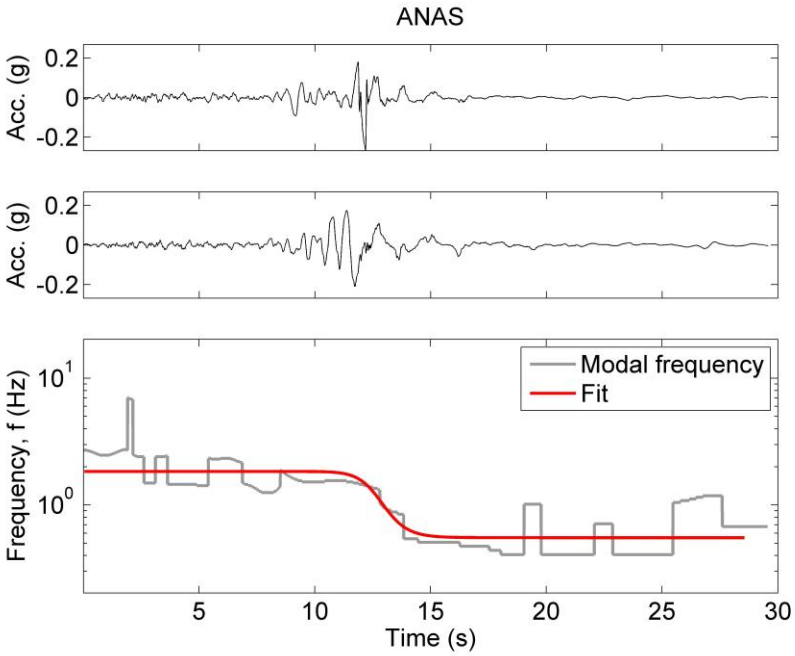

Figure B.4: Shift in modal frequency at ANAS

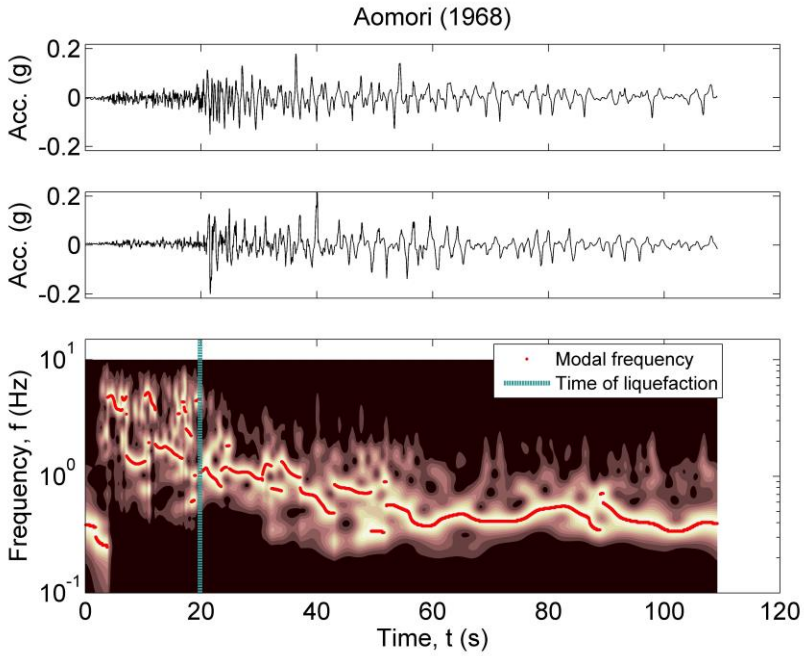

Figure B.5: Time of liquefaction at Aomori (1968)

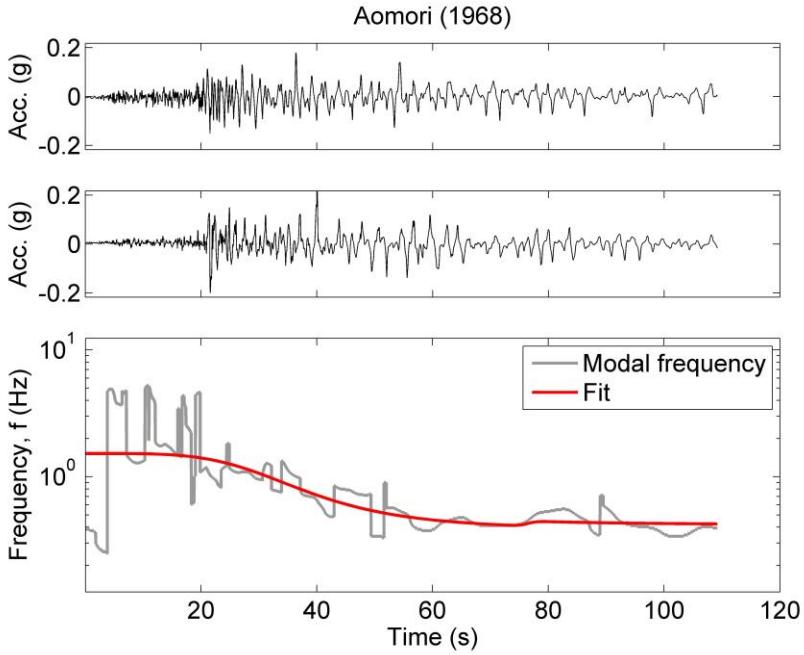

Figure B.6: Shift in modal frequency at Aomori (1968)

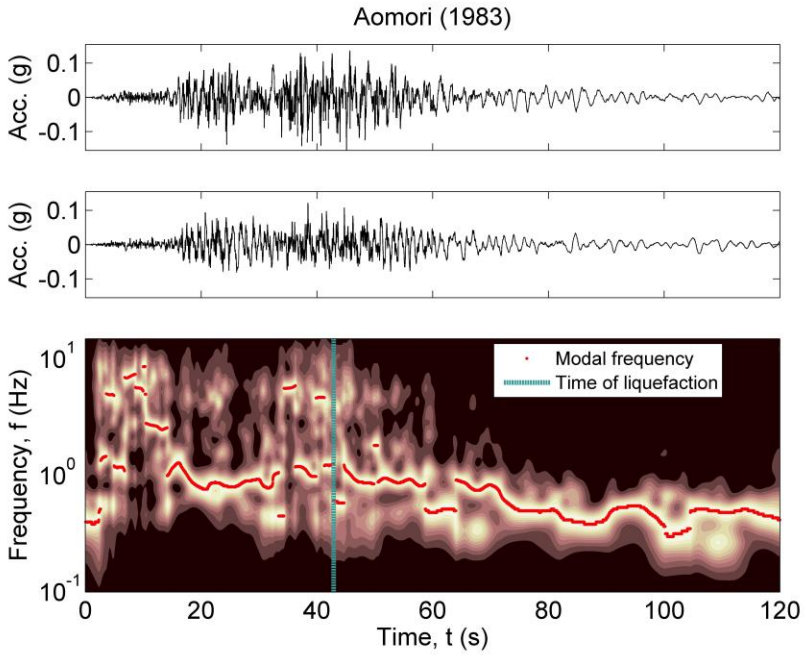

Figure B.7: Time of liquefaction at Aomori (1983)

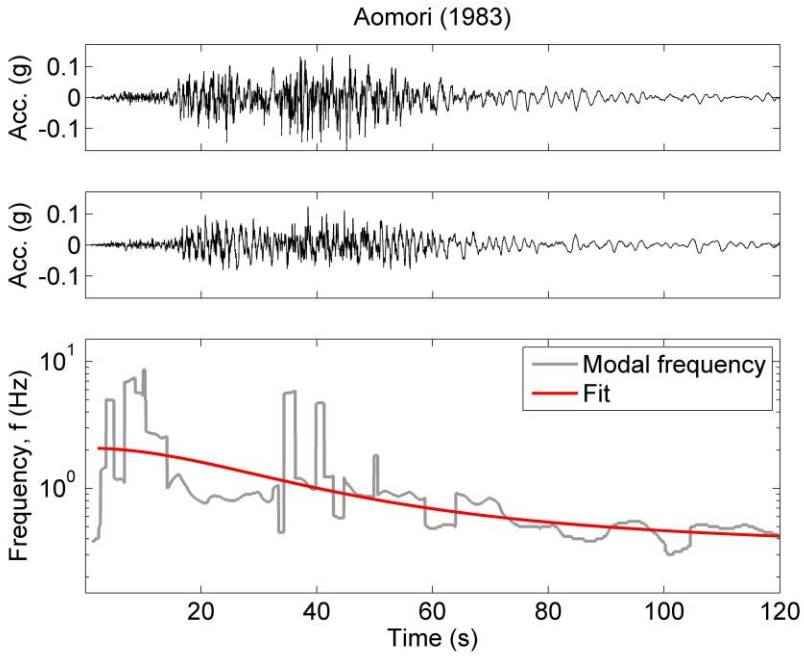

Figure B.8: Shift in modal frequency at Aomori (1983)

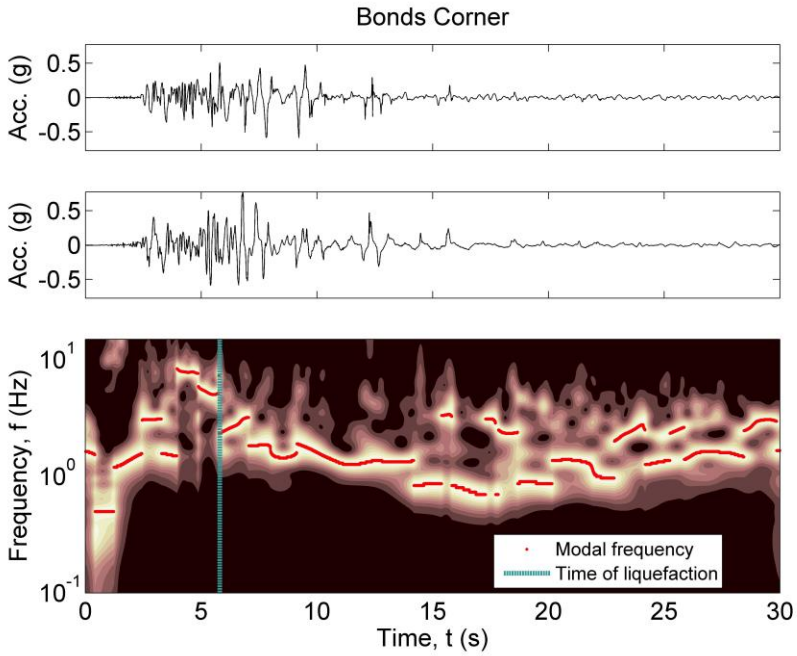

Figure B.9: Time of liquefaction at Bonds Corner

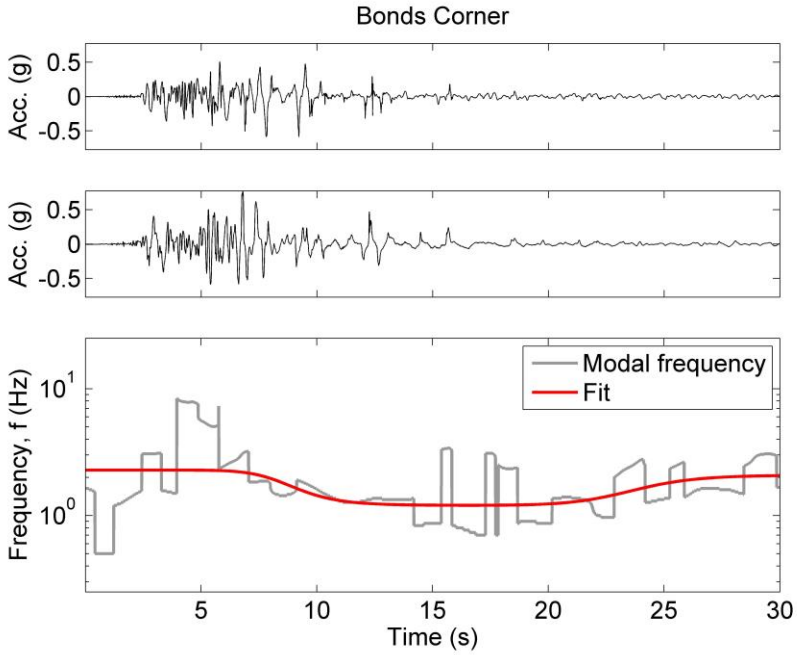

Figure B.10: Shift in modal frequency at Bonds Corner

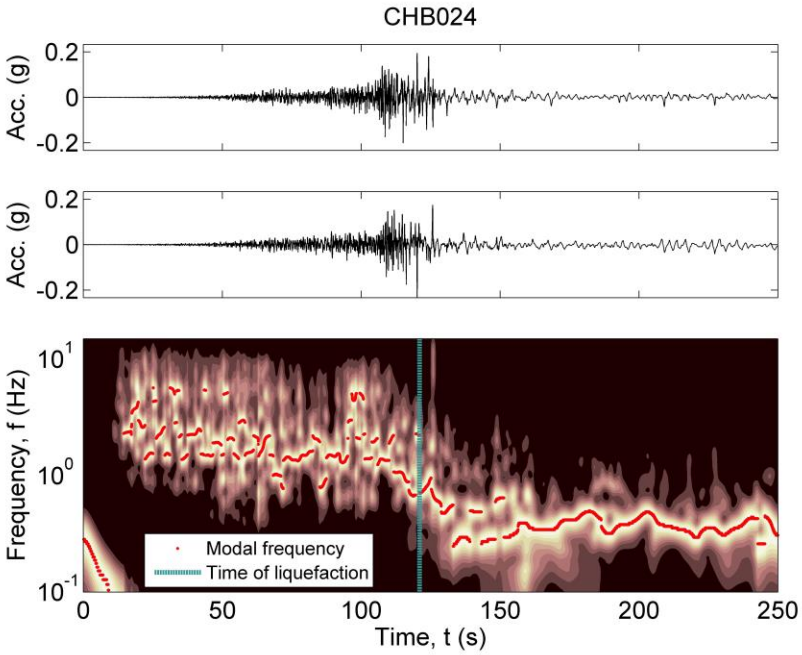

Figure B.11: Time of liquefaction at CHB024

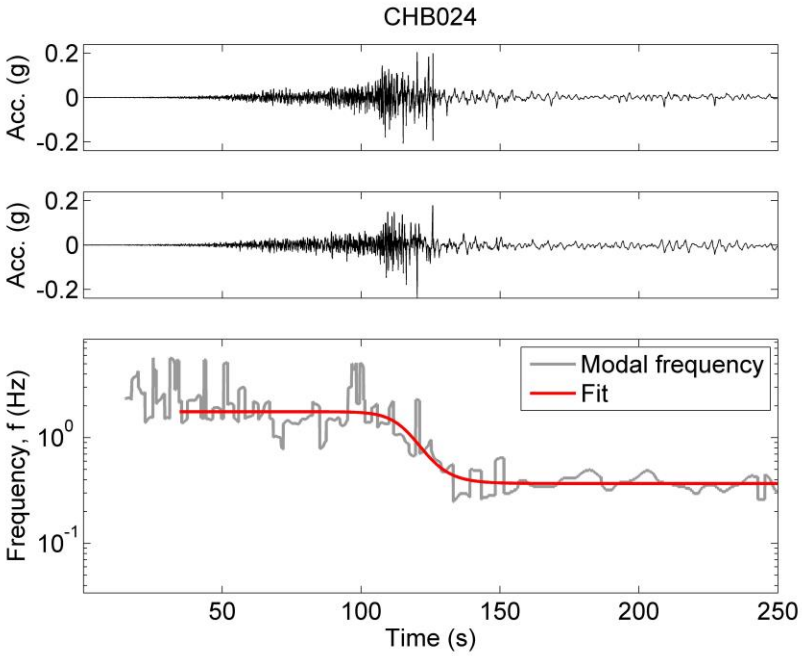

Figure B.12: Shift in modal frequency at CHB024

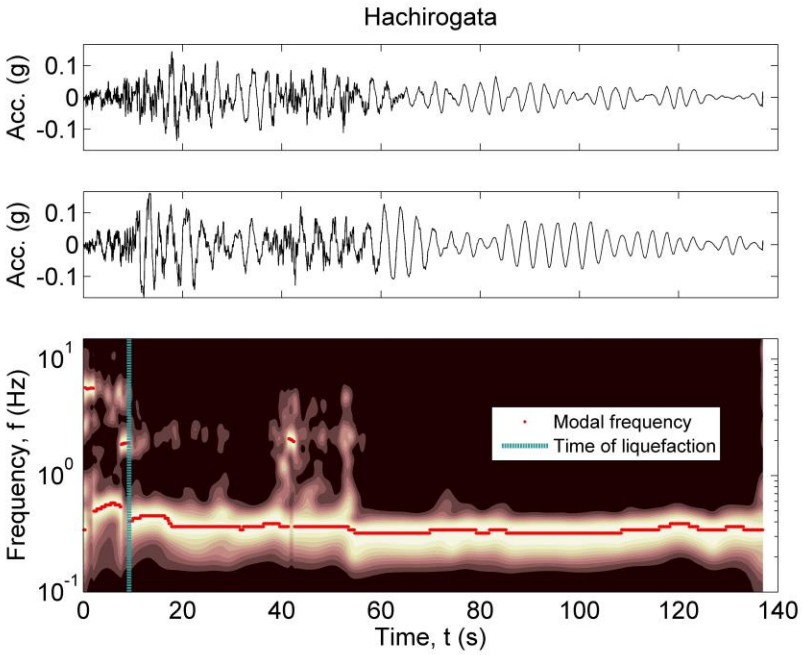

Figure B.13: Time of liquefaction at Hachirogata

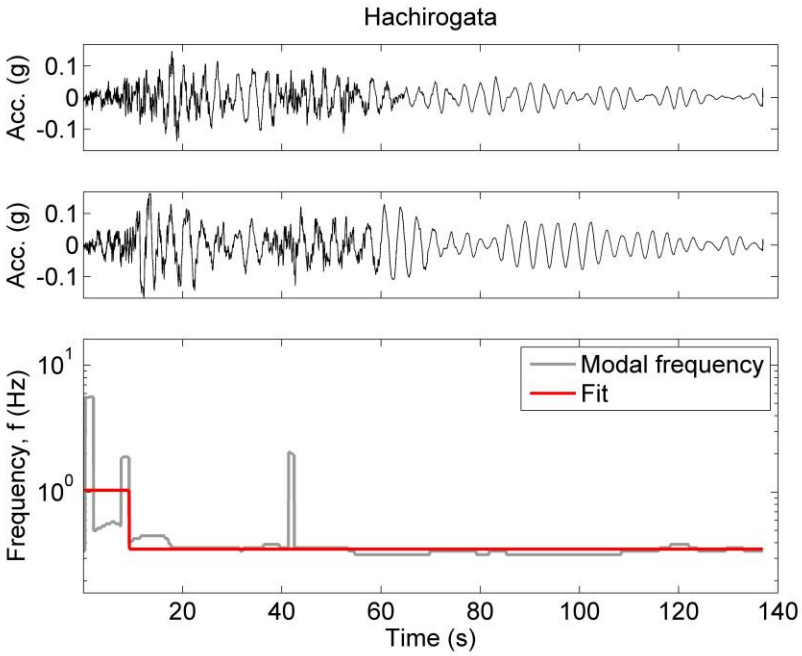

Figure B.14: Shift in modal frequency at Hachirogata

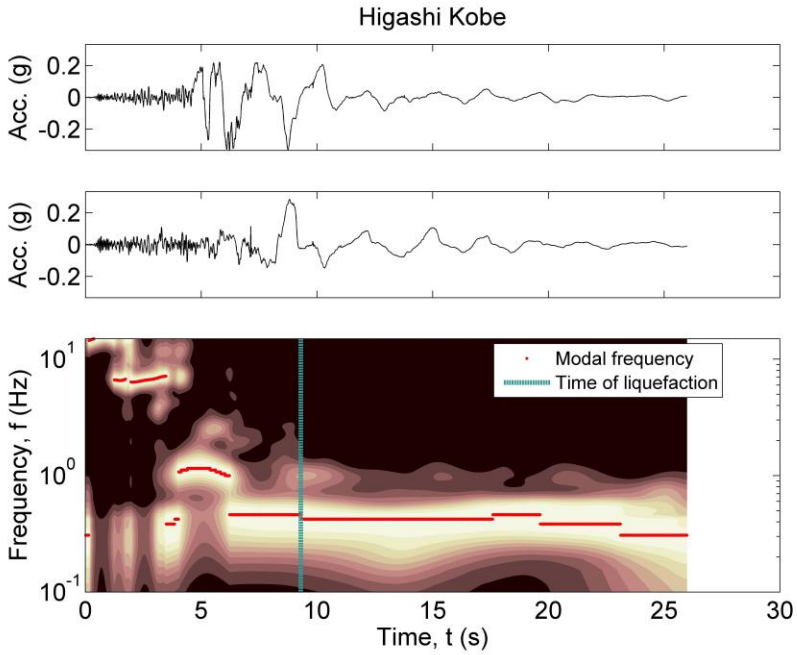

Figure B.15: Time of liquefaction at Higashi Kobe. H-Spectrum.

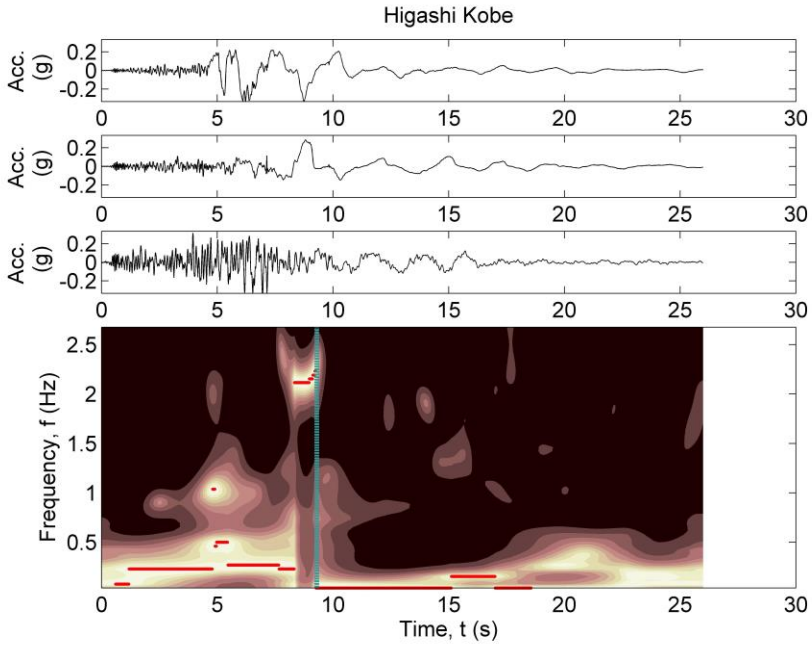

Figure B.16: Time of liquefaction at Higashi Kobe. H/V-Spectrum

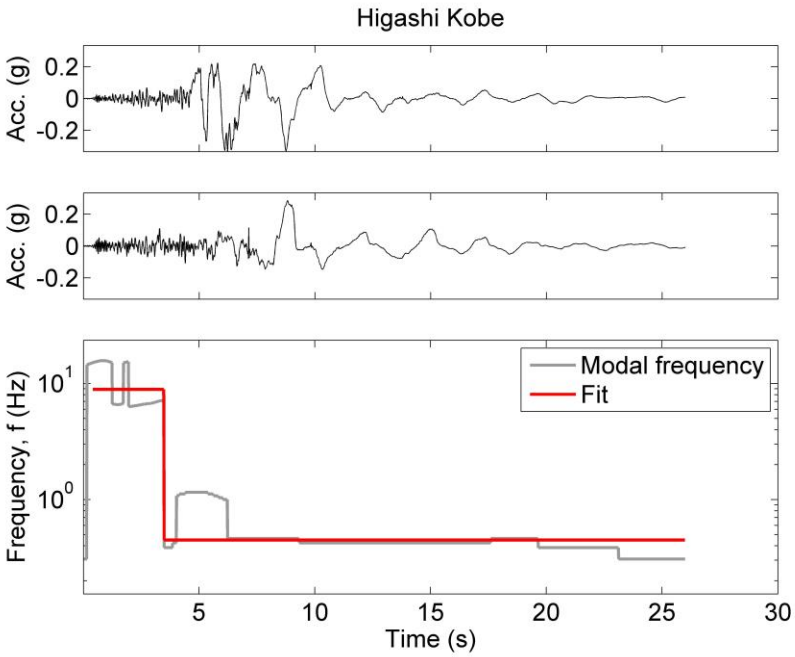

Figure B.17: Shift in modal frequency Higashi Kobe

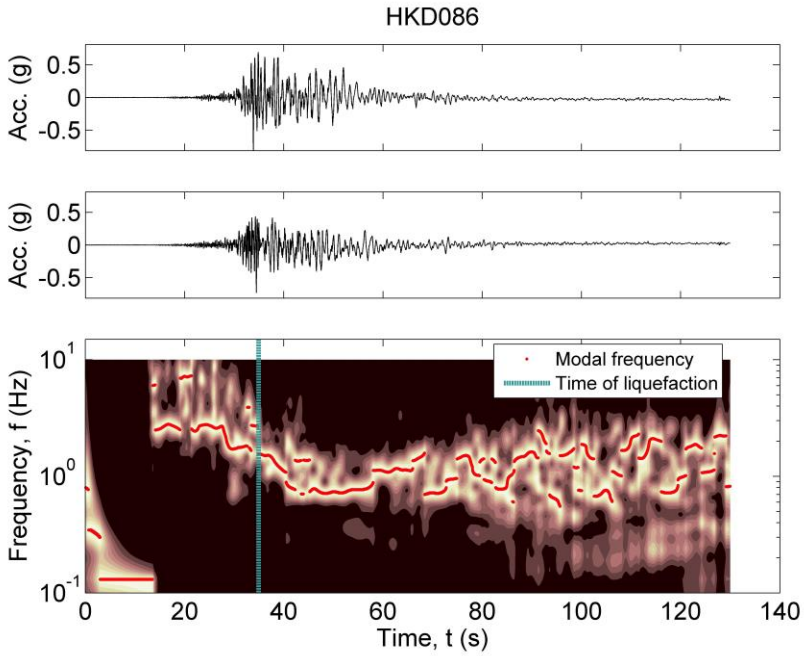

Figure B.18: Time of liquefaction at HKD086

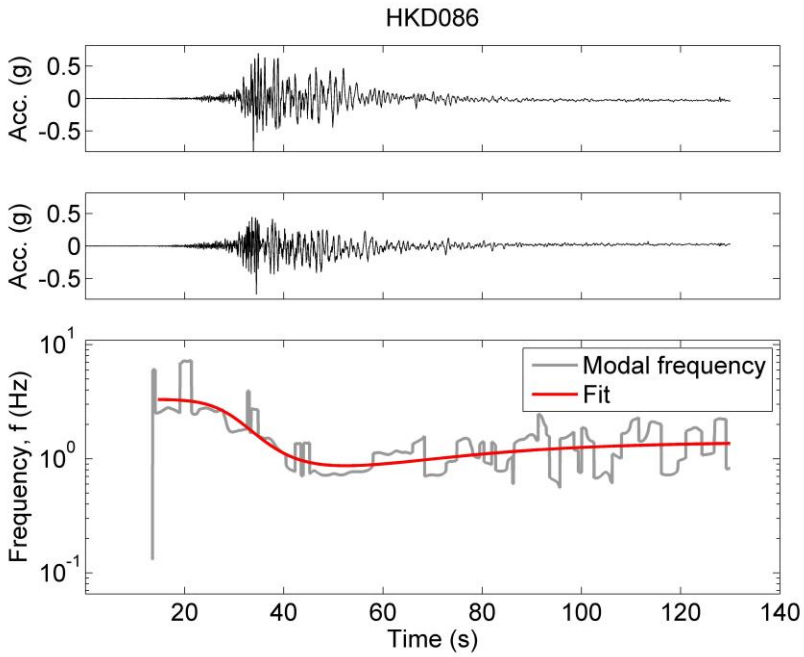

Figure B.19: Shift in modal frequency at HKD086

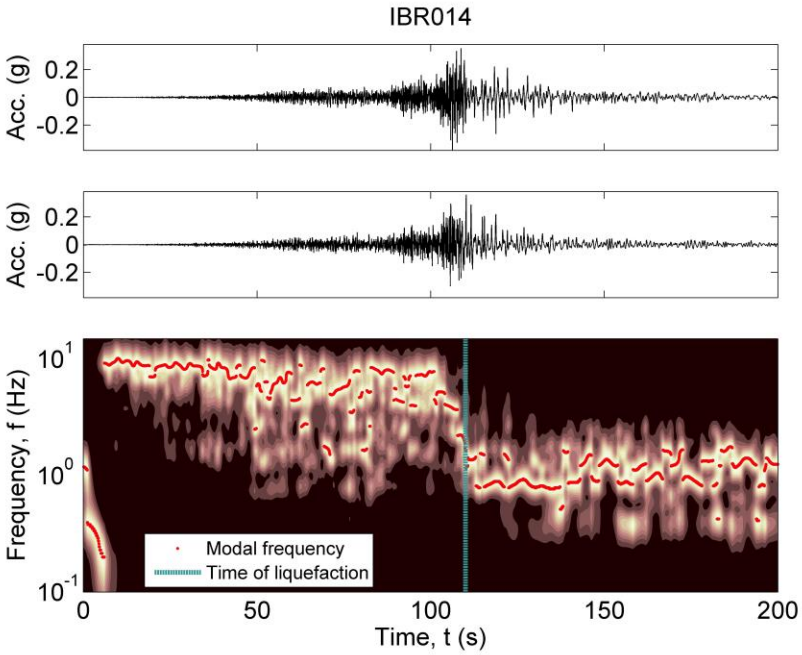

Figure B.20: Time of liquefaction IBR014

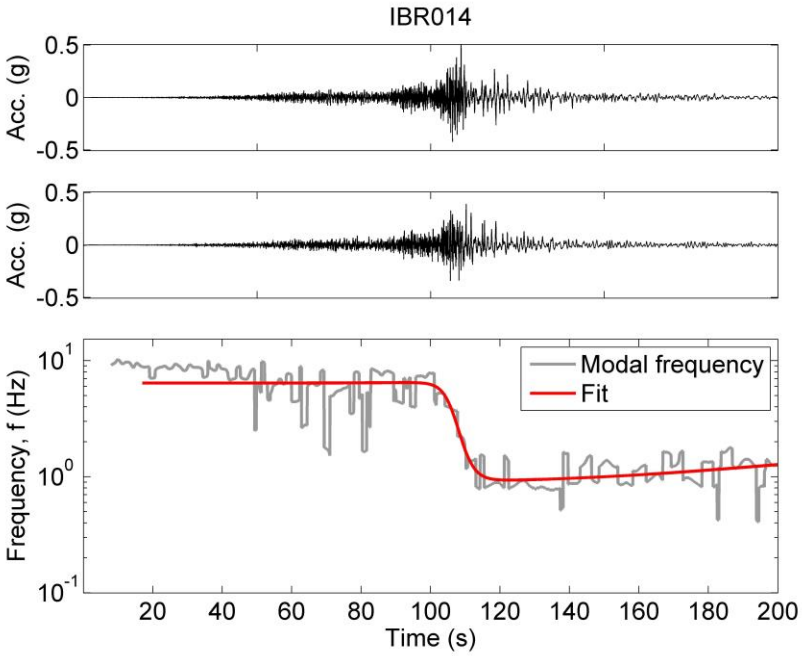

Figure B.21: Shift in modal frequency IBR014

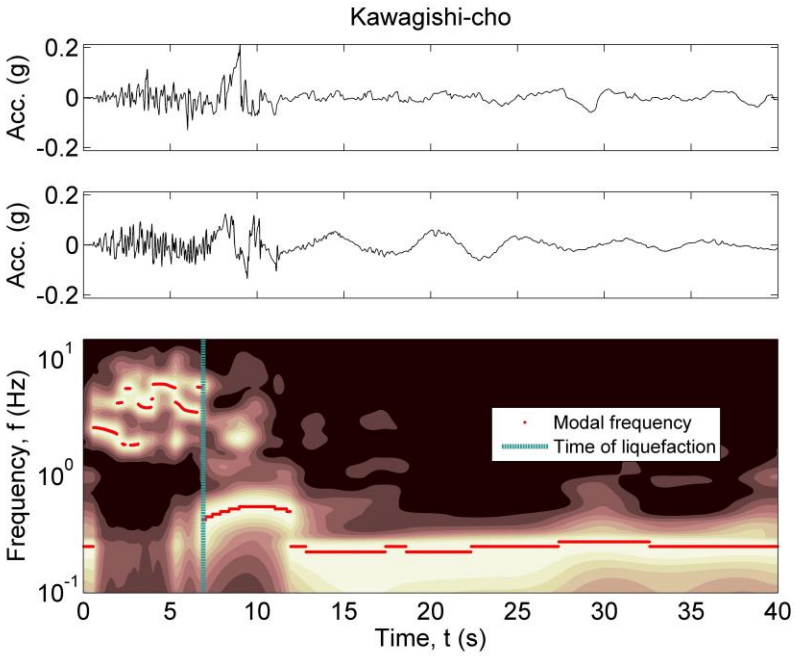

Figure B.22: Time of liquefaction at Kawagishi-cho

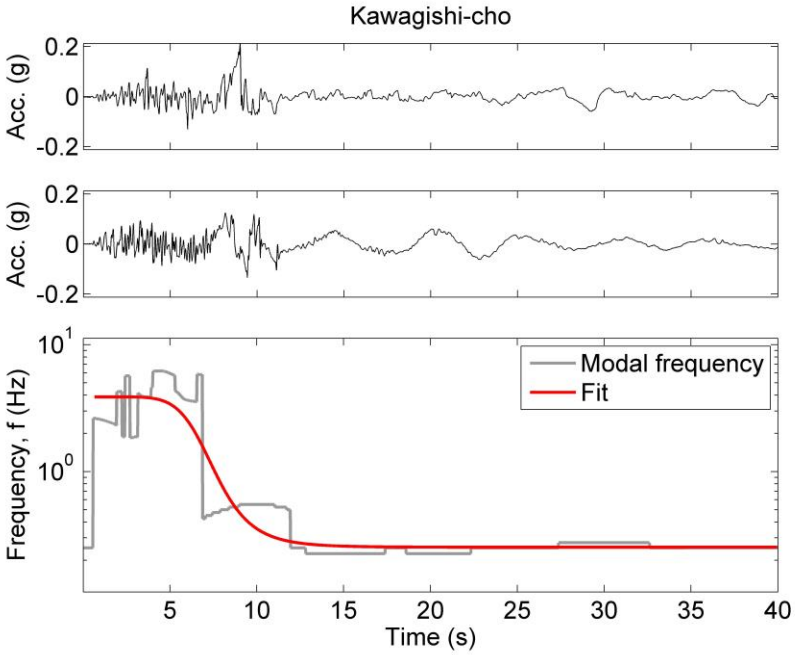

Figure B.23: Shift in modal frequency at Kawagishi-cho

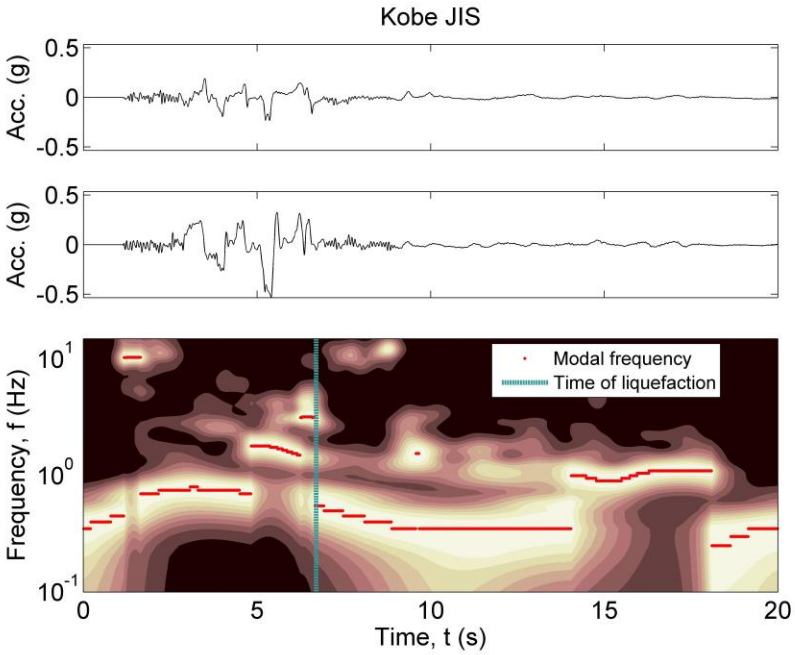

Figure B.24: Time of liquefaction at Kobe JIS

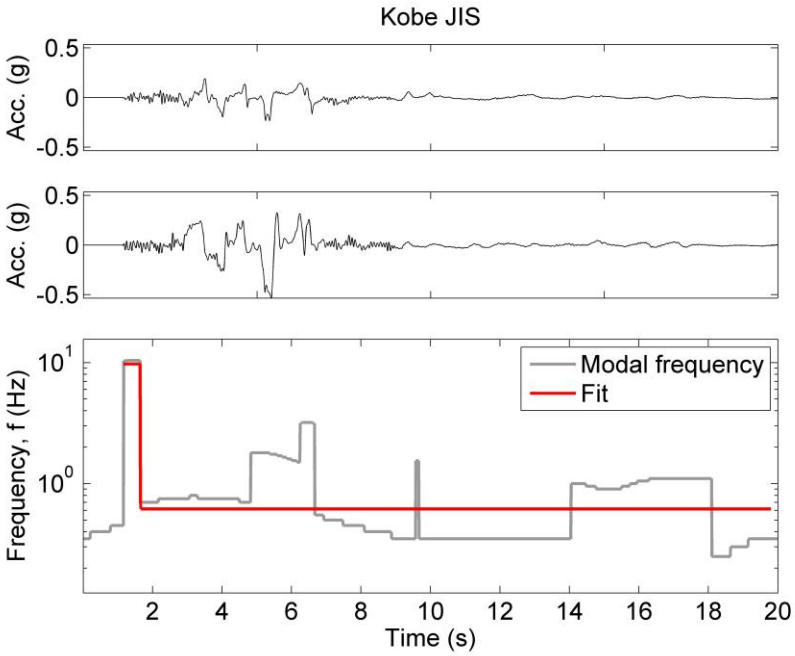

Figure B.25: Shift in modal frequency at Kobe JIS

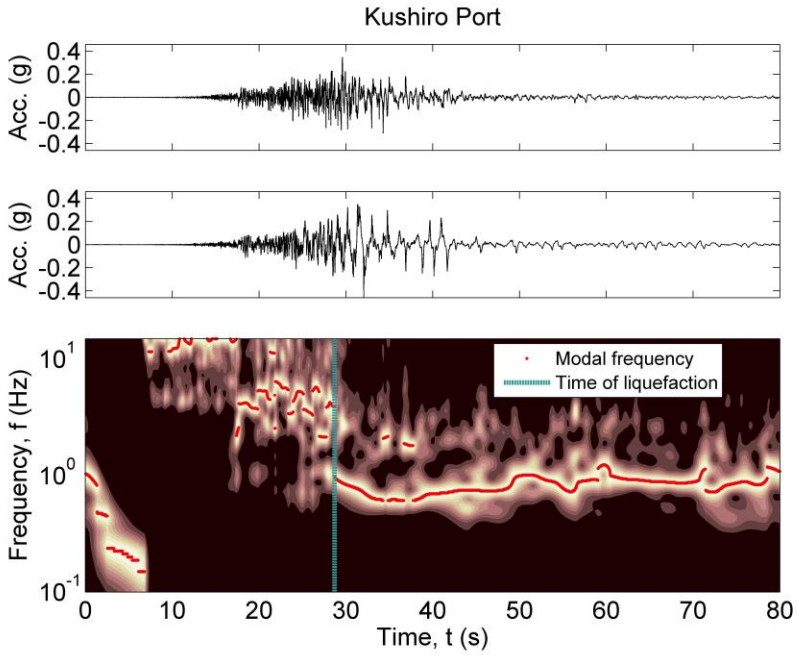

Figure B.26: Time of liquefaction at Kushiro Port

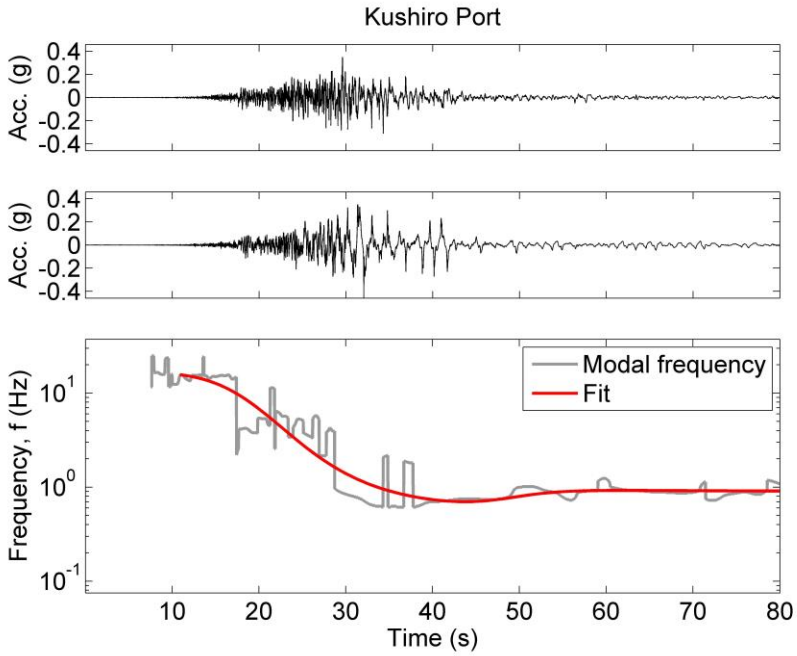

Figure B.27: Shift in modal frequency at Kushiro Port

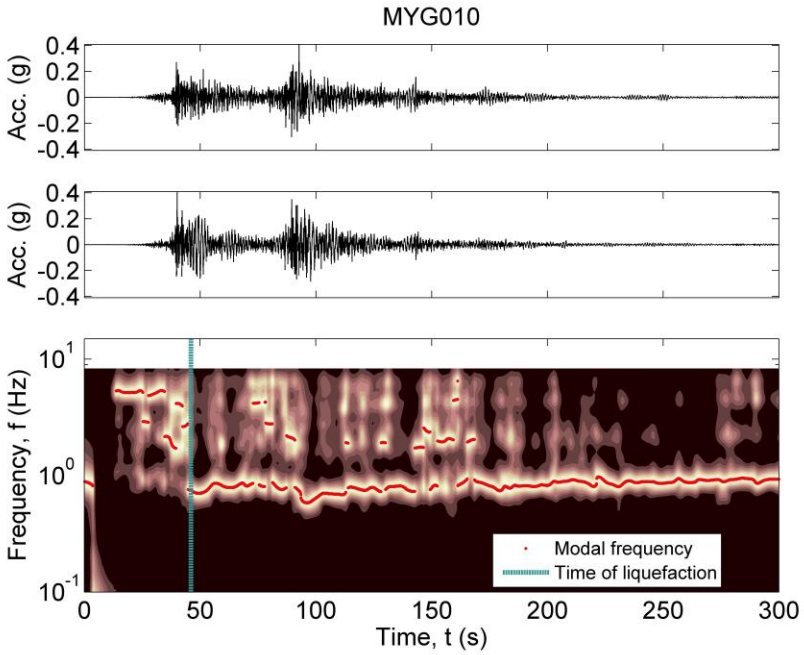

Figure B.28: Time of liquefaction at MYG010

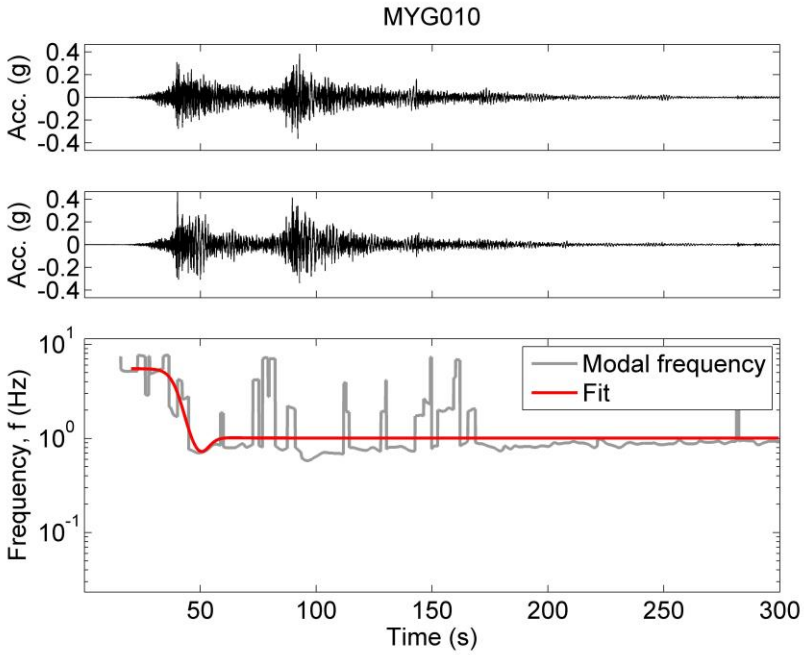

Figure B.29: Shift in modal frequency at MYG010

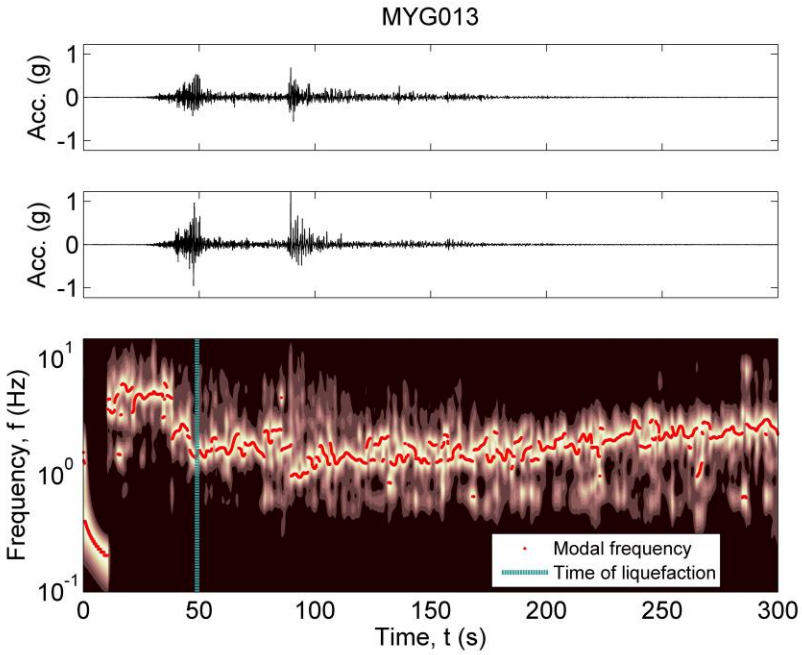

Figure B.30: Time of liquefaction at MYG013

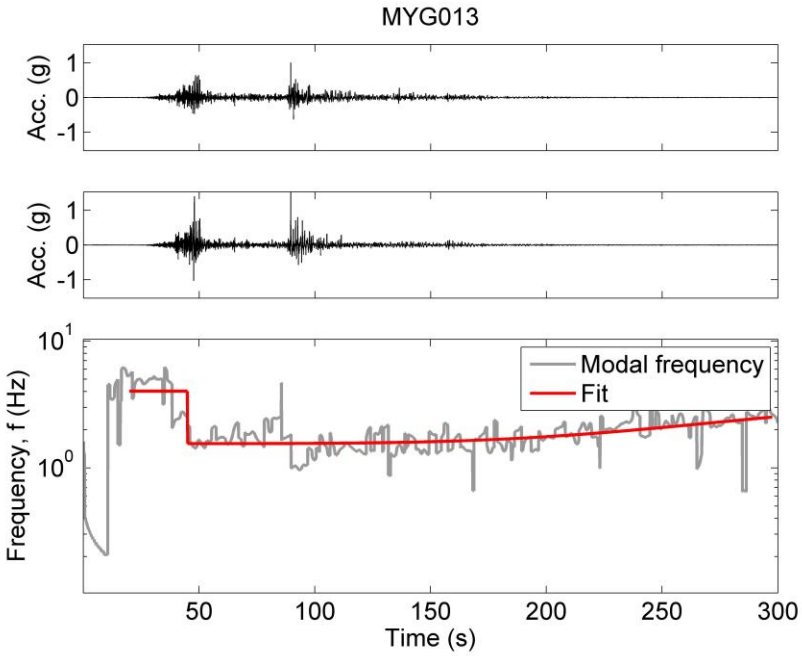

Figure B.31: Shift in modal frequency at MYG013

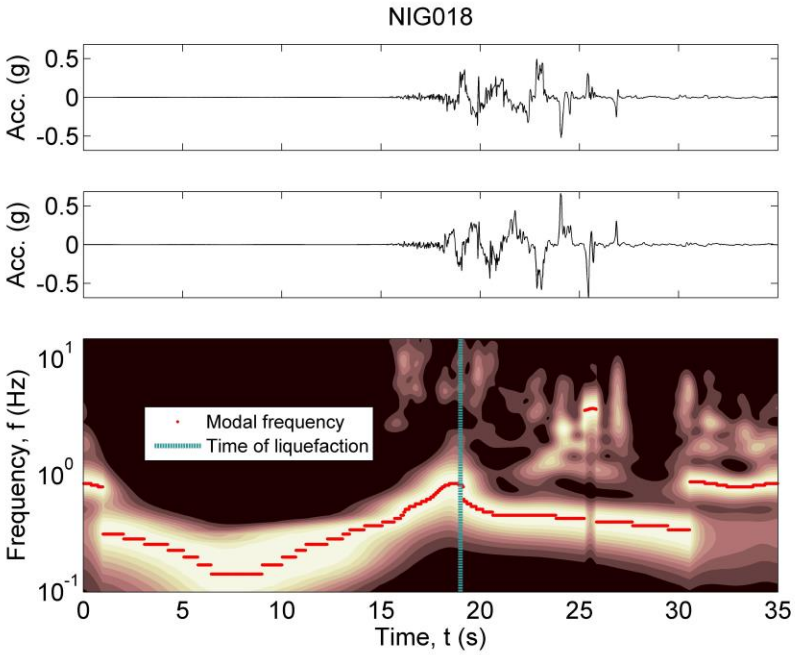

Figure B.32: Time of liquefaction at NIG018

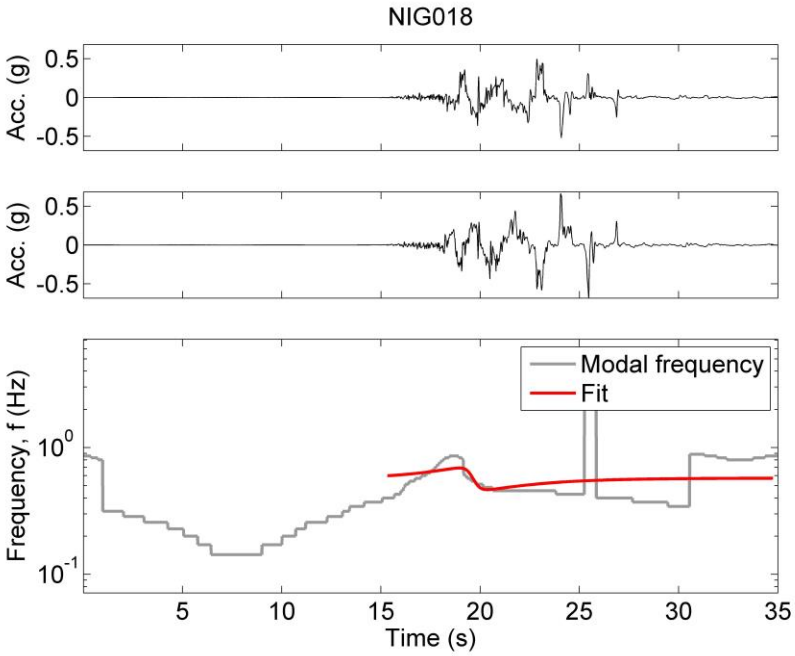

Figure B.33: Shift in modal frequency at NIG018

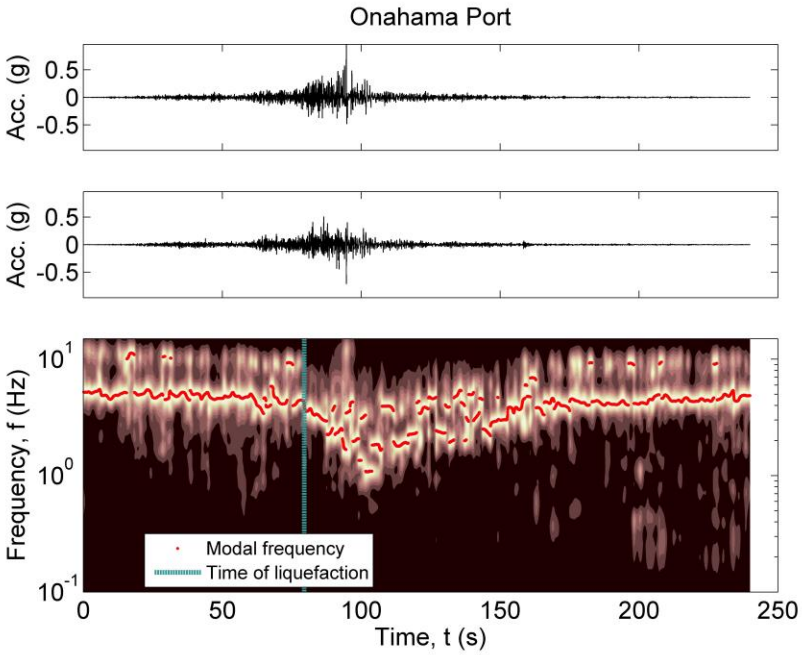

Figure B.34: Time of liquefaction at Onahama Port

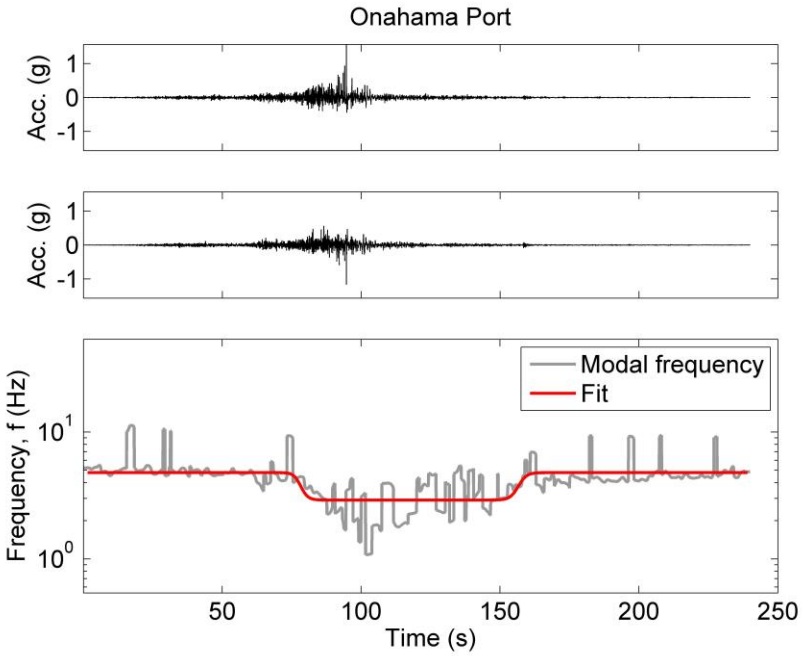

Figure B.35: Shift in modal frequency at Onahama Port

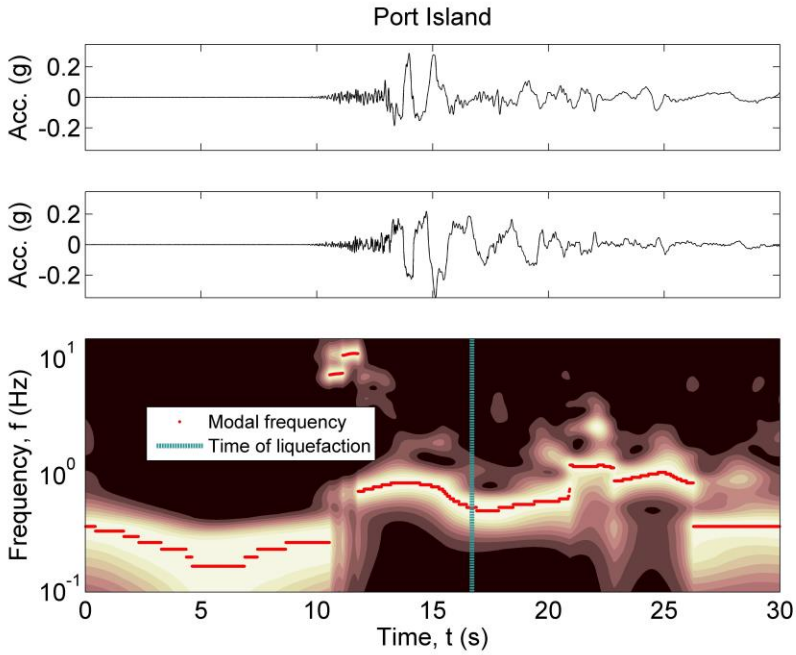

Figure B.36: Time of liquefaction at Port Island. H-spectrum

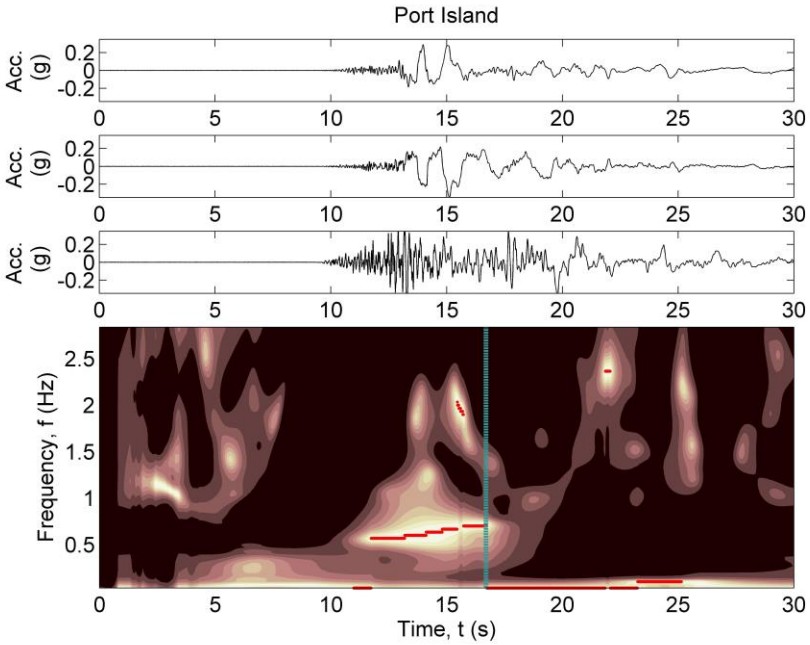

Figure B.37: Time of liquefaction at Port Island. H/V-spectrum.

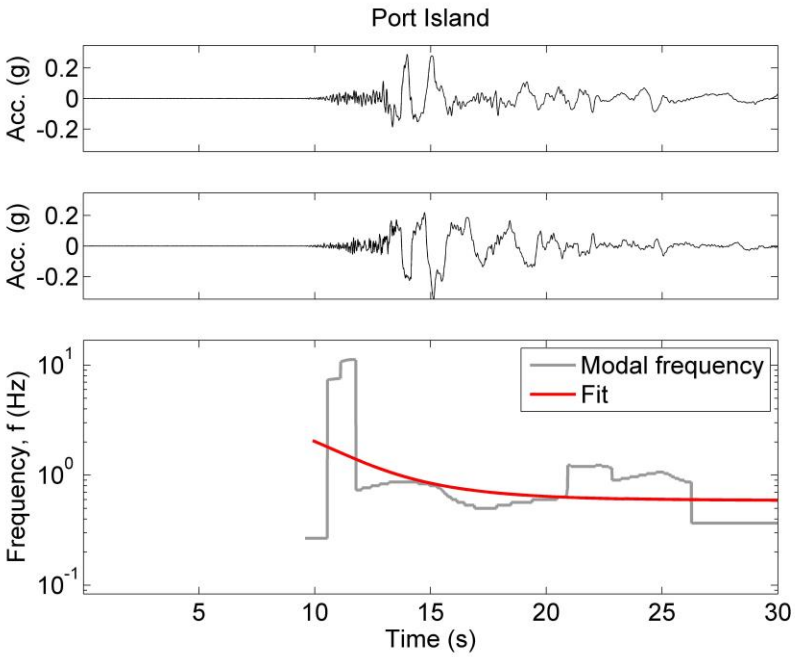

Figure B.38: Shift in modal frequency at Port Island

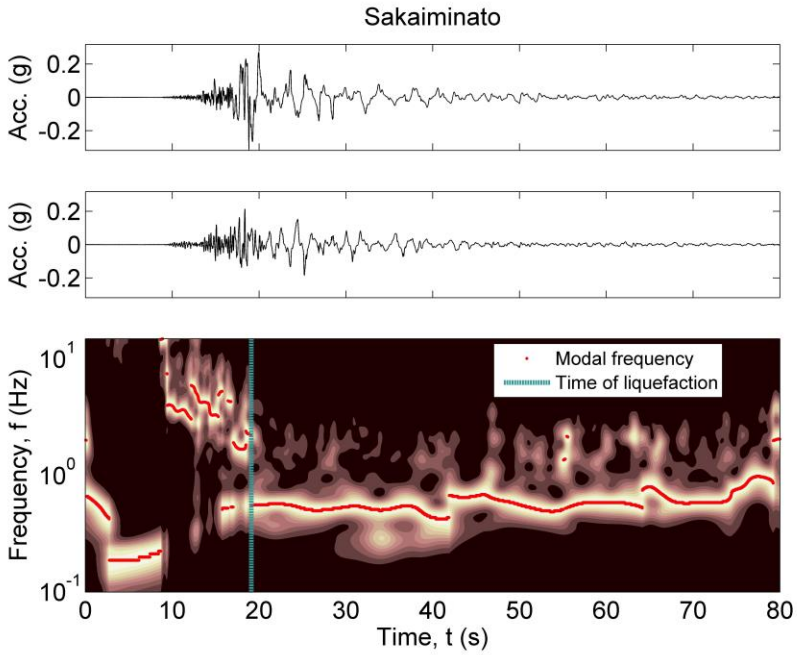

Figure B.39: Time of liquefaction at Sakaiminato

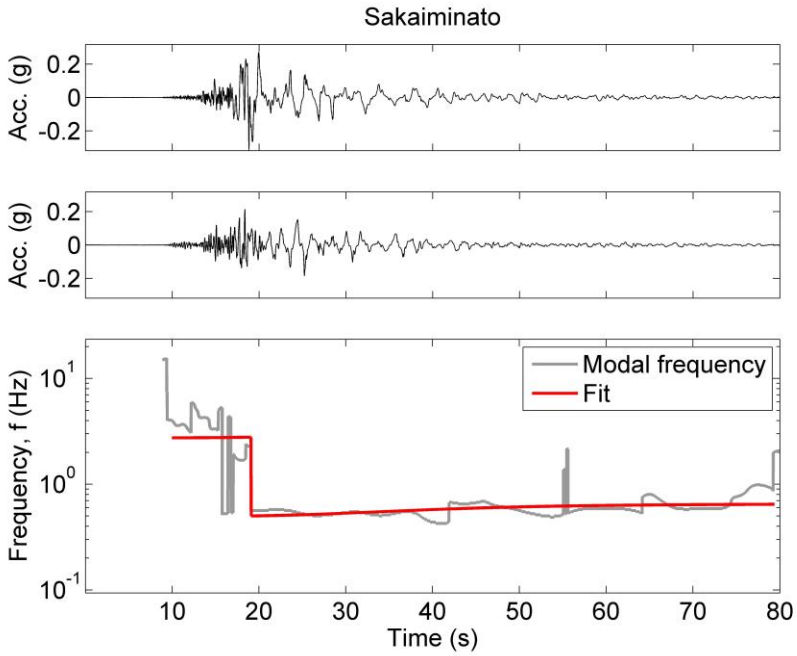

Figure B.40: Shift in modal frequency at Sakaiminato

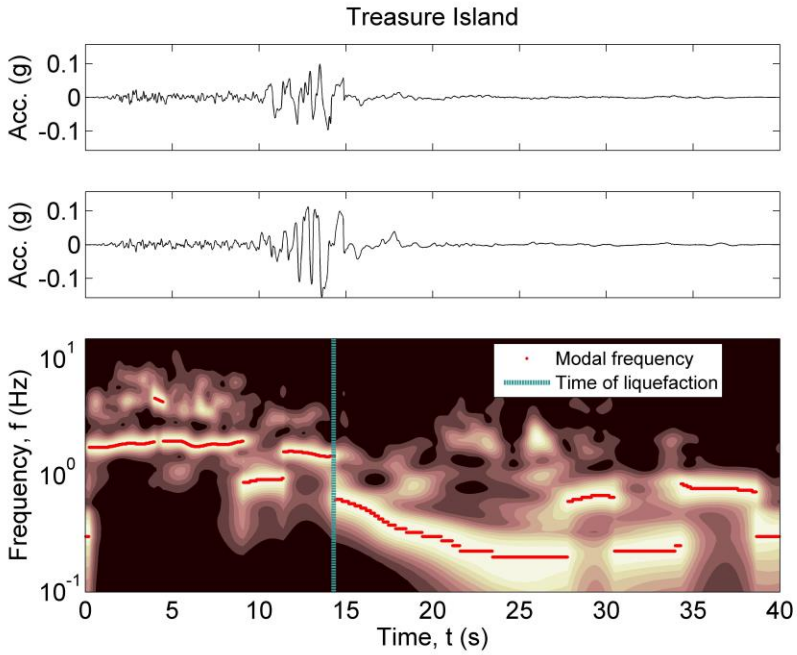

Figure B.41: Time of liquefaction at Treasure Island

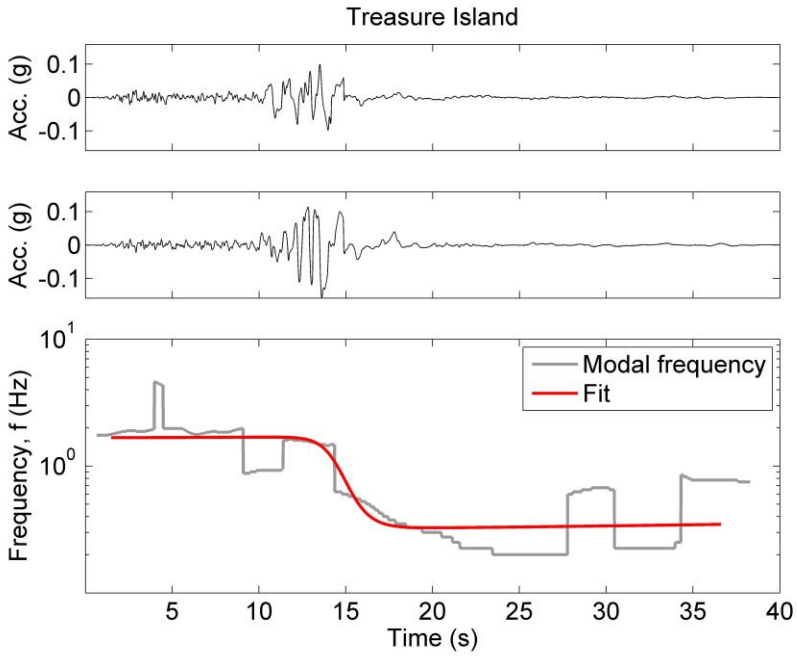

Figure B.42: Shift in modal frequency at Treasure Island

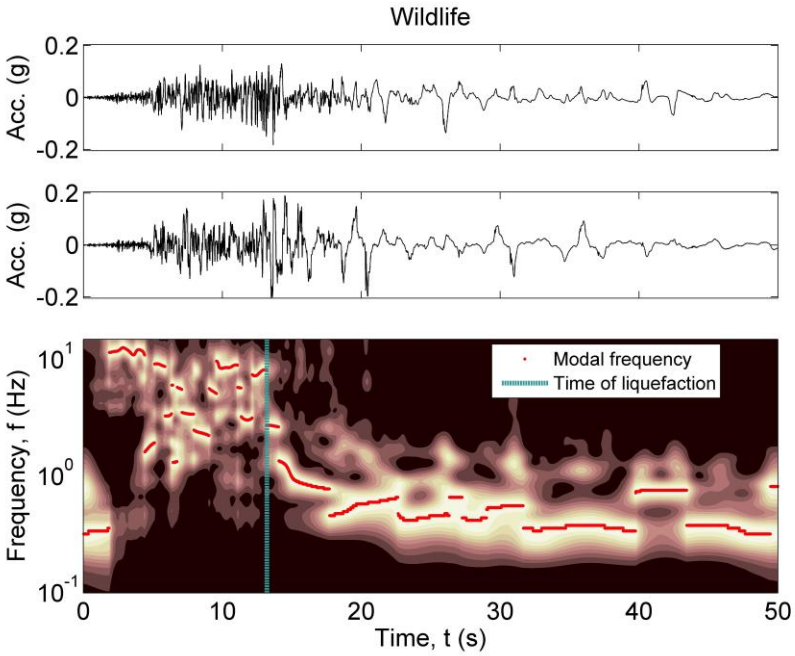

Figure B.43: Time of liquefaction at Wildlife

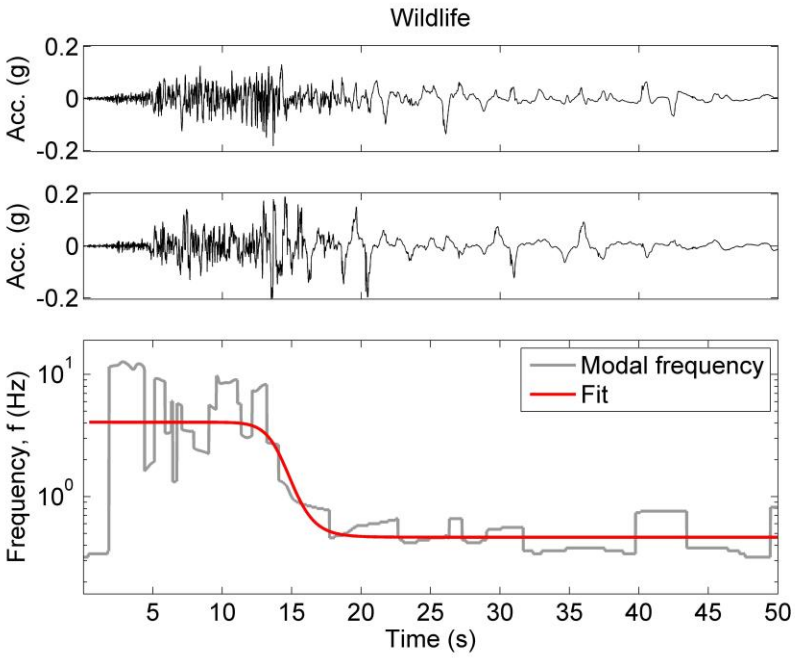

Figure B.44: Shift in modal frequency at Wildlife

VITA

Mike completed his B.S. and M.S. at Virginia Tech in 2006 and 2007. Afterwards, he worked as a geotechnical engineering consultant in Portland, Oregon, specializing in landslides, seismic hazards, and liquefaction mitigation design. In 2013, he and his wife, Sarah, left their consulting positions and biked from Fairbanks, Alaska to Baja, Mexico. Afterwards Mike began working on a PhD at the University of Washington, which he completing in 2017. Mike currently in Portland, where he works as a geotechnical and earthquake engineering consultant.